An Investigation into the Contribution of Receptive Fields in the Visual Cortex to Altered Perimetric Spatial Summation in Glaucoma

A thesis submitted to Cardiff University for the degree of Doctor of Philosophy

By

Melissa Emily Wright

School of Optometry and Vision Sciences &

School of Psychology, Cardiff University

January 2021

Supervised by Dr Tony Redmond, Professor Krish Singh, and Professor Simon Rushton

Acknowledgements

There are so many people I could thank who have helped to make this thesis possible and kept me going during these last four years! Firstly, I would like to thank all of my supervisors, Dr Tony Redmond, Prof. Krish Singh and Prof. Simon Rushton for your unwavering support and in-depth advice. I truly appreciate every time you pushed me out of my comfort zone and set an example of the kind of scientist I hope to be. I would also like to thank my advisor, Prof. Tom Margrain, for your in-depth guidance (especially with everything electrophysiology and wand-waving).

I would like to thank Fight for Sight, the Eye Research Charity, for funding this research and providing me with this opportunity. In addition, I would like to thank Cardiff University, particularly the School of Optometry and Vision Sciences, the School of Psychology, and the Cardiff University Brain Research Imaging Centre (CUBRIC). Thank you to everyone in the University who has supported and helped this project over the years; there are far too many to name. In particular, I would like to thank Dr Slawomir Kusmia for all of your support, expert MRI knowledge, and good humour. Thank you to Dr Fergal Ennis for the many hours spent sitting for piloting and methods development. Thank you also to Sue Hobbs and Cariad Sealy for all of your amazing support.

A huge thank you everyone who participated in my PhD research. None of this would be possible without you, and I can't count the amount of wonderful people I've had the pleasure of meeting. Thank you to Prof. James Morgan and everyone in the glaucoma clinics at University Hospital Wales who helped with recruitment. I would also like to thank all of the external collaborators on this work for all of their expert advice; in particular, Dr D Samuel Schwarzkopf, Dr Ed Silson, Dr Padraig Mulholland, and Victoria Stapely.

Thank you so much to all of my friends who, both face-to-face and online, kept me sane and never failed to brighten my days. In particular, big thanks go to Neema, Louise, Tom, Nikita, James, Suzie, Laura and Cassie. A huge thank you to my wonderful family, who have constantly encouraged and supported me no matter what; Mom, Dad, Amber, Lauren, Mark, Nan W, Nan H and Uncle Leigh. Thank you to Grandad.

And finally, a huge thank you to Connor, for supporting me in the highest highs and lowest lows and being all-round wonderful.

Summary

Classic literature on spatial summation suggests that the physiological basis for Ricco's area lies in retinal ganglion cell [RGC] receptive fields. However, the finding of an enlarged Ricco's area in glaucoma challenges this notion, as histological studies have found that RGC dendritic trees shrink before death in glaucoma, which should correspond to receptive field size shrinkage, rather than enlargement.

Evidence has suggested a cortical contribution to determining the size of Ricco's area, rather than a solely retinal basis. Pan & Swanson (2006) found that perimetric spatial summation could only be accounted for when considering cortical pooling by multiple spatial mechanisms. If an enlargement of cortical receptive fields is found in glaucoma, and if this is related to Ricco's area measurements, this might partly explain the basis for the increase in spatial summation in the condition. The current thesis therefore aims to investigate how receptive field sizes at the retina and cortex contribute to Ricco's area.

Pattern Electroretinography and functional MRI population receptive field [pRF] mapping were utilised to test for differences in retinal and cortical receptive field size respectively, in a sample of glaucoma patients and age-similar controls.

While there was no apparent enlargement of pRFs in glaucoma compared to controls, patients did demonstrate a significantly steeper relationship between pRF size and eccentricity in V1d. However, evidence for a cortical contribution to Ricco's area was not found in these data, despite replicating an enlargement of Ricco's area. In addition, though glaucoma patients demonstrated evidence for larger retinal receptive field sizes, this was not significantly associated with Ricco's area.

Overall, these results do not support the initial hypothesis of both retinal and cortical contributions to Ricco's area. However, future work with more specific cortical modelling is outlined for fully characterising the relationship between cortical receptive field sizes and Ricco's area.

Table of Contents

List of figures

Chapter one – Anatomy and physiology of the visual pathway

Chapter two – Glaucoma

Chapter three – Psychophysics

Chapter four – Objective Physiological Measurements

Chapter six – Establishing population receptive field sizes (pRFs) in the periphery of healthy young adults and associations with refractive error

Chapter 7. Methods Development for glaucoma investigations

Chapter 8. An investigation of receptive field size in the glaucomatous retina using pattern electrophysiology

Chapter 9. The Haemodynamic Response Function across the occipital lobe and primary visual areas in glaucoma.

Chapter 10. An exploration of receptive field properties in the glaucomatous visual cortex.

Chapter 11. Modelling the contribution of retina and cortex structure and function to Ricco's Area changes in glaucoma.

List of abbreviations

1.5/3/7T	1.5/3/7 Tesla
AFNI	Analysis of Functional NeuroImages
BET	Brain Extraction Tool
BOLD	Blood Oxygenation Level Dependant
cpd	cycles per degree
CAF	Contrast Attenuation Factor
D	Dioptre
dB	Decibels
DoG	Difference of Gaussian
EPI	Echo Planar Imaging
FEAT	FMRI Expert Analysis Tool
fMRI	functional Magnetic Resonance Imaging
FMRIB	Oxford Centre for Functional MRI of the Brain
FOV	Field of View
FSL	FMRIB Software Library
FWHM	Full-width-half-maximum
GCIPL	Ganglion Cell – Inner Plexiform Layer
GCL	Ganglion Cell Layer
HRF	Haemodynamic Response Function
IPL	Inner Plexiform Layer
MCFLIRT	Motion Correction using FMRIB's Linear Image Registration Tool
MRI	Magnetic Resonance Imaging
MTF	Modulation Transfer Function
OCT	Optical Coherence Tomography
PERG	Pattern Electroretinography
pRF	population Receptive Field
PSR	Pattern Specific Response
RGC	Retinal Ganglion Cell
RIR	Retinal Illuminance Response
RNFL	Retinal Nerve Fibre Layer

SAP	Standard Automated Perimetry
SNR	Signal-to-Noise Ratio
SPM	Statistical Parametric Mapping
TE	Echo Time
TI	Inversion Time
TR	Repetition Time
TTP	Time to Peak

Chapter 1 – Anatomy and Physiology of the visual pathway

1.1 Overview

The neural visual pathway is defined as the flow of visual information that is first detected by photosensitive rods and cones within the retina, and then passes through neural connections to the cortex and higher visual areas. A main aim of the current thesis is to investigate the contribution of receptive field size at multiple neural locations (within both the retina and cortex) to Ricco's area in a sample of glaucoma patients and controls. Before investigating the main aim of this thesis therefore, it is important to have a thorough understanding of these anatomical locations and how they function in health.

1.2 The anterior eye

The eye, specifically the anterior portion, is the first point of entry for light into the visual system (for an overview of the anterior eye structure, see Figure 1.1). At the frontmost region of the eye (i.e. the point at which light first enters) the surface bends outward and the fibres become more regularly organised to form the cornea. The spaces between the cornea and the iris, and the iris and the lens are called the anterior and posterior chambers respectively, which are filled with a watery liquid (the aqueous humour). This fluid serves a similar function to blood, but with the advantage of being transparent so that light can still pass through. It delivers oxygen and nutrients to surrounding tissue, as well as taking away metabolic waste productions. This aqueous humour is continuously produced from the ciliary epithelium and drained mainly via the trabecular meshwork. If this meshwork is suddenly blocked, it can cause a sudden increase in intra-ocular pressure and consequently closed-angle glaucoma, possibly resulting in permanent damage to the vision (the relationship between glaucoma and intraocular pressure is discussed further in Chapter 2). Light energy then passes the lens itself. Due to the optics of the lens, the trajectory of light is refracted, 'flipping' the overall image being viewed but critically maintaining the spatial organisation. Multiple factors can impact the quality of the refracted image as it transverses this anterior eye segment. For example, the lens shows accumulative opacity with age, which increases light scatter and reduces visual acuity even at non-cataract levels (Michael & Bron, 2011). Once it has passed the lens, light

energy transverses through the gelatinous vitreous humour before it reaches the retina and is finally translated into neural activity, entering the neural visual network.

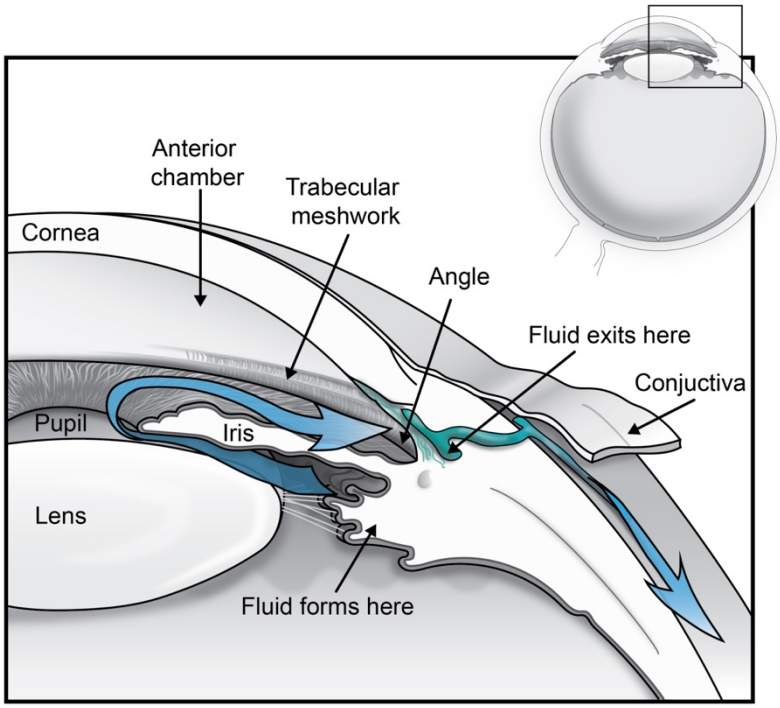

Figure 1.1 – Overview of anterior eye – reproduced from https://samstrongvision.com/illustrations/

1.3 Retina

The retina is the neural tissue lining the posterior of the eye that represents the first point at which light energy is translated into electrical neural activity. It is also the only point of the central nervous system (CNS) that can be directly visually examined without invasive techniques, so has the potential of providing easily accessible information about the CNS.

1.3.1 Retinal layers

The human retina can be subdivided into 10 distinct layers, namely: the retinal pigmented epithelium, the photoreceptor layer, the outer limiting membrane, the outer nuclear layer, the outer plexiform layer, the inner nuclear layer, the inner plexiform layer, the ganglion cell layer, the retinal nerve fibre layer, and the inner limiting membrane (as illustrated in Figure 1.2). The most outer layer, and the point at which light energy is first absorbed, is termed the photoreceptor layer. This layer contains the photosensitive segments of photoreceptors, the cell bodies of which are located in the outer nuclear layer. The photosensitive cells within this layer can be classified within two types; i) rods, which are highly sensitive and facilitate vision, and ii) cones, which are not as sensitive as rods but allow much higher acuity and facilitate vision during photopic (i.e. brightly lit) conditions. Cones are essential for colour vision and can be further categorised into short (S), medium (M), and long (L) wavelength variations, referring to the wavelength of light to which they are maximally sensitive. The distribution of these photoreceptors varies throughout the retina. The central fovea is entirely cone cells, and is where the majority of cone cells are located (Curcio *et al.*, 1991; Osterberg, 1935). Inner retinal layers are displaced radially, at the fovea, creating a foveal pit. This allows rays of light to reach the photoreceptor layer without being scattered and refracted by the inner retinal layers, in turn enabling finer resolution and maximum sensitivity. Moving further into the periphery, rod density exceeds that of cones (Osterberg, 1935). The axonal output of these photosensitive cells synapse with the dendritic trees of bipolar and horizontal cells in the outer plexiform layer, the cell bodies of which reside in the inner nuclear layer. Horizontal cells are interconnecting neurones that aid in lateral inhibition within the retina (Thoreson & Mangel, 2012). Bipolar cells on the other hand, can be either OFF (inhibitory) or ON (excitatory) and transfer information from the photoreceptors to the retinal ganglion cells (RGCs), which are the output cells of the retina. Bipolar cells synapse to these RGCs within the inner plexiform

layer. RGCs also receive input from the inner nuclear layer via the neuromodulatory amacrine cells, which have no clear axon but instead interact via their dendritic field. RGCs are of particular importance in glaucoma, as RGC degeneration is a primary characteristic of the disease.

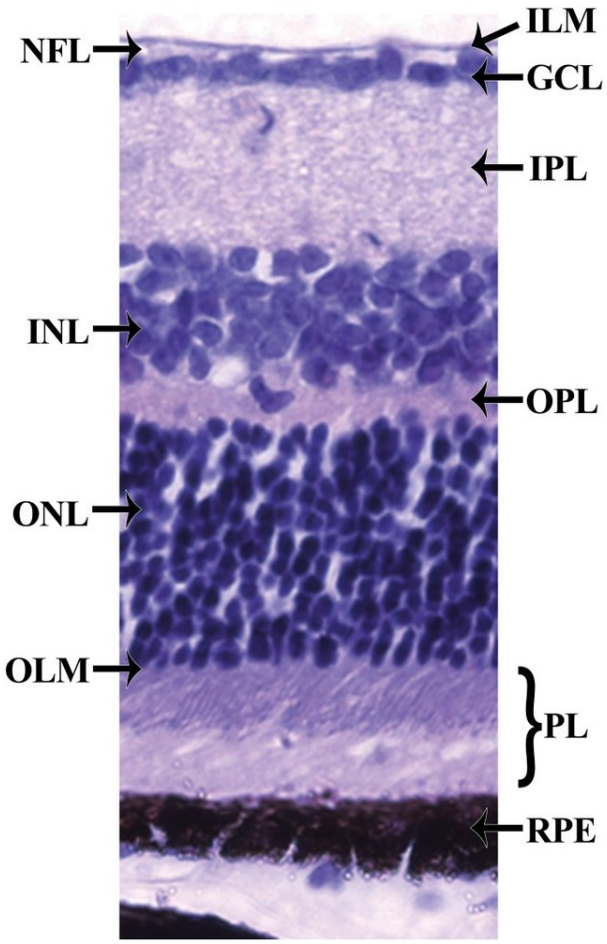

Figure 1.2 – Histology of the retina, with the 10 retinal layers labelled. ILM= Inner limiting membrane; NFL= Nerve fibre layer; GCL= Ganglion cell layer; IPL= Inner plexiform layer; INL= Inner nuclear layer; OPL= Outer plexiform layer; ONL= outer nuclear layer; OLM= Outer limiting membrane; PL= Photoreceptor layer; RPE= Retinal pigmented epithelium. Reproduced from Willermain et al., *(2014)*

The neurones that underlie the neural activity in the retina, and indeed the CNS as a whole, can be simplified into three major components (as illustrated in Figure 1.3; however, the exact structure of a neurone can vary widely depending on the exact subclass of cell):

1. The dendritic tree – these are multiple projections (i.e. dendrites) from the main cell body that receive input from other cells and can therefore sum information from a varying number of input cells, depending on size. The dendritic field is the total area covered by the overall structure of the dendritic tree. An illustration of these components can be seen in Figure 1.4. The larger the area of this dendritic field, the more cells can input to / synapse with it and thus the more information can be summed by the cell. Action potentials initiated in these projections are termed dendritic spikes, and typically travel towards the cell body.
2. The cell body or soma – the central component that contains the nucleus and the major processes that maintain the cell. If the cell is stimulated by incoming activation to a critical level (i.e. as to reach its threshold potential), an action potential is initiated which travels the length of the axon.
3. The axon – this carries the output of the cell from the cell body to its target, such as the dendrites on other cells (however, some neurones have no axon and instead interact via interconnections in the dendritic field). In many parts of the CNS, this portion of the neurone is insulated in a fatty myelin sheath, which block the movement of sodium ions that form the basis of action potentials, with occasional sections of unsheathed neurone termed the Nodes of Ranvier. This myelination speeds up transmission of action potentials as the neural activity is by saltatory propagation, rather than continuous propagation.

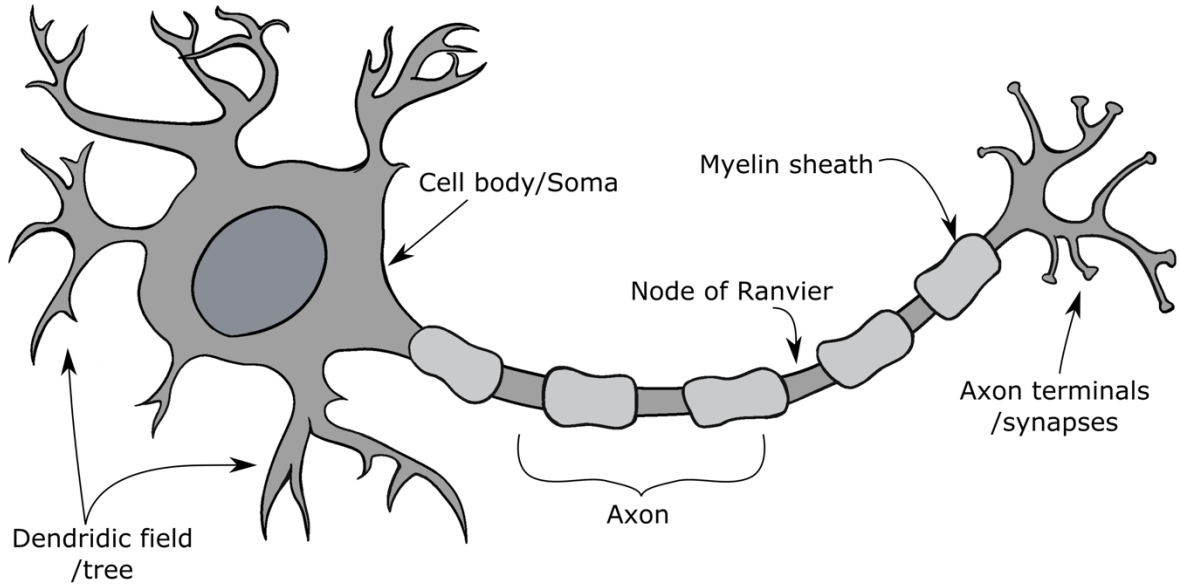

Figure 1.3 – Illustration of a neurone and its main components

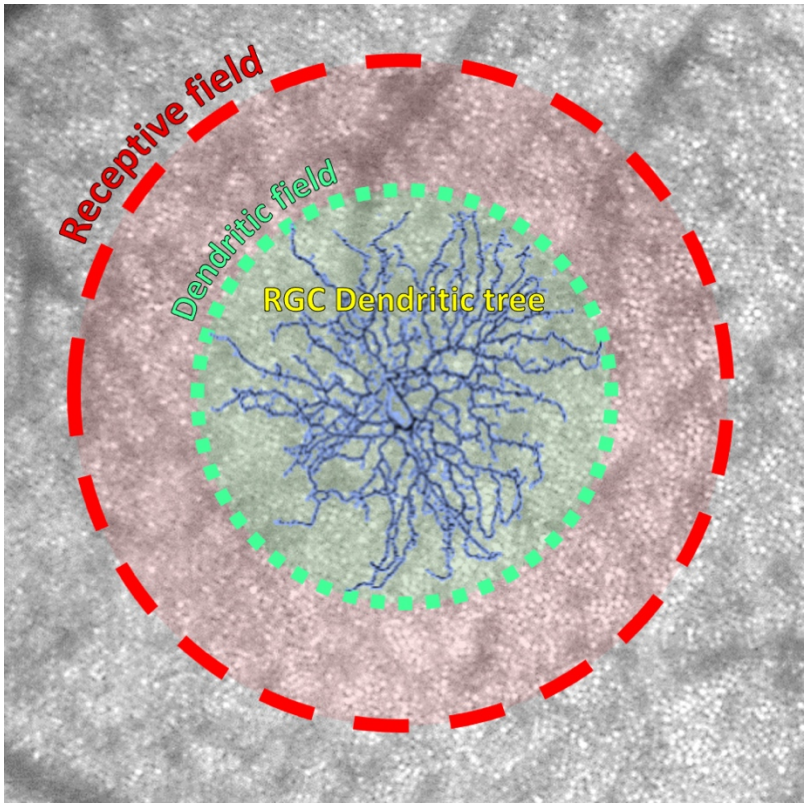

Figure 1.4 – A schematic of a retinal ganglion cell (RGC; highlighted in blue) superimposed on a cone mosaic. The RGC dendritic tree structure (comprising of individual dendrites) in labelled in yellow. The dendritic field is the area of the retina covered by the dendritic tree structure. The receptive field is indicated in red and refers to the retina area in which an action potential within the neurone can be elicited.

1.3.2 Retinal ganglion cells

RGCs are responsible for the transmission of signals from the retina to the lateral geniculate nucleus (LGN) in the midbrain. The dendritic trees of RGCs are located within the Inner Plexiform Layer (IPL). The cell bodies of RGCs are located in the Ganglion Cell Layer (GCL), while their axons travel towards the optic disc within the retinal nerve fibre layer (RNFL). These fibres come together to form the optic nerve and exit the eye towards the brain via the optic disc. Due to these fibres passing from the inner to the outer of the retina at this location, there are no photoreceptors at the optic disc, therefore forming a 'blind spot' within the visual field. RGCs axons move across the retina from the cell body to the optic disc in a distinct fashion, depending on where in the retina the RGC cell body is located. For example, for those located around the fovea or nasal retina, the associated axons travel roughly straight towards the optic disc. For those in the temporal retina however, axons demonstrate an arcuate pattern around the fovea, avoiding the obstruction of light travelling towards the foveal pit.

There are several classes and subclasses of RGCs. Classification of these RGCs, and indeed any retinal cell, can be complicated due to the large number of cell types, technical limitations, size variation with eccentricity, normal morphological variation within types, and the low probability of sampling rarer cell types (Gregg *et al.*, 2013). Cell classification tends to be based on factors such as morphology, electrophysiology, their patterns of connections, and their biochemistry. Another factor of particular importance to RGCs is the depth within the IPL at which their connections are found, which allows the specific RGC type to synapse to particular bipolar and amacrine cell processes (Gregg *et al.*, 2013). Animal work has suggested that the number of RGC types in the human retina is around 20, but this can differ depending on the criteria used (Masland, 2012a, 2012b). Three of the most commonly discussed RGCs will be briefly described here; midget RGCs, parasol RGCs, and small bistratified RGCs.

Midget cells represent the most populous form of RGCs, forming 70% of the RGC population in the central retina and 50% in the peripheral retina (Marshak, 2009). They are smaller than parasol cells, both in terms of dendritic tree and cell body, and in foveal and parafoveal vision can have a one-to-one relationship with a cone (Kolb & Dekorver, 1991; Kolb & Marshak, 2003). It follows therefore, that some midget cells will be colour-coded, as

they are primarily driven by a single cone sensitive to a particular wavelength range. These midget RGCs project onto the parvocellular layers of the Lateral Geniculate Nucleus (LGN). As opposed to this, parasol RGCs project mainly to the magnocellular layers of the LGN. These parasol cells sample uniformly from L- and M-cones (but not S-cones), indicating that they are not colour coded, and instead are more sensitive to luminance (Field *et al.*, 2010). They appear to have a greater absolute sensitivity to light than midget cells, potentially due to their greater input from rod cells and their larger dendritic field (which therefore sums information across a larger area; Marshak, 2009). Parasol RGCs comprise about 5% of all foveal RGCs, and approximately 15% in the peripheral retina (Marshak, 2009). Finally, while much smaller in number than either midget or parasol RGCs, the third most common form of RGC are small bistratified cells. They represent about 1-10% of the total RGC population, depending on eccentricity (Bock *et al.*, 2007; Marshak, 2009). Small bistratified cells receive input from short-wavelength (S-) cones and thus make an important contribution to blue-yellow vision (Dacey & Lee, 1994; Marshak, 2009). The dendritic fields of these RGCs are typically larger than those of midget cells and are more similar in size to those of parasol cells (Dacey & Lee, 1994), which may explain the reduced resolution acuity in this pathway compared to that in the achromatic pathway (Beirne *et al.*, 2005). While there are several morphological properties with which it is possible to distinguish these cell types, they also show varied functional receptive field properties. Consideration of the receptive field is vital when discussing the function and contribution of a cell to the wider visual network.

1.3.3. Receptive fields

How visual information is transferred and summated within the retina is dependent on receptive field size and characteristics. Within this context, the receptive field of a neurone can be defined as the area of visual field space that, if probed by a stimulus, would alter the firing rate from that neurone. These receptive fields differ in shape, size, and configuration throughout the visual system. It is important to note that this does not exclusively refer to excitatory responses; receptive fields can be inhibitory (in which a stimulus entering the receptive field will elicit an inhibitory response in the cell) or can have a configuration that involves both excitatory and inhibitory processes. These processes can also be split into spatially distinct components of the receptive field. For example, receptive fields of RGCs have a concentric centre-surround structure, which may include an ON-centre

and an OFF-surround, or the reverse (similar to bipolar cells, which synapse into RGCs). This centre-surround organisation leads to spatial antagonism in RGCs (or lateral inhibition). For this configuration of receptive field, a stimulus falling into the ON-centre would lead to an excitatory response/ action potential within the neurone (increased firing), while stimulating the OFF-surround would lead to an inhibitory response (decreased firing). A consequence of these centre-surround antagonistic receptive fields is that the visual system responds very strongly to luminance boundaries (or changes in local luminance) and RGCs also demonstrate spatial tuning characteristics in their responsiveness to differently sized stimuli. Spatial tuning is the phenomenon in which a RGC will respond with the greatest firing rate to stimulus of a certain size but will respond less strongly to larger or smaller stimuli. When plotting firing rate as a function of stimulus size therefore, a spatial tuning curve is seen, with the stimulus size that elicits the strongest response reflecting the size of the ON-centre (with response attenuation to smaller and larger stimuli). These spatial tuning characteristics have been investigated many times using stimuli with local luminance changes across space, such as luminance gratings (in which the stimulus cycles between high and low luminance bars of a certain spatial frequency; e.g. Enroth-Cugell & Robson, 1966; Kuffler, 1953; Thompson & Drasdo, 1987; White *et al.*, 2002). In such experiments, electrophysiological responses in retina are recorded (either on a single neurone level, such as with single-cell recordings, or at a global retinal level, such as with pattern electroretinography; PERG) while being presented with a high contrast grating. How the cell responds can inform experimenters of certain features of the receptive field, such as its size and configuration. For example, when the high luminance portion of a presented grating exactly covers the ON-centre of a receptive field with the low luminance falling on the OFF-surround, the cell will be at its most responsive (i.e. increased firing rate). If the phase is reversed however, so the low-luminance portion falls on the centre and the high-luminance on the surround, then the axonal firing of the cell will be actively supressed. Similarly, when the spatial frequency of such stimuli is increased or decreased, so that more of the OFF-surround or less of the ON-centre is being stimulated by the high-luminance portion of the stimulus respectively, firing rate will also decrease compared to the preferred spatial frequency that reflects ON-centre size. The concept of retinal spatial tuning curves and the measurement of these curves with PERG is discussed further in Chapter 4, as well as during PERG methods development in Chapter 7.

1.4. Lateral geniculate nucleus

RGC axons exit the eye in a bundled structure called the optic nerve (cranial nerve II), which projects towards the dorsal Lateral Geniculate Nucleus (LGN). An overview of the pathway between the retina and cortex can be seen in Figure 2.5. Along this projection, axons stemming from RGCs on the nasal side of the retina cross over, forming the optic chiasm. This has the consequence that, starting at the LGN, the right side of the visual field is processed by the left hemisphere, and vice versa (the topographic organisation of the retina is also maintained).

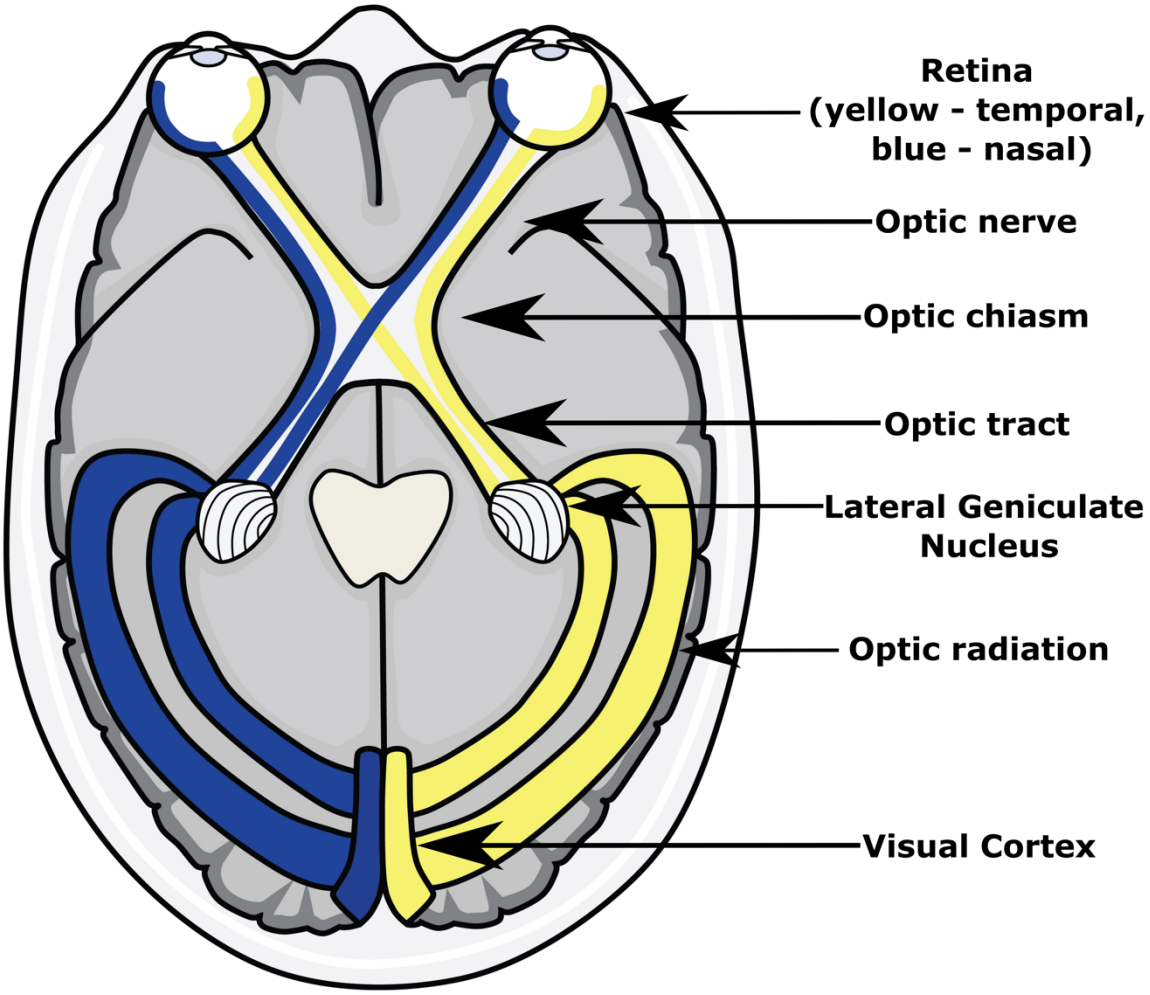

Figure 1.5 – Overview of the visual pathway from retina to cortex – reproduced from https://samstrongvision.com/illustrations/.

The LGN has a laminar structure, which is formed of six main layers. Layers 2, 3 and 5 receive input from the ipsilateral eye, while the remaining layers receive input from the contralateral eye. These layers can be further divided into the cells which constitute them, namely whether they are mainly comprised of Parvocellular (P-) cells (outer four layers; layers 3-6), Magnocellular (M-) cells (inner two layers; layers 1 and 2), or Koniocellular (K-) cells (six additional thin layers that sit below each main layer). M-, P- and K-cells comprise the major classes of thalmocortical cells within the LGN, and can be further distinguished by their spatiotemporal characteristics, many of which are inherited by the particular class of RGC that synapse with them. P-cells receive their input from midget RGCs, while M-cells receive input from parasol RGCs (Leventhal *et al.*, 1981). The retinal input to K-cells however, seems to mostly come from small bistratified RGCs (Dacey & Lee, 1994; Szmajda *et al.*, 2008). P-cells are tuned to higher spatial frequencies (due to their smaller receptive fields), but lower temporal frequencies than M-cells (Derrington & Lennie, 1984; O'Keefe *et al.*, 1998; So & Shapley, 1981; Usrey & Reid, 2000). Additionally, while M-cells are more sensitive to achromatic luminance contrast, P-cells show more sensitivity to red-green colour contrast (Hubel & Livingstone, 1990), due to P-cells demonstrating red-green colour opponency in their receptive field configurations (De Valois *et al.*, 1966, 2000; Reid & Shapley, 2002; Wiesel & Hubel, 1966). K-cells were discovered more recently (Dacey, 1993; Dacey & Lee, 1994), and appear to have more diverse properties. In general, they appear to have larger receptive fields than either M- or P-cells (leading to coarser spatial resolution), despite having smaller cell bodies (Tailby *et al.*, 2008; White *et al.*, 2001). Additionally, many show blue-yellow colour opponency (Chatterjee & Callaway, 2003; Szmajda *et al.*, 2008). These broad classes of cells (P-, M-, and K-cells) allow for different aspects of information to be processed optimally and this rough distinction between pathways continues into the cortex. It is also important to note that, when considering the functions of these pathways, how the population of cells work together as a whole is as important as the response properties of the individual cells. This may be why, although M-cells have a higher contrast sensitivity than P-cells, M-cell lesions do not always lead to contrast detection deficits, while P-cell lesions do (e.g. Merigan *et al.*, 1991). It may be that the higher population of P-cells affords it higher sensitivity than would be expected by looking at single cell sensitivity alone (Bruce *et al.*, 2000). Furthermore, the receptive field properties of LGN cells, such as the locations within the visual field to which they are tuned and the diameter of the excitatory

centre, can be further modulated by the extensive feedback from V1 (Wang *et al.*, 2016). The processing of these cells within the cortex is therefore modulated by, and should be considered in the context of, the wider visual system.

1.5. Visual Cortex

1.5.1. Primary visual areas

After the LGN, visual signals pass via the optic radiations to the primary visual areas. The first of these is V1 (also known as the striate cortex, primary visual cortex or Brodmann area 17). Similarly to the LGN, the tissue in V1 is layered, consisting of six principle layers. Input from the retina enters via layer 4C, with parvocellular and magnocellular neurones connecting to sublayers 4Cβ and 4Cα respectively. This represents the first point at which visual signals first generated by the photoreceptors enter the cortex and is the start of multiple processing pathways.

Cells within V1 can be classed as either simple or complex, with a multitude of subclasses and receptive field configurations within each. In a series of classic experiments, Hubel and Wiesel (1959, 1962, 1968) describe several different receptive field configurations found in V1. While some are concentric, similar to those in the LGN, others are constituted of elongated excitatory and inhibitory regions that sit adjacent to each other. There may be two or more of these regions in a single receptive field structure. Hubel and Wiesel (1968) termed these simple cells (though complex cells can also be of this configuration). By virtue of this elongated structure, these receptive fields demonstrate strong orientation preference that is only mildly seen in the LGN. For example, if a particular cell is tuned to stimuli orientated at 90° (as well as a specific spatial frequency and contrast), it will demonstrate the greatest firing rate when presented with a stimulus with this orientation. Its firing rate will start to reduce as the stimulus orientation is moved away from 90°. The particular orientation to which the cell is maximally responsive varies systematically across the cortex, roughly organised into orientation-sensitive columns. Simple cells can have several other response properties, focussed on processing different aspects of a visual stimulus. For example, some show colour-opponency, similar to the P-cells in the LGN (Thorell *et al.*, 1984), while others show more complex dual-opponency, whereby different regions of the receptive field show opposite colour-opponency responses, e.g. the double-

opponent cells (Livingstone & Hubel, 1984a; Michael, 1978). Another class of cells defined by Hubel and Wiesel's early work (1959, 1962) were complex cells. These have many similar properties to simple cells, such as in terms of showing orientation-preference and colour-opponency. However, as opposed to simple cells that respond (i.e. with an increase in firing rate) to stimuli that fall along the elongated excitatory component, complex cells will respond strongly to an orientation no matter where it falls within its receptive field and do not show clear excitatory/inhibitory regions (i.e. shows spatial phase invariance). It should be noted that this is a brief description of simple and complex cells and their associated receptive fields, and there are many other subtypes and response characteristics.

There are several characteristic features of the functional architecture of V1. Firstly, the retinotopic organisation of the visual information is inherited from the retina, so neighbouring neurones in V1 process neighbouring sections of the visual field. This organisation can be imaged using a functional neuroimaging technique termed retinotopic mapping (discussed in more detail in chapter 5). The fovea is disproportionately represented in the cortex, with the central 4° constituting 27% of the cortical surface (despite only accounting for 12% of the RGCs; Adams & Horton, 2003). Furthermore, similar to the retina, receptive fields are much smaller in the fovea and increase with eccentricity, which can be seen both in animal electrophysiological work (e.g. Cavanaugh *et al.*, 2002) and human neuroimaging studies (e.g. Dumoulin & Wandell, 2008). A second feature of the functional organisation of V1 is the existence of ocular dominance columns. While V1 cells tend to respond to stimuli binocularly (i.e. will respond to a preferred stimulus presented to either eye), they often respond more strongly to stimuli presented to one eye over the other. Cells that prefer the same eye tend to be organised into ocular dominance columns (Hubel & Wiesel, 1969). The width of these columns is relatively uniform across the visual field, but appear to be missing\fragmented at the blind spot and monocular crescent regions (i.e. the most peripheral part of the visual field, the perception of which is supported by input from just the ipsilateral eye; Adams et al., 2007). With the advent of ultra-high resolution neuroimaging techniques, these columns can be non-invasively imaged in humans with increasing feasibility (Cheng, 2012; Goodyear & Menon, 2001; Menezes de Oliveira *et al.*, 2019; Menon & Goodyear, 1999), allowing for further investigation into the function of these in humans and how they may reorganise in disease (e.g. Goodyear *et al.*, 2002). A

third feature of the striate cortex was revealed by staining the visual cortex for cytochrome oxidase (CO), which presents with higher levels in cells that are more metabolically present. This technique discovered 'blob' regions of highly metabolically active tissue, mostly in layers II and III, surrounded by 'inter-blob' regions (Edwards *et al.*, 1995; Hendrickson & Wilson, 1979; Livingstone & Hubel, 1984b; Wong-Riley, 1979). There are multiple properties distinguishing these two regions. For example, blob regions are more tuned to low spatial frequencies (~2.8 cycles per degree), while cells in inter-blob regions are tuned to a wider range of spatial frequencies (Edwards *et al.*, 1995). By keeping these functional aspects of the striate cortex in mind, we can better understand how and where features of the visual field are being processed within the cortex.

The next main visual areas (i.e. extra-striate cortices), are V2 and V3, which both continue to show retinotopic organisation and are split into dorsal and ventral regions, responsible for the lower and upper visual field respectively. These dorsal and ventral regions sit above and below V1. The initial main target of signals emerging from V1 is V2, the anatomically neighbouring area. Unlike V1, V2 doesn't show blob regions, but instead has thick-, thin-, and inter-stripes, as revealed by CO staining (Federer *et al.*, 2009; Livingstone & Hubel, 1984b). These regions receive inputs from the blob, blob/inter-blob border, and inter-blob regions of V1 respectively. Additionally, while all stripes receive projections from V1 layers 2/3 and 4A, differences are found with the amount of projections from V1 layer 4B, and these laminar differences may reflect different combinations of M-, P- and K-cells (Federer *et al.*, 2009). fMRI work has also reported M- or P-dominated cortical columns in V2 (and V3), based on functional distinctions between these streams (e.g. peak spatial frequency, luminance contrast sensitivity; Tootell & Nasr, 2017). Cells in the thick- and thin-stripes then continue into V3 (inter-stripes connect directly onto higher visual areas). As well as increasing with eccentricity, receptive field sizes increase gradually through these visual areas, which can be seen in both animal electrophysiological studies (e.g. Hubel & Wiesel, 1965; Keliris *et al.*, 2019) and human neuroimaging work (e.g. Alvarez *et al.*, 2015; Dumoulin & Wandell, 2008; Keliris *et al.*, 2019; Zuiderbaan *et al.*, 2012). Furthermore, cells continue to demonstrate colour and orientation selectivity in these regions (Felleman & Van Essen, 1987; Gegenfurtner *et al.*, 1997; Levitt *et al.*, 1994). These three areas (V1-3) are often referred to as 'early' visual areas.

1.5.2. Other visual areas

After processing by primary visual cortices, visual signals are then passed onto higher cortical regions that are responsible for a range of everyday visual tasks, such as vision-assisted reaching with the right intraparietal sulcus (e.g. Medina *et al.*, 2019) or global motion perception in visual area V5 (e.g. Schenk, 1997).

Broadly, the neural visual information is transferred down both a ventral and dorsal stream, with the former connecting to V4 and the inferotemporal cortex and the latter focused on areas such as V5/MT and the intra-parietal sulcus (Ungerleider & Mishkin, 1982). These two streams have been reported to be, not just anatomically, but also functionally distinct. Specifically, Goodale and Milner (1992) proposed an influential model that suggested the dorsal stream is responsible for the processing of visually-guided actions (the 'where' stream), while the ventral stream is involved with perception and memory-guided action (the 'what' stream). It is suggested that the dorsal stream is focused on real-time action and observer-focused visual information, while the ventral stream processes both object characteristics and context and is also involved with long-term memory. More recent evidence, however, has suggested that this early model is too simplistic, with evidence of multiple sub-streams with distinct anatomical and functional characteristics (Rizzolatti & Matelli, 2003) and also shared functions between the streams (Medendorp *et al.*, 2018; Schenk & McIntosh, 2010).

The visual pathway is a complex and highly organised neural stream that is vital for everyday functions. The structure and basic anatomy discussed in this chapter is important to understand before considering how it changes in glaucoma and what consequences these changes may have.

Chapter 2. Glaucoma

2.1. Introduction

Glaucoma is a chronic neurodegenerative condition, characterised by retinal ganglion cell (RGC) death elevated intra-ocular pressure, and slow, progressive, hitherto irreversible sight-loss. It is the world's leading cause of irreversible blindness, affecting approximately 500,000 people in England and Wales (Burr *et al.*, 2007), and 80 million people worldwide (Quigley, 2006). With an ageing population, prevalence of glaucoma is rising. Early detection of glaucoma means earlier and more effective treatment can be initiated (Guo *et al.*, 2007). Thus, there is a pressing need for a greater understanding, as well as timely diagnosis and treatment of the condition.

2.1.1. Subtypes

Glaucoma is regarded as a group of diseases with multiple subtypes (Weinreb *et al.*, 2014). For example, it can be primary (if the underlying cause is an unknown) or secondary (if the glaucoma is caused by another condition, such as uveitis or pigment dispersion syndrome). Glaucoma can also be divided into open-angle or closed-angle variants. The latter occurs when the iris moves anteriorly, narrowing or closing the angle formed by the cornea and iris, and thus inhibiting aqueous fluid drainage through the trabecular meshwork (as illustrated in Figure 2.1; the anterior eye was previously outlined in Chapter 1). This can happen suddenly, leading to an acute increase in intraocular pressure (IOP) and associated damage to the retina; this is known as acute angle closure glaucoma.

The most common form of glaucoma is termed Primary Open Angle Glaucoma (POAG). While raised IOP was once thought to be the defining characteristic of POAG, it has since been noted that some patients present with optic neuropathy and visual field loss (typical of glaucoma) but also with normal IOP (i.e. within 2 standard deviations of the population average). Additionally, other patients were found to have elevated IOP (i.e. above 2 standard deviations of the population average), but present with no optic neuropathy or visual field loss. These conditions have since been termed Normal Tension Glaucoma (NTG) and Optic Hypertension (OHT) respectively and suggest that the relationship between glaucoma and IOP is more complicated than once thought.

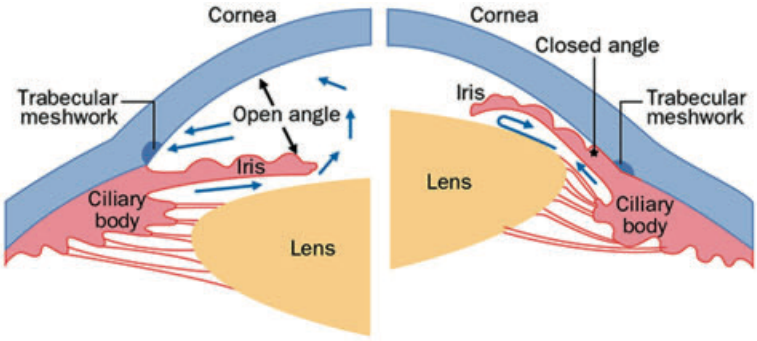

Figure 2.1 – Anterior segment of the eye in open-angle glaucoma (left) and closed-angle glaucoma (right). Blue arrows= the flow of the aqueous humor (formed by the ciliary body). Under normal conditions (i.e. open angle), this flows around the lends and iris and exits the eye via the Trabecular meshwork. In the closed angle example, the iris and lens are positioned anteriorly, blocking off the flow of the aqueous humor and preventing exit through the trabecular meshwork. This leads to an increase in intraocular pressure. Reproduced from Wiggs & Pasquale (2017).

The research presented in this thesis is primarily concerned with POAG, both normal-tension and high-tension subtypes, which is the most common form and presents with chronic RGC degeneration and vision loss. This is particularly relevant to the current thesis as visual adaptions to chronic neural damage (i.e. altered spatial summation mechanisms) and the neural contributions to these psychophysical changes in glaucoma will be investigated. The consequences of acute glaucomatous damage may be different.

2.2. Risk factors

There are various risk factors for glaucoma, including but not limited to:

- *Elevated Intraocular Pressure (IOP)* – This is one of the major risk factors and indications of glaucoma, with measurements of 22 millimetres of mercury (mmHg) and above considered higher than normal. While elevated IOP doesn't always progress to glaucoma and glaucoma is not always accompanied by elevated IOP, lowering IOP is currently the only evidence-based treatment for the condition (Weinreb *et al.*, 2014). However, lowering IOP is not always sufficient to halt the progress of the disease (Susanna *et al.*, 2015). The majority of animal models of experimental glaucoma involve artificially increasing IOP (Evangelho *et al.*, 2019; Johnson & Tomarev, 2010).

- *Age* – More than 2% of people over 49 years of age are affected by glaucoma, with prevalence rising to more than 5% in people over the age of 80 years. In black adults >80 years old, prevalence can reach 13% (Quigley & Vitale, 1997). Increasing age is a major risk factor for glaucoma (European Glaucoma Prevention Study (EGPS) Group *et al.*, 2007; Le *et al.*, 2003; Suzuki *et al.*, 2006). It has been suggested that rather being linked to age *per se*, this reflects increasing frailty with older age (McMonnies, 2017), which depends on the accumulation of health deficits and medications (Rockwood *et al.*, 2011; Song *et al.*, 2010). As such, a younger person with increased frailty may also have an increased risk of glaucoma (McMonnies, 2017).
- *Race* – Multiple studies have suggested race differences in the prevalence of glaucoma. Rudnicka *et al.,* (2006) completed a Bayesian meta-analysis to investigate how variations in POAG prevalence differs by race. They report that black populations had a higher prevalence of POAG compared to both white and Asian populations. White populations however, demonstrated the steepest increase of POAG with age. Glaucoma also appears to have an earlier onset in some sub-Saharan African populations; Ntim-Amponsah *et al.,* (2004) report an incidence of 6% in people aged 30 – 34 years. Furthermore, Nguyen *et al.,* (2018) investigated 5-year outcomes of trabeculectomy in 135 eyes of 105 patients of African descent and 135 eyes of 117 patients of European descent and found that the surgery was less successful in those of African descent. This difference in disease susceptibility has been suggested to reflect racial differences in anterior lamina cribrosa surface depth, which was associated with more severe glaucoma and higher IOP in those of African descent (Girkin *et al.*, 2019).
- *Family History* – Many individuals with glaucoma demonstrate a genetic disposition to the disease; for example, first-degree relatives of glaucoma patients were found to have a 22% lifetime risk of glaucoma, compared to 2.3% in relatives of healthy controls (Wolfs *et al.*, 1998). Multiple loci have been implicated in the development of POAG (ANZRAG Consortium *et al.*, 2016; Burdon *et al.*, 2011; Chen *et al.*, 2014; Li *et al.*, 2015; Osman *et al.*, 2012; Springelkamp *et al.*, 2015; Thorleifsson *et al.*, 2010; Wellcome Trust Case Control Consortium 2 *et al.*, 2014; Wiggs *et al.*, 2012) and NTG (Wiggs *et al.*, 2012). Rather than a single gene mutation demonstrating a large biological effect (such as APOE in Alzheimer's disease; Okuizumi *et al.*, 1994;

Strittmatter *et al.*, 1993), multiple genes with small effects appear to contribute to disease onset (Wiggs & Pasquale, 2017). For this reason, polygenic risk scores (PRS), a genome-wide risk score for a particular disease or trait, may be useful for investigating the impacts of an overall genetic disposition to glaucoma on the eye and wider visual neural system. Such PRS for IOP and POAG diagnosis have recently been published (Gao *et al.*, 2019; NEIGHBORHOOD consortium *et al.*, 2020; Qassim *et al.*, 2020), opening up this research area for further investigation.

2.3. Consequences to vision in glaucoma

Glaucoma leads to progressive vision loss starting in the peripheral visual field and, especially if left untreated, can lead to blindness. Traditionally, the damage to the retina in glaucoma was thought to present in the visual field of patients as 'tunnel-vision', with a ring of missing vision in the periphery corresponding to areas of RGC degeneration. Indeed, much publicity intended to raise awareness of glaucoma and associated symptoms includes pictures demonstrating this pattern of dense visual field loss (similar to print outs from clinical perimetric tests, which measure visual sensitivity thresholds across the visual field and graphically show vision loss as black areas). However, this doesn't seem to relate to what patients themselves report (e.g. Hu et al., 2014) and there is a poor association between clinical measures and self-perceptions (Jampel et al., 2002; Richman et al., 2010). While self-reports are vulnerable to several biases (such as the patient's knowledge of the disease or individual personality traits) they provide information about the patient's visual perception in glaucoma that is inaccessible via standard clinical visual sensitivity measures like Standard Automated Perimetry (SAP). For example, Crabb *et al.,* (2013) presented fifty glaucoma patients with images modified to mimic possibilities for perception in the disease (see Figure 2.2) and asked them to indicate which reflected their own vision. No patients chose the blacked-out 'tunnel vision'. Instead, the most commonly chosen image to represent the patient's own perception was the stimulus scene edited to include blurred patches in the periphery (which was chosen by 54% of patients). Later interviews with the participants reiterated that the prominent change in their perception was blurring or missing features in the periphery. This raises the question of why the majority of patients, at least in the early-to-moderate stages, don't report holes of 'missing' vision corresponding to areas of cell loss in the retina.

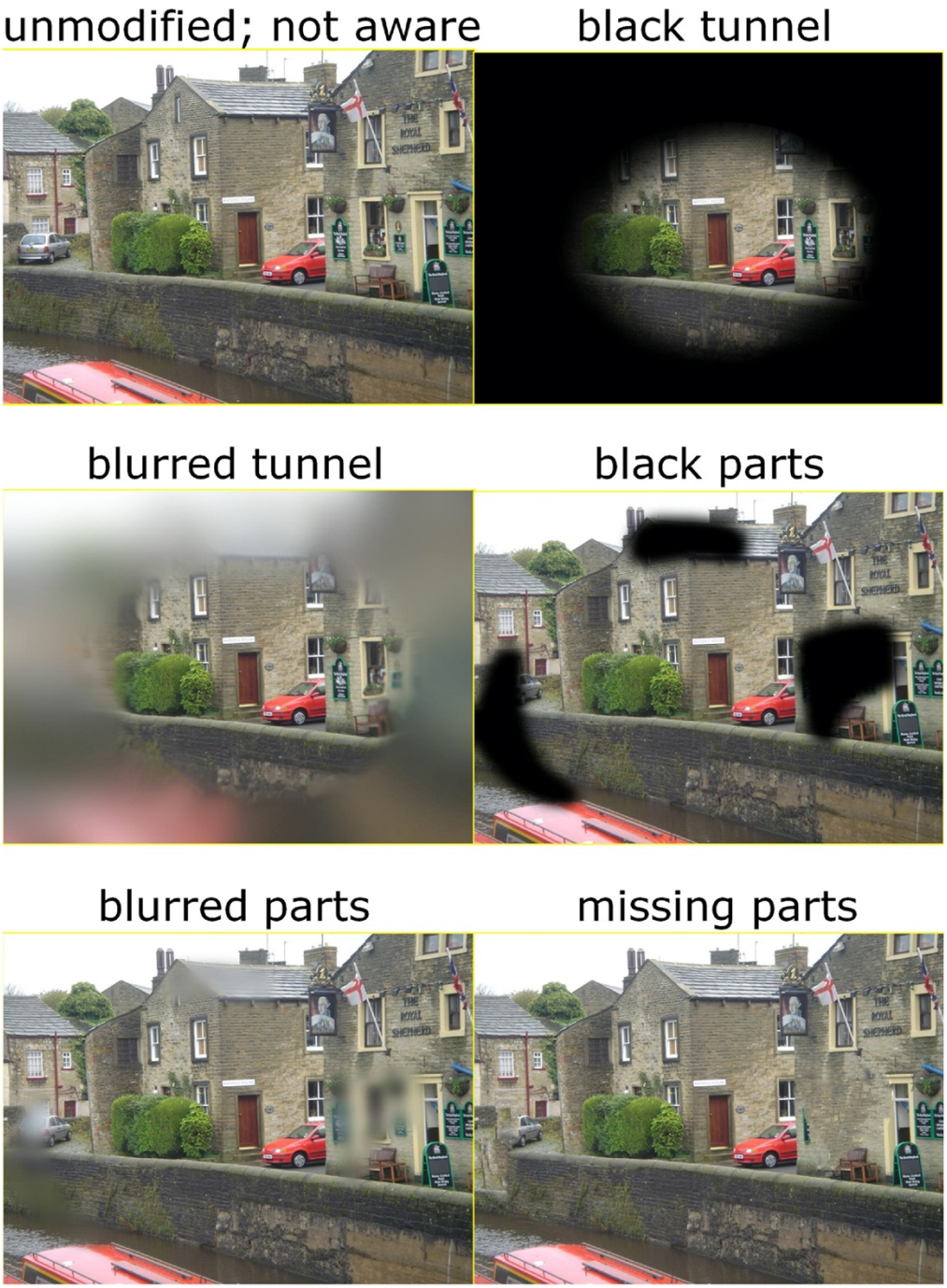

Figure 2.2 – Images used in the force-choice experiment described by Crabb et al., (2013).

It is likely that instead of this reported 'blurring' in peripheral vision reflecting actual optical defocus, it is the consequence of a reduction in RGC density as glaucoma progresses. As RGC density declines, resolution acuity will also decline with disease progression (Anderson *et al.*, 2002; Dacey, 1993). As resolution reduces but no 'holes' appear in the visual field, it therefore appears likely that there in some form of spatial pooling of visual information. Indeed, an enlarged Ricco's area (i.e. the area of complete spatial summation) is reported in glaucoma (Redmond *et al.*, 2010). However, the underlying physiology cause

of this increase in Ricco's area in glaucoma patients is still an unknown. While the size of Ricco's area was traditionally believed to reflect the underlying RGC receptive field size – and shows similar effects of eccentricity across the visual field (Graham & Bartlett, 1939; Vassilev *et al.*, 2003; Volbrecht *et al.*, 2000; Wilson, 1970) – more recent evidence suggests a potential cortical contribution. For example, histological animal work in glaucoma has suggested that RGC demonstrate shrinkage of the cell body, dendritic tree, and axon before cell death (Morgan, 2002). This therefore appear counterintuitive to the finding of Ricco's area enlarging in glaucoma if it had a purely retinal origin. A cortical contributor to determining the size of Ricco's area is also suggested by the finding that, in patients with amblyopia (a condition characterised by poorer vision in one eye compared to the other), Ricco's area enlarges when measured with the amblyopic eye but shrinks when measured with the fellow eye (Je *et al.*, 2015). Considering that there is no evidence of thinning of the RGC layers in amblyopia (Chen *et al.*, 2013; Ersan *et al.*, 2012; Szigeti *et al.*, 2014; Xu *et al.*, 2013) but there is evidence of cortical change (Conner *et al.*, 2007; Li *et al.*, 2007), it seems possible that this change in spatial summation has a cortical origin. Clavagnier, Dumoulin, and Hess (2015) found that fMRI-based estimates of cortical receptive field sizes in V1 were indeed enlarged when presenting stimuli to the amblyopic eye. Furthermore, Pan & Swanson (2006) demonstrate that spatial summation with perimetric stimuli can be accounted for by cortical pooling by multiple spatial mechanisms. Following this evidence, it therefore appears likely that Ricco's area has both retinal and cortical contributions. The topic of perimetric sensitivity and spatial summation in glaucoma is discussed fully in Chapter 3. This thesis will investigate how retinal and cortical receptive field sizes contribute to Ricco's area in a sample of glaucoma patients and age-similar controls. Before this can be investigated however, it is important to have a holistic understanding of the disease.

2.4. Structure-function relationships in glaucoma

A long standing debate in glaucoma literature is how visual loss relates to retinal damage, particularly the relationship between perimetric sensitivity and measures of retinal layer thickness or retinal ganglion cell density (Denniss *et al.*, 2019; e.g. Hood, 2019). For example, Harwerth *et al.,* (1999) compared RGC number (via histological examination) to performance in SAP in a sample of monkeys with unilateral experimental glaucoma. They report a curvi-linear relationship between light sensitivity and RGC number, suggesting that

perimetric loss in glaucoma is only observable after substantial RGC loss. However, this pattern may be an artefact due to comparing a linear measure (such as µm; used for quantifying retinal thickness) with a logarithmic scale (such as decibels [dB]; used for quantifying visual threshold). Such logarithmic scales are more sensitive to changes in low dB, but are less sensitive at high dB, leading to functional changes being initially less apparent and appearing to occur after structural changes (hence a curvilinear function). This was demonstrated by Garway-Heath *et al.,* (2002) who investigated structure-function relationships in a sample of 40 glaucoma patients and 34 healthy controls. They initially replicated previous reports of a curvilinear relationship between function (i.e. differential light sensitivity in dB) and structure (i.e. neuroretinal rim area and pattern electroretinogram amplitude) in their sample of glaucoma patients and age similar controls. However, these relationships became linear if dB was converted to 1/Lambert, a linear unit rather than logarithmic. They concluded that the impression of a functional reserve is given by the common use of a logarithmic scale to evaluate structure-function relationships, as well as the high test-retest variability of visual field tests (Katz *et al.*, 1995; Spry *et al.*, 2001), which hinders reproducible evidence of loss.

However, this has not always been replicated; for example Racette *et al.* (2003) found the opposite pattern, with dB showing linear patterns with structure, while 1/Lambert was curvilinear. This was shown in a similar sample to Garway-Heath *et al.* (2002; i.e. healthy controls and diagnosed glaucoma patients with reproducible visual field loss), as well as in patients with normal or unconfirmed visual field loss. One possible source of difference is that Garway-Heath *et al.* (2002) restricted their analysis to those of white ethnicity; as optic disk morphology seems to differ with ethnic group (e.g. Samarawickrama *et al.*, 2010), the structure-function relationship may also differ. In restricting their sample to those glaucoma patients with confirmed producible visual field and structural loss, bias may also be introduced to the original sample.

A consideration of such models is that once a substantial amount of visual field loss has occurred, measurements of retinal nerve fibre layer (RNFL) thickness (which thins in glaucoma due to the RGC degeneration and thus is often used in structure-function models) may stabilise due to residual glial cells and blood vessels within that retinal layer. It is suggested that this residual thickness in completely blind glaucomatous eyes is about

~45µm (Sihota *et al.*, 2006). Interpreting structure-function relationships is also complicated by the fact that RNFL thickness in healthy individuals can vary greatly (i.e. between 114.6-182.2µm; Hood & Kardon, 2007). In those with a naturally thick RNFL, it will be easier to identify functional visual loss before structural measures have thinned to an abnormal level, giving the impression that functional loss precedes structural loss. On the other hand, the opposite will occur with those with a naturally thin RNFL, for whom structural measures will approach abnormal levels earlier in disease and may seem to precede significant functional loss. High levels of myopia can also lead to thinner retinal thickness (e.g. Read *et al.*, 2017) independently to glaucoma or visual field loss. Retinal structural loss in glaucoma will be discussed further in Chapter 4.

Chapter 3. Psychophysics

Visual psychophysics allows for precise investigation of the visual system by quantitatively monitoring and manipulating a specific characteristic of a stimulus (e.g., luminance) and assessing how this impacts behaviour (e.g., detection). Psychophysical experiments give information about the limitations and functioning of a neural system underlying a particular perception and behavioural response.

3.1. Visual sensitivity

The psychophysical process can be understood in three stages (for an illustration of a typical psychophysical set-up, see Figure 3.1) Firstly, a characteristic of the stimulus, such as luminance, is varied systematically. It is vital that the parameters of this stimulus are precisely controlled so the response can be properly contextualised. For example, if one stimulus provokes a detection response but another does not, the reason for this can only be understood if the exact difference between the stimuli is known. For this reason, a single stimulus property is typically varied in a testing session, while the other parameters are kept constant. When a stimulus is detected, an internal representation is created within the neural visual system. This representation should change in a certain dimension with the particular stimulus property (e.g., the spatial extent of neural activation may increase with increasing stimulus size). Finally, a task-relevant response is produced, such as pressing a button to indicate that a stimulus has been detected. This is the basic set up of psychophysical experiments and the basis of perimetric testing (a measurement of visual sensitivity across the visual field commonly used in clinical diagnosis and monitoring).

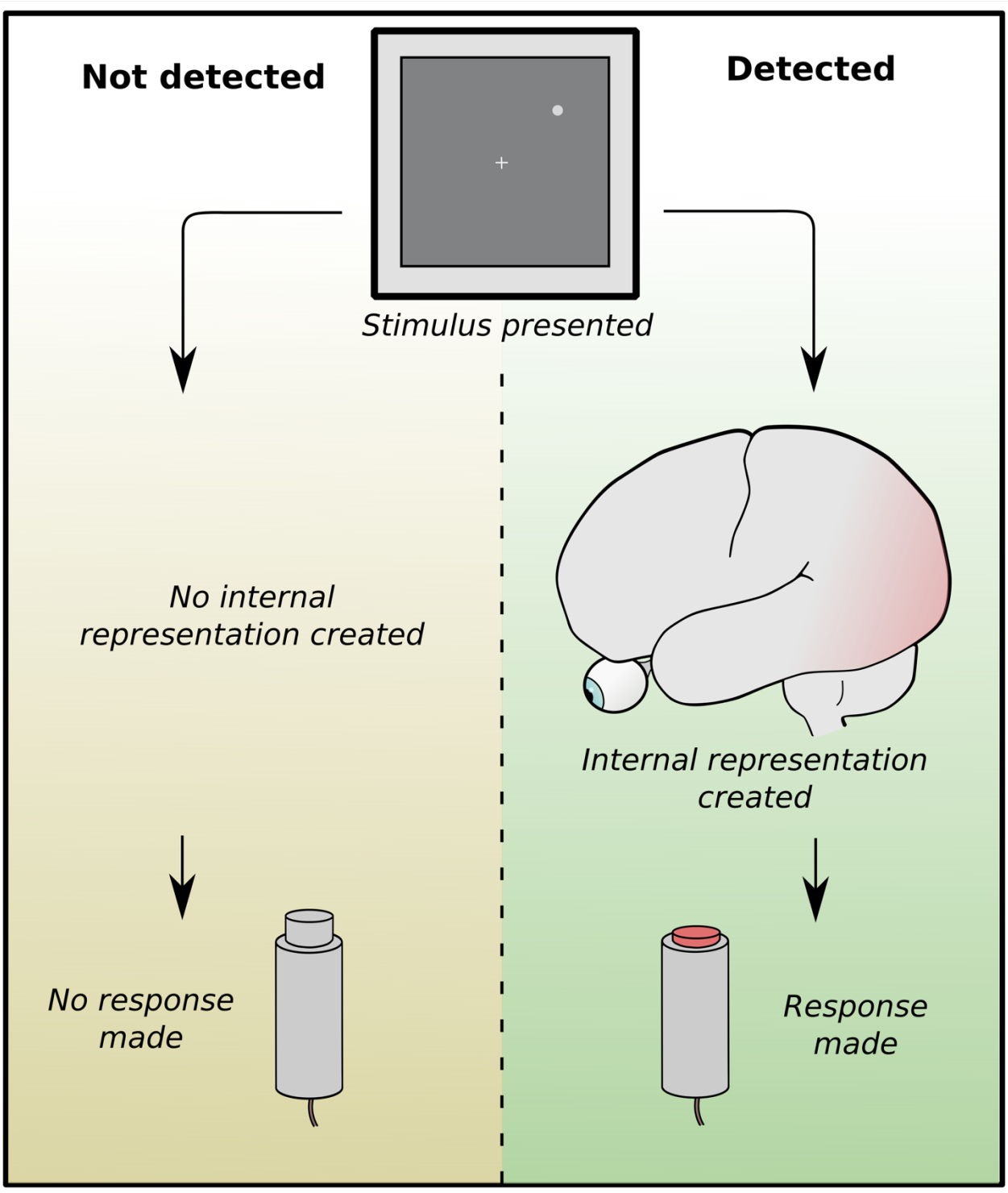

Figure 3.1 – Illustration of the typical psychophysical set up for investigating detection thresholds. A stimulus is presented to the observer, which is usually scaled on a particular parameter, such as intensity or size. Depending on how much the stimulus energy corresponds to the observer's visual threshold at that visual field location, the stimulus will either be detected or not. If detected, the underlying neural pathway will process and create an internal representation of the stimulus. This is then translated to a goal orientated behaviour, such as a 'detection' response.

One of the foundational domains of visual psychophysics is the measurement of visual sensitivity, typically done by measuring visual thresholds. A visual detection threshold is typically taken as the point at which a stimulus at a particular intensity is seen a certain percentage of times, such as 75%. This can be seen in the psychometric function plotted in Figure 3.2a, in which the probability of a stimulus being detected is plotted as a function of stimulus contrast against the background. In this instance, the contrast value at 75%

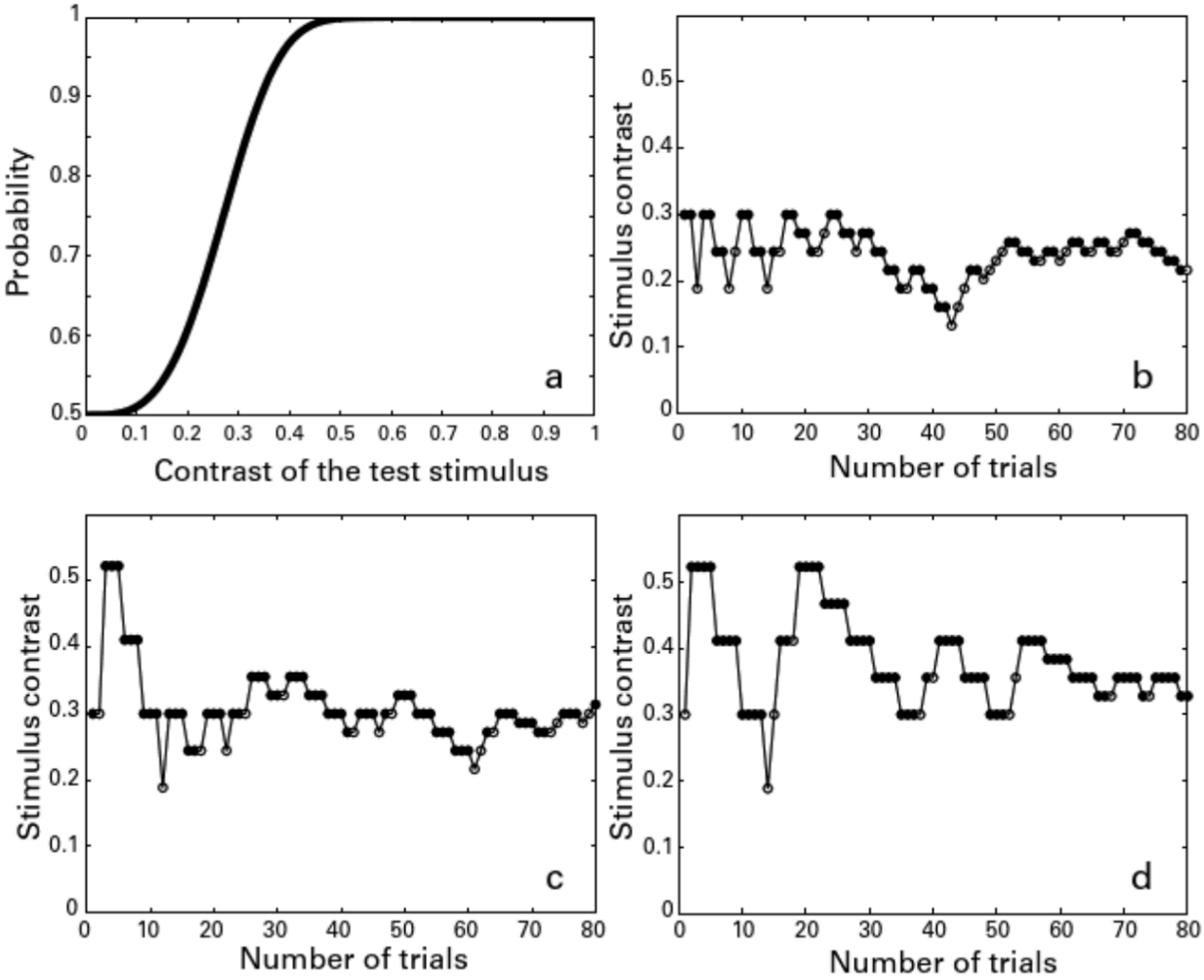

Figure 3.2 – Examples of multiple transformed staircases estimating the threshold for the same underlying psychometric function. a) The psychometric function demonstrating the probability of seeing for a range of stimulus contrasts. b) A 2-down, 1-up staircase, finding a threshold of 0.263 contrast at 70.7% probability of seeing. c) A 3-down, 1-up staircase, finding a threshold of 0.309 contrast at 79.4% probability of seeing. d) A 4-down, 1-up staircase, finding a threshold of 0.356 contrast at 84 .1% probability of seeing. All filled circles refer to correct responses (e.g. a detection response when a stimulus is shown), while unfilled circles indicate an incorrect response (e.g. no response to a shown stimulus). Reproduced from Lu and Dosher (2013).

is taken as the threshold. This kind of psychometric function underlies all threshold testing procedures. Various laws describe the relationship between a stimulus characteristic, such as intensity or size, and detection thresholds, some of which are described below (see 3.2. Spatial summation and changes in glaucoma). By examining thresholds and investigating the factors that influence them, we can infer the characteristics and limitations of the visual system. Three broad methods are commonly used to measure sensitivity thresholds (Lu & Dosher, 2013).

The method of limits – In this method, a stimulus is initially presented that is either substantially supra- or sub-threshold for the particular observer (method of descending or ascending limits respectively). If the stimulus is detected, the intensity of the next target is decreased. If the observer does not report detection, the intensity is increased. In this way, the intensity is adjusted up or down until the threshold is reliably identified. In some versions, the step size of the intensity adjustments decreases with each 'turn' (e.g. switch from increasing to decreasing), allowing for more precise identification. As the majority of presented intensities are concentrated around the threshold level, this is a relatively efficient method. It also does not assume *a priori* knowledge of the threshold, unlike the method of constant stimuli (below). However, without the use of stimuli at a very high or very low intensity, it has no in-built false negative or false positive tests, so participant attentiveness must be assumed. Participants may also be biased by habituation (i.e. when a participant has pressed a certain response a number of times and continues out of habit, leading to 'detected' responses for invisible stimuli or 'not detected' responses for visible stimuli) or anticipation errors (i.e. where the anticipation of seeing or not seeing a target leads to a false positive or false negative errors respectively).

The method of adjustment – In contrast to the above, in this method the participant manually adjusts the stimulus until it is just visible, rather than reporting detection to presented stimuli. This value of 'just visible' is estimated in this way a number of times, with different starting values, and then averaged to estimate the visual sensitivity threshold. This has the advantage of being relatively quick and easy, however it is also susceptible to participant errors such as habituation and anticipation errors.

The method of constant stimuli – This method differs from the above in that a range of intensities, which are assumed to range from supra-threshold to sub-threshold, are

determined beforehand. They are presented in a random order to participants, avoiding the problem of anticipation and habituation errors. This also provides a complete picture of sensitivity to a range of intensities. The inclusion of targets with a very high or low intensity also provides an in-built false negative or false positive test. However, unlike the above, it assumes knowledge of where the threshold will be, in order to define a range of intensities that encompasses it, which is especially problematic in clinical conditions where the threshold may be unknown. It is also a relatively lengthy test, as all intensities are administered, rather than just those surrounding the individual threshold. Long test times can introduce additional problems, such as participant fatigue and inattention.

3.1.1. Adaptive methods (staircases)

In many psychophysical experiments, multiple visual thresholds are estimated to multiple stimuli (that may vary in, for example, contrast), in order to plot a psychophysical function (such as the function illustrated in Figure 3.2a). For this reason, it is important that multiple thresholds can be calculated as efficiently as possible to avoid effects such as observer fatigue. Adaptive methods, which aim to find the threshold with the smallest number of targets while retaining accuracy, are therefore optimal. The method of limits is adaptive as it self-modifies the presented stimuli based on the participant's response, restricting the range of intensified presented.

Staircase procedures are a commonly used adaptive thresholding methodology. Up-Down staircases begin at a starting value – which is assumed to be either supra-threshold or sub-threshold – and change the intensity of the next target (i.e. stimulus to be detected) by a certain step size. The size and direction of this step size depends on the previous response (i.e. whether the participant has reported a certain integer of correct or erroneous responses; if the participant has reported a certain number of incorrect responses, the intensity may increase). This procedure ends when a certain stop rule, such as a certain number of reversals (e.g. changes in step direction), is reached. The starting value, step size, number of responses needed before the direction of the steps is reversed, and the stop rule all differ depending on the type of staircase used (nn example of different staircases and the underlying psychometric function [i.e. relationship between stimulus intensity and probability of detection] can be seen in Figure 3.2). A truncated (or 1/1) staircase is perhaps the most straightforward, in which intensity increases after one correct response and

decreases after one incorrect response, therefore converging on a threshold at which the participant has a 50% probability of detecting the stimulus. Thresholds at higher probabilities are obtained using transformed staircases that require a larger number of consecutive correct responses before reducing intensity and thus increasing difficulty (Lu & Dosher, 2013).

3.2. Spatial summation and changes in glaucoma

A characteristic of the visual system is that, to increase the signal-to-noise ratio, light is summated over both space (spatial summation) and time (temporal summation). For small stimuli, more light energy for unit area is required to remain at the detection threshold than is needed for larger stimuli. These complete spatial summation mechanisms in small stimuli (whereby all light over the area of the stimulus summates) have been described by Ricco's law (Ricco, 1877). This states that, at threshold, area and intensity of a stimulus are inversely proportional. This can be defined as:

$$I * A = k$$

whereby I refers to intensity, A refers to area, and k is a constant. An illustration of this relationship is given in Figure 3.3. However, this relationship breaks down once stimuli reaches a critical area (known as Ricco's area), after which k decreases and only partial summation (or incomplete summation) occurs (however, once stimuli reaches a certain stimulus size, there appears to be an absence of spatial summation; Glezer, 1965).

Several laws have been proposed for partial summation, such as Piper's law. This law suggests that the threshold for stimuli larger than a critical area (i.e. Ricco's area) is inversely proportional to the square root of the stimulus area (Howarth & Lowe, 1966; Piper, 1903). Other laws have also been proposed under various experimental conditions (such as strict fixation stabilisation methods; Piéron, 1929), which also suggest different values for the coefficient of summation (k); for example, Piéron's law (k=0.3), Goldmann's approximation (k=0.8), and Weber's law (k=0).

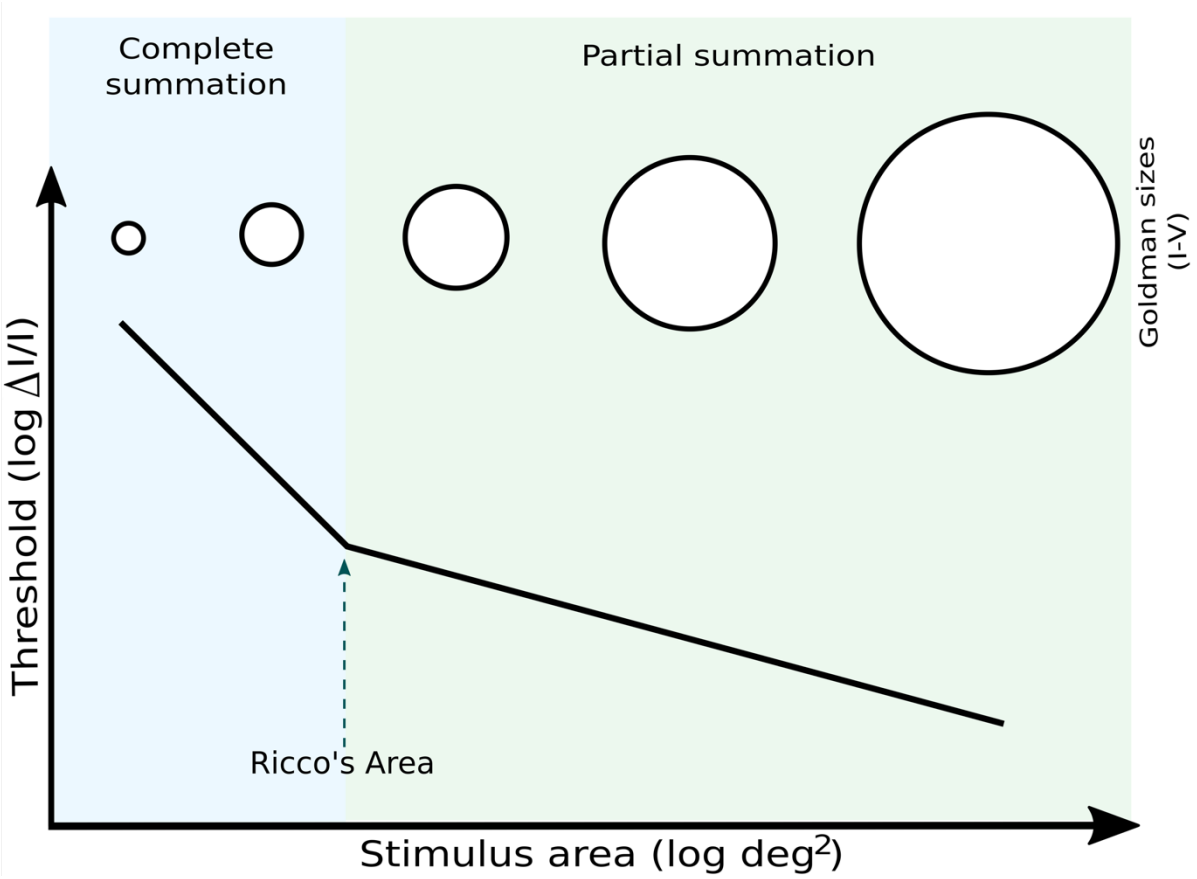

Figure 3.3 – A spatial summation curve at approximately 15 degrees eccentricity. The Y-axis shows visual thresholds, while the X-axis shows stimulus size, with the corresponding Goldman stimuli sizes illustrated along the top of the plot. Standard automated perimetry typically uses Goldman size III. Ricco's area is marked with a dashed arrow. With stimuli smaller than Ricco's area, the relationship between stimulus size and threshold is roughly -1, corresponding to Ricco's law and complete spatial summation. After that however, the relationship shallows and it moves to partial spatial summation. The degree of spatial summation and underlying law varies depends on experimental condition.

As mentioned, the largest area for which complete spatial summation occurs is termed Ricco's area (see Figure 3.3). Early studies estimated that, in healthy, photopic conditions, the diameter of Ricco's area is around 0.13° at 5° eccentricity and about 0.26° at 25° eccentricity (Wilson, 1970). Considering that clinical perimetry commonly involves the presentation of Goldman III size stimuli (diameter = 0.43°), the stimuli presented during a perimetric assessment are larger than Ricco's area for a large portion of the retina and therefore works within the range of partial spatial summation mechanisms. However, this assumes that Ricco's area stays stable across individuals and pathologies. Conversely, even under experimental conditions, Ricco's area seems to vary significantly between individuals (Redmond *et al.*, 2010b; Schefrin *et al.*, 1998; Volbrecht *et al.*, 2000a) and Ricco's area may

also enlarge with age in scotopic conditions (Schefrin *et al.*, 1998). It also appears to vary in conditions such as amblyopia (Je *et al.*, 2018) and, of particular importance for this thesis, glaucoma (e.g. Redmond *et al.*, 2010a). In certain conditions therefore, the stimuli presented in clinical perimetry may be smaller than Ricco's area, thereby passing from partial summation (as it the case in health) to complete spatial summation mechanisms.

Several studies have investigated this question of spatial summation changes in glaucoma compared to healthy controls. For example, Fellman *et al.*, (1989) demonstrated that glaucoma patients demonstrated a great improvement in retinal sensitivity to increasing size than they did for increasing the contrast of the stimulus. The opposite pattern was observed in healthy controls, with greater benefit to retinal sensitivity afforded by increasing stimulus size. They also found that lower background adaptation levels (which leads to an increase in Ricco's area; Barlow, 1958; Glezer, 1965) led to disproportionate improvements in contrast sensitivity for different retinal eccentricities for glaucoma patients compared to healthy controls. It was suggested that both of these results reflect altered spatial summation mechanisms (specifically an enlarged Ricco's area) in glaucoma (Anderson, 2006).

Redmond *et al.* (2010a) examined spatial summation curves in a sample of 24 early glaucoma patients and 26 age-similar controls, targeting both chromatic and achromatic pathways. Four visual field locations were examined after pupil dilation. Spatial summation curves were excluded if they did not reach a criterion model fit of $r^2 > 0.9$. For both conditions (i.e., chromatic and achromatic) and all hemifields, they found that Ricco's area was significantly larger in glaucoma patients compared to healthy controls, suggesting an increased pooling of light energy in the disease. Furthermore, this difference in Ricco's area

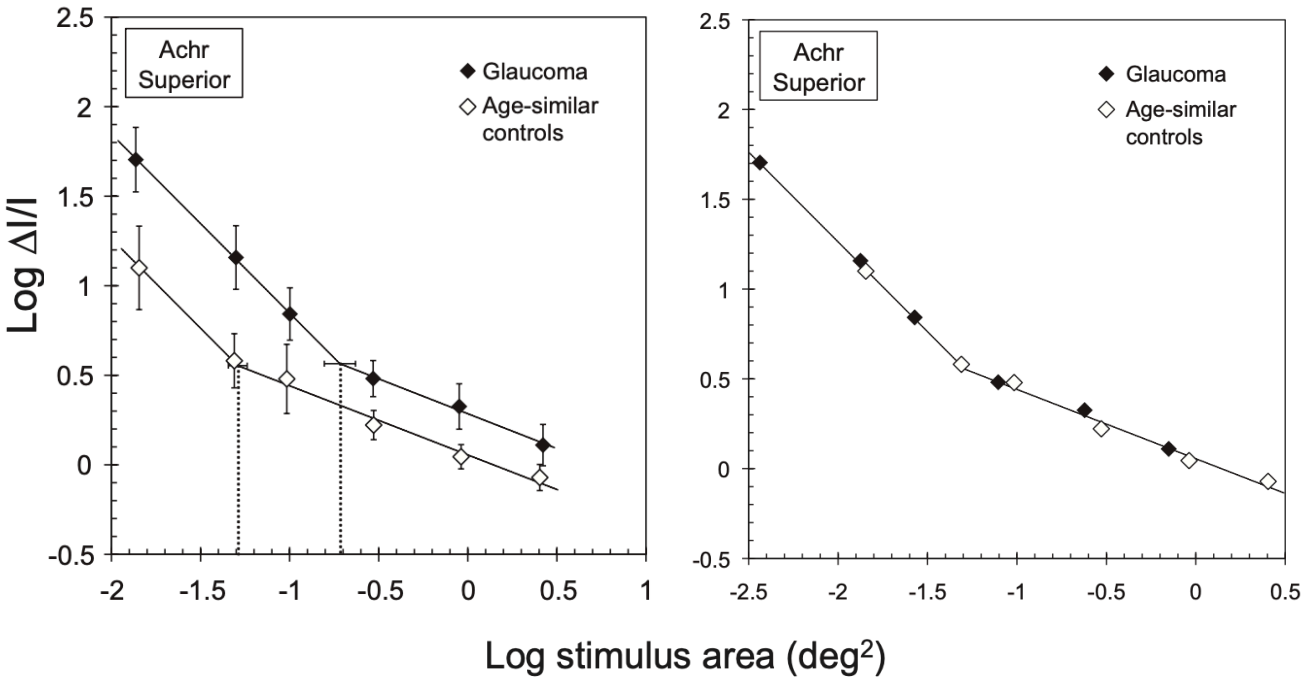

Figure 3.4 – Left panel: Average spatial summation functions for glaucoma patients and healthy controls for achromatic stimuli in the superior hemifield. Vertical dotted line= size of Ricco's area. Vertical error bars= 95% confidence intervals for each averaged point. Horizontal error bars= Standard Error of the Mean of Ricco's area values. Right panel: demonstration that if the average spatial summation function for glaucoma patients is shifted leftward along the size axis by an equal magnitude to the difference in Ricco's area, it overlaps completely with the average spatial summation function for healthy controls. Both plots adapted from Redmond et al. (2010).

completely accounted for the sensitivity difference between patients and healthy controls. This is illustrated in Figure 3.4. As can be seen from this figure, if the average spatial summation function for glaucoma patients is shifted leftward along the size axis by an equal magnitude to the difference in Ricco's area, it superimposes completely with the average spatial summation function for healthy controls. Thus, in regard to perimetric testing in early glaucoma, if a stimulus is scaled in size in accordance with the changing extent of spatial summation, the threshold sensitivity may be kept constant. Alternatively, if a fixed stimulus size is used, such as the use of Goldman size III stimuli in clinical perimetry, sensitivity will decline depending on the relative size of Ricco's area. Perimetric testing that involves the modulation of both area and intensity has been shown to be more efficient than traditional perimetry at detecting glaucomatous damage (Rountree *et al.*, 2018). Anderson (2006) has suggested that this enlargement of Ricco's area in glaucoma may lead to glaucomatous defects in visual sensitivity remaining undetected until Ricco's area

enlarges enough to match the size of the perimetric stimuli, at which point perimetric testing will start to pass into complete spatial summation. Understanding more about this psychophysical change in glaucoma will provide further information on the process of damage within the disease, as well as the neural underpinning of perimetric changes. The following section of this chapter will discuss various possible contributing factors throughout the visual system that may determine the size of Ricco's area.

3.2.1. Physiological basis of spatial summation changes in glaucoma

As yet, the exact physiological basis for determining the size of Ricco's area is uncertain. Experimental investigation has revealed several characteristics of Ricco's area, which may provide clues as to how it is determined. For example, the size of Ricco's area has been found to enlarge with increasing visual field eccentricity (Graham & Bartlett, 1939; Vassilev *et al.*, 2003; Volbrecht *et al.*, 2000a; Wilson, 1970), chromatic pathway (Redmond *et al.*, 2010b; Volbrecht *et al.*, 2000b) and temporal duration (Barlow, 1958; Wilson, 1970). It has also been found to vary with light conditions, with larger Ricco's area estimates reported for scotopic (i.e., rod-mediated vision) conditions compared to photopic (i.e. cone-mediated vision) conditions (Glezer, 1965). Any proposed theories of the physiological basis of Ricco's area would, therefore, need to provide explanations for these phenomena.

3.2.1.1. Optical contributions

Following comparisons between measured and simulated Ricco's area assessments, Davila and Geisler (1991) suggested that optical factors (such as the modulation transfer function [MTF], which determines how much contrast in the original object is maintained by the detector, i.e. retinal image) can account for most, if not all, of this phenomenon under photopic conditions. However, Schefrin *et al.* (1998) ran simulated models on various levels of MTF and intraocular scatter, and concluded that neither could account for their reported age-related changes in the size of Ricco's area. A later adaptive optics study found that while Ricco's area was reduced when removing the influence of optical factors, it remained present (Dalimier & Dainty, 2010), suggesting a post-optics influence. The sensitivity of Ricco's area to temporal duration (Wilson, 1970) also suggests a neural origin. There is also little evidence for large deviations in optical factors, such as MTF, in glaucoma (Holopigian *et al.*, 1990) suggesting that, these optical changes cannot explain the change in Ricco's area seen in this disease. Together, this work suggests that while optics has a role in determining

the size of Ricco's area, it is not the primary contributor and cannot seem to explain the observed change in glaucoma.

3.2.1.2. Retinal contributions

Much work has been done into the possibility of a major retinal component to Ricco's area. Multiple cell types are present in the retina and as the first point at which light energy is detected, the contribution of photoreceptors to spatial summation has been investigated. Brindley (1954) suggested that the lower acuity and increased area of spatial summation in the 'blue' pathway compared to 'red' or 'green' pathway may be explained by either the associated photoreceptors being very sparse or by a high level of convergence between the receptors and higher-level neurons. However, they found no sparsity of 'blue' photoreceptors that would explain an increase in spatial summation. In addition, as noted by Redmond (2009), rod photoreceptors are much more numerous than any cone subtypes, even though Ricco's area in rod-dominated scotopic conditions is larger than that in photopic conditions (e.g. Glezer, 1965). If photoreceptor density was the underlying basis of Ricco's area, increased density of photoreceptors would be expected to be associated with smaller Ricco's area estimates. Brindley (1954) therefore concluded that the most important factor in differing Ricco's area sizes between different pathways may be the convergence at the retinal ganglion cell (RGC) and bipolar cell level. The idea that RGC properties (e.g. density, receptive field size) are particularly important for determining Ricco's area size was collaborated by Volbrecht *et al.* (2000b), who found a stronger association between Ricco's area size and RGC density than either S- or L-cone density. This supports the proposal that it is RGC density, rather than photoreceptor density, that is relevant. Furthermore, an association is suggested by the fact that eccentricity-based changes in Ricco's area mirrors the changes in RGC density (Watson, 2014) and dendritic tree size (Vassilev *et al.*, 2003). Considering that RGC degeneration and death is a characteristic feature of glaucoma (e.g. Morgan, 2002), this is an important possible loci for the basis of Ricco's area and as such as been investigated further.

One suggestion is that the size of Ricco's area may be defined by RGC receptive field configuration (namely an excitatory centre and an inhibitory surround). Specifically, when a stimulus presented in the centre of a receptive field is smaller in area than that receptive field's excitatory centre, the light energy is summed by complete spatial summation. When

that stimulus is increased in size and starts to enter into the receptive field's inhibitory surround, it then enters into partial spatial summation mechanisms (such surround antagonistic receptive field configurations were described in chapter 1). Ricco's area should therefore by defined by the receptive field centre size and be limited by the amount of surrounding inhibition. This suggestion is supported by the finding that increasing the background luminance decreases the size of Ricco's area and also increases the involvement of lateral inhibition (or the OFF-centre surround; Barlow, 1958; Glezer, 1965; Lelkens & Zuidema, 1983). Davila and Geisler (1991) also suggested that low luminance conditions lead to an increased involvement of the magnocellular pathway, which has larger receptive field sizes and thus, may contribute to measurements of a larger Ricco's area. However, recent research has found that lateral inhibition in the retina, as measured psychophysically, appears to be normal within glaucoma (Junoy-Montolio *et al.*, 2016), suggesting that lateral inhibition does not underlie the enlarged Ricco's area in glaucoma.

Additionally, background-dependant changes in Ricco's area size have also been identified in the S-cone pathway (Redmond *et al.*, 2013). Receptive fields of RGCs underlying the S-cone signal response (the small bistratified cells; Dacey & Lee, 1994) are of the order S+/(L+M)- or S-/(L+M), so therefore do not show a surround inhibition configuration. However, this surround antagonism is found in the primary visual cortex (termed doubled-opponent cells; Conway, 2001; Conway & Livingstone, 2006; for a review, see Shapley & Hawken, 2011). This evidence suggests that, if Ricco's area reflects surround antagonism mechanisms, there may be a substantial cortical involvement to explain these findings in the S-cone pathway.

It has been theorised that Ricco's area may represent a critical number of RGCs, and that it increases with eccentricity due to increased RGC sparsity. If so, one would expect it to show age-related changes due to the decreases found in RGC density with age (e.g. Harwerth *et al.*, 2008). In line with this, Schefrin *et al.* (1998) found a small age-related increase with Ricco's area under scotopic conditions, suggested to correspond to an increased convergence to remaining RGCs. However, this finding is not universal; Redmond *et al.* (2010b) reported that, despite age-related decreases in overall contrast sensitivity and peripheral grating acuity (a marker of RGC density), there were no statistically significant decreases in Ricco's area with age in either photopic or S-cone conditions.

A recent investigation into the link between RGC density and spatial summation was carried out by Kwon and Liu (2019). A sample of 11-17 healthy adults with normal or corrected-to-normal vision were included, depending on the visual field location tested. For each of the seven tested visual field locations, estimated RGC density (based on previous literature; Drasdo *et al.*, 2007) and the measured Ricco's area was used to calculate the number of RGCs underlying Ricco's area. This number was found to be relatively consistent across the visual field, with about 14 RGCs underlying Ricco's area (which is less than has been previously estimated; Swanson *et al.*, 2004). Furthermore, they estimated that ~90% of variance in Ricco's area size can be explained by RGC density. There was some deviation close to the fovea, though this was suggested to reflect overestimation of RGC density in previous literature. This work was then extended to the cortex, using previous anatomical, psychophysical, and physiological literature to estimate cell density (Kwon & Liu, 2019). They estimated that ~12 magnocellular RGCs input into each 1mm of V1, while about 29 underlie a cortical receptive field. They propose a model whereby a certain number of RGCs underlie the area of complete spatial summation (i.e., Ricco's area), which then feed into the LGN with little interference, before the neural information is further pooled by V1 cortical neurons. When considering the enlargement of Ricco's area in glaucoma, the hypothesis of a critical number of RGCs underlying Ricco's area makes logical sense as RGCs degenerate throughout the condition. As this cell death occurs, Ricco's area may need to enlarge to retain a constant number of RGCs and thus sufficient signal-to-noise ratio for light to be detected. However, it could also be argued that when neighbouring cells die, RGC receptive fields may enlarge to compensate, which may lead to alterations in Ricco's area. It is also important to consider that RGCs show shrinkage before death (e.g. Morgan, 2002) so may not have the same output as a single healthy RGC. A similar model to that described by has been previously proposed by Pan and Swanson (2006; Swanson *et al.*, 2004), who suggested that spatial pooling by orientation-tuned cortical filters could account for the relationship between perimetric defects and RGC loss. Specifically, they found that a cortical-pooling model with strongly orientation-tuned neurons agreed more strongly with previously reported spatial summation curves than weakly tuned or RGC receptive field-based approaches. Critically, multiple pooling mechanisms throughout the visual pathway were needed to explain spatial summation across perimetric stimuli. Together, these

models highlight the importance of signal pooling at a cortical stage, which may be supported by a critical number of RGCs.

3.2.1.3. Cortical contributions

Several lines of evidence support the assertion of a substantial cortical involvement in determining the size of Ricco's area. For example, it was been reported that Ricco's area is larger in the Amblyopic eye compared to the non-amblyopic eye (Je *et al.*, 2018). Considering that there is no evidence of thinning of the RGC layers in Amblyopia (Chen *et al.*, 2013; Ersan *et al.*, 2012; Szigeti *et al.*, 2014; Xu *et al.*, 2013) but there is evidence of cortical changes (Conner *et al.*, 2007; Li *et al.*, 2007), it seems possible that this change in spatial summation has a cortical origin, possibly reflecting a compensatory increase in cortical receptive field sizes and thus spatial pooling. In support of this possibility, estimates of receptive fields in V1 show enlargement in the amblyopic eye, despite normal cortical magnification factor (Clavagnier *et al.*, 2015), though the relationship between cortical receptive field size and Ricco's area in amblyopia has yet to be tested directly. A cortical involvement in amblyopia has also been replicated in more recent work, which has also suggested that amblyopia also leads to reduced cortical responsiveness (Farivar *et al.*, 2019). Cortical receptive field sizes may therefore be an important limiting factor in Ricco's area size in amblyopia.

Could changing cortical receptive fields also be the basis of the increase in Ricco's area in glaucoma? There are several points that suggest some cortical involvement within glaucoma. For example, evidence from histological studies points to shrinkage of RGCs before death in glaucoma (Morgan, 2000, 2002). A shrinkage of the RGC dendritic tree should lead to a shrinkage (rather than enlargement) of associated receptive fields (Weber *et al.*, 1998). It therefore seems unlikely that the enlargement of Ricco's area in glaucoma has a solely retinal origin. Instead, it has been hypothesised that there may be compensatory enlargement of receptive fields higher up the visual pathway in order to pool more spatial information and maintain the physiological sensitivity of the visual system (Anderson, 2006; Redmond *et al.*, 2010a).

A small number of studies have investigated cortical receptive field size in glaucoma. This was first done by King *et al.,* (2006), who investigated superior colliculus receptive fields in a rat model of glaucoma, using electrophysiological recordings. Experimental glaucoma

was induced by artificially increasing intraocular pressure (IOP) via ocular surgery. An increase in cortical receptive field size was found, which was proportional to the percentage increase of IOP and the amount of time IOP had been elevated. However, as this was based in experimental glaucoma, the results may not be representative of the mechanisms underlying chronic glaucoma in humans, especially as it is not necessarily accompanied by an elevation in IOP (i.e. NTG). In terms of assessing cortical receptive field changes in human cases of glaucoma, only one study to date has investigated this directly, which was described in a conference abstract by Liu *et al.* (2007). Functional magnetic resonance imaging (fMRI) was used to investigate estimates of cortical receptive field sizes in the occipital lobes of two 70-year-old primary-open angle glaucoma (POAG) patients and three age-similar controls. fMRI time courses were recorded during viewing of an expanding ring stimulus, which subtended the central 12° of the visual field (in which the glaucoma patients showed 'normal' visual function; this methodology is termed retinotopic mapping, which is described fully in Chapter 4). When fitting reference functions to the resulting fMRI response profiles, they found that more voxels (the 3d pixel that constitutes an MRI image) within the occipital lobe in the glaucoma patients correlated with a 'wider width' model (28% of voxels) than a 'narrower width' model (11% of voxels), while controls demonstrated a more even distribution (percentage of voxels not provided). However, it is difficult to make firm conclusions with such a small sample, and there was no mention of correction for possible cerebrovascular differences; for example, this difference in the width of response profiles may reflect differences in the haemodynamic response function (HRF; a property of the fMRI signal reflecting neural and vascular contributions) between these participants. As Liu *et al.* (2007) is a conference abstract, there is also no information given on several methodological details such as the exact method of modelling, the exact definition of a 'wider width' model or clinical characteristics of the glaucoma patients, which limits a full interpretation of their results. Nevertheless, these results are supportive of the hypothesis of a difference in cortical receptive field sizes within the occipital lobe in human glaucoma compared to healthy controls; specifically, these studies suggest an enlargement of receptive field sizes in glaucoma, similar to the enlargement of psychophysical area of complete spatial summation (i.e. Ricco's area), reported in glaucoma (Redmond *et al.*, 2010a).

The models discussed above (Kwon & Liu, 2019; Pan & Swanson, 2006; Swanson *et al.*, 2004) have also highlighted the importance of cortical pooling, especially in the orientation-tuning neurons of V1. This pooling may be able to enlarge and adapt depending on the state of the visual system; for example, in glaucoma, V1 neurones may respond to the loss of RGCs by pooling the input of more RGCs in order to maintain a constant number and thus increase receptive field size.

While a limited number of studies have investigated cortical receptive fields in glaucoma, multiple studies have suggested cortical changes in glaucoma, in terms of cortical structure of grey and white matter (e.g. Frezzotti *et al.*, 2014; Jiang *et al.*, 2018; Kasi *et al.*, 2019; Wang *et al.*, 2016; Zhang *et al.*, 2015) and lower neural activity estimated as by fMRI signal (e.g. Borges *et al.*, 2015; Chen *et al.*, 2019; Dai *et al.*, 2015; Duncan *et al.*, 2007a, 2007b; Frezzotti *et al.*, 2014, 2016; Kasi *et al.*, 2019; Murphy *et al.*, 2016; Song *et al.*, 2014; Wang *et al.*, 2018). Studies have reports regions of decreased fMRI signal in glaucoma patients compared to age-matched controls, which correspond to regions of visual field loss (Duncan *et al.*, 2007a; Qing *et al.*, 2010; Zhou *et al.*, 2017) and also demonstrated associations with markers of optic disc damage, a characteristic clinical feature of glaucoma. (Duncan *et al.*, 2007b). This is discussed further in Chapter 4. There therefore appears to significant evidence of changes to cortical structure and function in glaucoma compared to healthy controls, possibly due to compensatory reorganisation or retrograde degeneration.

It is important to note that the size of Ricco's area may arise due to contributions from multiple locations. For example, the size of the receptive fields at a certain location in the neural pathway will be determined by the receptive fields of the cells that synapse into them. This is true for receptive fields all along the visual pathway, from the RGCs, to the lateral geniculate nucleus, to the visual cortex. Ricco's area may therefore represent the psychophysical consequence of the 'net' of these receptive fields. This thesis will be examining the contribution of both retinal and cortical receptive field sizes to Ricco's area in a sample of glaucoma patients and age-similar controls.

3.2.2. Statistical modelling of Ricco's area

As described above, Ricco's area is the largest area at which Ricco's law Ricco's law (Ricco, 1877) still applies. Ricco's law states that, at threshold, area and intensity are inversely proportional. This can be defined as:

$$I * A = k$$

whereby I refers to intensity, A refers to area, and k is a constant. One a stimulus is larger than Ricco's area, it moves from complete spatial summation (following Ricco's law), to partial spatial summation. In order to estimate the size of Ricco's area, the visual sensitivity thresholds to a range of stimuli sizes (encompassing the estimated size of Ricco's area) must be measured (as can be seen in the spatial summation curves shown in Figure 3.3 and Figure 3.4). The spatial summation function underlying these thresholds can then be statistically calculated. However, multiple methods have been used throughout the literature, which both limits the ability to directly compare between studies and also leads to a range of Ricco's area estimates for the same data (this can be seen in the temporal summation domain by Mulholland *et al.*, 2015). When choosing an appropriate statistical method to use, it is therefore important to consider which most reflects the underlying physiology and also introduces the least bias.

One method of estimating Ricco's area is manual estimation, in which the point at which the data deviates from a reference line of -1 (i.e., complete spatial summation) is manually approximated (e.g. Barlow, 1958; Wilson, 1970). However, this manual involvement introduces strong operator bias (especially if one is looking for a group-wise difference and is not blind to the participant group) and may lead to an over-estimation of the critical area (Mulholland *et al.*, 2015). Alternatively, a constricted least squares analysis has also been used, in which two lines are fit to the threshold data. In this method, the first line is constrained to -1 (following Ricco's law) and the second is constrained to 0.5 (due to Piper's law; e.g. Richards, 1967) or 0 (e.g. Davila & Geisler, 1991). The breakpoint of these lines is taken as Ricco's area. This method involves less operator bias than manual estimation, but assuming the slope of the second line introduces additional problems. For example, partial summation has been shown to occur in varying degrees under certain experimental conditions (Brindley, 1970; Schefrin *et al.*, 1998; Volbrecht *et al.*, 2000a). Additionally, a constriction of 0 assumes no spatial summation and, while it is reported in

varying degrees, it is usually reported to be present, unless testing very large stimuli (Glezer, 1965). As an alternative to these methods, various studies have used a two-phase regression method (e.g. Redmond *et al.*, 2010a; Schefrin *et al.*, 1998), in which two linear regression lines are fit to the data. The first line is constrained to -1, following Ricco's law, while the intercept of the first line, slope of the second line, and the breakpoint are allowed to vary. Once again, the breakpoint of these lines is taken as Ricco's area. Multiple iterations may be completed to model the final Ricco's area value. While this method is much less susceptible to operator bias than the manual method, it is still semi-subjective as it requires manual estimation of the initial breakpoint, the intercept of the first line and the slope of the second to be input. However, it has the significant advantage of being a close fit to the data while taking into account Ricco's law and the variable nature of partial summation. By not constraining the slope of the second line, no assumptions about the degree of partial summation are made, allowing for more flexibility across experimental conditions and visual field locations.

Considering the fact that the most suitable measure of Ricco's area should be one that introduces the least operator bias but still reflects the underlying physiology, the two-phase regression appears to be the most appropriate.

Chapter 4. Objective physiological measurements

In order to investigate the neural basis of Ricco's area, receptive field size and neural structure at both the retina and cortex must be objectively measured. While neural functioning can be inferred using psychophysical measurements, this suffers from two important limitations. Firstly, psychophysics are inherently subjective, allowing for the introduction of bias and greater between-session variability. Secondly, this methodology assesses the neural pathway as a whole; it is possible that alterations at different locations can have the same psychophysical result, even when isolating a particular pathway (e.g. S-cone). It is therefore important to *objectively* and *specifically* assess neural physiology at multiple locations within the visual pathway. This chapter will outline and explain a number of objective physiological measurements and introduce how these methodologies have been applied in glaucoma; specifically, optical coherence tomography (OCT), pattern electroretinography (PERG), and structural and functional magnetic resonance imaging (MRI and fMRI) will be discussed.

4.1. Optical coherence tomography

One of the defining characteristics of glaucoma is the degeneration of retinal ganglion cells (RGCs), which are an important marker of disease progression. RGCs are localised within certain retinal layers (as described in Chapter 1), which can be imaged and quantified non-invasively using OCT. This is an increasingly commonplace imaging technology that typically uses near-infrared light and the natural reflectiveness of retinal layers to create 3D images. Unlike other scanning modalities such as MRI, OCT is limited to a scanning depth of only a few millimetres, meaning it is very limited as to what it can image. However, it has the significant advantage of a high spatial resolution (down to the µm level), comparatively low-cost screening and fast scan speed. OCT is now an established method of imaging the structure of the posterior eye in both clinics and research facilities.

OCT is based on the concept of low-coherence optical interferometry (for an illustration, see Figure 4.1). This involves a beam projected onto a semi-silvered mirror and consequentially split into a measurement beam, which enters the eye, and a reference beam. When the measurement beam reaches the retina, small amounts are reflected back

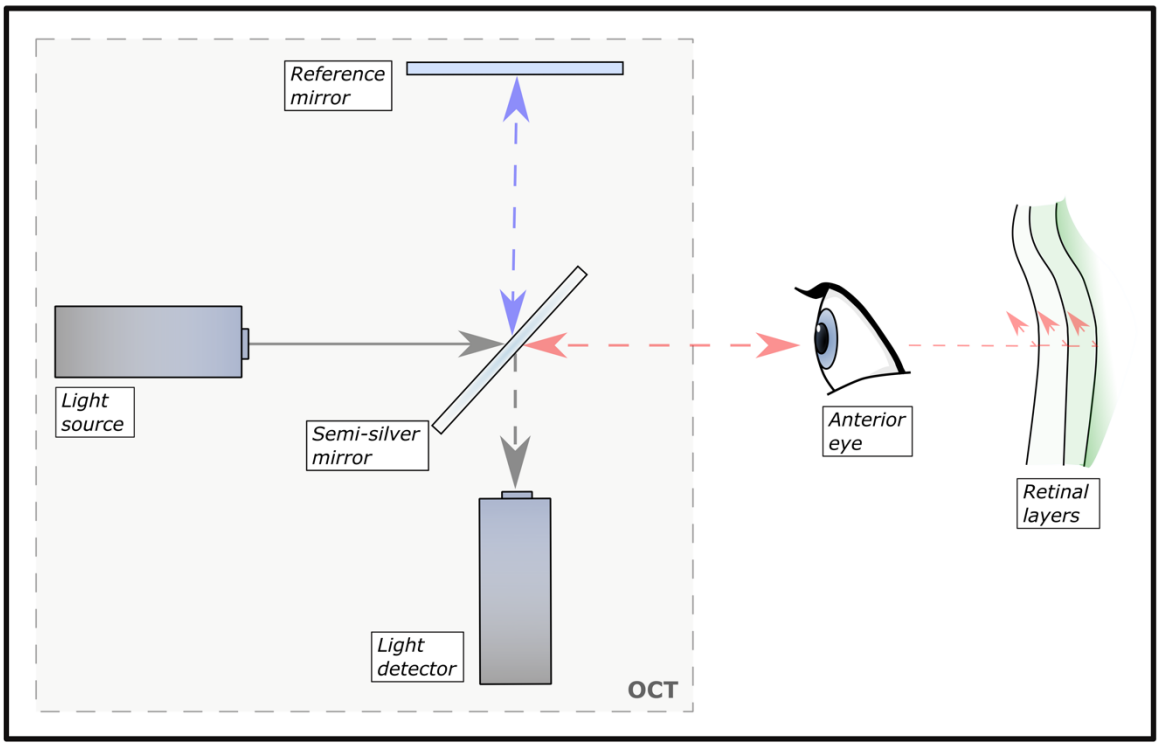

Figure 4.1 – Illustration of the workings of an Optical Coherence Tomography (OCT). Light first is emitted from a light source (grey solid arrow). Once it hits a semi-silvered mirror, it is split into a reference (blue arrow) and measurement beam (red arrow). The measurement beam enters the eye and is reflected back by the retina. As different retinal layers have different reflective properties, they are bounced back with different time delays, allowing for signals coming from different layers to be separated. When the measurement beam leaves the eye, it then re-enters the OCT and reforms with the reference beam (grey dashed arrow), which had been reflected back into its path by a reference mirror. Due to constructive and destructive interference, phase differences between the two beams can be analysed by a light detector, creating an A-scan. By moving the measurement beam across the retina, a three dimensional image can be reconstructed.

by each layer with different time delays. Each layer has different reflective properties, which allow different layers to be reflected in the reflected beam. The reflected measurement beam leaves the eye and reforms back into a single beam with the reference, which was reflected into position after the initial split using a reference mirror. This reference mirror is adjusted until the two optical paths are superimposed. Doing this gives information about the individual waveforms via constructive and destructive interference (for example, the amplitude of two waves with the same phase will add to each other, while those with opposite phases will subtract). The amplitude of this detected output allows for the construction of a 1D image of the retina (an axial a-scan). Intensity measurements will differ

at several depth points along this image (due to the reflective properties of different retinal layers) and thus allow for the distinction of different layers, depending on the resolution of the image *(though the ultimate depth of OCT imaging is restricted to a few millimetres due to light scattering and absorption; Huang* et al*., 1991)*. A 3D image is built up using many such measurements, which must be taken quickly to ensure patient comfort and to minimise movement. By moving the system laterally, a series of a-scans can be taken and used to form a 2D image (a b-scan), while adding a second direction produces a 3D structural image (a c-scan).

4.1.1 Applications in glaucoma

Following the first demonstration of OCT technology in 1991 (Huang *et al.*, 1991), the relevance of the technology to glaucoma detection and monitoring was quickly realised (Schuman *et al.*, 1995). While glaucoma progression can be tracked using visual field testing, these may require multiple visits, have poor test-retest reliability, and show learning effects (Katz *et al.*, 1995; Pierre-Filho *et al.*, 2010). The use of a more objective structural measure such as OCT therefore provides complimentary diagnostic information by imaging the optic nerve head, macula, or specific retinal layers. The diagnostic accuracy of OCT has been demonstrated across commercially available devices (i.e. Zeiss Stratus, Zeiss Cirrus, Heidelberg Spectralis and Optovue RTVue, and Topcon 3D-OCT), especially with increasing severity of glaucoma (Kansal *et al.*, 2018). Several parameters have proved to be informative for glaucoma diagnosis (Gracitelli *et al.*, 2015). Of particular interest in the macula are the retinal nerve fibre layer (RNFL), ganglion cell complex (GCC; composed of the macular nerve fibre layer, inner plexiform layer, and ganglion cell layer) and ganglion cell-inner plexiform layers (GCIPL), as retinal thinning in these layers are characteristic of RGC damage in glaucoma (see chapter 1 for a discussion of these retinal layers). Kansal *et al.* (2018) carried out a large-scale meta-analysis on 150 studies and over 16,000 glaucomatous eyes and reported high classification accuracy for the RNFL (area under the receiver operator characteristic curve [AUROC] = 0.897), macula GCC (AUROC = 0.885), and macula GCIPL (AUROC = 0.858). The diagnostic classification capability of these segmented layers was higher than the total macular thickness (AUROC = 0.795). Structure-function relationships in glaucoma have been discussed previously in Chapter 2.

4.2. Electroretinography

While OCT allows for structural imaging, this does not necessarily equate to functionality and cannot capture dysfunction or functional receptive field changes that may occur in disease state. To assess the retinal function that may contribute to psychophysical phenomenon in glaucoma, electroretinography (ERG), a retinal electrophysiological technique, was investigated.

ERG is a measure of transient changes in an eye's resting potential in response to light. Gross biological and background activity is removed with the aid of a nearby reference electrode. The shape of the recorded electrical waveform differs depending on the spatial, temporal, and frequency properties of the light stimulus used to elicit it. In the simplest form, an early receptor potential (ERP) can be recorded in response to an intense light flash with a short latency. This response typically occurs 1.5ms after stimulus onset and can be delineated into different 'waves' that reflect the response of different cell groups (see Figure 4.2.).

Following a flash, there is an initial negative-going response within a few milliseconds termed the *a-wave*, suggested to be of a majorly photoreceptor origin. In dark-adapted eyes, the *a-wave* is suggested to be mostly driven by rod cells and associated circuits, with the initial 'dip' dominated by the hyperpolarisation of the rod axon and synaptic terminals (Frishman, 2017). The amplitude of this is sensitive to rod photoreceptor degradation in an animal model (Hirota *et al.*, 2012), though it is also partly reflective of post-photoreceptor cells, as the amplitude also decreased once light-evoked horizontal cell and hyperpolarizing bipolar cell activity had been suppressed (Bush & Sieving, 1994).

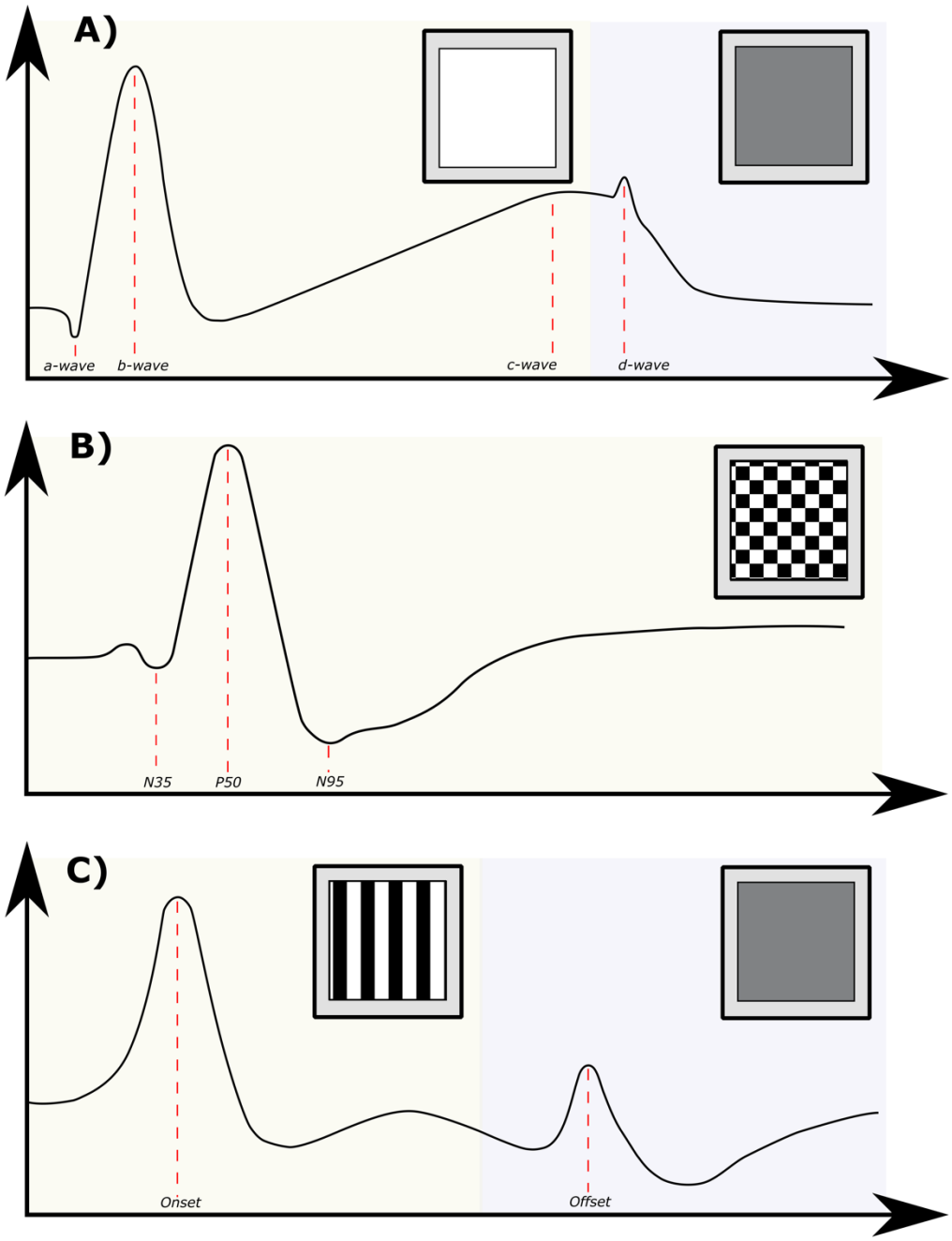

Figure 4.2 – Demonstration of traces typically recorded in response to A) flash electroretinogram (ERG), B) pattern-reversal ERG, and C) pattern onset-offset ERG. Monitor inserts show typical stimuli used to elicit these traces. The Y-axis is amplitude, while the X-axis is time (not to scale). Red dashed lined mark biologically relevant components.

The next major component is the *b-wave*. This is characterised by a large positive-going peak with a post-photoreceptor origin (e.g. Nilsson, 1971). Specifically, it is suggested to be dependent on ON-bipolar cell depolarisation and varies with stimulus intensity and contrast (Frishman, 2017; Stockton & Slaughter, 1989). Imposed on this *b-wave* are high-frequency, low-amplitude oscillatory potentials (OPs). Unlike the above components, they are optimally recorded in mesopic conditions, reflecting both scotopic and photopic processes, and their number and amplitude depend on the level of adaption and stimulus intensity (Thompson, 1987). It has been suggested that these OPs can be classified into early, intermediate, and late subgroups, which each have different likely generators, these being photoreceptors, non-spiking activity and spiking activity of ON-pathway cells (such as amacrine cells) respectively (Dong *et al.*, 2004; Wachtmeister, 1998). These have also been used for tracking nerve conductance from retina to cortex (Westner & Dalal, 2017).

The next major component is the *c-wave*, which depends on the integrity and complementary functioning of the pigment epithelium and rods (Thompson, 1987). Consequently, the *c-wave* is abnormal in vitelliruptive macular degeneration, which is a generalised defect of the pigment epithelium (Nilsson & Skoog, 1980).

Finally, the *d-wave* is suggested to be the depolarisation of OFF-bipolar cells and/or horizontal cells at the termination of illumination (Stockton & Slaughter, 1989).

The fact that different parts of this flash-ERG response can be mapped onto different cells allows specific retinal layers to be examined in different light conditions or pathology. However, to optimally examine the inner retina, which is primarily affected by glaucoma, another form of ERG is required.

4.2.1. Pattern ERG

Pattern ERG (PERG) is the bio-potential evoked by temporally modulated pattered stimuli, typically a grating or checkerboard, of constant mean luminance. It is assumed that since there is no change in the overall luminance, the linear responses described above (e.g. *b-wave*) should remain constant and only non-linear responses, sensitive to local changes in luminance, remain. It was first described by Riggs *et al.* (1964), who suggested it as a method of reducing stimulus-locked stray light due to the constant mean luminance. Compared to full-field ERGs, PERG has a very small amplitude, around 0.5-8µV (microvolts),

so extra attention must be paid to possible contaminating noise or artefacts, as well as maintaining low impedance in equipment.

A common form of PERG uses pattern-reversal stimuli, in which the high-luminance and low-luminance portions swap at a certain temporal frequency. The waveform this produces depends heavily on this temporal frequency, which further splits pattern-reversal PERG into two subtypes. The first is the transient PERG, produced when a pattern is reversing slowly at 3Hz or less. This produces a characteristic and reproducible wave form (Otto & Bach, 1997), shown in Figure 4.2., with the three main components; N35, P50, and N95 . These are typically described using latency – which is measured from onset – and amplitude – which is measured between peaks and troughs.

Some of the first studies investigating the origins of these transient PERG components looked at optic nerve sections in animals, which would lead to RGC degeneration but intact photoreceptors. These studies demonstrated that while full-field ERGs were maintained, the PERG signal was eliminated, suggesting that RGCs are a major contributor to PERG (Maffei & Fiorentini, 1981). However, later studies in human and animals found that P50 preservation could still be seen even after total RGC loss (Blondeau *et al.*, 1987; Harrison *et al.*, 1987), suggesting that RGCs were not the exclusive generator. N95 appears to mainly reflect RGC spiking activity, while non-spiking activity, possibly including nearby bipolar cells, is included in P50 amplitude (Luo & Frishman, 2011). Bach, Cuno and Hoffman (2018) therefore theorised that P50 reflects the spatial distribution and density of RGC bodies, while N95 is mostly reflective of the axonal spiking activity that occurs at the 90° fibre deflection at the optic nerve head. To investigate this, they used multifocal PERG at 30 retinal locations in 21 healthy participants. By examining retinal conduction speeds, they found that while both were influenced by eccentricity (with shorter speeds in the periphery), the N95-like signal was also influenced by distance from optic nerve head. This supports the hypothesis that while P50 reflects spiking and non-spiking activity near the ganglion cell body, N95 reflects RGC axonal spiking activity, particularly that which occurs at the turn into the optic nerve head.

When a higher temporal frequency of the pattern-reversal presentation is used, a steady-state PERG (SS-PERG) wave form is produced, which is a sinusoidal waveform that requires Fourier transform to extract amplitude and phase shift. This is suggested to be N95-

dominated (Holder, 2001), shows evidence of N95-like spatial tuning (Hess & Baker, 1984), and current source density analysis suggests a RGC origin (Baker *et al.*, 1988). While transient PERG components are suggested to be comprised of equal ON and OFF pathways, SS-PERG is found to be mainly reflective of ON-pathway spiking (Luo & Frishman, 2011).

Finally, an alternative form of PERG is the onset-offset PERG, which involves presenting a pattern for a set amount of time (onset), and then alternating it with a uniform mean-luminance field (offset) at a set temporal frequency. This produces a distinct onset and offset response, which can be seen in Figure 4.2. Similar to N95, the onset response seems to have a major RGC component; for example, when the luminance component of the response is removed to leave the pattern specific response (PSR), strong spatial tuning is evident at multiple eccentricities of the visual field (Drasdo *et al.*, 1987; Thompson & Drasdo, 1987) and it is found to correlate with RGC layer volume in healthy adults (Drasdo *et al.*, 1990). For achromatic luminance patterns, pattern onset-offset shows greater spatial tuning than pattern-reversal PERG despite lower average amplitudes (Korth & Rix, 1989), suggesting it may be more sensitive to RGC antagonistic centre-surround receptive field processes. Peak latency also increases with increasing spatial frequency, which could reflect a shift from cells with different response times and receptive field sizes.

4.2.2. Technology

The electrical response is directly recorded using an active electrode, which is placed in a location such as the edge of the lower fornix. Multiple types of active electrodes are available, from fibres to contact lens electrodes, though the latter are typically not used in PERG due to possible image degradation. Responses to visual stimuli can then be recorded, with background biological noise removed by recording activity at a nearby location with a reference electrode and subtracting this from the active recording. If these electrodes are close enough, it is assumed that the only difference should be the retinal response, so this is amplified. The ipsilateral outer canthus is typically used as a location for the reference electrode, as it is less susceptible to possible contamination from the fellow eye or cortical sources. A separate ground electrode is placed elsewhere on the body (such as the forehead) and is used for common mode rejection, preventing, for example, mains power from interfering with the biological response of interest (Biopac.com, 2014). Especially when recording a small signal, such as the PERG, it is important that these electrodes are placed

with as low impedance as possible, but at least below 5kΩ measured in situ (Bach *et al.*, 2013). This impedance can be improved with cleaning the skin and conductive gel inside the electrode. Additionally, if the electrodes are nominally non-polarizable silver/silver-chloride coated, then this must be monitored for if it is worn off then polarisation may occur and the input from that electrode will be imbalanced (Arden, 2006).

A large number of recordings (aka. sweeps) are typically taken (i.e. 100-300; Bach *et al.*, 2013), which are averaged into a single result (which may be then averaged again over multiple results for optimised signal to noise ratio). Dim or normal background illumination is recommended, with irrelevant bright lights out of view, which must be kept consistent across recordings. Pharmacological pupil dilation can be used for full-field ERG in order to ensure the stimuli hits the entire retinal surface, and thus assesses the entire retina and evokes the strongest response. While increasing flash luminance can also increase response amplitude, this cannot completely compensate for a small pupil size (Gagné *et al.*, 2010). However, this is not recommended for PERG due to the image degradation that will occur, which will blur high spatial frequency patterns.

It is important to be aware of and knowledgeable about possible artefacts that may distort the data. One of the most common causes of this is electrical mains noise, which operates at 50Hz. Notch 50Hz filtering may be used in some cases to remove mains power noise, but this is not recommended in PERG as it is a similar frequency to the response of interest. A notch filter may therefore remove some of this target response, so it is important to reduce mains noise using other methods, such as ensuring the room is electrically quiet. This can be done by enclosing electrical outlets in grounded, metallic casing or trunking. If possible, the room should also have a mains supply that is kept separate from the rest of the building to reduce contamination from other equipment (Arden, 2006).

Patient movement can also be a major source of artefacts in the data. This is due to electrical activity from the movement of muscles (e.g. jaw clenching, eye blinks/movements) or from the triboelectric effect, which is when a current is caused when the electrode is in contact with a material (i.e. the skin) and then is separated. A particular issue is the photomyoclonic reflex (Arden, 2006; Johnson & Massof, 1982), which is a rapid reflex in the eye and neck muscles in response to light. This has a delay of ~59ms, so can interfere with interpretation of the *b-wave* or the PERG signal. Habituation (repeated stimulus

presentations) or conditioned suppression (by pairing it with an auditory tone that does not elicit it) can reduce the amplitude, but Johnson & Massof (1982) suggest that while this reduces the effect, it makes it more difficult for automatic artefact rejection. Certain electrodes, such as the bipolar or gold foil, may also be more susceptible (Johnson & Massof, 1982). This effect is especially seen when the patient is uncomfortable and the neck in extended, highlighting the importance in making sure the participant is comfortable and given frequent breaks throughout a procedure. This was also initially demonstrated using flash ERG; it may be less impactful using PERG stimuli as the mean luminance stays constant. Excessive eye movements or blinks may also displace the active electrode, causing a sudden reduction in signal. Blinking can be prevented by using weaker flashes to evoke the scotopic threshold, using a fixation spot/cross, and asking the participant to blink before a flash occurs (Arden, 2006). The is also some evidence that PERG responses can change in glaucoma patients with head position (Ventura *et al.*, 2013), so this should also be kept consistent throughout participants with the use of, for example, a head and chin rest.

Filtering the data as it is being recorded can help artefact removal before it can contaminate the data, and it is recommended that this is set to a bandpass filter of 1-100Hz. Live artefact rejection is also considered essential and should be set as at least 100Hz, preferably less (Bach *et al.*, 2013). Manual removal of eye blinks from individual sweeps, characterised by sharp, steep increases in amplitude, may also be needed.

4.2.3. Applications in glaucoma

Different ERG methodologies allow for not only non-invasive assessment of retinal functioning, but also specific targeting of different cells and retinal layers. The electroretinography technique that has most often been translated to glaucoma is the PERG, due to its coupling with the typical site of glaucoma damage, the retinal nerve fibre layer. The first study into this reported that glaucoma patients exhibit a decrease in PERG amplitude in 1982 (May *et al.*, 1982), and since then a decrease in transient (P50 and N95) and sustained PERG amplitude (but not latency) has been demonstrated many times (e.g. Almrcegui Lafita *et al.*, 1997; Bach & Hoffmann, 2008; Bobak *et al.*, 1983; Ganekal *et al.*, 2013; Hiss & Fahl, 1991; Tiryaki Demir *et al.*, 2015; Uclés *et al.*, 1997; Viswanathan *et al.*, 2000; Wanger & Persson, 1983), showing associations with other established clinical measures (e.g. Bach *et al.*, 2006; Cvenkel *et al.*, 2017; Garway-Heath *et al.*, 2002; Hood *et*

al., 2005; Papst *et al.*, 1984; Wilsey *et al.*, 2017) and distinguishing between patterns of damage (Jung *et al.*, 2019; Salgarello *et al.*, 2018). Only one study did not report this difference, but this study was limited by the use of the fellow eye as a control (van den Berg *et al.*, 1986). As glaucoma is often bilateral and PERG deficits occur reliably before visual field damage (Arai *et al.*, 1993; Bach *et al.*, 2006; Karaśkiewicz *et al.*, 2014), it is likely that the amplitude in the fellow eye was already depressed. This diminished PERG amplitude in glaucomatous eyes makes sense when considering the loci of damage in the condition, the RGCs. For example, P50 is estimated to have approximately a third of its amplitude generated by pre-ganglionic retinal sources and the rest by non-spiking activity in the RGC cell body, while N95 is mostly RGC axonal spiking activity, especially at the optic nerve head (Bach *et al.*, 2018; Bach & Poloschek, 2013). Subsequently, P50 shows slightly less of reduction in animal models and human glaucoma patients than N95 (Bach & Hoffmann, 2008; Cvenkel *et al.*, 2017; Tiryaki Demir *et al.*, 2015; Viswanathan *et al.*, 2000).

PERG amplitudes have also proved useful in measuring the effectiveness of glaucoma treatments; for example, Karaśkiewicz and colleagues (2017) found that, in a sample of 24 patients with pre-perimetric (N=11) or early-stage glaucoma (N=13), intraocular pressure (IOP) lowering treatment also increased P50 and N95 amplitude by 28% and 38% respectively. This suggests that significantly lowering IOP in early glaucoma can improve or recover RGC function, possibly due to the reduction of mechanistic pressure deforming tissues and restricting perfusion. However, the inclusion of only pre-perimetric or early glaucoma also prevents investigation into at what point in the course of glaucoma progression RGC function can still be recovered. While other electrophysiological work supports this suggestion that RGC function can be improved (Parisi, 2005; Sehi *et al.*, 2010; Ventura & Porciatti, 2005; Wittström *et al.*, 2010) or function loss stabilised (Ventura *et al.*, 2012), other work is more mixed (Sehi *et al.*, 2011; Waisbourd *et al.*, 2016), possibly due to the range of methodologies, glaucoma subtype and treatment programs used.

In terms of diagnostic utility, it has been suggested that sustained PERG may be more efficacious than transient PERG, showing a greater glaucomatous decrease than either P50 or N95 (Bach & Hoffmann, 2008). However, this is only up to 18 reversals per second, possibly due to reduced signal to noise ratio reported at higher temporal frequencies (Hiss & Fahl, 1991). Furthermore, this effect also appears to be spatial frequency dependent.

Bach and colleagues (Bach *et al.*, 1988; Bach & Hoffmann, 2008; Bach & Holder, 1996) demonstrate that early glaucoma patients show a reduction in amplitude in response to small checks, while the response to large check is relatively spared (while responses to both sizes are reduced in severe glaucoma). This relative sparing of larger checks lead to the development of a metric termed the PERG ratio (Bach & Hoffmann, 2008), which is as follows:

$$\textit{PERG ratio} = \frac{PERG\ amplitude\ to\ 0.8°\ checks}{PERG\ amplitude\ to\ 16°\ checks}$$

This has proven to be a powerful methodology for detecting and predicting progression to glaucoma in high risk eyes up to four years before any visual field loss is apparent, as demonstrated in 1-year (Pfeiffer *et al.*, 1993), ~8-year (Bach *et al.*, 2006), and ~10-year longitudinal studies (Bode *et al.*, 2011). However, an important limitation is that, like any ratio approach, it becomes unreliable when the denominator becomes too small, so is less useful in more severe glaucoma cases. It is also less precise than transient PERG, with N95 and P50 associated with spiking and non-spiking activity near the ganglion cell body, and RGC axonal spiking activity respectively (Bach *et al.*, 2018) that may be more useful in research environments. It will also be confounded by anything that will systematically reduce image quality. For example, cataract or dioptric defocus will impact the PERG induced by the small cheques more than the larger cheques (Bach *et al.*, 1988), independently altering the ratio.

The onset-offset PERG methodology has been less utilised within the field of glaucoma, despite demonstrating more dramatic spatial tuning characteristics (Drasdo *et al.*, 1987; Korth & Rix, 1989). One such study was completed by Korth and colleagues (1989), who investigated changes in onset amplitude with age, with a sample of 147 healthy participants with ages ranging from 14-79 years, and with glaucoma, using a sample of 110 eyes from 65 patients with either primary open angle glaucoma (POAG; 83 eyes), closed angle glaucoma (CAG; 4 eyes), secondary open angle glaucoma (SOAG; 6 eyes), or ocular hypertension (OHT; 17 eyes). They recorded PERG responses to both a 0.2 cycles-per-degree (cpd) and 3.4cpd vertical square-wave grating, which was visible for 312ms and invisible for 291ms. The pattern was hidden by vibrating it using an optical scanner. They detected no change in space-averaged luminance during the stimulus cycle. The 3.4cpd onset peak

showed a steady decrease with age, cup-to-disc ratio, and visual field loss. When restricting the analysis to all healthy controls and glaucoma patients above 50 years old (59 and 74 participants respectively) they found a significant decrease in amplitude, but not latency (this was also found to a lesser degree with the OHT eyes). When comparing spatial frequencies within groups (24 controls and 26 glaucoma patients), they found that while controls show attenuation at the 0.2cpd stimulus, suggesting spatial tuning, this difference was not found in the glaucoma patients; the amplitudes were similar for both spatial frequencies. They suggested that this demonstrated a lack of spatial tuning in glaucoma. However, by only looking at two spatial frequencies, it is impossible to say whether the curve simply shifted, or differed in shape, rather than flattened.

4.3. Magnetic resonance imaging

Finally, to capture a full picture of the neural visual pathway, structural and functional imaging of the *in vivo* cortex was needed. Since the first full human body scan in 1977, magnetic resonance imaging (MRI) has become a mainstay of hospitals and academic research. From detecting tumours, to mapping functional activation, to plotting the white matter wiring of the entire human brain, MRI methods continue to develop and fuel investigation into the workings of the human body. In regard to imaging the brain, it remains one of the most popular tools of functional and structural investigation. While each body part has its own challenges for scanning, the brain has the advantage of being relatively close to the surface and far from the constant large-scale movement of the torso (though not completely free of physiological motion). Additionally, it receives a very dense blood supply, making it an ideal candidate for functional MRI, which relies on the neurovascular response. This section will first explain how the signal for both structural and functional MRI (sMRI and fMRI respectively) is derived, before discussing methods of investigating the visual cortex and cortical receptive field sizes, an area of particular relevance to this PhD.

4.3.1 The magnetic resonance signal

MRI works via the interaction between nuclei and the magnetic field, which is produced by a super-conducting magnet. Molecules with odd mass numbers, such as hydrogen, are termed MR-active as, due to having a net charge and being in motion, they acquire magnetic moments (MM) that align with an external magnetic field, such as the MR

magnet. They align either parallel (low-energy) or anti-parallel (high-energy). Together, the molecules within the tissue have a net magnetic vector (NMV), which reflects the balance between these populations. The scanner then applies a radiofrequency (RF) pulse at the Larmor frequency of the nuclei of interest, which is typically hydrogen. The Larmor frequency is the frequency that the MM is spinning and matching this causes a transfer of energy (resonance). This leads to some MMs passing from the low energy to the high-energy population, causing the NMV to move away from the external magnetic field. It also has the effect of causing the MMs to spin in phase with each other. When the RF pulse is turned off, the MNV again starts to realign to the external magnet, which has the effect of more energy in the longitudinal plane (more low-energy population, in alignment with the magnet; T1 recovery), and less in the transverse plane (less high-energy population, out of alignment; T2 decay). MMs also become less in phase with the process of T2 decay. This signal is collected using the receiver coil. Different tissues will have different T1 recovery and T2 decay times depending on properties such as the molecular density and molecular tumbling rate. The difference in these rates become the basis for contrasts within the MRI scan. For example, in a T1 structural scan, the contrast is due to the differences between tissues in T1 recovery time (fat has a fast recovery, so will produce a greater signal than water, which has a slow recovery). Other contrasts can be created by looking at different factors, such as the difference in T2 decay (T2-weighted image) or the displacement of water molecules (diffusion MRI). Depending on what aspect one is interested in – tissue volume, structural connectivity, pathology – a contrast can be selected that provides high resolution information anywhere in the brain.

4.3.2 Functional magnetic resonance imaging

A popular application of MRI technology is to estimate neural activity, termed functional MRI (fMRI). The most common way to estimate this is by using the blood-oxygen level dependant (BOLD) signal, which utilises the fact that oxyhaemoglobin and deoxyhaemoglobin have different magnetic properties and therefore changes in their ratio will disturb the magnetic field. This disruption produces the BOLD signal, from which neural activation can be inferred.

The process of BOLD fMRI can be roughly split into four stages following stimulation (e.g. a visual stimulus) or task (Iannetti & Wise, 2007). First is the neural activity itself. The

exact nature of the neural activity underlying the BOLD signal is complex. It appears to most strongly represent input and intracortical synaptic processing rather than the spiking output of a given cortical area, as seen by its greater associations with local field potentials rather than single- or multiple-unit recordings (Goense & Logothetis, 2008; Logothetis *et al.*, 2001). Task-based BOLD experiments also typically only show activation by comparing a 'task' or 'stimulated' state with a 'rest' or 'non-stimulated' state. Increases or decreases in BOLD activity may therefore represent many different balances of excitatory or inhibitory activity, so it difficult to delineate the exact processes underlying the change (Logothetis, 2008). For example, an increase in BOLD may represent an increase in excitatory activity, or a decrease in inhibitory activity, or a shift in the ratio between them.

Following neural activity, there is a corresponding increase in metabolic demand to meet the energy requirements. The neurons must therefore be able to signal to nearby vessels to increase local cerebral blood flow (CBF) and thus oxygen supply to the activated cells. There are a number of pathways through which this may be accomplished, such as metabolic (Bélanger *et al.*, 2011; Magistretti & Pellerin, 1999) or neurotransmitter signalling (Attwell & Iadecola, 2002). The exact mechanism is still not known and may differ across the brain. A recent review found that the most prominent signal mediator was neuronal nitric oxide, blockage of which led to a 64% reduction in the neurovascular response. Addition of other targets to this had no further effect, suggesting that the final third of neurovascular signalling works via a so far unknown mechanism (Hosford & Gourine, 2019).

The following stage is referred to as cerebrovascular reactivity and encompasses the group of processes that follow vessel signalling and lead to the haemodynamic changes within the tissue that underlie the BOLD response (Iannetti & Wise, 2007). This includes the increase in local CBF and cerebral blood volume (CBV) in response to signalling, as well as the changes in concentration of oxygenated blood and subsequent rate of oxygen metabolism. As these have a direct impact on the concentration of deoxygenated blood present, they have a direct impact on the BOLD signal and must therefore be considered in its interpretation.

When local neural activity leads to vasodilation, the coupled CBF increase is significantly larger than the metabolic demand (45% increase in CBF vs. 16% in demand), leading to an excessive increase in local oxygenated blood (Davis *et al.*, 1998). This means

that even though oxygen metabolism increases in order to meet the energy demand, paramagnetic deoxyhaemoglobin concentration still decreases. This shift in the sum magnetic properties is detected as the BOLD signal, the final stage in BOLD fMRI, and the exact characteristics of this, such as the resolution, depends on the scanner properties and scan parameters. The spatial resolution of a fMRI image is limited by the signal-to-noise ratio (SNR) of the signal, which itself is proportional to the static field strength, total scan time, and voxel size (Cheng, 2018). In general, longer scans and higher field strengths allow for greater SNR, which in turns allows for smaller voxel sizes and thus finer spatial resolution. Higher field strength fMRI is also less sensitive to large draining veins that may contaminate the signal (Uludağ & Blinder, 2018; Yacoub *et al.*, 2007), allowing for more accurate assessment of the target tissue and fine structures such as ocular dominance columns (Cheng, 2012, 2018). In addition, the time between presentation of the stimulus to the peak of the haemodynamic response is about 5 seconds. Due to this inherent, physiological lag, there is a limit on the temporal resolution that BOLD fMRI can achieve, which must be considered during analysis and methods design.

4.3.3 Retinotopic mapping

It was discovered early on that damage to certain parts of the occipital cortex lead to the loss of vision in certain parts of the visual field (Glickstein & Whitteridge, 1987; Holmes, 1918). This lead to the discovery of 'retinotopic maps' within the visual areas of the brain; essentially, the visual field is processed by a corresponding 'map' within the brain, with neighbouring neurons responsible for processing neighbouring sections of the visual field. Hence, when the superior portion of V1 (the primary visual area) is damaged, it reliably 'knocks out' the inferior portion of the visual field. These early researchers also made the important observations that one hemisphere processes the contralateral side of visual space and that the fovea appears to over-represented compared to the periphery (termed cortical magnification).

With the advent of fMRI, these retinotopic maps could be visualised, signalling a move from neuropsychological case studies of brain damaged patients and invasive neural recordings in animals to non-invasive human work. This traditionally used phase-encoding (or travelling wave) retinotopic mapping, so called because it relies on the phase of BOLD activation rather than the amplitude (Engel, 1997; Sereno *et al.*, 1995). Each point of the

visual field is systematically stimulated using a moving stimulus that elicits a strong visual response. The tissue that is most response to each visual field position is localised by comparing the stimulus and BOLD signal time courses. By examining the retinotopic maps representing eccentricity and polar angle, cortical visual areas have been identified across the neural hierarchy, from the primary visual areas (Dougherty *et al.*, 2003; Sereno *et al.*, 1995; Wandell *et al.*, 2007) to frontal and parietal regions (Silver & Kastner, 2009; Wandell *et al.*, 2007).

However, each fMRI voxel does not contain a single neuron with a single point in the visual field that it responds to. Instead, each voxel can contain up to millions of neurons (depending on voxel size), each with a certain amount of the visual field that it is responsive to (i.e. the associated receptive field sizes). These cortical receptive field sizes can be modelled using a method termed population receptive field (pRF) mapping.

4.3.3.1 Population receptive field mapping

While receptive fields are too small to image directly with MRI, they are possible to measure at the millimetre scale using a method termed population receptive field (pRF) mapping. This allows the receptive field of the population of neurons within a voxel to be estimated quantitatively (for an illustration of this, see Figure 4.3). The ability to detect pRFs within an fMRI time course was noted early on by Tootell et al. (1997), who found that V1 and V3A had different responses to retinotopic mapping stimuli. They suggested that this may reflect an enlargement of receptive field sizes in V3A compared to V1. Dumoulin and Wandell (2008) later developed a quantifiable framework to model pRF properties and importantly fit these to an fMRI time series from a traditional retinotopy dataset (see Figure 4.4). Their model suggested that pRFs can be represented by a 2D Gaussian curve, which can be defined by the following:

$$g(x,y) = \ exp\left(-\frac{(x-x_0)^2+(y-y_0)^2}{2\sigma^2}\right)$$

whereby x_0 and y_0 refer to the central visual field, σ is the standard deviation of the Gaussian curve (i.e. the pRF size), and x and y refers to the position of the pRF. All parameters are in degrees of visual angle (°), except for the amplitudes (% BOLD/deg^2/sec), and so rely on the dimensions of the effective stimulus. The stimulus is included in the

model as a binary model that varies across space and time, which assumes that the stimulus stimulates the cortex equally.

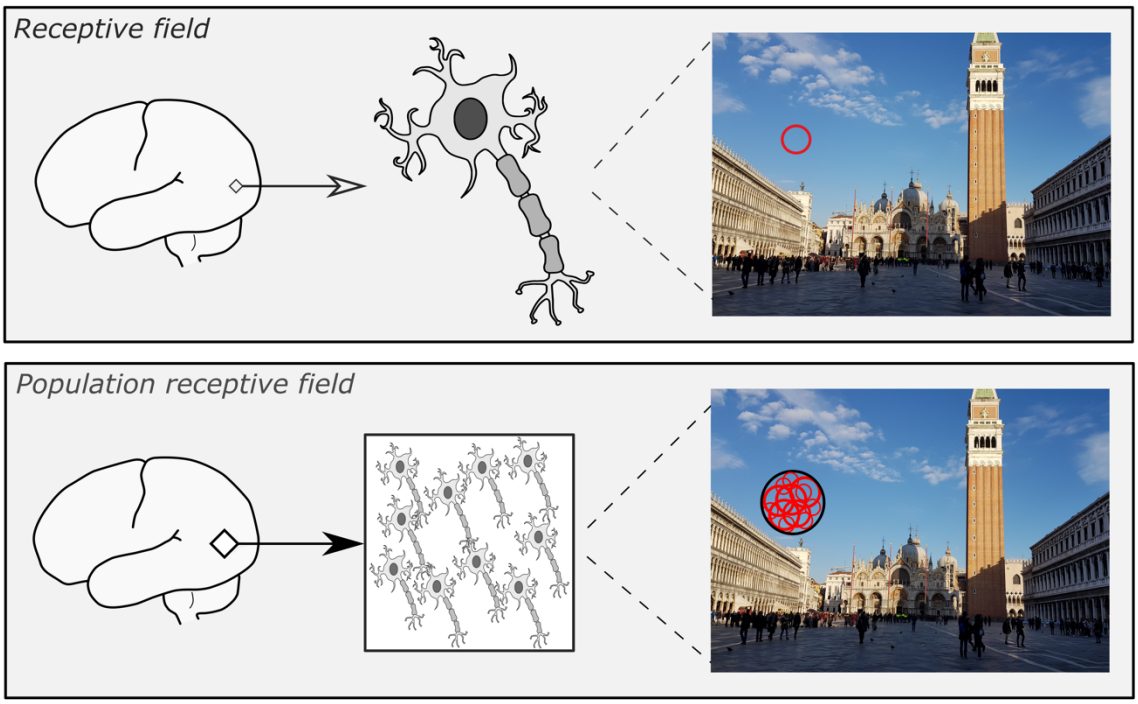

Figure 4.3 – Schematic illustration of a receptive field versus a population receptive field (pRF). The top row illustrates a neuron within a particular part of the visual cortex. The red circle on the image corresponds to that neuron's receptive field (i.e. the amount of the visual field in which a stimulus will elicit a response in that neurone). The bottom row shows a voxel within the visual cortex, which will encompass a large number of neurons. Each red circle in the image correspond to a neuron's receptive field, while the black circle surrounding these reflects the pRF. Using fMRI, the pRF can be modelled from the fMRI signal and inferences can be made about the underlying receptive field size.

Given the Gaussian model and stimulus, a predicted pRF time course can then be generated by calculating the overlap ($r(t)$) between a model pRF ($g(x, y)$) and the stimulus ($s(x, y, t)$) at each voxel, throughout the time course.

$$r(t) = \sum_{x,y} s(x, y, t)g(x, y)$$

This is then convolved with the haemodynamic response function (HRF; $h(t)$). A standard HRF can be used, or this can be individually estimated per participant to account for more variance in the data. This convolution is done as follows:

$$p(t) = r(t) * h(t)$$

With $p(t)$ being the final predicted time course. In order to calculate the optimum pRF parameters, goodness-of-fit is assessed in each voxel by computing the residual sum of squares (*RSS*) between the predicted ($p(t)$) and actual time course ($y(t)$).This calculation allows for the scale factor, β, which accounts for unknown units of the fMRI signal.

$$RSS = \sum_{t} (y(t) - p(t)\beta)^2$$

The *RSS* is minimised using a two-stage course-to-fine approach. After being projected onto the grey matter surface, the data is heavily smoothed for the first stage, increasing signal-to-noise ratio and allowing for a first estimate of the pRF parameters with minimal processing time. This can then be further refined in the second stage, during which no smoothing is applied. This course-to-fit approach minimises processing time and also increases the likelihood of finding a global minimum (Dumoulin & Wandell, 2008). The resulting estimated pRF sizes in V1-3 were found to correspond well to equivalents in primate and human electrophysiology (Victor *et al.*, 1994; Yoshor *et al.*, 2007), suggesting it represents a biologically relevant estimate of cortical receptive fields. A flowchart illustrating this modelling process can be found in Figure 4.4.

This pRF modelling has been used across multiple domains. pRF size appears to be a relatively age-resistant characteristic in early/mid-life (Dekker *et al.*, 2019) but shows some enlargement in senescence (Brewer & Barton, 2014). This enlargement may explain decreases in central visual acuity seen in older age (Brewer & Barton, 2014; Kline *et al.*,

2001), especially as fixation losses during retinotopic mapping do not appear to increase with age and therefore do not explain the results (Crossland *et al.*, 2008).

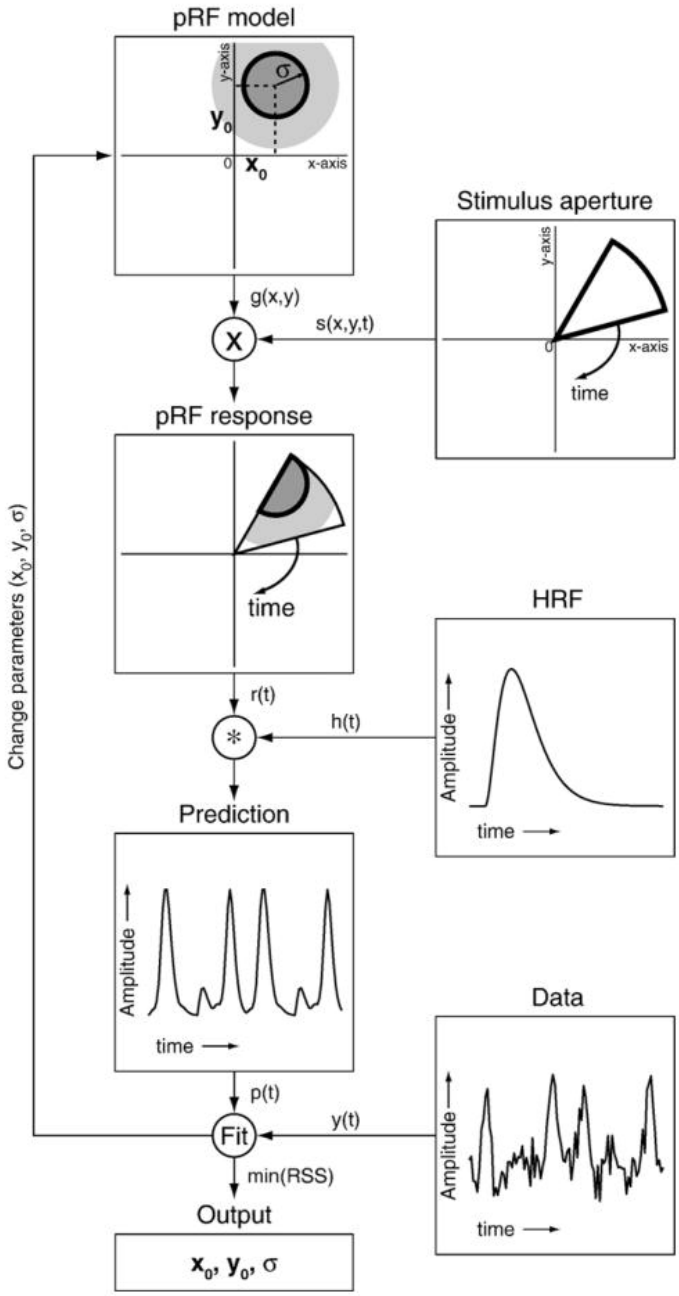

*Figure 4.4 – Flowchart of the population receptive field (pRF) analysis process. x_0 and y_0 refer to the central visual field, σ is the standard deviation of the Gaussian curve (i.e. the pRF size), x and y refers to the position of the pRF, ($r(t)$) is the overlap between a model pRF ($g(x,y)$) and the stimulus ($s(x,y,t)$), HRF is the haemodynamic response function, h(t) is the HRF time course to be used for convolution. The goodness-of-fit is assessed in each voxel by computing the residual sum of squares (*RSS*) between the predicted ($p(t)$) and actual time course ($y(t)$). Flowchart taken from Dumoulin and Wandell (2008).*

pRF metrics have been shown to differ in a number of conditions, such as Autism spectrum disorder (Schwarzkopf *et al.*, 2014), Alzheimer's disease (Brewer & Barton, 2014), albinism (Ahmadi *et al.*, 2019b), FHONDA-syndrome (Ahmadi *et al.*, 2019a), and macular degeneration (Shao *et al.*, 2013). Clavagnier, Dumoulin and Hess (2015) used pRF modelling to investigate cortical deficits in amblyopia, which is psychophysically characterised by loss of contrast sensitivity (Hess & Howell, 1977), spatial distortions (Lagreze & Sireteanu, 1991), reduced form and motion sensitivity (Aaen-Stockdale *et al.*, 2007), and increased Ricco's area (Je *et al.*, 2018). Eight amblyopic patients and four healthy controls underwent 3T retinotopic mapping with a moving bar stimulus (6° radius). As amblyopic patients can exhibit unsteady fixation, a simple fixation task and training session was used. It was found that pRF sizes increased in the amblyopic eye compared to the fixing eye (mirroring Ricco's area enlargement in the amblyopic eye; Je *et al.*, 2018), while cortical magnification factor was similar across eyes. This was consistent across visual areas and eccentricities (up to 6°). Furthermore, while pRF sizes in V2-3 can be explained by constant sampling of V1 in healthy controls and the fixing eye, this was not the case for the amblyopic eye. They suggest that this increase in pRF size may reflect increased positional scattering or simply a reduced contribution from smaller receptive field sizes.

Other work into retinal diseases, namely Stargardt disease (Ritter *et al.*, 2019), retinitis pigmentosa (Ritter *et al.*, 2019) and choroideremia (Silson *et al.*, 2018), has found that pRF coverage corresponds well to perimetric sensitivity, suggests it represents a more objective measure of preserved visual field. Subsequently, pRF mapping appears to be able to reliably map artificial scotomas in healthy individuals down to a radius of 2.35° (Hummer *et al.*, 2018). By comparing pRFs maps in those with real (i.e. caused by neurological damage) and artificial scotomas, the plasticity of receptive fields following damage can also be investigated. Papanikolaou *et al.* (2014) found that brain damaged patients with a visual scotoma had no large scale changes to V1 topography compared to controls with artificial scotomas. However, they did find that the distribution of V1 centres shifted slightly toward the scotoma border, pRF sizes were slightly enlarged on the border, and pRFs in the contralesional hemisphere were slightly enlarged. The fact that these changes were seen in patients but not those with artificial scotomas suggest that they arise due to longer-term reorganisation in V1. However, it could be argued that the scotomas were not entirely

matched; for example, while not detectable by perimetry, patients' scotomas may not look like the blank isoluminant masks presented. This is also the case for other conditions, such as glaucoma which may initially look like 'blurred' vision with 'missing features', rather than tunnel vision (Crabb *et al.*, 2013).

This method has also allowed examination of the dynamic nature of pRFs; the positional preference of pRFs (i.e. the position in the visual field they correspond to) differs, for example, with visual spatial attention, demonstrating shifts to the locus of attention (Bressler & Silver, 2010; Klein *et al.*, 2014, 2018). He and Fang (2015) found that following perceptive learning, an increase in V2 pRF size accompanied behavioural improvements in a crowding task. This suggests that not only are pRFs important to an aspect of crowding but may be susceptible to further fine tuning.

4.3.3.2 Difference-of-Gaussian mapping

While pRF mapping allows for the measurements of voxel-wise receptive fields, it assumes a symmetric Gaussian shape of activation and is therefore biased towards excitatory processing. However, a large number of receptive field configurations also involve a inhibitory portion, whereby a stimulus will cause a decrease or suppression of activity. This is typically present as 'surround suppression' and can be seen through electrophysiological and psychophysical studies (e.g. Cavanaugh *et al.*, 2002; Hubel & Wiesel, 1968; Petrov, 2005; Vanegas *et al.*, 2015). The presence of negative BOLD responses in the visual cortex following stimulation (Shmuel *et al.*, 2002, 2006) suggests that these suppressive surround responses can be measured at the scale of fMRI recordings. The pRF model above was therefore extended to incorporate the influence of suppressive surrounds by using a Difference-of-Gaussian (DoG) function rather than a single Gaussian (described by Zuiderbaan *et al.*, 2012). This DoG function is composed of a larger Gaussian subtracted from a smaller one. While the original pRF model has four parameters (describing size, position, and amplitude), the DoG model has two more; the size and amplitude of the surround. In order to ensure a centre-surround configuration (i.e. an excitatory centre and suppressive surround), the following restrictions are also in place:

1) The size of the surround must be larger than the size of the centre.
2) The amplitude of the surround must be negative, with an absolute value less than the amplitude of the centre.

Thus, the DoG pRF model can be defined as the following (Zuiderbaan *et al.*, 2012):

$$g^{+}(x,y) = exp - \left(\frac{(x-x_0)^2 + (y-y_0)^2}{2(\sigma_1)^2}\right)$$

$$g^{-}(x,y) = exp - \left(\frac{(x-x_0)^2 + (y-y_0)^2}{2(\sigma_2)^2}\right)$$

$$g(x,y) = \ g^{+}(x,y) - g^{-}(x,y)$$

Whereby g^{+} is the centre Gaussian, g^{-} is the surround Gaussian, x_0 and y_0 refer to the central visual field, x and y refer to the position of the pRF, σ_1 is the size of the centre Gaussian, σ_2 is the size of the surround Gaussian, and g is the overall DoG function. The rest of the procedure is similar to the pRF model above, with separate predictions generated for the positive and negative Gaussians. As a similar HRF is exhibited for both positive and negative responses (Shmuel *et al.*, 2006), the same HRF convolution is used in both (Zuiderbaan *et al.*, 2012). This model was found to account for more of the variance in the fMRI BOLD signal than the original single Gaussian in V1-3, with the most prominent gains in V1 (Zuiderbaan *et al.*, 2012). This asymmetry in gain also suggests that it is capturing a biologically relevant characteristic; if the improvement was just due to the increased degrees of freedom within the model, this increase would occur across the cortex.

By using sub-millimetre fMRI, it has been found that these metrics are depth-dependant, with both centre and surround size showing a U-shaped function with increasing cortical depth (Fracasso *et al.*, 2016). This reflects layer receptive field differences reported by invasive non-human neurophysiological studies (e.g. Chapin, 1986; Self *et al.*, 2014). Furthermore, this could not be explained by layer-dependant differences in HRF. Interestingly, the balance of centre and surround, namely the level of suppression, was kept constant throughout the layers suggesting that this may be kept constant across a neural column.

Considering the above, DoG modelling appears to capture biologically relevant characteristics of cortical receptive fields, without the bias to excitatory processing introduced by a single Gaussian. While it has been less utilised than the latter model, DoG modelling has also been used to examine processing in clinical conditions. For example, Anderson *et al.,* (2017) found that people with schizophrenia show reduced centre sizes, as

well as reduced size and depth of the surround suppression, possibly linked to suggestions of dysfunctions in schizophrenia with the inhibitory neurotransmitter, GABA (for a review, see de Jonge *et al.*, 2017). Recently, the receptive field architecture of the visual cortex was examined in a small sample of patients with posterior cortical atrophy with simultanagnosia and foveal crowding (de Best *et al.*, 2019). They found that patients showed smaller foveal (1-4°) but larger peripheral (4-8°) sizes of centre and surround estimates, particularly in earlier visual cortical areas (despite no damage to V1 in this cohort). This suggests feedback from high-level areas may be contributing to these changes in V1 receptive field architecture, while the changes found in extra-striate areas may reflect direct degeneration. Specifically, foveal crowding may occur due to enlarged pooling of spatial information (reflected by enlarged pRFs) in the fovea, while simultanagnosia may reflect shrinkage of receptive fields in the periphery and thus restricted input integration.

4.3.4 Applications in glaucoma

Due to the visual field location-specific neurodegeneration in glaucoma, fMRI holds particular promise for the investigation of neural activity changes in glaucoma. High spatial resolution allows for the precise investigation of particular areas of the visual field, allowing estimates of neural activity to be related to clinical or psychophysical measures. The possible imaging of the whole brain also allows for simultaneous imaging of the whole visual cortical pathway, including multiple cortical layer depths. This allows for a more complete picture of how visual information is being processed at multiple cortical hierarchies. The importance of examining functional cortical changes is also highlighted by reports of reduced grey matter thickness (Boucard *et al.*, 2009; Jiang *et al.*, 2018; Zhang *et al.*, 2015) and structural connectivity (Lu *et al.*, 2013; Wang *et al.*, 2018a, 2018b) in glaucoma patients, especially in regions retinotopically localised to areas of visual field damage.

Similar to findings of reduced grey matter, lower BOLD has also been reported in areas that correspond to visual field loss (Borges *et al.*, 2015; Duncan *et al.*, 2007), as well as V1 in general (Borges *et al.*, 2015; Gerente *et al.*, 2015; Song *et al.*, 2014; Wuerger *et al.*, 2015). This reduced signal may reflect dysfunction in retinal input, which is supported by the finding that this BOLD response correlated with retinal nerve fibre layer thickness and clinical visual field scores (Duncan *et al.*, 2007; Gerente *et al.*, 2015). This has also been reported to start pre-symptomatically (Murphy *et al.*, 2016), possibly in response to early

retinal ganglion cell shrinkage and death (Morgan, 2002), though this is not always seen in early stages (Gerente *et al.*, 2015; Zhang *et al.*, 2016). As these studies have relatively small sample sizes, with a mix of POAG and normal tension glaucoma (NTG) patients, this could reflect that this early effect is too subtle to be detected without sufficient statistical power.

BOLD fMRI has also been applied to other visual cortical areas, including the lateral geniculate nucleus (LGN), which demonstrates glaucomatous shrinkage that correlates with clinical measures (Dai *et al.*, 2011; Lee *et al.*, 2014). Contrary to V1, one study found BOLD signal increases in the glaucomatous LGN, potentially due to cortical feedback (Wuerger *et al.*, 2015). This was more pronounced in more severe glaucoma, though they only used a sample of 9 patients so the range of severities was limited. This result wasn't repeated by a more recent study, which did not find an increase in LGN-localised BOLD activity in their early glaucoma patients (Zhang *et al.*, 2016). Instead, BOLD activity was lower than controls, though this only occurred when using a stimulus that specifically activates the magnocellular pathway. When using a parvocellular stimulus, glaucoma patients showed no difference in LGN BOLD activation. This difference also did not appear to survive in V1, V2 or MT (Zhang *et al.*, 2016). This study appears to provide evidence that the magnocellular pathway may be the first to show functional damage in glaucoma. The difference between these studies may arise from the small sample sizes (the latter has ten POAG and eight NTG patients) and mix of glaucoma subtypes. Further work is needed to fully characterise LGN dysfunction in glaucoma.

Another avenue of fMRI research is functional connectivity (FC), which is defined as a statistical relationship between two or more anatomically distinct regions. Using various analysis techniques, studies have found both increases and decreases in FC in glaucoma in both visual and non-visual pathways (e.g. default mode network), which correlated with functional measures (Chen *et al.*, 2019; Frezzotti *et al.*, 2016; Song *et al.*, 2014; Wang *et al.*, 2018a, 2019). This suggests that glaucoma presents with global, general damage, which may worsen with symptom severity. What this FC change represents is up for debate; it may represent a 'reshuffle' of networks in order to better compensate for glaucoma, or simply a breakdown of structural connectivity (Wang *et al.*, 2018a).

A persistent problem within these studies is the lack of control for possible vascular confounds, such as lower cerebral blood flow (CBF), which has been reported in POAG and

NTG (Duncan *et al.*, 2012; Harris *et al.*, 2013; Sugiyama *et al.*, 2006; Zhang *et al.*, 2015). Lowered CBF would lead to a lower BOLD signal, independent of neural activity (for discussions, see: Iannetti & Wise, 2007; Wright & Wise, 2018). This may therefore be driving some of the findings above, especially as reductions in CBF seem to correlate with clinical symptoms and glaucomatous severity. However, these are not necessarily independent; lower CBF may impair functioning, and lower neural energy demand may lead to lower CBF. Altered functioning in V1 is suggested by other functional neuroimaging methods that do not rely on neurovascular coupling; for example, a study that reported lowered BOLD signal also found cortical cholinergic abnormalities associated with trans-neurodegeneration in V1 (Murphy *et al.*, 2016), and visual evoked potentials (an electrophysiological recording over the visual cortex) also show abnormalities in glaucoma (e.g. Bergua *et al.*, 2004; Bobak *et al.*, 1983; Fortune *et al.*, 2007; Hood & Greenstein, 2003; Jha *et al.*, 2017; Parisi *et al.*, 2001; Tai, 2018). A joint fMRI-EEG study would be able to help delineate these influences and help quantify gross neural changes in the visual cortex.

As of the time of writing, no study has used pRF mapping to quantify changes in glaucoma, though changes are suggested by an early estimate of cortical receptive field size in two glaucoma patients (Liu *et al.*, 2007). This PhD will describe research utilising OCT, PERG, and fMRI to interrogate retinal and cortical receptive field sizes and neural structure in glaucoma patients compared to age-similar controls and investigate whether these factors contribute to the size of Ricco's area.

Chapter 5. Outline of experimental chapters

The first section of this thesis has provided a brief introduction to the anatomy of the visual system, glaucoma (i.e., the disease investigated throughout the majority of this thesis), the concept of perceptual spatial summation and how this is estimated psychophysically, and finally an overview of different objective methodologies for imaging structure and/or function along the visual pathway. This lays the groundwork for the main research question that this thesis addresses; namely, to what extent do cortical and retinal receptive field sizes contribute to the size of Ricco's area in a sample of glaucoma patients and age-similar controls?

In order to investigate this, cortical receptive field sizes were estimated in the mid-periphery using functional Magnetic Resonance Imaging (fMRI). The first experimental chapter (Chapter 6) will therefore describe research establishing this methodology in a sample of healthy young adults. This chapter will also describe research investigating the relationship between axial eye length/refractive error and cortical population Receptive Field (pRF) size, in order to establish whether this is a confound that should be considered in future fMRI work.

Prior to undertaking any experiments with the main glaucoma sample, the methodologies to be used (i.e., psychophysics, fMRI, pattern electroretinography [PERG]) were first developed and optimised, as described in Chapter 7. This chapter also describes the inclusion and exclusion criteria used during recruitment of the full sample of glaucoma patients and healthy age-similar controls.

The following chapters then describe research investigating receptive field sizes in glaucoma patients and healthy controls at the retina and the cortex, establishing evidence of any group differences before these measures are related to Ricco's area. Chapter 8 describes research investigating group differences in estimated retinal receptive field size between glaucoma patients and controls using onset-offset PERG. When investigating receptive field size in the cortex, the fMRI protocol described and developed in Chapters 6-7 was utilised. This imaging technique relies on the fluctuation of blood flow that (after a certain haemodynamic delay) follows neural activity in order to meet the increased energy demand. The fMRI signal is typically convolved by the haemodynamic response function

(HRF) during analysis in order to model this response. The research outlined in Chapter 9 investigates whether the shape of this HRF varies between glaucoma patients and healthy controls, in order to establish whether this will introduce a source of bias if not controlled for. The research described in Chapter 10 will then use fMRI to investigate whether pRF sizes differ between the cortices of glaucoma patients and healthy age-similar controls as a function of eccentricity.

The final experimental chapter (Chapter 11) will describe work that addresses the main research question of this thesis. It will first investigate whether, as previously reported, an larger estimate of Ricco's area is found in this sample glaucoma patients compared to age-similar healthy controls (Redmond, Garway-Heath, et al., 2010), focusing on the mid-peripheral region sampled by the other imaging methodologies. Linear models will then be described that analyse the contribution of retinal and cortical receptive field size to Ricco's area (i.e., the area of complete spatial summation).

Finally, Chapter 12 will discuss the overall findings from this thesis and present suggestions for future research.

5.1. Statistical approach

For the most part, this thesis follows a frequentist approach to statistical hypothesis testing, which is commonly used across the scientific literature. Frequentist null hypothesis significance testing involves calculating a p-value, which is the probability of finding a given result (i.e. from the observed data), assuming that the null hypothesis is true (i.e. that there is no relationship/difference in the underlying population). This thesis follows common convention of using $p<0.05$ as a threshold for determining whether a result is statistically significant or not; if a statistical test on the observed data reports $p<0.05$, it would suggest that there is less than 5% probability that the effect occurs by chance alone, and there is therefore a high probability of it being reflective of a true difference/relationship in the population (i.e. the alternative hypothesis being true rather than the null hypothesis). However, there are a number of limitations to frequentist testing, one of which being that this approach does not explicitly test the null hypothesis (Gigerenzer *et al.*, 2004). If non-significance is found (commonly defined as $p>0.05$), such tests do not distinguish whether this indicates evidence towards the null hypothesis (e.g. no effect) or just that there is not

enough evidence to say one way or the other. Bayesian approaches however, allow for explicit testing of the null hypothesis. Bayesian testing produces Bayes Factors which, rather than arbitrary splitting results into 'significant' or 'non-significant', give information about the amount of evidence for a certain hypothesis being true based on prior probabilities (either the null or alternative can be tested this way). Within this thesis therefore, additional Bayesian statistics are used if a statistically non-significant effect is reported by frequentist statistics, in order to place that non-significant result into better context.

In addition, as fMRI and pRF mapping can be inherently noisy techniques, thresholding of resulting data is used as a data cleaning method throughout this thesis. Specifically, data are thresholded by the R^2 value, as a measure of the goodness-of-fit of the Gaussian pRF model on the collected data (as described in the previous section). This is a commonly used technique (e.g. Prabhakaran *et al.*, 2020; Schwarzkopf *et al.*, 2014; Welbourne *et al.*, 2018) and the exact values used for R^2 thresholding are detailed in the relevant chapters.

Chapter 6. Establishing population receptive field sizes (pRFs) in the periphery of healthy young adults and associations with refractive error

6.1. Introduction

In order to address the main research question of this thesis, cortical receptive field sizes will be measured in the mid-periphery of glaucoma patients and healthy controls using 7 Tesla (7T) functional Magnetic Resonance Imaging (fMRI). However, before investigating these cortical receptive fields, it is important to demonstrate and validate the methodology for measuring them at 7T in a healthy sample. This chapter will therefore describe research that establishes a methodology of measuring cortical receptive field sizes in central and mid-peripheral vision in a separate sample of healthy young adults within the constraints of the 7T MRI environment (the difficulties of which are described below). As a secondary exploratory aim, this chapter will also investigate whether refractive error and axial eye length are associated with fMRI-estimates of cortical receptive field size. If these factors are associated, it would suggest that this could be a potential confound for future fMRI studies investigating cortical receptive field size and this should be further investigated.

Unlike electrophysiology, when measuring cortical receptive fields using fMRI the receptive field of a single neurone is not being measured, but rather the whole population of neurones within a voxel (therefore summing over millimetres of cortex). This method is therefore termed population receptive field (pRF) mapping (Dumoulin & Wandell, 2008; outlined fully in Chapter 4; section 4.3.3.1 and 4.3.3.2). The pRF sizes in V1-3 estimated using this technique were found to correspond well (in terms of relative size across the visual areas) to equivalents in primate and human electrophysiology, using single- and multi-unit activity and local field potentials (Dumoulin & Wandell, 2008; Victor *et al.*, 1994; Yoshor *et al.*, 2007). This suggests that the pRFs estimated from the fMRI time course are reflective of the underlying neural structure of receptive fields. This fMRI-derived pRF mapping has the added benefit over other techniques (e.g. single-unit activity electrophysiology recording) of being non-invasive while retaining good spatial resolution. The size of receptive fields vary across the visual field, notably increasing with eccentricity (e.g.

Dumoulin & Wandell, 2008; Hammond, 1974; for more discussion on receptive fields within the visual system, please see chapter 2) and this healthy relationship between pRF size and visual field position has been very well replicated, prominently for 1.5T and 3T MRI (e.g. Alvarez *et al.*, 2015; Dekker *et al.*, 2019; Dumoulin & Wandell, 2008; Fracasso *et al.*, 2016; Schwarzkopf *et al.*, 2014; Zuiderbaan *et al.*, 2012). However, only a small number of studies have extended notably into peripheral vision. For example, Alvarez et al. (2015) used a stimulus that stimulated up to 16° eccentricity in a 3T MRI scanner, while the stimulus utilised in Smittenaar et al. (2016) stimulated up to 37.5° on a 1.5T scanner. pRF mapping is therefore a well-established methodology for modelling cortical receptive field sizes (both excitatory and inhibatory components; Zuiderbaan *et al.*, 2012), and has been used to characterise pRF size across the visual field, though 7T pRF studies in the periphery are currently lacking.

There are many advantages to using a 7T MRI system over lower magnet strength alternatives (i.e. 1.5T or 3T). For example, due to the increased magnet strength, these high-field 7T scanners also provide higher signal-to-noise ratios (SNR) and thus scans can use smaller voxels while keeping sufficient SNR (Stucht *et al.*, 2015). pRF maps can therefore not only be investigated in more detail, but can also be localised to increasingly specific features of the visual field (e.g. specific eccentricities) or cortical structures (e.g. cortical layers; Fracasso *et al.*, 2016). Furthermore, the 7T fMRI BOLD signal is less biased by large draining veins, meaning that the signal can be more accurately localised to the target tissue (Uludağ & Blinder, 2018) than at lower field strengths.

However, despite these advantages, there are several challenges to overcome and considerations that one needs to be aware of from the outset when conducting research into research questions such as those posed in this thesis. For example, there is a higher rate of image distortion due to field inhomogenities at 7T (Duchin *et al.*, 2012), compared to lower field strengths. In order to correct for this during the studies described in this thesis, phase and magnitude B0 mapping images will also be collected during data acquisition. A particular challenge at 7T is that of stimulating peripheral vision, which may contribute to the lack of 7T studies investing pRF size in the periphery (as mentioned previously). As a larger magnet coil is required, the bore itself is considerably smaller and longer within standard 7T MRI scanners than lower field-strength equivalents (e.g. 1.5T or 3T). This, in

turn, restricts the size of the screen that can be used for presentation of stimuli and thus the measurable field of view. A centred circular stimulus is typically only able to stimulate the central 5-8° (assuming central fixation). This therefore represents a significant challenge for using the 7T MRI for addressing vision science questions. Furthermore, the use of a head transmit coil at 7T, rather than a body transmit coil (as is more often used at lower field strengths, such as 3T), means that the head is more constrained and there is little room for instruments that may extend the visual field into the periphery (e.g. Wu *et al.*, 2012). While certain contact lenses may be able to magnify the image and thus extend the amount of visual field able to be stimulated at 7T, not all participants are able or willing to tolerate these, and long scanning sessions may lead to issues such as dry eyes which will result in reduced contrast of and, and in extreme cases, distortion of the stimulus on the retina. In order to capitalise on the advantages of 7T within this restrictive environment, the current study will map central and mid-peripheral vision in separate retinotopic runs by adjusting the position of the fixation mark. An illustration of the location of the fixation cross and pRF mapping area on the stimulus presentation screen is shown in Figure 6.1.

The secondary aim of the research described in this chapter is to investigate whether pRF estimates are associated with refractive error and axial eye length. A type of refractive error termed myopia (i.e. short-sightedness) is increasingly common across the world, and is predicted to effect up to 50% of the world's population in 2050 (Holden *et al.*, 2016). One cause of myopia is an increase in axial eye length, leading to incoming light converging at a point in front of the retina and therefore blurring once it reaches the retina's true location (see Figure 6.2 for an illustration). As varying levels of refractive error will be expected within our sample, it is prudent to establish whether we may expect it to impact our measurements despite the use of MR-safe vision correction.

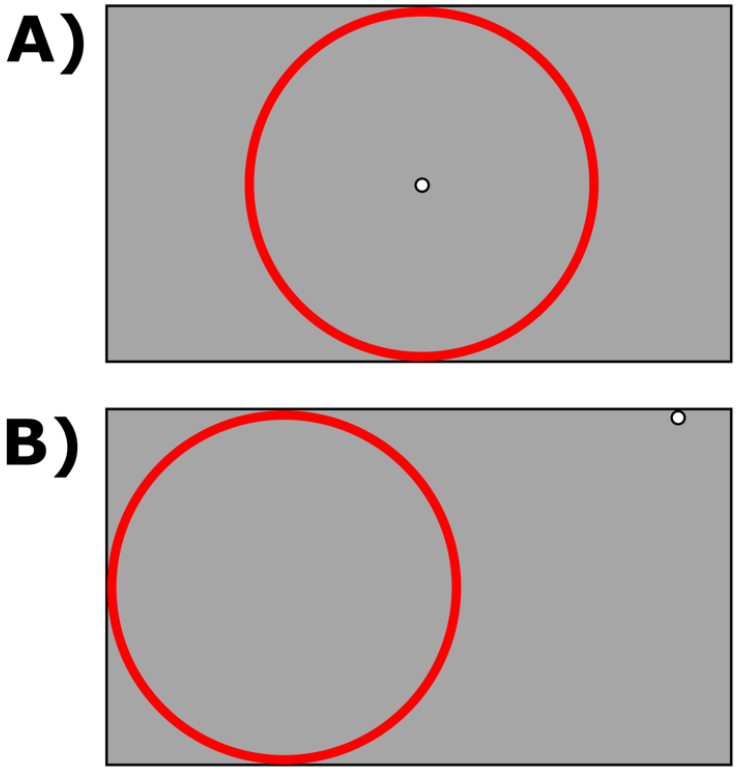

Figure 6.1 – An illustration of the position of the pRF mapping stimuli (the area marked by the red circle) and the fixation cross (indicated by the black circle with white fill) for A) the central mapping run, and B) the peripheral mapping run.

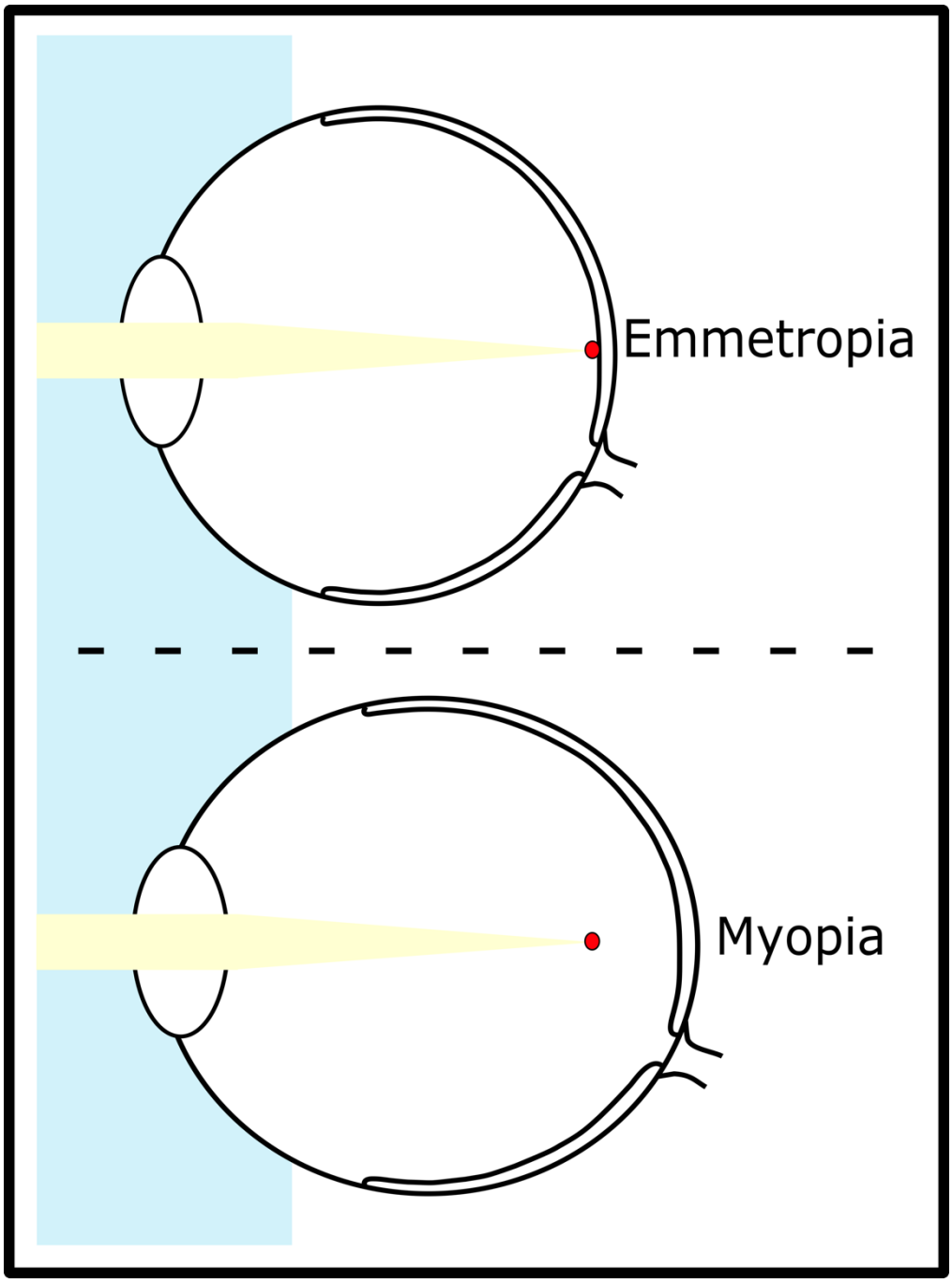

Figure 6.2 – Illustration of the difference between emmetropia (i.e. healthy normal vision) and myopia. Specifically, axial myopia is shown, in which the eye continues to grow length-wise, leading to a longer axial eye length than normal. Despite this, incoming light continues to be focused at the same point in the eye (as indicated on the figure by the red dot). As the eye has elongated, this point of focus therefore falls short of the retina. By the time light hits the retina in the myopic eye, it has begun to scatter and therefore will be perceived as blurred.

Several studies have investigated the impact of uncorrected myopic blur on the fMRI signal. A consistent finding is that introducing myopic blur with lenses significantly decreases fMRI responses, even at relatively low dioptre (i.e. refractive error) levels (Elbel *et al.*, 2002; Mirzajani *et al.*, 2011, 2017). Clearly, refractive error is an important factor to correct for in visual neuroimaging studies. However, many studies assume that, after being 'corrected to normal' (e.g. using MR-safe lens correction), no substantial impact of a myopic system should be introduced. However, several aspects suggest that this may not be true. Firstly, myopia introduces a systematic change to the structure of the visual system, such as with retinal stretching (and thus increased retinal image size). Even if there are no cortical neural changes per se, the input to the cortex from the retina may therefore be systemically different in myopia. For example, these retinal changes may lead to different perceptions of the same stimuli due to factors such as an increased retinal image size, which will impact upstream processing in the cortex. Studies have also found structural changes throughout the cortex in people with myopia, especially in visual and limbic systems (Huang *et al.*, 2018; Li *et al.*, 2012; Takeuchi *et al.*, 2018). For example, Pearce and Bridge (2013) reported a relationship between eyeball volume and visual cortex volume, which was independent of total brain size (though a later study suggested that there was a stronger relationship between orbital volume and frontal cortices; Masters *et al.*, 2015). Though cortical activity in corrected myopia has not yet been thoroughly examined, functional connectivity was found to be altered in an 'eyes closed' resting-state task in high myopes compared to emmetropes (gender, age and educational level matched), again implicating the occipital and limbic systems (Hu *et al.*, 2018). This work suggests that there may be a functional impact of structural changes in the myopic visual system, even when the visual input is the same (as it was an 'eyes closed' task). It is possible that the limbic system differences found in these group studies reflect the 'experience' of living with high myopia, as this system is central to emotional and memory processing (Rajmohan & Mohandas, 2007). It may also reflect a those with glasses being more likely to read outside of the education system, which would in turn impact emotional processing (e.g. Kumschick *et al.*, 2014). It is also important to consider that vision correction within the MRI scanner is often not optimal (i.e. due to the range of lenses available leading to a slightly inaccurate correction for refractive error or due to no correction for astigmatism), so even in 'corrected' myopia, the optical input may

be systematically different between groups, leading to fMRI signal differences. Ricco's area is also suggested to be enlarged in high myopia (Stapley *et al.*, 2019), which may be reflective of increased neural spatial pooling in myopia that may in turn be suggested in fMRI estimates. The relationship between corrected refractive error and pRF size was therefore considered in a small exploratory experiment in this chapter in order to determine whether a cut-off in refractive error should be included as a criterion in our clinical study.

6.1.1. Aims

The data presented within this chapter aims to demonstrate a method for extending current 7T pRF maps to the mid-periphery, despite hardware limitations. A small exploratory study will also be conducted to examine how these pRF estimates vary with varying levels of refractive error (this will use the same healthy sample, in addition to a small 'high myopia' sample in order to ensure sufficient range in axial eye length and refractive error values). Two locations will be stimulated using retinotopic mapping, with the fixation cross placed in the centre or top corner respectively (see Figure 6.1). Both central (0-5.5°) and mid-peripheral vision (7.7-18.7°; lower nasal quadrant) were mapped (Figure 6.3. illustrates the position of both runs of pRF mapping on a visual field plot). This peripheral region was chosen as it fits within the physical constraints of the scanner and also covers an area typically tested in clinical perimetry.

The research described in this chapter therefore has two specific aims:

1) To establish a method of testing pRF sizes in the peripheral visual field with 7T fMRI in a sample of healthy young adults.
2) To investigate the impact of refractive error and axial eye length in a small sample of high myopia patients and the non-high myopic control sample used in the first aim. This is an exploratory secondary aim, but from the previous literature suggesting an increase in perceptual spatial summation in myopia (Stapley *et al.*, 2019), it is predicted that pRF sizes may also increase with increasing axial eye length and more negative refractive error.

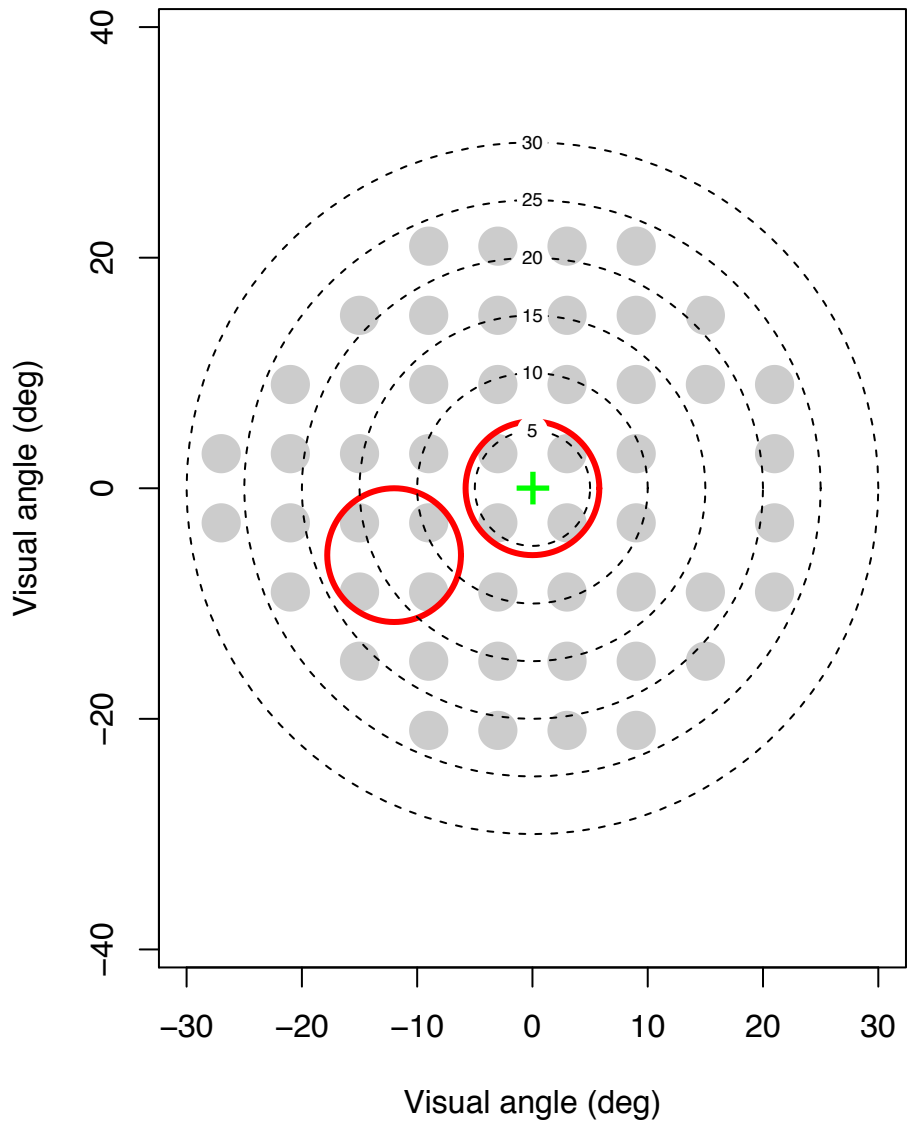

Figure 6.3 - Positions of central and peripheral stimulation during the MRI session (shown as red circles) in the visual field (x and y axes show visual angle in degrees [°]). Grey filled circles show locations tested in a standard 24-2 perimetry test pattern (right visual field) for reference. The green cross indicates fixation. Eccentricities are delineated in steps of 5 with dashed circles (with the embedded number referring to the eccentricity).

6.2. Methods

Twenty six healthy young adults were recruited for this cross sectional study. pRF mapping was completed in a 7T fMRI, in which both central and peripheral visual field regions were mapped, in order to develop this methodology for later experiments in a clinical glaucoma cohort. In addition, this sample was extended to include a small sample of individuals (6 recruited) with a greater refractive error, in order to examine relationships between myopia and pRF size.

6.2.1. Participants

MRI scanning was carried out in a sample of healthy young adults with varying levels of refractive error. The following inclusion criteria were used for recruiting participants:

- No diagnosis/immediate family history of glaucoma
- A healthy optic nerve, and clear optic media (apart from age-related changes)
- Age ≥18 years old

The following exclusion criteria was also used:

- No ocular surgery, and no optical/systematic condition or medication that impacts or may impact visual performance (including paediatric glaucoma)
- Unsafe for the 7T MRI environment (e.g. no implants or metallic dental work)

A sample of healthy young adults (N=26, >-5.00 dioptre [D]) were initially recruited following ethical approval from Cardiff University (Schools of Psychology and Optometry and Vision Sciences). All participants gave written consent before participation. One participant withdrew before completing the study, one was excluded because of a possible ocular impairment, and four were excluded due to retinotopic maps that were too noisy to delineate (i.e. did not show a clear fovea or polar angle reversals). This low-myopia (LM) group therefore consisted of 20 participants (14 female; mean [IQR] age: 20.76 years [19.31, 20.93]; mean [IQR] refractive error: -0.95D [-1.25, 0]; mean [IQR] mean deviation [MD; i.e. the overall amount of visual field sensitivity deviation from the population mean]: -1.15 dB [-1.61, -0.55).

In order to test the secondary aim, a high myopia (HM) group, defined as having a refractive error of -5.00D or greater in at least one eye, was also recruited (N=6). One

participant withdrew part-way through the study, leaving a sample of five HM participants (4 female; mean [IQR] age: 27.81 years [25.29, 30.52]; mean [IQR] refractive error: -7.70D [-7.75, -7.25]; mean [IQR] MD: -0.66 dB [-0.8, -0.63).

As a main aim of the current chapter was to optimise the MRI methodology for testing in a glaucoma population (which is a monocular/asymmetric condition), it was therefore important that this investigation was also done monocularly. Furthermore, monocular pRF mapping will allow for a more accurate comparison between refractive error/axial eye length and the cortical pRFs that the eye contributes to. An eye was randomly chosen to be tested within the study (LM group= 5 left eyes [OS]; HM group= 3 OS).

Ethical approval for this study was obtained from the Cardiff University School of Psychology School of Optometry and Vision Sciences research ethics committees. Participants were offered travel reimbursement or course credit (this latter option was for BSc psychology undergraduate students only). The study took place over two visits, both within Cardiff University (the School of Optometry and Vision Sciences and Cardiff University Brain Research Imaging Centre [CUBRIC]). The initial session allowed for an assessment of eye health (short discussion with the researcher, fundus photography [DRS fundus camera, Haag-Streit, Koeniz, Switzerland], Standard Automated Perimetry [SAP; SITA-Standard 24-2 grid, Humphrey Field Analyzer 3, HFA3, Carl Zeiss Meditec, Dublin, CA]) and of refractive error (assessed using an auto-refractor [TOPCON KR-7500 Kerato-refractometer, Topcon (Great Britain) Medical Limited, Newbury, UK]). Axial eye length was also measured using an IOL master (Carl-Zeiss Meditec, Dublin, CA, USA). The fMRI procedure was undertaken during a second session within CUBRIC.

6.2.2. MRI session

Images were acquired on a SIEMENS 7 Tesla (7T) MRI scanner (Siemens Medical Systems, Erlangen, Germany). Retinotopy scans were 1mm^3 resolution EPIs (Echo-Planar Image; TR= 3s, TE=26ms, 42 slices), manually positioned over the occipital lobe and dynamically motion-corrected by the scanner. As this had a limited FOV over the area of interest, a whole brain single-shot EPI was taken to aid with the registration to structural images. This had identical resolution and slice orientation to the retinotopy EPIs, but with

100 slices (TR= 5s, TE=31ms). To aid with distortion correction, phase and magnitude B0 mapping images were also taken. Finally, a T1-weighted MPRAGE sagittal structural scan was also completed at 0.7mm^3 resolution (TR=2.2s, TE=2.98ms). Foam head padding was used to limit head movements and either an eye patch or blackout lens was used to occlude the untested eye. MR-safe vision correction was provided if needed. All participants were asked to confirm that they could see the whole screen clearly (i.e. in focus) before scanning.

6.2.3. fMRI stimuli

The retinotopic stimuli used within this thesis is similar to what has been reported previously (e.g. Silson *et al.*, 2018). The stimuli used for retinotopic mapping was a moving bar-shaped window in a grey background, superimposed over a natural scene (an example of the stimuli is shown in Figure 6.4). This bar-shaped window moved across the screen in a set order and paused in 18 consecutive positions to cover a circular area of 11° diameter (each bar was 1.16° wide). The step size was half the bar width. Five background scenes were presented at each position for 0.6 seconds, totalling three seconds at a position before the bar moved to the next position (i.e. the length of one TR). The stimuli crossed the screen in the following order: left to right, bottom-right to top-left, top to bottom, bottom-left to top-right, and then the reverse. For the central run, the fixation point was positioned in the centre of the screen. To map the periphery, the fixation point was moved to the top corner of the screen (top left when testing the right eye and top right when testing the left eye) and the stimulus area was moved to the opposite side of the screen. For example, when examining the left eye, the fixation point appeared in the top right and the stimulus was moved to the bottom left of the screen. This is illustrated in Figure 6.1.The peripheral run mapped an area spanning 7.7-18.7° eccentricity (see Figure 6.3). Each run took ~7 minutes and each participant underwent 1-3 runs (averaged during analysis).

In order to ensure fixation, a simple fixation task was used. The fixation dot changed between red and black (with a white outline) at random irregular intervals throughout the run, and the participant was required to count in their head the number of times this happened. They were not required to make a response.

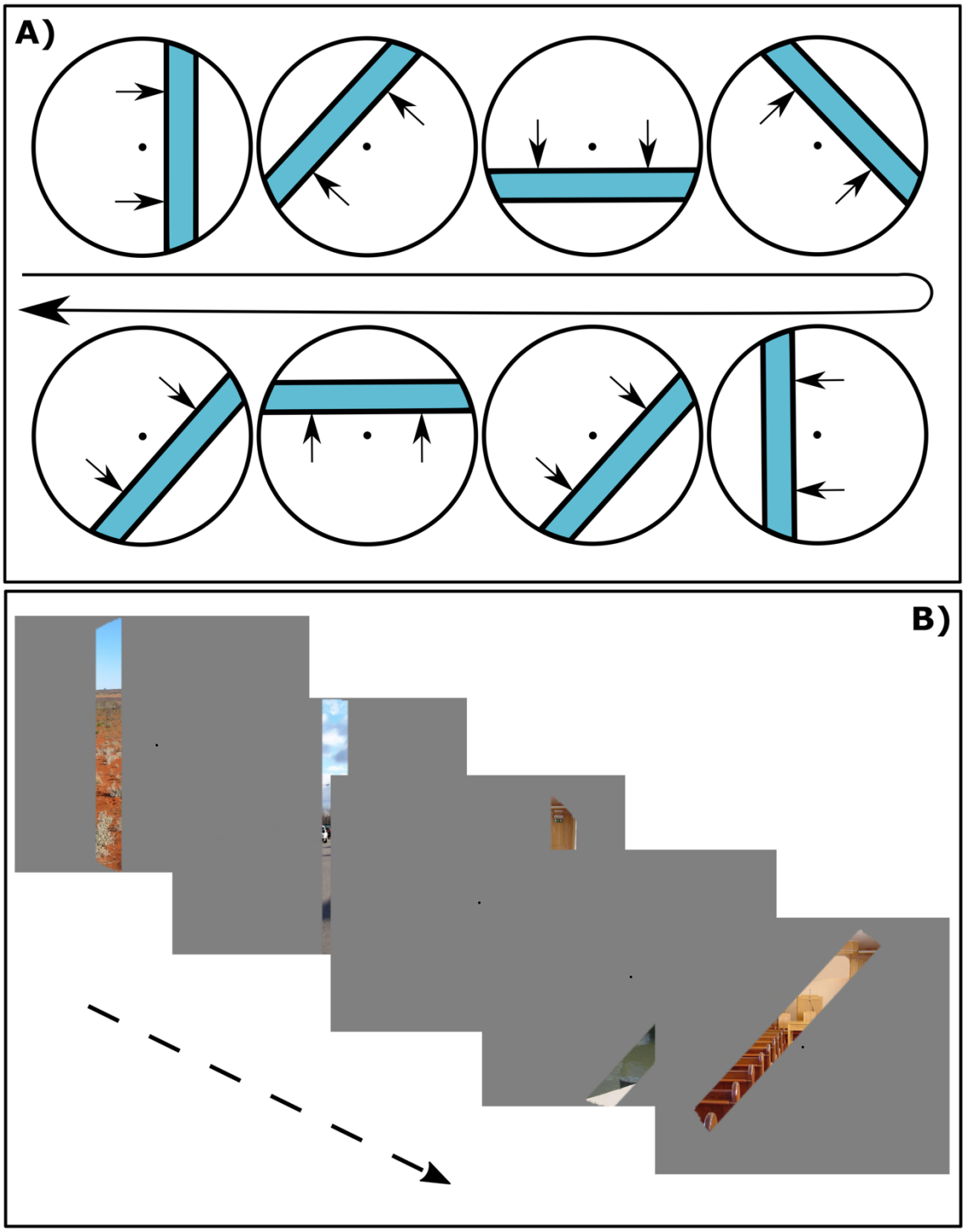

Figure 6.4 - Illustration of retinotopic stimuli used in population receptive field mapping. A moving bar aperture filled with multiple naturalistic scenes are used, which move to 18 consecutive positions in a particular direction. The filler scene changes five times per position, and position changes are timed with the repetition time (TR). The diagram in box A (top) illustrates the order of movements of the moving bars. Box B (bottom) displays screenshots of the actual stimuli moving across the visual field.

6.2.4. Pre-processing

The majority of pre-processing took place within FMRIB Software Library (FSL) toolkit (http://www.fmrib.ox.ac.uk/fsl/) and FMRI Expert Analysis Tool (FEAT) software packages (Jenkinson *et al.*, 2012; Woolrich *et al.*, 2001). Echo-planar Imaging (EPI) data underwent B0 distortion correction, motion correction (using the Motion Correction option of FMRIB's Linear Image Registration Tool; MCFLIRT; Jenkinson, Bannister, Brady, & Smith, 2002), brain extraction (Brain Extraction Tool; BET; Smith, 2002), and high-pass filtering (100s). Following this, registration of the partial-volume EPI to structural data (using the single-volume whole brain EPI as an intermediate step) took place in the Statistical Parametric Mapping (SPM) fMRI toolbox (http://www.fil.ion.ucl.ac.uk/spm/).

The MPRAGE structural image was first intensity-normalised within FSL, then segmented with FreeSurfer (Dale *et al.*, 1999; Fischl, 2012). This created a 3D mesh of the targeted hemisphere; one between the grey and white matter, and one at the outer pial boundary of the white matter. This mesh is made up of vertexes (i.e. triangular grey matter voxels). These cortical surfaces could be inflated to aid with visualisation of the data. Further analysis was restrained to a region-of-interest (ROI) that covered the occipital lobe, which was manually delineated in FreeSurfer using this inflated cortex and using the anterior end of the calcarine sulcus and the parieto-occiptal junction as anatomical landmarks.

6.2.5. Population receptive field mapping

Population receptive field (pRF) mapping was undertaken within the SamSrf v.5 Matlab toolbox (available at https://doi.org/10.6084/m9.figshare.1344765; see Schwarzkopf *et al.*, 2014 for more details). The retinotopic functional data was first projected onto the structural surface. To do this, the software determines the midpoint between the grey and white matter boundary and the pial surface for each vertex. A functional time series is created for each vertex by selecting the nearest voxel to this midpoint in the corresponding functional space. Linear detrending and z-score normalisation are then applied.

To complete the pRF mapping, a difference-of-Gaussian model of the underlying receptive field structure was chosen. Using this model as opposed to a single Gaussian model allowed for more variance within the data to be accounted for as both excitatory and

inhibitory responses could be modelled (Zuiderbaan *et al.*, 2012). The full analysis pipeline is discussed in Chapter 5 (in sections *5.3.3.1* and *5.3.3.2*). Briefly, the pRF modelling process is completed in two stages. In the initial, course fit stage, the data is heavily smoothed (5mm smoothing kernel). For the coarse fit, a standard 2D Gaussian model is used. The Pearson correlation is then calculated between the time series from each vertex and a search grid comprising of 15 × 15 × 34 combinations of x, y, and σ of the Gaussian. While all vertices were included in this initial fit, only those that demonstrated a Goodness-of-fit of $R^2 \geq 0.05$ were analysed further. The second stage was the fine fit, in which the optimum parameters found in the coarse fit are used as seeds for an optimization procedure (simplex search algorithm using the Nelder–Mead algorithm) to fit the pRF parameters to the unsmoothed time series (this time using the difference-of-Gaussian model) for each vertex. This was done by minimizing the residual sum of squares between the predicted and observed time series. Unlike the coarse fit, this model fitting stage included the β parameter for the amplitude.

This modelling produces four values for each vertex that will be examined in this chapter:

i) The excitatory centre (standard deviation [SD] of the excitatory Gaussian, representing the spatial spread of the pRF)
ii) The inhibitory surround (the SD of the larger, negative Gaussian)
iii) Suppression (defined as the ratio between the area under the inhibitory and excitatory Gaussians)
iv) The X- and Y- co-ordinates for the pRF centre

Functional visual areas were manually delineated using the SamSrf delineation tool and colour coded polar angle and eccentricity smoothed maps (such as those seen in Figure 6.5). Early visual areas were defined using standard criteria based on eccentricity and polar-angle reversal (e.g. Sereno *et al.*, 1995), while the outer edge was determined by looking for activation in the peripheral maps. It is assumed that the delineated visual areas would therefore cover all of the eccentricities stimulated by our stimuli.

6.2.6. Analysis

The first aim of the research described within this chapter was to establish a method of testing pRF sizes in the peripheral visual field with 7T fMRI in a sample of healthy young adults. In order to address this therefore, estimated of pRF centre, surround, and suppression level will be plotted as a function of eccentricity and visually examined. From previous research, a linear relationship is expected for pRF centre and surround sizes as a function of eccentricity, with the smallest sizes in V1 and the largest in V3. The level of suppression is expected to be relatively invariant with eccentricity.

The second aim to investigate the impact of refractive error and axial eye length in a small sample of high myopia patients and the non-high myopic control sample used in the first aim. All following analysis was carried out in JASP v.0.11.1 (JASP Team, 2019) unless otherwise specified. Demographic characteristics (namely refractive error and age) were first compared between groups using two-tailed student's T-tests to determine whether these factors differed significantly between groups. In order to address the second aim, the groups were combined, and a Spearman's rho correlation was completed to investigate the relationship between pRF sizes and both refractive error and axial eye length (in separate analyses). One-tailed correlations were used based on the initial hypotheses.

6.3. Results – Establishing pRFs in healthy adults

Examples of the retinotopic maps produced and the manual delineation of V1-3 for a single participant are shown in Figure 6.5.

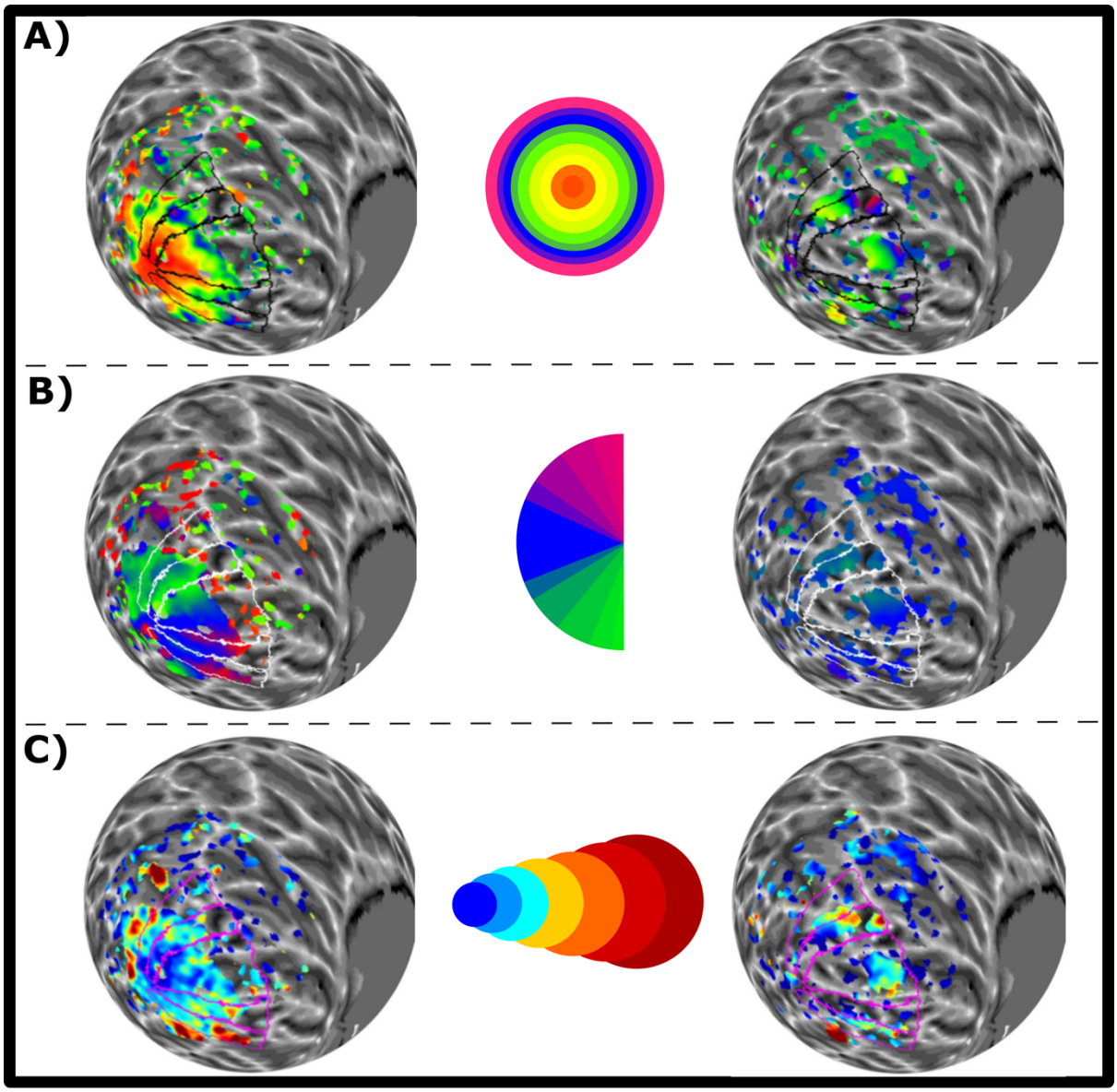

Figure 6.5 - Example retinotopic maps taken from a single participant, presented on an inflated cortical surface. Maps from the central stimuli shown in the left column, while maps from the peripheral stimuli are shown in the right column. Maps shown for A) eccentricity, B) polar angle, and C) population receptive field size (sigma). Manual delineations for areas V1-3 (both dorsal and ventral) are also shown.

In order to exclude noise from the data, an R^2 threshold was used to only include data that had satisfactory fit between the data and the associated pRF model. In order to choose this threshold (as the level chosen varies widely in previous literature), two graphs were plotted; firstly, the mean of the R^2 of the voxels that remain after thresholding was plotted for multiple R^2 thresholds, so that the effect of thresholding could be visualised. This is shown in Figure 6.6 (with separate colours indicating separate participants). As expected, the average model fit after thresholding increases for higher threshold levels. Specifically, it appears to start to increase at a threshold of around 0.04-0.05, with increases after

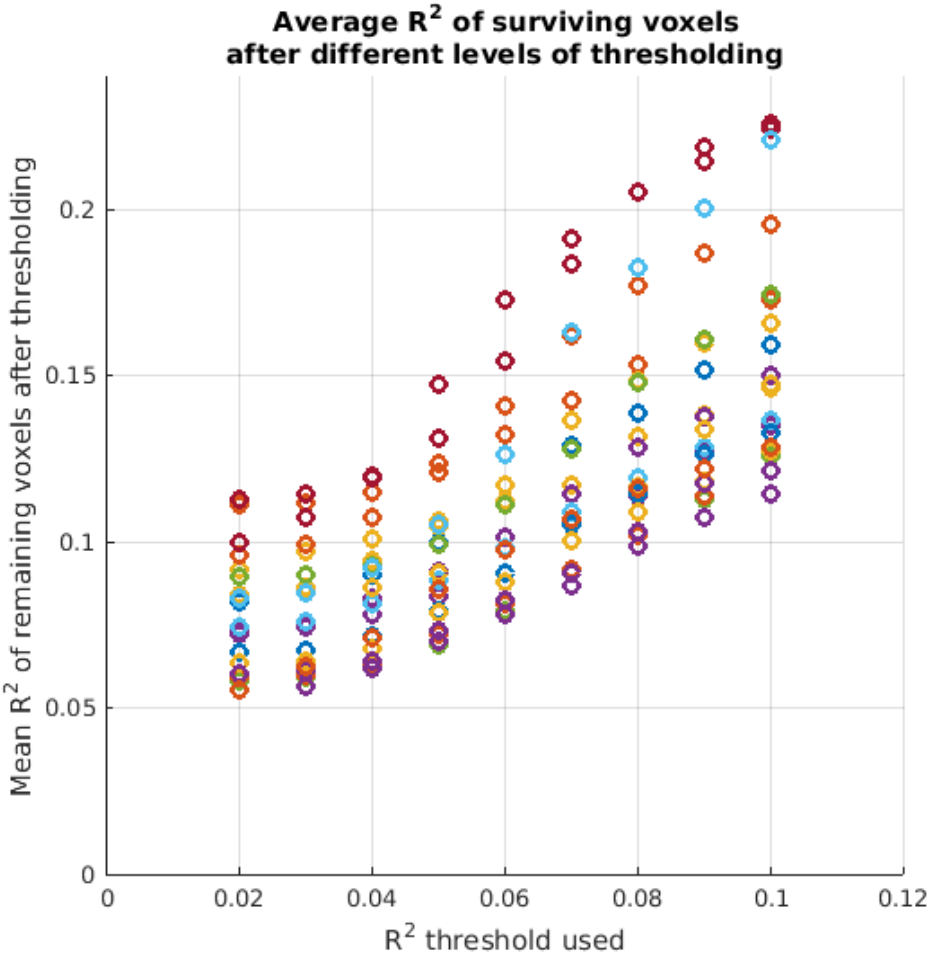

Figure 6.6 – pRF datasets were thresholded by different levels of Goodness-of-fit (defined as the R^2 between the model fit and the Difference-of-Gaussian pRF model). The R^2 of the surviving voxels were then averaged and plotted as a function of threshold to illustrate the influence of different levels of thresholding on the model fit of the surviving voxels. Different coloured datapoints refer to individual participants.

about 0.08-0.09 seeming more minimal. Secondly, the number of eccentricities with missing data at each threshold was examined (see Figure 6.7). As the threshold increases, more data is filtered out and it is increasingly possible that a certain eccentricity will have no remaining data corresponding to it. These histograms (Figure 6.7) illustrate the number of participants with a certain number of eccentricities with missing data. As expected, this increases with increasing threshold, particularly once reaching an R^2 threshold of about 0.07-0.08. While it is important to ensure that the data remaining post-thresholding has an acceptable level of model fit, it is also important to ensure that the threshold is not too conservative, as this would leave a substantial number of participants with large amounts of missing data. Taking both of these ways of plotting the data together, an R^2 threshold of 0.08 was decided to be the most appropriate for our data, as a balance between improving the R^2 of the surviving voxels and also not leaving too many participants with substantial areas of missing data.

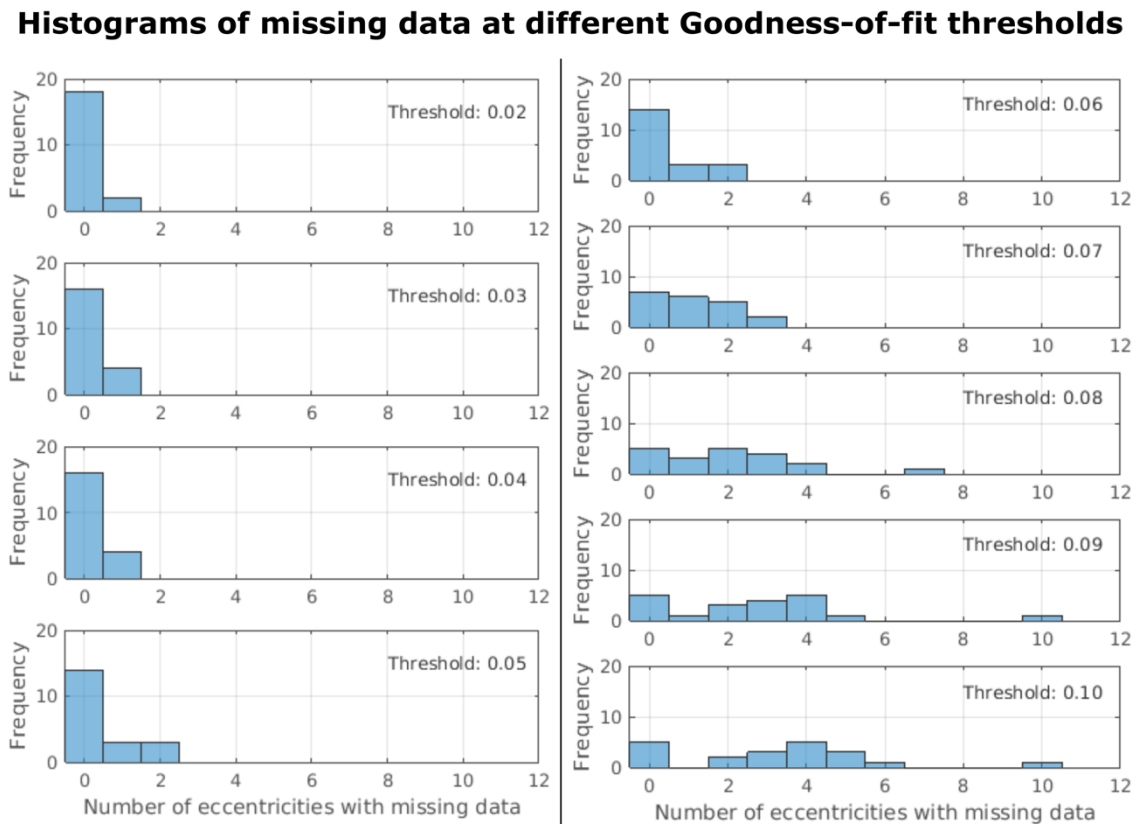

Figure 6.7 - A histogram illustrating the amount of participants with a certain number of eccentricities with missing data after thresholding. Data is presented for nine increasingly stringent R^2 thresholds.

After this thresholding was complete, the modelled parameters of the pRFs (namely the excitatory centre size, inhibitory surround size and suppression level) were extracted and plotted as a function of eccentricity for each visual area (see Figure 6.8). All data were binned across eccentricities, with the mean value at each eccentricity presented on Figure 6.8. All pRF plots demonstrate the expected transition from central stimuli to peripheral; for example, both centre and surround sizes steadily increase with eccentricity, while suppression values are relatively stable. This is supportive of the use of this methodology for mapping peripheral pRF values even in the restrictive environment of a 7T MRI. In general, the relationship between pRF metrics and eccentricity is as expected for V1-2 (i.e. larger in V2 than V1), but V3 estimates in the most peripheral region (i.e. 15° onwards) appear smaller than would be expected by the previous literature. While both centre and surround sizes in V3 should be consistently larger in V3 than V2, this is not always the case in the peripheral region, beyond around 15°. Possible reasons for this are discussed in section 6.5. One aspect to note in the peripheral regions is that a 'dip' of the pRF size estimation is observed at the most peripheral eccentricities for all visual areas (e.g. at 18.7°). This is likely due to the size of the receptive fields at this eccentricity; if the receptive field in question is large enough that it is only partially stimulated by the stimulus, a poorer model fit and under-estimation of the true pRF size would be expected. This 'clipping' or 'edge effect' is a known problem with pRF mapping paradigms but may be a greater problem in the periphery due to the larger pRF sizes.

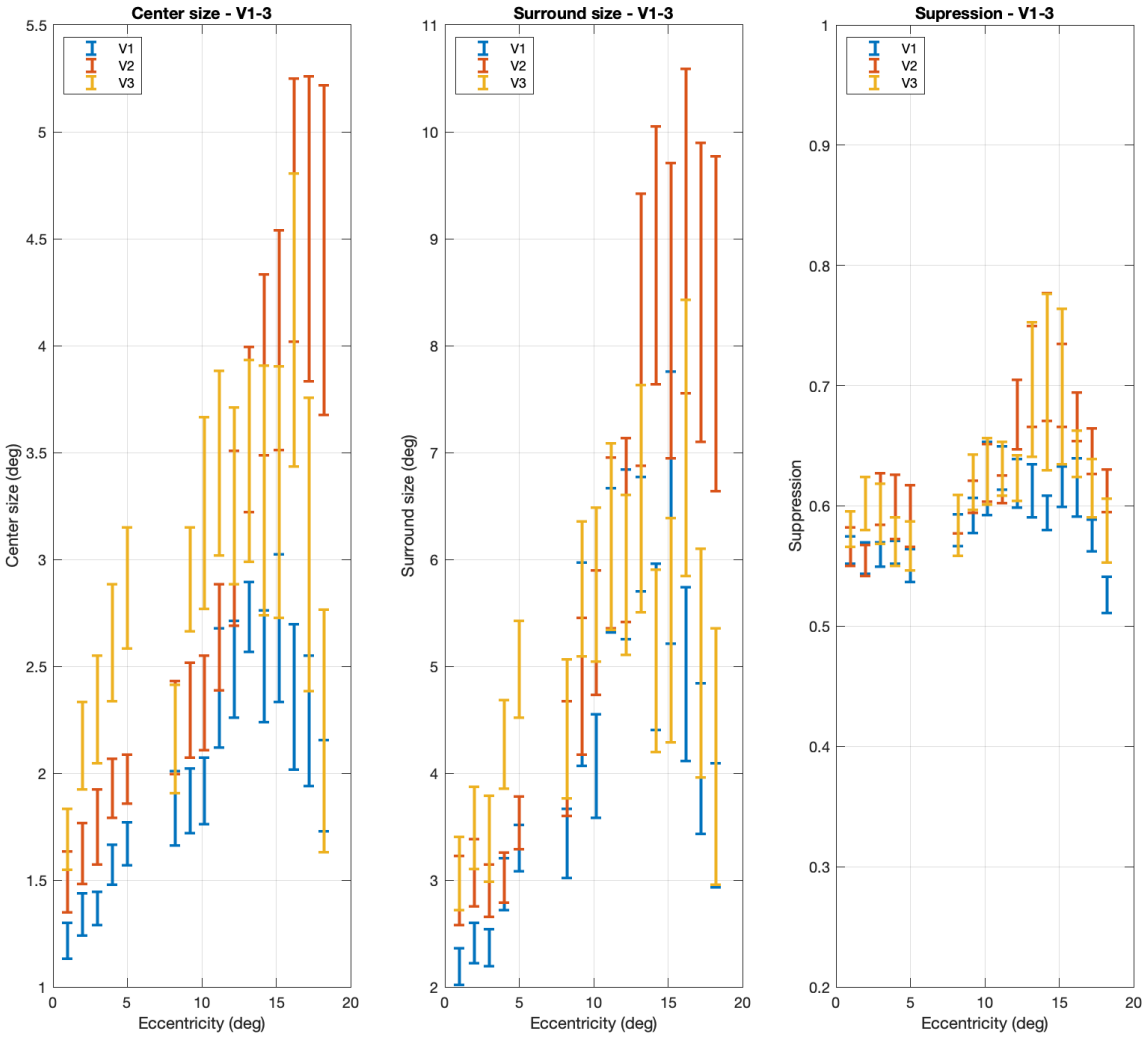

Figure 6.8 – Mean population receptive field metrics plotted as a function of eccentricity. Error bars refer to the standard error of the mean. Different colours refer to different visual areas (V1-3). Centre size and surround size are given in degrees of visual angle (deg). Suppression is defined as the ratio between the area under the inhibitory and excitatory Gaussians.

6.4. Results – Comparison to high myopic patients

The low myopia (LM) group discussed in the section above were then compared to an exploratory sample of young adults with a refractive error of -5.00D or greater (termed the high myopia [HM] group), in order to examine the impact of myopia on our outcome measures.

6.4.1. Comparison of group demographics

Levels of myopia were significantly higher (i.e. refractive error was significantly more negative) in the HM group (Mean[IQR]=-7.70D [-7.75, -7.25]) compared to the LM group (Mean [IQR]=-0.95D [-1.25, 0]; t=9.816; df=23; P<0.001; see Figure 6.9). Age was also

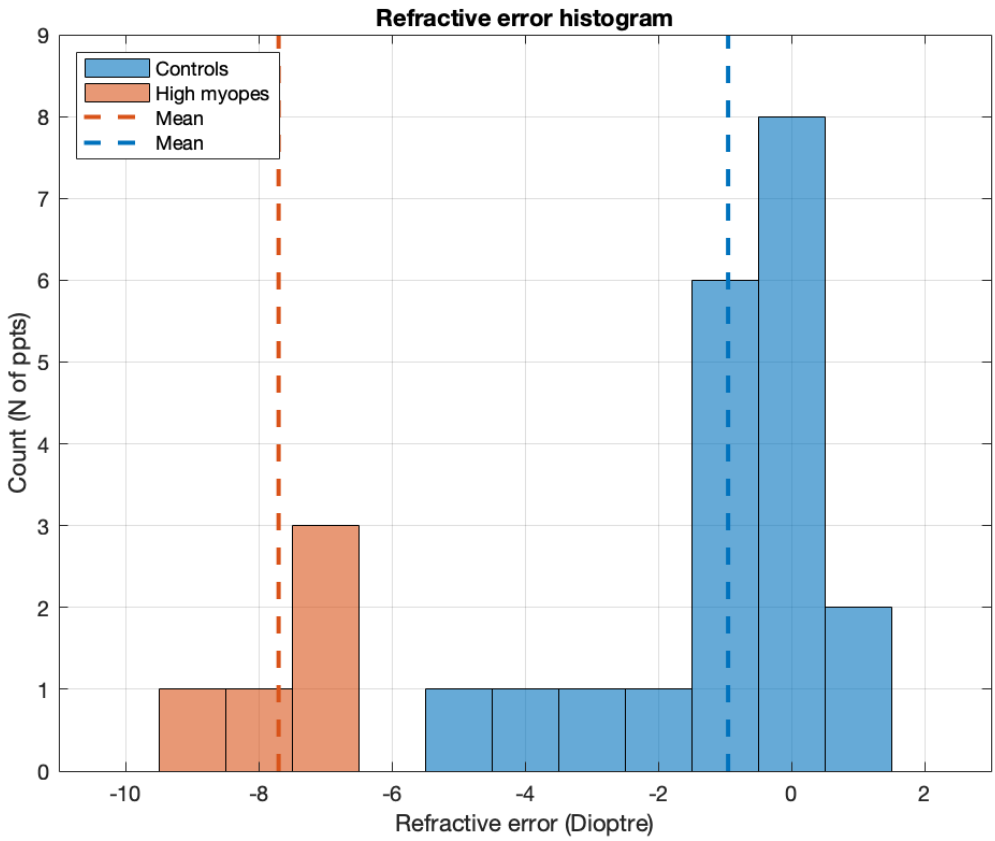

Figure 6.9 - Histogram of refractive error for the high myopia (orange) and non-myopia group (blue). Dashed lines show the means.

significantly different (t=-4.402; P<0.001;) between the HM group (Mean[IQR] = 27.81 years [25.29, 30.52]) and the LM group (Mean[IQR] = 20.76 years [19.31, 20.93]; see Figure 6.10). As previous reports demonstrate that pRFs are stable in childhood and young adults (Dekker *et al.*, 2019), it is unlikely that a change in pRF size would be present between these ages. While pRF size estimates may change in older adulthood (Brewer & Barton, 2014), it is unlikely to be a factor in the small range used here. In support of this, no relationship is found between age and V1 pRF parameters in the LM group (when averaged over all eccentricities; centre: Pearson's r=0.128, p=0.507; surround: r=0.308, p=0.186; suppression: r=0.054, p=0.821; CMF: r=-0.095, p=0.691).

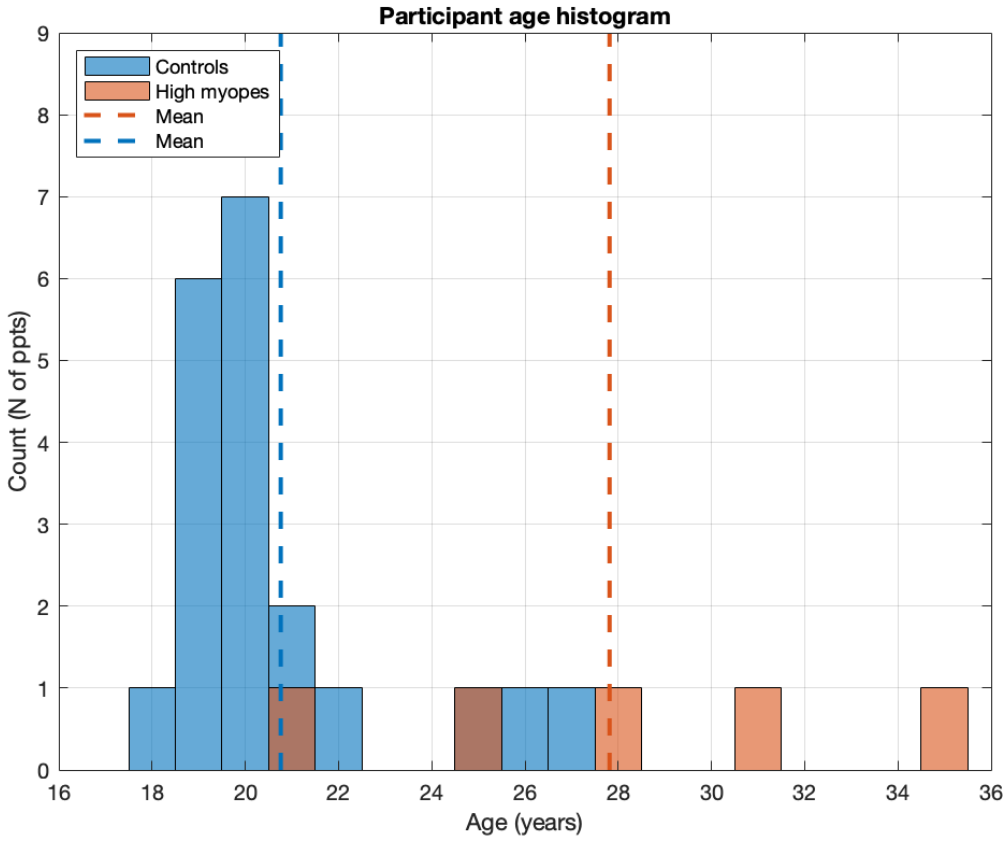

Figure 6.10 - Histogram of ages in years for the high myopia (orange) and non-myopia group (blue). Dashed lines show the means.

6.4.2. Group differences in population receptive field size as a function of eccentricity

Comparisons of the HM and LM group pRF metrics as a function of eccentricity are plotted in Figure 6.11, Figure 6.12 and Figure 6.13. From visual inspection of these plots, it can be seen that the HM group seem to show larger pRF centre sizes in the periphery for V1-3, as hypothesised by our initial aim. The HM group may also have larger surround sizes than the LM group, again focussing on the periphery. The suppression level however, appears relatively stable between groups.

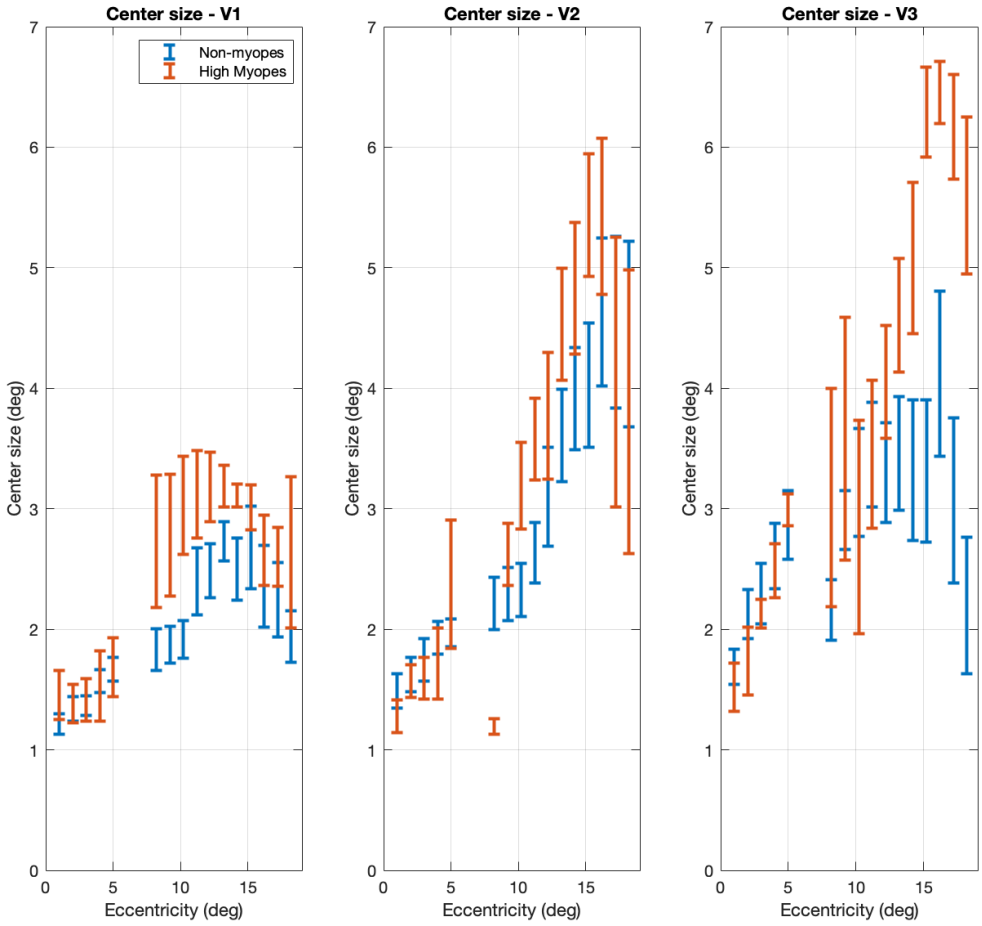

Figure 6.11 - Comparison of population receptive field centre sizes (°) for the high myopia (orange) and non-myopia (blue) groups. Values shown are the mean at each eccentricity.

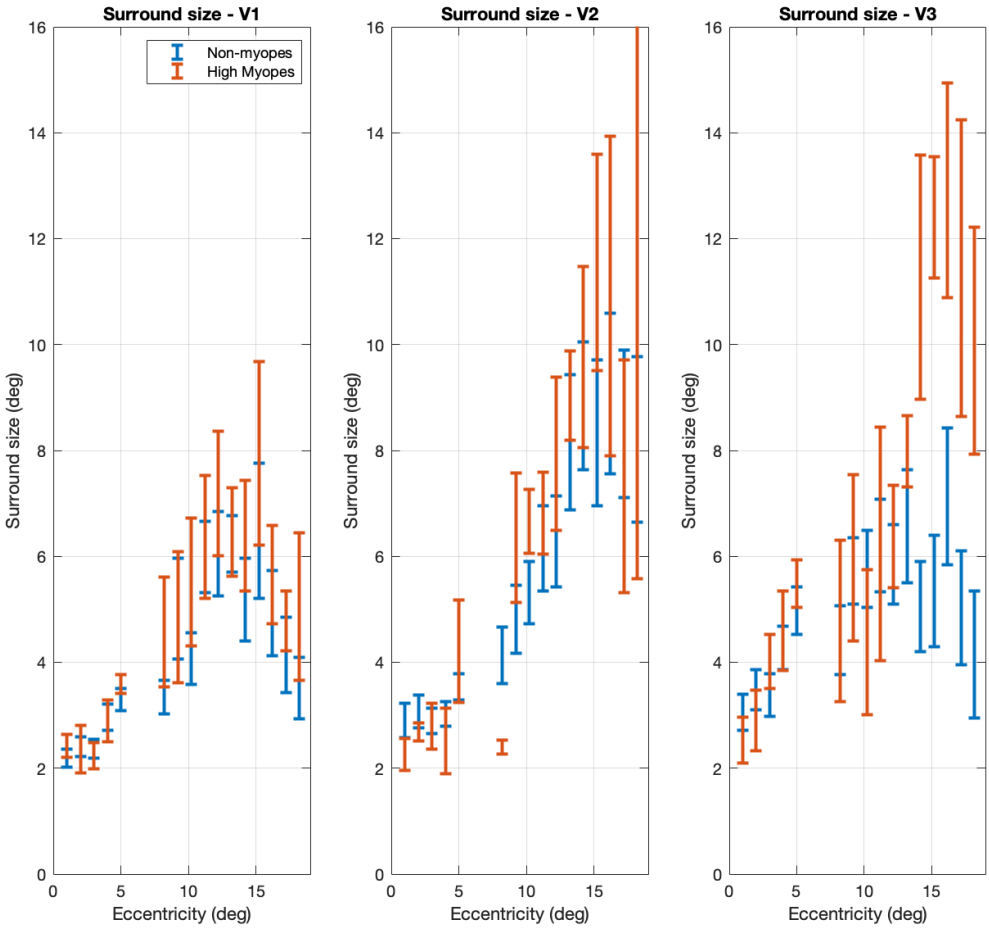

Figure 6.12 - Comparison of population receptive field surround sizes (°) for the high myopia (orange) and non-myopia (blue) groups. Values shown are the mean at each eccentricity.

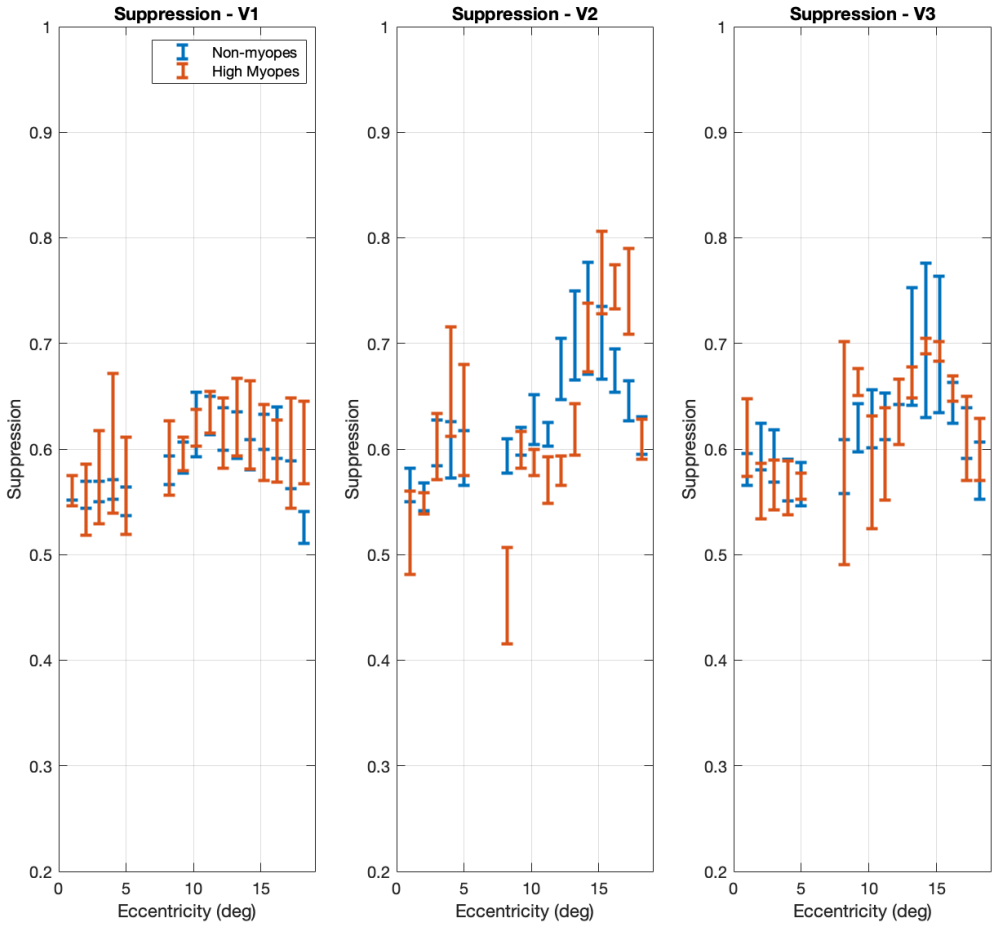

Figure 6.13 - Comparison of population receptive field suppression level (as defined as the ratio between the area under the curve of the centre and surround Gaussian curves) for the high myopia (orange) and non-myopia (blue) groups. Values shown are the mean at each eccentricity.

6.4.3. Relationship between refractive error and receptive field measures

In order to address the second aim of the research within this chapter, the groups were combined, and a correlation performed on the refractive error of the target eye and the centre size, due to the possible differences discussed above. In order to address possible effects of eccentricity, both the central and peripheral run were considered individually. For the central value therefore, pRF centre sizes were averaged across all central eccentricities (0-5.5°). An average peripheral value was created by averaging (mean) across peripheral eccentricities. However, as previously discussed, edge effects are apparent in our data, in which pRFs centred at the edge of the stimulus are underestimated. In order to exclude these pRFs therefore, pRF values at edge eccentricities were excluded (i.e. 8.2°, 17.2°, and 18.2) and pRF values across the remaining eccentricities (9.2°-16.2°) averaged over.

A Spearman's rho correlation was first performed between pRF centre size and refractive error. A negative correlation was hypothesised, with more negative refractive errors associated with larger centre sizes, so one-tailed Spearman's rho correlations were completed (for scatterplots, see Figure 6.14 and Figure 6.15). For V1, a significant relationship was found for central vision (r= -0.357; p= 0.040; slope= -0.027) and peripheral vision (r= -0.506; p= 0.005; slope= -0.123). Both retain significance after Bonferroni-Holm correction for multiple comparisons (Holm, 1979; Central p= 0.040; Peripheral p= 0.010), which was completed within MATLAB software (Groppe, 2020; *MATLAB*, 2018). For V2, the relationship between refractive error and central V2 centre size was not statistically significant (r= -0.280; p=0.087; slope= -0.020). The association with peripheral V2 centre sizes and refractive error however, was significant (r= -0.347; p= 0.048; slope= -0.181), though this did not survive Bonferroni-Holm correction for multiple comparisons (p= 0.0960). For V3, neither central centre sizes (r= -0.242; p= 0.122; slope= -0.028) or peripheral centre sizes (r= -0.170; p= 0.208; slope= -0.097) showed a statistically significant relationship with refractive error. It is notable that all relationships showed the hypothesised negative relationship, and the slope also increased between central and peripheral vision in all visual areas.

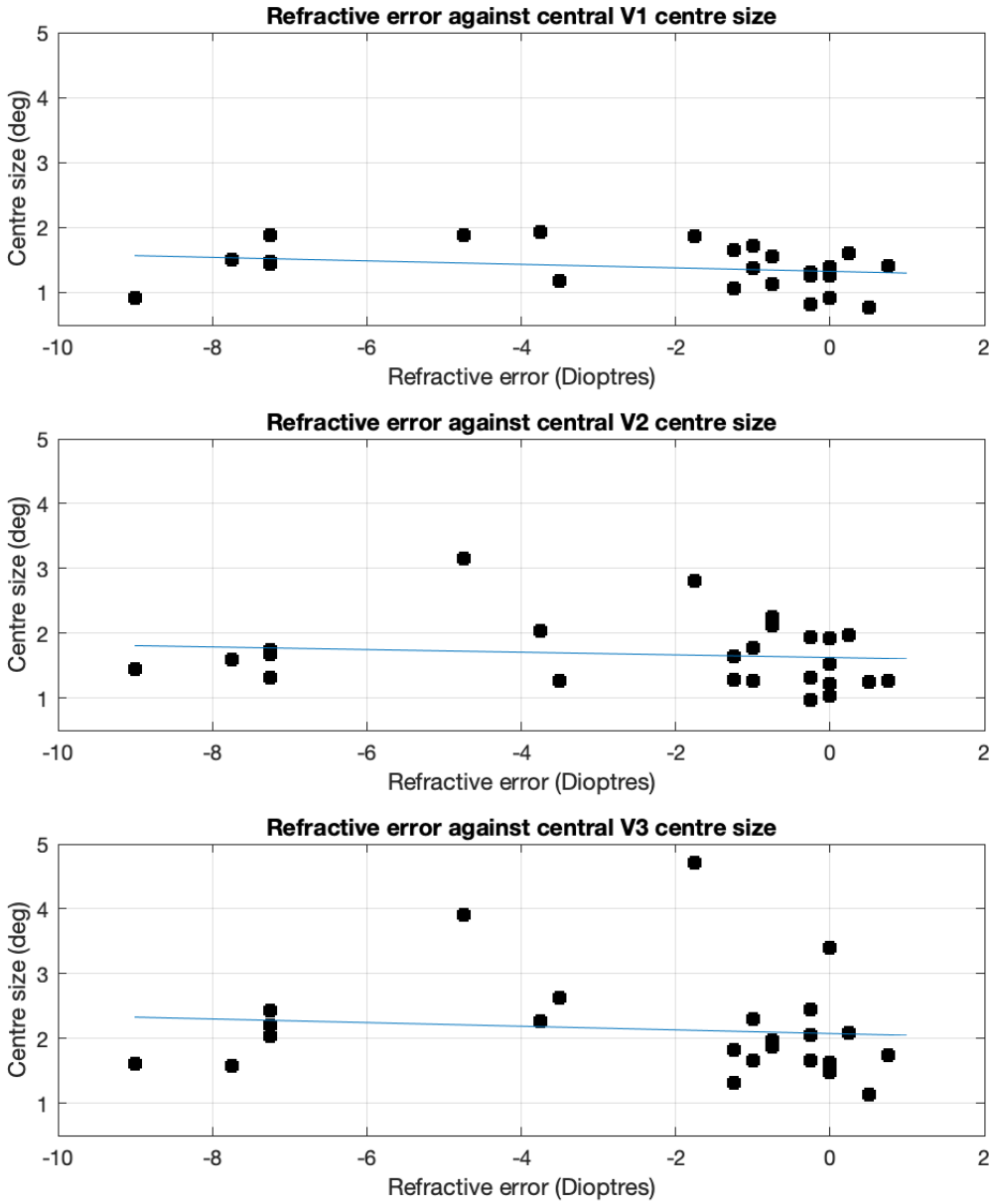

Figure 6.14 – Refractive error (Dioptre) plotted as a function of centre size (°) averaged across central eccentricities (0-5.5°) for V1-3. Line = line of best fit.

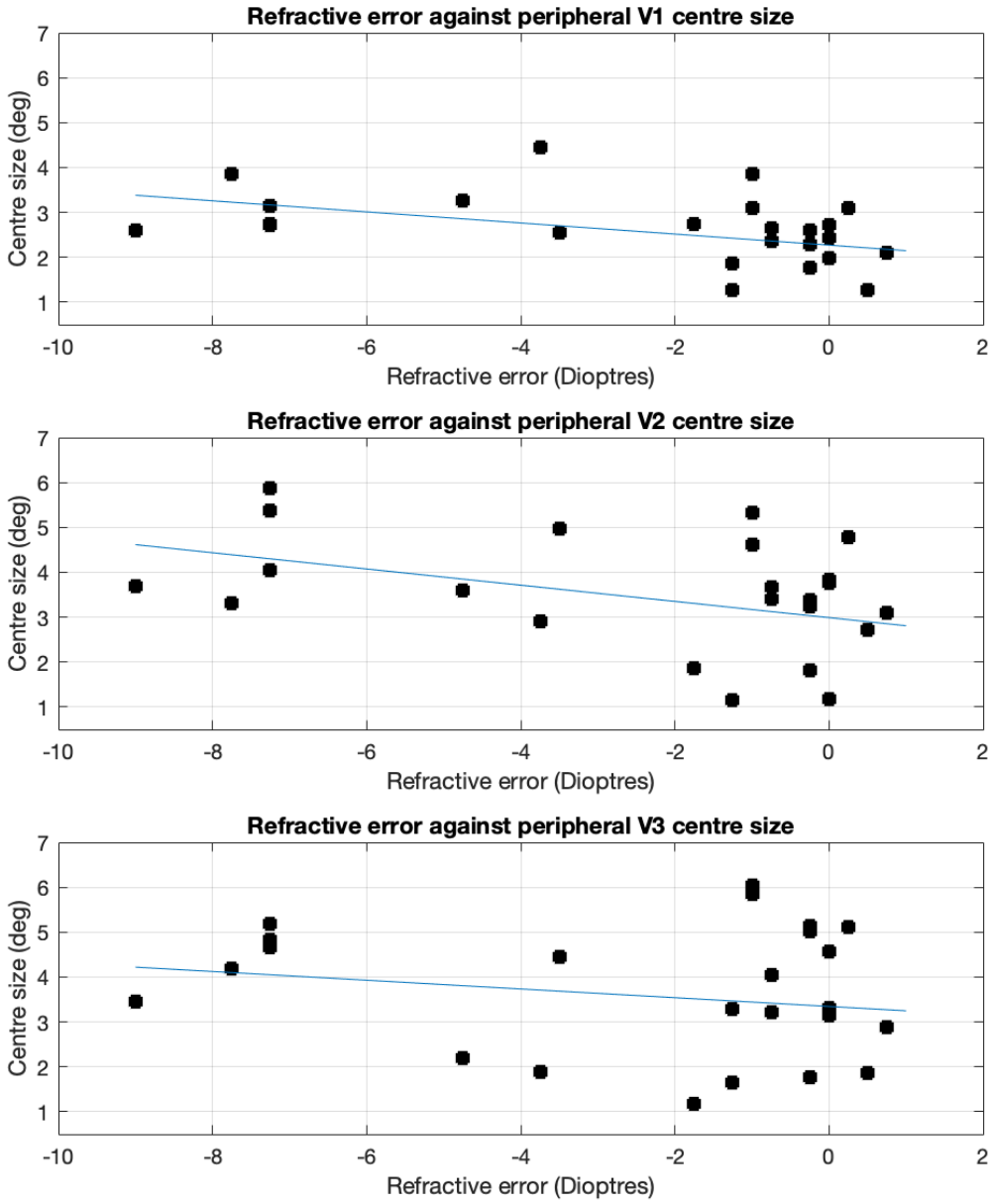

Figure 6.15 – Refractive error (Dioptre) plotted as a function of centre size (°) averaged across peripheral eccentricities (9.2-16.2°) for V1-3. Line = line of best fit.

In order to investigate whether axial eye length, which can be a causative factor in myopia, is also associated with pRF centre size, the correlations between axial eye length of the target eye and pRF centre sizes in V1-3 was also examined. Again, central and peripheral vision was examined separately. A positive relationship was hypothesised, as a longer axial eye length should lead to greater myopia and larger centre sizes. One-tailed Spearman's rho correlations were therefore run between axial eye length and pRF centre size in V1-3 for central and peripheral vision (for scatterplots, see Figure 6.16 and Figure 6.17). Similarly to above, V1 pRF centre size demonstrated a significant correlation with axial eye length in both central (r= 0.428; p= 0.017; slope= 0.093) and peripheral vision (r= 0.474; p= 0.009; slope= 0.301). Both retain significance after Bonferroni-Holm correction for multiple comparisons (Holm, 1979; central: p=0.018; peripheral p=0.018). For V2, the relationship did not meet statistical significance for central (r= 0.289; p= 0.080; slope= 0.088) or peripheral vision (r= 0.252; p= 0.117; slope= 0.269). For V3, the relationship also did not meet statistical significance for central (r= 0.077; p= 0.357; slope= 0.048) or peripheral vision (r= 0.117; p= 0.288; slope= 0.086). As with the correlations with refractive error, though not all relationships were significant, all showed the hypothesised positive relationship, and the slope also increased between central and peripheral vision in all visual areas.

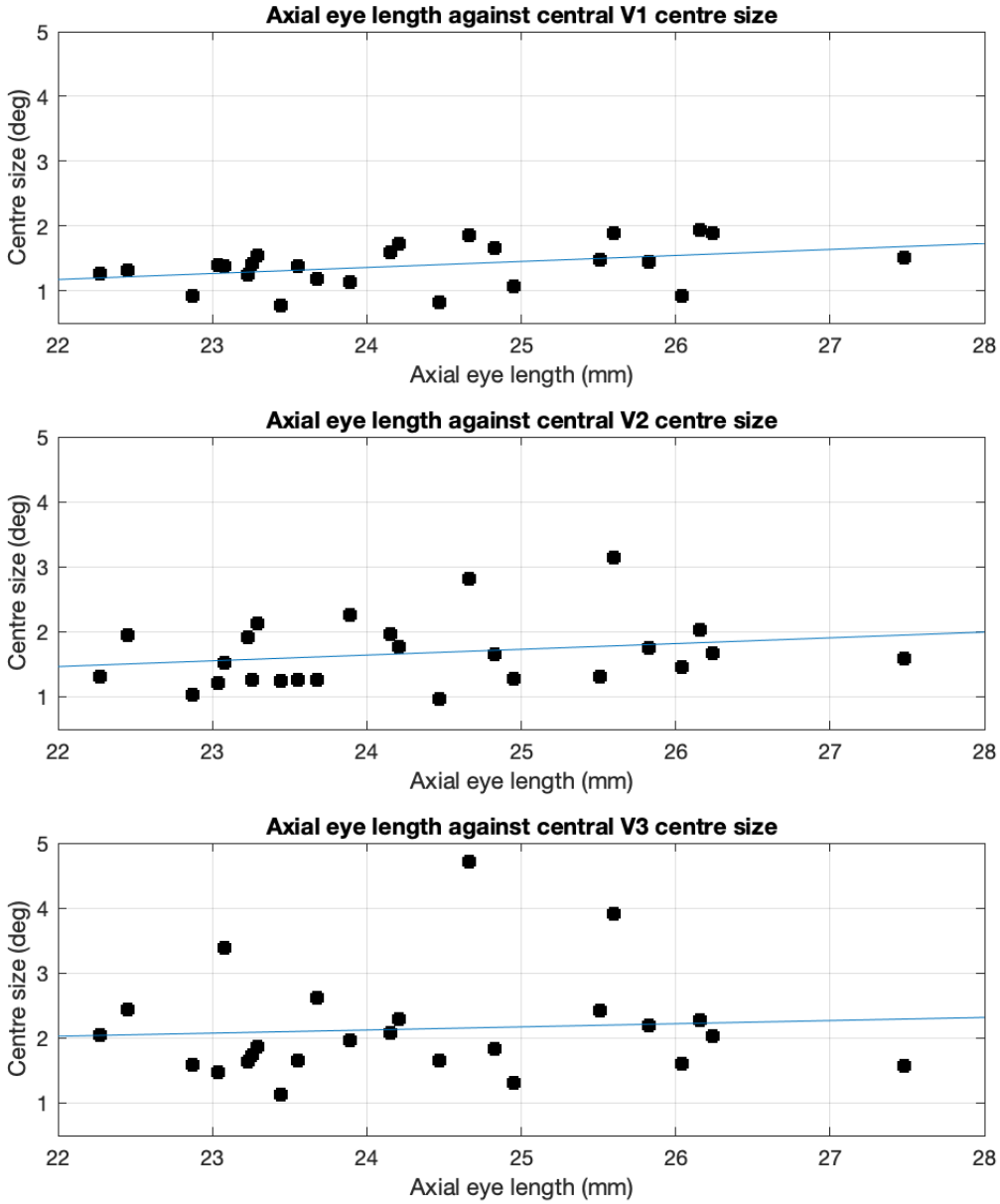

Figure 6.16 – Axial eye length (mm) plotted as a function of centre size (°) averaged across central eccentricities (0-5.5°) for V1-3. Line = line of best fit.

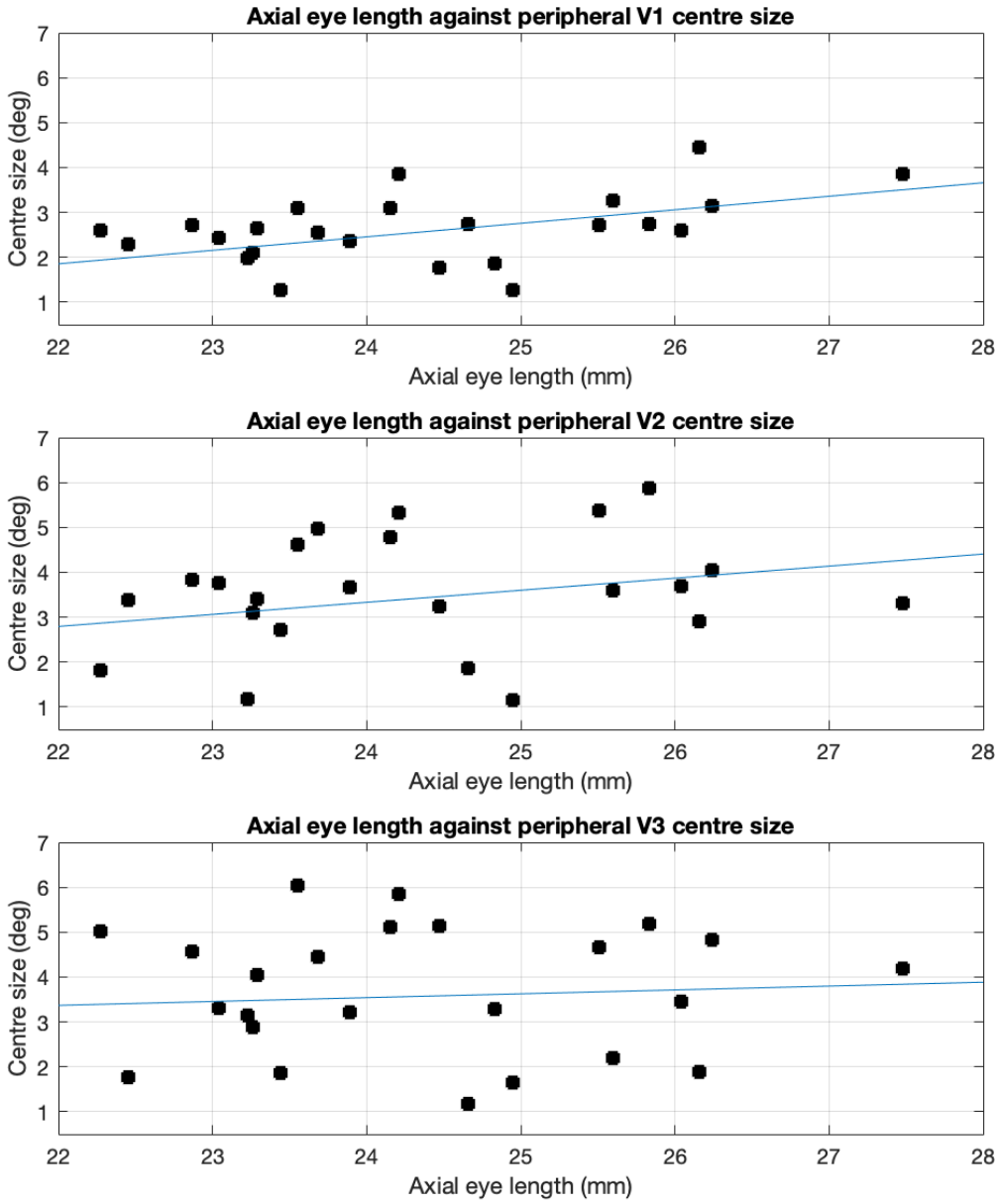

Figure 6.17 – Axial eye length (mm) plotted as a function of centre size (°) averaged across peripheral eccentricities (9.2-16.2°) for V1-3. Line = line of best fit.

6.4.4. Visual area size

As we can only examine the receptive fields of the neurons within a voxel as a whole, rather than the receptive fields directly (i.e. pRFs rather than receptive fields), it is possible that individual variation in visual area size will impact our pRF estimates. For example, a voxel of a fixed size in a participant with a large V1 will constitute a smaller percentage of V1 and thus cover a smaller amount of the visual field than a voxel of the same size in a participant with a very small V1, despite possibly having similar receptive field sizes. We therefore considered the possibility that this may introduce some bias into our findings, as previous work has suggested a possible relationship between orbital eye volume and visual cortex volumes (Masters *et al.*, 2015; Pearce & Bridge, 2013). However, it is also possible that smaller visual area sizes will lead to coarser sampling of pRF sizes at particular eccentricities, which may lead to poorer estimates that may not be necessarily larger. Another problem is how one may correct for this. For example, the size of V1 will not scale proportionately, but may be more compressed on one side of V1 (e.g. either more central or peripheral visual field) than the other. A global correction would therefore be not appropriate.

To ensure that the myopia investigations discussed would not be confounded by visual area size therefore, it was investigated whether visual area size (for V1, V2d, or V3d) were significantly different between the LM and HM groups. The visual area size was defined as the surface area (mm^2) of the visual areas delineated from the functional retinotopic maps. Two-way independent t-tests confirmed that there was no statistically significant group difference in visual area size (V1: t=1.24, p=0.23; V2d: t=0.27, p=0.79 V3d: t=0.43, p=0.67). This therefore suggests that visual area size should not systematically bias our results.

6.5. Discussion

The first aim of the research described within this chapter was to establish a method of measuring pRF sizes in the peripheral visual field with 7T fMRI in a sample of healthy young adults, as well as to highlight possible issues. This has been demonstrated using a difference-of-Gaussian pRF model, which allows for the relationship between pRF centre size, surround size, and suppression level as a function of eccentricity to examined. The

relationships between these pRF parameters and eccentricity in our healthy adult data appear mostly consistent with previous work, especially within central vision. All visual areas show an increase in pRF size with eccentricity, which continues out to the periphery. An edge effect is apparent from our data (as can be seen in Figure 6.8), in which there is an underestimation of pRF sizes at eccentricities that represent the 'edge' of the stimulus. This is a known problem in pRF mapping and may be due to receptive fields at these eccentricities not being completely covered by the stimulus, leading to coarser sampling of the receptive field and poorer pRF estimates. This partial stimulation may also lead to lower amplitude of responses, and thus poorer SNR at these locations. This effect appears to be greatest at the most peripheral eccentricities, which is likely due to the larger receptive fields centred in the periphery. For statistical analysis, eccentricities at these locations were therefore excluded, which is a method we can bring forward to our glaucomatous sample. pRF size also increases as expected from V1-3, as demonstrated by the scatter plots in Figure 6.8. However, the mapping for V3 appears to have estimated smaller sizes than one would expect based on previous literature (e.g. Alvarez *et al.*, 2015; Smith *et al.*, 2001), at more peripheral regions (i.e. 15+°). This doesn't appear to be problem in stimulating larger pRF sizes per se, as the larger estimates are found in V2. It may be that this stimulus is not optimal for stimulating V3, especially with the lower SNR we may expect in the smaller peripheral region, though natural scene retinotopy stimuli have been successfully used before (e.g. Alvarez *et al.*, 2015). It may also reflect a larger amount of 'clipping' in V3 due to the larger receptive fields. Overall, the results support the use of this methodology for mapping pRF sizes in peripheral vision, despite the constraints placed by the 7T scanning environment.

The second aim of this chapter was an exploratory investigation into the relationship between pRF sizes and refractive error/ axial eye length. It was hypothesised that, following findings of increased spatial summation in the visual system in myopia (i.e. Ricco's area; Stapley *et al.*, 2019), more negative refractive error and greater axial eye length would be associated with larger centre sizes, particularly in the periphery. A qualitative examination of the resulting scatterplots comparing centre sizes as a function of eccentricity relationships in the HM and LM groups support this initial hypothesis. Furthermore, this relationship was apparently across visual areas, though was most apparent in V1.

Correlations between pRF centre sizes and both refractive error and axial eye length were then quantitatively calculated (see Figure 6.14-17). In all visual areas, slopes in the hypothesised direction were found. Furthermore, all visual areas demonstrated an increase in the steepness of the relationship in the periphery compared to central vision. Similarly to observations from the group scatterplots, the relationships were strongest in V1, which was the only area in which significance passed corrections for multiple comparisons. There therefore appears to be a relationship between pRF centre size and refractive error/axial eye length, despite MR-safe vision correction, which suggests that this is an important factor to consider in future visual MRI studies, especially when examining pathologies that may be associated with a higher myopia rate.

There are several possible explanations for this finding, which need to be further teased apart in future work but are outside the scope of this thesis. For example, it may be hypothesised that in eyes with longer eye axial lengths (and thus greater refractive error), the retina is stretched (due to the same amount of retinal tissue having to cover a larger area) which may lead to the increase in Ricco's area discussed previously, as the retinal neurones are less dense and may summate information over a larger area to retain adequate coverage (Stapley *et al.*, 2019). This increased spatial summation at the retinal level would have upstream consequences and may lead to enlarged cortical pRF sizes. As retinal stretching has been found to occur to a greater extent in the periphery than the fovea (Lam *et al.*, 2007), this would also explain why stronger relationships were found within peripheral vision compared to central in the current study. The increased spatial pooling at the cortex may therefore be reflective of this increased pooling earlier on in the visual pathway due to eye growth and retinal stretching. However, this hypothesis would have to be directly tested in a larger sample with a more even distribution of axial eye lengths. Our results may also be explained by the decreased peripheral visual acuity reported in myopia (Chui *et al.*, 2005; Ehsaei *et al.*, 2013), especially as the steepness of the relationships increases in the periphery. It has been suggested that the linear axial stretching model is not enough to explain the decrease in peripheral visual acuity found in myopic eyes. Instead, it may be that rotation in the myopic eye is leading to disruption of usual photopic processes and thus misalignment of the receptors with the exit pupil (Nagra *et al.*, 2018). It may be that this misalignment of photoreceptors is leading to blurring in the

periphery and thus increased cortical pooling, which is reflective in our pRF results. It must also be considered that as a cross-sectional study, this cannot infer causality. For example, it may be that larger cortical receptive fields in development leads to additional growing in the eye. It has been found that pRF do not show much change in childhood and adolescence (Dekker *et al.*, 2019), whereas the eye continues to grow into teenage years (Fledelius *et al.*, 2014). This should be specifically investigated by measuring pRFs and refractive error in a sample of children at-risk of myopia, across multiple time points. Overall, a relationship between myopia and pRF sizes is demonstrated, despite the use of MR-size vision correction, especially in V1. The underlying cause of this relationship warrants further investigation but is outside the scope of this thesis.

A limitation to the method of 7T pRF mapping in the peripheral visual field described in this chapter is that the manual delineation of the peripheral region of the retinotopic map was more difficult than the central map, especially with the delineation of the boundary between V2 and V3 (V1 introduces less of an issue, as it lies in a separate section of cortex, as can be seen in the example retinotopic maps in Figure 6.5). For the central map, the polar angle reversals can be used to delineate V2 and V3 as all polar angles are sampled. For the peripheral stimulation however, the stimulus is centred around the horizontal meridian and there is a much smaller range of polar angles. While in this study the peripheral eccentricity maps and the central retinotopic maps were used to create an approximation of where this boundary should be (e.g. by continuing the projection of the polar angle reversals in the central map and by following the eccentricity gradient in the periphery map), it is possible that this was not always accurate, especially at the most peripheral eccentricities from fixation as these would be represented by the smallest region of cortex. When taking this methodology forward to our glaucoma study therefore, it may be useful to use a less manual method of delineating visual areas, such as using the structural predictive labels produced by FreeSurfer. This is discussed further in the following methods development chapter.

Overall, this chapter describes a viable method of investigating mid-periphery pRF sizes at 7T in early visual areas. By investigating this in a sample of young adults, healthy relationships could be established, and potential areas of improvement identified. The described exploratory myopia study has also highlighted the importance of considering

refractive error in our glaucomatous sample, as well as highlighting possible avenues of investigation outside the scope of this thesis.

Chapter 7. Methods Development for glaucoma investigations

7.1. Introduction

The main aim of this thesis is to investigate the neural basis of Ricco's area changes in glaucoma. This involves investigating structure and function at multiple locations throughout the visual pathway (i.e., at both the retina and the cortex), with a focus on how estimates of receptive field sizes differ along this pathway in glaucoma patients and healthy controls and then contributes to psychophysical changes. This is explored in Chapters 8-11. To generate the data for these investigations, a sample of glaucoma patients and age-similar healthy controls were recruited and completed the following experimental tests in two visits to Cardiff University:

1. A psychophysical measurement of Ricco's area
2. Optical Coherence Tomography (OCT)
3. Pattern Electroretinography (PERG)
4. Functional and structural Magnetic Resonance Imaging (MRI)

As well as this, a number of preliminary measurements were taken to ensure eligibility (i.e., clinical perimetry; see section 7.5). As some participants withdrew for certain tests (e.g., MRI) during testing, the demographics of the samples contributing to each chapter will be discussion within that chapter. To optimise the methodology for the definitive study in the glaucoma and control cohorts, we trialled our experimental techniques on small samples of healthy individuals.

7.2. Optimisation of Pattern Electroretinogram (PERG) measurement

As discussed previously (e.g. see Chapter 4.2), while the traditional explanation of Ricco's area was that it reflects the area of retinal receptive fields, recently, more evidence (e.g. Je *et al.*, 2018; Pan & Swanson, 2006; Redmond *et al.*, 2010) suggests a cortical component. However, considering that Retinal Ganglion Cell (RGC) dendritic trees have been found to shrink in the disease (e.g. Morgan, 2002) and changes at this level will directly impact the input to the cortex, it is prudent to also examine retinal receptive field sizes when investigating the contribution of cortical receptive field sizes to Ricco's area. Pattern Electroretinography (PERG) was therefore chosen to estimate functional receptive field sizes

within the retina (specifically Retinal Ganglion Cells; RGCs) in glaucoma patients and healthy controls (discussed further in Chapter 5). Before experimental tests were completed with this clinical sample, PERG methodology was optimised and trialled as detailed below.

7.2.1. Pattern reversal vs onset-offset

PERG allows for the direct electrophysiological recording of retinal function in response to patterned stimuli. An important characteristic of this methodology is that global stimulus luminance does not change throughout the recording session, but local luminance does, so that only spatially sensitive cells will show time-locked responses. A stimulus typically used for this type of recording is a high-contrast pattern with high- and low-luminance components that alternate across space (e.g., a grating or checkerboard) and time (e.g. onset-offset or pattern reversal). A method for investigating retinal receptive field sizes using PERG, which has been employed in previous studies (Drasdo *et al.*, 1987, 1990; Thompson, 1987), is the generation of PERG spatial tuning curves, whereby the amplitude of the electrophysiological response of interest differs with the presented spatial frequency of the stimulus. Typically, this amplitude increases with increasing spatial frequency, before reaching a peak (when the high-luminance portion completely fills the receptive field excitatory centre) and then decreasing again (when the high luminance portion expands and encroaches the inhibitory surround). This peak spatial frequency can be used as an estimate of the underlying average receptive field size. To delineate a spatial tuning curve, the PERG response amplitude must demonstrate both high and low spatial frequency attenuation (HSFA/LSFA; i.e. a decrease in PERG response amplitude to high or low spatial frequencies respectively). Two common PERG methodologies were therefore investigated for spatial tuning with a view to choosing the optimum methodology for employing in the experiments: i) pattern reversal, and ii) pattern onset-offset. For more discussion and description of these methodologies and their application in glaucoma, see Chapter 5.

Pattern reversal involves the high- and low-luminance portions of a stimulus alternating at a given temporal frequency. Depending on the temporal frequency, the PERG can be classed at either sustained/steady-state (high temporal frequency) or transient (low temporal frequency), with each having different response characteristics. Transient reversal PERG (temporal frequency <3Hz; Bach et al., 2013) is of particular interest, as N95 (a large negative-going peak at around 95ms post-reversal) is reflects RGC spiking activity. RGC

damage is a characteristic feature of glaucoma, and indeed, N95 is selectively reduced in glaucoma compared to controls (e.g. Bach & Hoffmann, 2008; Jafarzadehpour *et al.*, 2013). This component would therefore be useful for investigating RGC spatial tuning in a sample of glaucoma patients. However, HSFA and LSFA must both be demonstrated in the response amplitude (i.e., bandpass spatial tuning) if inferences about receptive field size are to be drawn. Two early studies have reported some spatial tuning properties in response to pattern reversal grating stimuli, with peaks at 2-5 cycles per degree (cpd; Fiorentini et al., 1981; Hess and Baker, 1984). However, both of these studies utilise steady-state PERGs (specifically, both use a reversal rate of 8Hz), which prevent the identification of components such as N95. Korth and Rix (1989) later investigated PERG response to a reversing grating stimuli with a much lower reversal rate (1.4Hz) and found only a very slight suggestion of spatial tuning, with a peak around 1.5 cpd. Faster reversals may therefore be more optimal for tapping into spatially selective mechanisms. However, other work has identified spatial tuning using transient reversal PERG (<3Hz) and with the use of a checkerboard, rather than a grating, stimulus (Holder et al., 2007), with N95 appearing especially likely to demonstrate spatial tuning (Arden & Vaegan, 1983; Bach & Holder, 1996; Berninger & Schuurmans, 1985). The peak spatial frequency for these tuning functions is smaller than that reported by steady state, at 1-2 cpd. Evidence of spatial tuning is also mostly found with smaller field sizes (e.g. Bach & Holder, 1996, found spatial tuning for a screen size of 16x14° but not 32x27°), possibly due to overlapping of larger receptive fields in the periphery. As the experiments in this thesis require a precise measure of spatial tuning functions, it will be important that the stimulus paradigm is optimised for this purpose.

An alternative technique is onset-offset PERG, for which there is more consistent evidence of spatial tuning, primarily in the onset response (e.g. Arden and Vaegan, 1983; Drasdo et al., 1987; Korth, 1983; Korth et al., 1989; Korth and Rix, 1989). This method records an onset response while a pattern is being displayed, and an offset response while a (typically mean-averaged) plain luminance screen is displayed. The pattern and solid luminance are alternated, though the temporal rate of this varies widely (i.e. 105-800ms onset, 106-1250ms offset; see Table 7.1). The majority of studies investigating spatial tuning using the onset response have identified a peak at around 3-4 cpd (e.g. Drasdo *et al.*, 1987; Korth, 1983; Korth *et al.*, 1989; Korth & Rix, 1989), though Arden and Vaegan (1983), who employed a checkerboard stimulus rather than a grating, found a peak at 2.27 cpd. This finding of studies employing a checkerboard stimulus reporting a lower cpd than those utilising a grating stimulus is similar to what is described above with pattern-reversal stimuli, suggesting that it may be a consistent effect that checkerboards elicit a spatial tuning peak at lower spatial frequencies. It has also been suggests that checkerboard stimuli are less optimal for investigating spatial tuning as multiple spatial frequencies are present (Bach & Holder, 1996), which may contribute to this difference in reported cpd.

Table 7.1 – Summary of previous research into spatial tuning curves with either pattern reversal or pattern onset-offset methodologies, which was used as a reference for the design of piloting methodology. Degrees are in visual angle; cpd = cycles-per-degree

Study	**Fiorentini et al. (1981)**	**Hess and Baker (1984)**	**Berninger and Schuurmans (1985)**	**Bach and Holder (1996)**	**Bach and Holder (1996)**	**Korth and Rix (1989)**
Method	Reversal	Reversal	Reversal (N95)	Reversal (N95)	Reversal (N95)	Reversal
Field size	24° and 12.5° radius	1.6x1.7°	14.5x18.5°	16x14°	32x27 °	15° radius
Temporal freq.	8Hz	8Hz		2.245Hz	2.245Hz	1.4 Hz
Stimuli	Vertical grating	Grating		Checkerboard	Checkerboard	Square-wave grating
Viewing distance	57cm or 114cm	7.15m		1.14m	0.57m	
Spatial freq.	0.2-6 cpd			0.26°, 0.52°, 1.2°, 4° and 8x7°	0.26°, 0.52°, 1.2°, 4°, 8° and 16x14°	0.3-8.55 cpd
Contrast	30%	100%		98%	98%	97%
Spatial tuning?	Yes	Yes	Yes	Yes (LSFA at 1.2-7)	No	Very slight
Estimated spatial tuning peak?	2-3 cpd	2-5 cpd		1-1.33 cpd		1.5 cpd
Study	**Arden and Vaegen (1983)**	**Drasdo et al (1987)**	**Korth and Rix (1989)**	**Korth et al. (1989)**	**Korth (1983)**	**Arden and Vaegen (1983)**
Method	Reversal	Onset-offset	Onset-offset	Onset-offset	Onset-offset	Onset-offset
Field size	4.74x7.5°	0-5.1°, 5.6-12.6°, 12.3-26.3° angular radius	15° radius	22° radius	40° diameter	23x17°
Temporal freq.	3Hz	105ms on, 106ms off	800ms on, 1200ms off	312ms on, 291ms off	800ms on, 1250 off	165ms on
Stimuli	Checkerboard	Vertical grating	Square-wave grating	Vertical square-wave grating	Grating	Checkerboard
Viewing distance		126, 50, or 22.5cm				
Spatial freq.	8, 4°, 2°, 1°, 30', 15', 7.5', and 3.8'	0.14-20 cpd	0.3-8.55 cpd	0.2 and 3.4 cpd	0.21 - 9.4 cpd	8, 4°, 2°, 1°, 30', 15', 7.5', and 3.8'
Contrast	87%	75%	97%		99%	96%
Spatial tuning?	Yes	Yes	Yes	Yes, but only 2 cpd used	Yes	Yes
Estimated spatial tuning peak?	2 cpd	4 cpd	3 cpd	3 cpd	3.5 cpd	2.27 cpd

Why might there be this difference in the strength of spatial tuning between pattern reversal and pattern onset-offset responses? The main difference between these methods is the change in local luminance, with pattern reversal stimuli associated with a higher luminance modulation depth (Korth & Rix, 1989). For example, while the high-luminance section of a 100% contrast reversal pattern will change from 100% (maximum luminance) to 0% luminance in a reversal, the high-luminance component of a 100% contrast onset/offset pattern will change 50% from the onset state (100%; maximum luminance) to the mean luminance offset state. It is possible that lower luminance changes are more optimal for investigating spatial tuning. By decreasing the contrast of the pattern reversal stimulus and thus decreasing the local luminance change, stronger spatial tuning functions may be found as the local luminance change will be similar to pattern onset-offset methodology. However, lower contrast stimuli would lead to smaller amplitudes and so the possibility of low signal to noise ratio in the pattern reversal PERG response. This was therefore also examined in the following methods development.

With these issues in mind, four PERG protocols were developed and tested to identify which would provide clear spatial tuning and therefore be a useful proxy for retinal receptive field size within this project. Specifically, the aim was to identify a protocol that demonstrates both HSFA and LSFA. A summary of previous studies investigating PERG responses to multiple spatial frequencies used as a reference for our methodology development is shown in Table 7.1

7.2.1.1. Methods

7.2.1.1.1 Measurement protocols

Based on previous literature, four protocols were selected for investigation, as well as seven spatial frequencies that subtended the estimated spatial tuning peak found in previous studies (see Table 7.1). For all protocols, the spatial frequencies used were (in cpd) 0.10, 0.32, 0.60, 1.20, 2.50, 5.00, and 7.40.

Firstly, two pattern reversal transient PERG protocols were investigated to examine whether HSFA and LSFA could be observed in the N95. Following the possibility that a lower contrast may produce more spatially selective responses, similar to the onset-offset response (which involves ~50% local luminance modulation rather than ~100%), two

different contrast levels were used with very similar mean luminance but different local luminance changes. The first was set to 96%, which was the highest contrast provided by the software and represented a more traditional PERG. The second was set to 46% to mimic the reduced local luminance modulation with onset-offset PERG. In order to specifically investigate the N95, a temporal frequency of 2.25 Hz was used for both pattern reversal protocols. This is slightly above the recommended 2Hz, as the above studies suggest that higher frequencies lead to stronger spatial tuning curves, but below the 3Hz cut off for N95 detection (Bach *et al.*, 2013). A checkerboard stimulus was used.

For the onset-offset PERGs, the temporal frequency was modulated between the two protocols tested, with the first at 200ms onset and the second at 100ms onset, both of which are similar to what has been used previously (Arden & Vaegan, 1983; Drasdo *et al.*, 1987; Korth *et al.*, 1989). One of the disadvantages of using this type of PERG is that it tends to be a longer protocol than the pattern reversal, which makes it more susceptible to participant fatigue and associated artefacts. The procedure at 200ms onset would take a minimum of 14-15 minutes of active recording, assuming:

- 3 results per spatial frequency with no repeats needed, which would require a perfect observer and is therefore unlikely.
- no breaks in-between, which would be expected to add another 5-10 minutes depending on the participant and the length/ frequency of breaks requested.

Table 7.2 – Methodologies tested during the first stage of piloting. cpd = cycles-per-degree

		Reversal
Stimulus Field	40x40° square with central 10° masked	40x40° square with central 10° masked
Timing	200ms and 100ms	2.254Hz
Stimuli	Grating	Checkerboard
Viewing distance	400mm	400mm
Spatial frequencies	7.4, 5, 2.5, 1.2, 0.6, 0.32, 0.1 cpd	7.4, 5, 2.5, 1.2, 0.6, 0.32, 0.1 cpd
Contrast	96%	96% and 46%

The 100ms onset procedure, however, would take about half that time. Although many studies use a duration longer than 100ms, spatial tuning has been robustly demonstrated using such a short time course (Drasdo *et al.*, 1987) and would make the protocol as patient-friendly as possible if similarly robust data could be replicated. A summary of the protocols tested during methods development are outlined in Table 7.2.

All protocols recorded 100 sweeps, which were averaged into a single result per protocol. Three results were recorded and averaged for each spatial frequency.

7.2.1.1.2 Apparatus & Procedure

A disposable Dawson-Trick-Litzcow (DTL) ERG fibre (Unimed Electrode Supplies Ltd) placed along the lower eyelid (near the lower limbus) was used for active recording. A ground electrode was placed on the forehead, and a reference near the ipsilateral canthus, as recommended by the International Society for Clinical Electrophysiology of Vision (ISCEV) protocol (Bach *et al.*, 2013). The skin was first prepared using Nuprep Skin Prep gel (Weaver and Company, Aurora, CO, USA), which acts to remove dry skin and dirt, and moisten the corneum skin layer. This improves conductivity and thus signal-to-noise in the final recording. The electrode was filled with Signa conductive electrolyte gel (Parker), which further improves conductivity. Finally, the electrodes were held in place using Blenderm surgical tape.

Stimuli were produced and recordings were taken using Diagnosys LLC Espion software (v.6.0.56; Diagnosys LLC, Cambridge, UK). All stimuli were presented on a CRT monitor (Mitsubishi Diamond Pro 2070sb, Mitsubishi, Tokyo, Japan; framerate= 50-160Hz; resolution= 1600x1200 pixels at 85Hz refresh rate) at a viewing distance of 400mm, powered via a Supra Lorad shielded mains power lead (Jenving Technology, Ljungskile, Sweden) to reduce mains interference. Stimuli were presented in a 40° x 40° square centred on fixation, with a superimposed 10° x 10° black Gaussian square also centred on fixation to ensure stimulation of the mid-periphery only. The remaining border of the screen was set at mean stimulus luminance. The participant was an experienced, healthy observer (24 years old, female), with no ocular or systemic impairment or condition which may affect visual performance.

7.2.1.1.3 Data analysis

To determine the spatial tuning curves, we firstly extracted peak amplitude values for each spatial frequency within each protocol. The peak was defined differently depending on the methodology. For the pattern reversal PERG, the peak was defined as N95, as this reflects RGC spiking activity and has demonstrated spatial tuning in previous studies (though evidence of spatial tuning can be inconsistent; Bach & Holder, 1996; Berninger & Schuurmans, 1985; Korth & Rix, 1989). The Diagnosys software automatically identifies N95 as a negative-going peak between 80-120ms. For the pattern onset response, the peak is defined as a large positive-going peak within the first 100m, which more consistently has shown spatial tuning (Arden & Vaegan, 1983; Drasdo *et al.*, 1987; Korth, 1983; Korth & Rix, 1989); the amplitude of this peak is extracted. These peak amplitude values could then be plot as a function of spatial frequency in order to investigate if they demonstrate HSFA and LSFA.

7.2.1.2. Results and discussion

Raw, averaged traces for each protocol are displayed in Figure 7.1. Both target responses (the N95 component and the onset response) were evident in the pattern reversal and onset-offset PERGs respectively, indicating that responses could be satisfactorily recorded with each experimental set-up and the area of stimulation.

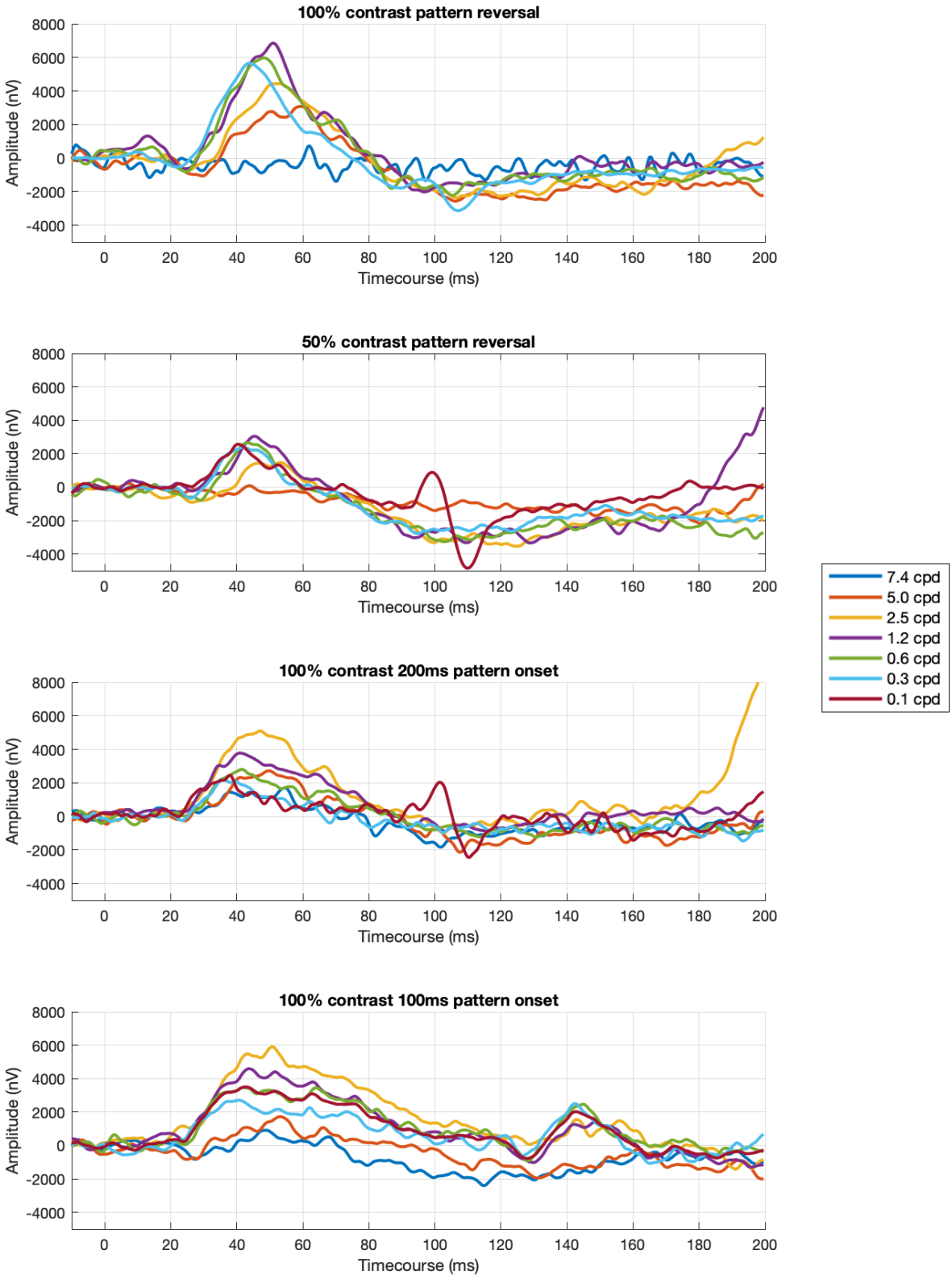

Figure 7.1 – Results of trialling four different PERG methodologies, in response to multiple spatial frequencies. First 200ms of each time course shown. cpd= cycles per degree.

Figure 7.2 shows the measured peak amplitude as a function of spatial frequency for all protocols. Both methods demonstrated a HSFA, which would be expected for stimuli smaller than the average receptive field excitatory centre and due to high spatial frequency filtering of the eye's optical system. However, neither pattern reversal spatial tuning plots show evidence of a LSFA, instead showing a steady increase in response with lower spatial frequencies. While lowering the contrast did appear to also lower the amplitude of N95 at certain frequencies, it did not make a substantial difference to the presence (or otherwise) of a LSFA.

For the pattern onset-offset PERG, a HSFA and LSFA were demonstrated for both variants. For both variations of the protocol, the spatial frequency that elicited the greatest amplitude response was 2.5 cpd. This is within the range reported in previous literature (see Table 7.1). This finding also supports the use of both time bases for investigating spatial tuning within our participants. The 100ms onset-offset was particularly desirable in that it affords a shorter test time for participants, which will help to reduce participant fatigue and also allows time for repeated recordings if needed (e.g. if a recording is affected by substantial movement or noise).

In conclusion, four protocols were trialled to investigate if they demonstrated evidence of spatial tuning (i.e., HSFA and LSFA). All protocols demonstrated the expected peaks (i.e., the onset peak or N95). However, neither 100% contrast reversal nor 50% reversal PERG demonstrated spatial tuning. Spatial tuning was evidence in the pattern onset-offset protocols. Out of these, the shorter protocol (100ms) was particularly desirable for the shorter test time afforded. Therefore, the 100ms onset-offset protocol was carried forward for our glaucoma patients and age-similar controls. Before carrying out this experimental testing within a clinical sample however, several other aspects were examined to ensure the quality of PERG recordings.

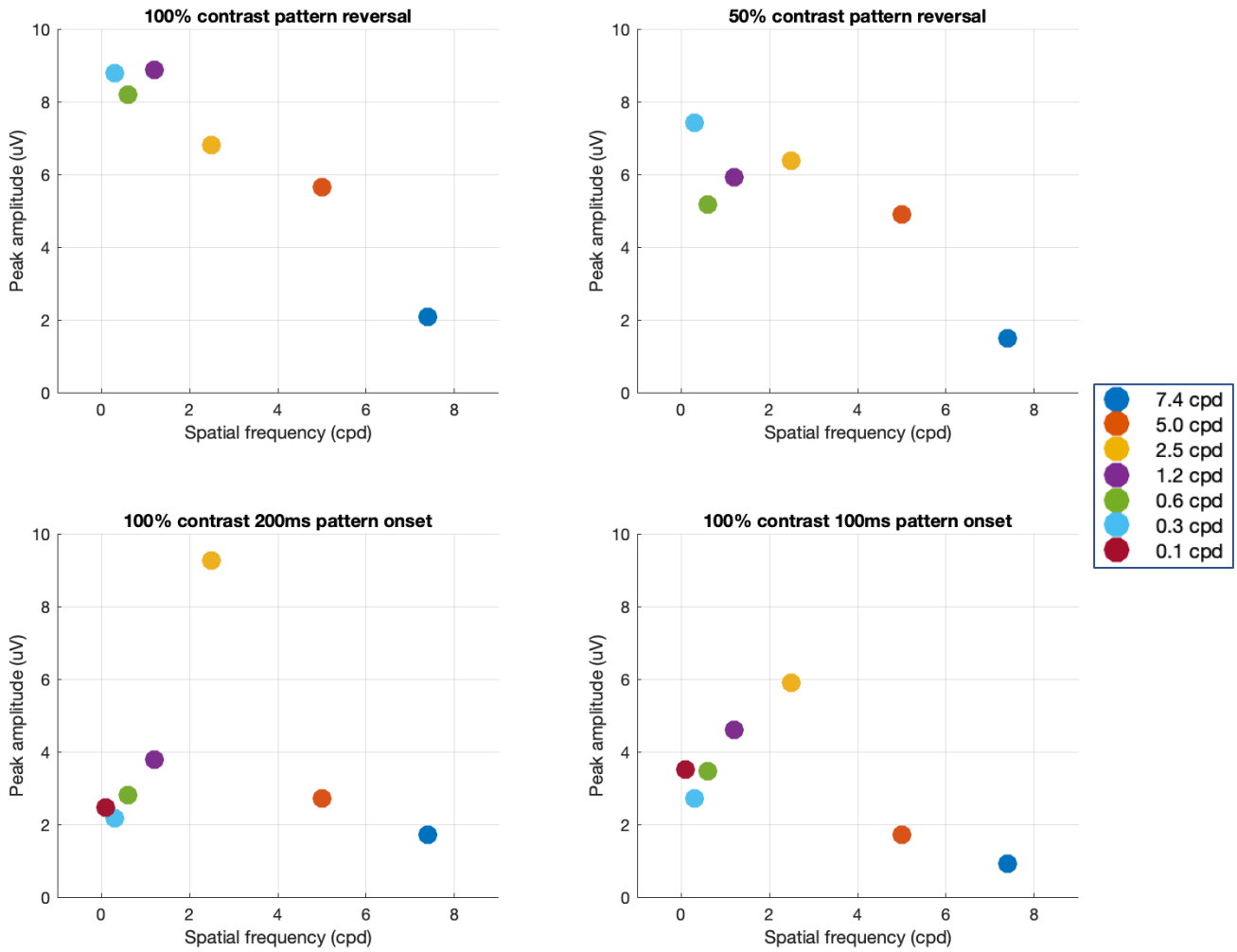

Figure 7.2 – Spatial tuning curves for four different methodologies tested during methods development. Low-frequency attenuation is only evident for the two pattern onset-offset tests. cpd= cycles-per-degree.

7.2.2. Offset mean luminance

In order to target spatially sensitive mechanisms rather than a global luminance response, it is important to establish that while there are local luminance changes between onset and offset stimuli, there are no global luminance differences (defined as the average luminance across the entire screen). If, for example, the onset stimulus had a much greater global luminance, it may be expected that the resulting response would be more dominated by a non-spatially specific luminance response. Furthermore, it was found that properties of the onset response significantly differs depending on whether a brighter or darker (in regards to global luminance) background/offset is used (Fritsch *et al.*, 2018). Specifically, higher luminance backgrounds/offsets are associated with less distinct onset response peaks, while lower luminance backgrounds/offsets are associated with sharper onset peaks. This may explain why our onset peaks recorded in the initial test (Figure 7.8) are less sharp than those recorded in Drasdo et al. (1987), as different methods of stimulation were used to produce the offset mean luminance. While this study used the mean luminance produced by the Espion software, displayed on a CRT monitor, Drasdo et al. (1987) used a diffusing shutter over the stimulus projection. If the offset mean luminance presentation had a higher luminance in our study than this previous study, this may explain the differences in onset traces.

To confirm that the global offset luminance being produced by the software in our protocol did not substantially differ from the global onset luminance, a handheld photometer was used to measure the global screen luminance at five times for both the onset and offset stimuli. The onset stimulus used was a 7.43cpd vertical grating presented on a full screen square CRT display (the same area, resolution, and frame rate as used in the experiment above), while the offset was mean grey luminance. The resulting luminance values (in cd/m^2) are displayed in Figure 7.3. A two-tailed independent samples t-test reported no significant difference ($t(8)= 1.5713$; $p=0.16$) between the mean luminance of the onset (Mean [M]= 51.44; Standard Deviation [SD]= 0.26) or offset stimuli (M= 51.64; SD= 0.11), suggesting that the only luminance modulations in our protocol are local changes in order to stimulate spatially sensitive cells.

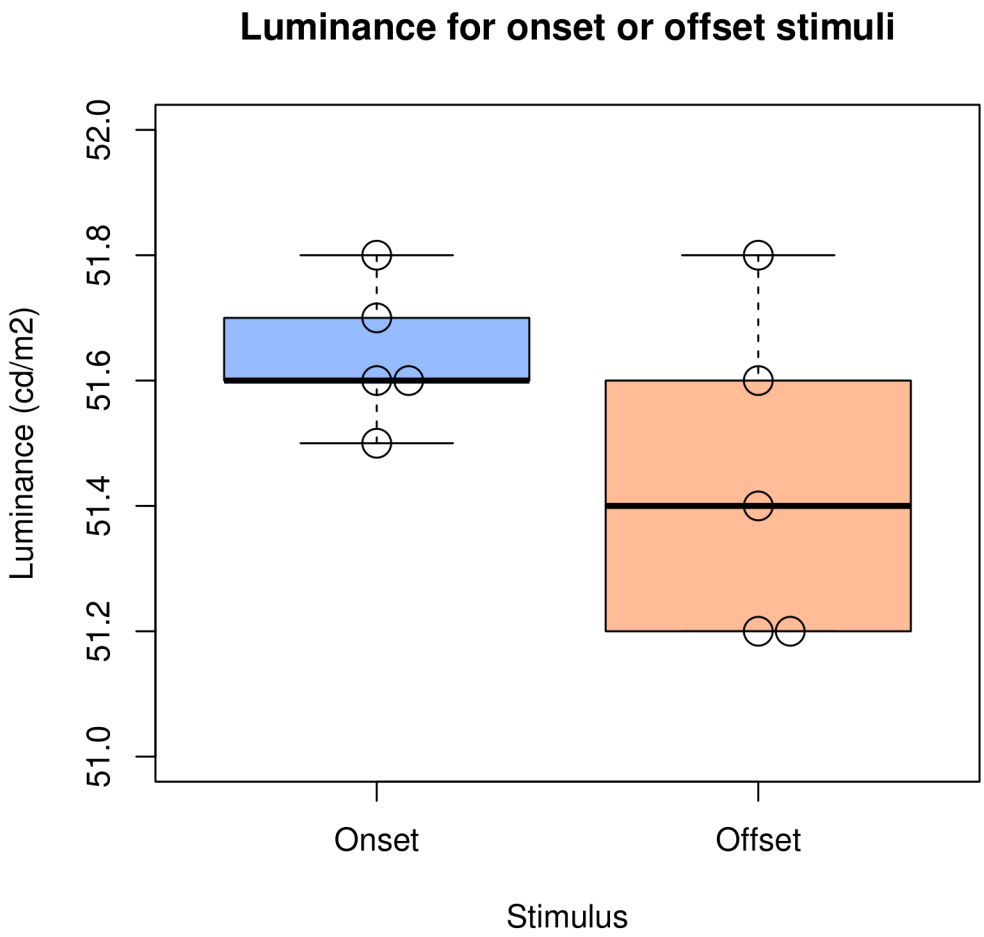

Figure 7.3 – Global luminance recorded from either the onset stimulus (7.43cpd vertical grating) or offset stimulus (mean grey luminance), recorded with a photometer.

7.2.3. Background noise

While conducting the above methods development on our methodology, a consistent issue that was discovered was high frequency electrical contamination, which was thought to be distorting the onset peak. While the PERG recording took place in electrically insulated lab dedicated to electrophysiology experiments, the PERG responses are very small (compared to other electrophysiology methodologies, such as flash ERG) and thus more susceptible to additional background noise. An example of this high frequency noise across multiple spatial frequencies can be seen in 7.3. While this is possible to filter out via Fourier analysis and smoothing, it was thought that this noise would also distort the trace to the extent that the peak characteristics would be less accurate; for example, if a 'noise' peak were to coincide with a response peak, the trace amplitude and timing would be obscured or distorted, even if the data were smoothed. Multiple setups were therefore investigated to identify the source of the contamination and how best to eliminate or minimise it in the final recordings.

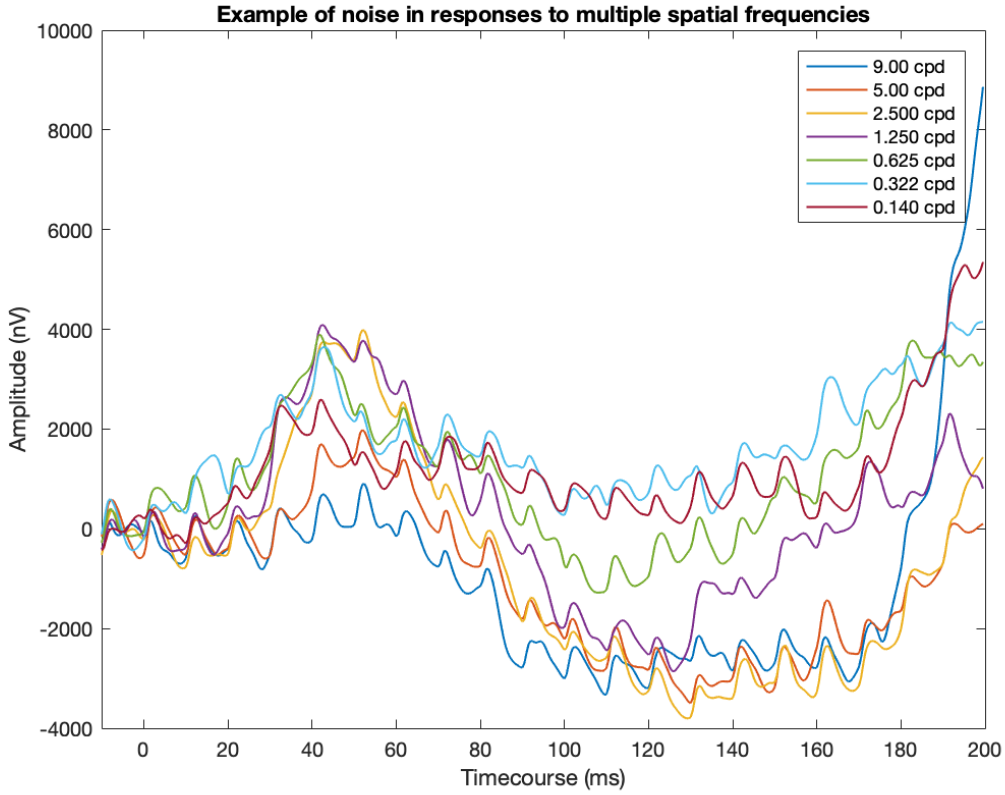

Figure 7.4 – Onset-offset PERG responses to multiple spatial frequencies. Interfering background noise is apparent as ~500-1000nV amplitude 105Hz spikes superimposed onto the traditional onset response. cpd= cycles-per-degree

7.2.3.1. Phase one – identifying the noise

The first stage was to isolate the source of the noise. To do this, a model eye was created using three 5K resistors and three electrode cables. This was positioned at head-rest height in order to take biologically-silent recordings (see Figure 7.5). This provided the same impedance as a human eye but with no biological electrical responses, so the only response recorded was the isolated background noise. This set-up was used to create the trace shown in Figure 7.6. The contamination was still present when the monitor was turned off, suggesting that this was not the source of the noise. To identify the frequency of this noise, Fourier analysis was run to 21 harmonics. The majority of the power was found within the 21st harmonic, suggesting that the noise was mostly around 105Hz (see Figure 7.6). Investigations continued with a LEADER LBO-522 oscilloscope (Leader Instruments Corp., Fort Lee, NJ, USA) and a lab-made probe that could be held at different locations in the room. Substantial 50Hz noise was found within a large part of the room, with a spike at approximately 105Hz imposed on top of the waveform. This therefore suggested that the contaminating noise may be a feature of the local mains power supply.

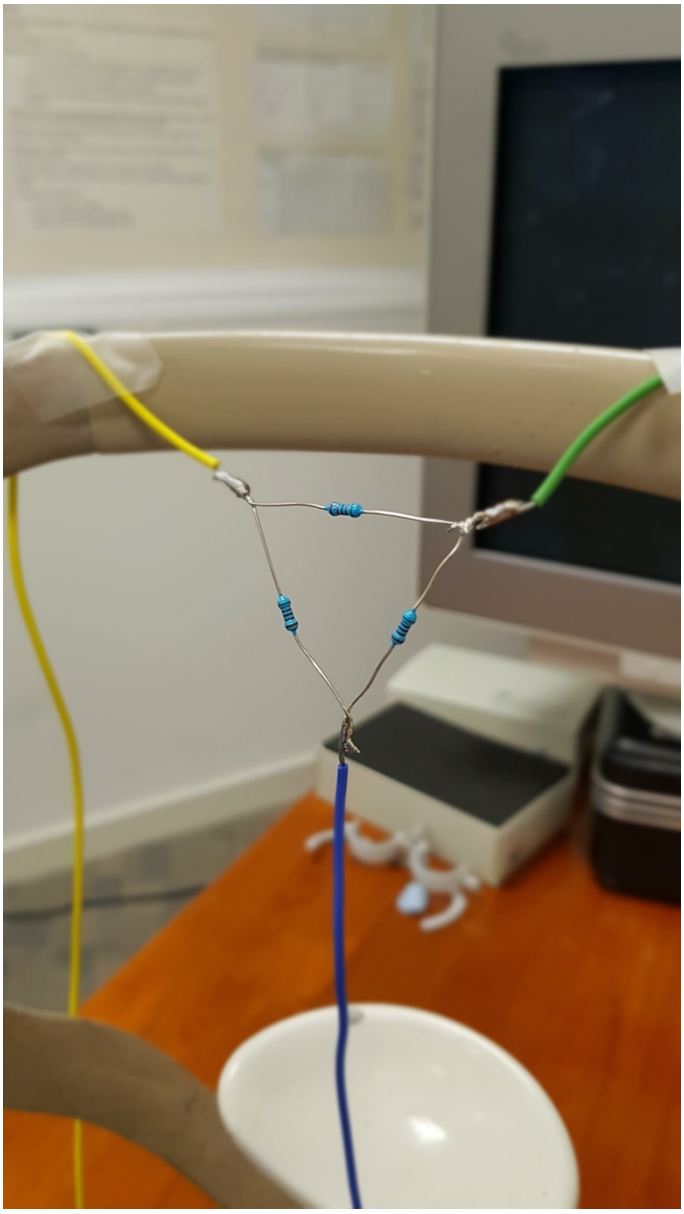

Figure 7.5 – Photo of a model eye used to pilot model to the electrophysiological room, made using three 5K resistors and three electrode cables, placed on the chin rest, where the participants' head is planned to be.

A)

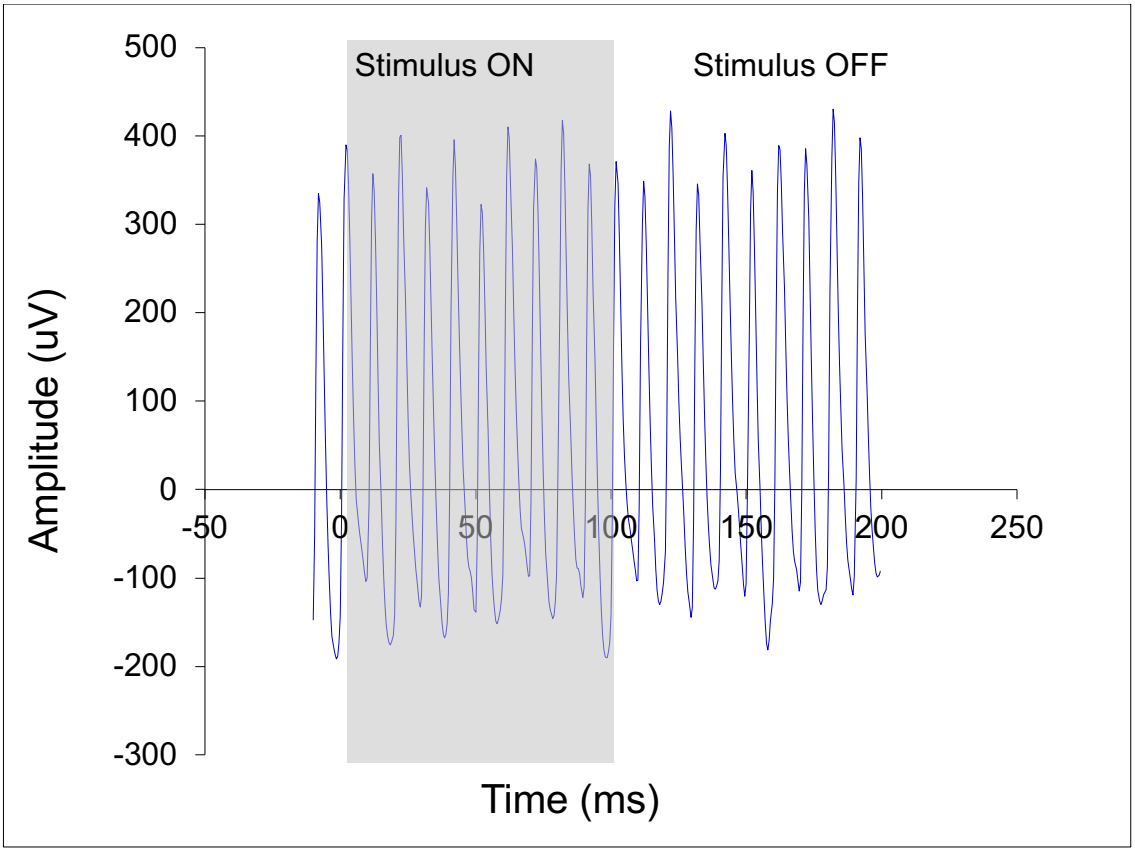

B)

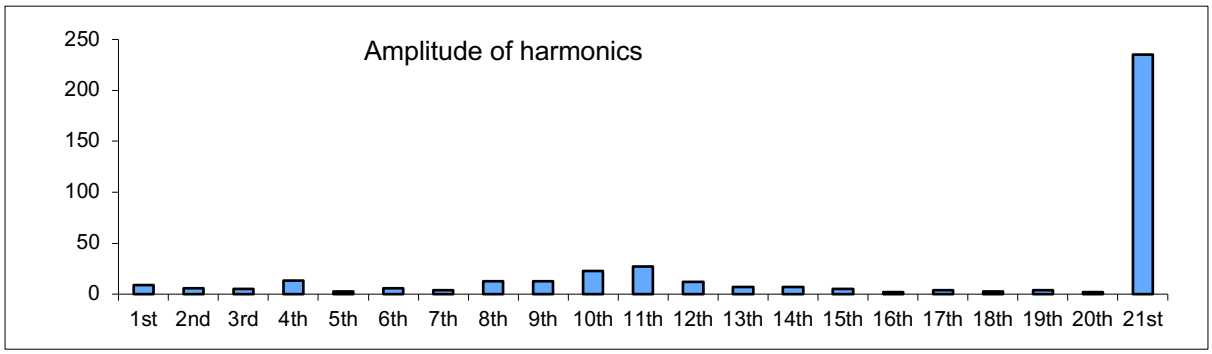

Figure 7.6 – A) Time course of the background noise taken with the model eye, avoiding biological noise. Grey section = stimulus on period. B) Amplitude of all harmonics extracted from time course using Fourier analysis. Demonstrates that the majority of noise comes from the 21st harmonic, corresponding to 105Hz.

7.2.3.2. Phase two – reducing mains frequency

An investigation of the lab itself found a number of issues that may be contributing to the increased noise found in our recording. Firstly, though shielded trunking was installed, a number of plug sockets within the room were unshielded, allowing mains frequency to 'escape'. There was also a number of electrically active cables and equipment in the immediate ceiling cavity that could not be switched off using the main switch, thus producing high-amplitude waveforms that could have been influencing recordings within the lab.

In an attempt to eliminate these interferences, an electrician replaced the plug sockets with shielded variants and connected all electrical equipment in the ceiling cavity to an additional switch so it could all be turned off during recording. In order to assess the impact these changes had on the level of mains noise, the amplitude of the frequency waveform was measured three times at three heights and two locations within the room, before and after the modifications (measurements taken with the oscilloscope and probe, as described above). The chosen heights were at i) ceiling level, ii) head-height (the level at which the chin rest had been set up; 1m 15cm), and iii) floor level. These recordings were taken at the testing location and also at a location in the room that demonstrated greatest amplitude of the mains frequency.

Average (mean) results are shown in Figure 7.7. Before room modifications, the amplitude of the noise decreased with increasing distance from the ceiling (i.e. towards floor level), suggesting the electrically active equipment in the ceiling cavity was a particular issue. As can be seen from Figure 7.7, the amplitude of the waveform (from the highest point to the lowest) substantially reduced after room modifications, especially nearer the ceiling. The modifications therefore appeared to be successful in reducing the mains contamination in the room. However, when taking another recording using the model eye described above, a reduced level of 105Hz contamination was still present (if no background noise is present, the model eye recording should produce a flat line). A number of hardware configurations (below) were trialled in an attempt to reduce the impact of this noise. A small temporal delay was added between sweeps in an attempt to cancel out the noise, but with no success, possibly due to rounding inherent in the ERG software.

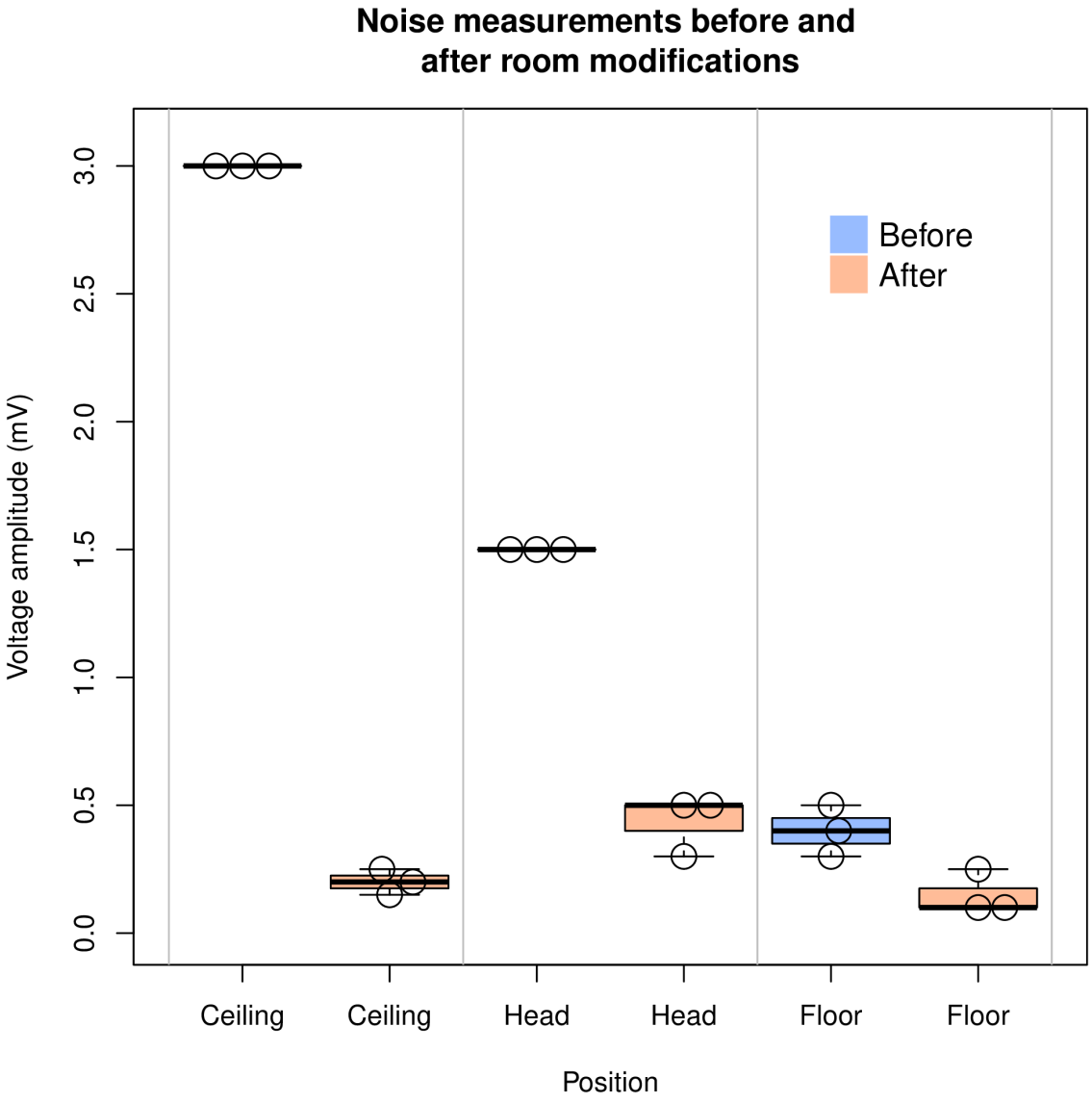

Figure 7.7 – Background room electrical noise recorded with an oscilloscope at the patient position within the room. Recordings are completed at ceiling level, head height, and floor level, both before (light blue) and after (light orange) room modifications. Unfilled circles= single measurements; error bars= interquartile range.

7.2.3.3. Phase three – modifying the set-up

For the next phase of our methods development, a number of different setups were tested with the aim of reducing the impact of the residual background noise. A description and rationale for each test is described in Table 7.3. For each test, three results were recorded with the model eye and averaged. To quantify the amount of background noise in the signal, the maximum minus minimum amplitude for each result was extracted and the mean average and standard deviation taken. These values are displayed for each test in Table 7.3. We found that the level of noise was slightly improved with increasing viewing distance and the addition of a 75Hz low-pass filter. However, by far the greatest reduction came from twisting the active and the reference electrode wires together. This essentially placed the active and reference electrodes in the same space, only deviating once reaching the eye. They should therefore be subject to the same amount of electrical interference (i.e. the background noise), with the only difference being at the eye itself. After demonstrating this in the model eye, we also demonstrated this effect with a healthy participant (who was an experienced observer) using the 100ms onset-offset PERG described above. Three results (containing 100 sweeps each) were averaged into a final recording for two different spatial frequency sine-wave gratings (1.25 and 5 cpd), with the electrode cables either twisted together or not. These spatial frequencies were chosen as the former should elicit very little response, while the latter typically elicits a larger peak. The results can be seen in Table 7.4. To avoid inclusion of the response peak, a difference value was extracted from the first 20ms post-onset of the trace. In all cases, the inclusion of twisting the electrode cables reduced the difference between the minimum and maximum recorded amplitude. This technique was therefore carried forward in the method for measuring the PERG in subsequent studies.

Table 7.3 – Hardware configurations piloted in order to reduce interfering background noise. Amp. = amplitude (nV); M = mean; SD = standard deviation; Diff = difference between maximum and minimum amplitude (nV) in recording.

	Description	Rationale	M diff.	SD diff.
Test 1	Baseline, 40cm viewing distance, ~50 cd/m^2	Initial baseline recording	552.66	15.32
Test 2	Increased viewing distance to 41.8cm	Increased viewing distance in case of noise coming from the screen or the associated power input	290.67	15.51
Test 3	Increased viewing distance to 46cm	As above	276.11	21.98
Test 4	Tightly twisted active and reference electrodes with ground next to them	Puts the two electrode in the same physical space, so the amplified difference between them will only be at the eye	57.43	2.85
Test 5	Separated all cables	Undo last change to confirm	337.49	19.75
Test 6	Tightly twisted active and reference electrodes with ground held separately	Repeating test 5 with ground held at a set distance away to investigate if ground position matters	86.10	21.46
Test 7	Ground held further away	Further testing if ground distance matters	98.52	40.52
Test 8	Active and reference only twisted very loosely	Investigated if minimal twisting is enough for a reduction in amp.	350.03	51.88
Test 9	Untwisted and 75Hz low-pass filter added	Investigated whether filtering at the recording level helps	240.71	15.51
Test 10	Active and reference twisted seven times	Find whether amp. reduction possible when twisting a set smaller amount	65.28	30.23

Table 7.4 – Testing the influence of twisting the active and reference electrode together on a participant's recorded trace. M = mean; SD = standard deviation; Difference = difference between maximum and minimum amplitude (nV) in first 20ms of recording; cpd = Cycles per degree.

	cpd	M Difference	SD Difference
Non-twisted	5.00	907.16	302.84
Twisted	5.00	493.45	229.56
Non-twisted	1.25	1251.37	466.49
Twisted	1.25	1159.84	355.39

7.3. Selection of population Receptive Field (pRF) modelling software

Up until this point, all pRF analysis have been undertaken with SamSrf v.5 software (which has been used in multiple previous publications; e.g. Dekker *et al.*, 2019; Hughes *et al.*, 2019; Infanti & Schwarzkopf, 2020). After initially analysising the clinical cohort (described in Chapter 10) with SamSrf v.5., it was also discovered that several issues may limit interpretation of this data, such as erroneous estimation of pRFs centred outside of the stimulation area and larger healthy control estimated pRF sizes than would be expected from previous research. Additionally, substantial noise in the data was evidenced from a visual inspection of the retinotopic maps and plots of pRF size as a function of eccentricity. It was therefore considered prudent to consider several options for pRF mapping software to be used in the clinical study. Several options were considered for the most appropriate software for analysing the pRF mapping dataset. The software packages trialled were the following:

- Two surface-based analysis packages, SamSrf v.5 (available at https://doi.org/10.6084/m9.figshare.1344765) and SamSrf v.7 (available at https://osf.io/2rgsm/)
- One volume-based package, the Analysis of Functional NeuroImages (AFNI) software package (Cox, 1996; provided in the public domain by the National Institutes of Health, Bethesda, MA, USA; http://afni.nimh.nih.gov/afni).

A small sample of healthy controls were selected and analysed in all three packages. The results were compared based on the final retinotopic maps, visual field coverage, levels of model fit, and pRF size as a function of eccentricity relationship. This section therefore aims to compare these software packages on various aspects in order to choose the most optimal for our dataset.

7.3.1. Methods

7.3.1.1. Participants

Three healthy controls (ages: 53.9-70.9; two females, all right-handed) from the main dataset were chosen to compare analysis packages (ppt9, ppt22, ppt62). These participants were chosen pseudo-randomly by the PhD student from those participants who demonstrated a clear retinotopic map after SamSrf v.5. processing (i.e. a map with distinct

phase reversals and an eccentricity gradient). For full detail on the inclusion and exclusion criteria, please see section 7.5. All participants were given MRI-safe vision correction during scanning.

7.3.1.2. MRI session

For full information on the MRI protocol and pre-processing steps, please see the methods section of Chapter 10. Briefly, monocular retinotopic mapping was completed (two left eyes [OS]) in a SIEMENS 7T MRI. These functional scans were 1.5mm^3 isotropic EPIs (Echo-Planar Images; TR= 1s, TE=25ms, flip angle=55°, 35 slices, 192x192 matrix, multiband=5). Haemodynamic Response Function (HRF) mapping was also completed with a 1.2mm^3 resolution EPI (TR= 2secs; TE= 25ms; flip angle= 76°; 33 slices; FOV= 984x984). All functional scans were positioned manually over the occipital lobe. To aid in distortion correction, a phase and magnitude image were also taken. Finally, a T1-weighted MPRAGE sagittal structural scan was completed at 1mm^3 resolution (TR=2.2s, TE=2.82ms, TI=1050ms).

The retinotopic stimulus was a moving bar design, which moved across the screen in 18 consecutive positions to cover a circular area of 11° diameter (each bar was 1.16° wide). The step size was half the bar width. The central region (0-5.5°) and peripheral region (7.7-18.7°) were mapped individually by moving the fixation dot to either the centre or corner of the screen (a methodology used in Chapter 6; see Figure 6.2). To encourage fixation, a simple task was used in which the participant had to silently count the number of times that the fixation dot flashed red, which happened randomly throughout the run. The fixation dot was generally black with a white outline. They were not required to make a response. The retinotopic mapping was repeated 3 times at each visual field location (central and mid-periphery).

The HRF stimulus was a 100% contrast black-and-white alternating radial checkerboard. This was presented to participants for 2 seconds (screen size: 19.5°x11.0°), followed by 20 seconds of blank grey. This was repeated ten times while the participant maintained central fixation. There was a 20 second period at the start of the sequence in which a blank grey screen was presented in order to establish a baseline of no stimulation, which was then removed for further analysis.

7.3.1.3. Pre-processing and analysis

In order to compare the software packages, the retinotopic data was processed separately through SamSrf v.5, SamSrf v.7, and AFNI, using a 2D Gaussian pRF model.

7.3.1.3.1. Haemodynamic response function

For all of the below pRF modelling techniques, the participants' individual HRF was used for convolution. Pre-processing of the HRF scan took place within FSL and FEAT software packages (Jenkinson *et al.*, 2012). EPI data underwent B0 distortion correction, motion correction (MCFLIRT; Jenkinson, Bannister, Brady, & Smith, 2002), brain extraction (BET; Smith, 2002), and high-pass filtering (100s). Following this, registration of the partial-volume EPIs to structural data, using the whole brain EPI as an intermediate step, took place in the spm-fMRI toolbox (http://www.fil.ion.ucl.ac.uk/spm/). The MPRAGE structural image was first intensity normalised within FSL, then processed within FreeSurfer (Dale *et al.*, 1999; Fischl, 2012) to allow estimation of the grey matter surface.

The functional data could then be projected onto this structural surface using SamSrf V.5 (with functional data at a cortical depth of 0.5mm sampled), before the HRF was extracted. This analysis was restricted to the occipital lobe, which was manually drawn on the inflated surface, using the anterior end of the calcarine sulcus and the parieto-occiptal junction as anatomical landmarks. The signals generated by the ten checkerboard stimulus blocks were first averaged within each vertex, excluding any outliers (defined as a time series that demonstrated greater than $\pm$1.5 standard deviation from mean). Analysis was also constrained to visually active regions to avoid analysing unrelated noise. This was defined as a vertex with a signal (averaged over the first five scans) that had a clear response (>1 standard error from the mean) to the checkerboard stimulation. A double-gamma function could then be fitted to the averaged response to estimate the HRF fit, from which the metrics discussed above could be extracted.

7.3.1.3.2. SamSrf

Pre-processing steps for both SamSrf versions were the same and took place mostly within FSL and FEAT software packages (Jenkinson *et al.*, 2012), using identical steps as described above for the HRF scans.

The modelling process used by SamSrf v.5. has been discussed previously in the methods section of Chapter 6 and within Chapter 5. There are several notable differences between the versions that may lead to one producing a better model fit than the other. This is namely in terms of improved precision of the fine fitting procedure, using a lower error tolerance threshold. Additionally, there was suggested to be an issue with SamSrf v.5 in which the HRF convolution before z-score convolution cases an artefactual undershoot in the convolved BOLD response, which in turn caused errors in the estimation of very large pRF sizes (S. Schwarzkopf, personal communication, 18th July 2020). The difference between weakly stimulated pRFs and partially stimulated pRFs is also ambiguous in v.5. Both of these issues are suggested to be resolved by removing z-score normalisation of the time series during the modelling process (S. Schwarzkopf, personal communication, 18th July 2020).

7.3.1.3.3. AFNI

For analysis in AFNI, B0 correction was carried out using FSL, while motion correction, detrending and averaging over runs was completed using AFNI tools.

pRF mapping based on the 2D Gaussian model was also completed within AFNI. For each voxel, a 200 by 200 search space is produced that covers the height and width of the stimulus (input as a binary mask). For each point in this search space, 100 levels of possible pRF size (sigma) are estimated, leading to 4 million possible combinations of x, y, and sigma. For each of these possible iterations, a stimulus time series (i.e. a binary mask of the stimulus position at each TR) is then used to create a predicted time series for each of those iterations. These can be compared to the actual data time series of each voxel using both Simplex and Powell optimization algorithms to find the best fitting model time series to the data (by minimising the least-squares error). This outputs the X-coordinate, Y-coordinate, pRF size (sigma) and R^2 for each voxel.

7.3.2. Results and discussion

The results of these pRF fitting procedures were compared based on several aspects in order to examine which would be most appropriate for our data:

- The visual field coverage – It was first examined how much of the visual field was sampled by the final pRFs, and how this matched the area of the visual field that was actually stimulated within the scanner.

- The estimated pRF size as a function of eccentricity – This was compared against what would be expected from previous literature. Although the exact values may be expected to vary with scan parameters and sample population, the positive relationship between these variables is well documented (e.g. Dumoulin & Wandell, 2008; Morgan & Schwarzkopf, 2020) and so would be expected within our data.
- The Goodness-of fit – Defined as the R^2 of the model fit (i.e. the data against the single Gaussian model), this was compared between software programs to examine whether one gave noticeably greater fit.
- The phase and eccentricity retinotopic maps – As these would be used for delineation of the early visual areas (i.e. V1-3), it is necessary that certain features are visible (such as polar-angle reversals and a clear fovea; e.g. Sereno *et al.*, 1995) as these are used to indicate the transition between visual areas.

All data points are extracted from V1 labels, which were manually drawn in each software with the aid of structural and functional landmarks (using either AFNI tools or SamSrf in-built functions). To enable fairer comparisons between packages, instead of selecting a goodness-of-fit level to threshold the data (as the optimal level of which may be different between packages), data was thresholded by only including the 200 voxels with the highest fit (unless otherwise stated). We therefore had 200 data points for the central run and 200 data points for the peripheral run.

7.3.2.1. Visual field coverage

To examine how well the results of each modelling technique sampled the visual field, the top 200 fitted voxels were plotted based on the estimated x and y positions of the associated pRF model within the visual field.

7.3.2.1.1. Central run

The area of the visual field that would be expected to be populated by pRFs in the central runs is shown in the top panel of Figure 7.8 (using an OD run as an example; an OS run would be the same but reflected into the right side of visual space). As can be seen in this illustration, it would be expected that the pRFs would be mainly constrained to the half of the stimulated region on the ipsilateral side to the test eye.

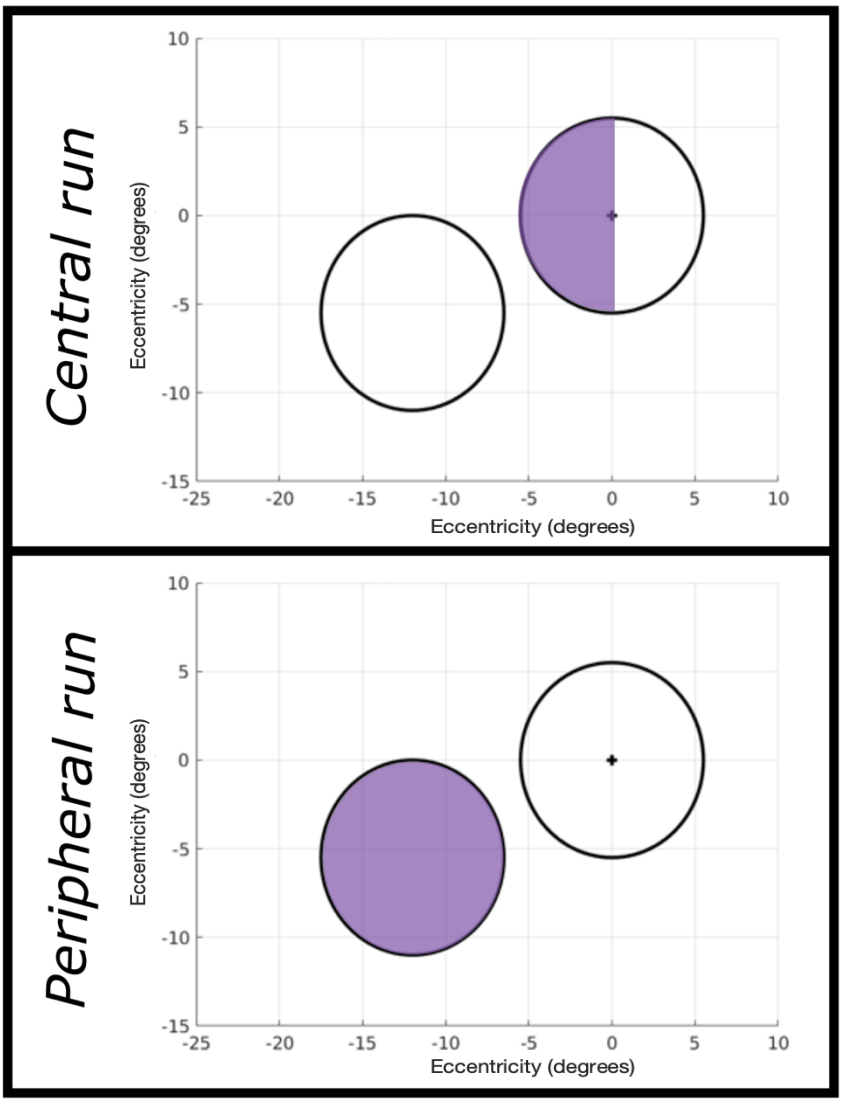

Figure 7.8 – Illustration of where in the visual field we would expect to be sampled using our pRF mapping method. The top plot shows the expected area for the central retinotopic run, while the bottom panel shows the expected region for the peripheral retinotopic run. The cross indicates fixation (i.e., 0° eccentricity on both axes)

The central plots for the three participants in each software package are presented in Figure 7.9. The black unfilled circles on the plots show the area of the visual field stimulated by the stimuli (with the fixation point indicated by a black cross), while the coloured filled circles refer to the estimated pRFs (with each data point being a single voxel). The sizes of the data points relate to the estimated pRF sigma size, while the opacity refers to the R2 value (higher R2 values being more opaque). Looking at the AFNI maps (leftmost column; Figure 7.9), the data points are mostly clustered around the fixation point, with a slight bias towards the expected hemisphere. As would be expected by the smaller search-space used, all estimates are within the stimulus area, though none show complete coverage of the expected hemisphere. In regard to SamSrf, all show a bias towards the expected hemisphere. SamSrf v.5 (middle column; Figure 7.9) demonstrates a significant number of estimated pRFs centred outside of the stimulus area. These pRFs may represent spurious fitting of noisy data (which is a likely explanation of the very small pRFs seen outside of the stimulus area) or may be reflecting real receptive fields (for example, if a larger pRF is partially stimulated by the stimulus, the modelling process may fit a pRF centred outside the stimulus area). Moving to SamSrf v.7 (rightmost column; Figure 7.9), fewer pRFs are estimated outside of the stimulus area, and are instead concentrated within the expected region, suggesting that these pRFs are being driven by the stimulus. While SamSrf v.7 appears to improve the fit from v.5 in this respect (i.e. with more realistic visual field coverage), it doesn't seem to improve the coverage in the case of ppt9, who had a poorer quality map (i.e. with more sparse coverage) than ppt22 or ppt62.

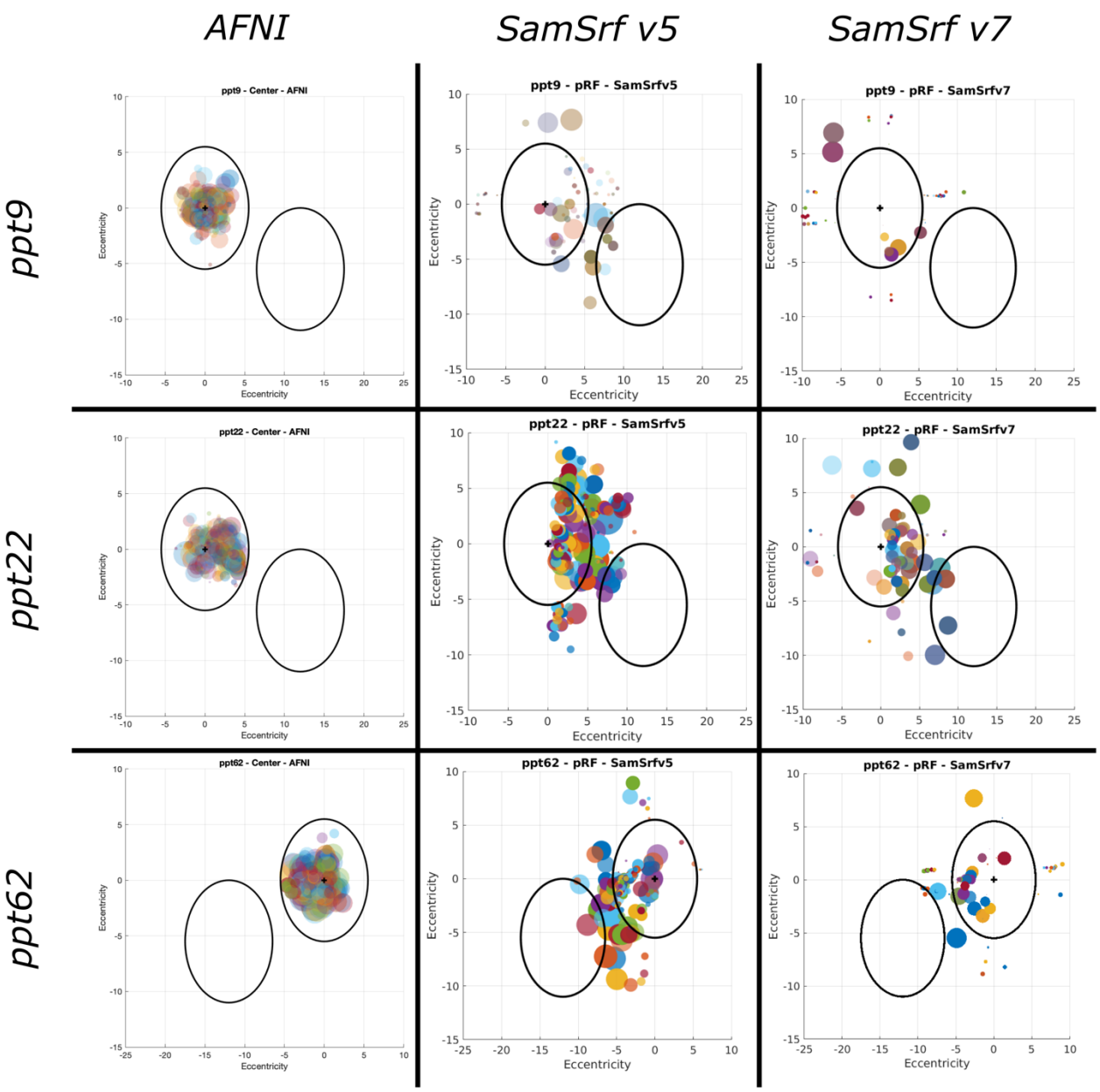

Figure 7.9 – Plots demonstrating where in the visual field are being sampled by the modelled pRFs for the central retinotopic mapping run. Fixation is shown with a black cross. The black unfilled circles show the area of the visual field stimulated by the stimuli. The coloured filled circles refer to the estimated pRFs (with each data point being a single voxel). The size of the data points relates to the estimated pRF sigma size, while the opacity refers to the R^2 value (higher R^2 values being more opaque). Each row is a different individual participant (healthy control), while each column is a different software package (indicated at the top of the column).

7.3.2.1.2. Peripheral run

For the data from the peripheral run, as it is already contained to one side of the visual field, pRF estimates are expected throughout the whole peripheral stimulated area, which is illustrated in the bottom panel of Figure 7.10. This pattern is indeed seen with the estimated pRFs from AFNI (leftmost column; Figure 7.10), though again this is mostly clustered towards the middle of the stimulus. No pRFs are estimated outside of the stimulus area. An issue that occurred during the process of model fitting with AFNI is that it failed to fit pRF estimates to the peripheral run of ppt62, possibly due to noise in the data or the relatively small area being mapped. Regarding SamSrf, a similar pattern to the central runs is seen, in which more of the visual field is being sampled by the pRFs modelled in v.5 (middle column; Figure 7.10), but with a substantial portion of pRFs being centred outside of the stimulated area (which is true for the majority of pRFs in some participants). Through there is less coverage in v.7 (rightmost column; Figure 7.10), the pRFs estimated are more constrained to the expected stimulated area, suggesting more realistic localisation. Most of the 'outside' pRFs have very small sizes in V.7, possibly suggesting that they reflect fitting of noisy data rather than actual receptive fields. In all cases, the whole of the stimulated area is not covered, which may be expected due to the lower signal-to-noise ratio (SNR) in this peripheral area compared to the central run (as it is sampling a relatively small amount of cortex).

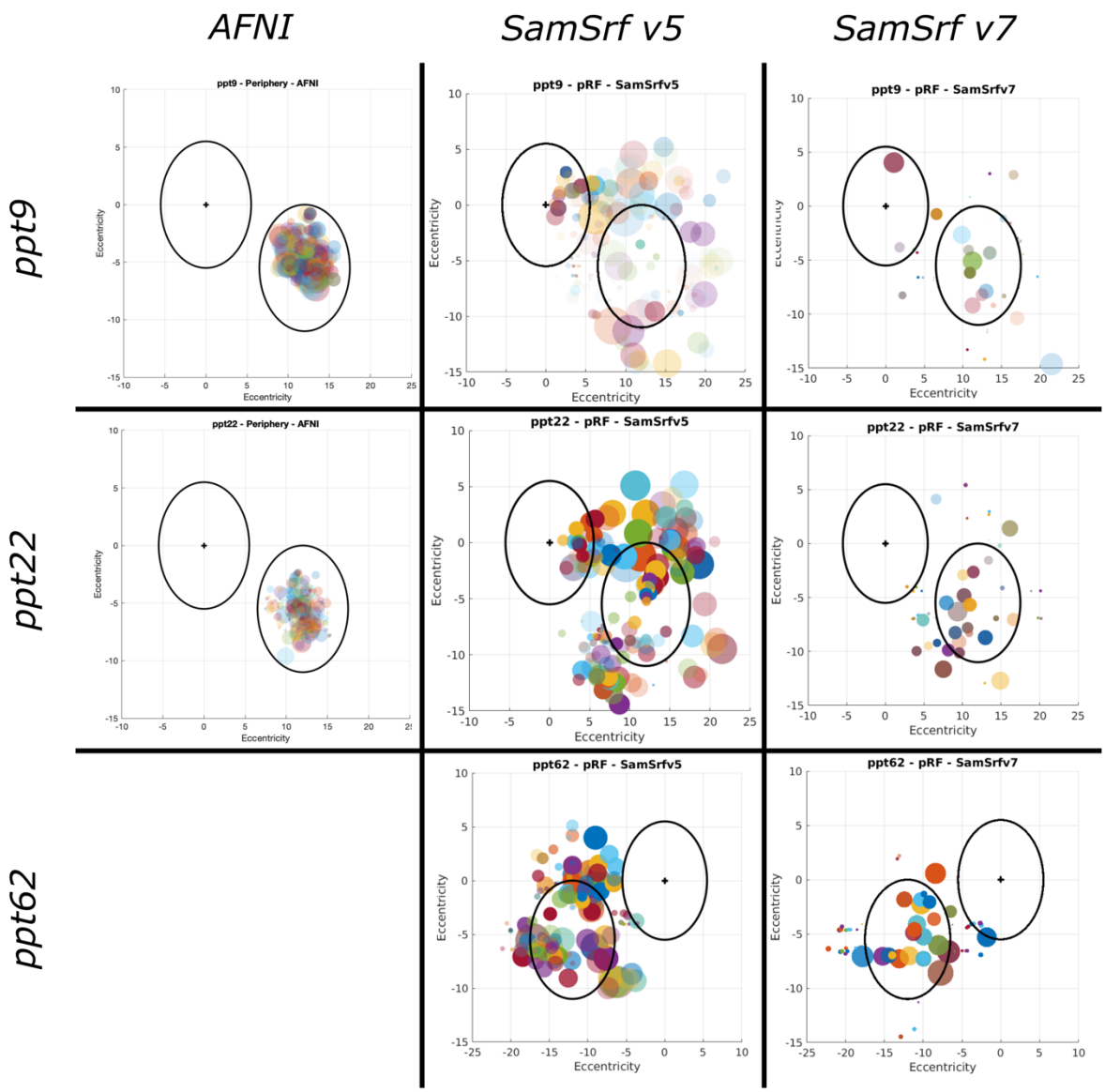

Figure 7.10 – Plots demonstrating where in the visual field are being sampled by the modelled pRFs for the peripheral retinotopic mapping run. Fixation is shown with a black cross. The black unfilled circles show the area of the visual field stimulated by the stimuli. The coloured filled circles refer to the estimated pRFs (with each data point being a single voxel). The size of the data points relate to the estimated pRF sigma size, while the opacity refers to the R^2 value (higher R^2 values being more opaque). Each row is a different individual participant (healthy control), while each column is a different software package (indicated at the top of the column).

7.3.2.3. Relationship between pRF size and eccentricity

There is an established positive relationship between fMRI-derived pRF size and eccentricity, which has been replicated many times. To compare our data to what has been previously published, pRF sizes were extracted from a sample of these previous papers (Amano *et al.*, 2009; Brewer & Barton, 2014; Dekker *et al.*, 2019; Harvey & Dumoulin, 2011; Morgan & Schwarzkopf, 2020; Schwarzkopf *et al.*, 2014) and were plotted in Figure 7.11. These were only from healthy participants (if the paper in question was comparing two samples of healthy participants, the group used is indicated on the plot), used a single Gaussian pRF model, and were from V1 only. From this plot, it can be seen that although there is some variation (especially with increasing eccentricity), a general trend can be seen, with size estimates starting at ~0.7° sigma size at 1° eccentricity and increasing to ~1.4° sigma size at 9° eccentricity. Of note, the single sample of healthy older adult participants demonstrated larger pRF estimates across eccentricities than the younger populations, as reported by Brewer and Barton (2014). As our glaucoma and healthy control participants are a similar age range to the older adult sample in Brewer and Barton (2014), we may see this bias towards larger pRF sizes compared to other studies using younger samples. As the voxel size determines the amount of cortex information regarding receptive field size is summed over, it would be expected that voxel size would impact pRF estimates, with larger voxels having larger coverage and thus larger pRF estimates. Based on the data extracted from these studies, estimated pRF sizes across the central 5° were also averaged and compared to voxel size (see Figure 7.12). Out of this sample of previous studies, only those with isotropic voxels were included for ease of comparison (see Table 7.5 for all included studies and associated voxel sizes). It can be seen in this limited sample that pRF size seems to increase with voxel size, which would be expected as the amount of cortex sampled (and thus summed over) within a single voxel is larger. As our scans use 1.5mm^3 isotropic resolution, we may therefore expect that our estimated sizes would be smaller than that of the older adult sample described by Brewer and Barton (2014), as they had a larger (non-isotropic) voxel size of 1.875×1.875×3mm. Though these studies cannot be directly compared to our work due to the different scanner protocols, pre-processing steps, analysis packages, and sample populations used, these plots can be used as a rough comparison for what estimated pRF sizes would be expected from our analysis.

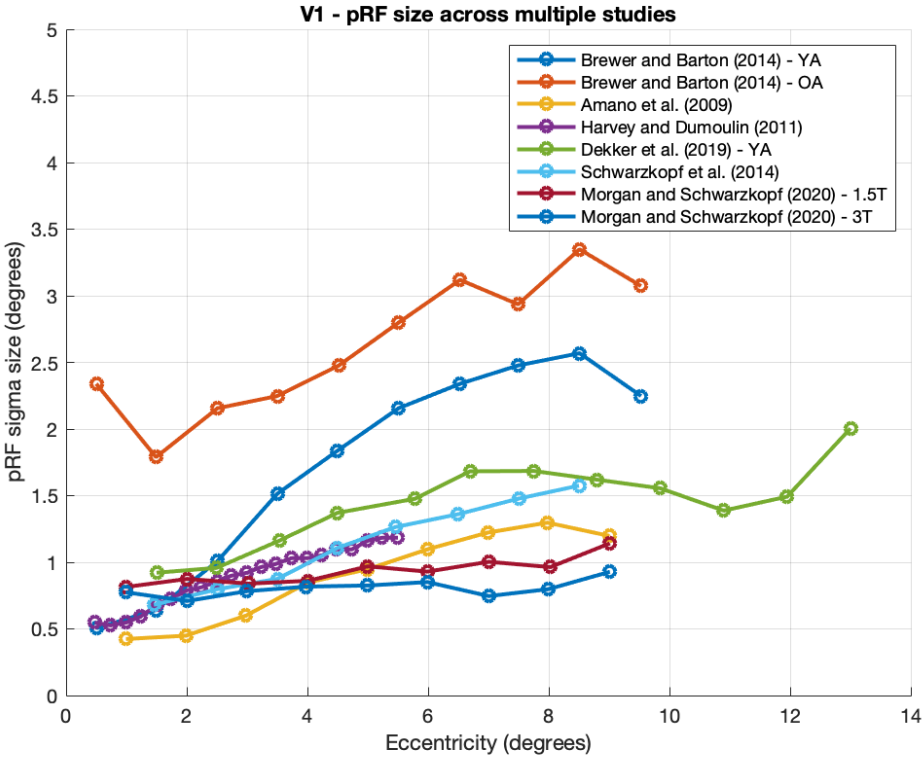

Figure 7.11 – V1 pRF estimates extracted from several previous studies. All studies use a 2D single Gaussian pRF model. Only data for healthy control participants are displayed. If the study used multiple healthy participant groups, these are distinguished in the figure legend. Eccentricity and pRF sigma size are both given in degrees. YA = Young Adult sample. OA = Older Adult sample. 1.5T and 3T refers to the magnet strength (Tesla; T) of the MRI used in that healthy sample, as this was compared between two groups in this study.

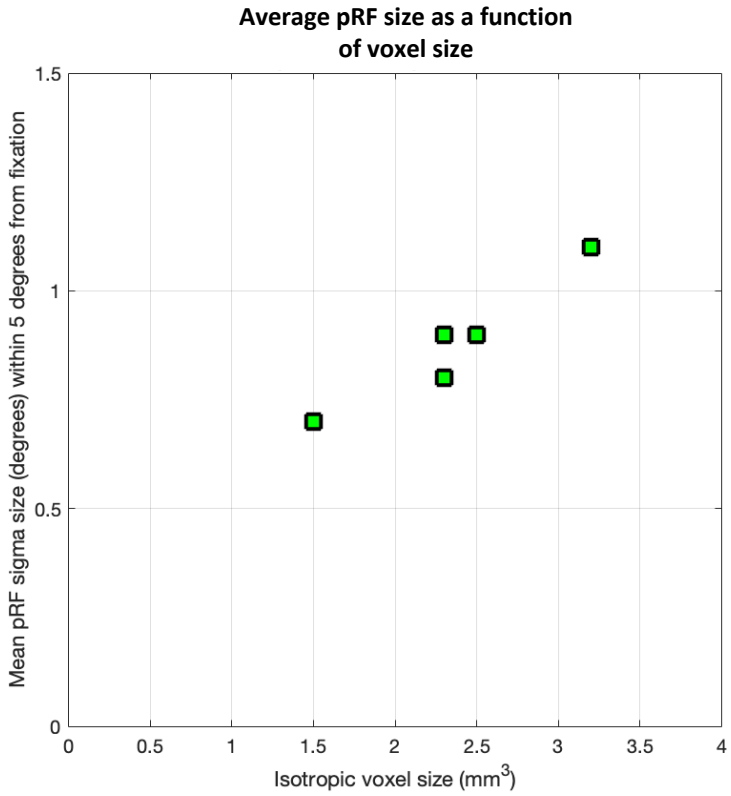

Figure 7.12 – Size of isotropic voxel as a function of the average V1 pRF size for the central 5° from a sample of previous studies. pRF sigma size is given in degrees. Isotropic voxel size is given in mm^3. Only healthy control groups are included.

Table 7.5 – Voxel size used in a sample of previous pRF mapping studies. Only those with isotropic voxels are included. Voxel size is given in mm^3. Only healthy control groups are included. If a sample includes more than one healthy sample (rather than, for example, comparing a healthy control group to a clinical population sample), then the group is specified. YA = Young Adult sample. 1.5T and 3T refers to the magnet strength (Tesla; T) of the MRI used in that healthy sample, as this was compared between two groups in this study.

Name of study	Voxel size (mm^3)
Amano et al. (2009)	*1.5*
Harvey and Dumoulin (2011)	*2.5*
Dekker et al. (2019) – YA group	*3.2*
Schwarzkopf et al. (2014)	*2.3*
Morgan and Schwarzkopf (2020) – 1.5T group	*2.3*
Morgan and Schwarzkopf (2020) – 3T group	*2.3*

To examine the relationship between pRF size and eccentricity from fixation in our data, the estimated pRF sigma size and associated eccentricity were plotted for the top 200 fitting voxels for each the central and peripheral runs (see Figure 7.13).

The pRF sizes estimated by AFNI appear mostly smaller than would be expected from Figure 7.11, and also show no obvious trend with eccentricity. Some of this issue may be due to how the AFNI pRF mapping estimates size. When generating the possible iterations, 100 sizes are chosen between 0 and half the stimulus width. This means that the maximum size that could be predicted based on the stimulus size used in this study would be 2.75°. From the estimates given by previous studies, this may start to limit the pRF sizes we could estimate, particularly once reaching the periphery. On the other hand, this should not impact estimates within central vision as these would be expected to be smaller than this, and our central AFNI estimates still do not appear to be showing the expected positive relationship. The pRF size estimates in the periphery are also not showing a ceiling effect of 2.75°. In contrast to this, the expected positive relationship can be observed for the two SamSrf versions, suggesting that they may be more accurately representing the underlying receptive field sizes. In terms of the average estimated sizes, those in SamSrf v.7 appear most comparable to those in previous studies, with sizes in SamSrf v.5 seeming larger than would be estimated. The very small pRFs seen in the SamSrf v.7. visual field plots (Figure 7.9 and Figure 7.10) are also evident in these scatterplots; upon further examination of the data, these are all very close to zero and thus unrealistically small. It may therefore be prudent to filter these from future data analysis.

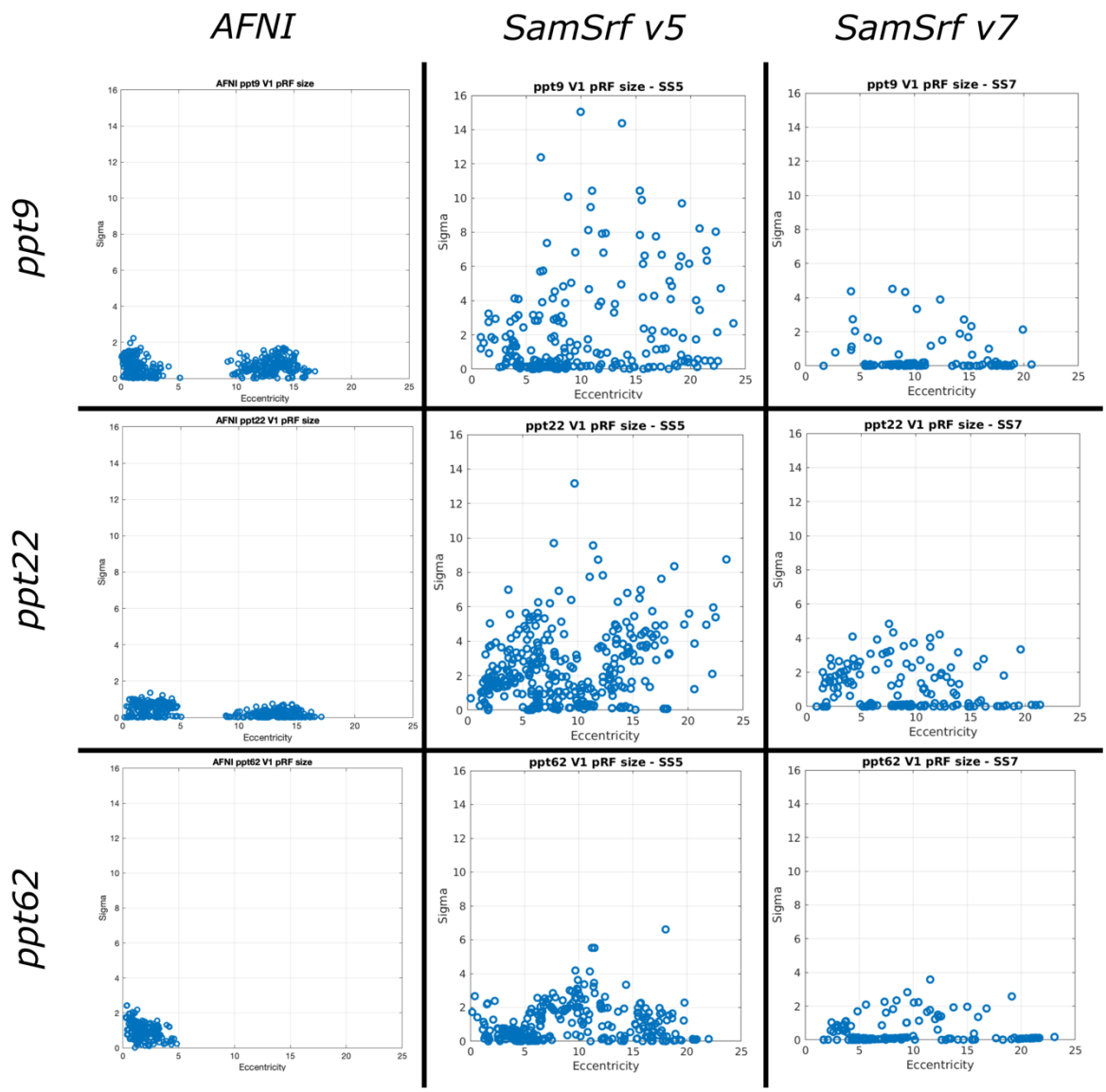

Figure 7.13 – Scatter plots demonstrating pRF sigma size as a function of eccentricity for each participant and each software package. Each data point represents a separate voxel. Both pRF size and eccentricity are given in visual degrees.

7.3.2.3. Goodness-of-fit

To examine how levels of Goodness-of-fit varied between software packages, the R2 associated with each voxel (i.e. how well the time course in that voxel fit with the estimated pRF model) was extracted and plotted as a histogram (these can be seen in Figure 7.14). This involved all voxels (i.e. not only the top 200) and central and peripheral runs were plotted separately. All packages show a 'peak' in R2 value, which appears to be higher for both AFNI and SamSrf v.7 compared to SamSrf v.5. The peak in the SamSrf v.5 fits appears to be relatively low, demonstrating a shape that would be expected in response to random data or, more likely in this case, data with a low SNR. The fact the R2 peak in AFNI and SamSrf v.7 is biased towards higher values – demonstrating a more distinct 'peak' shape – suggests that these fitting techniques lead to a greater SNR in the final data.

Several voxels in SamSrf v.7 gave a R2 value of 1, which seemed unrealistically high and can be seen in the histograms in the rightmost column Figure 7.14. Upon further inspection of the data, these voxels also gave a beta value of 0, suggesting that it would be useful to use this as a filter if this software was taken forward.

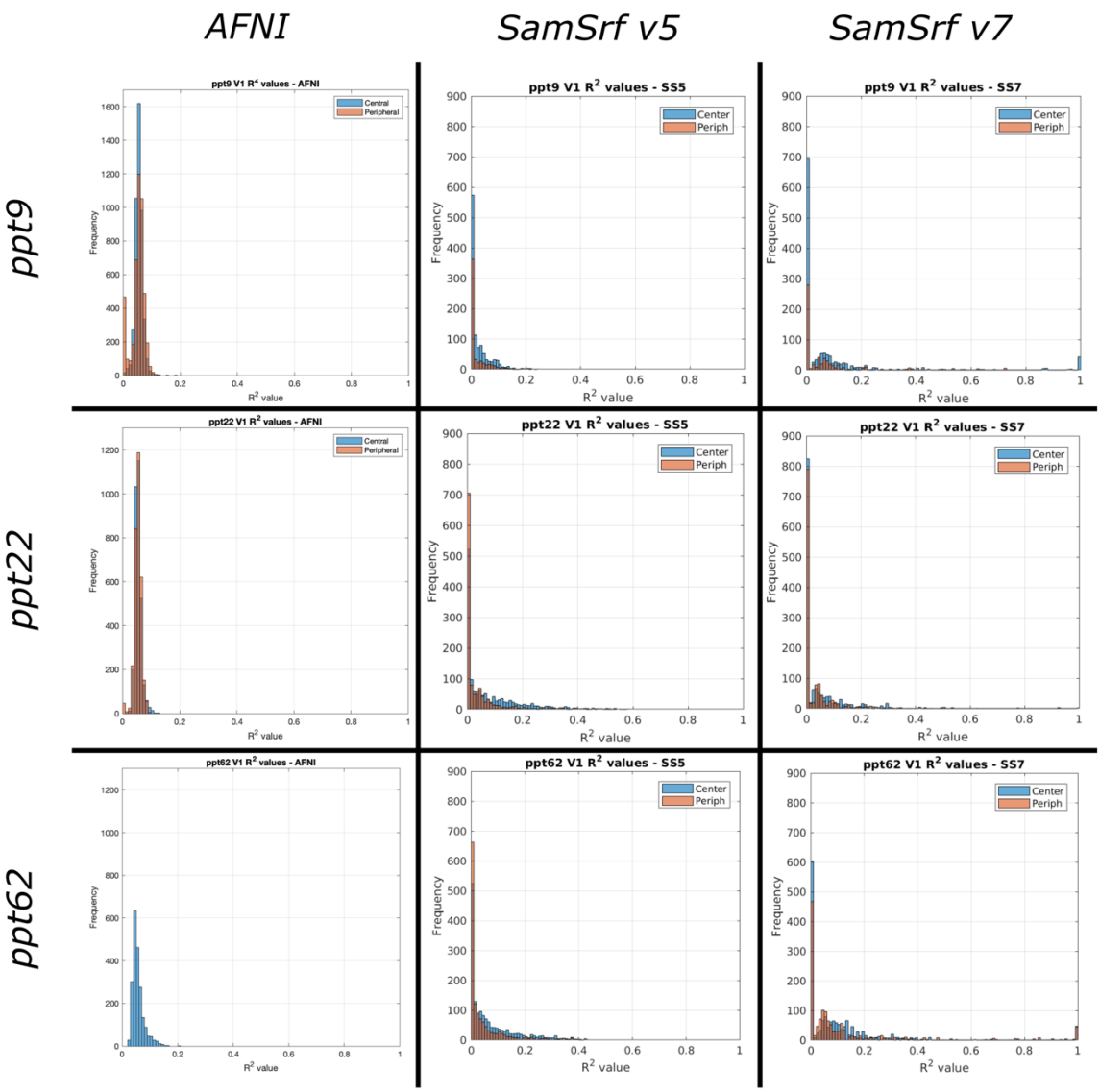

Figure 7.14 – Histograms of R^2 values across voxels for each participant (rows) and each software package (columns). R^2 is taken as the goodness-of-fit between the data and 2D Gaussian model fit. Data for the central and peripheral retinotopic run are plotted separately and indicated on the legend (central run = blue; peripheral run = orange).

7.3.2.4. Retinotopic maps

From the above comparisons, the AFNI analysis appears inappropriate for our data due to the lack of pRF size as a function of eccentricity relationship (as seen in Figure 7.13) and lack of hemifield bias in central visual field coverage (as seen in Figure 7.9), so the SamSrf software packages were taken forward for further comparison. The polar angle and eccentricity retinotopic maps for the SamSrf versions were compared. The maps presented (see Figures 7.18 and 7.19) are un-thresholded and smoothed at 5mm; this makes it easier to see features such as phase reversals as gaps in the map are averaged over. The quality of the final retinotopic map varies between participants (quality here defined as the ability to distinguish key features of the retinotopic map that are used in delineation, such polar reversals and an eccentricity gradient); for example, the phase reversals and fovea are very clear in ppt62, but are less easily observed in ppt9, who also had lower R2 values (as seen in Figure 7.14) and sparser visual field coverage (see Figure 7.9 and Figure 7.10). When comparing between packages, the features of the retinotopic maps produced by SamSrf v.5 are much clearer than those produced in SamSrf v.7 (though the features seem to be in the same spatial location in both versions). The eccentricity retinotopic maps in particular (Figure 7.15) in particular shows no clear pattern when calculated by SamSrf v.7, whereas the fovea is evidence when calculated by SamSrf V.5. Therefore, despite SamSrf v.7 seeming like it modelled more realistic pRF sizes and locations from the previous comparisons, it would be difficult to delineate the early visual areas from these maps, especially compared to SamSrf v.5 (in which V1-3 are visible).

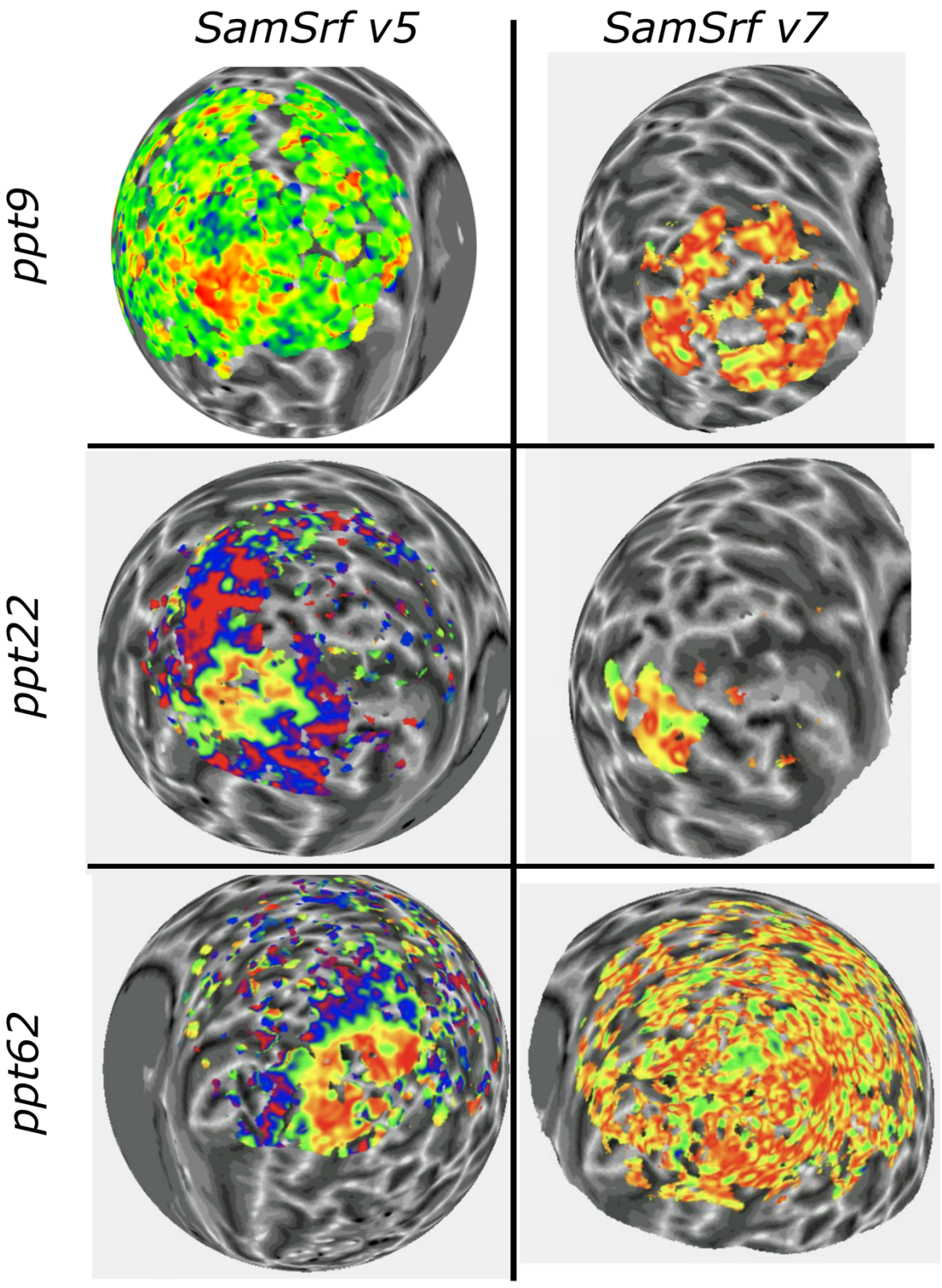

Figure 7.15 – Eccentricity retinotopic maps for three participants after analysis in SamSrf v.5 (left column) or SamSrf v.7 (right column)

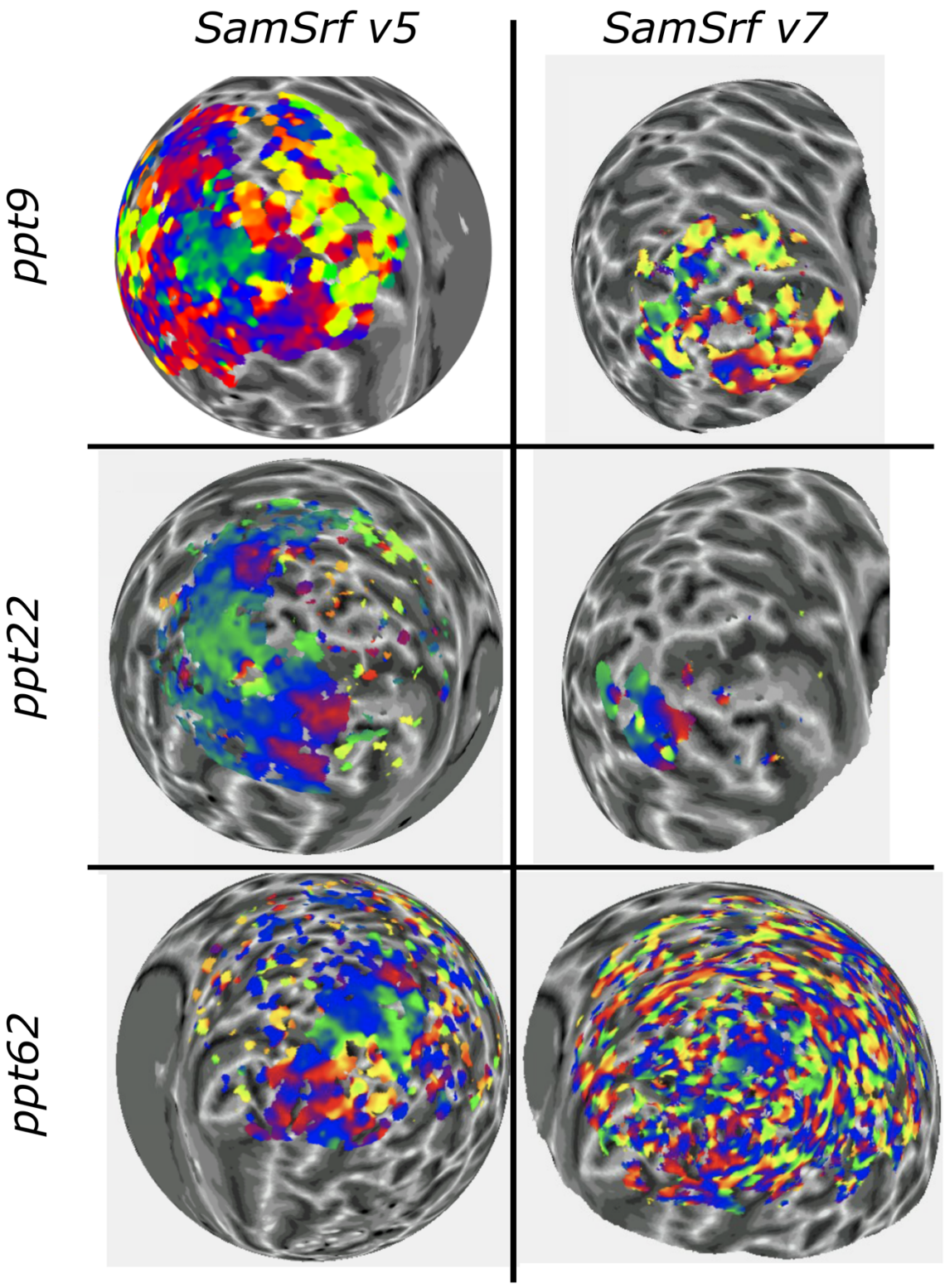

Figure 7.16 – Polar angle retinotopic maps for three participants after analysis in SamSrf v.5 (left column) or SamSrf v.7 (right column)

To see whether this could be improved, especially for noisier maps such as ppt9, the SamSrf v.7 analysis was rerun for this single participant with a modified surface projection step. Previously, the surface projection sampled the functional data at a cortical depth of 0.5mm. For this modified version, the data was sampled at 0.25mm, 0.5mm, and 0.75mm, and then an average was created. It was hypothesised that by increasing the amount of data sampled this would lead to higher SNR and thus improved retinotopic maps. Figure 7.10 shows the smoothed retinotopic maps without (panel A) and with (panel B) this averaging step. While the phase reversals seem to be slightly more distinct, the eccentricity still shows no obvious fovea. However, we then looked at the maps using unsmoothed data (panels C and D) and found that the fovea and appropriate eccentricity gradient was visible. It therefore seemed that the smoothing process caused this initial issue with the SamSrf v.7 maps. This was reassuring for the data discussed in the above sections, as these sections were based on unsmoothed data. The problem with smoothing may occur due to the noise in the data being averaged with true signal. Smoothing was performed based on distance on the spherical sphere; it was also performed based on Geodesic steps and Dijkstra's geodesic distance, but with a similar result. Comparing the unsmoothed maps with and without averaging, while there is not a large amount of difference, the averaged maps show more distinct retinotopic features.

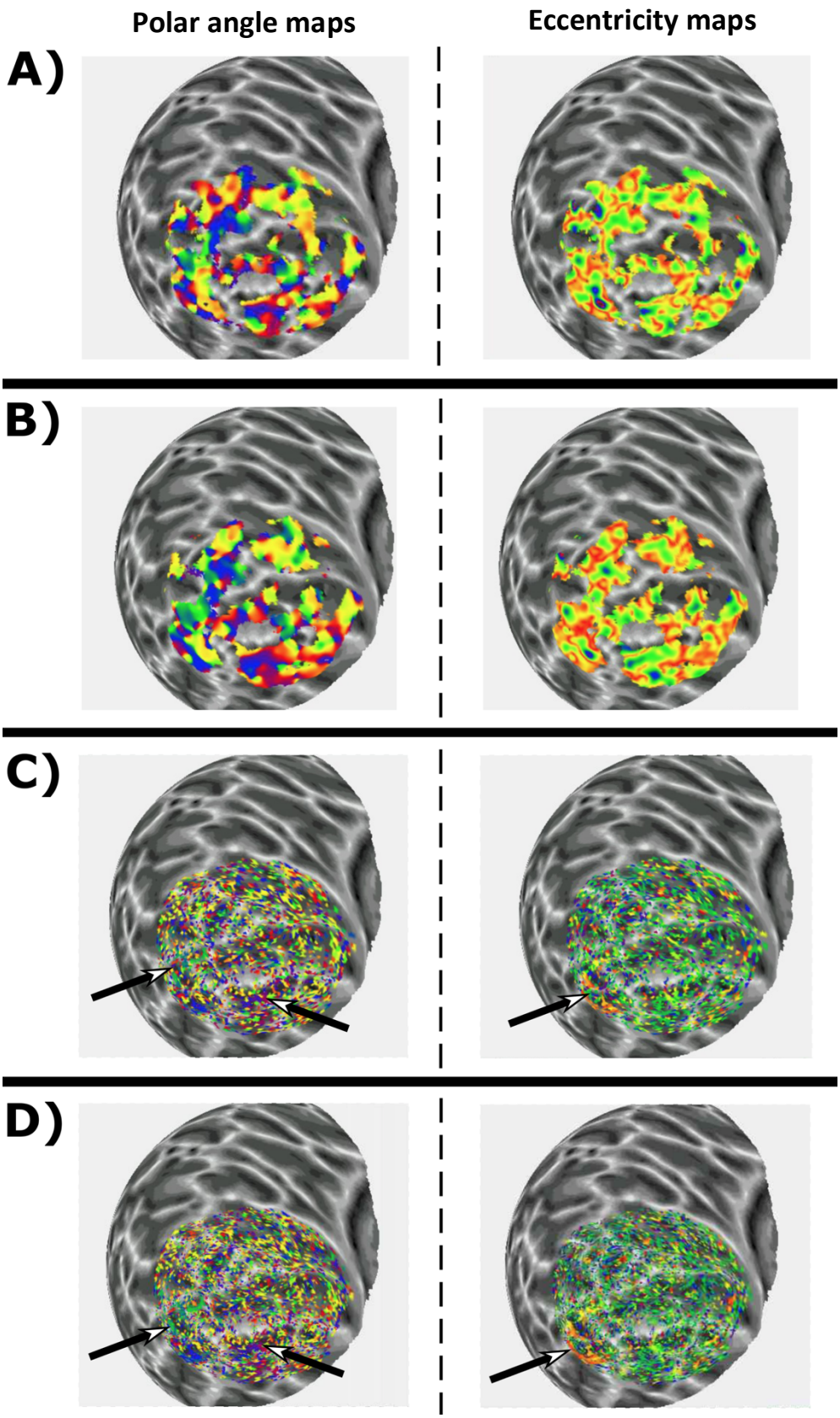

Figure 7.17 – Comparison of non-thresholded central retinotopic maps with or without averaging over cortical depths. A = Sampled at 0.5mm only (Smoothed map); B = Sampled at 0.25mm, 0.5mm, and 0.75mm (Smoothed map); C = Sampled at 0.5mm only (Unsmoothed map); D = Sampled at 0.25mm, 0.5mm, and 0.75mm (Unsmoothed map). The left column includes polar angle maps (with arrows indicating visible polar angle reversals, illustrated as a green or red stripe), while the right column includes eccentricity maps (with arrows indicating the foveal projection site).

7.3.3. Conclusion

This section focused on investigating three different pRF modelling software packages on a small sample of the healthy control participants from the larger clinical study. Several aspects of the final pRF data were considered to be important when deciding which software was the most appropriate for this dataset; namely, visual field coverage, the pRF size as a function of eccentricity relationship, goodness-of-fit of the pRF model, and retinotopic map quality. Considering these points and the results discussed above, SamSrf v.7 was considered to be the most appropriate for our data. Most of the estimated pRFs modelled by this software were constrained to the stimulated area of the visual field, and the estimated sizes more closely resembled previous literature compared to either of the other packages used. Furthermore, the goodness-of-fit of the modelled voxels showed a higher peak in SamSrf v.7. than SamSrf v.5. An issue that arose with this newer version however was with the smoothed retinotopic maps. While the key features could be seen in the unsmoothed data (namely the polar angle reversals and fovea), especially with an averaged surface projection, the eccentricity gradient was lost with smoothing, possibly due to averaging in of noise. While the data could be filtered prior to smoothing, this leaves a very partial amount of the map remaining, so would also make manual delineation of visual areas difficult. This level of noise in the data didn't appear to be due to the use of SamSrf v.7. *per se*, as this technique has been successfully used to generate distinct retinotopic maps in a participant from another dataset (3T data). Figure 7.18 demonstrates an unsmoothed retinotopic map from a healthy young adult, analysed using SamSrf V.7. As can be seen, even without smoothing a much lower level of noise is evident compared to the maps generated from the current cohort. Moving forwards, it may therefore be prudent to use visual area labels based on objective structural landmarks, such as using FreeSurfer generated probabilistic labels.

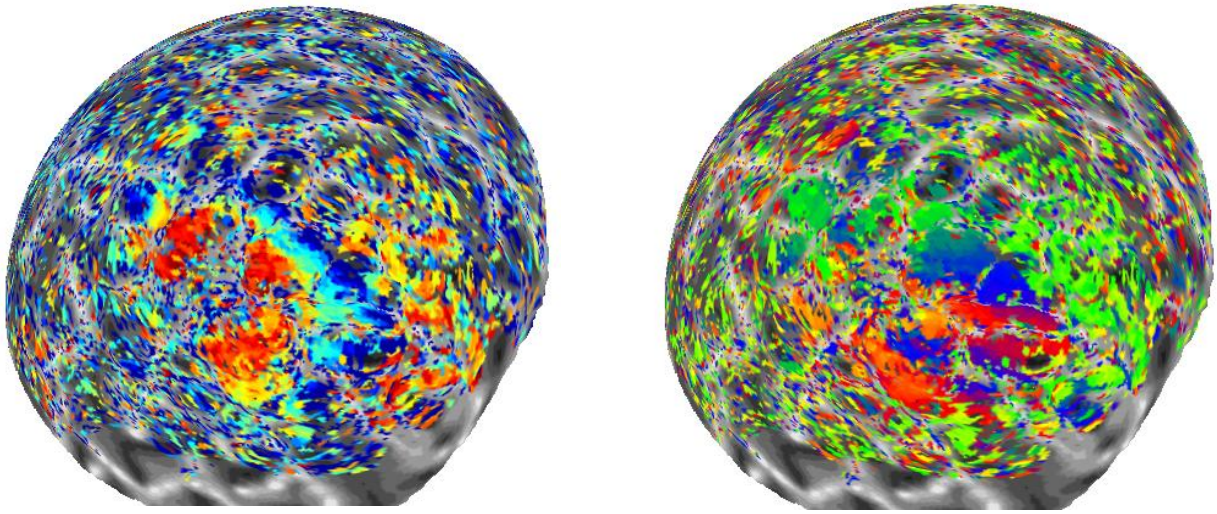

Figure 7.18 – Example retinotopic maps from a single healthy young participant from a separate dataset collected at 3T and analysed using SamSrf v.7. Left= Eccentricity map; Right= Polar angle map.

Another issue that arose during this development process was that several pRFs were estimated by SamSrf v.7 (mostly outside the stimulated area) with an unrealistically small size (e.g. 0.001°). Additionally, a number of pRFs in SamSrf v.7. had an R^2 value of 1, which was unrealistically high considering the majority of other data points were around 0.1 and this would suggest a perfect model fit of the Guassian 2d model. Closer inspection revealed that these data points demonstrating an R^2 value of 1 also had a beta value of 0, suggesting that they had no amplitude. These two issues therefore highlight possible data quality filtering that should be done in future analysis: namely the removal of very small pRF sizes, and of pRFs with a beta value of 0 (for a discussion of the implementation of these data quality filters, see Chapter 10).

In conclusion, based on several aspects of data quality, it was decided that SamSrf v.7 would be the most appropriate for pRF model fitting within our data. However, to ensure that only good quality data is included in our final measurements, several filters will be employed, the exact nature of which will be further discussed in Chapter 10.

7.4. Development of the spatial summation measurement protocol

As the principle aim of this thesis is to investigate the neural basis of the altered Ricco's area previously found in glaucoma (Redmond *et al.*, 2010), it is important to demonstrate that we can measure the expected spatial summation curves at multiple locations across the visual field. Prior to testing a clinical sample, it was considered prudent to trial and develop the measurement of spatial summation, and determine estimates for Ricco's area, in a sample of young healthy adults.

7.4.1. Methods

Spatial summation was measured psychophysically in a sample of healthy young adults in order to ensure that spatial summation curves could be estimated across the visual field locations to be tested in the wider clinical study.

7.4.1.1. Participants

A subset of participants from those recruited in the previous chapter (Chapter 6) were tested, following ethical approval from the Cardiff University School of Psychology and School of Optometry and Vision Sciences research ethics committees. This was a sample of 22 participants (16 females; median [IQR] age = 20.01[19.36, 21.31] years; median [IQR] MD = -0.89[-0.54, -1.45] dB). The test eye was chosen at random for each participant (OD = 5, OS = 5). The inclusion and exclusion criteria from the Chapter 6 (non-myopic sample) applied (see Section 6.2.1).

7.4.1.2. Psychophysical measurement

Contrast thresholds were measured with an Octopus 900 perimeter (Haag Streit AG, Koeniz, Switzerland) and the Open Perimetry Interface (OPI; v.1.6.2; Turpin *et al.*, 2012). OPI was ran through R software (v.3.0.2; R core team, 2013) Circular achromatic stimuli were presented at nine visual field locations (see Figure 7.19). These locations were chosen in order to cover the lower nasal region stimulated by the peripheral pRF mapping (see Chapter 6 and Figure 6.2) and also to sample locations from across the visual field. This latter point was to ensure participant's attention would not be overly biased towards the lower nasal quadrant and to encourage participants to keep centrally fixated (equal sampling in each quadrant was not completed in the interest of time and limiting participant fatigue). By sampling locations either side of the fixation, it also helps to prevent visual drift. Stimuli were presented on an achromatic background of 10 cd/m^2. A chin-and-forehead rest

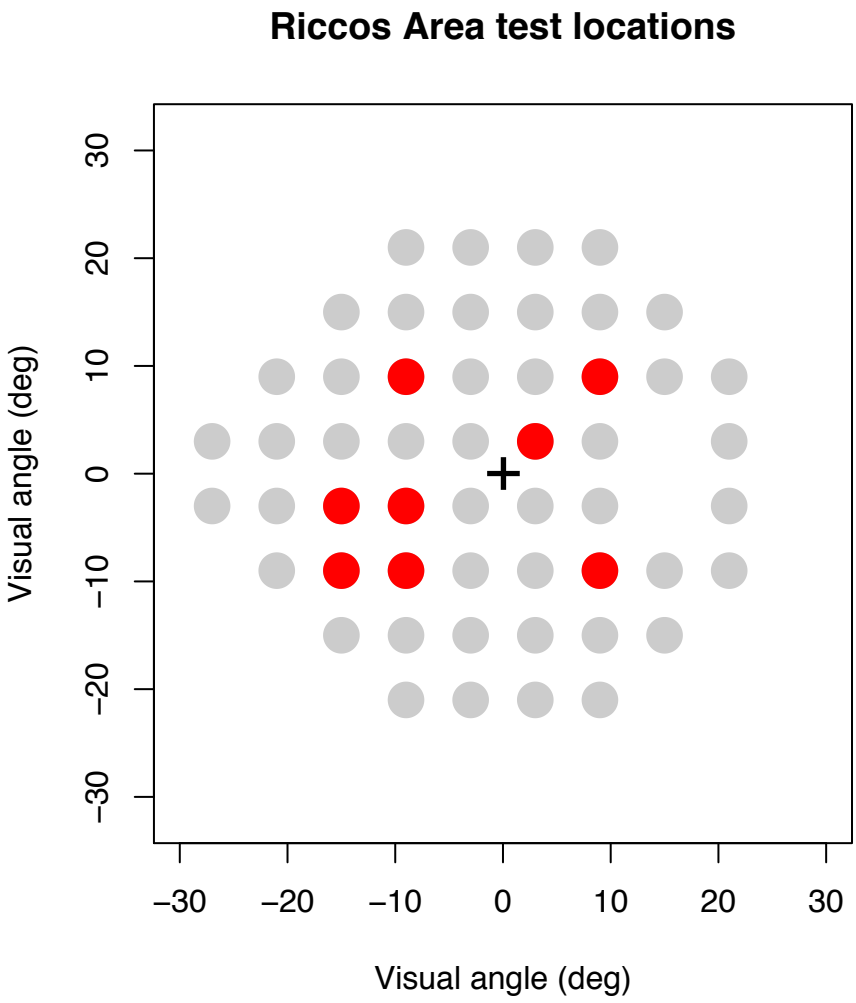

Figure 7.19 – Spatial summation test locations (red spots), defined by visual angle (°). The black cross denotes the fixation point, while the grey circles represent the locations of perimetric 24-2 testing for reference.

was used to aid in fixation. Fixation was also monitored visually and centred using an inbuilt camera display. Participants were given regular breaks throughout.

A 1-up:1-down staircase and Yes/No response criterion were used to determine individual thresholds (for more detail of these procedures, see chapter 4). Stimuli were consecutively presented to the nine visual field locations. At each location, luminance contrast thresholds were measured for the five Goldmann stimuli (I-V; areas: 0.01, 0.04, 0.15, 0.58, and 2.27 deg^2). Stimuli were presented for 200ms, with a square-wave temporal profile. After each stimulus area had been tested, the entire procedure was repeated, with three repetitions in total. The sensitivity could then be averaged across repetitions. The order that the Goldman stimulus areas were presented was randomised for each repetition.

Each location therefore ended with five contrast threshold measurements, one for each Goldmann stimulus area.

7.4.1.3. Ricco's area estimation

Ricco's area was estimated for each visual field location, using an iterative two-phase regression analysis (using MATLAB software). This two-phase regression methodology for fitting spatial summation data and estimating Ricco's area was discussed in Chapter 4.2.2. (Statistical modelling) and has been used in previous literature (e.g. Je *et al.*, 2018; Redmond *et al.*, 2010; Schefrin *et al.*, 1998). This fitting procedure constrains the slope of the first line to -1 (following Ricco's law), but allows the intercept of the first line, slope of the second line, and the breakpoint value to vary. The final estimated breakpoint value is used to represent Ricco's area.

Ricco's area was estimated for each visual field location per participant, along with an associated R^2 value in order to determine the goodness-of-fit of the two-phase regression line.

7.4.2. Results and discussion

7.4.2.1. Quality of fit

Figure 7.20 shows a histogram for all R^2 values (for all visual field locations combined). Encouragingly, the majority of these fits demonstrated an R^2 of above 0.9, suggesting a good level of fit between the data and the two-phase regression lines describing the spatial summation function. A repeated-measures ANOVA (Greenhouse-Geisser sphericity correction applied) also found no significant difference in R^2 values across visual field locations ($F(4.242, 76.361)= 1.123$; $p= 0.353$).

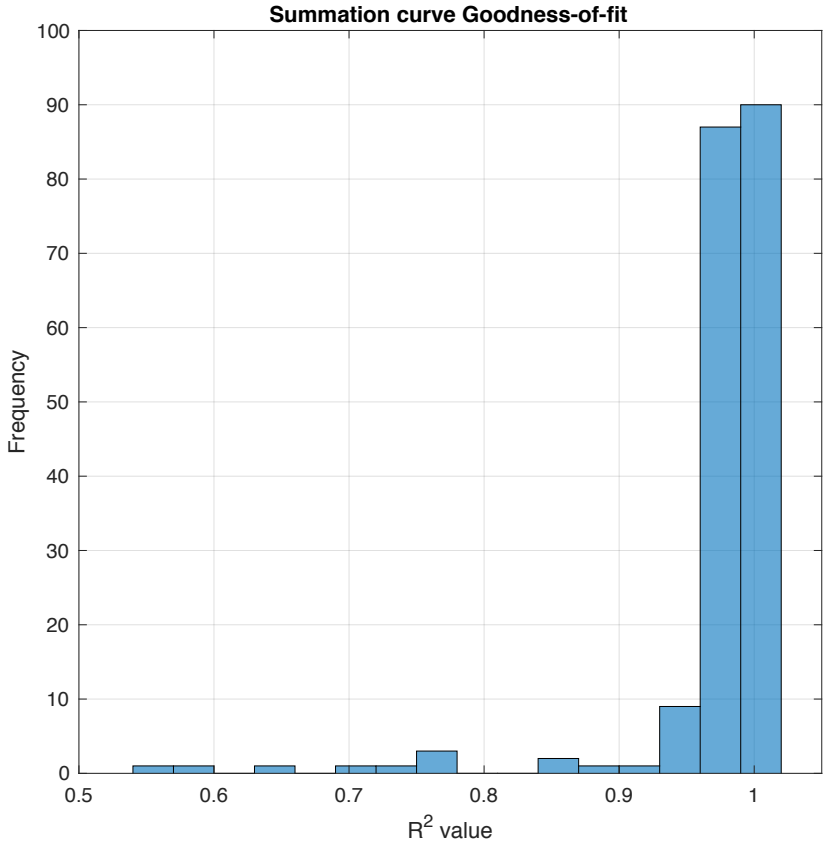

Figure 7.20 – Goodness-of-fit (R2 values) for a two-phase regression fit to participants' spatial summation data.

In order to ensure that only good quality fits are included in the final analysis, acceptability criteria were applied to the R^2 values. Firstly, only spatial summation curves with $R^2 > 0.9$ were included (which is a threshold that has been used previously; e.g. Redmond, Garway-Heath, et al., 2010). Representative examples of spatial summation functions at varying R^2 values are shown in Figure 7.24, which illustrates the fit of curves that would and would not be included in analysis, as a result of the criterion. Secondly, any Ricco's area estimation that fell outside of the range of stimulus sizes actually presented were also taken as unreliable and removed (i.e., outside of the range 0.01-2.27 deg^2). Out of 198 spatial summation functions (and associated Ricco's area estimates, eleven spatial summation functions were excluded due to poor fit, while six were excluded due to estimating Ricco's area estimates out of the presented range of stimulus areas. It should be noted that the majority (10/11) of spatial summation functions removed due to $R^2 < 0.9$ and all of the functions that were removed due to having Ricco's area estimates outside of the stimulated range, came from the same two participants. These participants were also included in the fMRI pRF mapping experiment described in Chapter 6 but demonstrated visual field maps that were too noisy to delineate. It is therefore possible that these two participants had generally poor fixation.

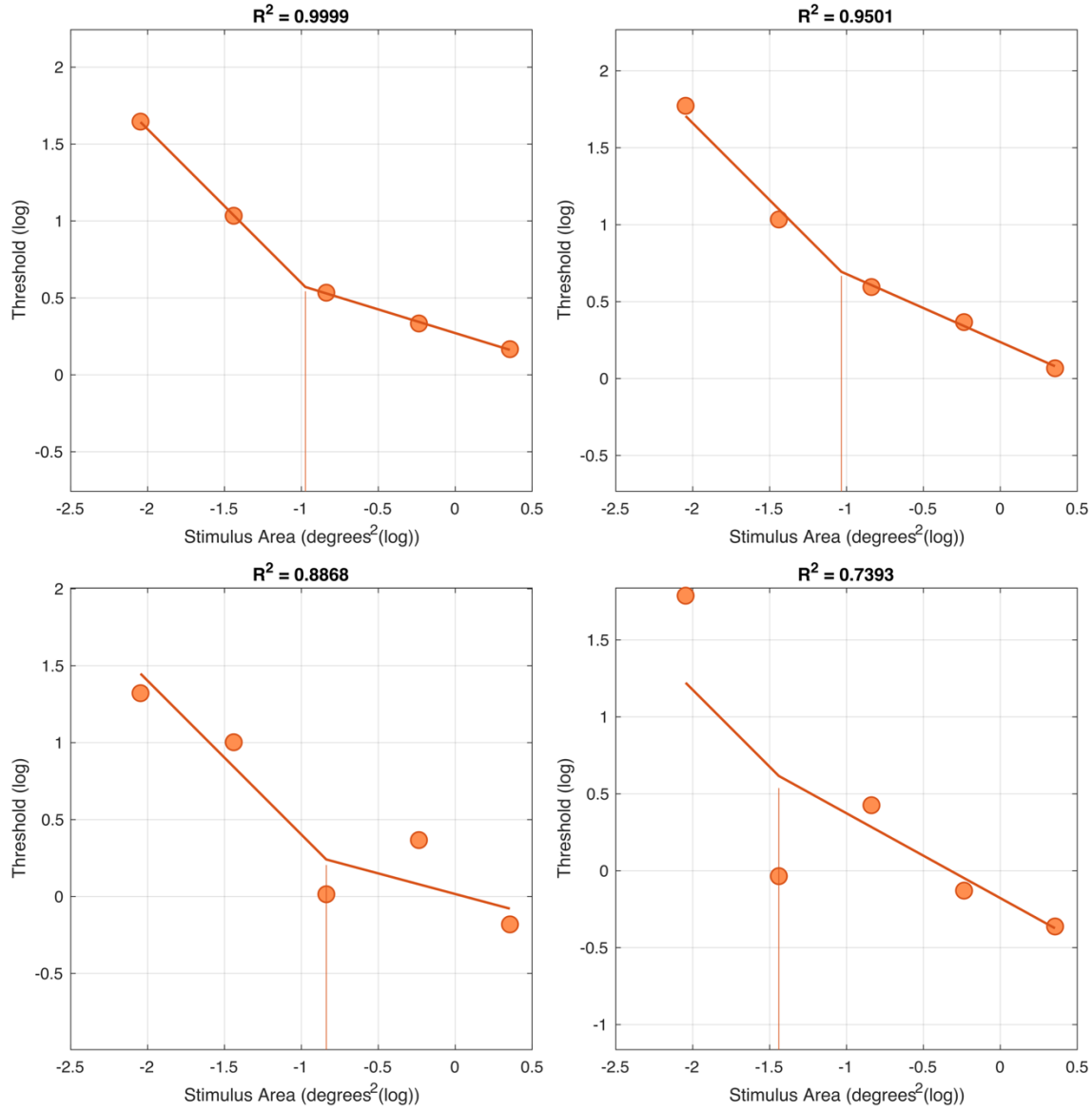

Figure 7. 21 - Example spatial summation curves taken from individual participants, illustrating different levels of Goodness-of-Fit (shown in R^2). The top two plots show representative curves above the 0.9 R^2 Goodness-of-fit criterion, while the bottom two plots illustrate curves that would be considered too poor a fit. All curves estimate a Ricco's area size that is within the stimulated region, and so would not be excluded for this reason. For each example, estimated threshold (shown in cd/m^2[logged]) is plotted as a function of stimulus area (shown in degrees^2[logged]). The summation curve is calculated using a two-phase regression and shown as a bold solid line. The red horizontal line indicates the estimated location of Ricco's area.

7.4.2.2. Ricco's area estimates

From those spatial summation curves that met the inclusion criteria, Ricco's area estimates were extracted and plotted as a function of eccentricity. Figure 7.25 illustrates this relationship for individuals (plot A) and for the group average (plot B). As expected from previous literature, Ricco's area shows a steady increase with eccentricity under photopic conditions. Furthermore, similar areas were found to those in the healthy control cohort described in Je *et al.* (2018) (who also used an Octopus 900 perimeter and used a similar procedure to the one described above), as well as the age-similar healthy participants in Redmond *et al.* (2010; who instead used a CRT monitor set-up).

These results suggest that the procedure described above can successfully measure good quality spatial summation curves (i.e., with a high goodness-of-fit value), and the resulting Ricco's area estimates agree with those in previous literature and vary across the visual field as expected. This procedure can therefore be brought forward to the sample of glaucoma patients and age-similar controls in future chapters.

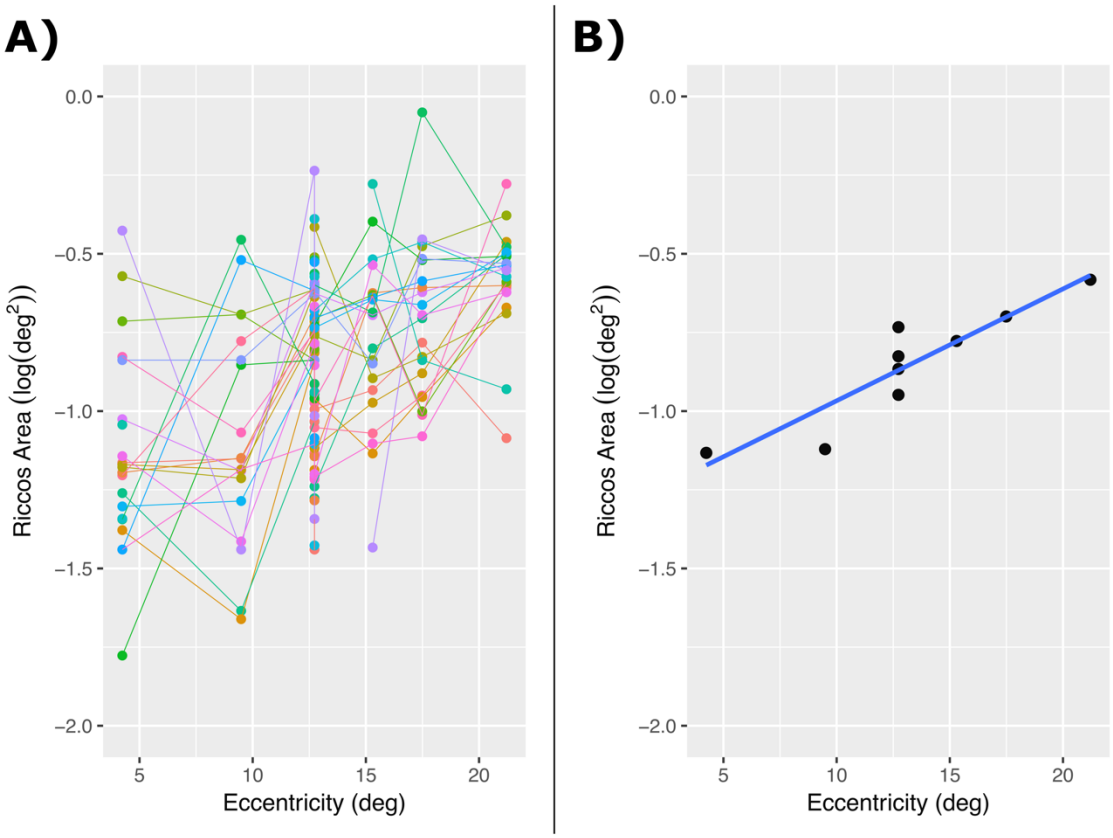

Figure 7.22 – Ricco's area estimates (degrees^2[logged]) plotted as a function of eccentricity of the visual field location at which it was measured. A) shows the individual datapoints for each participant (each colour is a separate participant), while B) is the group average. Blue solid line= line of best fit.

7.5. Participant inclusion and exclusion criteria

All participants (i.e., glaucoma patients and age-similar controls involved in the studies described in this thesis) had to meet strict eligibility criteria before being recruited, which were assessed either by their care team, by examination during a study session where an assessment by the care team was unavailable or not recent, or by self-report (where relevant). The inclusion criteria for participants, as well as the methods of assessment, are below. 'Self-report' refers to a questionnaire and discussion about visual and general health with the researcher at the start of testing. All participants also underwent assessment of the visual field using a ZEISS Humphrey Field Analyser 3 perimeter (Carl-Zeiss Meditec, Dublin, CA, USA; used the SITA standard strategy, program 24-2; examples of the visual field plots of glaucoma patients are given in Appendix A).

Glaucoma patients

a) Previous diagnoses of Normal Tension Glaucoma (NTG) or Primary Open Angle Glaucoma (POAG); assessed by the care team.
b) Glaucomatous nerve damage with corresponding visual field defect on two reliable visual fields tests; confirmed by the care team.

Healthy control participants

a) No previous diagnosis or immediate family history of glaucoma; self-report.

All participants

a) Clear ocular media, apart from normal age-related changes; assessed via the care team or in the participant visit.
b) Stable intraocular pressure (IOP) < 21mmHg – measured on the day of testing using a non-contact tonometer (CT-80 Non-Contact Computerized Tonometer, Topcon (Great Britain) Medical Limited, Newbury, UK) or, for glaucoma patients, confirmed by their care team.
c) Other abnormal ocular or systematic condition/medication that may affect visual performance (e.g., Age-related Macular Degeneration, diabetic retinopathy); assessed via the care team and self-report.
d) Paediatric glaucoma; assessed via the care team and self-report.
e) Age >18 years; self-report.

f) Refractive error > ±6.00 DS and > 2.50 DC (astigmatism) – assessed using an auto-refractor [TOPCON KR-7500 Kerato-refractometer, Topcon (Great Britain) Medical Limited, Newbury, UK]) on day of testing and (for glaucoma patients) confirmed by their ophthalmic care team.
g) Epilepsy; assessed via the care team and self-report.
h) Anything that would be considered unsafe to be within the MRI environment (e.g. pacemaker, head or neck tattoos, fixed dental work, metal implants); assessed via self-report and an MRI screening form completed on the day of scanning.

Chapter 8. An investigation of receptive field size in the glaucomatous retina using pattern electrophysiology

8.1. Introduction

It is important to consider the entire visual neural pathway when investigating glaucoma, as neurodegenerative effects have been shown at multiple neural hierarchies (e.g. Ersoz *et al.*, 2017; Jiang *et al.*, 2018; Zhang *et al.*, 2015). As discussed previously, the main aim of this thesis is to investigate the neural basis of Ricco's area changes in glaucoma compared to controls, specifically investigating the contribution of receptive field sizes at both the retina and the cortex. While it was previously suggested that Ricco's area reflects the size of retinal ganglion cell (RGC) receptive fields, more recent evidence suggests that it is unlikely to be solely a retinal phenomenon. For example, though Ricco's area enlarges in glaucoma (Redmond *et al.*, 2010), RGCs themselves shrink before cell death (Morgan, 2000, 2002). It has been hypothesised that there may be compensatory enlargement of receptive fields higher up the visual pathway in order to pool more spatial information and maintain the physiological sensitivity of the visual system (Redmond *et al.*, 2010). This thesis therefore aims to investigate how cortical receptive fields differ between glaucoma patients and healthy controls and how these receptive field sizes contribute to the extent of Ricco's area. Before investigating receptive field sizes within the visual cortices however, it is prudent to first investigate retinal receptive field sizes in glaucoma patients compared to controls, as these will shape the visual information being input from the retina to the cortex. In addition, as discussed in Chapter 2, the retina is the primary locus of damage within glaucoma.

Electroretinography (ERG) provides a direct method of assessing retinal neural functioning non-invasively and with excellent temporal resolution (described previously in Chapter 4). Multiple studies have used ERGs to investigate the retinal electrophysiological response amplitude in glaucoma compared to healthy controls (e.g. Bach & Hoffmann, 2008; Bach & Poloschek, 2013; Bergua *et al.*, 2004; Cvenkel *et al.*, 2017; Wilsey *et al.*, 2017). However, while studies have documented general RGC reductions in amplitude (e.g. using P50/N95 peaks or steady-state amplitude; for more discussion of the use of ERG in

glaucoma, see Chapter 4), the spatial selectivity of RGCs (and thus their receptive field sizes) has been less investigated. A method proposed for investigating the receptive field sizes of RGCs is pattern ERG (PERG) spatial tuning curves (Drasdo *et al.*, 1987, 1990).

PERG specifically involves recording the electrophysiological response elicited by patterned stimuli, which therefore target spatially sensitive cells. The presented stimulus is typically a high-contrast pattern, such as a grating or checkerboard, that alternates between high- and low-luminance portions across space at a particular spatial frequency. As discussed in Chapter 4 and during methods development in Chapter 7, this stimulus can be presented in a reversing pattern (with high- and low-luminance sections alternating at a set temporal frequency; reversal PERG) or it can be alternated with a blank mean-luminance background (onset-offset PERG) at a particular temporal frequency. The use of such PERG stimuli is an established method for investigating retinal receptive field structure (e.g. Enroth-Cugell & Robson, 1966; Thompson & Drasdo, 1987; White *et al.*, 2002).

By investigating the PERG response elicited by multiple spatial frequencies, a spatial tuning curve can be plotted. The amplitude of the PERG response varies depending on the spatial frequency of the presented stimulus, demonstrating both high- and low-spatial frequency attenuation (this type of spatial tuning curve is illustrated in Figure 8.1). This frequency-dependant attenuation occurs due to the centre-surround receptive field configuration of the retinal cells underlying the PERG response. For example, when the presented stimulus is at a relatively high spatial frequency (so that, for example, the width of the high-luminance portion is narrower than the target cell's receptive field centre), the high-luminance portion will fall within the excitatory centre of a retinal receptive field but will only stimulate a portion of it. The stimulus will therefore only elicit a relatively small response. On the other hand, if the high-luminance portion is large enough to encompass both the excitatory centre and the inhibitory surround (i.e. at a coarser spatial frequency), the response will also be attenuated due to the antagonistic action of the surround. The largest amplitude PERG response is elicited when the spatial frequency of the stimulus means that the high-luminance portion only encompasses the excitatory centre of the target cell's receptive field. When the amplitude of the PERG response is plotted as a function of the spatial frequency used to elicit it, a spatial tuning curve is produced and this

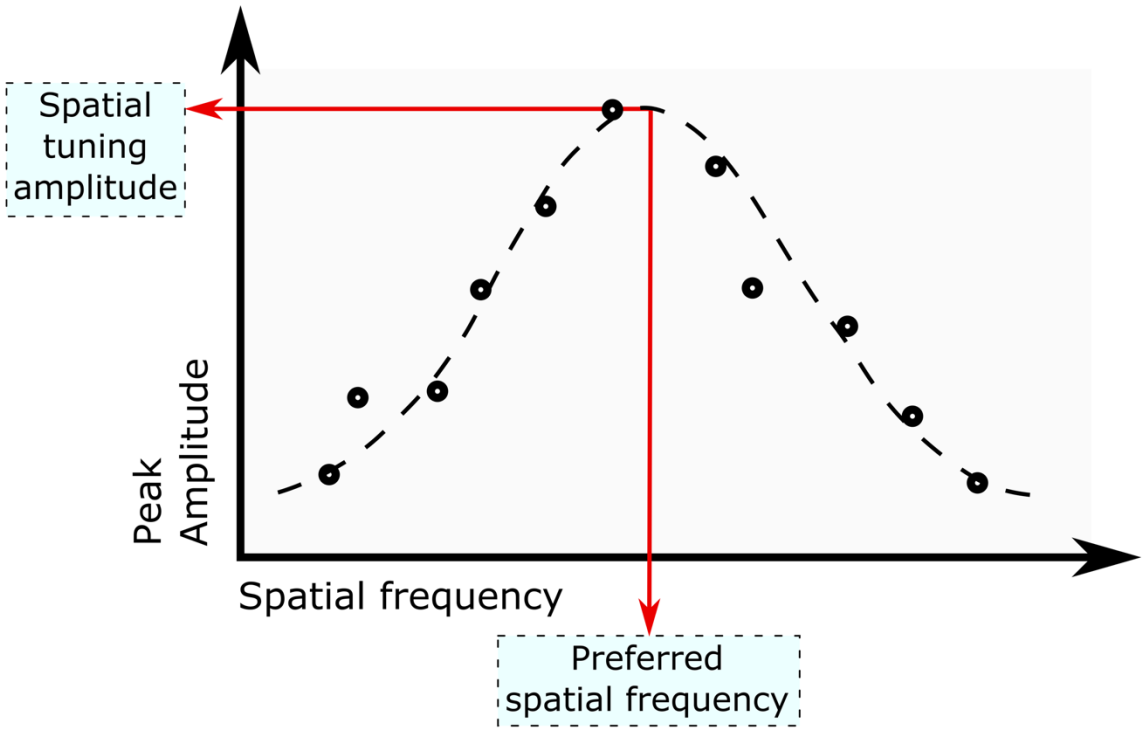

Figure 8.1 – Illustration of a spatial tuning curve and relevant metrics extracted for this study. Circles indicate possible response amplitudes to different spatial frequencies. Dashed curve indicates a Gaussian curve fit to the data as an estimate of the underlying spatial tuning function. Two metrics will be taken from this fit. A) The peak amplitude of the spatial tuning curve. B) the preferred spatial frequency that elicits the greatest amplitude response.

high- and low-spatial frequency attenuation can be seen (this is discussed further during PERG methods development in Chapter 7). The spatial frequency that elicits the peak of this spatial tuning curve (i.e. the preferred spatial frequency: illustrated in Figure 8.1) can be used as a proxy of average receptive field size over the stimulated area of the retina.

As both RGCs and bipolar cells show centre-surround antagonism in their receptive field organisation (e.g. Hammond, 1974; Kaneko, 1970; Lee, 1996), it is likely that they both contribute to the generation of these PERG spatial tuning curves. In order to more specifically target spatially sensitive cells, Drasdo *et al.* (1987) developed a method for refining the PERG response into separate components: the retinal illuminance response (RIR), driven by the distribution of retinal illuminance, and the pattern specific response (PSR), driven by the external stimulus luminance. They suggest that the PERG response to very low spatial frequencies contains negligible pattern specific components and mostly reflects the retinal illuminance. Furthermore, they suggest that the retinal illuminance component of higher spatial frequencies can be computed from the eye's optical transfer

function and the PERG response to very low spatial frequencies. From comparisons to different retinal layer thicknesses, it is suggested that the PSR mostly arises from RGCs, while the RIR mostly arises from bipolar cells (Drasdo *et al.*, 1990). This method described by Drasdo *etal., (1987)* therefore allows for the direct, non-invasive measurement of RGC receptive fields. Utilising this methodology for the current research has been described previously during PERG methods development (Chapter 7).

While no study has used the methodology described by Drasdo *et al.* (1987) to examine retinal receptive field sizes in glaucoma, a small number of studies have investigated the PERG response to multiple spatial frequency stimuli in samples of glaucoma patients and healthy controls. An early study by Korth *et al.* (1989) investigated onset-offset PERG responses to two frequencies of achromatic gratings (0.2 and 3.4 cycles-per-degree [cpd]) in 24 healthy controls and 26 glaucoma patients. While healthy controls, on average, showed an increase in PERG response amplitude with increasing cpd (i.e. a larger response to 3.4cpd stimuli than to 0.2cpd stimuli), no such difference was found in glaucoma patients (so a similar response was elicited by both spatial frequencies). This was interpreted as a lack of spatial tuning in these glaucoma patients, with the evidence of glaucomatous damage to retinal cells most evident at higher spatial frequencies (3.4 cpd). However, by only using two spatial frequencies, the whole profile of the spatial tuning curve (as is shown in Figure 8.1) could not be delineated so it cannot be said whether there was a lack of spatial tuning or if the curve had shifted to favour a smaller or larger receptive field size. Alternatively, the results may reflect a shallowing of the curve, without a particular directional shift.

A more recent study has also investigated spatial tuning in glaucoma, but using reversal PERG in the mid-periphery (Shorstein *et al.*, 1999). As mentioned previously (such as Chapter 4), the response to reversal PERG is comprised of a number of major components, such as P50 and N95, which are suggested to reflect spiking and non-spiking activity near the ganglion cell body, and RGC axonal spiking activity respectively (Bach *et al.*, 2018). In this study, the P50 component was investigated (N95 determined to be too variable due to the small amplitude), using a 3.2Hz reversing grating presented in a 12x12° stimulus area displayed in each quadrant separately. Healthy controls (N= 19) were presented with six spatial frequencies (0.25 to 6cpd), while glaucoma patients (N= 9) were

presented with three spatial frequencies (0.38, 0.75, 1.5cpd). They report evidence of expected spatial tuning in healthy controls, though the low spatial frequency attenuation discussed above was not always present. Glaucoma patients demonstrated significantly lower amplitudes in all quadrants, particularly for 1.5cpd stimuli (the response to which was also the only one to demonstrate a shortening of the time to peak). Conclusions about spatial tuning curves, however, are difficult to draw with only three spatial frequencies tested.

The current study aims to investigate spatial tuning curves in a sample of glaucoma patients and age-similar controls. A range of spatial frequencies will be utilised to ensure that the peak, and either side of the curve, can be estimated so that it will be possible to identify and investigate shifts in the curve between glaucoma patients and controls. Furthermore, the RGC receptive field signal will be more directly targeted by using the methodology detailed by Drasdo *et al.* (1987) to remove the non-pattern specific RIR. It is possible that, similar to findings of RGC dendritic tree shrinkage in glaucoma disease progression, the spatial tuning curve will be shifted towards coarser spatial frequencies in the glaucoma group compared to controls, reflecting a shrinking of average RGC receptive field size across the stimulated region. Alternatively, it is possible that there will be a compensatory enlargement of retinal receptive field sizes in glaucoma, possibly due to compensatory mechanisms of presynaptic cells which also contribute to retinal receptive field size (such as bipolar and amacrine cells; Peichl & Wässle, 1983). In support of this suggestion, previous work has reported increased synapse formation between bipolar and RGCs following chronic IOP elevation (Park *et al.*, 2014).

8.1.1. Aims

The study described in this chapter aims to extend previous research by investigating the full spatial tuning curve in glaucoma patients compared to age-similar controls, utilising methodology outlined by Drasdo *et al.* (1987) to remove the luminance response and investigate the pattern-specific response. The PERG methodology and chosen spatial frequencies were developed in Chapter 7. The mid-periphery will be stimulated, in order to investigate an area relevant to glaucomatous progression. It is also a region that can be stimulated in the MRI using the methodology described in Chapters 6 and 7, allowing for more meaningful comparisons between measurements taken from these methodologies

(which is done in Chapter 10). By extracting features from PERG spatial tuning curves (both outcome measures are demonstrated on Figure 8.1.), three main aims will be addressed:

1) To investigate whether there is a shift in the preferred spatial frequency in glaucoma patients compared to healthy controls, suggesting a change in RGC receptive field size.
2) To investigate whether the magnitude of the spatial tuning curve (i.e. the height/amplitude of the peak) decreases in glaucoma compared to age-similar healthy controls, as would be suggested by previous literature.
3) To investigate whether the above PERG outcome measures (i.e. peak spatial frequency or curve magnitude/amplitude) explains some of the variance in perimetric visual sensitivity. It is hypothesised that a positive relationship should be found between amplitude and visual sensitivity, with those with a lower sensitivity having more severe glaucomatous damage in this region and thus lower amplitude (following on from the aim above). In regard to peak spatial frequency, a direction is not specifically hypothesised.

8.2. Methods

PERG spatial tuning curves were measured in a sample of glaucoma patients and healthy age-similar controls, focussing on the mid-peripheral visual field. Outcome metrics describing these curves (i.e. preferred spatial frequency and curve amplitude; see Figure 8.1) were then compared between groups and associations with measurements of perimetric visual sensitivity investigated. Precise methodology is described below.

8.2.1. Participants

Ethical approval for this study was obtained from NHS Wales research ethics committee (Cardiff and Vale and Cwm Taf NHS health boards), as well as the Cardiff University Schools of Psychology and Optometry and Vision Sciences. Participants were recruited via NHS glaucoma clinics (at the Royal Glamorgan Hospital and University Hospital of Wales, as well as the School of Psychology community panel and Cardiff University Eye clinic. Participants were offered travel reimbursement. 29 healthy controls with a median age of 67.7 years (IQR= 63.0, 72.8; 16 females) and 25 diagnosed glaucoma patients (8 normal tension glaucoma [NTG] and 17 primary open angle glaucoma [POAG]) with a

median age of 67.8 years (IQR= 59.8, 71.5; 12 females) were recruited. There was no significant difference in age between the groups (t(52)= 0.263, p= 0.793). All experiments were carried out monocularly, on either a randomly chosen or glaucomatous eye (controls: 14 left eyes [OS]; glaucoma: 16 OS).

All participants met the eligibility criteria detailed in chapter 7. The intraocular pressure of the healthy controls (median= 15mmHg; IQR= 13, 16) and glaucoma patients (median= 14mmHg; IQR= 12,14) was not significantly different (t(52)= 1.09, p= 0.28). Similarly, pupil diameter in healthy controls (median= 3.20mm; IQR= 2.80, 3.70) and glaucoma patients (median= 3.40mm; IQR= 2.80,4.10) did not show a significant difference (t(49)= 0.13, p= 0.13), suggesting neither factor would be able to explain a difference in outcome variables between groups. As expected, mean deviation (MD; i.e. the overall amount of visual field sensitivity deviation from the population mean) for the glaucoma patients (median= -3.42dB; IQR= -11.19, -1.72) was significantly lower (t(52)= 5.29, p<0.001) than that of the age-similar controls (median= 0.04dB; IQR= -0.58, 0.47).

8.2.2. Electrophysiology

Electrophysiological recordings took place in an electrically quiet room (described within methods development; see Chapter 7). Following recommendations by the International Society for Clinical Electrophysiology of Vision (ISCEV) protocol (Bach *et al.*, 2013), a disposable DTL ERG fibre (Unimed Electrode Supplies Ltd) was placed along the lower eyelid of the target eye (near the lower limbus) and a reference electrode was placed near the ipsilateral canthus. The cables for these were twisted together along their length and secured to the participant's shoulder or upper back using Blenderm surgical tape. Finally, a ground electrode was placed on the forehead. Conductivity of the ground and reference electrodes was optimised using Nuprep Skin Prep gel (Weaver and company) and Signa conductive electrolyte gel (Parker). Electrodes were secured in place using Blenderm surgical tape. A chin-and-forehead rest was used to aid in keeping the participants' head still and relaxed during recordings. All participants were given appropriate vision correction for a working distance of 40cm.

Electrophysiological recordings were taken using the Diagnosys LLC Espion system (v.6.), which also generated the stimuli. Stimuli (described below) were presented on a CRT monitor (Mitsubishi Diamond Pro 2070sb; Mitsubishi Electric Corporation, Tokyo, Japan) at

a viewing distance of 40cm, powered via a Supra Lorad shielded mains power lead. The use of a shielded power lead avoided any electrical 'leakage' from the power supply, which would cause additional noise in the electrophysiological recordings. Participants were requested to keep their jaw relaxed and to fixate on a 1° green fixation cross in the centre of the screen. The stimuli subtended a 18° radius square, with the central 5.5° covered with a Gaussian dark-grey square patch in order to only stimulate the mid-periphery.

The 100ms onset-offset PERG methodology developed in Chapter 7 was used. A black and white grating (92% contrast) was presented for 100ms, followed by mean grey luminance for 110ms. Each sweep (i.e. response to single cycle) recording started at 10ms pre-onset and ended once the 110ms offset period was completed. 100 sweeps were averaged into a result. As an online quality check, results were recorded until at least three results satisfactorily superimposed (i.e. if the result was manually moved on top of the other, the overall shape of the response would overlap), which could then be taken forward. An in-built 10 second break was provided in between each result to allow the participant to rest their eyes if needed and reduce fatigue. Participants were also given a break between each spatial frequency and where requested. After recording, eye blinks were manually removed (at the sweep level; defined as sweeps that deviated from baseline by 50uV at any point along the timescale) and the superimposing results were averaged into a final trace. In order to assess the spatial tuning function, five gratings with increasing spatial frequencies were presented (0.14, 0.625, 1.25, 2.5, and 5 cycles per degree [cpd]). This range was chosen to encompass the spatial tuning peak previously reported in healthy individuals (between 1-4 cpd; e.g. Bach & Holder, 1996; Drasdo *et al.*, 1987). The 0.14 cpd grating is suggested to only include the luminance response due to the large width of the bars, so was included to allow removal of this component (as in Drasdo *et al.*, 1987). Each participant therefore ends with five traces, one for each spatial frequency grating. Fewer spatial frequencies were tested than during methods development in order minimise participant fatigue (and associated variability) and also to leave more time for repeating recordings if needed. Spatial frequencies were therefore chosen that sufficiently describe the curve found during methods development.

Spatial smoothing (i.e. low-pass temporal filtering) was completed using Fourier analysis (see Appendix B for code). As the target onset and offset response is a low frequency response, this allowed for the removal of higher frequency noise.

8.2.3. Perimetric visual field assessment

Participants completed standard clinical visual field assessment with a ZEISS Humphrey Field Analyser 3 perimeter (Carl-Zeiss Meditec, Dublin, CA, USA; SITA-standard, central 24-2). White-on-white perimetry was utilised, with a working distance of 33cm. The test procedure involved the participant resting on a chin-and-forehead rest, with appropriate spectacle correction calculated by the instrument, based on participant age and refractive error prescription. The eye was manually centred with the aid of a live eye monitor camera. The participant was required to fixate on a central fixation mark and indicate when they saw a circular stimulus anywhere in their visual field using a patient response button. Goldman size III stimuli were presented for 200ms at locations within the 24-2 test pattern, at sub- and supra-threshold levels. Each eye was tested separately (with the untested eye occluded with an eyepatch). Visual sensitivity thresholds were calculated and printed out by the device. The following quality check criteria were used based on metrics calculated by the instrument during testing to ensure the quality of the assessment (e.g. that the participant was paying sufficient attention):

- Blind spot errors: <25%
- False positive rate: <15%
- False negative rate: <15%

If one of these exclusion criteria were met, the visual field assessment was repeated on that eye.

8.2.4. Analysis

Following removal of the luminance component and fitting of the spatial tuning curves (discussed further in section 8.3.1), two metrics were extracted from each individual's curve:

1) The peak spatial frequency, defined as the spatial frequency corresponding to the peak of the curve fit (aim one).

2) The amplitude of spatial tuning present in the retinal cells, defined as the maximum amplitude along the fitted curve minus the minimum (aim two).
3) The goodness-of-fit of the curve fit, defined as the R^2.

A two-way frequentist ANOVA was used to compare the peak spatial frequency between groups. When looking at how one outcome variable differs between two groups, an ANOVA is essentially the same as a t-test – specifically, they produce the same p-value and the F-value is the T-statistic squared. However, the use of an ANOVA allows for the comparison to be weighted by the associated goodness-of-fit so that those with very poor fits will have less of an impact on the final result. Due to unequal variances between groups, a Welch ANOVA was used to compare PERG amplitude between groups, as this does not assume that the variances are equal. This was one-tailed, following our hypothesised direction, and was also weighted by goodness-of-fit.

As mentioned previously, the luminance component was removed to leave the Pattern Specific Response (PSR). In order to ensure that the removal of this component did not bias the group comparisons detailed above, the extracted luminance components were examined and compared between groups to see if there were any significant group-wise differences. To quantify this, Fréchet Distance was used, which is a measure of the similarity between two curves in space, defined as the minimum line-length which is sufficient to join each curve if simultaneously traversing the length of each. An illustration of Fréchet Distance is given in Figure 8. 2.

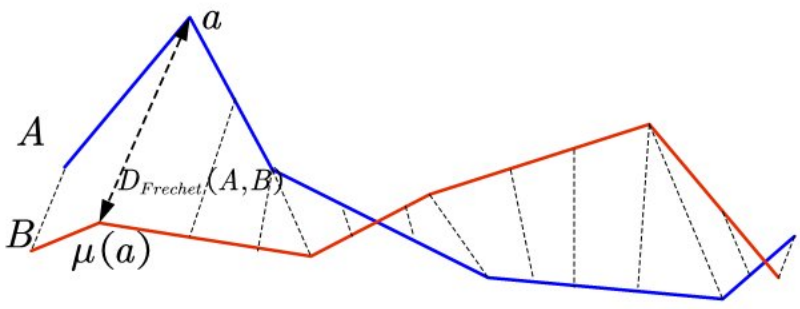

Figure 8. 2 – An illustration of Fréchet Distance (D) between two lines (A and B). Reproduced from Guo et al. (2017)

Finally, to address aim three, Ordinary Least Squares (OLS) multiple regressions were run to examine how much variance in visual sensitivity can be explained by the PERG outcome measures. Again, these are weighted by the curve goodness-of-fit. If any coefficients are significant, the slope of the relationship will be further examined quantitatively using a (transformation-method) Passing-Bablok regression (Bablok *et al.*, 1988). Unlike an OLS linear regression, such as that used above, Passing-Bablok regressions does not assume that either variable is free from measurement error and, due to its use of median values, is less affected by outliers and does not make assumptions from the underlying distribution (Bablok *et al.*, 1988; Redmond *et al.*, 2013). It is therefore suggested to be able to more accurately quantify the slope of the underlying relationship. However, this regression is only appropriate for use with linear relationships. Linearity was therefore tested in this dataset with the use of an OLS-based cumulative sum (CUSUM) test with alternative boundaries (which are proportional to the standard deviation and suggested to be better at detecting structural deviations from linearity; Hornik *et al.*, 2001; Zeileis, 2001). Passing-Bablok regressions also assume a positive relationship, which was confirmed by a one-tailed Kendall's Tau-b.

All statistical tests in sections 8.3.1-2, as well as t-tests and multiple regressions within sections 8.3.4-5, were computed using the computer software JASP v0.11 (JASP Team, 2019). Fréchet Distance values in section 8.3.3. was computed within MATLAB 2018b (*MATLAB*, 2018) using a Fréchet Disance calculator function (Ursell, 2013). CUSUM, Kendall's Tau-b, and Passing-Bablok regressions in sections 8.3.4-5 were computed within the software packages *R* v.4.0.0 (R core team, 2020) and *RStudio* v.1.0.153 (RStudio Team, 2016).

8.3. Results

8.3.1. Group spatial tuning curves

The pattern specific response (PSR) for each trace was initially calculated using the methodology outlined by Drasdo *et al.* (1987); the first step therefore was to recreate the group averaged curves seen in Drasdo *et al.* (1987) for our healthy control group. The final traces for each spatial frequency were averaged across participants, giving a group response for the healthy controls and glaucoma patients (first column in Figure 8.3 and Figure 8.4).

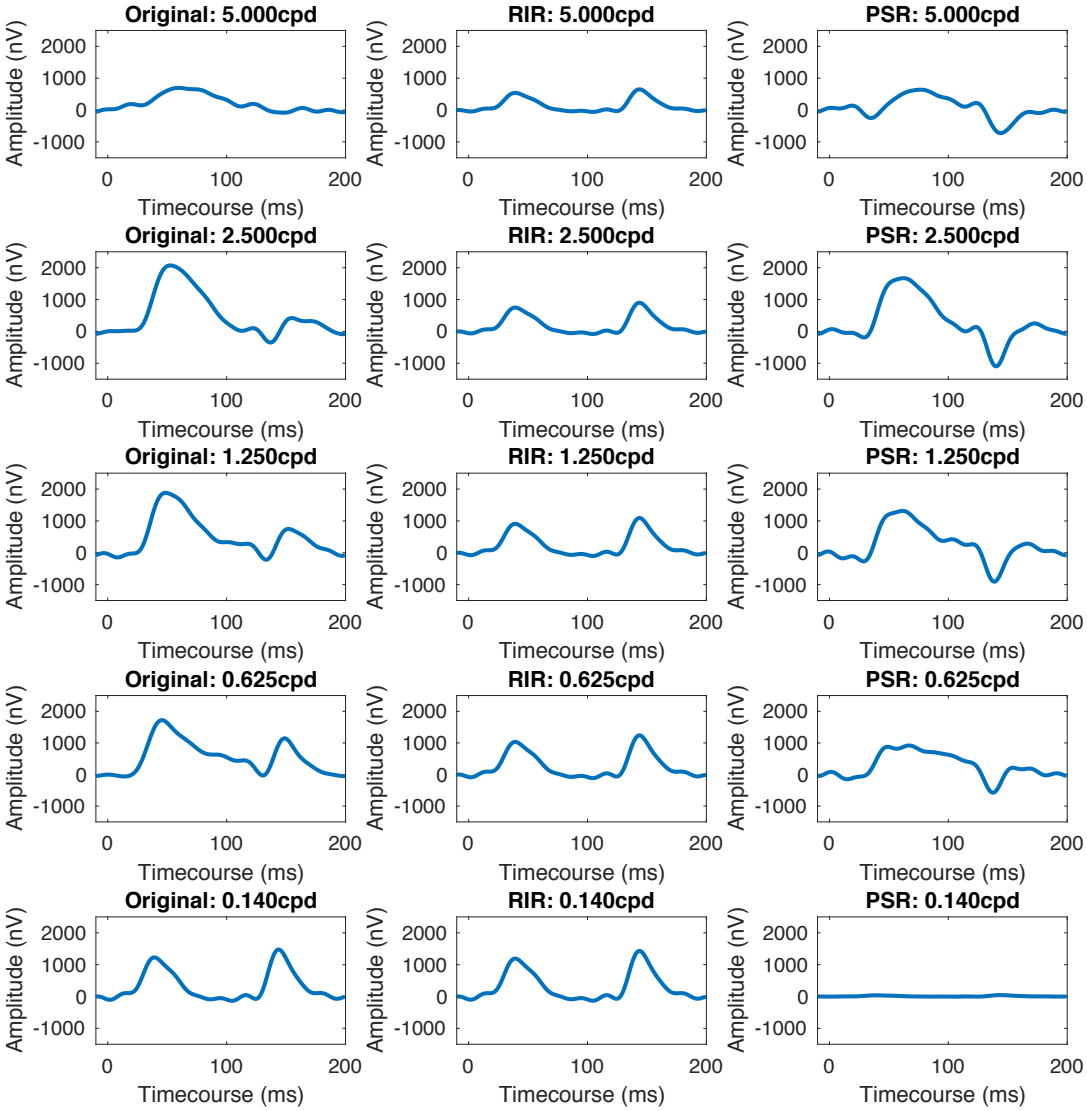

Figure 8.3 – Pattern Onset-offset group traces for the healthy controls. The first column shows the Fourier analysed raw data for each spatial frequency. The middle column show the retinal illuminance response (RIR), which are based on the 0.140cpd response then attenuated for each frequency by the contrast attenuation factor (CAF), retrieved from Drasdo et al. (1987). The RIR is subtracted from the average response, to produce the pattern specific response (PSR), shown in the third column. Cpd = cycles-per-degree. Amplitude in nV, while the time course is in ms.

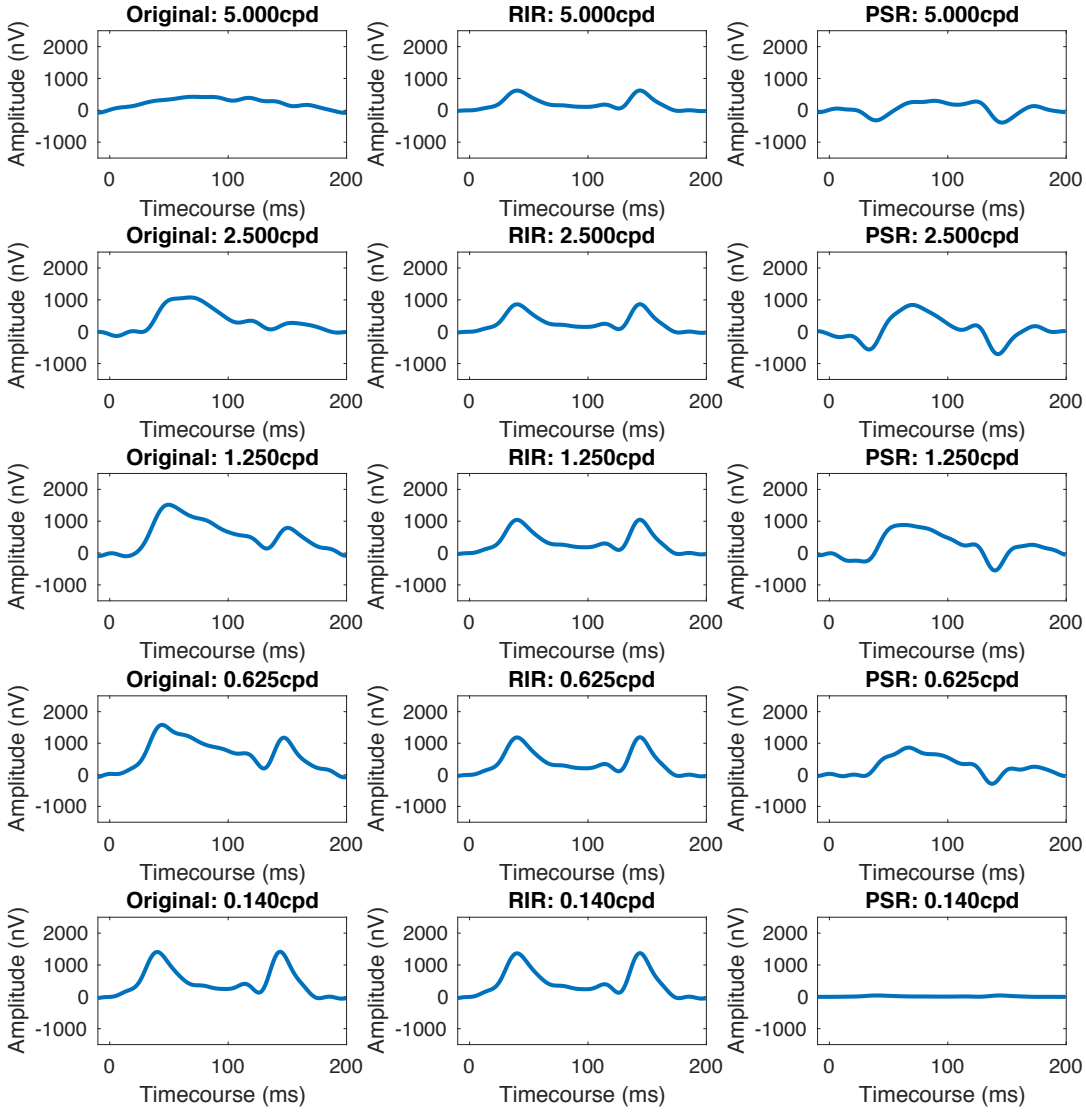

Figure 8.4 – Pattern Onset-offset group traces for the glaucoma patients. The first column shows the Fourier analysed raw data for each spatial frequency. The middle column show the retinal illuminance response (RIR), which are based on the 0.140cpd response then attenuated for each frequency by the contrast attenuation factor (CAF), retrieved from Drasdo et al. (1987). The RIR is subtracted from the average response, to produce the pattern specific response (PSR), shown in the third column. Cpd = cycles-per-degree. Amplitude in nV, while the time course is in ms.

The response to the coarsest grating (0.14 cpd) was taken as a mostly retinal illuminance response (RIR), which is linearly proportional to contrast. This linear relationship allows for the calculation of the RIR contribution to the response at other spatial frequencies, based on the 0.14 cpd response, using a correction factor to account for the contrast reduction due to optical degradation. This factor is termed the contrast attenuation factor (CAF) and is based on the modulation transfer function of the healthy eye. Values for the CAF at different spatial frequencies were taken from Drasdo *et al.* (1987). The RIR for each spatial frequency was computed by multiplying the 0.14 cpd response by the corresponding CAF for that frequency, essentially attenuating the RIR for higher spatial frequencies. The calculated RIRs can be seen in the second column of figures 8.2 and 8.3. The final PSR is therefore the original trace with this RIR removed, as seen in the third column of figures 8.2 and 8.3. Finally, the peak response (defined as the peak-to-trough amplitude) was extracted for each PSR and plotted as a function of logged spatial frequency. A Gaussian curve is then fitted to the data. Figure 8.5 illustrates this final spatial tuning curve for healthy controls compared to the spatial tuning curves from Dradso *et al.* (1987).

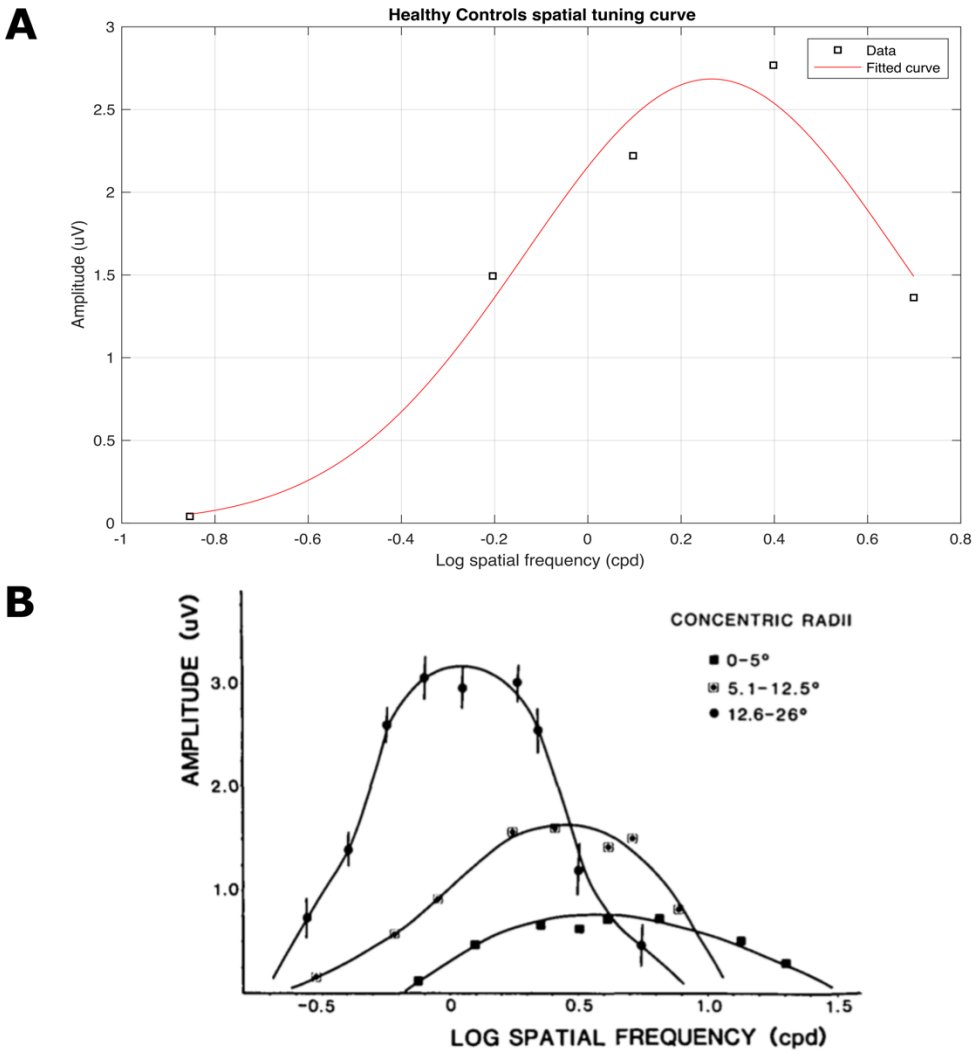

Figure 8.5 – Comparison of (A) healthy spatial tuning curves in the current healthy control sample (stimulated region= 5.5-18 degrees eccentricity), and (B) spatial tuning curves found in Drasdo et al. (1987; different regions of stimulation shown). Spatial frequency shown in log cycles-per-degree (cpd). Y-axis shows the peak amplitude, defined in this study as the onset peak-to-trough amplitude.

Clearly defined onset responses are visible in our traces (Figure 8.3), occurring around the 40-70ms mark, with the smaller offset response expected at a rate of 100ms onset-offset (Drasdo *et al.*, 1987). Drasdo *et al.* (1987) and Thompson and Drasdo (1987) also found that the RIR peaks were quite flat in the central visual field but increased greatly to be near equivalent to the PSR in the periphery. The amplitude of our RIR traces seems to be a midpoint between the RIR described at these eccentricities and are therefore consistent with previous results, considering that the current study stimulated 5.5 - 18° and Drasdo et al. (1987) report that their unshown 5.6 - 12.6° stimulation showed an intermediate amplitude. Clear bandpass spatial tuning (i.e. both low and high spatial frequency amplitude attenuation) is found in our healthy controls (Figure 8.5), with a peak at approximately 0.3 log cpd (~2cpd on a linear scale). This is slightly lower than the peripheral responses described in Drasdo et al. (1987; see plot B in Figure 8.5 for curves at different regions of stimulation) and Thompson and Drasdo (1987), possibly due to the older age in our sample. Slightly higher amplitude is also reported in our sample, which may be due to defining the peak as peak-to-trough, as has been done by previous papers, rather than maximum amplitude.

Glaucoma patients (Figure 8.4) also show clear spatial tuning. The RIR is similar to that in healthy controls across spatial frequencies, suggesting an unaffected illuminance response. The PSR however, shows a substantially diminished onset peak, though with a similar time-to-peak. These averaged responses were plotted as a spatial tuning curve and compared between glaucoma patients and healthy controls (Figure 8.6). A substantial shallowing of the tuning curve is seen. The peak spatial frequency appears to be slightly shifted towards lower frequencies in the glaucoma patients, but this change appears small. Curve metrics are statistically compared below.

8.3.2. Spatial tuning analysis

The above methodology was again used to extract the PSR traces, but this time on an individual basis to allow for individual metrics to be calculated and compared. The onset peak, defined as the peak-to-trough amplitude (with the peak occurring between 20-100ms post onset and with the trough occurring between 78-165ms post onset; this range was used to encompass all individual variation present in the data), was extracted for each

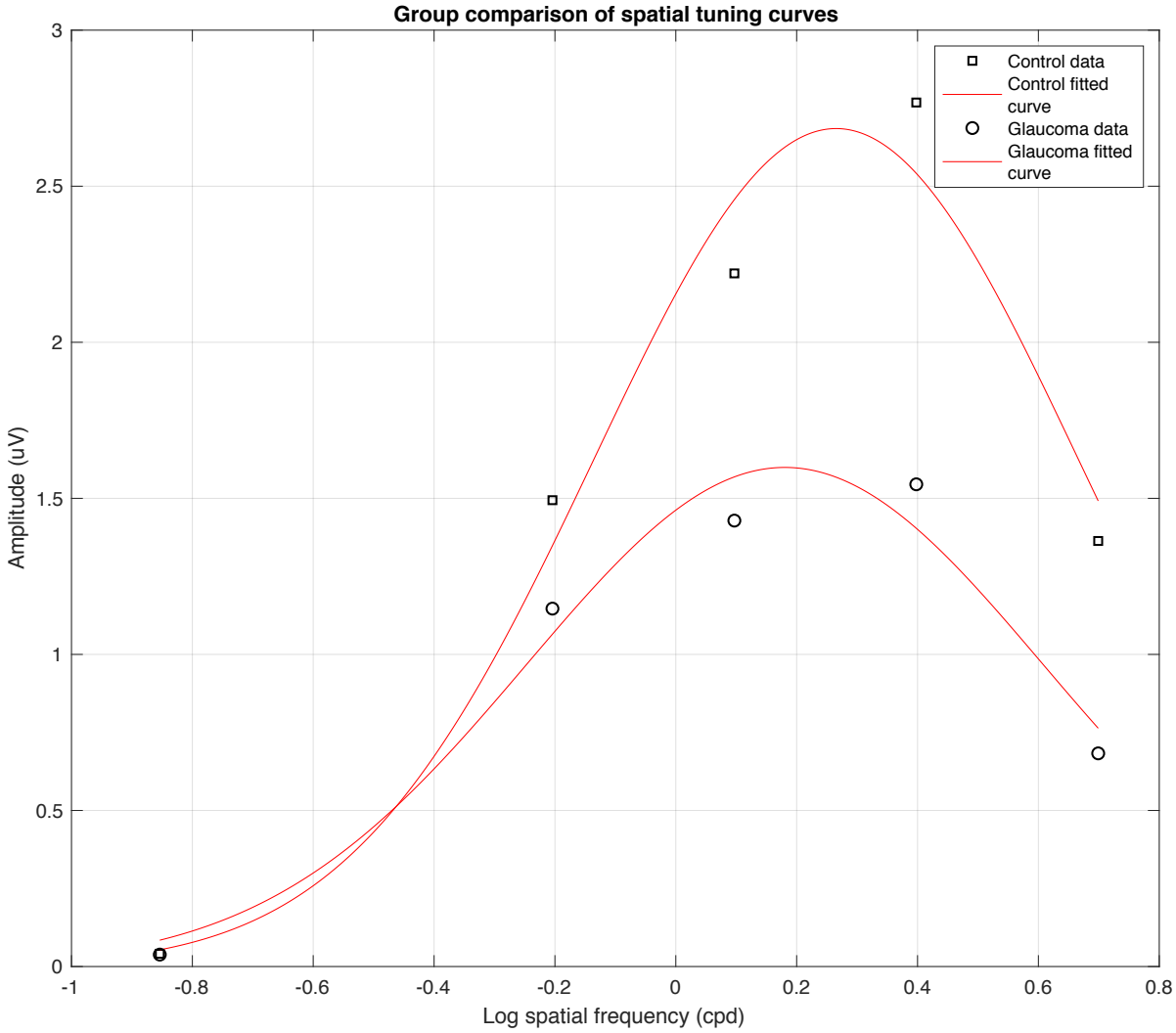

Figure 8.6 – Spatial tuning curves for glaucoma patients (circles) compared to healthy age-similar controls (squares). Spatial frequency shown in log cycles-per-degree (cpd). Red lines show the Gaussian curve fit. Peak amplitude plotted on y-axis, defined as the onset response peak-to-trough (in uV).

spatial frequency. These peak amplitudes were then plotted as a function of log spatial frequency and a Gaussian curve fitted (as was done with the group averages in Figure 8.5 and Figure 8.6). A Gaussian curve was determined to best represent the underlying physiological receptive field population. Peak spatial frequency and PERG amplitude were extracted from this curve fit.

In order to quality check our data, the goodness-of-fit of the individual spatial tuning curves (defined as the R^2 of the Gaussian curve fits) was examined. A histogram of all R^2 values is shown in Figure 8.7, with glaucoma patients represented as orange and healthy controls as blue. No notable difference is seen between groups, which is confirmed by an

independent, two-tailed t-test (t[52]= 0.721, p= 0.474). Reassuringly, most participants (15 glaucoma patients and 17 controls) show a high level of Goodness-of-Fit (R^2>0.95). Figure 8.8 shows representative curves at different levels of Goodness-of-fit, from 0.99-0.39. In order to account for differing levels of fit in the data, which will impact the confidence one can have in the estimated curve metrics, the below statistics will be weighted by the associated R^2 score.

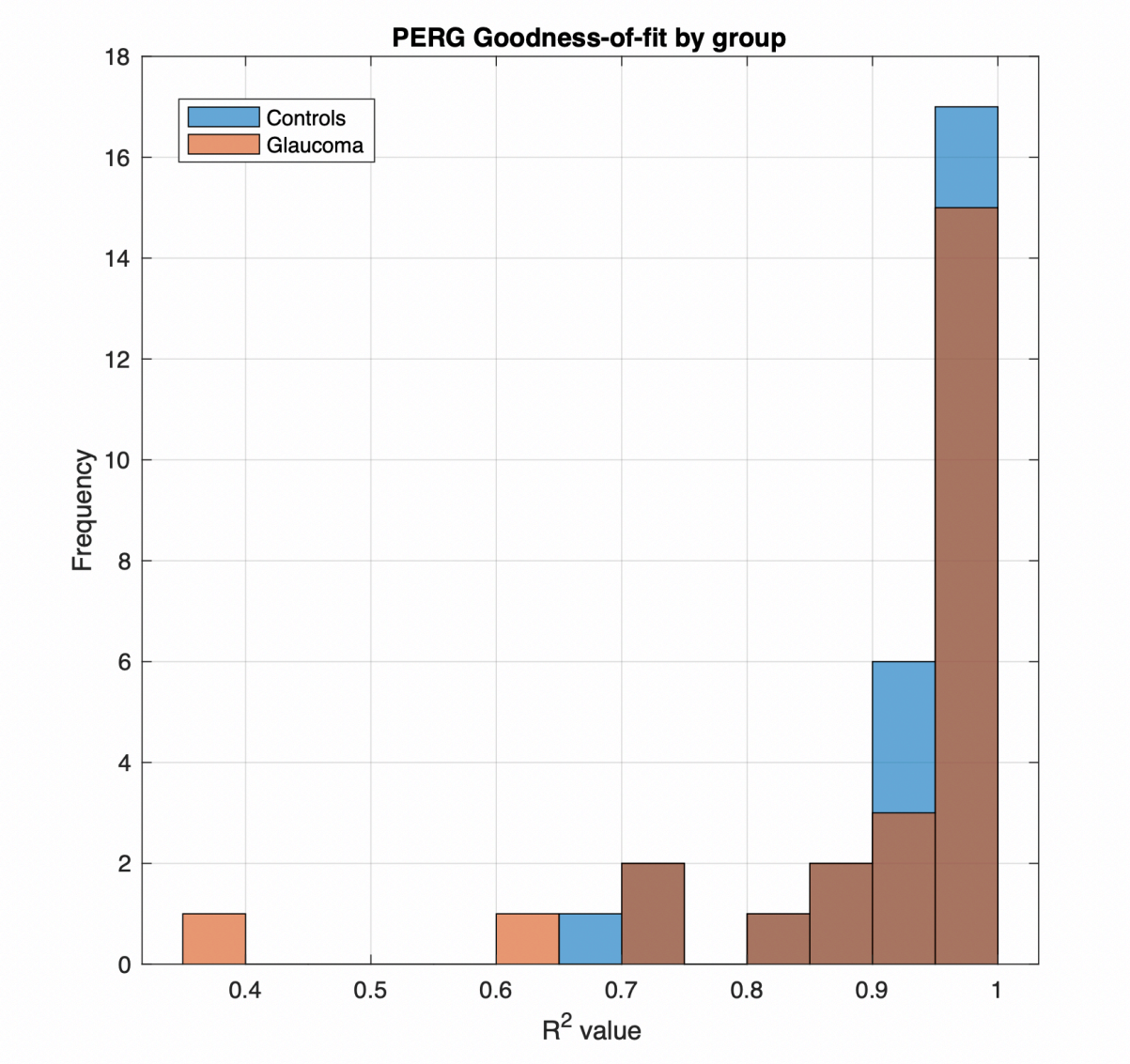

Figure 8.7 – Histogram of Goodness-of-fit (R^2 values) for a Gaussian curve fit to participants' spatial tuning data. Orange bars represent glaucoma patients, while blue bars represent healthy controls.

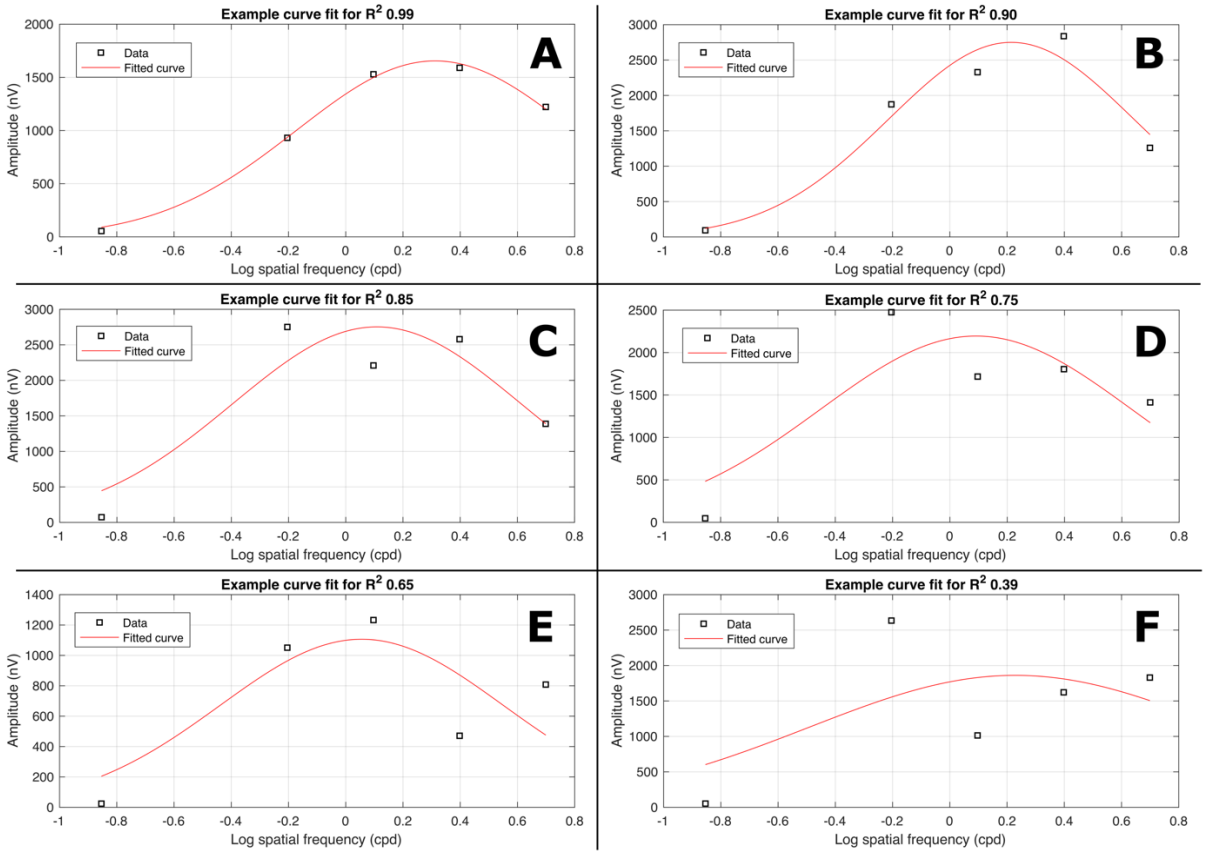

Figure 8.8 – Example of curve fitting for spatial tuning curves from individual participants. Gaussian curves are fit (shown as a red line) on the peak amplitude (shown in nV) extracted from each presented spatial frequency (shown in log cycles-per-degree [cpd]). The Goodness-of-fit is represented as the R^2 of the curve fit. Plots A-F show example curves with descending Goodness-of-fit.

The median peak spatial frequency (see Figure 8.9) was 1.80cpd for healthy controls (IQR= 1.46, 2.14) and 1.64cpd for glaucoma patients (IQR= 1.33, 1.84), suggesting a shift in peak spatial frequency (and so average RGC functional receptive field size) towards lower spatial frequencies, possibly reflecting a compensatory enlargement of functional receptive fields, despite the shrinkage of dendritic trees (Morgan, 2002). This is supported by a two-way ANOVA, weighted by R^2 value ($F(1,52)= 4.84$, $p= 0.03$).

The median tuning amplitude (see Figure 8.10) for healthy controls was 2548.28nV (IQR= 1857.79nV, 4233.69nV) and 1711.77nV for glaucoma patients (IQR= 1371.10nV, 2160.05nV). A Welch one-way ANOVA, weighted by the R^2 value, was carried out and a significantly lower amplitude in the glaucoma group ($F[1,39.30]= 17.25$, $p<0.001$) was observed.

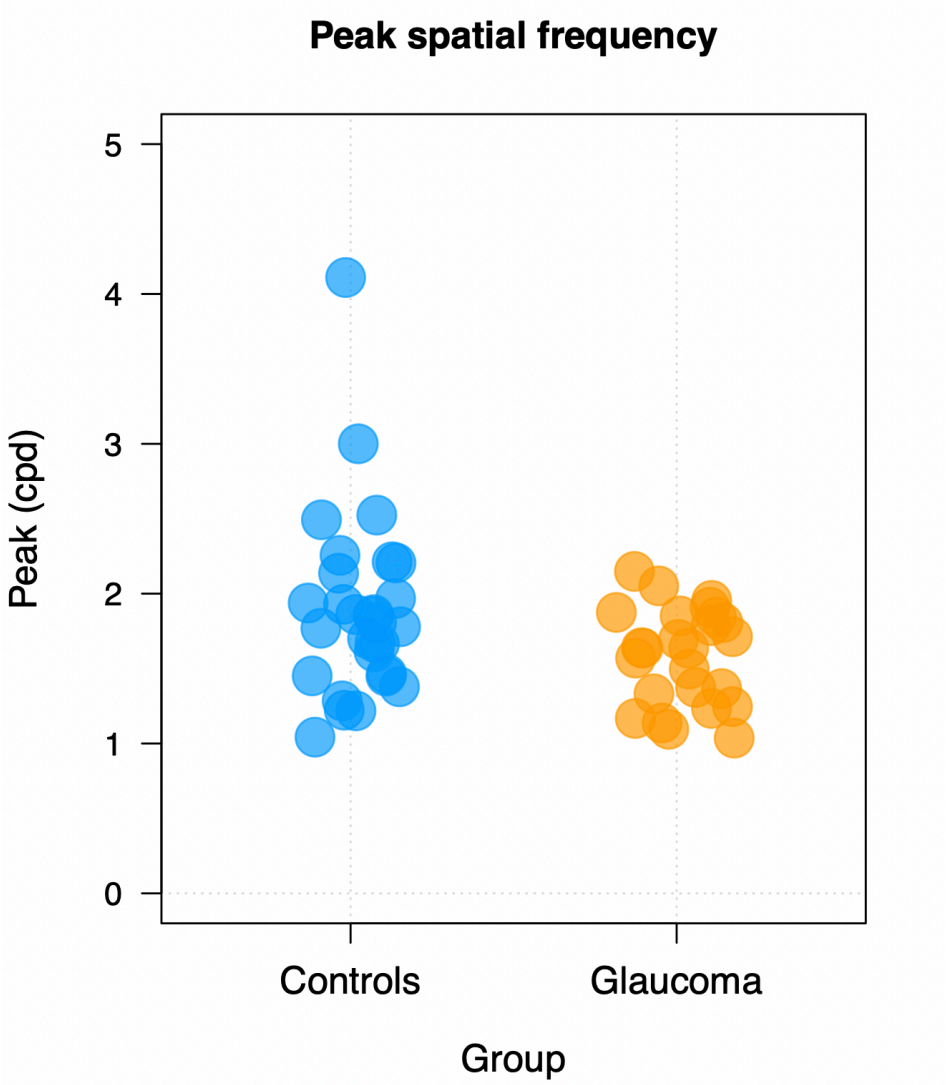

Figure 8.9 – Spatial frequency that caused the strongest amplitude response, extracted from the fitted Gaussian spatial tuning curves. Preferred spatial frequency given in cycles-per-degree (cpd).

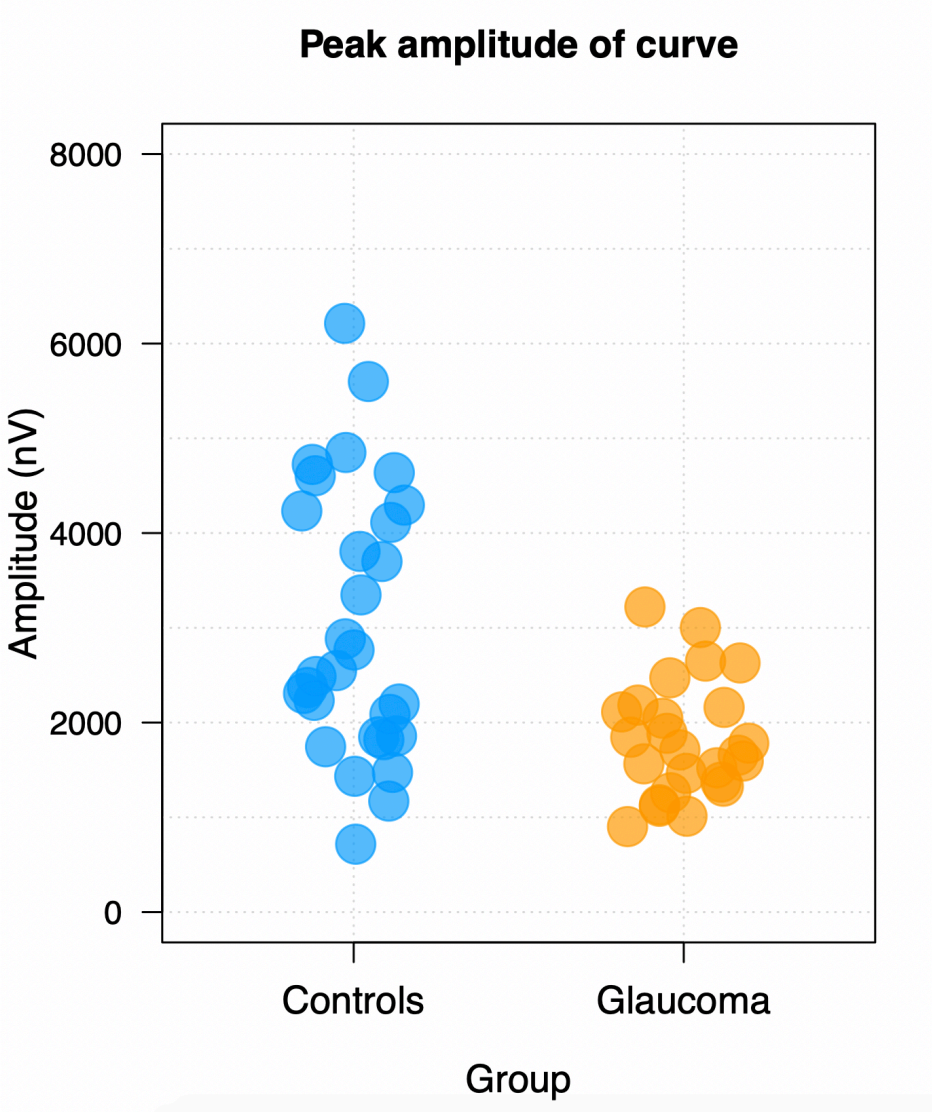

Figure 8.10 – The peak amplitude (nV) of the spatial tuning curves, defined as the maximum minus the minimum amplitude of the Gaussian fit.

8.3.3. Comparison of luminance response

It is assumed that the extracted luminance response is similar across groups and does not introduce bias in this process. It was therefore important to test this assumption. The Retinal Illuminance Response (RIR) for the 0.14cpd grating, which is the maximal luminance response, was compared between groups. From visual inspection of these responses in Figure 8.3 and Figure 8.4, these seem very similar, and are also comparable to the RIR reported by Drasdo et al., (1987). This is supported by a Fréchet Distance value between the two traces of 147.6nV (Ursell, 2013), which is relatively low considering the average amplitude of this response is 309.74nV in healthy controls and 423.23nV in glaucoma patients.

To investigate the impact of luminance removal on the final results, spatial tuning curves were also generated without the removal of this component. A comparison of the resulting curves (on a group level) can be seen in Figure 8.11. The same direction of group differences can be seen (i.e. smaller amplitude and lower preferred cpd in the glaucoma group compared to the controls) even without isolating the pattern specific response. In terms of the peak spatial frequency, this is likely partially driven by the maintained luminance response (which is particularly present in lower cpd stimuli) in glaucoma patients compared the reduced spatially sensitive response pulling the curve to these lower cpds. There was also a much poorer fit of the Gaussian curve, presumably due to the larger response at the finer frequencies, suggesting that this curve fit is less appropriate for this data. Overall, this suggests that the removal of the luminance response did not bias the results.

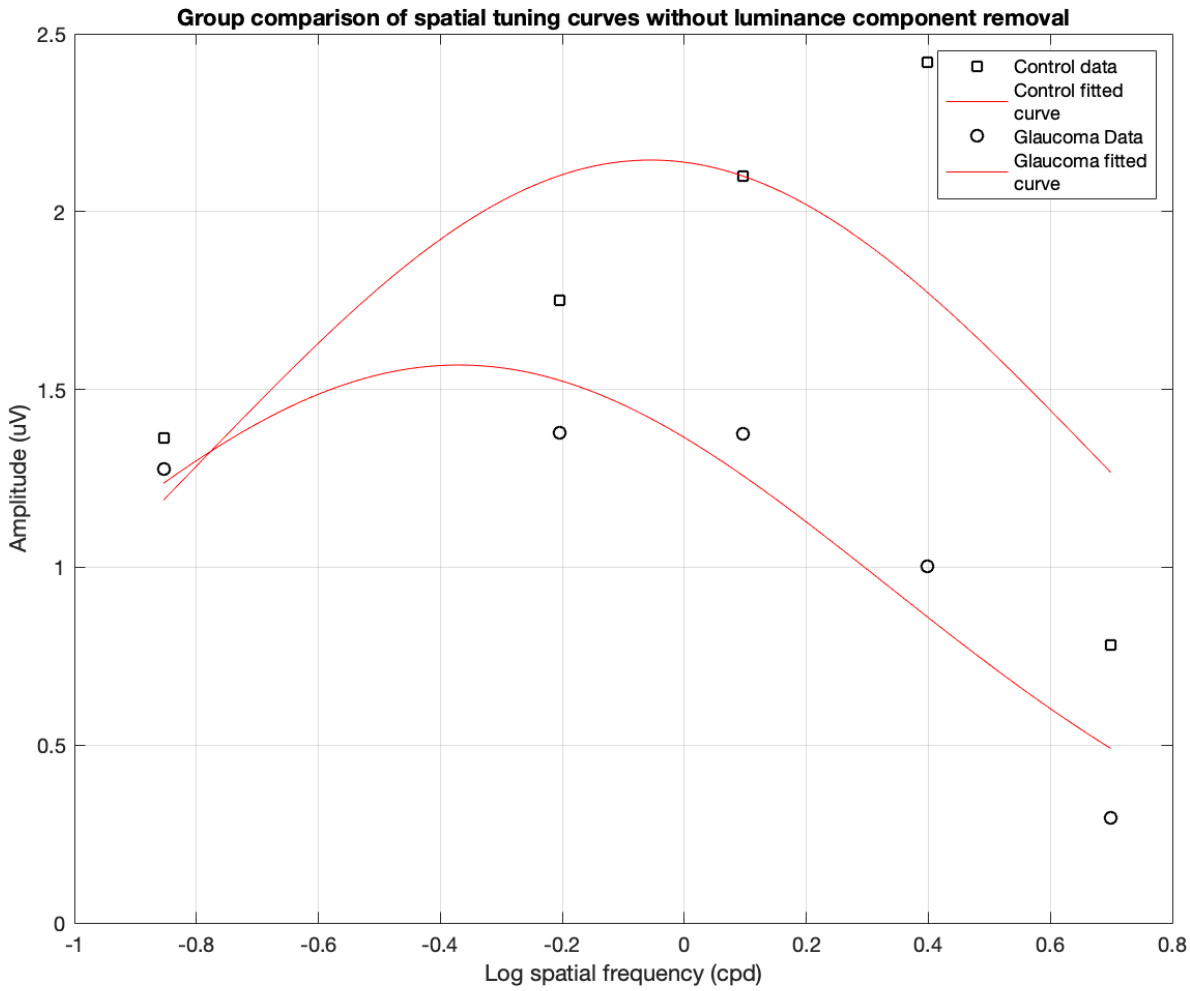

Figure 8.11 – Spatial tuning curves without the luminance response removed for glaucoma patients (circles) compared to healthy age-similar controls (squares). Spatial frequency shown in log cycles-per-degree (cpd). Red lines show the Gaussian curve fit. Peak amplitude plotted on y-axis, defined as the onset response peak-to-trough (in uV).

8.3.4. Associations with visual sensitivity

The relationships between the PERG outcome measures and perimetric sensitivity was then investigated. In order to address aim 3, perimetric visual sensitivity scores from ZEISS Humphrey Field Analyser 3 perimetric testing 24-2 protocol (Carl-Zeiss Meditec, Dublin, CA, USA; used the SITA standard strategy) were averaged (i.e. unlogged, mean taken, re-logged) over the region of the visual field tested via PERG (see Figure 8.12 for an illustration of the test region on a visual field plot). The associations between the above outcome measures (logged) and perimetric visual sensitivity (decibels; dB) were addressed with a R^2-weighted multiple linear regression. Using the Enter method, it was found that the overall model effect of PERG outcome measures against sensitivity scores was significant ($F(2,51)= 5.666$; $p= 0.006$; $R^2= 0.182$; $R^2_{Adjusted}= 0.150$). As an individual coefficient, PERG amplitude did explain a significant amount of variance in perimetric sensitivity (standardised $\beta= 0.420$; $t= 3.247$; 95% confidence intervals [CIs]= 1.404, 5.950; $p= 0.002$), while peak spatial frequency did not explain a significant proportion of visual sensitivity variance (standardised $\beta= 0.025$; $t= 0.193$; 95% CIs= -3.824, 4.638; $p= 0.848$).

A Passing-Bablok regression was ran to estimate the slope of this relationship (Bablok *et al.*, 1988). An OLS-based CUSUM test reported non-significant deviations from linearity (therefore suggesting a linear relationship) in the combined (all participants) dataset ($p= 0.379$), glaucoma group alone ($p= 0.905$), and healthy control group alone ($p= 0.384$). Passing-Bablok regressions also assume a positive relationship, which was suggested by a one-tailed Kendall's Tau-b (combined: tau-b= 0.281; $p= 0.001$; glaucoma only: tau-b= 0.327; $p= 0.011$; controls only: tau-b= 0.165; $p= 0.104$). Passing-Bablok regressions were run for the whole dataset, as well as the glaucoma and healthy control groups separately (regression lines shown in Figure 8.13). For the combined sample, the slope of the relationship between PERG amplitude and visual sensitivity was 6.741 (CIs= 4.587, 10.724), while the intercept was 8.360 (CIs= -4.847, 15.722). This suggests that, for this sample, for an increase of 1nV(log) in PERG amplitude, there is a corresponding increase of about 6.741dB in visual sensitivity in the test region. When looking at the groups separately, the healthy controls show a slope of 5.202 (CIs= 2.323, 8.933) and an intercept of 13.708 (CIs= 0.409, 24.076). The glaucoma group, however, shows a steeper slope of 11.707 (CIs= 4.810, 22.783) and a lower intercept of -7.481 (CIs= -43.202, 14.877).

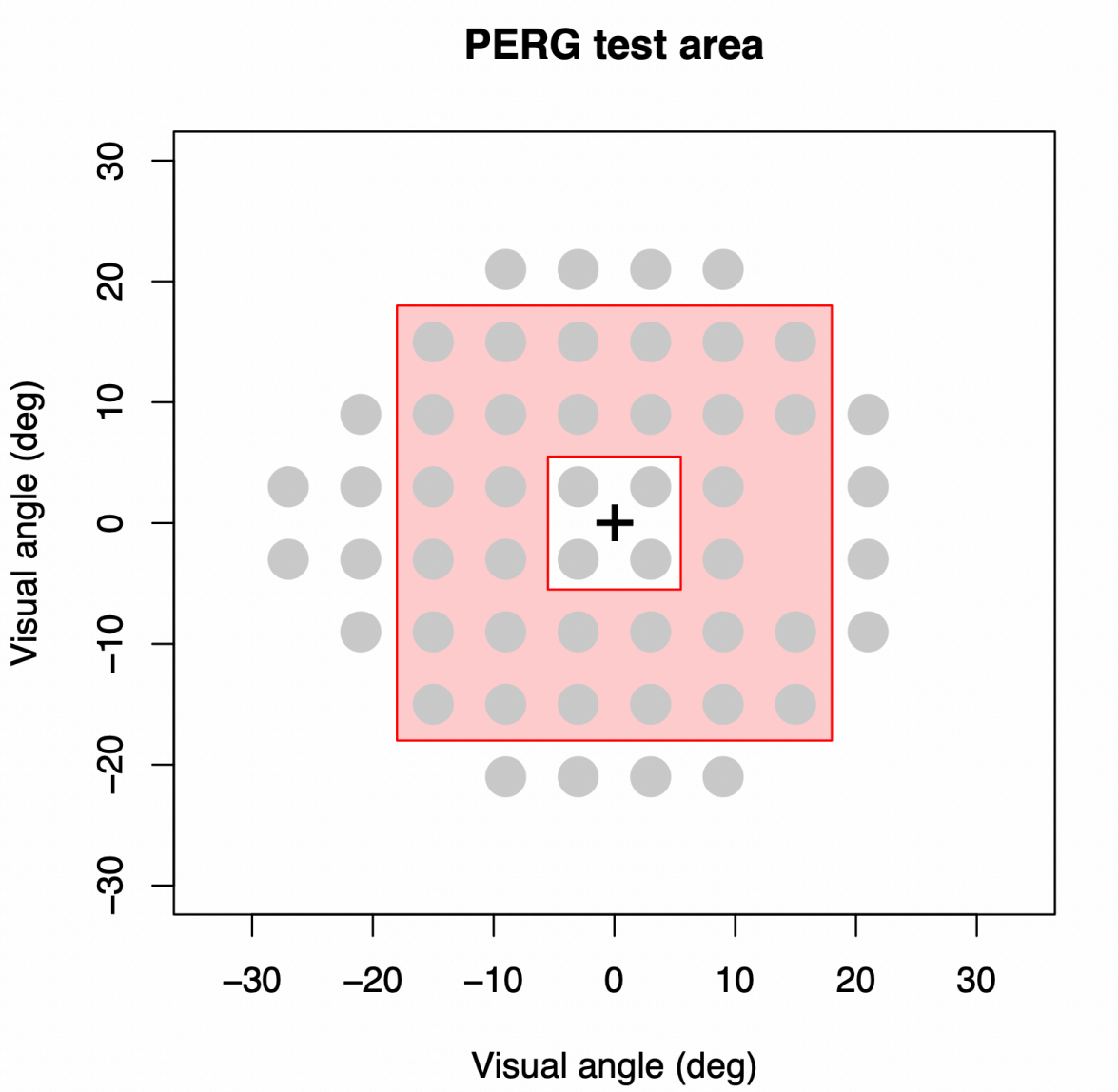

Figure 8.12 – PERG test area on a visual field plot (defined by visual angle [°]). PERG test area is shown by the shaded red region. The black cross indicates fixation, while the grey circles represent the locations of perimetric 24-2 testing for reference. In order to compare the visual sensitivity of this region to the PERG response, visual sensitivity values of all those spots contained with the red region were averaged.

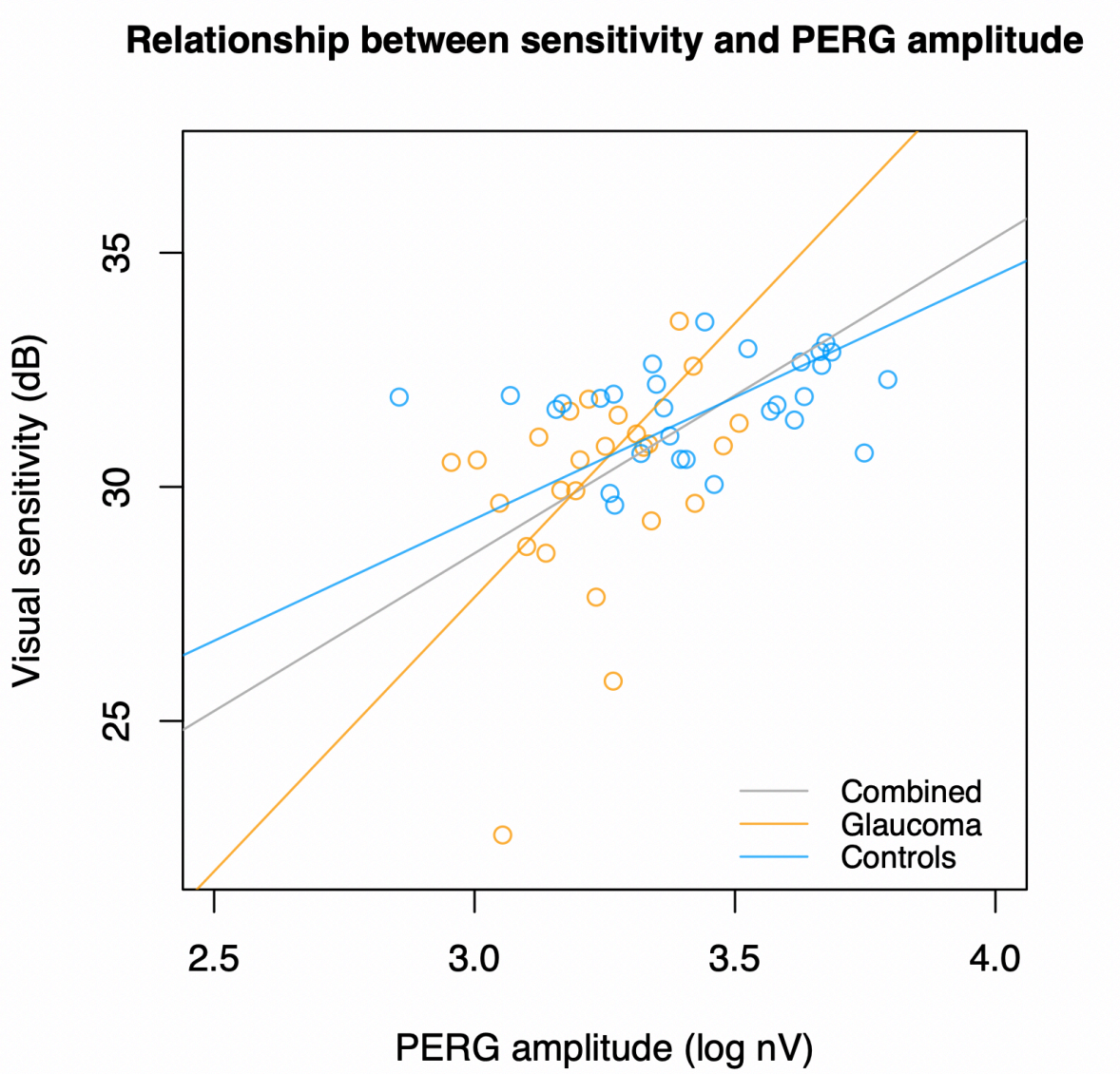

Figure 8.13 – PERG spatial tuning curve amplitude as a function of perimetric visual sensitivity. Amplitude of the PERG spatial tuning curve in given in logged nanovolts (nV), and visual sensitivity is given in decibels (dB). Regression lines are from Passing-Bablok regressions. Data from glaucoma patients are shown in orange, healthy controls are shown in blue and the regression line for the combined dataset in given in grey.

8.4. Discussion

The aim of the current chapter was to use the methodology developed in Chapter 7 to investigate spatial tuning curves in glaucoma patients compared to age-similar healthy controls, as a proxy for RGC receptive field sizes. There were three main hypotheses. Firstly, that the amplitude of spatial tuning curve would decrease in glaucoma, reflecting spatially-sensitive RGC damage and death. The second hypothesis was that the preferred spatial frequency, as estimated by the fitted spatial tuning curve, would be shifted in glaucoma, reflecting a change in average retinal receptive field size of the stimulated area. A direction was not hypothesised, as it could shift to finer spatial frequencies, reflecting the shrinkage of RGC dendritic trees (Morgan, 2002), or coarser spatial frequencies, reflecting compensatory enlargement of receptive fields. The third hypothesis was that these outcome measures would show a relationship with the visual sensitivity of the same region of the visual field, as measured by a clinical perimeter.

Regarding the first aim, evidence was found in favour of the initial hypothesis; specifically, that glaucoma patients would show a reduction in amplitude in their PSR spatial tuning curve compared to healthy controls (see Figure 8.10). Furthermore, this reduction in amplitude significantly predicted variation in visual sensitivity, suggesting that this is a functionally relevant effect. This is consistent with previous work finding reductions in PERG amplitude in glaucoma patients compared to controls (e.g. Almrcegui Lafita *et al.*, 1997; Bach & Hoffmann, 2008; Bobak *et al.*, 1983; Ganekal *et al.*, 2013; Hiss & Fahl, 1991; Tiryaki Demir *et al.*, 2015; Uclés *et al.*, 1997; Viswanathan *et al.*, 2000; Wanger & Persson, 1983), as well as associations with clinically-relevant measures (e.g. Bach *et al.*, 2006; Cvenkel *et al.*, 2017; Garway-Heath *et al.*, 2002; Hood *et al.*, 2005; Papst *et al.*, 1984; Wilsey *et al.*, 2017). Considering this reduction of amplitude, but the relative preservation of the RIR in glaucoma (see section 8.3.3), it is likely that this reflects damage and death of spatially sensitive RGCs and their receptive fields. Additionally, the glaucoma patients showed a smaller range of amplitude values compared to healthy controls, despite a range of glaucoma severities being included (MD IQR= -11.190, -1.720; range= 22.180), suggesting that this decrease occurs early in glaucoma progression and is a common characteristic of the disease. To examine at which stage this effect originates, possible future work should examine this longitudinally and expand to those with ocular hypertension or family history of glaucoma,

both of which are significant risk factors for the condition (Sommer *et al.*, 1991; Wiggs & Pasquale, 2017). Alternatively, there may be a floor effect in our measurement, with the response amplitude supported by other spatially sensitive retinal cells (e.g. bipolar cells). This would explain why neither group have amplitudes that go lower than ~900nV, which is the same across groups (rather than being lower in the glaucoma group).

In terms of the second hypothesis, a statistically significant group difference was found in peak spatial frequency (i.e. the spatial frequency that elicited the highest amplitude response, as estimated via the spatial tuning curve; see Figure 8.9). A lower preferred spatial frequency was found in glaucoma patients (median= 1.636 cpd), compared to healthy controls (median= 1.806 cpd). This therefore suggests a larger size of RGC receptive fields, despite reports of the loss and reduction of RGC dendritic branches before cell death (Tribble *et al.*, 2019), with cell soma size changes in both larger Magnocellular-pathway (M-pathway) and finer Parvocellular (P-pathway) cells (Weber *et al.*, 1998). Our result may reflect a compensatory enlarging of the functional receptive fields of neighbouring 'healthy' RGC or other retinal cells (e.g. bipolar). This may explain why histological studies can find a selective loss of larger RGCs (initially interpreted as a selective loss of M-pathway cells; Glovinsky *et al.*, 1991; Morgan, 2002; Quigley *et al.*, 1989), but this is not always reflected in the psychophysical results, which do not always demonstrate a deficit in response to M-pathway stimuli, despite reductions in the electrophysiological response to the same stimuli (Vaegan & Hollows, 2006). However, it should be noted that peak spatial frequency was not significantly predictive of visual sensitivity. The size of the difference in cpd was also relatively small. It may therefore be that an enlargement of the functional receptive field size is present in just a subset of patients, or in a subset of the retina; for example, enlargement of fMRI-derived estimates of cortical receptive fields have been found specifically along the edge of a visual field deficit (Papanikolaou *et al.*, 2014). It may be that a similar effect is happening with these patients, but this is hard to delineate with such a global measure. Future studies that investigate more specific regions of the visual field will be able to assess relationships between patterns of visual field loss and shifts in peak spatial frequency.

One of the motivations for looking at functional correlates of retinal receptive field sizes in this thesis was to investigate the neural basis of glaucomatous changes in Ricco's

area. One of the suggested explanations for the size of Ricco's area (i.e. complete perceptual spatial summation) is that it reflects the size of the underlying retinal receptive field sizes. The slightly larger estimates of receptive field sizes that were found in this cohort of glaucoma patients compared to healthy controls may reflect increased summation of spatial information at the retina and therefore be contributing to the increase in Ricco's area in glaucoma (Redmond *et al.*, 2010; further investigated in Chapter 11). However, there may be simultaneous changes along the visual neural pathway that are contributing to this psychophysical difference. Indeed, previous work has emphasised the importance of multiple neural pooling mechanisms in determining perimetric sensitivity (e.g. Pan & Swanson, 2006). Furthermore, this possible change in receptive field size may have consequences to neural processing further up the visual neural pathway, in terms of how spatial neural information is pooled; an important next step taken in this thesis is to examine how this estimate of receptive field size in the retina relates to estimates of cortical receptive field size. The following chapters will therefore examine these questions.

The third aim of the current chapter was to investigate the relationship between clinical visual sensitivity and our PERG outcome measures. As mentioned above, visual perimetric sensitivity of the test region was significantly associated with the amplitude of the spatial tuning curve (though the relationship between visual sensitivity and preferred spatial frequency was not significant). A Passing-Bablok regression was used to quantify the slope between visual sensitivity and PERG amplitude (see Figure 8.13) and found that the slope of this relationship was steeper for glaucoma patients than for healthy controls. This suggests that the maximum amplitude of the spatially specific cells is associated with the overall functioning of the visual system, especially in glaucoma. While these results do not necessarily imply causality, they suggest that the functioning of these spatially specific RGCs are functionally relevant and may therefore contribute to overall visual sensitivity. While the CUSUM test suggested a linear relationship between our variables, the pattern of the relationship between visual sensitivity and logged PERG amplitude shows similarities to the curvilinear relationship that has been reported previously by other studies examining the relationship between sensitivity (dB) and logged electrophysiological measures, such as by Garway-Heath et al. (2002). This is also suggested by the increase in slope between healthy controls and glaucoma patients. However, due to most of our patients showing little defect

in the target region, there is not an even distribution of patents across severities. It is therefore difficult to make conclusions about how this relationship differs across all severities with this sample; it is possible that with a greater range of sensitivities, a clearer curvilinear relationship would have been found. Overall, our data highlights a relationship between the peak amplitude of spatially sensitive RGCs and visual sensitivity in the mid-periphery of healthy controls and glaucoma patients.

There are limitations to the above study that should be considered. Firstly, following guidelines on retaining retinal image quality during PERG recordings, dilation was not used (Bach *et al.*, 2013) so pupils sizes were relatively small due to the age of the participant sample (mean= 3.4mm), as well as showing some inter-subject variability (range= 2-5.8mm). The average pupil size in Drasdo *et al.* (1987) was ~5mm (due to the younger ages in their sample; 22-52 years, N= 4). While pupil size can have a sizeable effect on some ERG responses (e.g. Gagné *et al.*, 2010; Gonzalez *et al.*, 2004), there appears to be less of an impact on PERG (e.g. Anders *et al.*, 2019; Bach *et al.*, 2013), and smaller pupil sizes have been used in previous papers (e.g. Shorstein *et al.*, 1999), so it is unlikely that our sample of pupil sizes would impact our PERG recordings. An area in which this varying pupil size may have an impact is the calculation of CAF (used to calculate the RIR at each spatial frequency), which was initially calculated based on the modulation transfer function (MTF) of pupil sizes of 4.9mm (Campbell & Gubisch, 1966; Thompson & Drasdo, 1987). It would be expected that this MTF would differ between pupil sizes (Campbell & Gubisch, 1966), which may lead to some eyes in our data being slightly over- or under-corrected. However, as pupil sizes were similar across groups, any effect of this should affect both groups equally and thus it is unlikely that this would have had an impact on group-level comparisons. This is supported by the fact that similar group differences are found with or without the removal of the luminance component based on CAF and MTF calculations (see section 8.3.3). In addition, pupil size showed no association with either of our PERG outcome measures, as assessed using Pearson's r and logged values (Amplitude: r= -0.100; p= 0.477; preferred frequency: r= -0.214; p= 0.124). It could also be argued that by only using five spatial frequencies, more subtle shifts in the spatial tuning curves may be missed. Curves could also be more accurately delineated with more measurements. The five spatial frequencies used within this study were chosen from the seven initially investigated in methods development

in Chapter 7 as they were judged to sufficiently describe the spatial tuning function (i.e. with spatial frequencies delineating either side of the peak). The use of this slightly lower number of spatial frequencies also allowed for more recording repeats without unreasonably bloating the test time, which helped in limiting participant fatigue. However, it may be beneficial for future studies to refine this result with an increased number of tested frequencies.

In summary, this chapter aimed to investigate electrophysiological spatial tuning curves in glaucoma compared to age-similar controls in order to assess the amplitude and peak spatial frequency of underlying spatially sensitive RGCs. It was found that the amplitude of these curves was significantly reduced in glaucoma compared to controls, which was also associated with visual sensitivity. The peak spatial frequency was also slightly lower in glaucoma compared to controls, suggesting larger retinal receptive field sizes. How these outcomes relate to cortical receptive fields and psychophysical measures of spatial summation will be further investigated in Chapter 11.

Chapter 9. The Haemodynamic Response Function across the occipital lobe and primary visual areas in glaucoma

9.1 Introduction

One of the overall aims of this thesis is to determine how receptive field sizes across the visual pathway contribute to the measured size of Ricco's area in individuals with glaucoma and healthy controls. In order to assess the contribution of cortical receptive field sizes to Ricco's area, functional Magnetic Resonance Imaging (fMRI) and a methodology termed population Receptive Field (pRF) mapping will be utilised. An important step in pRF analysis is the convolution of the predicted time course by a Haemodynamic Response Function (HRF), which accounts for the typical shape of the Blood Oxygenated-Level Dependant (BOLD) signal (an example of a canonical HRF can be seen in Figure 9.1). While the shape of an individual's HRF can be expected to be similar across, for example, a healthy young adult group, there is still inter-individual variation in HRF parameters that can introduce noise into pRF estimates if not accounted for. To account for this variability, an individual's HRF can be measured using fMRI and used for convolution. The influence of the HRF fit shape is demonstrated by considering how variations in the full-width-at-half-maximum (FWHM; see Figure 9.1) of a HRF used in convolution impacts estimated pRF size. While HRF metrics and pRF size vary independently across the cortex (Fracasso *et al.*, 2016), when used in convolution, the FWHM of the HRF fit appears to have a relationship with estimates of pRF size. Specially, larger FWHMs result in smaller pRF estimates in V1-3 in the same dataset, though the relative pRF sizes between visual areas was consistent across FWHM values (see Appendix C of Dumoulin & Wandell, 2008). Given this relationship between the HRF fit parameters and the final pRF estimates, more accurate pRF estimates would be expected if the HRF parameters more closely resemble the individual's underlying HRF. A particular problem is introduced when considering group studies. If one group (e.g. a patient group) shows a difference in HRF when compared to the other (e.g. healthy control) group, this will introduce a systematic bias in pRF estimates if individual HRFs are not used in convolution. Therefore, it is important to examine whether there are differences in HRFs in glaucoma which should be controlled for. It is also useful to investigate possible

differences in HRF for reference in future studies, as convolving signals by an HRF is also a feature in other fMRI analysis pipelines.

The upper panel of Figure 9.1 illustrates a typical HRF. Following a brief visual stimulus (e.g., a high-contrast reversal checkerboard shown for a couple of seconds), the BOLD signal will increase, reflecting the corresponding increase in blood oxygenation to meet the neural energy demand. This peaks at around 4-6 seconds post-stimulus before decreasing, undershooting, and then returning to baseline (Buxton *et al.*, 2004). Some investigators have identified a small dip in activation before the initial positive-going peak (Ernst & Hennig, 1994; Hu *et al.*, 1997; Menon *et al.*, 1995), which may represent a local and rapid increase in oxygen metabolism before the energy demand can be met by an increase in

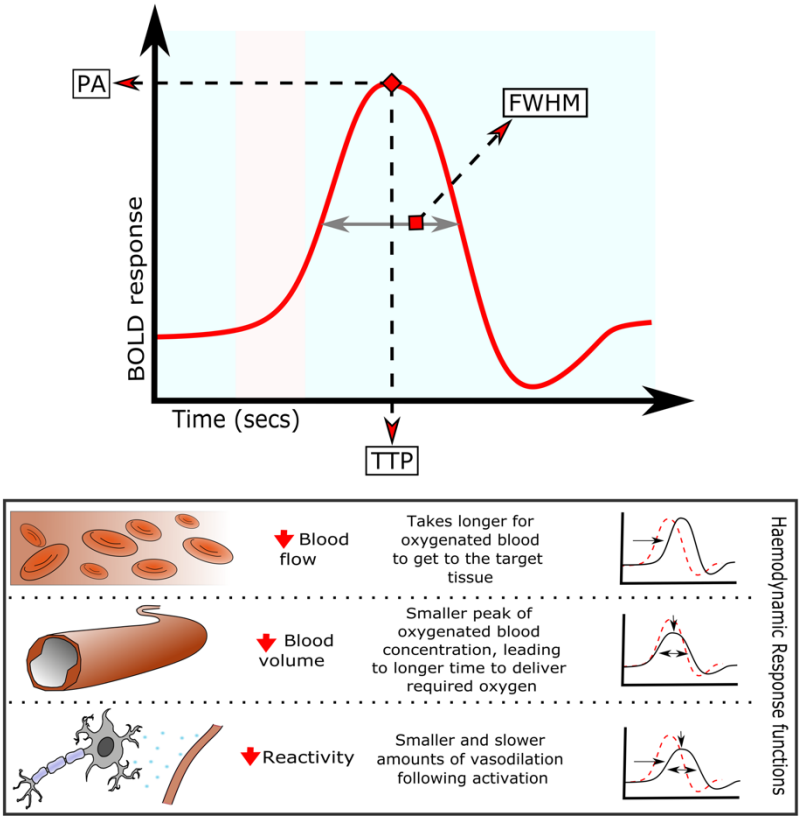

Figure 9.1 – Illustration of a haemodynamic response function (HRF) and how it may be impacted by different vascular changes. The top plot shows a canonical HRF with the main metrics used to describe it within this chapter labelled. PA = Peak Amplitude. TTP = Time-To-Peak. FWHM= Full-Width-Half-Max. Time is shown in seconds. The shaded red area indicates stimulation triggering the HRF, such as a visual stimulus.
The bottom plot illustrates how changes in cerebral blood flow, blood volume and vascular reactivity may theoretically impact the shape of the HRF. For example, slower blood flow means it takes longer for blood to get to target tissue, which then delays the HRF curve.

regional blood flow (Ernst & Hennig, 1994; Malonek & Grinvald, 1996). However, this dip is small and not always present (Buxton, 2001; Menon *et al.*, 1995). Several methods may be used to describe the HRF shape, but three parameters (highlighted in Figure 9.1) will be examined in this study, following similar approaches in previous clinical research (e.g. Bonakdarpour *et al.*, 2007; Mayer *et al.*, 2014). These characteristics are the Peak Amplitude (PA), the Time-To-Peak (TTP), and the FWHM (of the positive peak); when used in convolution, the HRF PA is not defined and only TTP and FWHM would have an impact on the convolved BOLD signal and thus the pRF estimate, but PA is investigated here for completeness. Several factors may influence these parameters (and hence the shape) of the HRF (Buxton *et al.*, 2004). With reference to the schematics in the lower panel of Figure 9.1, these factors include cerebral blood flow (CBF), cerebral blood volume (CBV), and cerebrovascular reactivity (CVR). CBF has an important influence on BOLD signal. CBF refers to the perfusion of blood in the brain and is broadly dependant on cerebral perfusion pressure and cerebrovascular resistance (Powers, 2016). If the level of CBF was, for example, reduced in a participant, it would take longer for the oxygenated blood to reach the target tissue following stimulation. This may be reflected in a delay in the HRF curve, extending the TTP. The HRF response is also dependant on CBV, which determines the amount of blood present in a voxel. For example, if CBV were reduced in a participant, assuming stable neural activity, the peak amplitude would be limited as there would be less blood per voxel. One may also expect the FWHM to be extended, allowing more time for the required oxygenated blood to reach the target tissue. Another important contributor to the BOLD response is CVR, which characterises the ability of the surrounding vessels to respond to, for example, increased energy demand from a neuron. If this changes, it may cause a lag in the HRF TTP compared to healthy controls. It may also cause insufficient increases in cerebral blood flow in response to an energy demand (such as an activated neuron), leading to a shallower but extended response to meet the energy demand. It should be noted that the BOLD response is a complex signal which is impacted by a multitude of factors and this is not an exhaustive discussion of what variables can underlie a shift in HRF. For example, resting GABA concentration (involved in neural inhibition) is associated with smaller and wider HRFs, independent of resting blood flow (Muthukumaraswamy *et al.*, 2012).

Though changes in the HRF shape have not been explicitly tested in glaucoma, a change may be expected based on previous literature. For example, glaucoma patients demonstrating lower PA than healthy controls in response to a brief HRF-mapping stimulus is suggested by the finding of a reduced BOLD signal reported in glaucoma groups in response to various other stimuli (e.g. Duncan *et al.*, 2007; Murphy *et al.*, 2016). Whether this lower BOLD signal compared to controls is due to lower neural activity or changes in the vascular functions supporting BOLD fMRI is unclear from the BOLD response alone, especially as lower levels of neurotransmitter (Murphy *et al.*, 2016) and vascular factors (e.g. CBF and CVR; Duncan *et al.*, 2012; Harris *et al.*, 2013; Sugiyama *et al.*, 2006; Zhang *et al.*, 2015, 2016) have been reported in brains of individuals with glaucoma, compared to those in healthy control. Indeed, these variables are not necessarily independent and can impact upon each other. Additionally, it is possible that the TTP and FWHM may also be altered in the glaucomatous brain. Specifically, they may be delayed and extended respectively in glaucoma, due to findings of decreased CVR following visual stimulation compared to healthy controls (Zhang *et al.*, 2016). Importantly, CVR disruption previously found in glaucoma by Zhang et al. (2016) appeared functionally relevant, as it showed a significant relationship with pattern standard deviation in Standard Automated Perimetry, which is an indicator of a localised loss of visual field sensitivity. However, CVR in the study of Zhang et al was measured using transcranial Doppler sonography across only the posterior cerebral arteries, so cannot be spatially resolved to a particular cortical region. CBF, on the other hand, has been measured using more spatially resolved methodology (i.e. arterial spin labelling MRI). Using this methodology, lower rates of CBF have been found within V1 in glaucoma patients compared to controls (e.g. Duncan *et al.*, 2012). This reduced CBF may be reflected in the HRF as a downward shift of PA and widening of the FWHM. However, it should also be noted that the HRF is a complex response, with many underlying contributing factors that are not completely understood, so precise changes in the HRF in glaucoma may be difficult to predict or interpret.

The aim of the research described in this chapter is to investigate the shape of the HRF across the occipital lobe and primary visual areas in patients with glaucoma, compared with that in healthy controls. The effect of glaucoma on pRF size will be investigated in Chapter 10 and the temporal profile of the BOLD response will be used to infer pRF location

and width. As this is influenced by differences in the temporal characteristics of the HRF, such as FWHM and TTP (e.g. Dumoulin & Wandell, 2008), it is important to investigate whether or not there are any group differences in the HRF shape that need to be accounted for with individual HRF mapping. Specifically, surface-based 2D analysis will be used in the determination of the HRF, as opposed to 3D volume-based analysis, as it is most relevant to the surface-based pRF mapping used in the determination of pRF sizes described in Chapters 6, 7, 10 and 11, but also because it brings advantages in the form of superior localisation and statistical power (Anticevic *et al.*, 2008).

9.1.1 Aims

The research outlined here is an exploratory study into the impact of glaucoma of the HRF, ahead of future investigation into pRF sizes in glaucoma compared to age-similar controls (Chapter 10). There are three aims to the research described in this chapter:

1. To estimate the HRF in the occipital lobe of people with glaucoma and age-similar healthy controls.
2. To investigate generalisability of the results from the first aim to individual primary visual areas (i.e. V1 and V2). It may be that differences are only found, or are primarily driven by, disruption in these areas, as previous studies have reported BOLD disruption in the early visual cortices (e.g. Murphy *et al.*, 2016).
3. To investigate any differences in the HRF response with distance across V1. If there are indeed differences in the HRF in glaucoma compared to healthy controls, these might be more identifiable in regions of the cortex associated with the peripheral visual field, where glaucomatous damage primarily manifests.

9.2. Methods

In this cross-sectional study, HRFs were measured and possible group differences investigated using 7 Tesla (7T) fMRI in the visual cortices of a cohort of glaucoma patients and age-similar controls. This was an exploratory study to investigate whether HRF metrics (i.e. PA, TTP and FWHM) are different in glaucoma patients compared to healthy controls, ahead of investigating group differences in pRF size in a later study (see Chapter 10).

9.2.1 Participants

Ethical approval for this study was obtained from NHS Wales research ethics committee (Cardiff and Vale and Cwm Taf NHS health boards), as well as the Cardiff University Schools of Psychology and Optometry and Vision Sciences. Participants were recruited via NHS glaucoma clinics (at the Royal Glamorgan Hospital and University Hospital of Wales, as well as the School of Psychology community panel and Cardiff University Eye clinic. Participants were offered travel reimbursement.

fMRI imaging was carried out in 28 healthy controls (median age=66.6; IQR=59.6, 70.6; 15 females) and 28 glaucoma patients (median age=67.6; IQR=59.4, 71.7; 13 females; 8 normal-tension, 20 primary-open-angle). HRF mapping was carried out monocularly with either the glaucomatous or a randomly chosen eye (controls OS=15; glaucoma OS=16).

A Mann-Whitney U independent t-test found no significant difference in age (W=382.00; p= 0.71) or intraocular pressure (glaucoma: median[IQR]= 14[12,15]; controls: median[IQR]= 15[13,16]; W= 470.50; p= 0.30). Glaucoma patients showed significantly worse Mean Deviation and Pattern Standard Deviation (PSD) than controls (MD [glaucoma]: median[IQR]= -4.61[-10.10, -2.10]; MD [controls]: median[IQR]= 0.08[-0.77, 0.50]; W= 751.00; p<0.001; PSD [glaucoma]: median[IQR]= 5.57[3.07, 10.12]; PSD [controls]: median[IQR]= 1.47[1.31,1.85]; W= 49.50; p<0.001).

9.2.2 MRI protocol

fMRI images were acquired on a SEIMENS 7T MRI scanner. HRF mapping was undertaken with a 1.2mm^3 resolution EPI (TR= 2s; TE= 25ms; flip angle= 76°; 33 slices; FOV= 984 x 984mm), positioned manually over the occipital lobe. As this had a limited FOV over the area of interest, a whole brain single-shot EPI with same slice orientation was taken to aid with registration to structural images (TR= 5s, TE = 31s, 100 slices, 1.2mm^3 isotropic). To aid in distortion correction, phase and magnitude B0 mapping images were also taken. Finally, a T1-weighted MPRAGE sagittal structural scan was completed at 1mm^3 resolution (TR= 2.2s, TE= 2.82ms, TI= 1050ms).

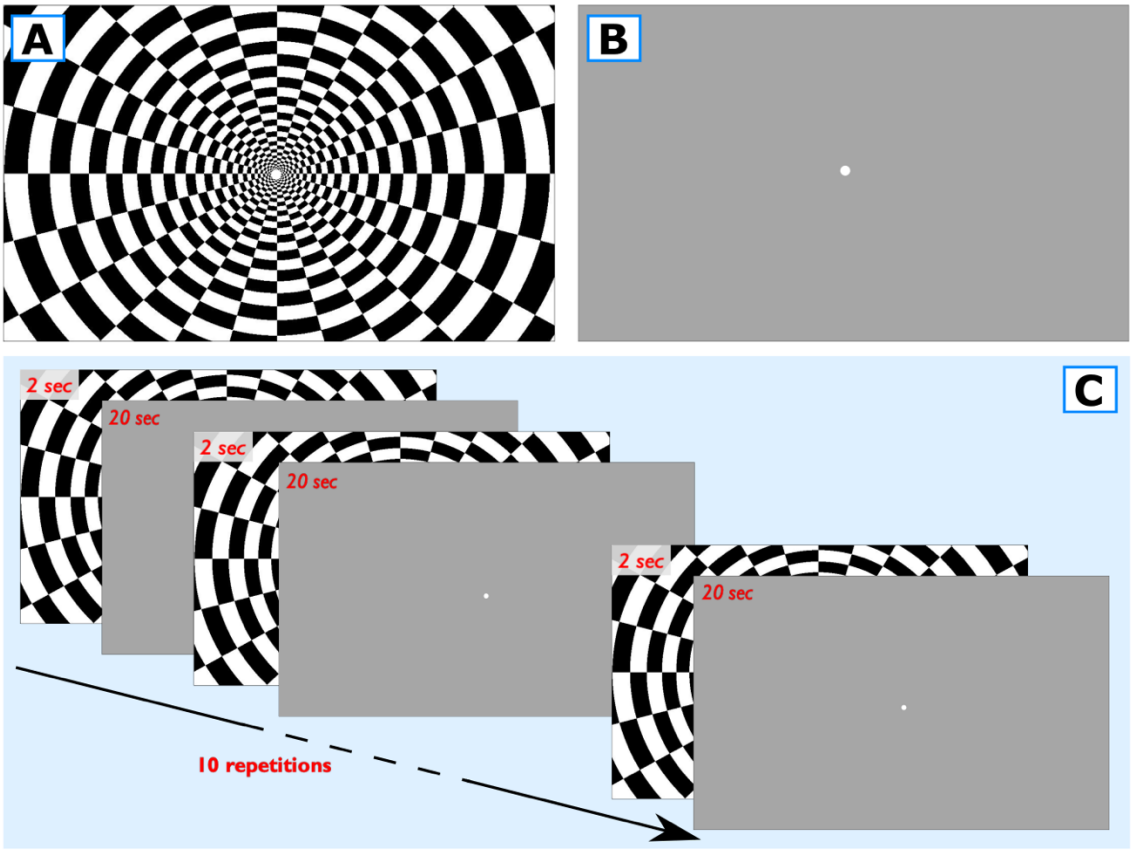

Figure 9.2 – The stimulus used for Haemodynamic Response Function (HRF) mapping in the scanner. A: The radial checkerboard stimulation. B: Mean grey rest stimuli. C: diagram of the procedure of stimulation during the HRF mapping scan. Checkerboard stimulation is displayed for one Repetition Time (TR; 2 seconds), followed by ten TR of rest stimuli (20 seconds). This is repeated ten times.

Foam head padding was paced below and on each side of the head to limit head movements, and blackout lens was used to occlude the untested eye. MR-safe vision correction for the working distance was provided where required. All participants were asked to confirm that they could see the whole screen clearly (i.e. in focus) before scanning.

9.2.3 fMRI stimuli

The HRF was mapped with a 100% contrast black-and-white alternating radial checkerboard (see Figure 9.2). This was presented to participants for 2 seconds (monocular stimulation; screen size: 19.5°x11.0°), followed by a blank grey screen for 20 seconds. This sequence was repeated ten times while the participant was asked to maintain focus on a central fixation. 20 seconds of mean luminance was also included at the start of the sequence to establish a baseline of no stimulation, then removed for further analysis.

In order to maintain fixation, a simple fixation task was used. The fixation dot changed from white to red at random irregular intervals throughout the run, and the participant was required to count in their head the number of times this happened. They were not required to make a response or remember this number.

9.2.4 Pre-processing and structural analysis

The majority of pre-processing took place within FSL and FEAT software packages (Jenkinson *et al.*, 2012). EPI data underwent B0 distortion correction, motion correction (MCFLIRT; Jenkinson, Bannister, Brady, & Smith, 2002), brain extraction (BET; Smith, 2002), and high-pass filtering (100s). Following this, registration of the partial-volume HRF EPIs to structural data, using the whole brain EPI as an intermediate step, took place within the spm fMRI toolbox (http://www.fil.ion.ucl.ac.uk/spm/).

The MPRAGE structural image was first intensity-normalised within FSL, then segmented with FreeSurfer (Dale *et al.*, 1999; Fischl, 2012). This created two 3D meshes of the targeted hemisphere: one between the grey and white matter, and one at the outer pial boundary. The cortex was then split into vertexes (i.e. triangular grey matter voxels). These cortical surfaces could be inflated to aid visualisation of the data.

Freesurfer software was also used to generate the following ROI labels for use in future analysis. These labels were generated using each individual's structural scan, to allow for generation of the HRF in each participant's local space.

1. Occipital lobe – this was drawn manually on the inflated surface, using the anterior end of the calcarine sulcus and the parieto-occiptal junction as anatomical landmarks. (Aim 1)
2. Structural probabilistic masks of V1 and V2. (Aim 2)
3. V1 segments – The Freesurfer-generated probabilistic mask of V1 was split into five even length segments along its long axis. This produced five labels associated with increasing eccentricity. An example of V1 segment labels made in this way is shown in Figure 9.3. (Aim 3)

9.2.5 Haemodynamic response function estimation

HRF model fitting was completed within the SamSrf v.5 toolbox. This analysis was restricted to a specific Freesurfer-generated label, depending on the aim being investigated.

The BOLD signals generated by the ten checkerboard photic bursts were first averaged within each vertex, excluding any outliers (defined as a time series that demonstrated greater than $\pm$1.5 standard deviation from mean). Analysis was also confined to only visually active regions to avoid noise. This was defined as a vertex with a signal (averaged over the first five scans) that had a clear response (>1 standard error from the mean) to the photic stimulation. A double-gamma function was then fitted to the averaged response to estimate the HRF fit, from which the metrics discussed above could be extracted.

There were four free parameters involved in the fitting of the double-gamma function:

1. The peak response latency (i.e. time-to-peak; TTP)
2. The latency of the undershoot
3. The peak amplitude (PA)
4. The ratio of the peak and undershoot amplitudes

This generated a modelled HRF fit. An associated Goodness-of-fit value (defined as the R^2 of this curve fit) was also generated.

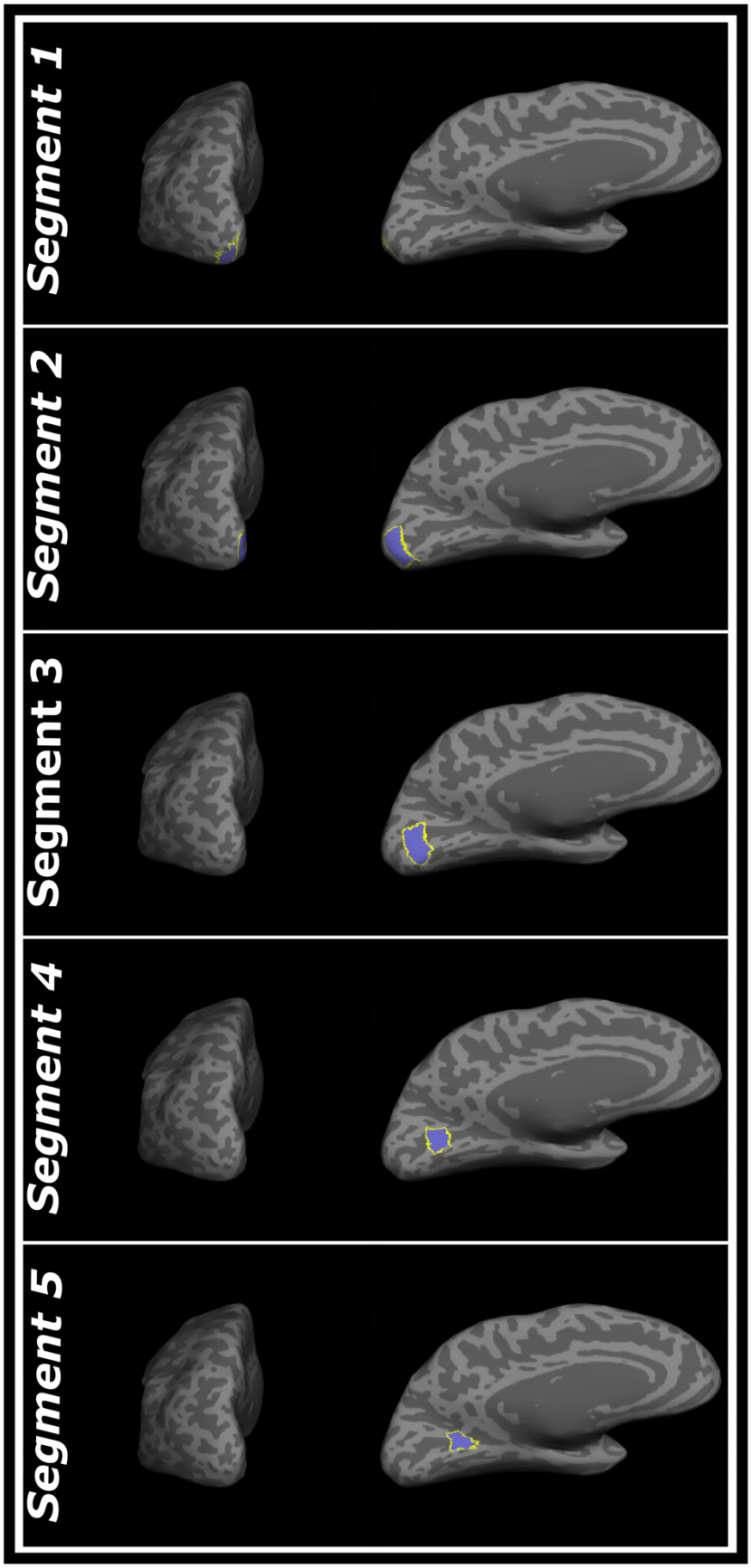

Figure 9.3 – Example of Freesurfer-generated V1 segments for a single participant (displayed on an inflated structural T1 scan). Segment labels are shown in blue and delineated in yellow.

To address all aims, three metrics were extracted from these fits to describe the final HRF shape and allow for quantitative comparisons between groups. These metrics were the Peak Amplitude (PA, defined as the peak z-score value), the Time-To-Peak (TTP, defined as the corresponding time [in seconds] to reach the PA), and the Full-Width-Half-Maximum (FWHM, measured across the initial positive Gaussian peak in seconds). See Figure 9.1 for an illustration.

9.2.6 Analysis

Analysis of this dataset was split into sections to reflect each of the three aims. Both frequentist and Bayesian t-tests and ANOVAs were carried out in Jasp v.011.1 (JASP Team, 2019). Frequentist tests were used to statistically tests the aims. Bayesian tests were added to those measures demonstrating non-significant results in order to provide evidence for the null hypothesis. All linear and mixed linear models were computed in the freely available open-source statistical environment, R (R core team, 2020) with the 'lme4' package (Bates *et al.*, 2015).

9.2.6.1. Haemodynamic response function across the occipital lobe

Before addressing the main analysis, the goodness-of-fit of the HRF curve fit (as defined by the R^2 was first investigated for any group differences between the glaucoma patient cohort and healthy age-matched controls. If, for example, glaucoma patients demonstrated significantly lower HRF goodness-of-fit values compared to age-matched controls, this could be the driving force behind a group difference in a metric HRF, rather than a genuine difference in the HRF. Goodness-of-fit of the HRF curve fits in glaucoma patients and healthy controls was therefore investigated using an independent samples Mann-Whitney U t-test to investigate group differences between glaucoma patients and healthy controls (both frequentist and Bayesian). For non-significant results, evidence for the null hypothesis was supported by a Bayesian Mann-Whitney U t-test (1000 iterations; BF01; non-directional).

Group differences in PA, TTP, and FWHM, extracted from the occipital lobe HRF, could then be investigated. To account for interdependence between PA, TTP, and FWHM, linear models were constructed. With all models, residual plots were first visually inspected to ensure they demonstrated no notable deviations from homoskedasticity or normality

(which is assumed by the model). Three models were created, so a singular HRF metric could be investigated at a time (e.g. PA), while the other metrics were controlled for (e.g. FWHM and TTP). In order to investigate whether there are group-level differences in HRF metrics in the occipital lobes of glaucoma patients and age matched controls therefore, three models in total were created:

- The effects of group (i.e. glaucoma patient or control), TTP and FWHM on PA
- The effects of group, PA and FWHM on TTP
- The effects of group, PA and TTP on FWHM

9.2.6.2. Haemodynamic response function in specific visual areas

The HRF was then investigated in early visual areas (V1 and V2) in order to address the second aim. A repeated-measures ANOVA (between-subject variable= group; within-subject variable= visual area) was used initially to investigate whether there was a difference in goodness-of-fit between groups and visual areas (or the interaction of these variables), that could lead to a bias in the results (i.e. if one group or visual area has a significantly difference level of goodness-of-fit than the other). For non-significant results, evidence for the null hypothesis was supported by a Bayesian repeated-measures ANOVA (BF01; compared against null model).

A linear mixed model analysis was then completed for each metric of interest to investigate group differences. To investigate a particular HRF outcome variable (e.g. PA), the other metrics (e.g. TTP, FWHM), group, and visual area were added as fixed effects, in order to control for interdependence between these variables (i.e. shared variation). Participant intercept was used as a random effect, in order to control for participant variation across visual areas. Three models were therefore tested:

1) To investigate changes in PA, group (i.e. glaucoma patient or control), visual area (i.e. V1 or V2), TTP, FWHM and a group by visual area interaction were added as fixed effects, while participant intercept was added as a random effect. The effect of group, visual area, and a group by visual area interaction on PA was statistically tested.
2) To investigate changes in TTP, group, visual area, PA, FWHM and a group by visual area interaction were added as fixed effects, while participant intercept was added

as a random effect. The effect of group, visual area, and a group by visual area interaction on TTP was statistically tested.

3) To investigate changes in FWHM, group, visual area, PA, TTP and a group by visual area interaction were added as fixed effects, while participant intercept was added as a random effect. The effect of group, visual area, and a group by visual area interaction on FWHM was statistically tested.

Visual inspection of residual plots was carried out to ensure no notable deviations from homoskedasticity or normality, which are assumptions of the model. P-values were obtained by likelihood ratio tests of the full model against the model without the effect in question (e.g. to investigate the effect of group, a model with this as a fixed effect and without this as a fixed effect were compared using an ANOVA). If the interaction term was non-significant, it was removed to keep the model as simple as possible.

9.2.6.3. Haemodynamic response function metrics as a function of V1 cortical distance

Finally, the third aim was addressed by investigating differences in HRFs from glaucoma patients and healthy controls as a function of cortical V1 segments. A Greenhouse-Geisser-corrected repeated-measures ANOVA (between-subject variable= group; within-subject variable= V1 segment) was first used to investigate whether goodness-of-fit varied between groups or across V1 segments.

As above, a linear mixed model analysis was completed for each metric of interest to investigate group differences. The structure of these models (in terms of fixed effects) was similar to those ran for the analysis for visual area (section 9.2.6.2), but with cortical segment as a fixed effect rather than visual area. The models created to address this aim were therefore as follows:

1) To investigate changes in PA, group (i.e. glaucoma patient or control), cortical segment, TTP, FWHM and a group by cortical segment interaction were added as fixed effects, while participant intercept was added as a random effect. The effect of group, cortical segment, and a group by cortical segment interaction on PA was statistically tested.
2) To investigate changes in TTP, group, cortical segment, PA, FWHM and a group by cortical segment interaction were added as fixed effects, while participant intercept

was added as a random effect. The effect of group, cortical segment, and a group by cortical segment interaction on TTP was statistically tested.

3) To investigate changes in FWHM, group, cortical segment, PA, TTP and a group by cortical segment interaction were added as fixed effects, while participant intercept was added as a random effect. The effect of group, cortical segment, and a group by cortical segment interaction on FWHM was statistically tested.

Visual inspection of residual plots ensured no deviations from homoscedasticity or normality. P-values were obtained by likelihood ratio tests of the full model against the model without the effect in question, as in Section 9.2.6.2. If the interaction term was non-significant, it was removed to keep the model as simple as possible.

9.3. Results

9.3.1. Haemodynamic response function across the occipital lobe

Results based on the preliminary analysis of this dataset were presented at the Association for Research in Vision and Ophthalmology (ARVO) 2019 meeting and published in abstract form (Wright *et al.*, 2019).

In order to address aim 1, the HRF across the whole occipital lobe was investigated in glaucoma patients and healthy controls using linear models. From a visual inspection of histograms of R^2 values from the fit of the HRF curve fits (Figure 9.4), the majority of participants had an $R^2 > 0.7$ and all participants had an $R^2 > 0.5$ (Plot A). There was also no apparent group difference that could introduce bias to the results (i.e., if one group had significantly difference R^2 values, this could confound group effects in the main analysis; see Plot B). This was confirmed with a Mann-Whitney U t-test (W=418.000; p=0.855). A lack of difference was also supported by a Bayesian Independent samples Mann-Whitney U t-test, which estimated a Bayes factor of 3.673 (W= 394.00). This suggests a moderate level of evidence in favour of the null hypothesis.

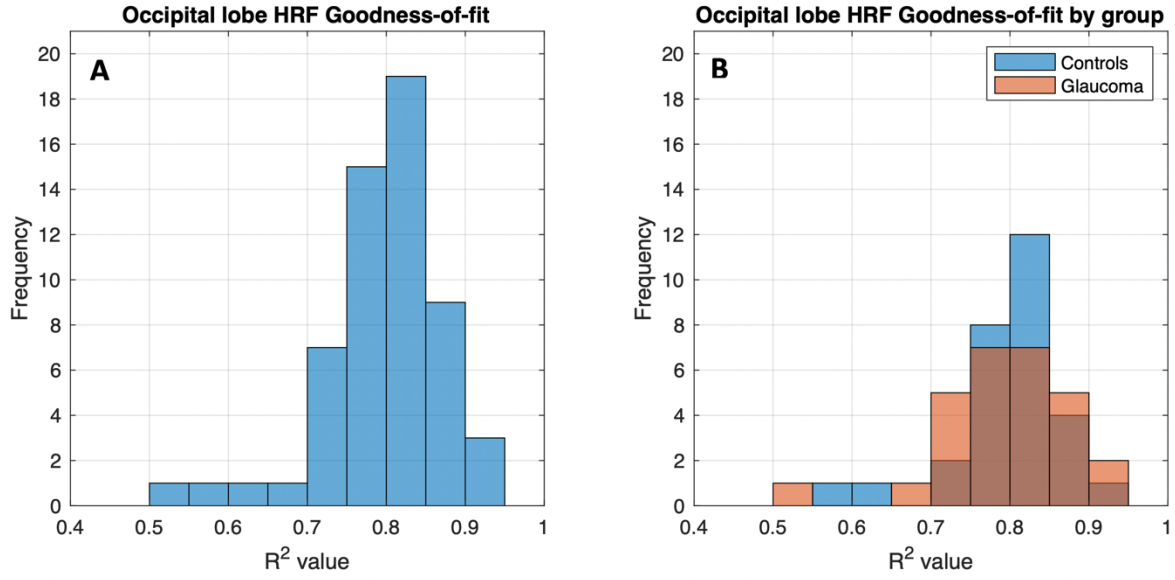

Figure 9.4 – Histograms of the Goodness-of-fit (shown in R^2) of the occipital lobe Haemodynamic Response Functions (HRFs). A: The R^2 values of the full sample. B: R^2 values split by group. Glaucoma data= orange. Healthy control data= blue.

Figure 9.5 illustrates the average HRF response and associated double-gamma fit per group, with a shaded area showing the associated 95% confidence interval. PA, TTP, and FWHM were extracted from individual curves for each participant, which are plotted in Figure 9.6. Data for the healthy controls (PA: median [IQR] = 0.552 [0.472, 0.592] z-score; TTP: median [IQR] = 5.700 [4.900,6.200] secs; FWHM: median [IQR] = 7.000 [6.400, 7.500] secs) were similar to what has been reported in previously published literature (e.g. Kim *et al.*, 2019; Mayer *et al.*, 2014).

Linear models were used to investigate the effect of group on occipital lobe HRF metrics (i.e., PA, TTP, or FWHM). With all models, residual plots were visually inspected and showed no notable deviations from homoscedasticity or normality.

For PA, a linear model of PA as a function of group (i.e. glaucoma patient or healthy control), FWHM and TTP was created. Overall, this model (i.e. the effect of group, TTP, and FWHM on PA) was significant ($F(52,3)= 9.034$; $p<0.001$), with the overall model accounting for 30.5% of the variance in PA ($R^2_{adj}= 0.305$). Looking at the parameters individually, the effect of both group (t= -1.721; p=0.091) and FWHM (t= -1.738; p=0.088) on PA showed a trend but did not reach $p<0.05$ statistical significance. TTP however, contributed significantly to the model (t = 4.269; $p<0.001$; estimate [±SE] = 0.061 [±0.0.14]).

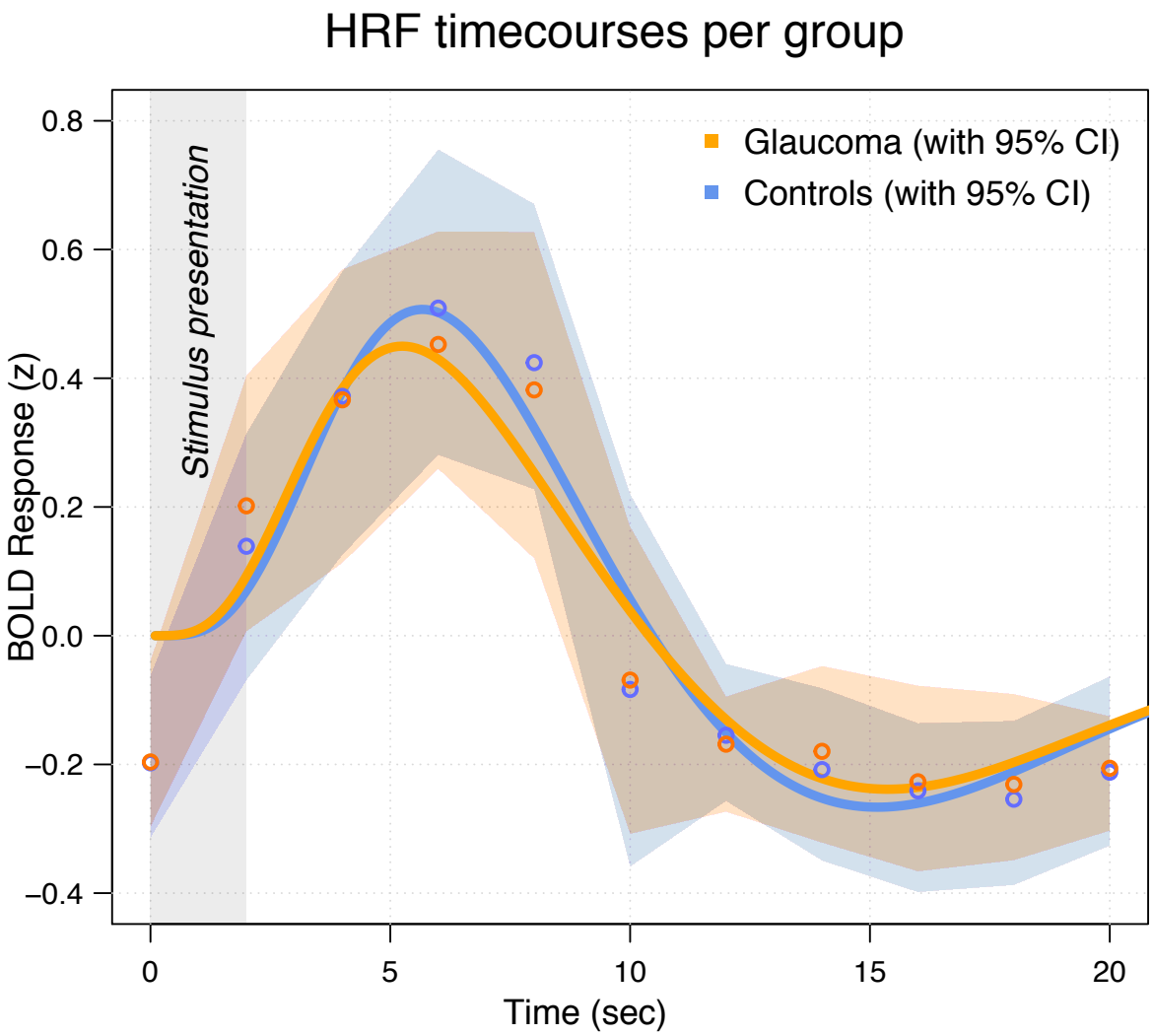

Figure 9.5 – Plot showing the mean Haemodynamic Response Functions (HRFs) fits for each group (averaged raw data shown as circles). The BOLD response is given as a z-score (which is calculated as follows: $z = \frac{x-\mu}{\sigma}$) , while time is in seconds. The coloured shaded segments indicate the 95% confidence intervals (CI) for the associated group. Stimulus presentation is shown with the labelled grey shaded section. Glaucoma data = orange. Control data = blue.

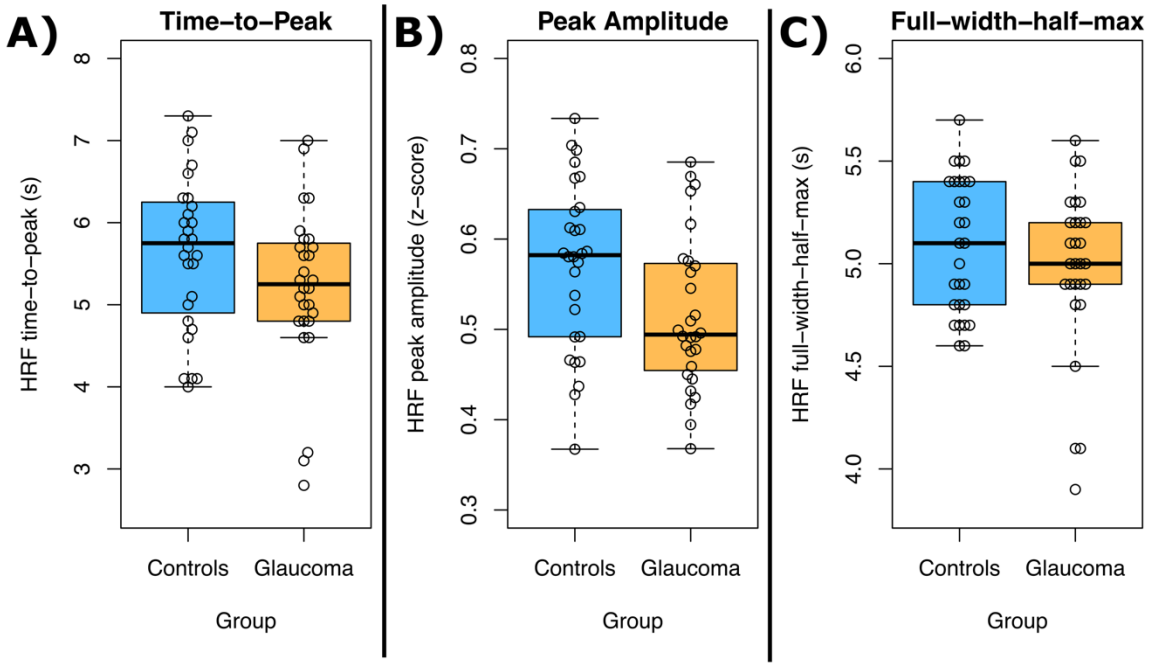

Figure 9.6 – Boxplots of the extracted metrics from the occipital lobe Haemodynamic Response Functions (HRFs). Time-to-peak and Full-Width-Half-Max values are given in seconds, and peak amplitude is shown in z-score. Glaucoma data = orange. Control data = blue. Unfilled circles = individual data points.

For TTP, a similar linear model was created with group, PA, and FWHM as fixed effects. This model was also significant overall ($F(52,3) = 25.01$; $p<0.001$), accounting for 56.7% of the variance in TTP ($R^2_{adj}= 0.567$). Both FWHM ($t = 6.358$; $p<0.001$; estimate [±SE]= 1.517 [±0.239]) and PA (t-value= 4.269; $p<0.001$; estimate[±SE]= 4.226[±0.990]) significantly contributed to TTP. The effect of group on TTP however, was non-significant (t-value= -0.087; p= 0.931).

Finally, a third linear model was constructed for FWHM as a function of group, PA, and TTP. This model was significant ($F(52,3)= 15.05$; $p<0.001$), explaining 43.4% of the variance in FWHM ($R^2_{adj}= 0.434$). Looking at the individual coefficients, neither group (t= -0.501; p= 0.619), nor PA (t= -1.738; p= 0.088) were statistically significant. However, TTP did contribute to the model by a statistically significant amount (t= 6.358; $p<0.001$; estimate [±SE]= -0.288 [±0.045]).

9.3.2. Haemodynamic response function in specific visual areas

To explore whether there are any differences in HRF between glaucoma patients and age-similar controls in specific visual areas (i.e. V1 and V2), HRF analysis was restricted to the structural probabilistic labels of V1 and V2 (separately) and the same metrics as above (i.e., PA, TTP, and FWHM of the HRF) extracted. The goodness-of-fit was compared between groups and a repeated-measures ANOVA reported no statistically significant difference in R2 between groups ($F(1,55) = 0.002$; $p = 0.964$), visual areas ($F(1,55) = 1.426$; $p = 0.238$) The interaction term between group and visual area also showed no significant effect on R^2 ($F(1,55) = 2.474$; $p = 0.121$). This suggests that there is no groupwise difference in R^2 that would confound the main analysis below. This was supported by a Bayesian repeated-measures ANOVA (BF01; compared against null model), which found a Bayes factor of 4.727 for the combined main effects (individual main effects: group = 1.810; visual area = 2.677) and a factor of 6.690 for a model with both main effects and interaction.

9.3.2.1. Peak amplitude

To investigate changes in peak amplitude (PA; see Figure 9.7), group (i.e. glaucoma patient or control), visual area (i.e. V1 or V2), TTP, and FWHM were added as fixed effects, and an interaction term between group and visual area was also included. Participant intercept was used as a random effect. Visual inspection of residual plots suggested no notable deviations from homoskedasticity or normality. The effect of group, visual area, and group*visual area interaction on PA was investigated.

Group/visual area did not have a significant effect on PA ($\chi^2(1) = 0.345$; $p = 0.557$), so was therefore removed from the model to allow for inspection of the main effects. Visual area was found to have a significant effect on PA ($\chi^2(1) = 29.986$; $p<0.001$), increasing it by about 0.037 ±0.005 (SE) between V1 and V2. While PA values appear lower in glaucoma based on a visual inspection of the associated plot (see Figure 9.7), this effect was not statistically significant ($\chi^2(1) = 3.802$; $p = 0.051$).

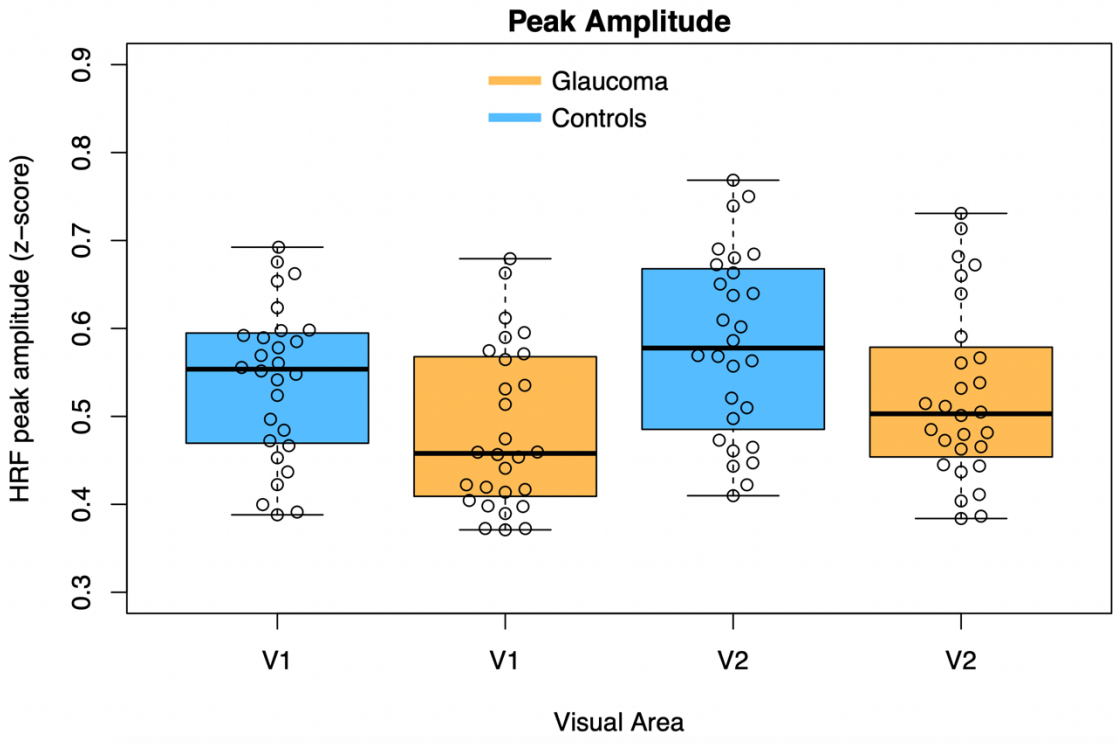

Figure 9.7 – Peak amplitude from the visual area (i.e. V1 and V2) Haemodynamic Response Functions (HRFs). Peak amplitude is shown in z-score. Glaucoma= orange. Control= blue. Unfilled circles = individual data points.

9.3.2.2. Time to peak

Time-To-Peak (TTP) was investigated similarly (see Figure 9.8). Group, visual area, PA, and FWHM were added as fixed effects, as well as an interaction term between group and visual area. Participant intercept was used as a random effect. Visual inspection of residual plots suggested no notable deviations from homoscedasticity or normality. No significant effects were found for the interaction term ($\chi^2(1)= 1.4315$; p= 0.232), or, once the interaction term had been removed from the model, either main effect (group: $\chi^2(1)= 0.527$; p= 0.468; visual area: $\chi^2(1)= 0.339$; p= 0.561).

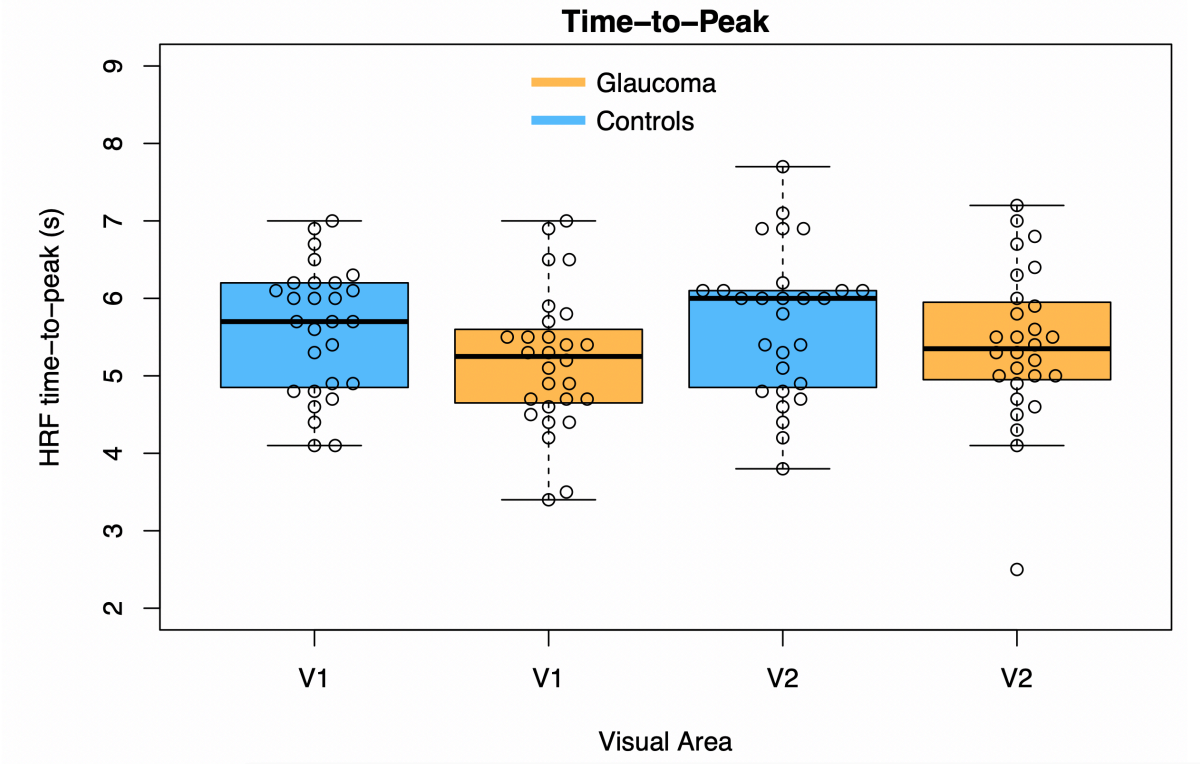

Figure 9.8 – Time-to-peak from the visual area (i.e. V1 and V2) Haemodynamic Response Functions (HRFs). Time-to-peak is shown in seconds. Glaucoma= orange. Controls = blue. Unfilled circles = individual data points.

9.3.2.3. Full-width half-max

Finally, Full-Width Half-Max (FWHM) of the HRFs were investigated using the same methodology (see Figure 9.9). Group, visual area, TTP, and FWHM were added as fixed effects. An interaction term between the main effects, group and visual area, was also initially added. Participant intercept was used as a random effect. Visual inspection of residual plots suggested no notable deviations from homoskedasticity or normality. No significant effects were found for the interaction term between visual area and group on FWHM ($\chi^2(1)= 0.600$; p= 0.4385), or, once the interaction term had been removed, either main effect (group: $\chi^2(1) = 0.043$; p = 0.836; visual area: $\chi^2(1) = 1.767$; p = 0.184). As with the analysis considering the whole occipital lobe, FWHM and TTP appear relatively unchanged in glaucoma across visual areas.

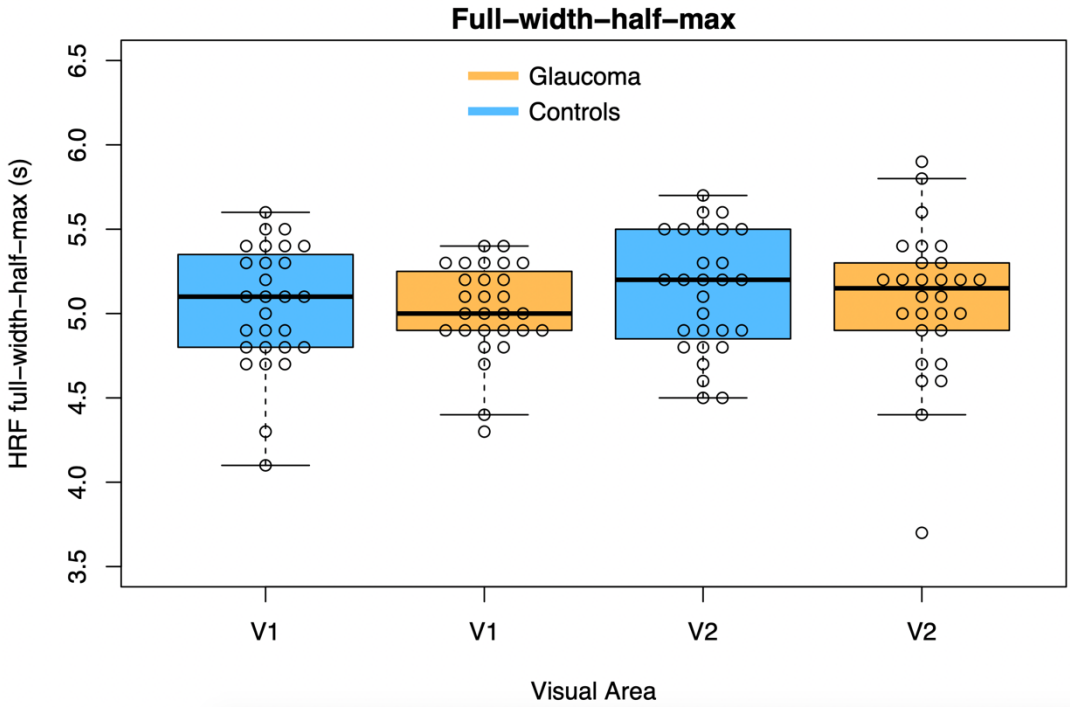

Figure 9.9 – Full-width-half-max from the visual area (i.e. V1 and V2) Haemodynamic Response Functions (HRFs). Full-width-half-max is shown in seconds. Glaucoma= orange. Control= blue. Unfilled circles = individual data points.

Table 9.1 – Table of post hoc comparisons for Haemodynamic Response Function (HRF) Goodness-of-fit as it varies across V1 segments. Seg1 represents the segment at the occipital pole (and therefore reflects foveal vision), with increasing numbered segments (Seg2, Seg3 etc.) representing more anterior sections of the calcarine (and thus more peripheral regions of the visual field).

Post Hoc Comparisons – V1 segments

		Mean Difference	SE	t	p_{holm}
Seg1	Seg2	-0.052	0.022	-2.341	0.075
	Seg3	-0.055	0.018	-3.035	0.018
	Seg4	0.094	0.028	3.366	0.009
	Seg5	0.153	0.034	4.549	< .001
Seg2	Seg3	-0.003	0.013	-0.238	0.813
	Seg4	0.146	0.024	6.060	< .001
	Seg5	0.204	0.031	6.656	< .001
Seg3	Seg4	0.149	0.025	6.018	< .001
	Seg5	0.207	0.027	7.640	< .001
Seg4	Seg5	0.058	0.030	1.913	0.127

9.3.3. Haemodynamic response function metrics as a function of V1 cortical distance

The V1 HRF was then examined in more detail by investigating how it varied with cortical distance in V1 between glaucoma patients and healthy controls. A HRF was generated within each V1 segment label. The goodness-of-fit (R^2) of the HRF within each segment was investigated using a Greenhouse-Geisser-corrected repeated-measures ANOVA, in order to establish whether R^2 was significantly affected by either group or cortical segment. There was no statistically significant effect of group ($F(1,35) = 0.186$; $p = 0.669$) or group-segment interaction ($F(2.830,99.036) = 0.786$; $p = 0.498$) on R^2. The effect of segment on R^2 however, was significant ($F(2.830,99.036) = 25.602$; $p<0.001$). This was investigated further with post-hoc testing, the results of which can be seen in Table 9.1. Of note, there was a small but significant increase in R^2 between segment 1 and segment 3 ($t = -3.035$; $p = 0.018$). Both segment 4 and 5 demonstrated a significantly lower R^2 compared to the other segments (all $P<0.01$), though segments 4 and 5 did not significantly differ from each other ($t= 1.913$; $p=0.127$). This makes sense when considering the size of stimulation screen available (screen size: 19.5°x11.0°) and the fact that segments 4 and 5 relate to the peripheral visual field. Though this will differ depending on the cortical magnification factor of each participant, previous estimates (Horton, 1991) would suggest that while segments 1-3 will be fully stimulated by a stimulation screen of this size, the edge of the screen will fall

within segment 4 (which covers roughly 10 to 25° of the visual field). HRF responses in segments 4 and 5 therefore, may be mostly driven by stray light and stimulation from the inside of the MRI core (which would be uniform luminance and low contrast). Because of this difference in stimulation across the segments, only segments 1-3 were included for further analysis.

In order to investigate group differences, a linear mixed effects model analysis of the relationship between group and our HRF parameters across V1 segments (for an example of V1 segments, see Figure 9.3) was undertaken.

9.3.3.1. Peak amplitude

PA values across V1 segment for each group are presented in Figure 9.10. From a visual inspection, PA in V1 segments, similar to the PA results above, appears to be lower in glaucoma compared t0 heathy controls. Residual plots were visually inspected to ensure no assumption violations. An interaction term between group and V1 segment was initially included, which was found to have a non-significant ($\chi^2(1) = 0.019$; p = 0.892) effect on PA. The main effects were then examined, which suggested that neither group ($\chi^2(1) = 2.000$; p = 0.157) nor V1 segment ($\chi^2(1) = 2.670$; p = 0.102) explained a significant amount of PA variance (i.e. there was no significant difference in PA between V1 segments or group).

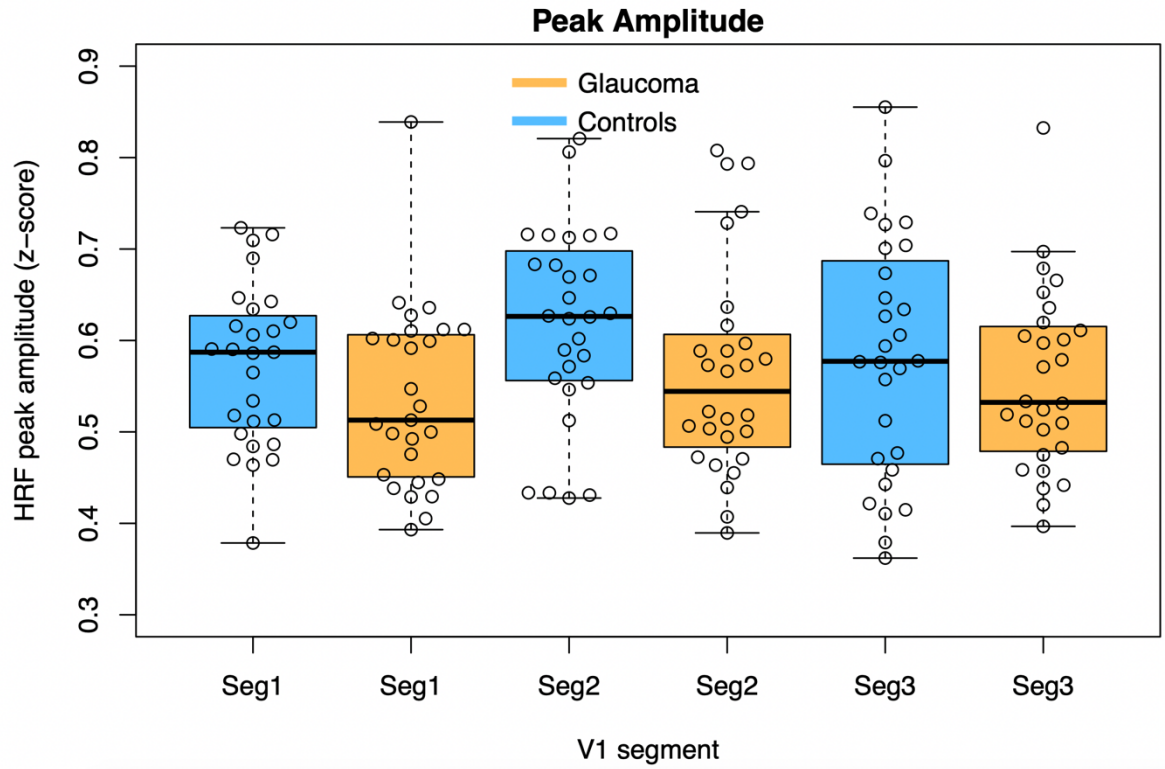

Figure 9.10 – Peak amplitude across V1 segments. Seg= segment; Glaucoma = orange. Controls = blue. Unfilled circles = individual data points. Seg1 represents the segment at the occipital pole (and therefore reflects foveal vision), with increasing numbered segments representing more anterior sections of the calcarine (and thus more peripheral regions of the visual field).

9.3.3.2. Time to peak

It was then investigated whether TTP of HRFs differs by group (i.e. glaucoma patients or healthy controls) or V1 segment. TTP values across V1 segments for each group can be seen in Figure 9.11. As before, a visual inspection of the residual plots ensured no obvious deviations from homoscedasticity or normality. This analysis suggested that neither the interaction effect ($\chi^2(1) = 2.000$; p = 0.157) nor the group main effect ($\chi^2(1) = 0.040$; p = 0.841) were significant. However, V1 segment did significantly explain some of the variance in TTP ($\chi^2(1) = 5.385$; p = 0.020), with TTP shortening by ~ -0.164 seconds ± 0.070 (SE) across V1 segments.

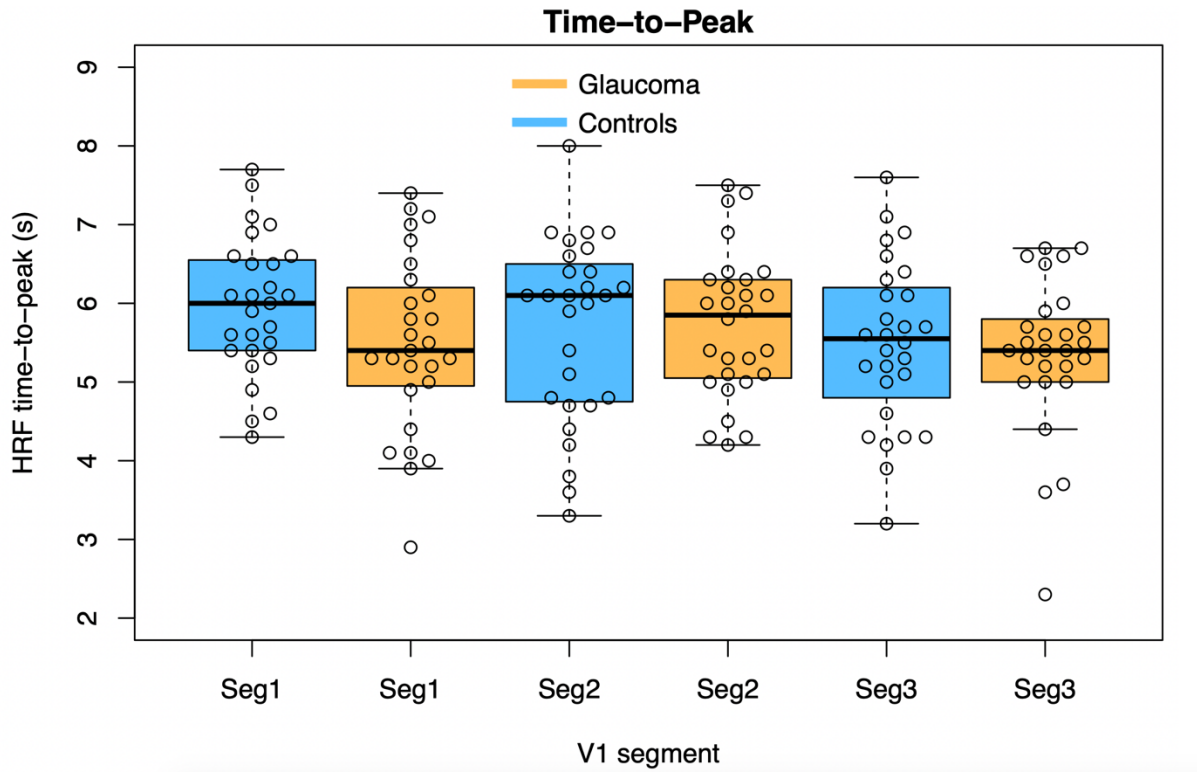

Figure 9.11 – Time-to-peak across V1 segments (seg= segment). Glaucoma = orange. Control = blue. Unfilled circles = individual data points. Seg1 represents the segment at the occipital pole (and therefore reflects foveal vision), with increasing numbered segments representing more anterior sections of the calcarine (and thus more peripheral regions of the visual field).

9.3.3.3. Full-width half-max

Finally, FWHM of HRFs across V1 segments was investigated for differences between group (i.e. glaucoma patients or controls) or V1 segment. No obvious effects were apparent from a visual inspection of the associated plot (see Figure 9.12). This was then investigated statistically using the linear mixed model approach described in section 9.2.6.3. The linear mixed model found no significant contribution of an interaction term between group and V1 segment ($\chi^2(1)= 0.168$; p = 0.682), group ($\chi^2(1) = 0.4217$; p = 0.516), or V1 segments ($\chi^2(1) = 0.2302$; p = 0.6314) on the FWHM of the HRF.

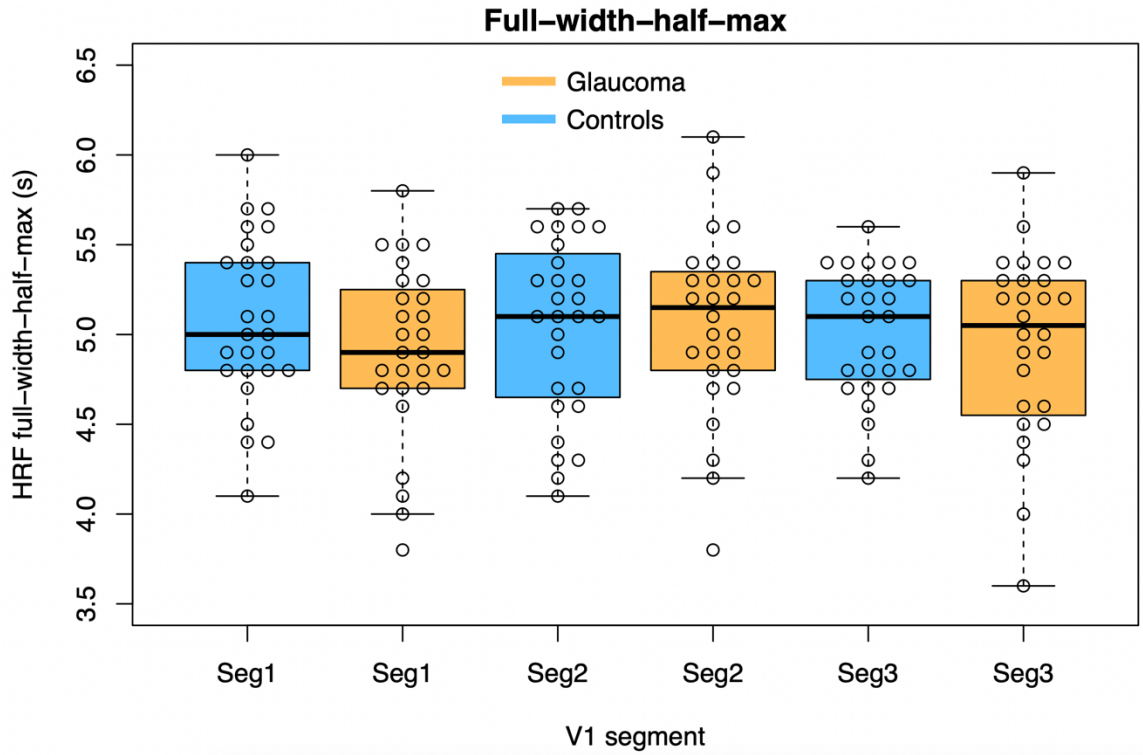

Figure 9.12 – Full-width-half-max across V1 segments (seg= segment). Glaucoma = orange. Controls = blue. Unfilled circles = individual data points. Seg1 represents the segment at the occipital pole (and therefore reflects foveal vision), with increasing numbered segments representing more anterior sections of the calcarine (and thus more peripheral regions of the visual field).

9.4. Discussion

This chapter aimed to investigate the impact of glaucoma on HRF characteristics at various scales across the cortical surface. As pRF mapping involves HRF signal convolution of the BOLD time course, it is important to firstly investigate whether the HRF differs between groups; if there is a systematic shift in HRF, this should be considered in the interpretation of any differences in pRF size that may be found between groups. FWHM is particularly impactful for pRF size estimates, as demonstrated by Dumoulin and Wandell (2008).

The first aim of this chapter aimed to investigate whether there was any shift in the occipital lobe surface-based HRF between glaucoma patients and age-similar controls, which could then be used for individual HRF convolution in Chapter 10. It was found that TTP, PA, and FWHM were similar across groups. While lower PA in the glaucoma group compared to age-similar controls was implied by visual inspection of the plot (Figure 9.6), PA only demonstrated a trend ($p=0.091$) towards being lower in glaucoma patients, and this did not reach statistical significance. The initial hypothesis follows predictions from previous literature, which found a decrease in BOLD amplitude in response to various other visual stimuli in glaucoma patients compared to healthy controls (e.g. Duncan *et al.*, 2007; Murphy *et al.*, 2016; Song *et al.*, 2014, 2014; Zhou *et al.*, 2017). The fact that this study did not reach statistical significance at the $p<0.05$ level may be due to the fact that the glaucoma patients included in this sample were at a relatively mild stage of the disease. It may be that a more pronounced effect would be seen if patients with more extensive retinal and/or visual field damage were included, especially as previous work has reported larger differences at more severe stages of disease progression compared to controls (Murphy *et al.*, 2016). Alternatively, it may be that the brief HRF mapping stimulus used in this experiment doesn't produce a strong enough BOLD signal (i.e. with sufficient SNR) for the differences between glaucoma patients and controls that have been previously reported (e.g. Murphy *et al.*, 2016; Zhou *et al.*, 2017).

In terms of pRF modelling, the FWHM and TTP characteristics of the HRF would be expected to influence the final pRF size estimates. Though no group differences were found in the FWHM and TTP occipital lobe models, there was notable inter-individual variation in HRF TTP and FWHM (as can be seen in Figure 9.6). This highlights the importance of mapping individual HRFs for convolution, as substantial noise would otherwise be introduced.

The interaction between HRF parameters in the occipital lobe is also highlighted; for example, FWHM explained a significant amount of variance of TTP, with later TTP also demonstrating larger FWHM. This positive relationship between FWHM and TTP has also been demonstrated by previous work (Taylor *et al.*, 2018), potentially reflecting variation in cerebrovascular reactivity (CVR). As illustrated in Figure 9.1, lowered CVR would lead to smaller or slower amounts of vasodilation following neural activity (and associated metabolic demand), which would in turn lead to later TTP and wider FWHM. In addition, a decrease in CVR is hypothesised to lead to decreased PA (Figure 9.1), which would explain the link between PA and TTP in our occipital-lobe findings. The link between these HRF metrics may therefore reflect underlying variation in the cerebrovascular system that supports the BOLD response, notably CVR.

The second and third aims of the research described here investigated whether the HRF in individuals with glaucoma is different to that in controls in the primary visual areas or across the cortical length of V1 respectively. In both cases, lower PA in the glaucoma group compared to controls was implied by visual inspection of the plot. Similar to the wider occipital lobe, it was not statistically significant at the $p<0.05$ level (visual areas: $p=0.051$; V1 segments: $p= 0.157$). As mentioned, it is possible that the differences in vascular and neural factors in glaucoma reported previously (e.g. Duncan *et al.*, 2012; Murphy *et al.*, 2016; Zhang *et al.*, 2015) are not evident when using such a brief stimulus. Additionally, the fact that this analysis is surface-based means that the contribution of non-cortical blood vessels will be minimalised, which may have had a larger influence in previous BOLD fMRI studies. This is particularly true when using 7T MRI, which is less biased towards large non-cortical vessels than lower magnet strengths (Uludağ & Blinder, 2018). It is possible that larger differences between glaucoma patients and controls are found when considering BOLD signals with a larger contribution from these larger draining veins. Therefore, while these results suggest minimal difference between surface-based HRFs in individuals with glaucoma and healthy controls, the same may not be true in volume-based analysis or at lower field strengths. This would be important to assess therefore, before investigating the brain in glaucoma patients compared to healthy controls using these alternative methodologies.

The finding of similar HRF metrics across V1 and V2 reported by this study follows previous findings, which suggests that HRF metrics are similar for these early visual areas, and then begin to diverge for extra-striate visual areas, reflecting underlying variation in metabolism and vasculature (Puckett *et al.*, 2014). The current study also found that TTP shortened with increasing cortical distance along V1, suggesting that the most rapid HRF peaks occurred in more peripheral cortical representations. Similar findings of decreasing latency with increasing eccentricity has been reported previously in V1 (Lin *et al.*, 2018). This possibly reflects reducing metabolic demand in more peripheral regions of the visual field cortical representation. Reduced metabolic demand would lead to a lowered rate of oxygen removal from the vessels and thus it would be faster to reach a peak in BOLD signal (which depends on the ratio of oxygenated to deoxygenated blood). It has been found that cerebral metabolism in V1 shows greater increases with directed attention than the BOLD signal (Moradi *et al.*, 2012). As attention was diverted towards central vision in this study (by asking the participant to fixate on the fixation spot and count whenever it randomly changed colour), this may have led to an increase in metabolism in central V1 segments compared to more peripheral V1 segments, which is not necessarily present in the BOLD signal PA. Alternatively, many metabolic, neuronal, and vascular factors underlie the HRF, which may vary across the cortical surface and lead to this effect. For example, as illustrated in Figure 9.1, shortened TTP can occur due to increased cerebral blood flow or increased cerebrovascular reactivity.

One of the limitations of this investigation was the available stimulus screen size, which was limited by the 7T MRI environment. The whole of the visual field, and thus the cortex, was therefore not equally stimulated. This was particularly a problem when investigating V1 segments, as only the central three out of five segments were similarly stimulated by the mapping checkerboard and could therefore be fairly compared. Though the exact location along the cortex will differ depending on the cortical magnification factor of each participant, previous estimates (Horton, 1991) would suggest that the edge of the screen will fall within segment 4 (which covers roughly 10 to 25° of the visual field). HRF responses in segments 4 and 5 therefore, may be mostly driven by stray light and stimulation from the inside of the MRI core (which would be uniform luminance and low contrast), while segments 1-3 will be fully stimulated by the checkerboard stimuli. This is

evident in the drop-off in goodness-of-fit when moving from the foveal three segments to the more peripheral two segments. To fully investigate how HRF differs across the entire length of V1, either stimulation with a much larger field-of-view or stimulation that targets particular areas of the visual field should be used in future.

A factor that should be taken into consideration when generalising these results to other work is the use of monocular stimulation. On one hand, this allows better inferences to be made between the health of an eye and the associated cortical response, and thus provide an appropriate baseline for future work investigating the effects of monocular eye disease. However, there is also the possibility that these results may not hold when compared to the same experiment completed with binocular vision. For example, visual attention may be differently employed when attending through only one eye, which can impact neural responses (Luck *et al.*, 1997).

In conclusion, the research in this chapter has investigated the impact of glaucoma on surface-based HRF estimates across the occipital lobe and visual cortices. Lower HRF PA in glaucoma patients compared to healthy controls was suggested by visual plots but this did not meet $P<0.05$ statistical significance. Regarding future chapters within this thesis, the inter-participant variability in this study has highlighted the importance of controlling for HRF differences, which will be done for future pRF convolution modelling.

Chapter 10. An exploration of receptive field properties in the glaucomatous visual cortex

10.1. Introduction

Classic literature on normal spatial summation has suggested that the physiological basis for Ricco's area lies in the receptive fields of retinal ganglion cells (Glezer, 1965). However, the finding of an enlarged Ricco's area in glaucoma challenges this notion for the following reasons: a) evidence from histological studies points to shrinkage of retinal ganglion cells in early glaucoma and a shrinkage of the dendritic tree should lead to a shrinkage (rather than enlargement) of receptive fields (Morgan, 2000, 2002; Weber *et al.*, 1998); b) differences in Ricco's area between eyes in amblyopia (a condition with no retinal involvement; Je *et al.*, 2018), and in comparison of normally-sighted individuals suggests a cortical basis; c) Ricco's area is enlarged in the S-cone pathway in glaucoma (Redmond *et al.*, 2010) and is smaller with increased blue background luminance in healthy individuals in the S-cone pathway (Redmond *et al.*, 2013) – given that centre-surround antagonism is required for these effects and that they are first encountered in the visual cortex (e.g. double-opponent cells of S+/S- form; Conway, 2001; Conway & Livingstone, 2006), this points to a cortical basis; d) Pan & Swanson (2006) found that perimetric spatial summation could be accounted for by cortical pooling by multiple spatial mechanisms. Thus, taken together, recent evidence suggests that Ricco's area is likely not confined to the retina, but may actually have a sizeable cortical component, that it is shaped by the combination and interaction of receptive fields at multiple hierarchies in the visual pathway, and that it is affected by damage and adaptation at different stages of the visual pathway. The primary aim of the research described in this thesis is to investigate the contribution of receptive field size, at multiple neural hierarchies, to Ricco's area in glaucoma patients and age-similar controls. A critical first step, however, is to independently investigate and characterise the size of receptive fields in glaucoma patients compared to those in healthy controls.

In Chapter 8, the peak of spatial tuning functions (estimated with the pattern onset-offset electroretinography response to multiple spatial frequencies) was used to determine a surrogate estimate of (global) receptive field size at the retinal level. These estimates were

then compared between glaucoma patients and healthy controls. It was found that the spatial tuning function was shifted to lower spatial frequencies in glaucoma patients compared to controls, suggesting statistically significantly larger retinal receptive field sizes in glaucoma patients, though this was not associated with perimetric visual sensitivity (i.e. visual sensitivity measured across the visual field using a clinical perimeter and set stimulus size). The association with Ricco's area will be investigated in Chapter 11.

In this chapter, cortical receptive field size is measured and compared between glaucoma patients and healthy controls with fMRI. Cortical function has previously been measured in glaucoma with fMRI by measuring responses to stimuli or resting state. For example, Murphy *et al.* (2016) presented flickering checkerboards to the upper or lower hemifield of glaucoma patients (13 early stage and 13 advanced) and nine age-similar controls during an fMRI scan. The researchers found that the Blood Oxygen Level Dependent (BOLD) responses to both hemifield stimulations were lower in patients compared to controls, with the greatest difference in more advanced glaucoma. The BOLD signal was also significantly associated with clinically-relevant measures (retinal thickness and perimetric sensitivity). This difference in BOLD signal may not necessarily represent damage or dysfunction in the visual cortex in glaucoma; it is also possible that such differences are a result of normal cortical processing of altered neuro-visual input resulting from glaucomatous damage at the retina. This lower BOLD response in glaucoma patients compared to that in controls has been replicated in other research, especially in regions of the cortex retinotopically localised to regions of visual field loss in glaucoma patients (e.g. Qing *et al.*, 2010; Zhou *et al.*, 2017). However, such studies commonly make such comparisons by methods such as comparing percentage increases in the BOLD signal (e.g. Murphy *et al.*, 2016). This is problematic as it limits the number of specific conclusions and questions that can be addressed. For example, BOLD itself cannot delineate between neural activity or cerebrovascular functioning as both contribute to the signal (as discussed in Chapter 9). A lower BOLD response in a particular group may therefore be driven by a difference in neural activity, cerebro-vasculature, or both. Without using modelling techniques, such investigations also cannot make inferences about the underlying pattern of neural responsivity (e.g. receptive fields), which is particularly relevant to the current thesis. Furthermore, previous studies of cortical function in glaucoma with fMRI tend to identify

gross changes that relate to large geographical areas of moderate-advanced visual field loss. While interesting, these methods cannot inform how altered visual input in early glaucoma is dealt with by the visual cortex and, by extension, the consequences for perimetric sensitivity and perception of natural scenes. Given that Ricco's area, hypothesised to be a 'net' measure of receptive field size along the visual pathway is enlarged in glaucoma such that it completely accounts for changes in perimetric sensitivity loss, it would be prudent to investigate whether or not there is any difference in the size of cortical receptive fields in glaucoma, relative to those in healthy controls. This can be done quantitatively and non-invasively with population Receptive Field (pRF) mapping in fMRI, which models the size of the sum of receptive fields within a voxel (as discussed in previous chapters). While cortical pRF mapping has not been performed in glaucoma, it has been successfully applied to other primarily retinal conditions, such as Stargardt disease (Ritter *et al.*, 2019), retinitis pigmentosa (Ritter *et al.*, 2019), and choroideremia (Silson *et al.*, 2018a). In addition, pRF mapping has been used to demonstrate that, in a sample of five patients with visual field deficits, pRFs centred on the edge of the scotoma were enlarged compared to controls with artificial scotomas (Papanikolaou *et al.*, 2014).

A small number of previous studies have investigated cortical receptive field size in glaucoma. This was first done by King *et al.,* (2006), who investigated superior colliculus receptive fields in a rat model of glaucoma, using electrophysiological recordings. Experimental glaucoma was induced by artificially increasing intraocular pressure (IOP) via ocular surgery. They found an increase in receptive field size, which was proportional to the percentage increase of IOP and the amount of time IOP had been elevated. However, the data also suggested that increases in receptive field size didn't occur until IOP had been increased by 50-60%. Additionally, as this was based in experimental glaucoma, the results may not be representative of the mechanisms underlying glaucoma in humans. For example, it involved the rapid increase of IOP, whereas open-angle glaucoma is a chronic condition and may not involve a significant increase in IOP at all (i.e. normal-tension glaucoma; NTG). In terms of assessing cortical receptive field changes in human cases of glaucoma, only one study to date has investigated this directly, which was described in a conference abstract by Liu *et al.* (2007). fMRI retinotopy was carried out on two 70-year-old primary-open angle glaucoma (POAG) patients and three age-similar controls to map out

the central 12° of the visual field (in which the glaucoma patients showed 'normal' visual function). When fitting reference functions to the resulting BOLD response profiles, they found that more voxels within the occipital lobe in the glaucoma patients correlated with a 'wider width' model (28% of voxels) than a 'narrower width' model (11% of voxels), while controls demonstrated a more even distribution (percentage of voxels not provided). However, it is difficult to make firm conclusions with such a small sample, and there was no mention of correction for possible cerebrovascular differences; for example, this difference in the width of response profiles may reflect differences in the haemodynamic response function (HRF; a property of the fMRI signal reflecting neural and vascular contributions) between these participants. As Liu *et al.* (2007) is a conference abstract, there is also no information given on several methodological details such as the exact method of modelling, the exact definition of a 'wider width' model or clinical characteristics of the glaucoma patients, which limits a full interpretation of their results. Nevertheless, these results are supportive of the hypothesis of a difference in cortical receptive field sizes within the occipital lobe in human glaucoma compared to healthy controls; specifically, these studies suggest an enlargement of receptive field sizes in glaucoma, similar to the enlargement of psychophysical area of complete spatial summation (i.e. Ricco's area), reported in glaucoma (Redmond *et al.*, 2010).

This chapter will describe research investigating pRF size in central and mid-peripheral regions of the visual field of glaucoma patients and healthy controls. The size of pRFs will be estimated with a single Gaussian modelling approach that has been demonstrated previously (e.g. Dumoulin & Wandell, 2008; Schwarzkopf *et al.*, 2014). As the first point of entry of visual information to the cortex, V1 is of particular interest, especially as reduced activity in this region in glaucoma is more strongly associated with retinal structural changes compared to higher-order cortices (Murphy *et al.*, 2016).

10.1.1. Aim

The following are specific aims of the research in this Chapter:

4. To test for a difference in pRF size between glaucoma patients and healthy controls at different locations in the central and mid-peripheral visual field in V1 - V3. Given the enlargement of Ricco's area in glaucoma, it is hypothesised that pRFs will be

larger in glaucoma relative to those in healthy controls, especially in the mid-peripheral visual field.

5. To investigate if pRF size is associated with perimetric sensitivity in our glaucoma patients and healthy controls in V1-3.

10.2. Methods

In this cross-sectional study, 7T fMRI was used to complete pRF mapping in the visual cortices of a sample of glaucoma patients and age-similar healthy controls. pRF sizes were compared between glaucoma patients and controls. In addition, visual sensitivity was measured using a clinical perimeter. An association between visual sensitivity and pRF size was tested in order to investigate whether glaucomatous loss of visual field sensitivity was related to pRF size in the same visual field region.

10.2.1. Participants

Ethical approval for this study was obtained from NHS Wales Research Ethics Committee (Cardiff and Vale and Cwm Taf NHS health boards), as well as the Research Ethics Committees within the Cardiff University Schools of Psychology and Optometry and Vision Sciences. Participants were recruited via NHS glaucoma clinics (at the Royal Glamorgan Hospital and University Hospital of Wales), as well as the School of Psychology community panel and Cardiff University Eye Clinic. The participants described in Chapter 9 also took part in this experiment (HRF and pRF mapping took place within the same scanning session). Twenty-eight glaucoma patients (8 normal-tension [NTG], 20 primary-open-angle [POAG]) and twenty-eight healthy age-similar controls were recruited and tested. All experimental tests were carried out monocularly (controls OS [left eye]= 15; glaucoma OS= 16). The same procedure of selecting the experimental eye was used for all chapters. For healthy controls, whether the right or left eye was tested was chosen randomly by the PhD student. For glaucoma patients, either the glaucomatous eye or, if the glaucoma was bilateral, a randomly chosen eye was chosen for experimental testing. In cases of bilateral glaucoma where complete visual field loss in one eye included the mid-peripheral region targeted in pRF mapping, the eye without this visual field loss was tested. When comparing across eyes throughout the thesis, the nasal and temporal sides of the visual fields were matched.

There was no statistically significant difference in age or intra-ocular pressure (all $p>0.05$; see chapter 9 for statistical comparison). As part of the eligibility testing procedure discussed in Chapter 7, perimetric sensitivity was measured using a ZEISS Humphrey Field Analyser 3 perimeter (Carl-Zeiss Meditec, Dublin, CA, USA; SITA-Standard, central 24-2).

10.2.2. MRI protocol

Images were acquired on a SIEMENS 7 tesla (7T) MRI scanner (Siemens Medical Systems, Erlangen, Germany). Retinotopy scans were 1.5mm^3 isotropic EPIs (Echo-Planar Images; TR= 1s, TE=25ms, Flip angle=55°, 35 slices, 192x192 matrix, multiband=5), manually positioned over the occipital lobe and dynamically motion-corrected by the scanner. The use of multiband imaging allowed for a shorter scan time to be used, to aid in minimising participant fatigue. By reducing the TR from 3s (as used previously in Chapter 6) to 1s, the time of a single retinotopic fMRI run reduced from 7.5 minutes to 2.5 minutes. This meant that the minimum time required to map both the central and peripheral regions (with a single repeat of each and not counting set up time), was reduced from 15 minutes to 5 minutes. As this had a limited FOV over the area of interest, a whole brain single-volume EPI with same slice orientation was taken to aid with registration to structural images (TR= 5s, TE= 31s, 100 slices, 1.2mm^3 isotropic). To aid in distortion correction, a phase and magnitude image were also taken. Finally, a T1-weighted MPRAGE structural scan was also completed at 1mm^3 resolution (TR= 2.2s, TE= 2.82ms, TI= 1050ms). HRF mapping was undertaken with a 1.2mm^3 resolution EPI (TR= 2s; TE= 25ms; flip angle= 76°; 33 slices; FOV= 984x984), which was positioned manually over the occipital lobe.

Foam head padding was used to limit head movements and either an eye patch or blackout lens was used to occlude the untested eye. MR-safe vision correction was provided if needed. All participants were asked to confirm that they could see the screen clearly (i.e. confirming that none of the screen was occluded by and the screen was in sharp focus) before scanning (the fixation mark and 'Get ready' text was on the screen while this was asked).

10.2.3. fMRI stimuli

The same pRF mapping stimulus used in Chapter 6 was used again here, with adjusted timings to account for a TR of 1 second, rather than 3 seconds as previously used. For an

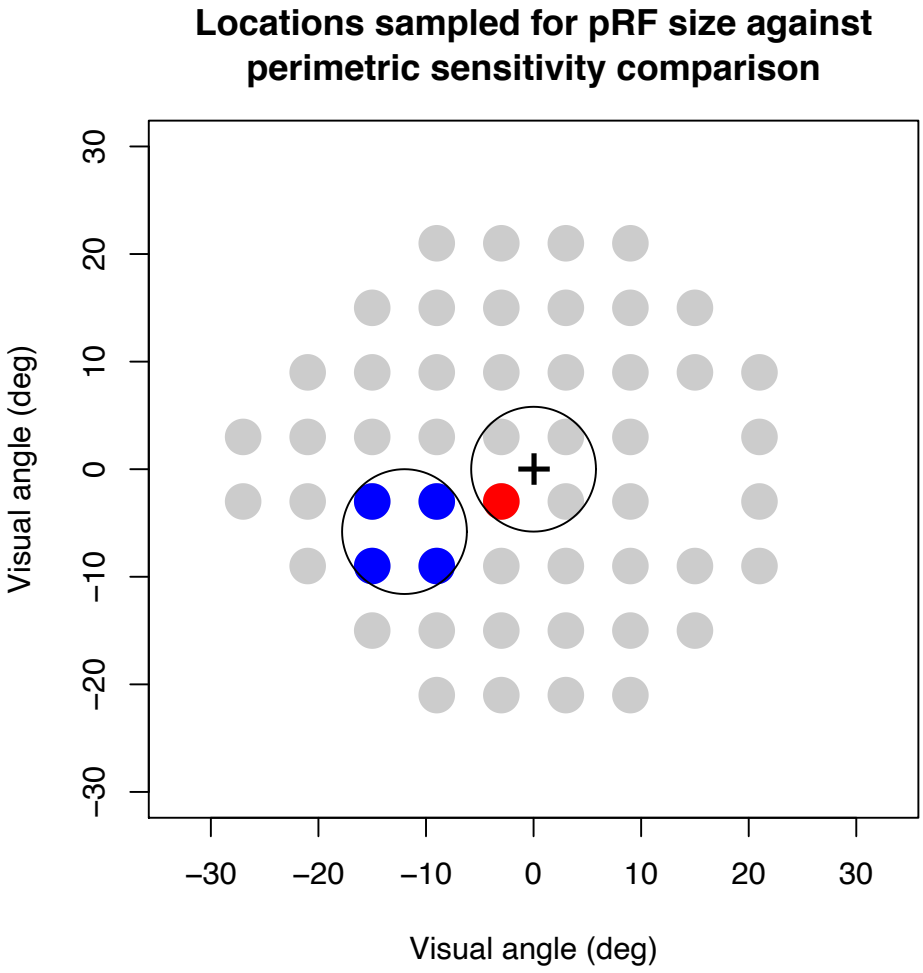

Figure 10.1 – fMRI pRF mapping stimulation areas on a visual field plot (defined by visual angle degrees [°]). pRF mapping regions are illustrated by black circles. The black cross indicates fixation, while the grey circles represent the locations of perimetric 24-2 testing for reference. In order to compare the visual sensitivity of this region to the estimated pRF size for the central and peripheral regions, the averaged centre pRF size is compared to the perimetric sensitivity sampled at the red filled circles, while the averaged peripheral pRF size is compared the perimetric sensitivity sampled at the locations indicated by the blue filled circles (averaged).

illustration of the stimuli and the region of visual field stimulated, see Figure 6.1, Figure 6.3 and Figure 6.4, in Chapter 6. Briefly, the stimulus was a moving bar aperture filled with a complex natural scene that changed five times per TR (0.2 seconds each). The bar moved to 18 consecutive positions to cover a circular area of 11° diameter. Each bar was 1.16° wide, and the step size was half the bar width. The stimulus crossed the screen in the following order: left to right, bottom-right to top-left, top to bottom, bottom-left to top-right, and then the reverse. The central region (-5.5° to 5.5°) and peripheral region (7.7 to 18.7°) were mapped individually by placing the fixation dot to the centre or the corner of the screen,

respectively. The regions of the visual field scanned are illustrated as black circles on a perimetric 24-2 testing grid in Figure 10.1. Each participant underwent 1-3 runs (averaged during analysis).

The HRF was mapped using stimuli described in Chapter 9. Briefly, this was a high-contrast reversing radial checkerboard, which filled the entire screen (screen size: 19.5° x 11.0°) and was presented to participants for 2 seconds. This stimulation period was followed by 20 seconds of a blank grey screen.

In order to maintain fixation, a simple fixation task was used for both HRF and pRF mapping. The fixation dot changed from white to red at random irregular intervals throughout the run, and the participant was required to count in their head the number of times this happened. They were not required to make a response or remember this number.

10.2.4. Pre-processing and structural analysis

FMRIB Software Library (FSL) toolkit (http://www.fmrib.ox.ac.uk/fsl/) and FEAT software packages (Jenkinson *et al.*, 2012; Woolrich *et al.*, 2001) were used for the majority of pre-processing. Both retinotopy and HRF EPI data underwent B0 distortion correction, motion correction (MCFLIRT; Jenkinson, Bannister, Brady, & Smith, 2002), brain extraction (BET; Smith, 2002), and high-pass filtering (100s). Following this, registration of the partial-volume EPIs (both retinotopy and HRF runs) to structural data, using the whole brain EPI as an intermediate step, took place in spm fMRI toolbox (http://www.fil.ion.ucl.ac.uk/spm/).

As described previously, the MPRAGE structural image was first intensity normalised within FSL, then segmented with FreeSurfer (Dale *et al.*, 1999; Fischl, 2012). This process divided the structural data into vertices (i.e. triangular 3-D pixels), which could be 'inflated' to provide a smoothed projection of the cortical surface for use in functional data projection and visualisation. FreeSurfer software was also used to generate an occipital lobe label to constrain pRF mapping analysis, which was generated based on manually located landmarks on the inflated brain surface (i.e. at the anterior end of the calcarine sulcus and the parieto-occipital function).

10.2.5. Haemodynamic response function estimation

HRF model fitting was completed within SamSrf v.7 software and was restricted to the occipital lobe (using the label described above). The BOLD signals generated by the ten

checkerboard photic bursts were first averaged within each vertex, excluding any outliers (defined as a time series that demonstrated greater than ±1.5 standard deviation from mean). Analysis was also constrained to only visually active regions to avoid noise. This was defined as a vertex with a signal (averaged over the first five scans) that had a clear response (>1 standard error from the mean) to the photic stimulation. A double-gamma function could then be fitted to the averaged response to estimate the HRF fit, from which the metrics discussed above could be extracted. There were four free parameters involved in the fitting of the double-gamma function:

5. The peak response latency (i.e. time-to-peak; TTP)
6. The latency of the undershoot
7. The peak amplitude (PA)
8. The ratio of the peak and undershoot amplitudes

The modelled HRF fit could then be used for an individual participants' pRF convolution, as described in the next section.

10.2.6. Population receptive field (pRF) mapping

Following methods development and the comparison of different software packages carried out in Chapter 7 (section 7.6), population receptive field (pRF) mapping was undertaken within the SamSrf Matlab toolbox v.7 (available at https://osf.io/2rgsm/). The functional data (averaged over runs) were first projected onto the structural surface. As discussed in Chapter 7, the functional timeseries for the voxels at 0 at three points defined as a proportion of the cortical thickness (0.25, 0.5 and 0.75) were sampled and averaged into each vertex. The time series for each run were then z-score-normalized and linear detrending was applied.

To calculate the pRF for each vertex, a forward-modelling approach was used with a 2D Gaussian model. This has been previously discussed in detail in this thesis (see Chapter 4, section 4.3.3). The final best-model fitting parameters provides estimates of the retinotopic location (X and Y coordinates), the spatial spread or size (σ; the standard deviation of the model Gaussian) and amplitude (β) of the pRF model. This also provides an R^2 value of model fit for each vertex, which can be used for thresholding.

10.2.7. Visual area delineation

As discussed previously (see Chapter 7), it was desirable to use an objective method for delineating visual areas. This would be beneficial as it would allow for the delineation of the early visual areas despite the issues with smoothing and general noise found during methods development with SamSrf v.7. and it would also aid in the clarification of the boundary between the area of peripheral stimulation in V2d and V3d, which is relatively ambiguous due to the relatively small amount of cortex stimulated (see Chapter 6). Therefore, a set of probabilistic labels for V1d, V2d, and V3d were generated based on each individual's structural data. These surface-based labels were based on the atlas described by Wang *et al.* (2015), based on traditional retinotopic fMRI maps (which extended to an eccentricity of 30°). These labels were 'probabilistic' in that they are defined by the likelihood of a given coordinate being associated with a given visual area. Specifically, the labels used were generated by a maximum probability topographic map. This is calculated by classifying each coordinate on the structural surface as the visual area it has the highest probability to be. As demonstrated in Figure 10.2, there is a fairly good agreement between manually drawn V1 (green outline) and probabilistic estimates of V1d (yellow outline) and V1v (black outline).

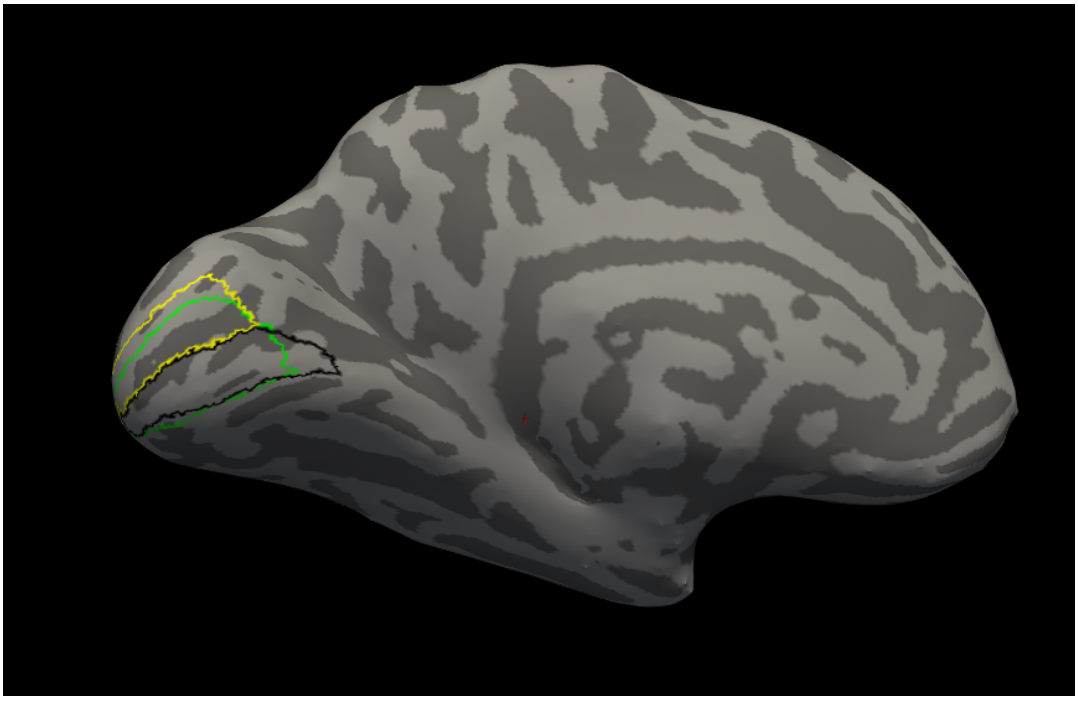

Figure 10.2 – Comparison of manually drawn V1 (green outline) and probabilistic estimates of V1d (yellow outline) and V1v (black outline) on an inflated brain.

10.2.8. Retinotopic map quality check

To ensure the inclusion of only maps in which delineation would theoretically be possible, all central retinotopic maps were visually inspected for evidence of a fovea in the eccentricity map and polar angle reversals in the polar angle map, which are standard markers for manual retinotopic delineation (e.g. Sereno *et al.*, 1995). Polar angle reversals indicate the locations of vertical meridians and so can be used to highlight the borders of visual areas. Each target dorsal region (V1d, V2d, V3d) will contain a quarter-field representation of the lower (dorsal ROIs) contralateral visual field. The difference between a map which does meet this criterion and one which fails to demonstrate these visual features is illustrated on Figure 10.3. After this process, one healthy control participant and ten glaucoma patients were excluded.

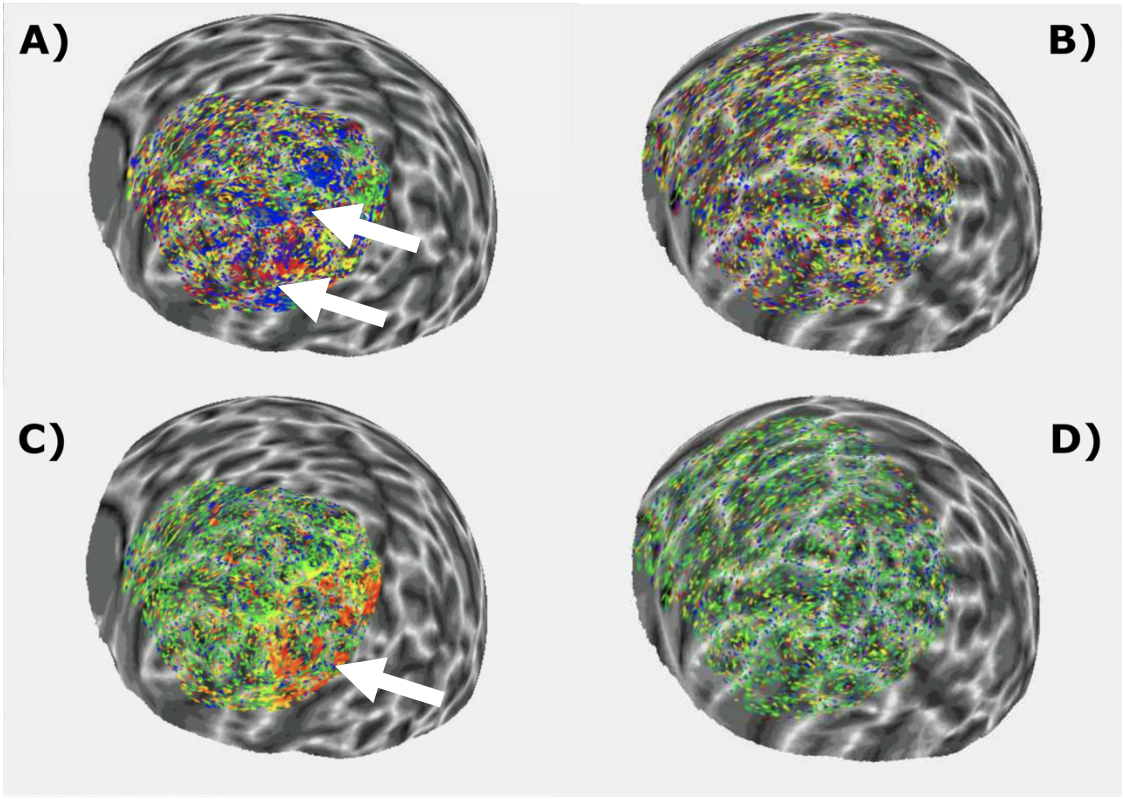

Figure 10.3 - Example of a map which would (maps A and C) and would not (maps B and D) pass manual inspection. In order to be deemed a retinotopic map of acceptable quality, the fovea must be visible in the eccentricity maps (maps C and D) and polar angle reversals must be present in the polar angle maps (maps A and B). Examples of these features are highlighted by arrows on maps A and C. In terms of the phase reversal maps (e.g. map A) the green polar angle reversal (the green stripe indicated by the arrow) refers to the lower vertical meridian, while the red polar angle reversal refers to the upper vertical meridian. The middle of the blue stripes therefore refers to the horizontal meridian.

It is notable that there were substantially more glaucoma patients excluded after this quality check than healthy controls. This may reflect increased movement in the glaucoma patients compared to the healthy controls, leading to poorer quality retinotopic maps. However, it seems unlikely that there would be systematically more movement in the glaucoma group, as it is not a motor or cognitive condition and the groups also included similar ages. The larger exclusion rate in the glaucoma group compared to the healthy controls may also suggest an increased difficulty in modelling the visual cortical response in the glaucoma patients, potentially due to altered input from the retina following glaucomatous damage.

10.2.9. Population receptive field data quality filters

To ensure that only good quality pRF data were used in the final analysis, several data quality filters were employed.

Firstly, methods development discussed in Chapter 7 revealed edge effects in the pRF data, whereby the size of pRFs centred on eccentricities at the edge of the stimulus were smaller than would be expected from a linear trend (i.e. show a 'dip' away from linearity) and from previous literature. For the central stimulus, this is evident for pRFs at eccentricities above ~4.5°, whereas for the central stimulus, this is evident for pRFs at eccentricities below ~8.7° and those above ~17°. Based on previous pRF size estimates in V1, these eccentricities also represent points at which the amount of the pRF covered by the stimulus goes below ~50%, so measures may be less reliable. Such edge effects are common in pRF studies (e.g. Harvey & Dumoulin, 2011; Schwarzkopf *et al.*, 2014; Smittenaar *et al.*, 2016) Therefore, only data centred on 0 - 4.5° for the central scan and 8.7 - 17° for the peripheral scan were included.

Secondly, it became evident in the methods development chapter that an irregularity with SamSrf v.7 was the inclusion of extremely small pRF sizes (i.e. near zero). Considering the unrealistically small size of these pRFs, it is most likely that these values are not real pRF sizes and reflect spurious fitting of noisy data. Therefore, a high-pass filter was used to filter out these points. When choosing a size to be used as a lower limit in this high-pass filter, we had to consider what would be an unreasonably small size, and therefore immeasurable using this fMRI protocol. One possible influencing factor be fixation stability. Though a fixation task was used to encourage stable fixation, micro-saccades (i.e. small involuntary

eye movements of about 0.3-1°; Martinez-Conde *et al.*, 2009) may still be a source of noise. Micro-saccades measured during a simple fixation task in the course of an MRI scan were found to be ~0.7° (Smith *et al.*, 2001). Fixation within static tasks also appears to be similar between glaucoma patients and healthy controls (Longhin *et al.*, 2013). Therefore, if these small eye movements do represent a lower limit of the pRF sizes estimated, we would at least expect this to be similar between groups. A number of studies have investigated whether eye movements have an impact on pRF mapping results. Levin *et al.,* (2010) compared retinotopic maps a patient who demonstrated eye movements around fixation (around 2 - 3°) to healthy controls. They found that even with large eye movements, the V1 map could still be estimated. When running a simulation that amplified the healthy controls' natural eye movements during pRF mapping, they also found no statistically significant difference in the retinotopic maps (in terms of the spatial cortical representation of the visual field). Estimated pRF sizes only increased once simulated eye movements were exaggerated to 4 times the patient's eye movements (simulated up to 10 - 15°). Similar results were also found in later simulation work (Klein *et al.*, 2014). Together, this work suggests that the fixational eye movements we would expect in our sample are unlikely to have a substantial impact on pRF size estimates and therefore are unlikely to provide a lower limit for this filter. Another factor which is likely to impact what the lower limit of this filter is the pRF stimulus itself. The pRF mapping stimulus used was a drifting bar with a width of 1.16° and a step size of 0.58°. It might therefore be expected that ~0.5° represents the smallest pRF that can be accurately estimated, as it is the smallest difference between the bar stimuli when changing positions on the screen. This was therefore examined with our dataset. All estimated healthy control pRF sizes (that met the rest of the criteria/filters described in this section) within each visual area were plotted as histograms and are presented in Figure 10.4. As can be seen from these plots, there are two clear peaks in the sizes estimated. The peak corresponding to the smallest sizes has a peak at very close to zero, suggesting it likely represents the very small pRF estimates identified in the small sub-sample (three healthy controls) described in Chapter 7. Between this 'noisy' peak and what can be assumed to be the 'signal' peak (which is entered around larger pRF sizes), there is a clear dip at around 0.5°, supporting the conclusion that this would be a reasonable point at

which to threshold these small pRF sizes. We chose a lower threshold of 0.5, rather than 0.58 exactly, in order to avoid cutting out any 'real' data.

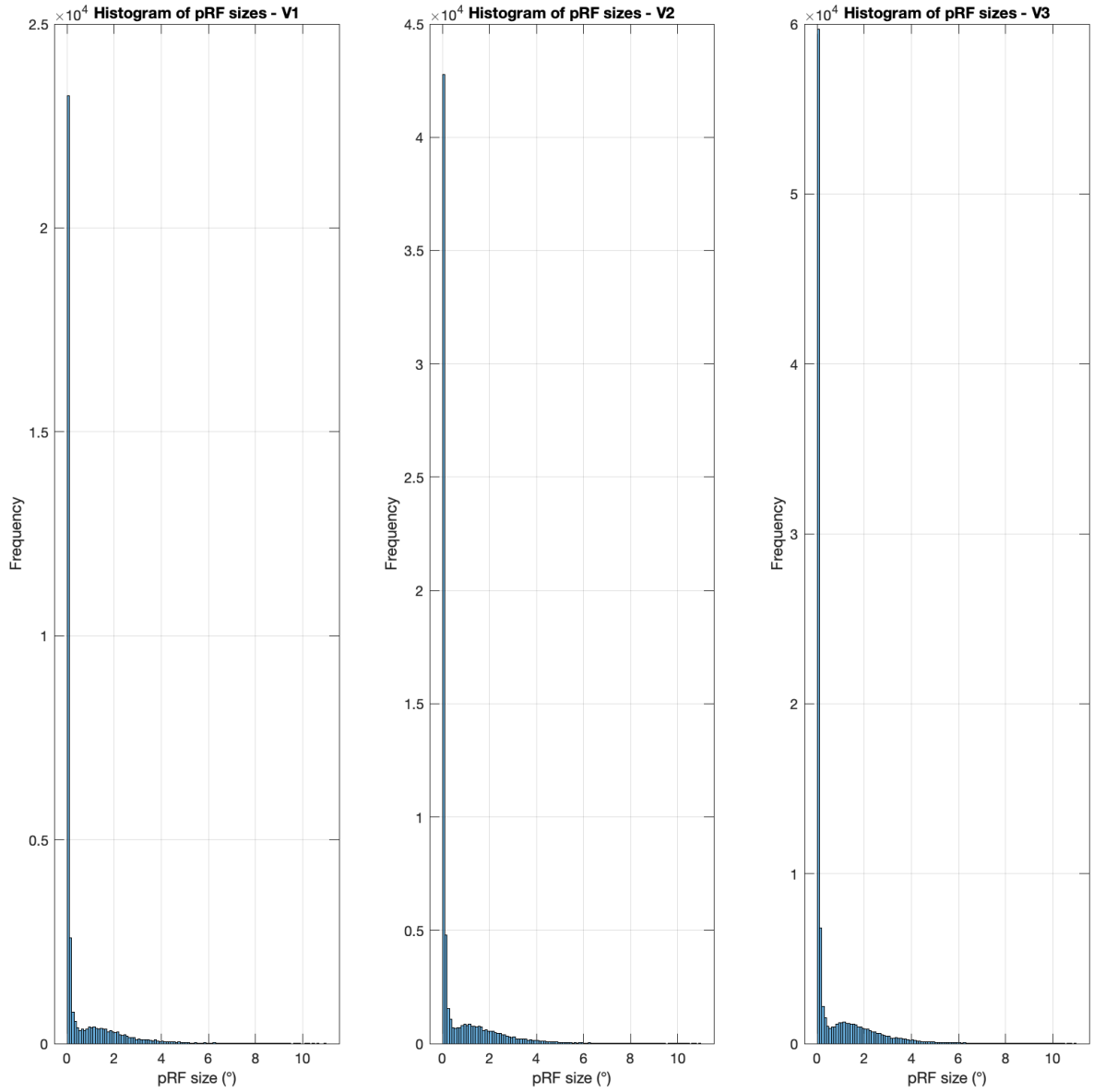

Figure 10.4 – Frequency of different pRFs sizes, separated by visual area. All participants are included. Data presented here has been threshold at R^2= 0.1 but has not undergone any of the other filtering steps detailed in this section.

Thirdly, an issue discussed in the methods development chapter (Chapter 7) was that there was a small number of vertices that demonstrated a goodness-of-fit of R^2=1 in the SamSrf v.7 analysis. Encountering such a high value is highly unlikely, considering the generally noisy nature of fMRI data. Upon closer inspection, it was found that all of these had a Beta value of 0, suggesting that the pRF model fits had no amplitude. For the final dataset therefore, all vertices with a Beta value of 0 or less were also excluded.

Next, only pRF estimates within the lower nasal quadrant were included for further analysis. As the peripheral stimulation was only within this quadrant, the analysis was constrained to the dorsal regions of the early visual areas, which process this portion of the visual field. As only pRFs within the lower nasal quadrant should be processed by these early visual areas (i.e. V1d, V2d, V3d), pRFs estimated outside of this region were assumed to be unreliable and were not included in the analysis. To keep this consistent, this was done for both the peripheral and central stimulation runs.

Finally, all pRF data were also filtered with an R^2 threshold. This is a standard filtering technique when completing pRF mapping and ensures that only data demonstrating a reasonable agreement with the Gaussian pRF model are included. The SamSrf v.7. software generated an R^2 threshold of 0.1 based on the TR and amount of datapoints in the current dataset and this value was used in the current study. Basing the R^2 threshold on the TR in this way accounts for the finding that shorter TR sequences tend to have lower R^2 values due to the addition of higher frequency noise (Morgan & Schwarzkopf, 2020).

In summary, the filters used were as follows:

- Eccentricities were restricted to avoid edge effects
- Unrealistic pRF sizes below 0.5° were removed
- Modelled pRFs with a Beta of 0 or less were removed
- All results were thresholded so only fits with an R^2 of 0.1 or above were included
- Only data corresponding to the lower nasal quadrant of the visual field (which should be represented within the dorsal visual areas) are included.

While this is a more thorough set of criteria than would be typically used, it ensures that the highest quality data are being brought forward to final analysis and addresses the issues that occurred in our data after SamSrf v.7 analysis (see Chapter 7).

10.2.10. Perimetric visual field assessment

Participants completed standard clinical visual field assessment with a ZEISS Humphrey Field Analyser 3 perimeter (Carl-Zeiss Meditec, Dublin, CA, USA; SITA-standard, central 24-2). White-on-white perimetry was utilised, with a working distance of 33cm. The test procedure involved the participant resting on a chin-and-forehead rest, with appropriate spectacle correction calculated by the instrument, based on participant age and refractive error prescription. The eye was manually centred with the aid of a live eye monitor camera. The participant was required to fixate on a central fixation mark and indicate when they saw a circular stimulus anywhere in their visual field using a patient response button. Goldman size III stimuli were presented for 200ms at locations within the 24-2 test pattern, at sub- and supra-threshold levels. Each eye was tested separately (with the untested eye occluded with an eyepatch). Visual sensitivity thresholds were calculated and printed out by the device. The following quality check criteria were used based on metrics calculated by the instrument during testing to ensure the quality of the assessment (e.g. that the participant was paying sufficient attention):

- Blind spot errors: <25%
- False positive rate: <15%
- False negative rate: <15%

If one of these exclusion criteria were met, the visual field assessment was repeated on that eye.

10.2.11. Post-processing analysis

The first aim test for a difference in pRF size between glaucoma patients and healthy controls at different locations in the central and mid-peripheral visual field in V1 - V3. In order to quantify the relationship between pRF size and eccentricity, a linear least squares fit was used to quantify the relationship between pRF size and eccentricity for each individual participant (using MATLAB software; *MATLAB*, 2018). The slope values and associated confidence interval (CI) widths from these fits were then extracted. A one-way ANOVA, weighted by the CI width, was used to test whether there was a significant difference between the individual slopes of the pRF size-eccentricity relationship for each visual area and between groups.

The second aim was to investigate if pRF size is associated with perimetric sensitivity in our glaucoma patients and healthy controls in V1 - V3. A Spearman's Rho was therefore carried out to test for an association between pRF size and perimetric sensitivity (due to non-normality in the data, as determined by a Shapiro-Wilk test). Central and peripheral values were investigated separately. For the central and peripheral investigations therefore, pRF size values from the central and peripheral retinotopic run were averaged over all eccentricities (median) within each run and logged, in order to give a single median 'central' pRF size value and a median 'peripheral' pRF size value. Perimetric sensitivity (dB) was extracted from the corresponding visual field locations (tested with the ZEISS Humphrey Field Analyser 3 perimeter; Carl-Zeiss Meditec, Dublin, CA, USA; used the SITA-Standard, central24-2 strategy). For the central stimulation, this was just one location, but for the peripheral stimulation, the area sampled during pRF testing subtended four perimetric locations. In order to compare sensitivity in this region to the peripheral pRF size, sensitivity thresholds in these four visual field locations were unlogged, averaged (mean), then relogged. See Figure 10.1 for an illustration of the visual field locations extracted for this analysis.

10.3. Results

10.3.1. Data quality filters

All pRF mapping data underwent the data quality filters discussed above. In order to illustrate the influence of these filters on the data, Figure 10.5 demonstrates the pRF size as a function of eccentricity for all healthy control participants in V1d. As can be seen from the comparison between the red (filtered) and blue (unfiltered) points, the relationship appears a lot more reasonable and in line with previous work after these filtering steps have been undergone.

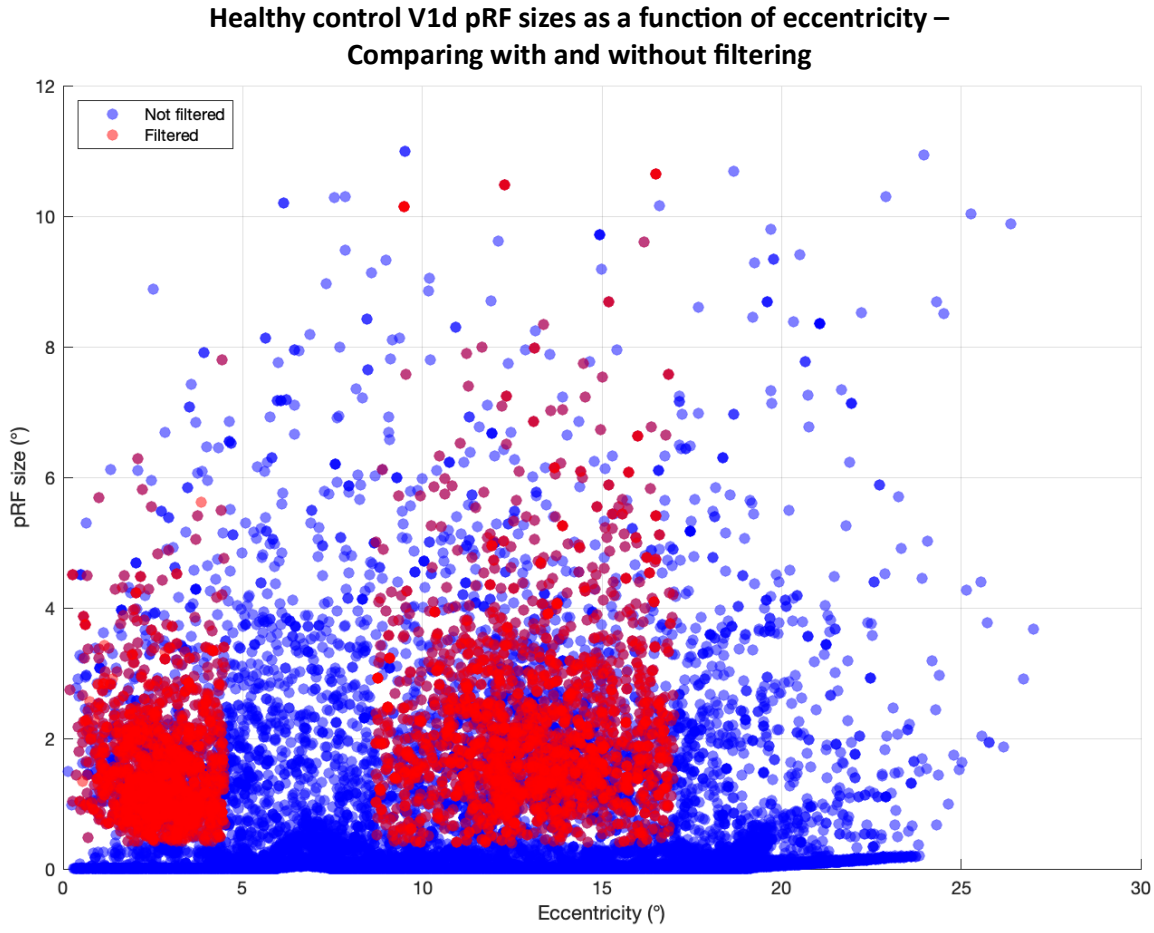

Figure 10.5 – V1d pRF sizes as a function of eccentricity for both the central and peripheral scans. Data are pooled from all healthy control participants and thresholded at R2>0.1. Datapoints in blue represent data which has undergone no additional filtering, while the datapoints in red represent data after undergoing all filtering procedures detailed in this section. pRF size is the sigma of the final fit. Both pRF size and eccentricity are given in visual degrees (°).

10.3.2. Population receptive field size

pRF estimates were extracted from each visual area region of interest and then plotted as a function of the estimated eccentricity (Figure 10.6). The data was not binned by eccentricity, for two reasons: 1) to utilise all of the data rather than a summary statistic, 2) it has been suggested that binning in pRF experiments can lead to certain biases, such as regression to the mean (Stoll *et al.*, 2020). While the relationship in healthy controls is not as steep as might be expected from previous work, the plots in Figure 10.6 demonstrate the expected positive relationship between estimated pRF size and eccentricity in all visual areas. Furthermore, the slope of the relationship between pRF size and eccentricity appears to increase systematically from V1d to V3d, as predicted from previous work.

The slope values from linear Bisquare fits were then extracted and compared between glaucoma patients and healthy controls (see Figure 10.7). As a number of possible outliers can be seen from a visual inspection of these figures, these were removed from all analysis within this section in order to prevent these values having a disproportionate influence on the statistical tests. In addition, these potential outliers demonstrated negative slopes of around -0.25 between pRF size and eccentricity, which would be implausible considering the underlying physiology and previous work (Cavanaugh *et al.*, 2002; Dumoulin & Wandell, 2008). Outliers were defined as data points with values more than 1.5 IQR away from the mean in either direction (Howitt, 2013). This excluded one glaucoma patient from V1 analysis, two glaucoma patients from V2 analysis, and one glaucoma patient from V3 analysis. A one-way two-tailed ANOVA, weighted by the confidence interval (CI) width, was used to compare the individual slopes of the pRF size-eccentricity relationship for between groups. This was completed for each visual area. For V1, a statistically significant difference was found ($F(1,42)= 5.687$; $p= 0.022$), with glaucoma patients demonstrating steeper slopes (controls: weighted mean[weighted standard deviation; SD]= 0.048[0.048]; glaucoma: weighted mean[weighted SD]= 0.012[0.049]). For V2, no statistically significant difference was found ($F(1,41)= 0.280$; $p= 0.600$) between healthy controls (weighted mean[weighted SD]= 0.063[0.039]) or glaucoma patients (weighted mean[weighted SD]= 0.039[0.040]). Finally, for V3, there was also no statistically significant difference ($F(1,42)= 2.032$; $p= 0.161$) between healthy controls (weighted mean[weighted SD]= 0.049[0.046]) or glaucoma patients (weighted mean[weighted SD]= 0.021[0.038]).

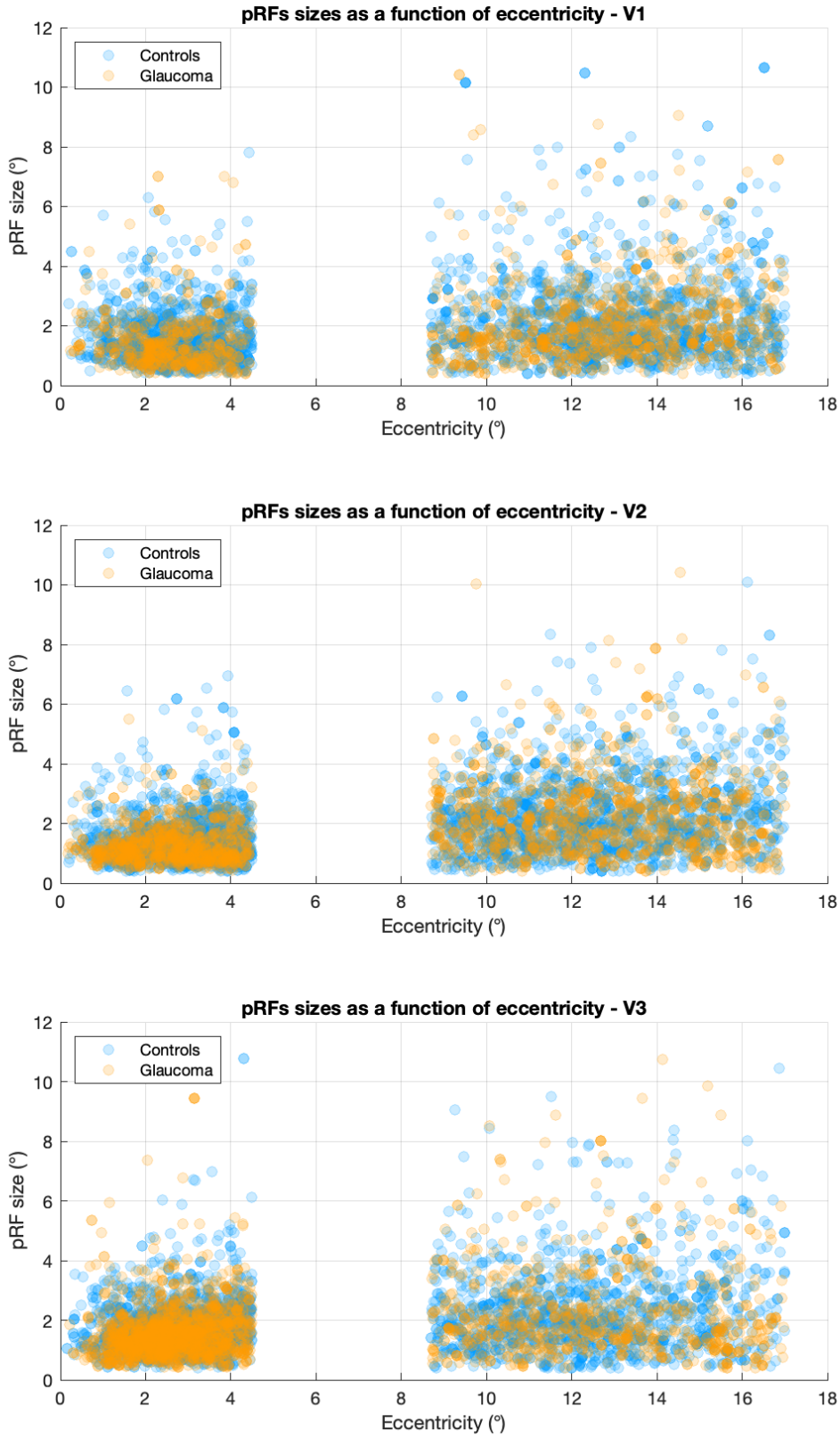

Figure 10.6 – pRF sigma size plotted as a function of eccentricity for both glaucoma patients (orange datapoints) and healthy controls (blue datapoints) in V1-3 (only dorsal regions). Both pRF size and eccentricity are given in degrees (°). All datapoints that pass the data quality filtering (section 10.2.7) and R^2 threshold of 0.1 are displayed.

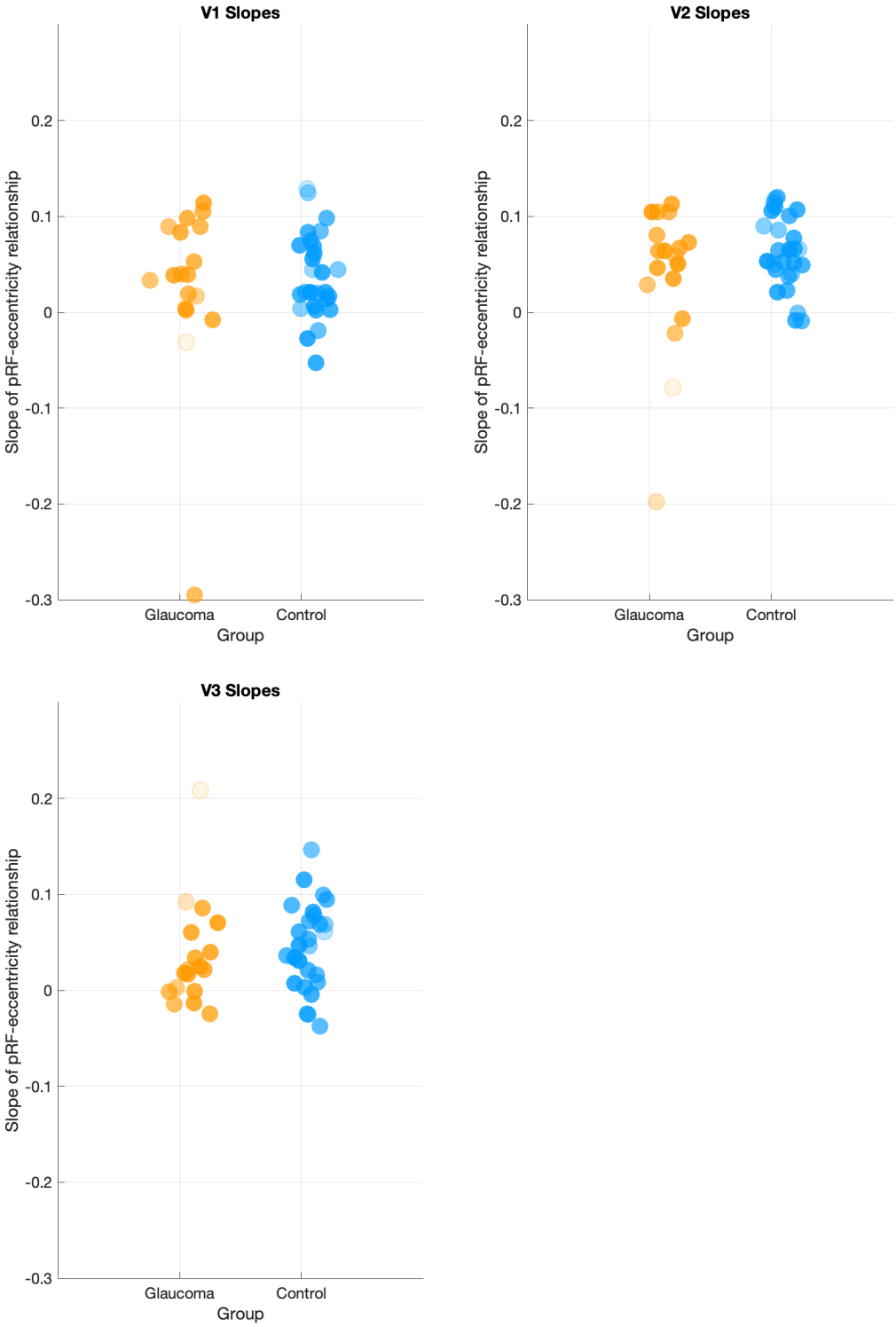

Figure 10.7 – Estimated slopes for the linear least squared fits (with Bisquare weighting) on the individual datasets for V1-3 (dorsal regions only). Glaucoma patients are displayed in orange, while healthy controls are displayed in blue. Opacity of the datapoints refers to the associated confidence interval width.

As a statistically significant difference between glaucoma patients and healthy controls in the steepness of the relationship between V1d pRF size and eccentricity was found, a linear least square fit (with Bisquare weighting) was rerun on the group data and the relationship plotted (see Figure 10.8). As can be seen from this figure, the steepness of the relationship in the glaucoma group (slope [95% CIs]= 0.054 [0.045, 0.062]; interval= 1.179) compared to the healthy control group (slope [95% CIs]= 0.038 [0.032, 0.044]; interval= 1.381) seems to be due to a depression in pRF size for more central eccentricities (i.e. 0-10°), and a possible increase at the furthest eccentricities (i.e. 16-18°).

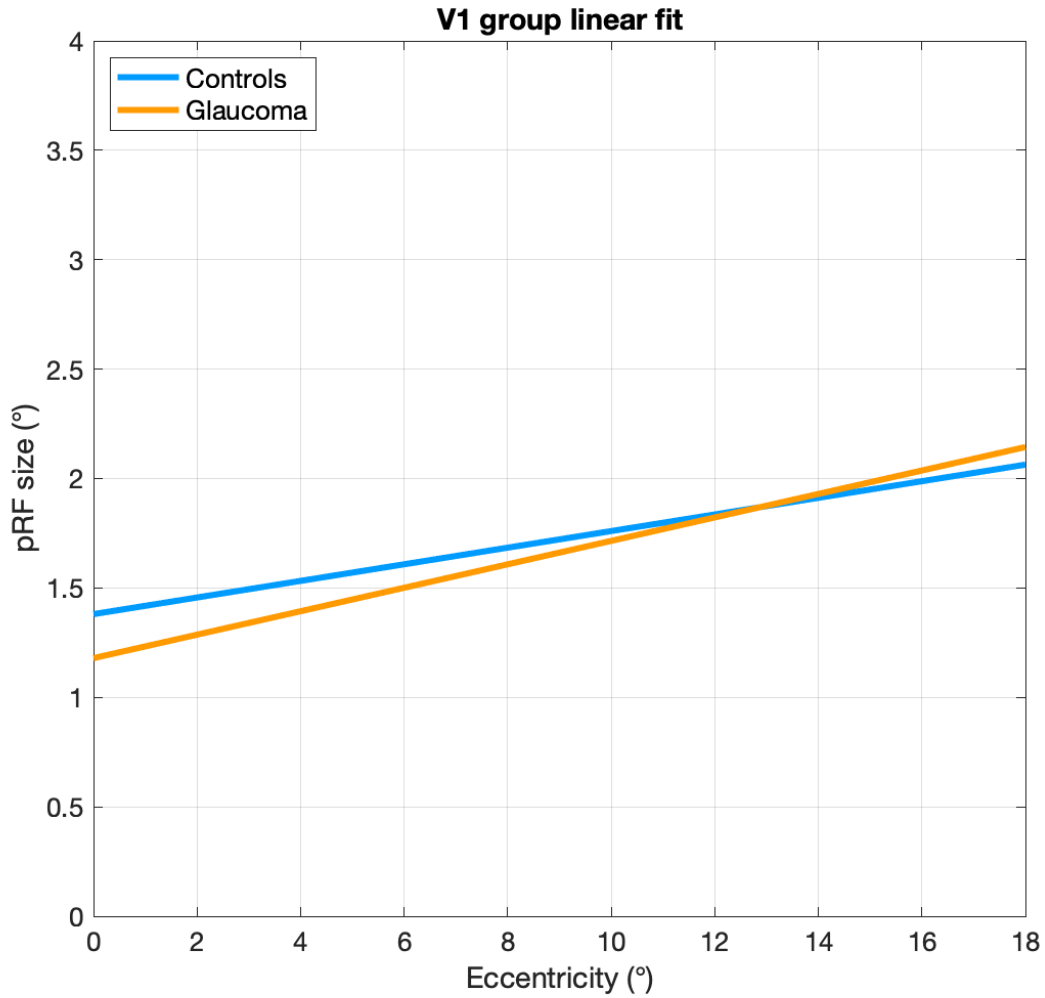

Figure 10.8 – A linear least square fit (with Bisquare weighting) completed on the group level data for dorsal V1. Orange line = Glaucoma patients; Blue line = healthy controls.

It is possible that there are isolated alterations in pRF size in individual locations in glaucoma patients relating to areas of damage in the retina, the location of which may vary between patients. The slope of the relationship between pRF size and eccentricity investigated above may mask individual local and subtle irregularities to the relationship. An approach to investigating such individual irregularities would be to perform a LOESS (locally estimated scatterplot smoothing) regression analysis. However, this analysis is heavily dependent on user input and potentially biased by the weighting the user applies to outlying data. Another approach is to investigate local departures from a linear relationship how levels of goodness-of-fit of a polynomial regression curve differs as the number of orders is systematically increased. As the relationship between pRF size and eccentricity is expected to be linear in healthy controls, there should be a minimal increase in goodness-of-fit as the number of orders are increased. By investigating if this pattern also holds in glaucoma patients, the nature of the relationship can be better interrogated. For example, if glaucoma patients show less of a smooth relationship (i.e. deviations from linearity) between pRF size and eccentricity than healthy controls (e.g. possibly due to a deviation in pRF size at specific eccentricities corresponding to areas of retinal damage), it is possible that they will demonstrate a greater increase in goodness-of-fit when the orders in a polynomial fit are increased compared to healthy controls. It is important to note that this is not being done as a way to model the data, but to further investigate the relationship between pRF size and eccentricity in glaucoma and how it may differ from the same relationship in healthy controls. Goodness-of-fit is defined as the adjusted R^2 of the corresponding polynomial fit. Orders from 1 to 6 were investigated. Bisquare weighting was used in all cases to reduce the influence of outliers. The individual data are shown in the upper panel of Figure 10.9, and the averaged (median) data are shown in the lower panel. These data show a similar trend as to what was hypothesised, with healthy controls demonstrating similar R^2 values across the number of orders, while glaucoma patients demonstrating an overall increase in R^2 with increasing number of polynomial orders. This is evident in both the individual data and the averaged data. A Greenhouse-Geiser repeated measures ANOVA (between-subject variable = group; within subject variable = number of orders) did not find the interaction between group and number of orders to have a statistically significant effect on R^2 ($F(5,1.757)= 1.637$; $p= 0.204$). The main effects were also statistically non-significant (Number of orders: $F(5,1.757)= 2.960$; $p= 0.064$; Group: $F(1,43)=$

0.116; p= 0.753). When examining the averaged relationship in the other tested visual areas (V2d and V3d), similar trends in the data are seen (more so in V2; see Figure 10.10), in which the relationship between R^2 and the number of orders in healthy controls is relatively flat, while an increase in R^2 values is seen in glaucoma patients. These trends in the data may suggest that some glaucoma patients are demonstrating localised changes, which is leading to a better fit with a larger number of polynomial orders. Healthy controls, however, show the expected linear response, and therefore goodness-of-fit values are similar despite increasing the number of orders.

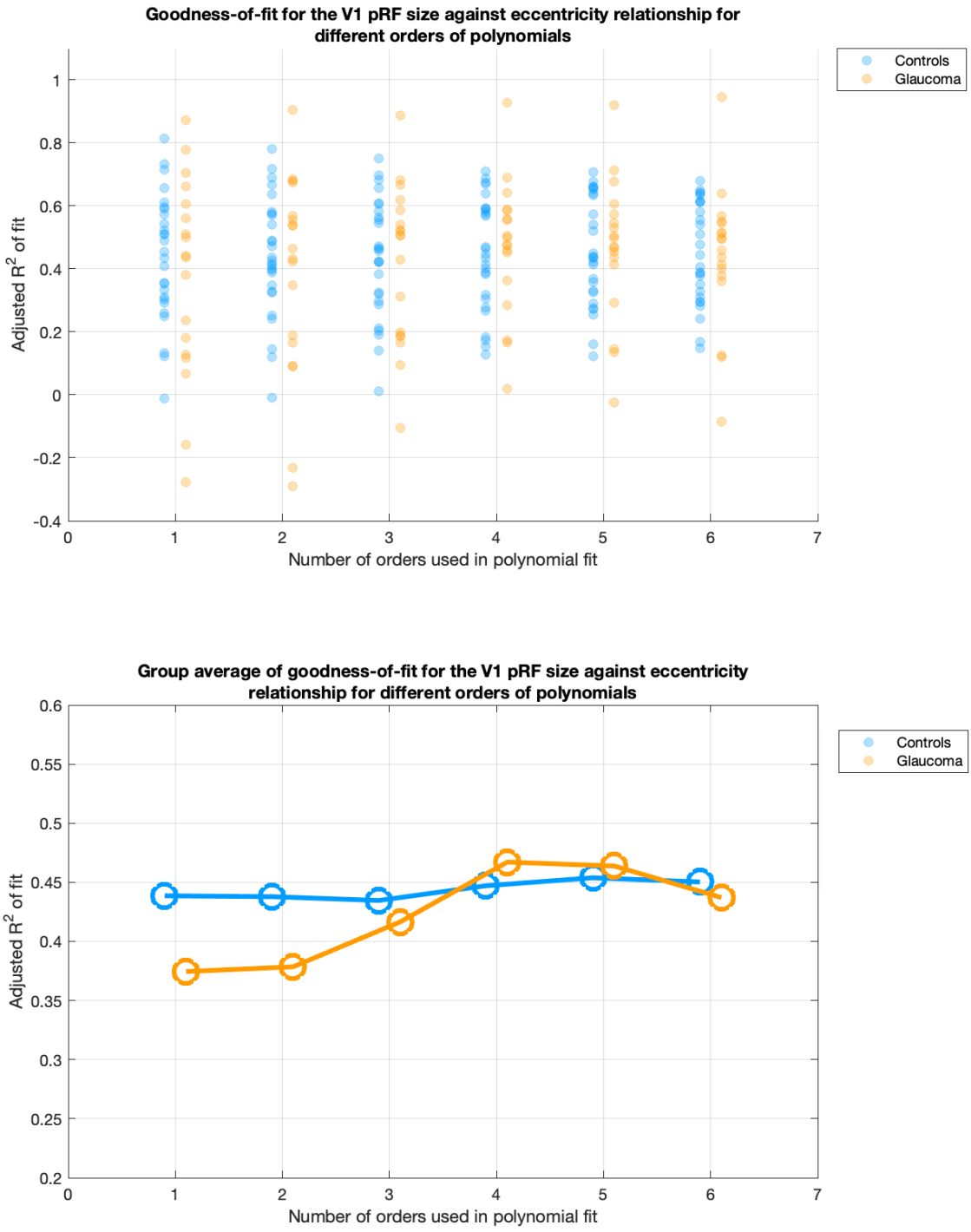

Figure 10.9 – Level of goodness-of-fit as a function of number of orders in a polynomial fit (with Bisquare weighting) for V1 (dorsal only). Goodness-of-fit is represented by the adjusted R^2 of the polynomial fit against the actual data (i.e. the pRF size as a function of eccentricity relationship). The individual data points are shown in the upper plot, while the average values (median) are shown in the lower plot. Orange datapoints = glaucoma patients. Blue datapoints = Healthy controls.

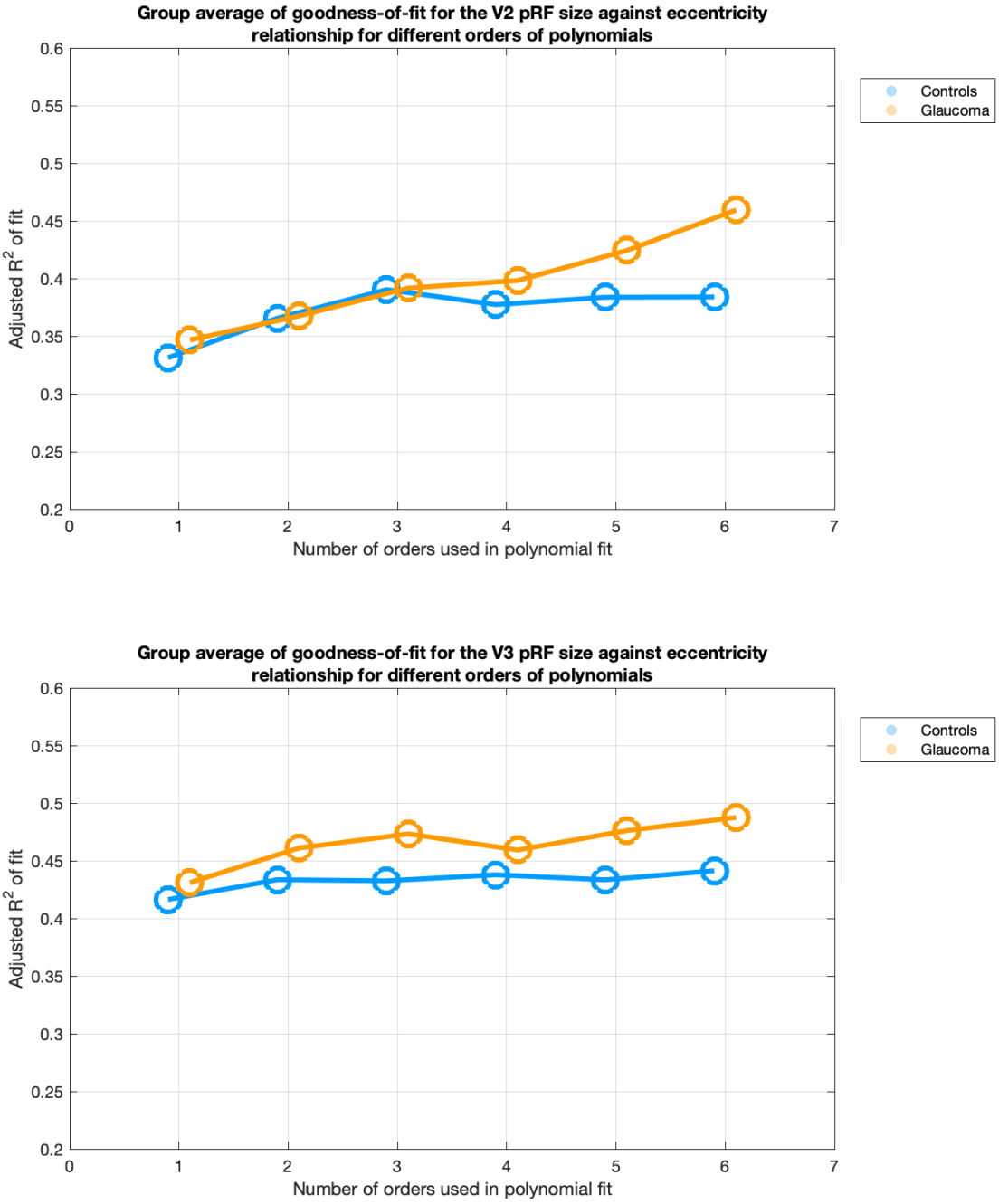

Figure 10.10 – Averaged (median) goodness-of-fit values for different number of orders in polynomial fits (with Bisquare weighting) on the pRF size as a function of eccentricity relationship for V2 and V3 (dorsal regions only). Orange datapoints = glaucoma patients. Blue datapoints = Healthy controls.

10.3.3. Relationship between population receptive field size and perimetric sensitivity

In order to address the second aim of the research discussed in this chapter, pRF size in the centre and periphery were correlated as a function of the perimetric visual sensitivity (decibels; dB) in the corresponding region of the visual field (see Figure 10.1) in V1 - V3. Scatterplots are shown in Figure 10.11. A Spearman regression test was performed on the data. For V1, the relationship between perimetric sensitivity and average pRF size was found to be statistically non-significant in both central (*rho*= -0.023; p= 0.883) and peripheral regions (*rho*= 0.012; p= 0.939). This relationship was also statistically non-significant in V2 for the central (*rho*= 0.042; p= 0.748) and peripheral regions (*rho*= 0.028; p= 0.853). Finally, in V3 this relationship was also statistically non-significant for the central (*rho*= 0.137; p= 0.370) and peripheral regions (*rho*= 0.054; p= 0.726).

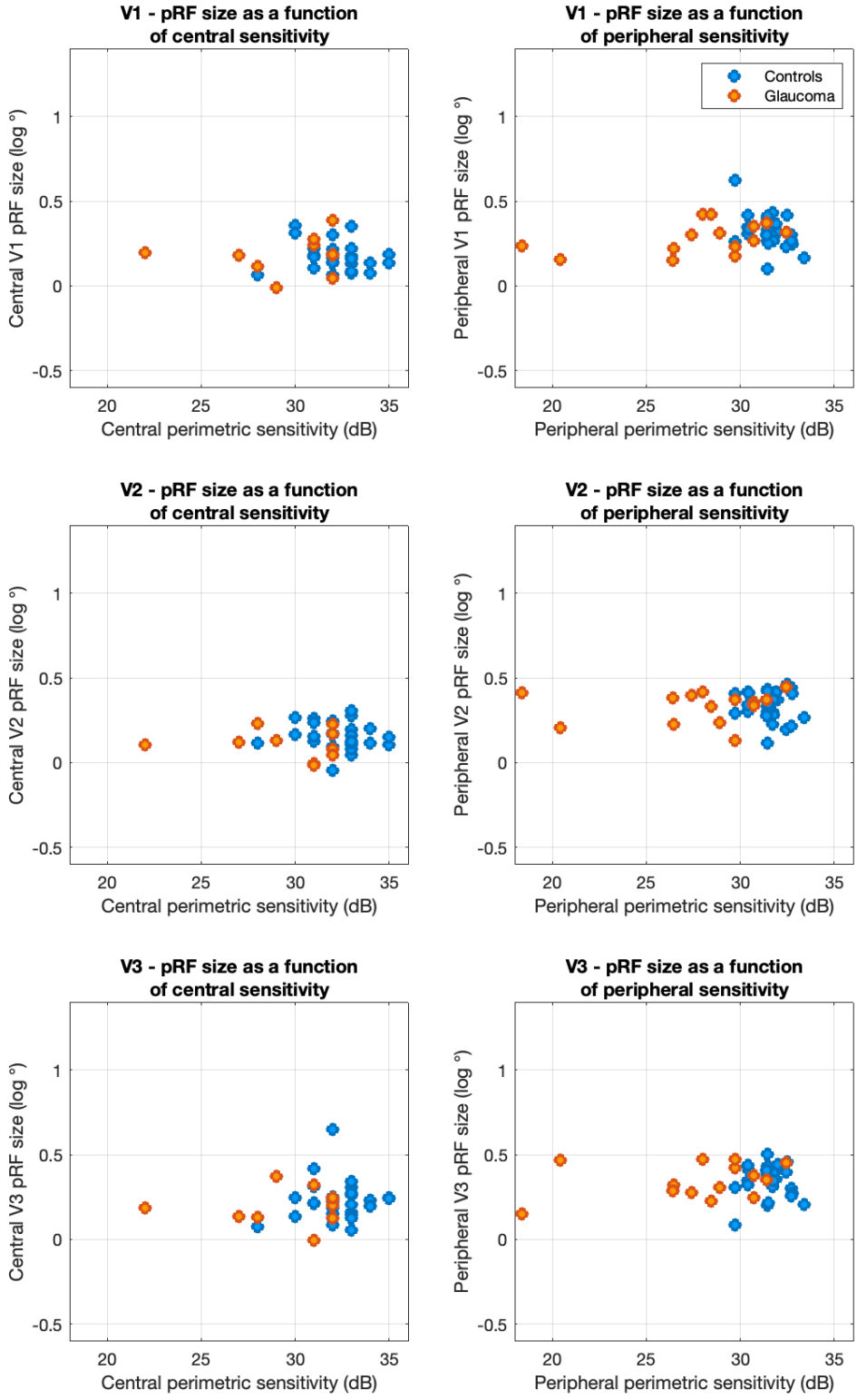

Figure 10.11 – pRF size plotted as a function of perimetric sensitivity in V1 (top row), V2 (middle row), and V3 (bottom row). The first column shows data sampled from the central visual field (0-5.5°, lower nasal quadrant), and the second column shows data sampled from a region in the mid-peripheral visual field (8.7-17°, lower nasal quadrant). pRF size is given in degrees (°) logged. Perimetric sensitivity is given in decibels (dB). Orange datapoints = glaucoma patients. Blue datapoints = Healthy controls.

10.3.4. Comparison of visual area size

As discussed in section 6.4.4 in Chapter 6, it is possible that, as receptive field properties being reported are averages within a single voxel rather than individual receptive fields, individual variation in visual area surface size will influence results. For example, a voxel of a fixed size in a participant with a large V1 will constitute a smaller percentage of V1 and thus cover a smaller amount of the visual field than a voxel of the same size in a participant with a very small V1, despite possibly having similar receptive field sizes. In order to investigate whether there was a group difference in visual area size that may influence the results, the surface area of V1d, V2d, and V3d were compared between groups, using a repeated measures ANOVA (between-subject factor= group; within-subject factor= visual area). Mauchly's test indicated that the assumption of sphericity had been violated ($\chi^2(2)$= 9.810, p= 0.047), therefore degrees of freedom were corrected using Huynh-Feldt estimates of sphericity (ε= 0.857). No significant differences between groups were found (F(1,43)= 0.001; p= 0.981), and there was also no evidence for a group-visual area interaction (F(1.713,73.665)= 0.321; p= 0.692). There was however, a significant effect of visual area, as might be expected from previous literature (F((1.713,73.665)= 51.757; p<0.001). Three paired samples t-tests were used to make *post hoc* comparisons between conditions. A first paired samples t-test indicated that there was a significant difference in the surface area of V1d (M= 822mm^2; SD= 138mm^2) and V2d (M= 705mm^2; SD= 123mm^2; t(44)= -5.817; p<0.001). A second paired samples t-test indicated that there was also a significant difference in area between V1d (M= 822mm^2; SD= 138mm^2) and V3d (M= 616mm^2; SD= 123mm^2) surface area (t(44)= 10.138; p<0.001). Finally, a third paired samples t-test indicated that there was also a significant difference between V2d (M= 705mm^2; SD= 123mm^2) and V3d (M= 616mm^2; SD= 123mm^2) surface area (t(44)= 4.321; p<0.001). Surface area therefore appears to shrink with higher visual areas, which can be seen in the retinotopic maps presented. However, importantly for the pRF analysis discussed elsewhere in this chapter, there is no difference in surface area size between groups, suggesting that this is unlikely to lead to any systematic bias that would impact group pRF comparisons.

10.4. Low contrast population receptive field mapping

One of the main aims of this chapter was to investigate how pRF sizes in glaucoma patients compare to those of healthy controls in dorsal V1-3. Following previous findings of

a larger Ricco's area in glaucoma patients compared to controls at similar eccentricities (Redmond *et al.*, 2010), it was hypothesised that evidence of larger pRF sizes in this sample of glaucoma patients compared to healthy controls would be found in the peripheral visual field. However, as illustrated in Figure 10.8, the difference in pRF size as a function of eccentricity slopes between the glaucoma sample and age-similar controls appears to be driven by smaller pRF sizes at more central locations.

A possible reason for this apparent discrepancy between psychophysical and pRF results could lie with the stimulus used during the fMRI retinotopic mapping. The retinotopic stimulus used by this experiment was a moving bar filled with a high-contrast alternating scene, as has been previously used by pRF mapping studies (e.g. Silson *et al.*, 2018b). One of the reasons that this stimulus is used is that it drives a wide range of neurons, thus resulting in a high signal-to-noise (SNR) BOLD signal (Yildirim *et al.*, 2018). However, a high-contrast stimulus could perhaps also have the effect of over-saturating larger receptive field sizes that usually have a higher sensitivity than smaller receptive fields (at the expense of resolution). If it is the case that certain 'compensatory' receptive fields are enlarging in glaucoma (as is suggested by the enlarged Ricco's area), it could be that they become saturated by the high-contrast stimulus and don't contribute to the stimulus response. The effect of this would be that only smaller pRFs would be measurable by our routine. Furthermore, estimating Ricco's area involves measures of luminance thresholds to spot stimuli of different area. Thus, if the abovementioned hypothesis is true, it could be that pathologically larger receptive fields contribute to the measurement of Ricco's area, but not to the pRF measurement.

There is some suggestion from the animal electrophysiology literature of increased spatial pooling in V1 when presented with low contrast stimuli (e.g. Nauhaus *et al.*, 2009; Victor *et al.*, 1994), which may be reflective of increased contribution of larger receptive field sizes. Use of low contrast stimuli during pRF mapping might therefore enable larger receptive fields to contribute to the response in patients and controls. To investigate this possible explanation for our findings therefore, a small exploratory study was completed using a sub-sample of participants from the larger study described above. pRF sizes measured during low contrast pRF mapping could be compared to pRF sizes measured with the same stimuli at high contrast (larger study).

10.4.1. Aims

The exploratory study had two main aims:

1) To investigate whether the use of low contrast pRF mapping stimuli leads to larger pRFs in healthy controls being measurable.
2) To investigate if the hypothesised larger peripheral pRFs in glaucoma compared to healthy controls discussed previously (section 10.1) are revealed when using low contrast stimuli instead of traditional high contrast stimuli.

10.4.2. Methods

10.4.2.1. Participants

Ethical approval for this study was obtained from NHS Wales Research Ethics Committee (Cardiff and Vale and Cwm Taf NHS health boards), as well as the Research Ethics Committees within the Cardiff University Schools of Psychology and Optometry and Vision Sciences. A small subset of participants from the main pRF mapping study described in this chapter was invited back to complete an additional MRI session. These participants were randomly chosen out of those who demonstrated a clear retinotopic map (i.e. with a observable fovea and polar angle reversals, determined manually) after the initial analysis of the dataset with SamSrf v.5. This sample consisted of four glaucoma patients (1 NTG, 3 POAG; median age [IQR]= 58.1 years [52.6, 62.6]) and six healthy controls (median age [IQR]= 62.4 years [55.6, 69.0]). All pRF mapping was completed monocularly (glaucoma = 1 OS; healthy controls = 3 OS). Intraocular pressure (IOP) was similar between glaucoma patients (median IOP [IQR]= 11.5 mmHg [10.5, 12.5]) and healthy controls (median IOP [IQR]= 14.0 mmHg[13.0, 15.75]). As expected, (as it is a measure of general visual field sensitivity) Mean Deviation (MD) was worse for glaucoma patients (median MD [IQR]= -5.9 dB [-9.2, -4.0]) compared to that of controls (median MD [IQR]= 0.32 dB [0.0, 0.5]). Pattern Standard Deviation (PSD) was higher in glaucoma patients (median PSD [IQR]= 7.4 dB [4.8, 10.5]) compared to that in the age-similar controls (median PSD [IQR]=1.3 dB [1.2, 1.3]).

10.4.2.2. MRI protocol

Scanning took place in a 7T SEIMENS MRI at Cardiff University Brain Research Imaging Centre (CUBRIC), using foam head and neck padding for participant comfort and to limit head movements. Retinotopic EPI scans were 1.5mm resolution images (TR= 1s, TE=

26ms, 46 slices, 192x192mm matrix size), using a multiband of 5. Each participant completed 1-3 central retinotopic runs and 2-4 peripheral retinotopic runs. In addition, a single volume whole brain EPI with the same orientation (TR= 5s, TE= 31ms) and field mapping images (phase and magnitude scans) were also taken in order to aid with registration and distortion correction respectively. HRF mapping was undertaken with a 1.2mm^3 resolution EPI (TR= 2s; TE= 25ms; flip angle= 76°; 33 slices; FOV= 984x984), which was positioned manually over the occipital lobe. Finally, a T1 MPRAGE sagittal structural scan was also completed at 0.7mm resolution (TR=2.2s, TE=2.98ms, TI=1050ms).

10.4.2.3. fMRI stimuli

To carry out low-contrast pRF mapping, the retinotopic stimulus described elsewhere in this thesis (e.g. section 10.2.3) was edited so that the naturalistic scene was 20% of its original contrast (for a comparison of the natural scene stimuli used in each version of the pRF mapping sequence, please see Figure 10.12). Other parameters of the stimulus were identical. HRF mapping was also completed at 20% contrast.

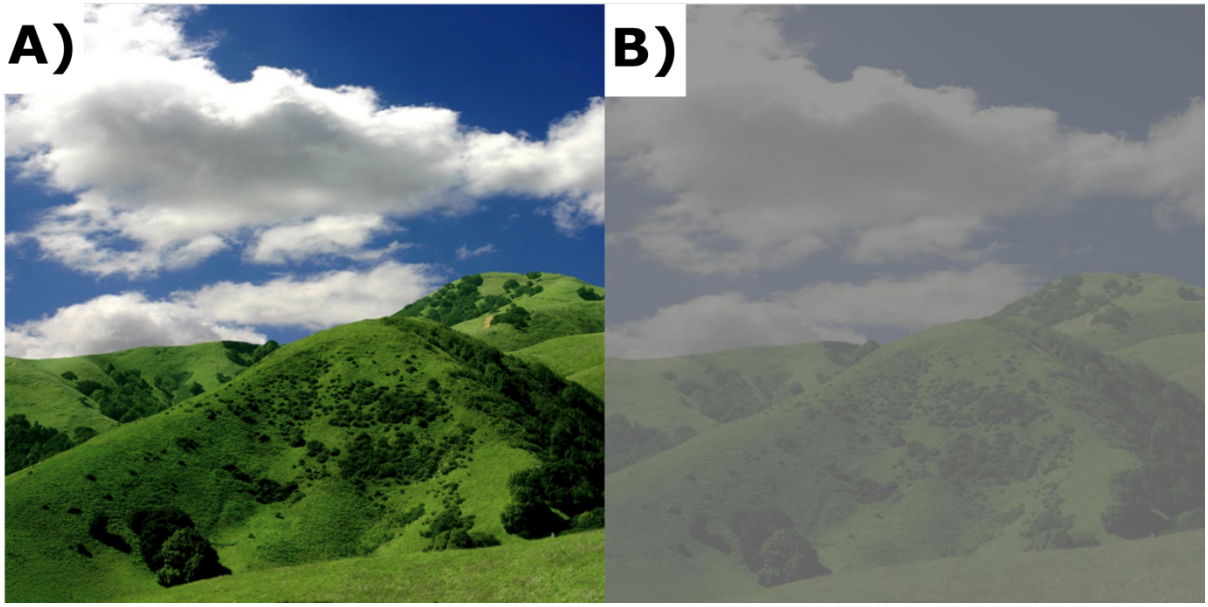

Figure 10.12 – Comparison of natural scene stimuli used in A) traditional high-contrast pRF mapping, and B) 20% contrast pRF mapping.

10.4.2.4. MRI pre-processing and modelling

As previously, the majority of pre-processing took place within FSL and FEAT (Jenkinson *et al.*, 2012). EPI data underwent B0 distortion correction, motion correction (MCFLIRT; Jenkinson, Bannister, Brady, & Smith, 2002), brain extraction (BET; Smith, 2002), and high-pass filtering (100s). The structural data were intensity normalised using FSL, then processed using FreeSurfer (Dale *et al.*, 1999; Fischl, 2012). Following this, registration of the partial-volume EPI to structural data, using the whole brain EPI as an intermediate step, took place in SPM fMRI toolbox (http://www.fil.ion.ucl.ac.uk/spm/).

Structural probabilistic labels for V1d, V2d, and V3d were generated based on the atlas described by Wang et al., (2015) to allow pRF size estimates in separate visual areas to be investigated. The generation of these is described more fully in section 10.2.7.

Both HRF and pRF modelling were carried out in SamSrf v.7 (described in sections 10.2.5. and 10.2.6). A 2D Gaussian pRF was used. The pRF modelling process provides estimates of the retinotopic location (X and Y coordinates), the spatial spread/size (σ) and amplitude (β) of the pRF model. This also provides an R^2 value of model fit for each vertex, which can be used for thresholding.

Once again, all retinotopic maps underwent a visual check to ensure that features such as clear polar angle reversals and a fovea (which are traditionally used to delineate visual areas; Sereno *et al.*, 1995). This stage excluded one glaucoma patient and one healthy control, leaving three glaucoma patients and five healthy controls. All pRF data then underwent the same filtering steps as discussed in section 10.2.8. As an overview, these filters were as follows:

- Eccentricities samples were restricted to avoid edge effects.
- Unrealistic pRF sizes below 0.5° were determined to be noise and removed.
- Modelled pRFs with a β of 0 or less were also removed.
- All results were thresholded so only fits with an R^2 of 0.1 or above were included.
- Only data corresponding to the lower nasal quadrant of the visual field (which should be represented within the dorsal visual areas) were included.

10.4.2.5. Analysis

In order to address the two aims of this small exploratory study, the data were plotted in two ways; firstly, low-contrast pRF size was plotted as a function of eccentricity (as was done in Figure 10.6) for the glaucoma patients and age-similar controls. This allows for the relationship between pRF size and eccentricity to be visualised and investigated in comparison to the data collected during the larger study using traditional high-contrast pRF mapping. Secondly, as the slope of the relationship between V1 pRF size and eccentricity was found to the significantly steeper in glaucoma patients compared to that in age-matched controls during the larger study (see Figure 10.8), the group-level slopes of this relationship were plotted for this low-contrast data and compared between high- and low-contrast pRF mapping runs. As this was an exploratory study with a small sample, quantitative statistics were not used.

10.4.3. Results and discussion

Plots of pRF size as a function of eccentricity are shown in Figure 10.13 and Figure 10.14.

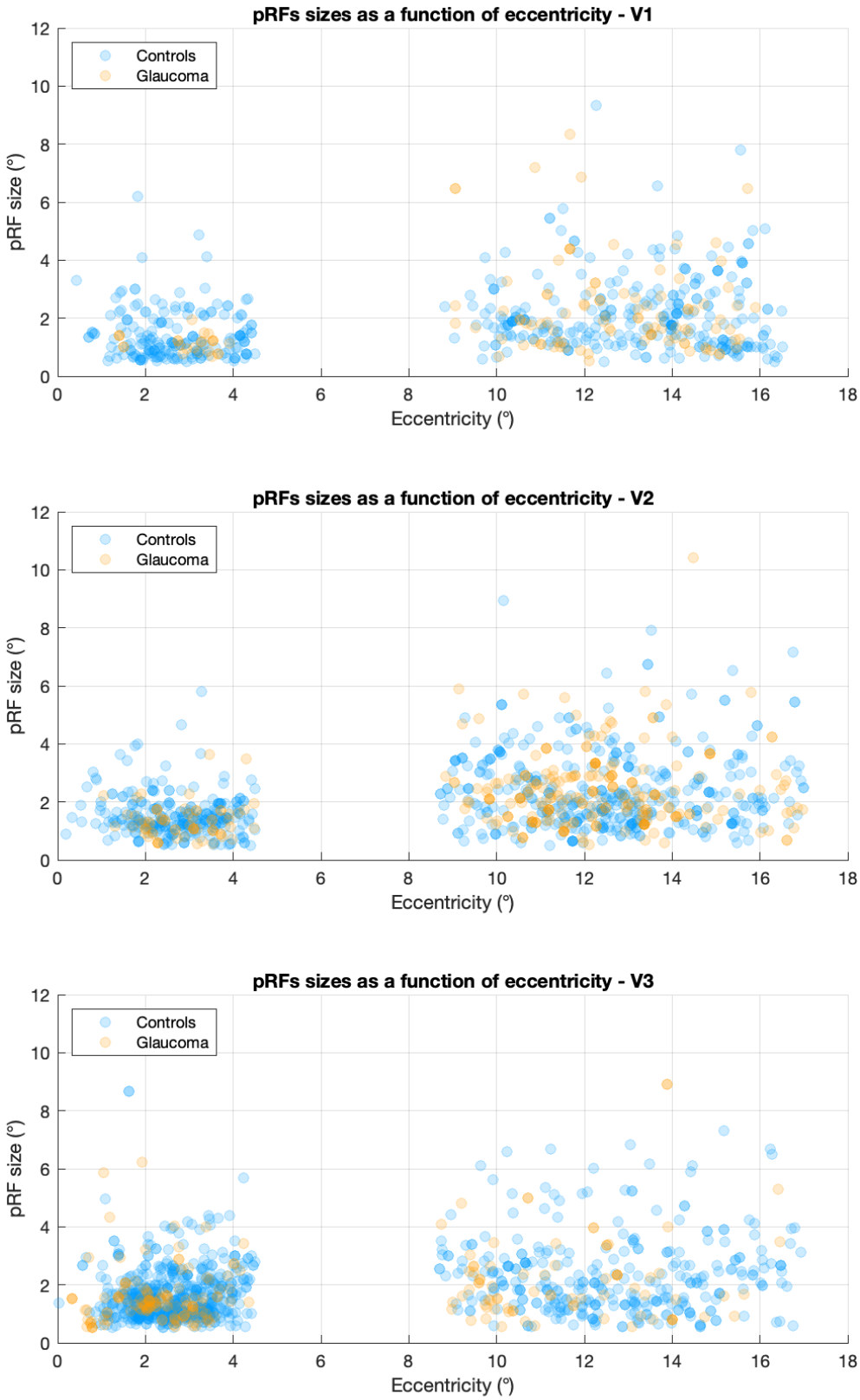

Figure 10.13 – pRF sigma size following low-contrast pRF mapping plotted as a function of eccentricity for both glaucoma patients (orange datapoints) and healthy controls (blue datapoints) in V1-3 (only dorsal regions). Both pRF size and eccentricity are given in degrees (°). All datapoints that pass the data quality filtering (section 10.2.7) and R^2 threshold of 0.1 are displayed.

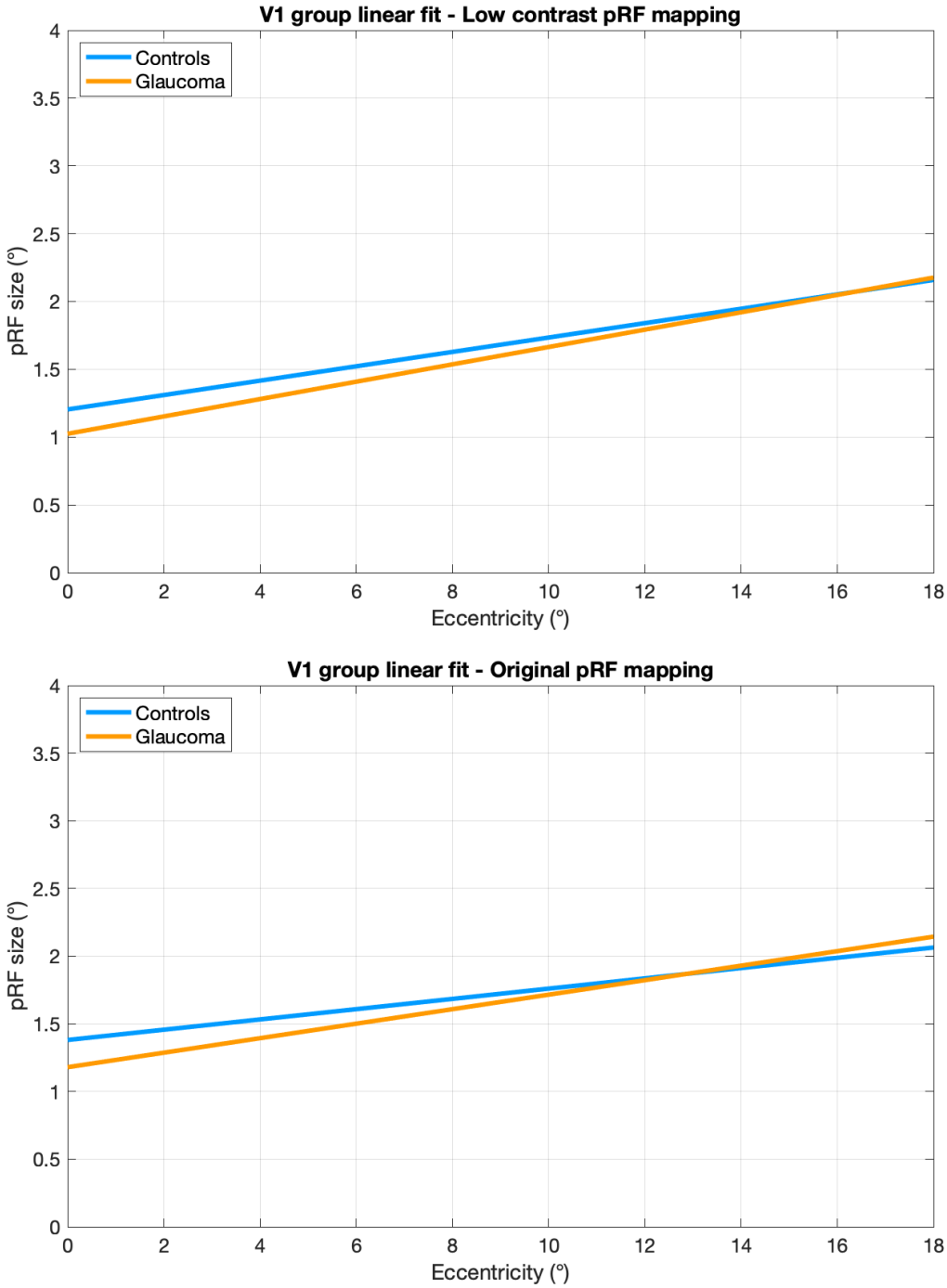

Figure 10.14 – A linear least square fit (with Bisquare weighting) completed on the group level data for dorsal V1 for low-contrast pRF mapping (top plot) and the original high-contrast pRF mapping (bottom plot). Orange line = Glaucoma patients; Blue line = healthy controls.

Comparing the low-contrast pRF size as a function of eccentricity data in Figure 10.13 to the same from traditional retinotopic stimuli in Figure 10.5, a similar pattern to the data can be seen, in terms of average pRF size and slope. The use of low-contrast stimuli does not appear to have made a substantial difference to the reported pRF sizes in any visual area. In reference to the first aim therefore, it appears that the use of low contrast pRF stimuli does not recruit substantially larger receptive fields within the healthy population, despite evidence to the contrary from electrophysiology studies (e.g. Nauhaus *et al.*, 2009; Victor *et al.*, 1994). However, it is possible that a difference in pRF size would be found if lower contrast levels were used. A contrast level of 20% was employed within the current study to ensure that high enough SNR BOLD signal could be elicited for the limited number of central and peripheral runs possible within a single session. In order to fully address this question in future research therefore, pRF mapping to a range of stimulus contrasts, especially lower contrasts, should be completed, with enough runs to ensure sufficient SNR at each contrast level.

In terms of the second aim of the research described here, the slopes of the relationship between low-contrast pRF size and eccentricity in V1d of individuals with glaucoma and healthy controls and between the original pRF size and eccentricity in V1d of individuals with glaucoma and healthy controls are shown in Figure 10.14. As can be seen from these plots, a similar trend is apparent in both sets of data; namely, a steeper slope in glaucoma patients than controls, possibly driven by a decrease in foveal pRF sizes. Very similar pRF sizes are reported for both contrast levels, across groups. This follows the finding to aim 1; if both contrast levels are targeting the same neurones, rather than lower contrast stimuli allowing for a greater contribution of larger receptive field sizes to be measured, then similar results would be expected. In this way, this work provides a replication of the larger result using low contrast pRF mapping stimuli.

10.5. Overall discussion and conclusion

The research described in this chapter was an investigation into pRF sizes in the visual cortices of glaucoma patients compared to those in healthy controls, using high-resolution 7T MRI. A difference in pRF size between these groups was hypothesised, due in part to an enlargement of Ricco's area in glaucoma (Redmond *et al.*, 2010). The research described in this chapter aimed to quantitatively investigating whether pRF sizes differ in glaucoma compared to that in healthy controls and how pRF size relates to perimetric sensitivity.

The first aim of the research was to investigate whether pRF sizes in glaucoma patients differ to those in healthy age-similar controls in V1-3. It was found that glaucoma patients demonstrated a steeper relationship between pRF size and eccentricity compared to controls, mainly due to smaller pRF sizes in central vision in glaucoma patients compared to healthy controls (see Figure 10.8). These group slopes also suggest that pRF sizes may be larger in the far periphery (16+°), but this is at the edge of our peripheral stimulus and so some of this is extrapolation from the slope found for the actual data (assuming that this relationship continues linearly into the far periphery with the same slope). Regarding the second aim of the research described in this chapter, we also did not find a significant association between pRF size and perimetric sensitivity, in either central or peripheral regions.

These results are inconsistent with our initial hypothesis, which was that larger pRF sizes would be estimated in the visual cortices of glaucoma patients compared to healthy age-similar controls, reflecting an increase in spatial summation across altered retinal inputs (due to cell death in glaucoma). While pRF sizes have not previously been investigated in glaucoma, the question of cortical receptive field sizes in human glaucoma was addressed by an early conference abstract, which compared BOLD responses across the occipital lobe to retinotopic stimuli between two early glaucoma patients and three age-matched controls (Liu *et al.*, 2007). BOLD responses were cross-corelated with 7 functions, representing a range of receptive field widths. They reported that more voxels in glaucoma patients correlated to wider width models compared to narrower models, especially at the posterior pole of the occipital cortex, though data from individual visual areas and direct comparisons between the pRF size as a function of eccentricity relationships in glaucoma patients and

controls are unavailable. Additionally, information regarding the exact eccentricities showing 'wider' response profiles is also not available, as was clinical information regarding the two glaucoma patients. It is possible that only eccentricities beyond (i.e. more peripheral than) what was tested in the current study demonstrated wider response profiles. These issues limit possible interpretation and comparison with this research. The current study is the first to describe and quantitatively investigate pRF sizes in a cohort of glaucoma patients and age-similar controls, using the pRF modelling approach first described by Dumoulin and Wandell (2008).

One possible reason for these results is a reorganisation of the retinotopic map, specifically an enlargement of central representation. Though differences weren't found when comparing overall visual area size, it is possible that due to decreased input from the peripheral retina, the cortical representation of central vision, which tends to be impacted later in the course of the disease, enlarges. A larger portion of V1 would therefore, be dedicated to central vision. Voxels centred in this region would have less of the visual field to cover (i.e. each voxel would represent a smaller percentage of the visual field if the central representation is spread over a larger amount of cortex), thus leading to smaller pRF estimates. This suggestion is supported by Zhou *et al.,* (2017) who found that, in a sample of 9 glaucoma patients and 9 age-matched controls, glaucoma patients demonstrated greater cortical magnification than controls in the central visual field (7°), but not the peripheral visual field. Glaucoma patients therefore demonstrated an enlarged foveal cortical representation. This effect could explain the decrease in pRF size at the fovea in this cohort of glaucoma patients compared to controls within the current study, and may suggest that the receptive fields themselves are not shrinking but are instead shifting towards a more central representation.

A possible mechanism by which this effect may occur is a difference in attentional allocation between glaucoma patients and healthy controls. It has been found that attentional allocation to a particular location within the visual field leads to a shift of receptive field position preference to the attended stimulus. This attention modulation of cortical receptive fields was first described in animal studies (e.g. Luck *et al.*, 1997; Womelsdorf *et al.*, 2008) and later in human fMRI pRF mapping work (Klein *et al.*, 2014, 2018) across cortical layers (Klein *et al.*, 2018). The effect of this modulation appears

greatest in higher visual areas, particularly extra-striate areas, but has also been observed in V1 using fMRI (Klein *et al.*, 2014, 2018). It is possible that, following a decrease in visual sensitivity in the periphery, patients with glaucoma start to reallocate attentional resources to areas of preserved vision, namely central vision, leading to a shift in pRF position preference and thus enlargement of central cortical representation. While this has not been tested in glaucoma, it has been found that attention modulation of BOLD responses in central vision is increased in a different peripheral retinal condition (inherited peripheral retinal degeneration) compared to healthy controls (Ferreira *et al.*, 2019). While the onset for this condition is at an earlier age than in glaucoma (the age range of patients in Ferreira *et al*., 2019, was 20-66 years), different compensatory mechanisms may be involved (as the brain is more plastic in younger life), a similar effect of enhanced attention modulation may be present in glaucoma compared to controls. This may also explain the greater effect of attention on pRF position preference in glaucoma patients compared to controls (i.e., though groups were fixating at the fixation point, enhanced attentional modulation of neuronal responses in glaucoma compared to healthy controls may lead to pRF position preference to shift to greater magnitude and thus enlarge central representation). If the impact of an enlarged central representation is a less linear relationship between pRF size and eccentricity, this may also explain why the current study found that glaucoma patients showed a greater gain in goodness-of-fit with increasing order of polynomial fit over controls (who demonstrated minimal increases, see Figure 10.9 and Figure 10.10). An expansion of central cortical representation due to attentional bias would therefore be a possible explanation for the findings discussed in this chapter. Future research should investigate whether cortical attention modulation of cortical responses in various regions of the visual field differs in a cohort of glaucoma patients versus age-matched controls (by investigating the effect of attentional demands on BOLD fMRI visual responses).

Previous research has investigated the impact of less peripheral stimulation on pRF size. Prabhakaran *et al.*, (2020) found that the extent of the visual field stimulated (i.e. mapping either the central 14°, 7°, or 4°) impacted pRF size. Specifically, larger peripheral scotomas (i.e. less peripheral stimulation, such as in the 4° radius condition rather than the 14° radius condition) led to larger foveal pRF sizes in a sample of healthy adults. The authors caution that this effect should be taken into account when investigating patients with actual

peripheral scotomas, as findings of larger pRFs sizes may reflect this effect (i.e. of a reduced area of stimulation) rather than actual cortical reorganisation. The fact that the opposite effect was reported here, with smaller pRF sizes found in the fovea of glaucoma patients compared to healthy controls, suggests that this phenomenon is not the cause of our results.

As mentioned previously, an advantage of the traditional high-luminance contrast used in the main study described in this chapter is that, by stimulating a broad range of neurones due to the high contrast and range of spatial frequencies involved in the natural scenes, the BOLD signal has a higher SNR than would otherwise be elicited. However, this also means that if there any differences in glaucoma patients compared to controls in specific neural sub-populations, they may be overshadowed by the majority and difficult to discern (i.e. there may by high 'redundancy'). While a similar pattern of results was found even when using low-contrast pRF mapping stimuli (section 10.4), future studies may aim to address the question of pRF size changes in glaucoma compared to controls using a range of stimuli in order to target specific neuronal populations. For example, Welbourne *et al.,* (2018) mapped pRF sizes using either achromatic or chromatic (L-M or S-cone pathways) stimuli, in order to isolate these specific neural populations. Similarly, pRF mapping has been completed using stimuli defined by orientation contrast (Yildirim *et al.*, 2018) or contour properties (Dumoulin *et al.*, 2014) in order to target neuron populations sensitive to these properties, especially in extra-striate visual areas.

The second aim of the current study was to investigate the relationship between pRF size and visual field sensitivity at the corresponding location in a combined sample of glaucoma patients and controls (which allowed for a range of sensitivities to be included). A relationship was hypothesised by modelling work carried out by Pan and Swanson (2006), who demonstrate that spatial summation with perimetric stimuli can be accounted for by cortical pooling by multiple orientation-sensitive mechanisms. However, a statistically significant relationship between pRF size and visual perimetric sensitivity in corresponding regions of the visual field was not found in this cohort. Positive relationships between pRF size and perimetric sensitivity were reported by Silson *et al.,* (2018a) in a sample of four patients with choroideremia and four healthy controls. However, this was not demonstrated in healthy controls, and was only apparent when considering choroideremia patients with a

large range of severities. It is possible that a relationship was not observed in our data due to most patients demonstrating relatively mild visual field loss, as a relationship in either group is not apparent in Figure 10.11. Additionally, choroideremia is an inherited disease, with visual loss occurring much younger than in glaucoma (i.e. within childhood and adolescence) so may respond differently to reduced retinal input. Regarding the relationship suggested by the data described in Pan and Swanson (2006), it is possible that by utilising stimuli that better target orientation-sensitive neurones, a stronger relationship between cortical responses and perimetric sensitivity would be found. For example, previous work modelling elongated pRF functions have found a relationships between pRF elongation and orientation selectivity (Merkel *et al.*, 2020). Population spatial frequency tuning can also be mapped across the cortex (Aghajari *et al.*, 2020), which may better target these spatially sensitive mechanisms. The relationship between pRF size and perimetric spatial summation is addressed more fully in the next chapter (Chapter 11).

A limitation of the current study is the limited amount of visual field sampled. Due to the restrictions of the 7T MRI environment (i.e. restrictive head coil, small field-of-view of stimulation screen), only a stimulus with a radius of 5.5° could be employed. In order to sample the periphery, therefore, the central and peripheral regions had to be scanned separately (see Chapter 6 for further discussion of this methodology). This leads to a number of potential limitations. Firstly, only a relatively small portion of the peripheral visual field was sampled (rather than the whole visual field at a certain peripheral eccentricity). As only a small amount of the cortex will be responsible for this region (due to cortical magnification favouring central vision), this also leads to lower SNR in this peripheral region than if the entire visual field up to the maximum peripheral eccentricity were stimulated. It would be prudent therefore to replicate these results in a 3T MRI, with the possibility of extending the stimulus field-of-view to more peripheral eccentricities than was possible in this study. Replication of this work with a larger field of view would also be beneficial considering that differences in pRF size are found depending on size of area of stimulation (Prabhakaran *et al.*, 2020). Furthermore, as only the lower visual field was sampled, only data within the dorsal visual areas could be analysed. This raises the possibility that these results will not generalise to pRFs estimated in ventral visual field areas. This may explain the smaller pRF sizes reported in this work compared to some

previously discussed work, as pRF sizes have been found to be smaller in the dorsal regions (Silson *et al.*, 2018b). By replicating this study at 3T with a larger field-of-view both ventral and dorsal regions could be sampled simultaneously (as for example, the larger inner bore used at 3T allows for a larger stimulation screen to be used).

The main limitation of this research is the unexpected level of noise in the data which, although reduced following re-analysis with SamSrf v.7, still remains a limiting factor (as discussed during methods development in Chapter 7). This led to the use of probabilistic labels of the early visual areas rather than manually drawn labels based on the retinotopic maps, which opens the possibility of inaccuracies in visual area borders. This noise in the data led to a relatively high rate of exclusion due to poor quality retinotopic maps (10 glaucoma patients and 1 healthy control). The use of strict data filtering criteria however, aided in ensuring the inclusion of the best quality data available.

An advantage of the research described here is the use of individual HRF mapping in pRF modelling. As shown in Chapter 9, though there was no group difference in HRF, the shape of the HRF can vary substantially between individuals. This in turn can influence the estimated pRF size due to the HRF convolution involved in the modelling process. By mapping each individual participants' HRF and using that for convolution, this potential additional source of noise in the pRF estimates is minimised, helping to account for vascular differences (e.g. in cerebral blood flow) that may underlie HRF individual differences.

The use of 7T fMRI in the research described here also brings certain advantages over 3T. For example, due to the increased magnet strength, high-field 7T scanners provide higher signal-to-noise ratios (SNR) and thus scans can use smaller voxels while keeping sufficient SNR (Stucht *et al.*, 2015). Additionally, 7T fMRI studies are less biased by large draining veins, meaning that the signal can be more accurately localised to the target tissue (Uludağ & Blinder, 2018), in this case, within the early dorsal visual areas.

Overall, the research described in this chapter aimed to investigate whether pRF sizes differ in the visual cortices of individuals with glaucoma compared to age-similar controls. We found that glaucoma patients show a steeper pRF size as a function of eccentricity relationship than healthy controls, primarily driven by a decrease in foveal receptive field size. This result was repeated in a sub-sample of participants using low-contrast pRF mapping. One of the main motivations of this thesis was to investigate the contribution of

cortical receptive field sizes to the finding of an enlarged Ricco's area in glaucoma patients relative to that in healthy controls (Redmond *et al.,* 2010).The following chapter will therefore investigate how these observed pRF sizes contribute to measurements of Ricco's area in the mid-periphery of the same sample of glaucoma patients and age-similar controls.

Chapter 11. Modelling the contribution of retina and cortex structure and function to Ricco's area changes in glaucoma

11.1. Introduction

In Chapters 8 and 10, pattern electroretinography (PERG) and functional magnetic resonance imaging (fMRI) were utilised to estimate retinal and cortical receptive field sizes, respectively, and investigate whether these receptive field sizes differed between glaucoma patients and healthy controls. In Chapter 8, evidence was found to suggest larger global retinal receptive field sizes in the mid peripheral visual field of glaucoma patients compared to those in healthy controls. In Chapter 10, it was found that, compared to controls, glaucoma patients demonstrated a steeper relationship between pRF size and eccentricity, possibly driven by relatively smaller pRF sizes found within central vision (0 to 10°). Additionally, a polynomial function was fitted to the data (i.e. the pRF size as a function of eccentricity relationship) with an increasing number of polynomial orders (1-6), in order to investigate the effect that this had on the goodness-of-fit of the function and therefore have an initial insight into the likelihood of group differences. For healthy controls, increasing the number of orders made little to no difference to the goodness-of-fit (defined by the R^2), which would be expected from a monotone linear relationship. For glaucoma patients however, the goodness-of-fit increased with increasing number of orders used in the polynomial fit, a trend that was evident in all visual areas. One of the possible reasons for this is that the pRF size as a function of eccentricity relationship was deviating from linearity at certain eccentricities in the glaucoma patients, possibly relating to areas of glaucomatous damage in the retina or, as discussed in Chapter 10, a compensatory expansion of the cortical representation of the central visual field. In the current chapter, the main aim of this thesis will be addressed; namely, to investigate how receptive field sizes at the retina and cortex contribute to Ricco's area in a sample of glaucoma patients and age-similar controls.

Initially, research discussed in this chapter will investigate whether Ricco's area measured within the target region in the mid-peripheral visual field (see Figure 11.1) differs between glaucoma patients and age-similar controls. Ricco's area is the maximum size at

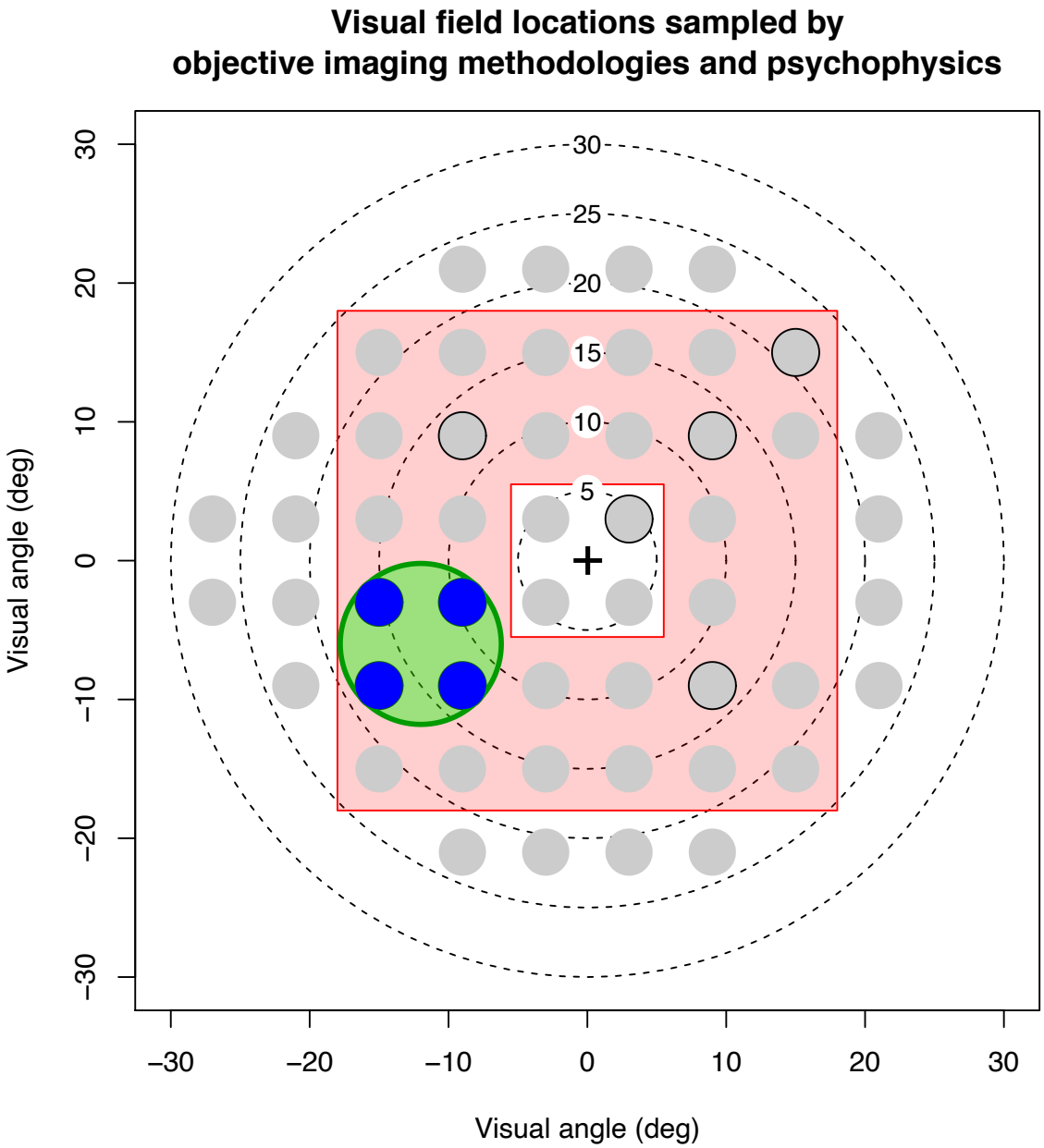

Figure 11.1 – Visual field locations sampled by experimental procedures used in this chapter. PERG test area is shown by the shaded red region. The black cross indicates fixation, while the grey circles represent the locations of perimetric 24-2 testing for reference. Visual field locations at which Ricco's area was measured are indicated by a black outline. Blue-filled circles with black outlines are those Ricco's area measurements that are analysed within this chapter. The green filled circle represents the area of the visual sampled by the ganglion cell- inner plexiform layer (GCIPL) thickness measurement (at the corresponding retinal location) and peripheral population receptive field (pRF) run.

which Ricco's law (which states that, at threshold, area and intensity are inversely proportional; Ricco, 1877), and thus complete spatial summation, is maintained. Once a

stimulus is larger than Ricco's area, threshold is determined by partial summation (discussed further in Chapter 3). Multiple early studies suggested the possibility of spatial summation changes in glaucoma. For example, Fellman *et al.*, (1989) demonstrated that, for glaucoma patients, increasing stimulus size provided a greater benefit to retinal sensitivity than did increasing contrast. Healthy controls however, demonstrated the opposite pattern. They also found that lower background adaptation levels (which leads to an increase in Ricco's area; Barlow, 1958; Glezer, 1965) led to disproportionate improvements in contrast sensitivity for different retinal eccentricities for glaucoma patients compared to healthy controls. It was suggested that both of these results reflect altered spatial summation mechanisms (specifically an enlarged Ricco's area) in glaucoma (Anderson, 2006). Spatial summation of a range of perimetric stimuli (both chromatic and achromatic) was therefore investigated by Redmond *et al.* (2010). Sensitivity thresholds to multiple perimetric stimulus areas were measured at 10° retinal eccentricity in four diagonal visual field meridian. It was found that glaucoma patients demonstrated a larger Ricco's area than healthy controls in both achromatic and chromatic (S-cone) pathways, and in both inferior and superior hemifields. Furthermore, this difference in Ricco's area completely accounted for sensitivity loss in the patient group. When individual stimulus areas were scaled to match the size of the change in Ricco's area, sensitivity in patients and healthy controls completely overlapped (described further in Chapter 3). Due to these spatial summation changes in glaucoma, when a fixed stimulus size is used for assessing visual sensitivity, such as the use of Goldman size III stimuli in standard automated perimetry (SAP; a commonly-used clinical tool for glaucoma detection and monitoring that relies on spatial summation mechanisms), the rate at which sensitivity declines as a function of RGC loss can be predicted on the basis of the relative area of the stimulus and Ricco's area. Before investigating the possible neural underpinnings of this change, the first aim of the research described in this chapter was to replicate the finding of a larger Ricco's area in glaucoma patients compared to that in age-similar controls.

It was traditionally thought that the size of Ricco's area was determined by retinal receptive field size, particularly those of retinal ganglion cells (RGC; e.g. Brindley, 1954; Volbrecht *et al.*, 2000). However, as discussed previously (Chapter 3), multiple lines of evidence suggest a cortical contribution to Ricco's area. For example, while Ricco's area

enlarges in glaucoma (Redmond *et al.*, 2010), histological studies of experimental glaucoma have found that RGC dendritic trees shrink before cell death in glaucoma, which would assumably lead to shrinkage of the associated receptive field (Morgan, 2000, 2002; Peichl & Wässle, 1983; Weber *et al.*, 1998). In addition, Ricco's area decreases as the blue-background luminance increases (Redmond *et al.*, 2013). The same phenomenon, observed with achromatic stimuli, is attributed to increased contribution from the antagonistic retinal receptive field surround. However, concentric centre-surround receptive field configurations are not found within the retina; RGCs mediating the blue/yellow response (small and large bistratified cells) have receptive fields that are co-extensive (Dacey & Lee, 1994). Spatial antagonism in receptive fields of the form S+/S- associated with the blue/yellow pathway (required for such changes with blue background luminance) are first encountered in the visual cortex (the double-opponent cells; Conway, 2001; Conway & Livingstone, 2006). A cortical contribution to Ricco's area is also suggested by the finding that, in individuals with amblyopia (characterised by poorer vision in one eye compared to the other in the absence of ocular disease), Ricco's area is larger than normal when measured with the amblyopic eye but smaller than normal when measured with the fellow eye (Je *et al.*, 2015). Furthermore, binocularly-measured Ricco's area in amblyopes is closer in size to that in non-amblyopic controls. Considering that there is no evidence of thinning of the RGC layers in amblyopia (Chen *et al.*, 2013; Ersan *et al.*, 2012; Szigeti *et al.*, 2014; Xu *et al.*, 2013) but there is evidence of cortical changes in visual responsiveness (Conner *et al.*, 2007; Li *et al.*, 2007), it seems possible that this change in spatial summation has a cortical origin. Clavagnier, Dumoulin, and Hess (2015) found that fMRI-based estimates of cortical receptive field sizes in V1 were indeed enlarged when presenting stimuli to the amblyopic eye. Furthermore, Pan & Swanson (2006) demonstrate that spatial summation with perimetric stimuli can be accounted for by cortical pooling by multiple spatial mechanisms. With all of this evidence in mind, it is entirely plausible, likely in fact, that Ricco's area has a sizeable cortical component.

The research in this chapter therefore aims to investigate the question of how retinal and cortical receptive field sizes contribute to the Ricco's area in a sample of glaucoma patients and age-similar controls, using a combination of psychophysics, electrophysiology, and fMRI. Specifically, it is hypothesised that larger receptive field sizes (at all neural

locations) would be associated with larger estimates of Ricco's area, particularly in the glaucoma cohort. In addition to investigating retinal and cortical receptive field size contributions to Ricco's area, the association between Ricco's area and neural structure at the retina and cortex will also form a secondary investigation. Specifically, the contribution of retinal ganglion cell complex - inner plexiform layer (GCIPL) thickness, as well as cortical thickness and surface area of the early visual area cortices (i.e. V1-3), to the size of Ricco's area will be investigated in both glaucoma patients and healthy controls. It is expected that GCIPL thickness will show a negative association with Ricco's area. Firstly, as mentioned, both RGC shrinkage and degeneration, as well as Ricco's area enlargement, have been found in glaucoma (Morgan, 2000, 2002; Redmond *et al.*, 2010). In addition, there is a statistically significant, albeit weak, relationship between Ricco's area and peripheral grating resolution acuity (a surrogate measure of RGC density) in a combined sample of glaucoma patients and age-similar controls (Redmond *et al.*, 2010). In terms of cortical structure, smaller V1 surface area has been reported to be associated with greater illusion strength (suggesting larger contextual effects and more lateral connections; Schwarzkopf *et al.*, 2011), lower visual acuity (Song *et al.*, 2013, 2015) and stronger, but less precise mental imagery (Bergmann *et al.*, 2016). Furthermore, surface area and cortical thickness appear to have opposed associations with perceptual functions. For example, Song *et al.,* (2015) found that while smaller V1 sizes were associated with lower visual acuity and coarser neural population tuning than larger V1 surface area, thinner V1 cortical thickness was statistically significantly associated with higher visual acuity and finer neural population tuning. This may reflect differences in levels of interconnectivity (Song *et al.*, 2013), which decreases with expanding surface area in order to maintain neural computational speed (Kaas, 2000; Ringo, 1991). The result from Song *et al.,* (2015) not only highlights the importance of examining these measurements of cortical structure separately (rather than with a composite measure, such as volume), but also suggests a direction in which one would expect an association between these variables (i.e. cortical surface area and thickness) and Ricco's area. With this in mind, though the relationship between Ricco's area and cortical structure has not been investigated directly, the hypothesis is that cortical surface area has a negative association with Ricco's area (i.e. smaller surface areas associated with a larger Ricco's area) and that cortical thickness has a positive association with Ricco's area (i.e. thicker cortices will be associated with larger Ricco's area). As the evidence outlined here

suggests a clear direction for the relationship between Ricco's area and the above variables, one-tailed statistical analyses will be undertaken.

11.1.1. Aims

There were two aims of the research described in this chapter:

1) To investigate the size of Ricco's area in glaucoma patients compared to healthy controls in a mid-peripheral region of the visual field. Specifically, it is hypothesised that Ricco's area is larger in glaucoma patients compared to that in controls, similar to what has been previous reported by Redmond *et al.* (2010; tested in different visual field locations).
2) To investigate the contributions of retinal and cortical receptive field size and neural structure to the size of Ricco's area in a cohort of glaucoma patients and age-similar controls using linear modelling.

11.2. Methods

In this cross-sectional study, estimates of receptive field size (at multiple neural locations) and Ricco's area were investigated in a cohort of 34 glaucoma patients and 38 healthy age-similar controls. The aims of the research described here were addressed using a multi-disciplinary approach. Firstly, Ricco's area was estimated at multiple visual field locations using the psychophysical thresholding methodology discussed in previous chapters (e.g., Chapter 7; section 7.4.). Receptive field size in retinal and cortical regions corresponding to the mid-peripheral visual field are estimated via onset-offset PERG (described in Chapter 8) and fMRI pRF mapping (described in Chapter 10;) respectively. OCT was used to calculate ganglion cell – inner plexiform layer thickness (GCIPL; consisting of the ganglion cell layer and the inner plexiform layers) at the retina and structural MRI was used to image grey matter thickness at V1-3d in the cortex. Figure 11.1 illustrates the regions of the visual field sampled by each methodology, superimposed on a standard 24-2 visual field plot. All methodologies were designed to overlap and sample a region in the mid-periphery, which will be focused on for the majority of the analysis and comparisons in this chapter. This region was selected as glaucoma primarily impacts peripheral vision and it also is accessible within the constraints of all imaging technologies.

The PERG and MRI methodology and data described below have been previously described and investigated in Chapters 8 and 10 respectively.

11.2.1. Participants

Ethical approval for this study was obtained from NHS Wales research ethics committee (Cardiff and Vale and Cwm Taf NHS health boards), as well as the Research Ethics Committees within the Cardiff University Schools of Psychology and Optometry and Vision Sciences. Participants were recruited via NHS glaucoma clinics at the Royal Glamorgan Hospital and University Hospital of Wales, as well as via the School of Psychology community panel and Cardiff University Eye clinic. Thirty-four glaucoma patients (median age [IQR]= 67.6 years [59.6,72.5]; 25 primary open angle and 9 normal tension glaucoma) and 38 healthy controls (median age [IQR]= 67.6 years [60.4, 71.9]) were tested. All experimental procedures were carried out monocularly (glaucoma patients left eye [OS]= 20; controls OS= 19).

Due to factors such as drop out (for reasons including discomfort with the MRI environment or PERG procedure), the MRI screening criteria, and incomplete participation due to the COVID-19 pandemic near the end of the study, there were some experimental procedures for which data were unavailable. Table 11.1 provides a list of the number of participants contributing to each measure, as well as the number of participants who have a full dataset. Demographical characteristics are also present in Table 11.1.

Table 11.1 – Participant demographics split via methodology. The 'total sample' refers to every participant recruited for the study, while the 'full dataset' refers to participants with data from every methodology (i.e. MRI, OCT, Ricco's area, PERG).

		Total participant number	Age (years)	MD (dB)	IOP (mmHg)
			Median (IQR)	*Median (IQR)*	*Median (IQR)*
Total sample	*Glaucoma*	34	67.6 (59.6, 72.5)	-4.60 (-8.75, -1.85)	14.50 (12.00, 17.75)
	Healthy Controls	38	67.4 (60.5, 71.9)	0.00 (-0.80, 0.44)	15.00 (13.00, 16.00)
MRI sample	*Glaucoma*	28	67.6 (59.4, 71.7)	-4.60 (-10.10, -1.10)	14.00 (12.00, 15.50)
	Healthy Controls	28	66.6 (59.6, 70.6)	0.08 (-0.77, 0.48)	15.00 (13.00, 16.25)
OCT sample	*Glaucoma*	26	68.0 (58.5, 72.0)	-4.60 (-9.50, -2.44)	13.50 (12.00, 16.50)
	Healthy Controls	33	67.6 (60.8, 72.0)	0.04 (-0.58, 0.47)	15.00 (13.00, 16.00)
Ricco's area sample	*Glaucoma*	32	68.0 (59.1, 73.0)	-4.60 (-8.62, -2.10)	14.00 (12.00, 16.25)
	Healthy Controls	34	66.6 (59.8, 70.6)	0.06 (-0.71, 0.48)	15.00 (13.00, 16.00)
PERG sample	*Glaucoma*	25	67.7 (59.8, 71.5)	-3.42 (-11.19, -1.72)	14.00 (12.00, 15.00)
	Healthy Controls	29	67.7 (63.0, 72.8)	0.04 (-0.58, 0.47)	15.00 (13.00, 16.00)
Full dataset	*Glaucoma*	20	70.5 (64.7, 72.3)	-3.89 (-11.44, -2.10)	13.50 (11.75, 15.00)
	Healthy Controls	20	67.4 (62.4, 70.9)	0.08 (-0.64, 0.49)	15.00 (13.00, 16.00)

11.2.2. Psychophysical estimation of Ricco's area

Measurements of Ricco's area were the same as has been previously described during methods development (see Chapter 7).

Briefly, contrast thresholds were measured with an Octopus 900 perimeter (Haag Streit AG, Koeniz, Switzerland) and the Open Perimetry Interface (OPI; v.1.6.2; Turpin *et al.*, 2012). The OPI is specified in R (v.3.0.2; R core team, 2013) Circular achromatic stimuli were presented at nine visual field locations (see Figure 11.1). Stimuli were presented on an achromatic background of 10 cd/m^2. A chin-and-forehead rest was used to aid in fixation.

A 1-up:1-down staircase and Yes/No response criterion were used to determine individual thresholds (for more detail of these procedures, see chapter 4). Stimuli were consecutively presented to the nine visual field locations. At each location, luminance contrast thresholds were measured for the five Goldmann stimuli (I-V; areas: 0.01, 0.04, 0.15, 0.58, and 2.27 deg^2). Stimuli were presented for 200ms, with a square-wave temporal profile. After each visual field location had been tested, the entire procedure was repeated, with three repetitions in total. The sensitivity threshold could then be averaged across repetitions. The order that the Goldman stimulus areas were presented was randomised for each repetition.

Ricco's area was estimated for each visual field location, using an iterative two-phase regression analysis (using MATLAB software). This two-phase regression methodology for fitting spatial summation data and estimating Ricco's area was discussed in Chapter 4 (section 4.2.2) and has been used in previous literature (e.g. Je *et al.*, 2018; Redmond *et al.*, 2010; Schefrin *et al.*, 1998). This fitting procedure constrains the slope of the first line to -1 (following Ricco's law), but allows the intercept of the first line, slope of the second line, and the breakpoint value to vary. The final estimated breakpoint value is used to represent Ricco's area. Ricco's area was estimated for each visual field location per participant, along with an associated R^2 value in order to determine the goodness-of-fit of the two-phase regression line.

11.2.3. OCT measurement

OCT scans were acquired using a Zeiss Cirrus HD-OCT (Carl Zeiss Meditec, Dublin, CA). As measures of axial eye length (AEL) were required for correct scaling of the OCT

images, AEL was measured using an average of 5 readings from an IOLMaster (Carl Zeiss, Jena, Germany). Macula cube volume scans were taken from the target eye, comprising of 200 x 200 A-scans. The scan angle was 20° x 20° degrees. Two images were taken, with at least a 7/10 quality rating (given by the instrument). The first scan was centred on the fovea (for reference only), and the second scan imaged the upper temporal quadrant of the retina, in order to ensure that the area of retina corresponding to the target region of visual field (in the lower nasal visual field; see Figure 11.1) was included. To do this, the scan was positioned on the retina so that the fovea was in the lower nasal corner of the OCT scan area. Eye-tracking was enabled to minimise the contribution of eye movements. Natural pupils were used, but all images were obtained with minimal room lighting to ensure maximum pupil size (which would thus allow the retina to be more easily imaged).

11.2.3.1. OCT pre-processing

The following processing steps were carried out in the Java-based image processing package Fiji, an open source distribution of ImageJ (Rasband; National Institute of Health, USA; Schindelin *et al.*, 2012; Schneider *et al.*, 2012). As images are initially inverted (i.e. with the foveal pit facing downwards), they are first vertically transformed. Vertical cropping was also completed to remove reflection artefacts that may occur due to stray light within the imaging system. By cropping the images so just the relevant structures remained (i.e. removing excess vitreous and post-choroid, so only the retina and choroid remained), the file size and thus processing times for subsequent steps are reduced.

The image is then converted into TIFF format and loaded into OCT explorer software (The Iowa Reference Algorithms, Retinal Image Analysis Lab, Iowa Institute for Biomedical Imaging, Iowa City, IA; freely available for non-commercial research; e.g. Bogunovi *et al.*, 2015; Guo *et al.*, 2017; Kang Li *et al.*, 2006) for further analysis. Due to optics of both the instrument and participant's eye, magnification effects influence the transverse plane of the OCT scans. In order to ensure accurate structural measurements from these scans, a correction for the individual's AEL was performed (inaccuracy errors associated with not correcting for AEL are outlined by Odell *et al.*, 2011). Lateral scaling for this was calculated as follows:

$$Lateral\ scaling = \frac{2\pi R(\frac{A}{360})}{N_p}$$

Whereby R is the 'retina to nodal point' distance, or vitreous chamber depth, A is the scan angle (in this case, 20°), and N_p is the number of pixels in the scan. R can be calculated using the AEL as follows:

$$R = \left(\frac{AEL - 1.6}{1.34}\right)$$

Whereby AEL is the axial eye length in mm. By using these calculations, the image size in pixels can be converted to feature size in microns.

This software was also used to complete automated segmentation of ten retinal layers (11 boundaries). For an illustration of these layers see Figure 11.2. In order to assess retinal layer thickness from just the area of the retina corresponding to the target peripheral region (see Figure 11.1), a circular mask was used. The radius of this mask was calculated as follows, in order to match the area stimulated by the pRF mapping stimulus:

$$Radius = \left(\frac{L}{A}\right) * PR$$

Whereby L is the image width in mm (which was scaled by the AEL above), A is the scan angle (in this case, 20°), and PR is the radius of the pRF stimulation area to be matched. This mask was centred to be 5.5° superior and 12.5° nasally from the centre coordinate of the fovea. Average GCIPL thickness was extracted from this region and taken forward for future analysis.

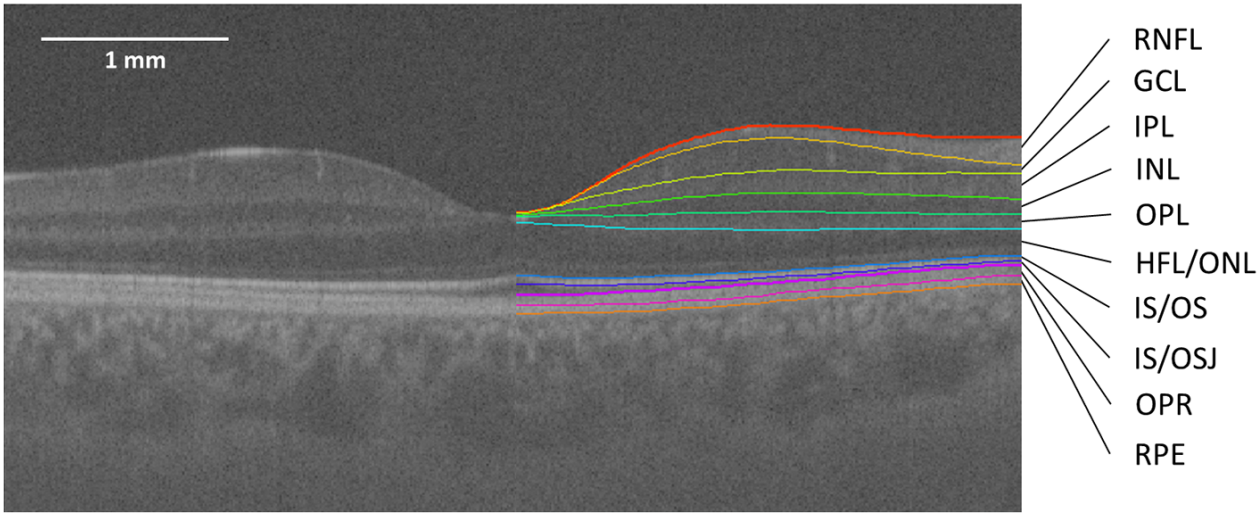

Figure 11.2 – Retinal layers segmented by OCT explorer software, reproduced from Terry et al., (2016). RNFL= retinal nerve fibre layer; GCL= ganglion cell layer; IPL= inner plexiform layer; INL= inner nuclear layer; OPL = outer plexiform layer; HFL/ONL= Henle's fibre layer and outer nuclear layer; IS/OS= photoreceptor inner/outer segments; IS/OSJ= inner/outer segment junction; OPR= outer segment photoreceptor/retinal pigment epithelium complex; RPE= retinal pigment epithelium.

11.2.4. MRI measurement

11.2.4.1. MRI protocol

The MRI data and associated protocol were discussed in detail in chapter 10.

Briefly, fMRI retinotopy scans were acquired on a SIEMENS 7 tesla (7T) MRI scanner (1.5mm^3 isotropic EPIs; TR= 1s, TE= 25ms, Flip angle= 55°, 35 slices, 192 x 192 matrix, multiband= 5). HRF mapping was undertaken with a 1.2mm^3 resolution EPI (TR= 2s; TE= 25ms; flip angle= 76°; 33 slices; FOV= 984 x 984).

11.2.4.2. fMRI stimuli

The stimulus used during the retinotopic mapping fMRI scans was been described previously (see Chapter 6, Chapter 7, and Chapter 10; for an illustration of the stimuli, see Figure 6.4).

The haemodynamic response function (HRF) was mapped using stimuli described in Chapters 9 and 10.

11.2.4.3. Pre-processing and population receptive field mapping

The pre-processing and structural analysis steps are outlined in Chapter 10. FMRIB Software Library (FSL) toolkit (http://www.fmrib.ox.ac.uk/fsl/), FEAT software packages (Jenkinson *et al.*, 2012; Woolrich *et al.*, 2001) and spm fMRI toolbox (http://www.fil.ion.ucl.ac.uk/spm/) was used for pre-processing.

Segmentation and creation of an occipital lobe region-of interest was carried out in FreeSurfer software (Dale *et al.*, 1999; Fischl, 2012).

11.2.4.4. Population receptive field mapping

Following methods development and the comparison of different software packages carried out in chapter 7 (section 7.6), population receptive field (pRF) mapping was undertaken within the SamSrf Matlab toolbox v.7 (available at https://osf.io/2rgsm/). The choice of software package for pRF mapping was discussed during methods development (Chapter 7). The pRF modelling process was the same has been described in Chapter 7 and 10.

11.2.4.5. Retinotopic map quality check and data filtering

As discussed in more detail in Chapter 10 (section 10.2.8), to ensure the inclusion of only maps in which delineation would theoretically be possible, all central retinotopic maps were visually inspected for evidence of a fovea in the eccentricity map and polar angle reversals in the polar angle map, which are standard markers for manual retinotopic delineation (e.g. Sereno *et al.*, 1995). After this process, one healthy control participant and ten glaucoma patients were excluded. Due to the data quality issues with the fMRI data, all pRF data then underwent the same filtering steps as discussed in section 10.2.8. As an overview, these filters were as follows:

- Eccentricities samples were restricted to avoid edge effects. As only the peripheral region is being sampled for this analysis, these eccentricities were 8.7-17°.
- Unrealistic pRF sizes below 0.5° were determined to be noise and removed.
- Modelled pRFs with a β of 0 or less were also removed.
- All results were thresholded so only fits with an R^2 of 0.1 or above were included.
- Only data corresponding to the lower nasal quadrant of the visual field (which should be represented within the dorsal visual areas) were included.

The final pRF sizes were averaged over peripheral eccentricities (8.7-17°) for V1-3d to produce a single peripheral pRF size value for each visual area.

11.2.4.6. Visual area delineation

As discussed previously, it was beneficial for this dataset to utilise an objective basis of delineating visual areas. This was due to inherent noise in the fMRI data leading to difficulties with manual delineation of the retinotopic maps with SamSrf v.7. (see Chapter 7). It also aids in the clarification of the boundary between the area of peripheral stimulation in V2d and V3d, which is relatively ambiguous due to the relatively small amount of cortex stimulated (see Chapter 6). Therefore, a set of probabilistic surface-based labels for V1d, V2d, and V3d were generated on each individual's structural data, modelled on an atlas described by Wang *et al.* (2015). This atlas was constructed using traditional retinotopic fMRI maps (which extended to an eccentricity of 30°). These labels were 'probabilistic' in that they are defined by the likelihood of a given coordinate being associated with a given visual area. Specifically, the labels used were generated by a maximum probability topographic map. This is calculated by classifying each coordinate on the structural surface as the visual area it has the highest probability to be. Due to the atlas being based on retinotopic maps with a maximum eccentricity of 30°, these visual area labels are therefore expected to both include the area of peripheral stimulation used in the current study. To ensure that only cortex corresponding to peripheral vision was included, the visual areas (i.e. V1d, V2d and V3d) were divided into two even length segments along their long axis. This created a 'central representation' segment and a 'peripheral representation' segment. The peripheral segment corresponds to a visual field eccentricity of ~7°-30° of the lower nasal quadrant of the visual field, so will encompass the target region and was taken forward for further analysis. More precise estimation would require cortical magnification or clear peripheral retinotopic maps from all participants and manual estimation; using the current data, the boundary of the visual area may be ambiguous in some participants. By utilising structural estimates of the early dorsal visual areas, structural data could be extracted for all participants, even if, for example, the retinotopic map was excluded.

Using these peripheral labels, FreeSurfer-generated statistics for grey matter cortical thickness (mm) and surface area (mm^2) were extracted for each of the visual areas.

11.2.5. PERG measurement

The PERG protocol and associated data have been described in detail in Chapter 8. To summarise the key points here, onset-offset PERG responses were recorded for a range of spatial frequencies chosen during methods development (see Chapter 7). In order to produce a more spatially specific response, the luminance component of the response was subtracted from the PERG response for each spatial frequency (based on the PERG response to the 1.4 c/deg grating, which is assumed to be only driven by luminance, and the contrast attenuation factor; CAF; based on the methodology outlined by Drasdo *et al.*, 1987), leaving the pattern-specific response (PSR). Using the onset peaks from the recorded PSRs plotted as a function of spatial frequency, a spatial tuning curve can be created. The preferred spatial frequency (i.e. the spatial frequency corresponding to the predicted peak response) of the spatial tuning curve is taken as an estimate of retinal receptive field size.

11.2.6. Analysis

Frequentist tests were carried out in Jasp v.011.1 (JASP Team, 2019). Multiple imputation was completed within the freely available open-source statistical environment, R (R core team, 2020), using the 'mice' package (v.3.12.0; Buuren & Groothuis-Oudshoorn, 2011). Linear models were also computed in R, with the 'lme4' package v1.1 (Bates *et al.*, 2015).

11.2.6.1. Ricco's area in patients with glaucoma and healthy controls

The first aim of the research was to test for a difference in Ricco's area in glaucoma patients compared to that in healthy controls, as reported by Redmond *et al*., (2010) This was done as a way of validating the methods employed here. The four visual field locations in the region of interest in the inferior nasal field (Figure 11.1) were taken forward for all subsequent analysis. Firstly, the goodness-of-fit of the spatial summation functions was investigated. As each spatial summation function has an associated R^2 value describing the strength of the relationship between ΔI and stimuli area, a repeated-measures ANOVA (Greenhouse-Geisser sphericity correction applied) was used to test if the level of goodness-of-fit differed between visual field location or group. Then, in order to ensure that only spatial summation functions with good quality fits between the actual data and the two-

phase regression lines were included in all analysis, the same criteria as discussed previously (Chapter 7) were employed. Thus, Ricco's area values were only included if:

1) The R^2 goodness-of-fit value of the summation curves was above or equal to 0.9, which is a threshold that was been previously used to ensure good quality fit of spatial summation curves (e.g. Je *et al.*, 2018; Redmond *et al.*, 2010).
2) The estimated Ricco's area value was within the range actually presented (i.e. within of the range 0.01 - 2.27 deg^2) to avoid including any spurious estimates.

In order to address the first main aim, the surviving Ricco's area estimates were then compared between glaucoma patients and healthy controls using a repeated-measures ANOVA (between-subject factor: group; within-subject factor: visual field location). The surviving data points were then averaged (i.e. unlogged, the mean taken, then re-logged) for future analysis. As this averaged metric was going to be taken forward, it was also tested for differences between glaucoma patients and healthy controls using a one-tailed independent samples Student's t-test. A one-tailed, directional t-test were used as we had a clear hypothesis of the direction we expected the results to go (i.e. a larger estimate of Ricco's area in glaucoma patients compared to controls) based on previous literature (Redmond *et al.*, 2010).

11.2.6.2. The contribution of retinal and cortical structure and function to Ricco's area

The second aim of the research described within this chapter was to investigate to investigate the contributions of retinal and cortical structure and function to the size of Ricco's area in this cohort of glaucoma patients and age-similar controls. All variables were expressed as log(variable in linear terms) for subsequent analysis.

As a first pass, relationships between all variables were investigated using Pearson's r correlations in a cross-correlation matrix. The purpose of this initial investigation was to identify any possible interdependencies between variables that might be important for subsequent linear modelling. Specifically, relationships between the following variables were investigated:

- Ricco's area
- The spatial frequency corresponding to the peak of the PERG spatial tuning curve
- fMRI-derived measurements of pRF size in V1d, V2d and V3d

- OCT-derived measurements of GCIPL thickness
- MRI-derived measurements of V1d, V2d and V3d surface area
- MRI-derived measurements of V1d, V2d and V3d grey matter thickness

As mentioned previously, an issue with the current dataset is that not all participants completed every experimental procedure. This missing data would lead to pairwise deletion of the whole participant during linear model analysis, leading to only those with a full dataset being analysed. In order to maximise the power obtainable from this dataset and fully utilise the data available, multiple imputation using chain equations (MICE; White *et al.*, 2011) was used to impute missing data. This uses a distribution of observed variables (i.e. the non-missing data) to estimate a set of plausible values for the missing data (plus a random component). MICE generated these data imputations based on a set of imputation models, which can differ per variable; in this case, a linear regression model was used. This process starts with the variable missing the least data (in this case, OCT GCIPL thickness; 11.7% missing), and ends with the variable with the most missing data (in this case, fMRI pRF sizes; 28.9% missing). Multiple imputation cycles were run for all variables in order to stabilise the result and create the final dataset. Following previous guidelines (White *et al.*, 2011), a general rule-of-thumb is to run the least the same about of imputation cycles as there are missing data for the variable with highest amount of missing data, which in this case in 28.9%. Thirty imputation cycles were therefore completed. To avoid bias, all variables were included in imputation. As Ricco's area was the planned output variable of the following linear model (i.e. the variable to be predicted), no imputed data were used for this variable. Therefore, only participants who had Ricco's area data, which had survived the data quality steps described above in at least one of the four visual field locations, were included in MICE and further analysis (34 healthy controls and 28 glaucoma patients).

After an imputed dataset had been generated, the main aim could be addressed; namely, how receptive field size estimates at multiple neural locations contribute to Ricco's area in this cohort of glaucoma patients and age-similar controls. To do this, two sets of models were created. As there were strong predictions for the direction of these effects, one-tailed analyses were performed.

1. Firstly, the effects of the functional variables (fixed effects) on the size of Ricco's area were investigated. Namely, the effect of peak spatial frequency of the PERG

spatial tuning curve, V1d pRF size, V2d pRF size, and V3d pRF size on Ricco's area was investigated. It was hypothesised that all receptive field size variables would show a positive relationship with Ricco's area (H1: beta>0).

2. Secondly, the effect of structural measurements at these neural locations (fixed effects) on Ricco's area was investigated. Specifically, the effect of OCT-derived measurements of GCIPL thickness, V1-3d surface area, and V1-3d grey matter thickness on Ricco's area was investigated. It was hypothesised that both GCIPL thickness and cortical surface area would demonstrate a negative relationship with Ricco's area (H1: beta<0), whereas cortical thickness would show a positive relationship with Ricco's area (H1: beta>0).

In both cases, visual inspection of residual plots was carried out to ensure no notable deviations from homoskedasticity or normality, which are assumptions of the model. Separate models were generated for glaucoma patients and controls in order to investigate whether any significant associations that may be found in healthy individuals may change in disease. Alternatively, relationships may not be apparent in healthy control data, which then become more apparent when the measurement range is extended in glaucoma. To ensure that use of imputed data introduced no bias to the models (as may occur if that data are not missing at random; White *et al.*, 2011), models were rerun with only the complete dataset (i.e. participants who have data for each variables, with no imputed data). These models were examined to ensure that, in all cases, the estimate of each coefficient was similar in both dataset (e.g. went in the same direction) and similar shapes in the residual plots were seen.

The code used for MICE and linear modelling is included in Appendix C.

11.3. Results

11.3.1 Ricco's area between glaucoma patients and healthy controls

11.3.1.1. Spatial summation curves

No significant differences in R^2 were found between group ($F(1,64)= 3.240$; $p= 0.077$), visual field location ($F(2.187, 139.960)= 1.276$; $p= 0.284$), or the interaction term between group and visual field location ($F(2.187, 139.960)= 0.217$; $p= 0.824$).

In order to ensure that only those spatial summation functions with an acceptable fit were taken forward for future analysis, the criteria described above (section 11.2.6.1) were employed. In total (including all 66 participants who underwent psychophysical testing and all four visual field locations), there were 264 spatial summation functions. Out of these, 35 had an $R^2<0.9$, while 23 estimated a Ricco's area value outside of the presented range of stimulus areas. There was a large overlap between these functions (i.e. a spatial summation functions that demonstrated a poor fit defined by one criterion also tended to have a poor fit as defined by the other criterion). Forty-three spatial summation functions were removed due to these criteria, leaving 221 spatial summation functions from 62 participants (28 glaucoma patients and 34 healthy controls).

Figure 11.3 illustrates a representative 'good' (i.e. with an associated $R^2>0.9$) and 'bad' (i.e. with an associated $R^2<0.9$) fitting spatial summation curve for a glaucoma patient and healthy control to demonstrate the difference between a spatial summation function that would and would not be included based on the R^2 criterion.

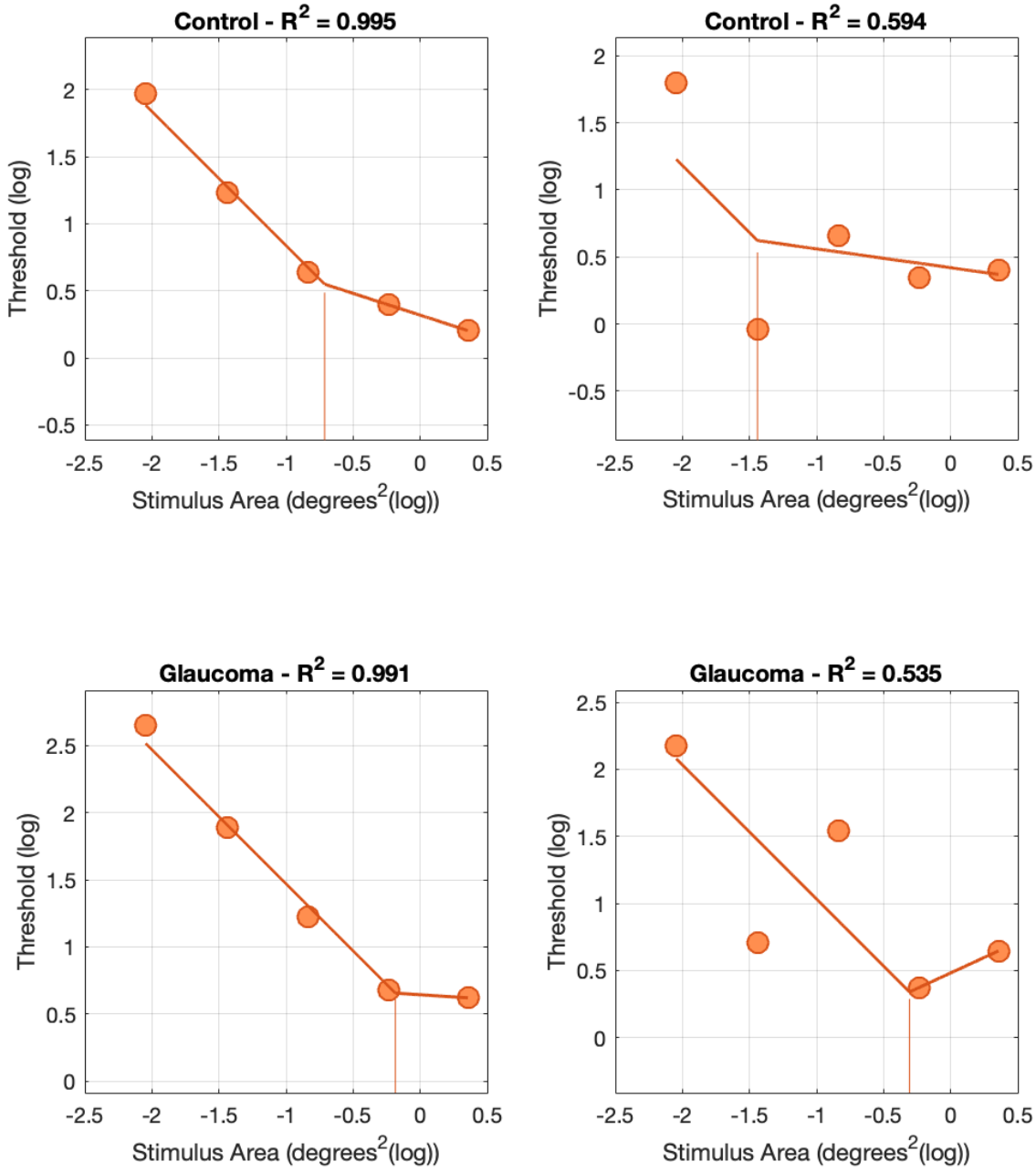

Figure 11.3 – Example spatial summation curves taken from individual participants, illustrating fits that would be above and below the R^2 inclusion criteria for glaucoma patients and healthy controls. The top two plots are from healthy controls, while the bottom two plots are from glaucoma patients. The left two plots are representative spatial summation curves that would be above the 0.9 R^2 goodness-of-fit cut off, whereas the right two plots are representative plots that would be excluded by this criterion. Exact goodness-of-fit values are given above each plot. All curves estimate a Ricco's area (indicated by a red horizontal line) that is within the range of presented stimulus sizes, and so these spatial summation curves would not be excluded for this reason. All curves are from the same visual field location (12.73° eccentricity).

11.3.1.2. Estimates of Ricco's area

The relationship between eccentricity and Ricco's area for the four target locations is illustrated in Figure 11.4 (panel A shows the individual level data while panel B shows the average data for glaucoma patients and healthy controls). As can be seen from these plots, there is a clear positive relationship between eccentricity and Ricco's area estimate, which would be expected from previous literature under photopic conditions (e.g. Je *et al.*, 2018). Also as expected from previous work (Redmond *et al.*, 2010), the glaucoma group demonstrates larger Ricco's area estimates compared to healthy controls across visual field locations. This was tested statistically using a repeated-measures ANOVA (between-subject factor: group; within-subject factor: visual field location). This found the effect of visual field location (i.e. eccentricity) on Ricco's area to be statistically significant ($F(3,135)= 5.528$; $p= 0.001$). However, statistical significance at the $p= 0.05$ level was not reached for group ($F(1,45)= 0.790$; $p= 0.379$) or the interaction term between group and visual field location ($F(3,135)= 0.399$; $p= 0.754$).

The Ricco's area estimates were then averaged across visual field locations (i.e. unlogged, the mean taken, and then relogged) to produce a single peripheral Ricco's area value. To examine whether Ricco's area was significantly enlarged in glaucoma patients compared to healthy controls, a one-tailed Student's t-test was completed. It was found that glaucoma patients (Ricco's area mean= -0.605; Standard Deviation [SD]= 0.306) had a statistically significant larger Ricco's area compared to healthy controls (Ricco's area mean= -0.736; SD= 0.255) in the mid-periphery ($t(60)= -1.843$; $p= 0.035$).

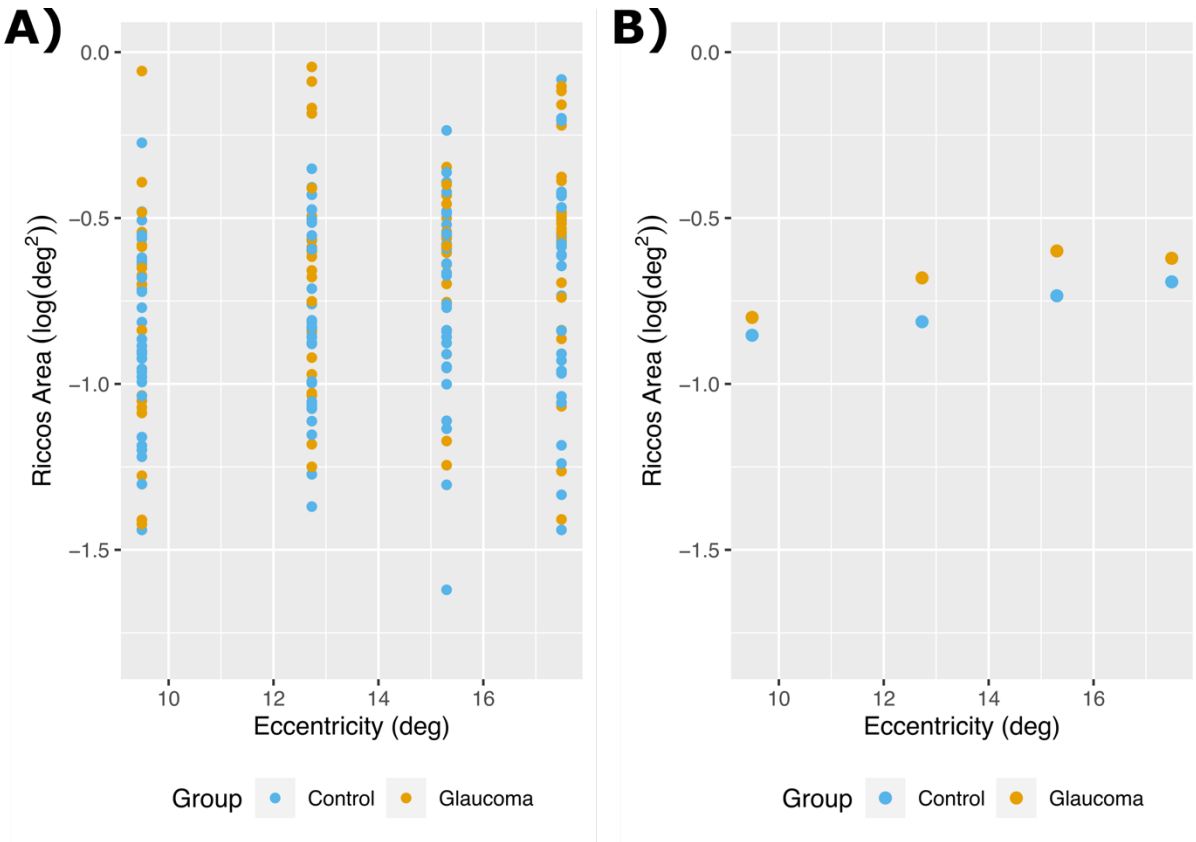

Figure 11.4 – Ricco's area estimated (log stimulus area) as a function of eccentricity of the visual field location at which it was measured, split by group. Orange= Glaucoma. Blue= Controls. A) individual datapoints for each participant. B) group averages.

11.3.2. Cross-correlation matrix

A cross-correlation matrix (Pearson's r correlation coefficient) between experimental variables. The statistical values from this correlation matrix are detailed in

Table 11.2 and also presented a heatmap in Figure 11.5. As expected, several relationships between structural cortical variables are seen, which may be driven in part by overall brain size. Specifically, V1d surface area was significantly and positively related to V2d surface area ($r(56)= 0.471$; $p<0.001$) and V3d surface area ($r(56)= 0.366$; $p= 0.006$). Additionally, V2d cortical thickness is positively associated with V3d cortical thickness ($r(56)= 0.370$; $p= 0.005$), as well as with V2d pRF sizes ($r(45)= 0.310$; $p= 0.038$). pRF sizes from V1d and V2d also demonstrated a significant positive correlation ($r(45)= 0.302$; $p= 0.043$), possibly reflecting the relationship between surface area measurements in V1d and V2d.

Interestingly, GCIPL thickness showed a significant relationship with several cortical measurements. GCIPL thickness was significantly and positively associated with V1d cortical thickness ($r(50)= 0.358$; $p= 0.011$) and also V3 pRF size ($r(40)= 0.405$; $p= 0.009$).

Ricco's area did not show a statistically significant correlation with any variable.

*Table 11.2 – Pearson's r correlation matrix. Significant correlations are bolded and underlined. PERG= pattern electroretinography; pRF= population receptive field; GCIPL= ganglion cell- inner plexiform layer. The dorsal regions of all visual areas (V1-3) sampled. *= p<0.05, **= p<0.01, ***= p<0.001*

Variable		Ricco's area	PERG peak	V1 pRF	V2 pRF	V3 pRF	V1 surface	V1 thickness	V2 surface	V2 thickness	V3 surface	V3 thickness	GCIPL thickness
1. Ricco's area	n	—											
	Pearson's r	—											
	p-value	—											
2. PERG peak	n	48	—										
	Pearson's r	-0.178	—										
	p-value	0.226	—										
3. V1 pRF	n	43	37	—									
	Pearson's r	-0.133	-0.016	—									
	p-value	0.395	0.925	—									
4. V2 pRF	n	43	37	**45**	—								
	Pearson's r	-0.133	0.101	**0.302** *	—								
	p-value	0.394	0.553	**0.043**	—								
5. V3 pRF	n	43	37	45	45	—							
	Pearson's r	0.042	7.433e -4	0.253	0.134	—							
	p-value	0.791	0.997	0.094	0.382	—							
6. V1 surface	n	52	45	45	45	45	—						
	Pearson's r	-0.017	0.084	-0.193	0.053	-0.086	—						
	p-value	0.906	0.584	0.205	0.731	0.574	—						
7. V1 thickness	n	52	45	45	45	45	56	—					
	Pearson's r	-0.169	0.163	0.023	0.108	0.084	0.011	—					
	p-value	0.231	0.284	0.879	0.479	0.584	0.934	—					
8. V2 surface	n	52	45	45	**45**	45	**56**	56	—				
	Pearson's r	-0.137	0.170	0.019	**0.310** *	0.136	**0.471** ***	0.012	—				
	p-value	0.333	0.264	0.900	**0.038**	0.373	**< .001**	0.931	—				
9. V2 thickness	n	52	45	45	45	45	56	56	56	—			
	Pearson's r	-0.132	0.183	-0.165	-0.130	0.041	0.179	0.226	0.093	—			
	p-value	0.352	0.230	0.278	0.394	0.788	0.187	0.094	0.497	—			
10. V3 surface	n	52	45	45	45	45	**56**	56	56	56	—		
	Pearson's r	0.130	0.268	-0.131	-0.217	-0.205	**0.366** **	-0.037	0.216	0.146	—		
	p-value	0.357	0.075	0.393	0.153	0.176	**0.006**	0.785	0.110	0.284	—		
11. V3 thickness	n	52	45	45	45	45	56	56	56	**56**	56	—	
	Pearson's r	-0.050	0.255	-0.111	0.169	0.027	0.018	-0.007	-0.026	**0.370** **	-0.065	—	
	p-value	0.727	0.090	0.469	0.268	0.859	0.895	0.961	0.851	**0.005**	0.635	—	
12. GCIPL thickness	n	51	48	40	40	**40**	50	**50**	50	50	50	50	—
	Pearson's r	-0.137	-0.047	0.122	0.037	**0.405** **	-0.136	**0.358** *	-0.063	0.238	-0.179	0.187	—
	p-value	0.339	0.750	0.453	0.821	**0.009**	0.346	**0.011**	0.666	0.097	0.214	0.194	—

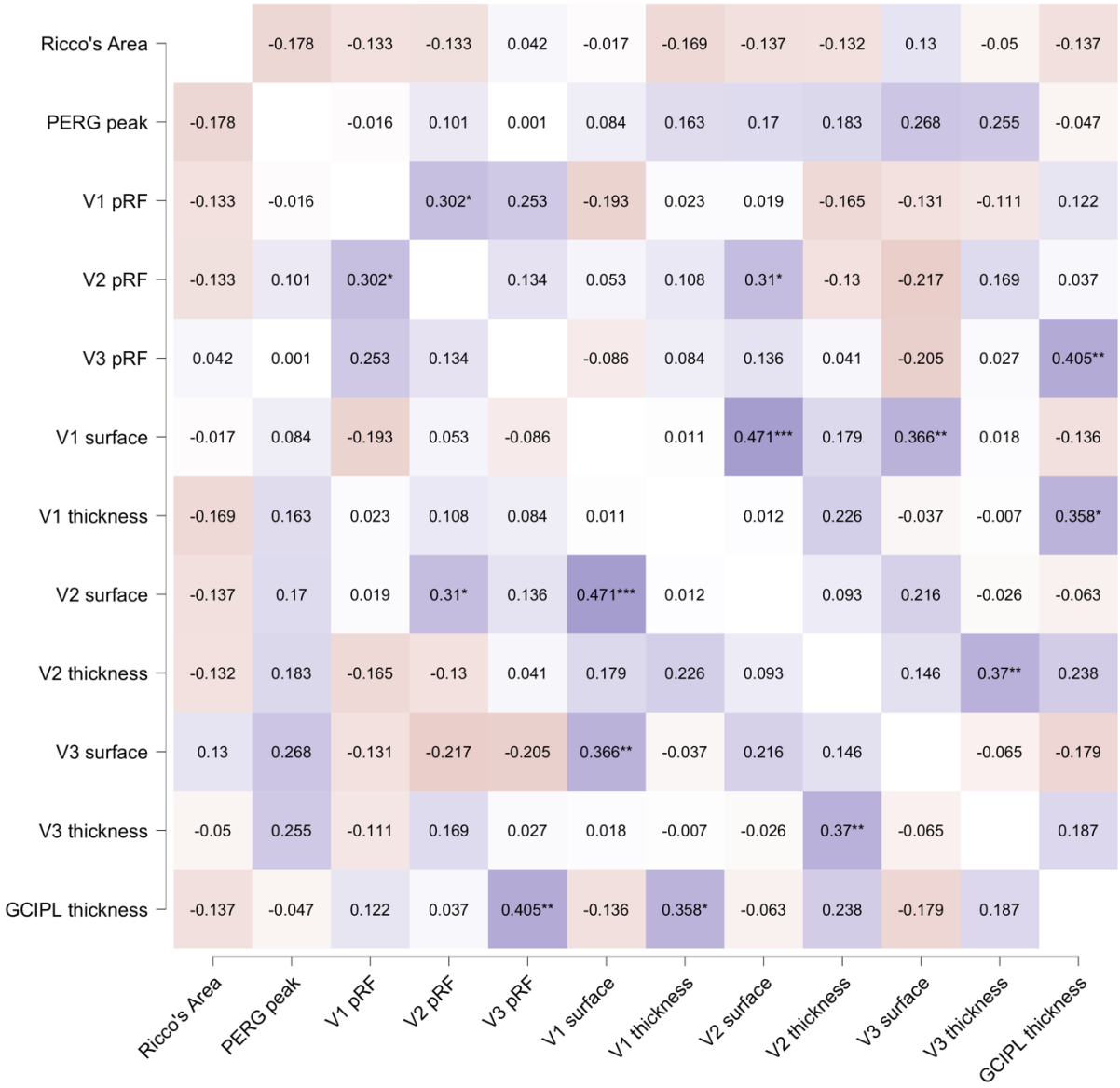

Figure 11.5 – Heatmap of Pearson's r correlation matrix. Cool colours= more positive Pearson's r; Warm colours= more negative Pearson's r. PERG= pattern electroretinography; pRF= population receptive field; GCIPL= ganglion cell- inner plexiform layer.

**= p<0.05, **= p<0.01, ***= p<0.001*

11.3.3. Modelling of retinal and cortical receptive field size contributions to Ricco's area

11.3.3.1. Functional model

In order to investigate the contribution of receptive field sizes at the retina and V1-3d to Ricco's area, linear models were computed for both glaucoma patients and healthy

controls separately. With all models, residual plots were visually inspected and showed no notable deviations from homoscedasticity or normality.

For healthy controls, this model was not statistically significant ($F(4,29)= 1.34$; $p= 0.279$; $R^2= 0.156$; $R^2_{Adj} = 0.040$). From the individual parameters, PERG peak spatial frequency did not significantly predict Ricco's area in healthy controls (estimate = -0.289; 95% confidence intervals [CIs]= -1.120, 0.537; p= 0.760). The effect of pRF size in V1d on Ricco's area was also not statistically significant (estimate = -0.0003; 95% CIs= -1.095, 1.095; p= 0.500), nor was the effect of pRF size in V2d (estimate = -0.915; 95% CIs= -2.105, 0.275; p= 0.937), or V3d (estimate= 0.757; 95% CIs= -0.330, 1.845; p= 0.083).

For glaucoma patients, the overall model was also not statistically significant ($F(4,23) = 0.569$; $p = 0.688$; $R^2= 0.090$; $R^2_{Adj}= -0.069$). Looking at the individual parameters, PERG peak spatial frequency did not significantly predict Ricco's area in glaucoma patients (estimate= -0.382; 95% CIs= -1.789, 1.025; p= 0.710). The effect of pRF size on Ricco's area in V1d was also not statistically significant (estimate= -1.232; 95% CIs= -3.277, 0.812; p= 0.888), nor was the effect of pRF size in V2d (estimate= -0.385; 95% CIs= -1.668, 0.899; p= 0.729) or V3d (estimate= 0.523; 95% CIs= -1.305, 2.350; p= 0.280).

All models were repeated with non-imputed data and a manual inspection found no marked changes in coefficient estimates or residual plots compared to models run with imputed data, suggesting that no bias was introduced with the use of imputed data.

11.3.3.2. Structural models

In order to investigate the contribution of retinal and cortical structure to Ricco's area, linear models were computed separately for both glaucoma patients and healthy controls. With all models, residual plots were visually inspected and showed no notable deviations from homoscedasticity or normality.

For healthy controls, the overall structural model did explain a significant amount of variance in Ricco's area ($F(7,26)= 3.048$; $p= 0.0176$; $R^2= 0.451$; $R^2_{Adj}= 0.303$). This suggests that this model explained 30.3% of variance in Ricco's area values in this cohort of healthy controls. Looking at the individual one-tailed parameters, GCIPL thickness did not have a significant effect on Ricco's area in healthy controls (estimate= 2.509; 95% CIs= 0.708, 4.309; p= 0.996). In terms of surface area measurements, no statistically significant contribution to

Ricco's area was found in V1d (estimate= 0.350; 95% CIs= -1.336, 2.063; p= 0.663), V2d (estimate= -0.893; 95% CIs= -2.128, 0.342; p= 0.075), or V3d (estimate= 1.448; 95% CIs= 0.593, 2.303; p= 0.999). In terms of average grey matter thickness between the different visual areas, no statistically significant contribution to Ricco's area was found in V1d (estimate= -3.064; 95% CIs= -5.369, -0.759; p= 0.994), V2d (estimate= -1.499; 95% CIs= -3.321, 0.324; p= 0.948) or V3d (estimate= 0.908; 95% CIs= -1.758, 3.574; p= 0.245).

For glaucoma patients, the overall structural model did not explain a significant amount of variance in Ricco's area ($F(7,20)= 0.6172$; $p= 0.7356$; $R^2= 0.178$; $R^2_{Adj}= -0.110$). Looking at the individual one-tailed parameters, GCIPL thickness did not have a significant effect on Ricco's area in glaucoma patients (estimate= -3.705; 95% CIs= -8.566, 1.156; p= 0.064). In terms of cortical surface area, no statistically significant effect on Ricco's area was found in V1d (estimate= 0.509; 95% CIs= -2.101, 3.119; p= 0.656), V2d (estimate= -0.342; 95% CIs= -2.122, 1.439; p= 0.347), or V3d (estimate= -0.466; 95% CIs= -2.277, 1.345; p= 0.299). In terms of cortical grey matter thickness, no statistically significant effect on Ricco's area was not found in V1d (estimate= 0.6963; 95% CIs= -2.357, 3.749; p= 0.320), V2d (estimate= -1.635; 95% CIs= -5.096, 1.825; p= 0.832), or V3d (estimate= 1.106; 95% CIs= -3.053, 5.086; p= 0.304).

All models were repeated with non-imputed data and a manual inspection found no marked differences in the direction of coefficient estimates or residual plots compared to models run with imputed data, suggesting that no bias was introduced with the use of imputed data.

11.4. Discussion

The research described in this chapter was an investigation of how receptive field size at multiple neural hierarchies contribute to the size of Ricco's area in glaucoma patients and age-similar controls. In order to estimate receptive field sizes at both the retinal and cortical level, spatial tuning curves (PERG) and pRF maps (fMRI) were measured respectively. In addition, the contribution of structural measurements (GCIPL thickness, cortical thickness, surface area) to Ricco's area was also investigated with OCT and structural MRI.

The first aim of the research described here was to replicate previous results reporting an enlarged Ricco's area in glaucoma patients compared to that in age-similar controls (Redmond *et al.*, 2010). The expected increase in Ricco's area with eccentricity (e.g. as in Wilson, 1970) was found in both groups. While glaucoma patients in this cohort also demonstrated an enlarged Ricco's area on average when compared to healthy controls, this was not significant when tested using a repeated-measures ANOVA. This may be due to the fact that glaucoma patients may not demonstrate enlargement of Ricco's area across all eccentricities due to localised retinal damage. Therefore, glaucoma patients would demonstrate greater variance than healthy controls, reducing the likelihood of finding a statistically significant difference. Alternatively, this may be due to the fact this test handles missing data via pairwise deletion, leading to a reduced sample size (pairwise deletion of participants with missing data left 16 glaucoma patients and 31 controls). When Ricco's area values were averaged over the peripheral region, so that any participant with a least one well-fitting spatial summation function in the test region was included, glaucoma patients were found to have a significantly larger Ricco's area value compared to healthy controls. This result therefore replicates the original finding reported by Redmond *et al.,* (2010) in several different visual field locations within the mid-periphery.

The second aim of this research was to investigate the contribution of retinal and cortical receptive field size and structural parameters to Ricco's area in glaucoma patients and age-similar controls. To address this aim, multiple methodologies were utilised in order to measure retinal GCIPL thickness, retinal receptive field size, cortical receptive field size, and visual area cortical thickness and surface area (using OCT, PERG spatial tuning curves, fMRI pRF mapping and structural MRI respectively).

Relationships between these variables were initially explored using a Pearson's r cross-correlation matrix. Several relationships were found between cortical structural measurements in the cross-correlation table, such as between V1-3d surface areas, replicating previous work (e.g. Song *et al.*, 2015). This likely reflects an effect of overall brain size on the size of the visual areas as a whole. Specifically, larger brains have been found to be associated with smaller V1 surface areas (Schwarzkopf *et al.*, 2011). If this relationship holds true across visual areas, this may explain the relationships between visual areas reported in the current study. Another significant finding was a positive association between

GCIPL thickness and V1 thickness in this sample of glaucoma patients and age similar controls (r= 0.358). Jorge *et al.,* (2020b) found that V1 cortical thickness, ganglion cell layer (GCL) thickness, and inner plexiform layer (IPL) thickness all demonstrate a significant negative correlation with age in a sample of healthy participants aged 23 to 79 years old. Furthermore, they found that V1 thickness demonstrated a significant positive correlation with multiple retinal layers, including GCIPL, though suggested that this relationship may be mostly explained by age effects. In line with our results, other research has also suggested a link between GCIPL thickness and occipital lobe grey matter volume (Liu *et al.*, 2016), though the use of volume as a structural metric prevents the separate effects of surface area and cortical thickness to be investigated, as was done with the current study. Jorge *et al.,* (2020a) investigated the link between V1 cortical thickness and IPL thickness in a sample of AD patients and healthy age-, education- and sex-matched controls. They found that thicker IPLs were significantly associated with thicker V1 cortices, though this occurred only in the patient group. Overall, these studies highlight the relationship between GCIPL and V1 cortical thickness, which was replicated here in a mid-peripheral region a sample of glaucoma patients and age-similar controls. Multiple studies have found decreased cortical thickness in glaucoma patients compared to that in healthy controls (Wang *et al.*, 2016; Yu *et al.*, 2014, 2015), which was related to other retinal structures, namely cup-to-disc ratio (Wang *et al.*, 2016) and retinal nerve fibre layer thickness (Yu *et al.*, 2015). The relationship between V1d surface area and GCIPL thickness in glaucoma should be further interrogated by investigating the relationship between GCIPL thickness at both central and peripheral regions compared to cortical thickness of the corresponding area of V1. Considering that glaucoma is primarily a peripheral disease and had previously demonstrated reduced grey matter volume at the anterior portion of V1 (corresponding to peripheral regions; Zhang *et al.*, 2015), it may be predicted that this relationship would be particularly strong in the periphery.

Linear models were then used to investigate the contribution of receptive field size at the retina and cortex to Ricco's area values. Relationships within healthy controls and glaucoma groups were tested for separately. Similar results were found in each group, with neither retinal receptive field sizes (estimated using PERG spatial tuning curves) nor V1-3d cortical pRF sizes significantly explaining variation in Ricco's area. The initial hypothesis

could not, therefore, be accepted on the basis of these data. This apparent disconnect between pRF sizes and psychophysical results has been found in previous research. For example, Welbourne *et al.,* (2018) investigated the relationship between psychophysically measured spatial selectivity and pRF size in achromatic, L-M-cone, or S-cone isolating conditions. They found that, despite psychophysical responses to achromatic stimuli demonstrating a bias for higher spatial frequencies compared to the chromatic stimuli, there was no difference in pRF sizes in either the chromatic or achromatic conditions. The authors suggest that this may be due to the population of simple verses complex cells that contribute to the pRF signal. The individual contribution of these cell types may be indistinguishable in the BOLD signal, as it mostly reflects local field potentials (Logothetis *et al.*, 2001). The relationship between spatial tuning and receptive field size is present in simple cells but breaks down with complex cells (Movshon *et al.*, 1978). It is possible that a contribution of complex cells may also explain the lack of relationship between Ricco's area and pRF size in the current study. This may be better addressed using stimuli that specifically target spatial tuning of cortical cells rather than pRF size (e.g. population spatial frequency tuning mapping; Aghajari *et al.*, 2020). Calderone *et al.* (2013) also report a disconnect between psychophysical and fMRI results, in that psychophysically-measured contrast sensitivity deficits present in schizophrenia patients compared to those in controls were not reflected in fMRI responses to the same stimuli. However, the psychophysical results were reflected in electrophysiological steady-state visual evoked potentials. This may suggest that while the psychophysical results may reflect the underlying neural activity, this relationship is obscured by the metabolic and neurovascular process that connect neural activity to BOLD fMRI signal.

One of the possible reasons for the lack of association found between Ricco's area and peak spatial frequency from the PERG spatial tuning curve is the region of retina sampled. Due to the inherently small signal afforded by PERGs, a relatively large region of retina needs to be stimulated in order to obtain a useable signal. In the current study, a sizeable region of the mid-periphery was sampled in order to gain sufficient PERG signal for comparison with our other measures. The caveat was that this region was much larger than that region within which Ricco's area was measured and thus, in patients with early glaucoma, localised defects may have had less influence on the measurement than

surrounding healthy regions. This, in turn, may have limited the glaucoma signal with the PERG, i.e. the difference in the measure between patients and healthy controls, and thus the ability to precisely relate PERG features to psychophysical and objective measures. However, efforts were made to limit the boundaries of the stimulated region to those most likely to be affected in glaucoma while maintaining sufficient signal. Another potential issue (as mentioned previously in the discussion section of Chapter 10) is differences between stimuli used in the psychophysics, fMRI and PERG experimental tests. Stimuli used in the determination of detection thresholds and subsequently the estimation of Ricco's area have a brief presentation duration and only those neural units with the highest sensitivity determine threshold. The stimuli for PERG and fMRI however, have 100% contrast and are substantially supra-threshold, in order to ensure sufficient SNR in the elicited signal. These stimuli are more likely to be detectable by neural units with lower sensitivity than those that are sensitive enough to mediate vision near threshold. There may therefore be different (or different proportions of) neuronal sub-populations contributing to the signals. On the other hand, similar pRF sizes in a subsample of glaucoma patients and healthy controls were found when compared traditional high-contrast and 20% contrast pRF stimuli in an exploratory study in Chapter 10. However, it is possible that differences would have been found if the contrast was reduced further to threshold (e.g. 2%).

Another possible contributor to the lack of a statistically significant association between the functional variables in this study is the level of noise in the imaging methodologies used, which may arise from different sources depending on the particular methodology. For example, the BOLD signal relies on numerous physiological factors (e.g. basal cerebral blood flow; Brown *et al.*, 2003; Cohen *et al.*, 2002; Stefanovic *et al.*, 2006; for further discussion, see Chapters 4 and 9), which can in turn be influenced by numerous external factors, such as caffeine intake (e.g., Addicott *et al.*, 2009; Perthen *et al.*, 2008), time of day (e.g. Conroy *et al.*, 2005; Elvsåshagen *et al.*, 2019), or amount of sleep (e.g. Elvsåshagen *et al.*, 2019). While it seems unlikely that these factors would differ between groups (i.e. healthy controls compared to glaucoma patients) and the influence of these is somewhat controlled for by the use of individual HRFs for convolution, it is possible that varying levels in these external factors could lead to increased variation in some of the physiological processes underlying the BOLD signal, leading to within-group noise in the

dataset. Similarly, the PERG signal is relatively small and can be noisy, varying with factors such as exact placement under the lower fornix, which is difficult to standardise between participants. It is possible that these sources of noise in the different methodologies caused an increased difficulty in detecting a statistically significant relationship between the experimental variables.

Finally, it should also be considered that, though evidence suggests that there is a cortical contribution to Ricco's area, this may not lie in the early visual areas tested in this study. These locations (i.e. v1-3) were initially considered as Pan and Swanson (2006) highlighted the importance of orientation-sensitive cortical pooling processes in the processing of perimetric stimuli, which start to become prevalent in V1 (e.g. Hubel & Wiesel, 1959). However, it is possible that the cortical contribution to Ricco's area lies higher up the cortical visual hierarchy. For example, glaucoma patients demonstrate reduced cerebral blood flow and functional connectivity across the brain, including extra striate visual areas (involved in the 'what' and 'where' visual streams; Wang *et al.*, 2018, 2020) and executive function networks (Wang *et al.*, 2020). These results may therefore suggest that a more thorough investigation of pRF sizes across the cortex is necessary in glaucoma patients, with direct comparison to Ricco's area.

Models were then created to investigate the contribution of structural measures to estimates of Ricco's area. Similar to the investigations of the contribution of functional measures to Ricco's area described above, no significant effects of structural measures were reported in either group. This may be due to the range of glaucoma severities included. As the majority of participants had early glaucoma (as enough residual vision had to be present for the retinotopic fMRI mapping to be completed), it is possible that there was an insufficient range of values (e.g. in Ricco's area and GCIPL thickness) for relationships to be identified. The absence of a statistically significant relationship between GCIPL thickness and Ricco's area could also reflect the fact that, as noted by Redmond *et al.*, (2010), the relationship between RGC density (using peripheral grating acuity as a surrogate marker) and Ricco's area was relatively weak.

An interesting note is that, while the individual parameters did not show a significant association in the hypothesised direction, the structural model for Ricco's area in healthy controls (but not glaucoma patients) was statistically significant overall. An examination of

the estimates and CIs for the individual parameters suggest that this may be driven by GCIPL thickness, V3d surface area, and V1d cortical thickness, which show estimates in the opposite direction as was hypothesised (with CIs that do not cross zero). This is counter to what may be predicted based on previous research; for example, smaller surface area and larger cortical thickness are associated with lower visual acuity (Song *et al.*, 2015), and acuity is inversely related to spatial summation. It therefore appears contradictory that smaller surface area and larger cortical thickness would be statistically associated with a smaller Ricco's area in the healthy control sample described here. However, this could reflect a possible constant number of cortical cells underlying Ricco's area (possibly determined in turn by the underlying number of RGCs that underlie Ricco's area, which is suggested to be ~14 [Kwon & Liu, 2019] or 31 RGCs [Swanson *et al.*, 2004] depending on the model). Larger visual areas have a larger number of neurones, but at a lower density, with more non-neural cortical tissue between neuronal soma (de Sousa *et al.*, 2010; de Sousa & Proulx, 2014). Ricco's area may therefore reflect the density of neurones within the visual cortex, a relationship which then breaks down in disease (possibly due to other compensatory mechanisms leading to the increase in Ricco's area). However, as the models described by Kwon and Liu (2019) and Pan and Swanson (2006) specifically investigate and find evidence for V1 cortical pooling mechanisms, this would not explain why the association between surface area and Ricco's area was found for V3d and not V1d in the current study.

A possible limitation to these data is the previously described noise in the pRF data (see Chapter 7 and 10). For example, the slope of the relationship between pRF size and eccentricity in healthy controls appears to be less than that found in previously published research. Also, glaucoma patients demonstrated a higher level of exclusion due to poor retinotopic maps compared to healthy controls. This may suggest that in general, the glaucoma patients in this cohort had noisier fMRI data than healthy controls, possibly due to lower SNR across the visual system. It is also possible that cortical receptive fields in glaucoma demonstrate a deviation from the 2D Gaussian model commonly used in pRF modelling, which may better represent pRF models in healthy controls. If, for example, the underlying pRF in glaucoma demonstrates a more elongated shape, this may not be discernible when modelling with a Gaussian fit and may only be reflected as poorer model

fits. It may then be beneficial to investigate this issue using less rigid pRF mapping, such as multivariate Gaussian models (which allows for modelling of horizontal and vertical pRF axis) or model-free approaches. It should also be reiterated that substantial noise in pRF data was found across both groups, which lead to difficulties with visual area delineation (described in Chapter 7).

Overall, the data described in this chapter do not provide evidence to support the initial hypothesis that cortical receptive field sizes would make a significant contribution to determining the size of Ricco's area. However, this is not to say that evidence has been found *against* a contribution of retinal or cortical receptive field size to Ricco's area. With the evidence for both a cortical and retinal contribution to Ricco's area in mind, as well as the sources of noise described in these data, it is possible that this noise is obscuring underlying relationships in the data, despite steps taken to minimise this (e.g. pRF software selection in Chapter 7). However, the finding of an increased steepness in the relationship between V1d pRF size and eccentricity in glaucoma patients compared to controls warrants further investigation. In addition, several cortical modelling approaches have been suggested that may better reflect the underlying relationship between cortical receptive field sizes and Ricco's area.

Chapter 12 – Overall discussion and future work

12.1. Overall discussion

The main aim of this thesis was to investigate the contribution of retinal and cortical receptive field size to Ricco's area in a sample of glaucoma patients and age-similar controls. Ricco's area has been found to enlarge in glaucoma compared to healthy observers in both chromatic and achromatic pathways (Redmond *et al.*, 2010). As outlined at multiple points throughout this thesis (specifically Chapter 3), while Ricco's area was traditionally thought to reflect retinal receptive field size, several lines of evidence suggest that there may be a substantial cortical contribution. Pan and Swanson (2006; Swanson *et al.*, 2004) describe a two-stage neural model for spatial summation across perimetric stimuli and demonstrate that only by including cortical pooling by multiple spatial mechanisms (as opposed to retinal ganglion cell [RGC] probability summation alone) can perimetric spatial summation be explained. The studies described in this thesis interrogated receptive field size across the visual pathway in a sample of glaucoma patients and healthy age-similar controls in order to investigate the factors that determine the size of Ricco's area.

Prior to investigating cortical receptive field sizes within this clinical cohort, development of the associated method was carried out within Chapter 6 and Chapter 7. Due to field of view and space restrictions within the 7 Tesla (7T) magnetic resonance imaging (MRI) environment, mapping of cortical receptive field sizes (via population receptive field [pRF] mapping; Dumoulin & Wandell, 2008) had to be completed in two separate runs; one for central vision (mapping out to 5.5°) and one for a region in the mid-periphery (7.7 to 18.7°), which was also targeted with other objective imaging methodologies later in the thesis. Mapping the periphery with pRF mapping in this way was completed successfully in a sample of healthy young adults.

Several issues were brought to light during this pRF methodology development, which was later addressed in further methods development in Chapter 7. For example, the original pRF mapping run was quite long at ~7.5 minutes per run (mapping both central and peripheral vision would therefore take ~15 minutes, and this was typically repeated at least twice) so multiband imaging was introduced in Chapter 10 to cut time and help reduce

participant fatigue in the older sample. This cut the time for a single run to ~2.5 minutes. After initially analysing pRF data from the clinical cohort with SamSrf v.5., it was also discovered that several issues may limit interpretation of this data, such as erroneous estimation, in many cases, of pRFs centred outside of the stimulation area. Multiple software packages were therefore investigated (SamSrf v.5., SamSrf v.7., and AFNI) in a small sample of healthy controls and it was decided that SamSrf v.7. was most appropriate for this dataset. However, substantial noise was discovered within the data, which lead to the need for stringent data quality criteria (discussed in Chapter 10). This noise in the final maps led to difficulties in using the standard approach of manual parcellation of the retinotopic maps. Manual delineation of visual areas (e.g. V1-3) is commonly carried out on smoothed retinotopic maps in order to smooth over gaps in the map and make important features (such as polar angle phase reversals or the foveal eccentricity gradient; e.g. Sereno *et al.*, 1995) easier to distinguish. However, the low SNR of this dataset led to this smoothing removing such features from the maps, despite being visible in the unsmoothed maps. An additional issue with manual delineation was that the boundary between the peripheral regions of V2 and V3 was difficult to delineate in most participants, as the stimulated region is close to the horizontal meridian and a relatively small amount of the cortex is stimulated. Probabilistic visual area labels based on the individual structural scans and the atlas described by Wang *et al.,* (2015) were therefore used in the main pRF investigations in the glaucoma cohort.

As part of these early experiments, associations between pRF size and myopia were also investigated by extending the original healthy young adult sample to include additional participants with high refractive error (i.e. 7.00+ dioptre refractive error). A significant correlation was found between pRF centre size and refractive error/axial eye length, despite MR-safe vision correction, suggesting that more myopic participants demonstrate larger pRF sizes, especially in the periphery. This result suggests that myopia is an important factor to consider in future visual MRI studies, especially when examining pathologies that may be associated with a higher myopia rate as this may confound results despite visual correction. This finding may be due to the output from the retina changing with myopia despite refractive error correction (e.g. due to retinal stretching), consistent with studies showing that Ricco's area also varies with myopia with spectacle correction (Stapley *et al.*, 2020). In

the main glaucoma cohort, an exclusion criterion was therefore put in place to exclude participants with a refractive error greater than 6 dioptres.

Chapter 8 described research investigating retinal receptive field sizes in glaucoma compared to healthy controls. To do this, pattern electroretinography (PERG) spatial tuning curves were measured, with the predicted peak used to generate an estimate of average retinal receptive field size for the stimulated area. Furthermore, following methodology outlined by Drasdo *et al.* (1987), the component of the PERG response that was purely elicited by luminance was removed from each PERG response, leaving the pattern-specific response (PSR). It is suggested that the PSR better reflects spatially-selective RGCs (Drasdo *et al.*, 1990). It was found that the peak of the generated spatial tuning curve was at a statistically significantly lower spatial frequency (in cycles per degree) in glaucoma compared to controls, suggesting slightly larger retinal receptive field sizes, possibly due to compensatory effects of surrounding cells (as discussed in Chapter 8). It was also found that the amplitude of the spatial tuning curve was significantly decreased in glaucoma patients compared to controls. This PERG amplitude was also found to explain a significant amount of variation in perimetric sensitivity. This supports previous findings suggesting a loss of PERG amplitude in glaucoma patients compared to controls (e.g. Almrcegui Lafita *et al.*, 1997; Bach & Hoffmann, 2008; Bobak *et al.*, 1983; Ganekal *et al.*, 2013; Hiss & Fahl, 1991; Tiryaki Demir *et al.*, 2015; Uclés *et al.*, 1997; Viswanathan *et al.*, 2000; Wanger & Persson, 1983), likely due to damage and degeneration of spatially-selective RGCs.

Before discussing the research into the cortex in glaucoma, it should be noted that any findings of differences in cortical responses between healthy controls and glaucoma patients do not necessarily represent pathological cortical processing (i.e. a direct impact of glaucoma on the cortex), but may instead represent normal processing of pathological input from the retina. Multiple studies, including that reported in Chapter 8, have reported a decrease in electrophysiological amplitude in the retina (e.g. Bach *et al.*, 1988; Fortune *et al.*, 2007; Karaśkiewicz *et al.*, 2014; Korth *et al.*, 1989; Salgarello *et al.*, 2018), potentially due to RGC cell death. However, even before cell death, RGC output may be altered, such as due to the shrinking of the dendritic tree (Morgan, 2002) or a change in spatial tuning (Chapter 8). This change of retinal processing in glaucoma will inevitably be reflected in the cortical responses to this input, such as a lower blood oxygen-level dependant (BOLD) signal in

response to visual stimuli in glaucoma patients versus healthy controls (e.g. Duncan *et al.*, 2007; Murphy *et al.*, 2016; Wuerger *et al.*, 2015). In response to this lowered input (from RGC dysfunction or reduced density), cortical cells may summate over a larger number of retinal cells in order to retain the same SNR or number of spikes (Kwon & Liu, 2019; Pan & Swanson, 2006). It was hypothesised that an increased summation in the cortex in glaucoma may contribute to the enlargement of Ricco's area in glaucoma patients compared to healthy controls. This was therefore investigated in this thesis using population receptive field (pRF) mapping methodology.

During pRF mapping in the sample of glaucoma patients and age-matched controls, individual HRF mapping was completed and used for convolutions. Although no group level differences in HRF time-to-peak (TTP) or full-width-at-half-maximum (FWHM) were found in Chapter 9, a substantial amount of inter-participant variability was noted. Variation in these parameters can directly impact pRF mapping estimates, with larger FWHMs associated with smaller pRF estimates in V1-3 in the same dataset, though the relative pRF sizes between visual areas was consistent across FWHM values (see Appendix C of Dumoulin & Wandell, 2008). Given this relationship between the HRF fit parameters used in convolution and the final pRF estimates, more accurate pRF estimates are expected if the HRF parameters more closely resemble the individual's underlying HRF. By doing so with the pRF mapping data described in Chapter 10 and Chapter 11 therefore, this potential source of extra variation in the data is accounted for.

Chapter 10 describes research investigating pRF sizes in glaucoma patients compared to healthy age-similar controls. It was found that glaucoma patients demonstrated a significantly steeper relationship between pRF size and eccentricity compared to controls, mainly due to smaller pRF sizes in central vision in glaucoma patients compared to healthy controls (see Figure 10.6Figure 10.8). This is opposed to our initial hypothesis, which was that pRF sizes would enlarge in glaucoma patients compared to controls, following suggestions of a cortical contribution to the size of Ricco's area in glaucoma (discussed in Chapter 3, 10, and 11) and following suggestion of larger receptive field sizes by some early work into this question (Liu *et al.*, 2007).

One of the possible reasons for this unexpected finding was the type of stimuli used in our pRF mapping, which is different to that commonly used to measure Ricco's area. The

stimuli used in the main study described in Chapter 10 employed high contrast retinotopic stimuli, as is most commonly used in such pRF mapping experiments. The advantage of this is that, due to this high contrast and the range of spatial frequencies involved, a broad range of neurones are stimulated and thus the BOLD signal has a higher SNR than would otherwise be elicited. However, this also means that if there are any differences in glaucoma patients compared to controls in specific neural sub-populations, they may be overshadowed by the majority and difficult to discern. Additionally, a high-contrast stimulus could perhaps also have the effect of over-saturating larger receptive field sizes that usually have a higher sensitivity than smaller receptive fields (at the expense of resolution). If it is the case that certain 'compensatory' receptive fields are enlarging in glaucoma (as is suggested by the enlarged Ricco's area), it could be that they become saturated by the high-contrast stimulus and don't contribute to the stimulus response. The effect of this would be that only smaller pRFs would be measurable by our routine. In order to investigate this possibility, pRF mapping was repeated with 20% contrast retinotopic stimuli in a small sample of glaucoma patients and healthy controls in an exploratory study. However, similar results to the high-contrast stimuli were found, with glaucoma patients demonstrating reduced pRF size in central vision. This work therefore suggests that similar neural sub-populations were being stimulated by both high contrast and low contrast natural scene pRF mapping stimuli and provides a replication of the main result using low contrast pRF mapping stimuli.

In order to address the main aim of this thesis, which was to investigate the contribution of cortical and retinal receptive field size to Ricco's area in this sample of glaucoma patients and age-similar controls, linear models were created (as described in Chapter 11). Relationships within healthy control and glaucoma patient groups were examined separately. Neither retinal or cortical (V1-3d) receptive field size estimates were found to be predictive of Ricco's area, in either glaucoma patients or controls. While this was against our initial hypotheses, it is similar to multiple previous studies that report a disconnect between pRF sizes and psychophysical results. For example, Welbourne *et al.,* (2018) found that, despite behavioural responses to achromatic stimuli demonstrating a bias for higher spatial frequencies compared to the chromatic stimuli, there was no differences in pRF sizes in either the chromatic or achromatic conditions. This disconnect may be due to the contribution of complex cells in the cortex to the BOLD signal, which,

unlike simple cells, show a weak relationship between spatial tuning and receptive field size (Movshon *et al.*, 1978). Additionally, a fundamental characteristic of pRF mapping is that it is based on a population of neurones, so changes to smaller numbers of cortical receptive fields may be lost. In terms of the PERG, it may also reflect that PERG is a relatively global measure, whereas Ricco's area is measured at specific locations in the retina.

12.2. Overall conclusions

The main aim of this thesis was to investigate the contribution of cortical and retinal receptive field sizes to the size of Ricco's area in a sample of glaucoma patients and age-similar healthy controls. However, the data described in this thesis do not support the contribution of cortical or retinal receptive field sizes to Ricco's area, despite evidence from models of perimetric spatial summation mechanisms (Pan & Swanson, 2006; Swanson *et al.*, 2004). On the other hand, this result should not be taken as suggesting evidence *against* a contribution of retinal or cortical receptive field size to Ricco's area. With the evidence for both a cortical and retinal contribution to Ricco's area in mind, as well as the sources of noise described in these data, it is possible that this noise is obscuring underlying relationships in the data, despite steps taken to minimise this (e.g. pRF software selection in Chapter 7). Several possible future avenues have been highlighted by the work described here, which may better characterise the relationship between cortical receptive field sizes and Ricco's area.

12.3. Future work

12.3.1. Attention modulation in glaucoma

As mentioned above, one of the findings from Chapter 10 was that glaucoma patients demonstrated a statistically significantly steeper relationship between pRF size and eccentricity compared to controls, possibly driven by smaller pRF sizes in central vision in glaucoma patients compared to healthy controls (see Figure 10.6Figure 10.8). One of the possible explanations for this is an enlargement of the area of the retinotopic map corresponding to central vision, which is supported by previous research (Zhou *et al.*, 2017). Each voxel would represent a smaller percentage of the visual field if central representation was spread over a larger amount of cortex, leading to smaller pRF sizes. As attention to a particular location leads to a shift in pRF position preference (i.e. the position in the visual

field that a pRF responds to) to that location (e.g. Klein *et al.*, 2014, 2018; Luck *et al.*, 1997; Womelsdorf *et al.*, 2008), it may be that glaucoma patients show enhanced attentional modulation towards central vision to compensate for peripheral vision loss. In support of this, attention modulation of BOLD responses have been found to increase in inherited peripheral degeneration in response to the same attentional task (Ferreira *et al.*, 2019). The effect of attention modulation on BOLD responses and pRF position preference should therefore be investigated in a sample of glaucoma patients and healthy controls to investigate this as a possible reason for the results described in Chapter 10.

12.3.2. Spatial tuning stimuli

One of the possible suggestions for the lack of relationship between pRF sizes and psychophysical measurements is the population of simple verses complex cells that are contributing to the BOLD fMRI signal. The contribution of such cells may be indistinguishable in the BOLD signal, as it mostly reflects local field potentials within the cortical tissue (Logothetis *et al.*, 2001). The relationship between spatial tuning and receptive field size is present in simple cells but breaks down with complex cells (Movshon *et al.*, 1978). An analysis that specifically investigates the spatial tuning of cortical neuronal populations may therefore be a more sensitive probe of the cortical mechanisms underlying Ricco's area. For example, a model-driven methodology (termed population spatial frequency tuning mapping) has recently been discussed that specifically maps spatial tuning bandwidth across the cortex (Aghajari *et al.*, 2020).

12.3.3. Alternate pRF models

Multiple different pRF models have been utilised in the literature as an alternative to the single 2D Gaussian utilised in the glaucoma cohort described in Chapters 8-11. For example, as described previously (e.g. Chapter 4), a Difference-of-Gaussian (DoG) model allows for the investigation of inhibitory surrounds in the cortex and thus explain a larger about of variance in the retinotopic signal (Zuiderbaan *et al.*, 2012). While the size of the cortical receptive field centre was assumed to be most reflective of the cortical pooling mechanisms underlying Ricco's area, analysis using a DoG model would allow for the configuration of pRFs and their associated contribution to psychophysical phenomena to be more fully investigated.

Additionally, it should be kept in mind that the underlying orientation sensitive neurones in the early cortical areas are elongated in shape, rather than the DoG receptive field organisation found in the retina (Hubel & Wiesel, 1959, 1962, 1968; Kuffler, 1953; Lee, 1996). It is when averaging over all receptive fields within a voxel, as is done with pRF mapping, that a Gaussian shape can be used to model the response. However, work using elongated Gaussian pRF models have suggested that the degree of radial bias for the long axis of pRFs better reflects the underlying orientation sensitivity (Merkel *et al.*, 2020). As the model from Pan and Swanson (2006) suggests that spatial summation over perimetric stimuli can only be explained by considering cortical pooling by orientation sensitive receptive fields, it may be that this method of modelling pRF responses would better tap into the cortical mechanisms underlying Ricco's area.

References

Aaen-Stockdale, C., Ledgeway, T., & Hess, R. F. (2007). Second-Order Optic Flow Deficits in Amblyopia. *Investigative Opthalmology & Visual Science*, *48*(12), 5532. https://doi.org/10.1167/iovs.07-0447

Adams, D. L., & Horton, J. C. (2003). A Precise Retinotopic Map of Primate Striate Cortex Generated from the Representation of Angioscotomas. *The Journal of Neuroscience*, *23*(9), 3771–3789. https://doi.org/10.1523/JNEUROSCI.23-09-03771.2003

Adams, D. L., Sincich, L. C., & Horton, J. C. (2007). Complete Pattern of Ocular Dominance Columns in Human Primary Visual Cortex. *Journal of Neuroscience*, *27*(39), 10391–10403. https://doi.org/10.1523/JNEUROSCI.2923-07.2007

Addicott, M. A., Yang, L. L., Peiffer, A. M., Burnett, L. R., Burdette, J. H., Chen, M. Y., Hayasaka, S., Kraft, R. A., Maldjian, J. A., & Laurienti, P. J. (2009). The effect of daily caffeine use on cerebral blood flow: How much caffeine can we tolerate? *Human Brain Mapping*, *30*(10), 3102–3114. https://doi.org/10.1002/hbm.20732

Aghajari, S., Vinke, L. N., & Ling, S. (2020). Population spatial frequency tuning in human early visual cortex. *Journal of Neurophysiology*, *123*(2), 773–785. https://doi.org/10.1152/jn.00291.2019

Ahmadi, K., Fracasso, A., van Dijk, J. A., Kruijt, C., van Genderen, M., Dumoulin, S. O., & Hoffmann, M. B. (2019). Altered organization of the visual cortex in FHONDA syndrome. *NeuroImage*, *190*, 224–231. https://doi.org/10.1016/j.neuroimage.2018.02.053

Ahmadi, K., Herbik, A., Wagner, M., Kanowski, M., Thieme, H., & Hoffmann, M. B. (2019). Population receptive field and connectivity properties of the early visual cortex in

human albinism. *NeuroImage*, *202*, 116105. https://doi.org/10.1016/j.neuroimage.2019.116105

Almrcegui Lafita, C., Fernandez Tirado, J., Melcon Sanchez Friera, B., Ucls Moreno, P., Valdizn Us?n, J., & Honrubia Lupez, F. (1997). Components of PERG in Glaucoma. *Neurophysiologie Clinique/Clinical Neurophysiology*, *27*(2), 109–115. https://doi.org/10.1016/S0987-7053(97)85663-8

Alvarez, I., de Haas, B., Clark, C. A., Rees, G., & Schwarzkopf, D. S. (2015). Comparing different stimulus configurations for population receptive field mapping in human fMRI. *Frontiers in Human Neuroscience*, *9*. https://doi.org/10.3389/fnhum.2015.00096

Amano, K., Wandell, B. A., & Dumoulin, S. O. (2009). Visual Field Maps, Population Receptive Field Sizes, and Visual Field Coverage in the Human MT+ Complex. *Journal of Neurophysiology*, *102*(5), 2704–2718. https://doi.org/10.1152/jn.00102.2009

Anders, L.-M., Heinrich, S. P., Lagrèze, W. A., & Joachimsen, L. (2019). Little effect of 0.01% atropine eye drops as used in myopia prevention on the pattern electroretinogram. *Documenta Ophthalmologica*, *138*(2), 85–95. https://doi.org/10.1007/s10633-019-09671-0

Anderson, E. J., Tibber, M. S., Schwarzkopf, D. S., Shergill, S. S., Fernandez-Egea, E., Rees, G., & Dakin, S. C. (2017). Visual Population Receptive Fields in People with Schizophrenia Have Reduced Inhibitory Surrounds. *The Journal of Neuroscience*, *37*(6), 1546–1556. https://doi.org/10.1523/JNEUROSCI.3620-15.2016

Anderson, R. S. (2006). The psychophysics of glaucoma: Improving the structure/function relationship. *Progress in Retinal and Eye Research*, *25*(1), 79–97. https://doi.org/10.1016/j.preteyeres.2005.06.001

Anderson, R. S., Zlatkova, M. B., & Demirel, S. (2002). What limits detection and resolution of short-wavelength sinusoidal gratings across the retina? *Vision Research*, *42*(8), 981–990. https://doi.org/10.1016/S0042-6989(02)00013-5

Anticevic, A., Dierker, D. L., Gillespie, S. K., Repovs, G., Csernansky, J. G., Van Essen, D. C., & Barch, D. M. (2008). Comparing surface-based and volume-based analyses of functional neuroimaging data in patients with schizophrenia. *NeuroImage*, *41*(3), 835–848. https://doi.org/10.1016/j.neuroimage.2008.02.052

ANZRAG Consortium, Bailey, J. N. C., Loomis, S. J., Kang, J. H., Allingham, R. R., Gharahkhani, P., Khor, C. C., Burdon, K. P., Aschard, H., Chasman, D. I., Igo, R. P., Hysi, P. G., Glastonbury, C. A., Ashley-Koch, A., Brilliant, M., Brown, A. A., Budenz, D. L., Buil, A., Cheng, C.-Y., … Wiggs, J. L. (2016). Genome-wide association analysis identifies TXNRD2, ATXN2 and FOXC1 as susceptibility loci for primary open-angle glaucoma. *Nature Genetics*, *48*(2), 189–194. https://doi.org/10.1038/ng.3482

Arai, M., Yoshimura, N., Sakaue, H., Chihara, E., & Honda, Y. (1993). A 3-Year Follow-Up Study of Ocular Hypertension by Pattern Electroretinogram. *Ophthalmologica*, *207*(4), 187–195. https://doi.org/10.1159/000310431

Arden, G. B. (2006). Causes and cures of artefacts. In J. R. Heckenlively & G. B. Arden (Eds.), *Principles and practice of clinical electrophysiology of vision*. MIT Press.

Arden, G. B., & Vaegan. (1983). Electroretinograms evoked in man by local uniform or patterned stimulation. *Journal of Physiology*, *341*, 85–104.

Attwell, D., & Iadecola, C. (2002). The neural basis of functional brain imaging signals. *Trends in Neurosciences*, *25*(12), 621–625. https://doi.org/10.1016/S0166-2236(02)02264-6

Bablok, W., Passing, H., Bender, R., & Schneider, B. (1988). A General Regression Procedure for Method Transformation. Application of Linear Regression Procedures for Method

Comparison Studies in Clinical Chemistry, Part III. *Clinical Chemistry and Laboratory Medicine*, *26*(11). https://doi.org/10.1515/cclm.1988.26.11.783

Bach, M., Brigell, M. G., Hawlina, M., Holder, G. E., Johnson, M. A., McCulloch, D. L., Meigen, T., & Viswanathan, S. (2013). ISCEV standard for clinical pattern electroretinography (PERG): 2012 update. *Documenta Ophthalmologica*, *126*(1), 1–7. https://doi.org/10.1007/s10633-012-9353-y

Bach, M., Cuno, A.-K., & Hoffmann, M. B. (2018). Retinal conduction speed analysis reveals different origins of the P50 and N95 components of the (multifocal) pattern electroretinogram. *Experimental Eye Research*, *169*, 48–53. https://doi.org/10.1016/j.exer.2018.01.021

Bach, M., Hiss, P., & Röver, J. (1988). Check-size specific changes of pattern electroretinogram in patients with early open-angle glaucoma. *Documenta Ophthalmologica. Advances in Ophthalmology*, *69*(3), 315–322.

Bach, M., & Hoffmann, M. B. (2008). Update on the Pattern Electroretinogram in Glaucoma: *Optometry and Vision Science*, *85*(6), 386–395. https://doi.org/10.1097/OPX.0b013e318177ebf3

Bach, M., & Holder, G. E. (1996). Check size tuning of the pattern electroretingoram: A reappraisal. *Documenta Ophthalmologica*, *92*(3), 193–202.

Bach, M., & Poloschek, C. M. (2013). Electrophysiology and glaucoma: Current status and future challenges. *Cell and Tissue Research*, *353*(2), 287–296. https://doi.org/10.1007/s00441-013-1598-6

Bach, M., Unsoeld, A. S., Philippin, H., Staubach, F., Maier, P., Walter, H. S., Bomer, T. G., & Funk, J. (2006). Pattern ERG as an Early Glaucoma Indicator in Ocular Hypertension:

A Long-Term, Prospective Study. *Investigative Opthalmology & Visual Science*, *47*(11), 4881. https://doi.org/10.1167/iovs.05-0875

Baker, C. L., Hess, R. R., Olsen, B. T., & Zrenner, E. (1988). Current source density analysis of linear and non-linear components of the primate electroretinogram. *The Journal of Physiology*, *407*(1), 155–176. https://doi.org/10.1113/jphysiol.1988.sp017408

Barlow, H. B. (1958). Temporal and spatial summation in human vision at different background intensities. *The Journal of Physiology*, *141*(2), 337–350.

Bates, D., Mächler, M., Bolker, B., & Walker, S. (2015). Fitting Linear Mixed-Effects Models Using **lme4**. *Journal of Statistical Software*, *67*(1). https://doi.org/10.18637/jss.v067.i01

Beirne, R. O., Zlatkova, M. B., & Anderson, R. S. (2005). Changes in human short-wavelength-sensitive and achromatic resolution acuity with retinal eccentricity and meridian. *Visual Neuroscience*, *22*(1), 79–86. https://doi.org/10.1017/S0952523805221119

Bélanger, M., Allaman, I., & Magistretti, P. J. (2011). Brain Energy Metabolism: Focus on Astrocyte-Neuron Metabolic Cooperation. *Cell Metabolism*, *14*(6), 724–738. https://doi.org/10.1016/j.cmet.2011.08.016

Bergmann, J., Genç, E., Kohler, A., Singer, W., & Pearson, J. (2016). Smaller Primary Visual Cortex Is Associated with Stronger, but Less Precise Mental Imagery. *Cerebral Cortex*, *26*(9), 3838–3850. https://doi.org/10.1093/cercor/bhv186

Bergua, A., Horn, F. K., Martus, P., Jünemann, A. M., & Korth, M. (2004). Stereoscopic visual evoked potentials in normal subjects and patients with open-angle glaucomas. *Graefe's Archive for Clinical and Experimental Ophthalmology*, *242*(3), 197–203. https://doi.org/10.1007/s00417-003-0797-3

Berninger, T., & Schuurmans, R. P. (1985). Spatial tuning of the pattern ERG across temporal frequency. *Documenta Ophthalmologica*, *61*(1), 17–25.

Biopac.com. (2014, December 31). *Ground vs Reference for EEG Recording*. https://www.biopac.com/knowledge-base/ground-vs-reference-for-eeg-recording/

Blondeau, P., Lamarche, J., Lafond, G., & Brunette, J. R. (1987). Pattern electroretinogram and optic nerve section in pigeons. *Current Eye Research*, *6*(6), 747–756. https://doi.org/10.3109/02713688709034841

Bobak, P., Bodis-Wollner, I., Podos, S., Harnois, C., Mylin, L., Maffei, L., & Thornton, J. (1983). Pattern Electroretinograms and Visual-Evoked Potentials in Glaucoma and Multiple Sclerosis. *American Journal of Ophthalmology*, *96*(1), 72–83. https://doi.org/10.1016/0002-9394(83)90457-9

Bock, G. R., Goode, J. A., & Dacey, D. M. (2007). Physiology, Morphology and Spatial Densities of Identified Ganglion Cell Types in Primate Retina. *Novartis Foundation Symposia*, 12–34. https://doi.org/10.1002/9780470514610.ch2

Bode, S. F. N., Jehle, T., & Bach, M. (2011). Pattern Electroretinogram in Glaucoma Suspects: New Findings from a Longitudinal Study. *Investigative Opthalmology & Visual Science*, *52*(7), 4300. https://doi.org/10.1167/iovs.10-6381

Bogunovi, H., Kwon, Y. H., Rashid, A., Lee, K., Critser, D. B., Garvin, M. K., Sonka, M., & Abramoff, M. D. (2015). Relationships of Retinal Structure and Humphrey 24-2 Visual Field Thresholds in Patients With Glaucoma. *Investigative Ophthalmology & Visual Science*, *56*(1), 259–271. https://doi.org/10.1167/iovs.14-15885

Bonakdarpour, B., Parrish, T. B., & Thompson, C. K. (2007). Hemodynamic response function in patients with stroke-induced aphasia: Implications for fMRI data analysis. *NeuroImage*, *36*(2), 322–331. https://doi.org/10.1016/j.neuroimage.2007.02.035

Borges, V. M., Danesh-Meyer, H. V., Black, J. M., & Thompson, B. (2015). Functional effects of unilateral open-angle glaucoma on the primary and extrastriate visual cortex. *Journal of Vision*, *15*(15), 9. https://doi.org/10.1167/15.15.9

Boucard, C. C., Hernowo, A. T., Maguire, R. P., Jansonius, N. M., Roerdink, J. B. T. M., Hooymans, J. M. M., & Cornelissen, F. W. (2009). Changes in cortical grey matter density associated with long-standing retinal visual field defects. *Brain*, *132*(7), 1898–1906. https://doi.org/10.1093/brain/awp119

Bressler, D., & Silver, M. (2010). The effects of spatial attention and population receptive field size estimation on fMRI topographic mapping signals. *Journal of Vision*, *8*(6), 803–803. https://doi.org/10.1167/8.6.803

Brewer, A. A., & Barton, B. (2014). Visual cortex in aging and Alzheimer's disease: Changes in visual field maps and population receptive fields. *Frontiers in Psychology*, *5*. https://doi.org/10.3389/fpsyg.2014.00074

Brindley, G. S. (1954). The summation areas of human colour-receptive mechanisms at increment threshold. *The Journal of Physiology*, *124*(2), 400–408. https://doi.org/10.1113/jphysiol.1954.sp005116

Brindley, G. S. (1970). *Physiology of the retina and visual pathway* (2nd ed). Edward Arnold.

Brown, G. G., Zorrilla, L. T. E., Georgy, B., Kindermann, S. S., Wong, E. C., & Buxton, R. B. (2003). BOLD and Perfusion Response to Finger-Thumb Apposition after Acetazolamide Administration: Differential Relationship to Global Perfusion. *Journal of Cerebral Blood Flow & Metabolism*, *23*(7), 829–837. https://doi.org/10.1097/01.WCB.0000071887.63724.B2

Bruce, V., Green, P. R., & Georgeson, M. A. (2000). *Visual perception: Physiology, psychology, and ecology* (3. ed, reprinted). Psychology Press.

Burdon, K. P., Macgregor, S., Hewitt, A. W., Sharma, S., Chidlow, G., Mills, R. A., Danoy, P., Casson, R., Viswanathan, A. C., Liu, J. Z., Landers, J., Henders, A. K., Wood, J., Souzeau, E., Crawford, A., Leo, P., Wang, J. J., Rochtchina, E., Nyholt, D. R., … Craig, J. E. (2011). Genome-wide association study identifies susceptibility loci for open angle glaucoma at TMCO1 and CDKN2B-AS1. *Nature Genetics*, *43*(6), 574–578. https://doi.org/10.1038/ng.824

Burr, J., Mowatt, G., Hernández, R., Siddiqui, M., Cook, J., Lourenco, T., Ramsay, C., Vale, L., Fraser, C., Azuara-Blanco, A., Deeks, J., Cairns, J., Wormald, R., McPherson, S., Rabindranath, K., & Grant, A. (2007). The clinical effectiveness and cost-effectiveness of screening for open angle glaucoma: A systematic review and economic evaluation. *Health Technology Assessment*, *11*(41). https://doi.org/10.3310/hta11410

Bush, R. A., & Sieving, P. A. (1994). A proximal retinal component in the primate photopic ERG a-wave. *Investigative Ophthalmology & Visual Science*, *35*(2), 635–645.

Buuren, S. van, & Groothuis-Oudshoorn, K. (2011). MICE: Multivariate Imputation by Chained Equations in R. *Journal of Statistical Software*, *45*(3). https://doi.org/10.18637/jss.v045.i03

Buxton, R. B. (2001). The Elusive Initial Dip. *NeuroImage*, *13*(6), 953–958. https://doi.org/10.1006/nimg.2001.0814

Buxton, R. B., Uludağ, K., Dubowitz, D. J., & Liu, T. T. (2004). Modeling the hemodynamic response to brain activation. *NeuroImage*, *23*, S220–S233. https://doi.org/10.1016/j.neuroimage.2004.07.013

Calderone, D. J., Martinez, A., Zemon, V., Hoptman, M. J., Hu, G., Watkins, J. E., Javitt, D. C., & Butler, P. D. (2013). Comparison of psychophysical, electrophysiological, and fMRI

assessment of visual contrast responses in patients with schizophrenia. *NeuroImage*, *67*, 153–162. https://doi.org/10.1016/j.neuroimage.2012.11.019

Campbell, F. W., & Gubisch, R. W. (1966). Optical quality of the human eye. *The Journal of Physiology*, *186*(3), 558–578. https://doi.org/10.1113/jphysiol.1966.sp008056

Cavanaugh, J. R., Bair, W., & Movshon, J. A. (2002). Nature and Interaction of Signals From the Receptive Field Center and Surround in Macaque V1 Neurons. *Journal of Neurophysiology*, *88*(5), 2530–2546. https://doi.org/10.1152/jn.00692.2001

Chapin, J. K. (1986). Laminar differences in sizes, shapes, and response profiles of cutaneous receptive fields in the rat SI cortex. *Experimental Brain Research*, *62*(3). https://doi.org/10.1007/BF00236033

Chatterjee, S., & Callaway, E. M. (2003). Parallel colour-opponent pathways to primary visual cortex. *Nature*, *426*(6967), 668–671. https://doi.org/10.1038/nature02167

Chen, L., Li, S., Cai, F., Wu, L., Gong, H., Pei, C., Zhou, F., & Zeng, X. (2019). Altered functional connectivity density in primary angle-closure glaucoma patients at resting-state. *Quantitative Imaging in Medicine and Surgery*, *9*(4), 603–614. https://doi.org/10.21037/qims.2019.04.13

Chen, W., Chen, J., Huang, J., Xu, J., Zhang, F., & Lu, F. (2013). Comparison of Macular and Retinal Nerve Fiber Layer Thickness in Untreated and Treated Binocular Amblyopia. *Current Eye Research*, *38*(12), 1248–1254. https://doi.org/10.3109/02713683.2013.805233

Chen, Y., Lin, Y., Vithana, E. N., Jia, L., Zuo, X., Wong, T. Y., Chen, L. J., Zhu, X., Tam, P. O. S., Gong, B., Qian, S., Li, Z., Liu, X., Mani, B., Luo, Q., Guzman, C., Leung, C. K. S., Li, X., Cao, W., … Yang, Z. (2014). Common variants near ABCA1 and in PMM2 are

associated with primary open-angle glaucoma. *Nature Genetics*, *46*(10), 1115–1119. https://doi.org/10.1038/ng.3078

Cheng, K. (2012). Revealing human ocular dominance columns using high-resolution functional magnetic resonance imaging. *NeuroImage*, *62*(2), 1029–1034. https://doi.org/10.1016/j.neuroimage.2011.08.086

Cheng, K. (2018). Exploration of human visual cortex using high spatial resolution functional magnetic resonance imaging. *NeuroImage*, *164*, 4–9. https://doi.org/10.1016/j.neuroimage.2016.11.018

Chui, T. Y. P., Yap, M. K. H., Chan, H. H. L., & Thibos, L. N. (2005). Retinal stretching limits peripheral visual acuity in myopia. *Vision Research*, *45*(5), 593–605. https://doi.org/10.1016/j.visres.2004.09.016

Clavagnier, S., Dumoulin, S. O., & Hess, R. F. (2015). Is the Cortical Deficit in Amblyopia Due to Reduced Cortical Magnification, Loss of Neural Resolution, or Neural Disorganization? *Journal of Neuroscience*, *35*(44), 14740–14755. https://doi.org/10.1523/JNEUROSCI.1101-15.2015

Cohen, E. R., Ugurbil, K., & Kim, S.-G. (2002). Effect of Basal Conditions on the Magnitude and Dynamics of the Blood Oxygenation Level-Dependent fMRI Response. *Journal of Cerebral Blood Flow & Metabolism*, *22*(9), 1042–1053. https://doi.org/10.1097/00004647-200209000-00002

Conner, I. P., Odom, J. V., Schwartz, T. L., & Mendola, J. D. (2007). Monocular activation of V1 and V2 in amblyopic adults measured with functional magnetic resonance imaging. *Journal of American Association for Pediatric Ophthalmology and Strabismus*, *11*(4), 341–350. https://doi.org/10.1016/j.jaapos.2007.01.119

Conroy, D. A., Spielman, A. J., & Scott, R. Q. (2005). Daily rhythm of cerebral blood flow velocity. *Journal of Circadian Rhythms*, *3*(0), 3. https://doi.org/10.1186/1740-3391-3-3

Conway, B. R. (2001). Spatial structure of cone inputs to color cells in alert macaque primary visual cortex (V-1). *Journal of Neuroscience*, *21*(8), 2768–2783.

Conway, B. R., & Livingstone, M. S. (2006). Spatial and temporal properties of cone signals in alert macaque primary visual cortex. *Journal of Neuroscience*, *26*(42), 10826–10846. https://doi.org/10.1523/JNEUROSCI.2091-06.2006

Cox, R. W. (1996). AFNI: Software for Analysis and Visualization of Functional Magnetic Resonance Neuroimages. *Computers and Biomedical Research*, *29*(3), 162–173. https://doi.org/10.1006/cbmr.1996.0014

Crabb, D. P., Smith, N. D., Glen, F. C., Burton, R., & Garway-Heath, D. F. (2013). How Does Glaucoma Look?: Patient Perception of Visual Field Loss. *Ophthalmology*, *120*(6), 1120–1126. https://doi.org/10.1016/j.ophtha.2012.11.043

Crossland, M. D., Morland, A. B., Feely, M. P., von dem Hagen, E., & Rubin, G. S. (2008). The Effect of Age and Fixation Instability on Retinotopic Mapping of Primary Visual Cortex. *Investigative Opthalmology & Visual Science*, *49*(8), 3734. https://doi.org/10.1167/iovs.07-1621

Curcio, C. A., Allen, K. A., Sloan, K. R., Lerea, C. L., Hurley, J. B., Klock, I. B., & Milam, A. H. (1991). Distribution and morphology of human cone photoreceptors stained with anti-blue opsin. *The Journal of Comparative Neurology*, *312*(4), 610–624. https://doi.org/10.1002/cne.903120411

Cvenkel, B., Sustar, M., & Perovšek, D. (2017). Ganglion cell loss in early glaucoma, as assessed by photopic negative response, pattern electroretinogram, and spectral-

domain optical coherence tomography. *Documenta Ophthalmologica*, *135*(1), 17–28. https://doi.org/10.1007/s10633-017-9595-9

Dacey, D. (1993). The mosaic of midget ganglion cells in the human retina. *The Journal of Neuroscience*, *13*(12), 5334–5355. https://doi.org/10.1523/JNEUROSCI.13-12-05334.1993

Dacey, D. M. (1993). Morphology of a small-field bistratified ganglion cell type in the macaque and human retina. *Visual Neuroscience*, *10*(6), 1081–1098. https://doi.org/10.1017/S0952523800010191

Dacey, D. M., & Lee, B. B. (1994). The "blue-on" opponent pathway in primate retina originates from a distinct bistratified ganglion cell type. *Nature*, *367*(6465), 731–735. https://doi.org/10.1038/367731a0

Dai, H., Mu, K. T., Qi, J. P., Wang, C. Y., Zhu, W. Z., Xia, L. M., Chen, Z. Q., Zhang, H., Ai, F., & Morelli, J. N. (2011). Assessment of Lateral Geniculate Nucleus Atrophy with 3T MR Imaging and Correlation with Clinical Stage of Glaucoma. *American Journal of Neuroradiology*, *32*(7), 1347–1353. https://doi.org/10.3174/ajnr.A2486

Dai, X., Huang, X., Zhong, Y., Zhou, F., Hu, P.-H., Shao, Y., Pei, C.-G., Liu, X.-H., & Zeng, X.-J. (2015). Disturbed spontaneous brain activity pattern in patients with primary angle-closure glaucoma using amplitude of low-frequency fluctuation: A fMRI study. *Neuropsychiatric Disease and Treatment*, 1877. https://doi.org/10.2147/NDT.S87596

Dale, A. M., Fischl, B., & Sereno, M. I. (1999). Cortical Surface-Based Analysis. *NeuroImage*, *9*(2), 179–194. https://doi.org/10.1006/nimg.1998.0395

Dalimier, E., & Dainty, C. (2010). Role of ocular aberrations in photopic spatial summation in the fovea. *Optics Letters*, *35*(4), 589–591.

Davila, K. d, & Geisler, W. S. (1991). The relative contributions of pre-neural and neural factors to areal summation in the fovea. *Vision Research*, *31*(7–8), 1369–1380.

Davis, T. L., Kwong, K. K., Weisskoff, R. M., & Rosen, B. R. (1998). Calibrated functional MRI: Mapping the dynamics of oxidative metabolism. *Proceedings of the National Academy of Sciences*, *95*(4), 1834–1839. https://doi.org/10.1073/pnas.95.4.1834

de Best, P. B., Raz, N., Guy, N., Ben-Hur, T., Dumoulin, S. O., Pertzov, Y., & Levin, N. (2019). Role of Population Receptive Field Size in Complex Visual Dysfunctions: A Posterior Cortical Atrophy Model. *JAMA Neurology*. https://doi.org/10.1001/jamaneurol.2019.2447

de Jonge, J. C., Vinkers, C. H., Hulshoff Pol, H. E., & Marsman, A. (2017). GABAergic Mechanisms in Schizophrenia: Linking Postmortem and In Vivo Studies. *Frontiers in Psychiatry*, *8*, 118. https://doi.org/10.3389/fpsyt.2017.00118

de Sousa, A. A., & Proulx, M. J. (2014). What can volumes reveal about human brain evolution? A framework for bridging behavioral, histometric, and volumetric perspectives. *Frontiers in Neuroanatomy*, *8*. https://doi.org/10.3389/fnana.2014.00051

de Sousa, A. A., Sherwood, C. C., Schleicher, A., Amunts, K., MacLeod, C. E., Hof, P. R., & Zilles, K. (2010). Comparative Cytoarchitectural Analyses of Striate and Extrastriate Areas in Hominoids. *Cerebral Cortex*, *20*(4), 966–981. https://doi.org/10.1093/cercor/bhp158

De Valois, R. L., Abramov, I., & Jacobs, G. H. (1966). Analysis of Response Patterns of LGN Cells. *Journal of the Optical Society of America*, *56*(7), 966. https://doi.org/10.1364/JOSA.56.000966

De Valois, R. L., Cottaris, N. P., Elfar, S. D., Mahon, L. E., & Wilson, J. A. (2000). Some transformations of color information from lateral geniculate nucleus to striate cortex. *Proceedings of the National Academy of Sciences*, *97*(9), 4997–5002. https://doi.org/10.1073/pnas.97.9.4997

Dekker, T. M., Schwarzkopf, D. S., de Haas, B., Nardini, M., & Sereno, M. I. (2019). Population receptive field tuning properties of visual cortex during childhood. *Developmental Cognitive Neuroscience*, *37*, 100614. https://doi.org/10.1016/j.dcn.2019.01.001

Denniss, J., Turpin, A., & McKendrick, A. M. (2019). Relating optical coherence tomography to visual fields in glaucoma: Structure–function mapping, limitations and future applications. *Clinical and Experimental Optometry*, *102*(3), 291–299. https://doi.org/10.1111/cxo.12844

Derrington, A. M., & Lennie, P. (1984). Spatial and temporal contrast sensitivities of neurones in lateral geniculate nucleus of macaque. *The Journal of Physiology*, *357*(1), 219–240. https://doi.org/10.1113/jphysiol.1984.sp015498

Dong, C.-J., Agey, P., & Hare, W. A. (2004). Origins of the electroretinogram oscillatory potentials in the rabbit retina. *Visual Neuroscience*, *21*(4), 533–543. https://doi.org/10.1017/S0952523804214043

Dougherty, R. F., Koch, V. M., Brewer, A. A., Fischer, B., Modersitzki, J., & Wandell, B. A. (2003). Visual field representations and locations of visual areas V1/2/3 in human visual cortex. *Journal of Vision*, *3*(10), 1. https://doi.org/10.1167/3.10.1

Drasdo, N., Millican, C. L., Katholi, C. R., & Curcio, C. A. (2007). The length of Henle fibers in the human retina and a model of ganglion receptive field density in the visual field. *Vision Research*, *47*(22), 2901–2911. https://doi.org/10.1016/j.visres.2007.01.007

Drasdo, N., Thompson, D. A., & Arden, G. B. (1990). A comparison of pattern ERG amplitudes and nuclear layer thickness in different zones of the retina. *Clin Vis Sci.*, *5*(4), 415–420.

Drasdo, N., Thompson, D. A., Thompson, C. M., & Edwards, L. (1987). Complementary components and local variations of the Pattern Electroretinogram. *Investigative Ophthalmology and Visual Science*, *28*, 158–162.

Duchin, Y., Abosch, A., Yacoub, E., Sapiro, G., & Harel, N. (2012). Feasibility of Using Ultra-High Field (7 T) MRI for Clinical Surgical Targeting. *PLoS ONE*, *7*(5), e37328. https://doi.org/10.1371/journal.pone.0037328

Dumoulin, S. O., Hess, R. F., May, K. A., Harvey, B. M., Rokers, B., & Barendregt, M. (2014). Contour extracting networks in early extrastriate cortex. *Journal of Vision*, *14*(5), 18–18. https://doi.org/10.1167/14.5.18

Dumoulin, S. O., & Wandell, B. A. (2008). Population receptive field estimates in human visual cortex. *NeuroImage*, *39*(2), 647–660. https://doi.org/10.1016/j.neuroimage.2007.09.034

Duncan, R. O., Sample, P. A., Bowd, C., Weinreb, R. N., & Zangwill, L. M. (2012). Arterial spin labeling fMRI measurements of decreased blood flow in primary visual cortex correlates with decreased visual function in human glaucoma. *Vision Research*, *60*, 51–60. https://doi.org/10.1016/j.visres.2012.03.012

Duncan, R. O., Sample, P. A., Weinreb, R. N., Bowd, C., & Zangwill, L. M. (2007a). Retinotopic organization of primary visual cortex in glaucoma: Comparing fMRI measurements of cortical function with visual field loss. *Progress in Retinal and Eye Research*, *26*(1), 38–56. https://doi.org/10.1016/j.preteyeres.2006.10.001

Duncan, R. O., Sample, P. A., Weinreb, R. N., Bowd, C., & Zangwill, L. M. (2007b). Retinotopic organization of primary visual cortex in glaucoma: A method for comparing cortical function with damage to the optic disk. *Investigative Opthalmology & Visual Science*, *48*(2), 733. https://doi.org/10.1167/iovs.06-0773

Edwards, D. P., Purpura, K. P., & Kaplan, E. (1995). Contrast sensitivity and spatial frequency response of primate cortical neurons in and around the cytochrome oxidase blobs. *Vision Research*, *35*(11), 1501–1523. https://doi.org/10.1016/0042-6989(94)00253-I

Ehsaei, A., Chisholm, C. M., Pacey, I. E., & Mallen, E. A. H. (2013). Visual performance fall-off with eccentricity in myopes versus emmetropes. *Journal of Optometry*, *6*(1), 36–44. https://doi.org/10.1016/j.optom.2012.07.001

Elbel, G. K., Kaufmann, C., Schaefers, S., Buser, A., & Auer, D. P. (2002). Refractive anomalies and visual activation in functional magnetic resonance imaging (fMRI): A versatile and low-cost MR-compatible device to correct a potential confound. *Journal of Magnetic Resonance Imaging*, *15*(1), 101–107. https://doi.org/10.1002/jmri.10031

Elvsåshagen, T., Mutsaerts, H. JMM., Zak, N., Norbom, L. B., Quraishi, S. H., Pedersen, P. Ø., Malt, U. F., Westlye, L. T., van Someren, E. JW., Bjørnerud, A., & Groote, I. R. (2019). Cerebral blood flow changes after a day of wake, sleep, and sleep deprivation. *NeuroImage*, *186*, 497–509. https://doi.org/10.1016/j.neuroimage.2018.11.032

Engel, S. (1997). Retinotopic organization in human visual cortex and the spatial precision of functional MRI. *Cerebral Cortex*, *7*(2), 181–192. https://doi.org/10.1093/cercor/7.2.181

Enroth-Cugell, C., & Robson, J. G. (1966). The contrast sensitivity of retinal ganglion cells of the cat. *The Journal of Physiology*, *187*(3), 517–552. https://doi.org/10.1113/jphysiol.1966.sp008107

Ernst, T., & Hennig, J. (1994). Observation of a fast response in functional MR. *Magnetic Resonance in Medicine*, *32*(1), 146–149. https://doi.org/10.1002/mrm.1910320122

Ersan, I., Zengin, N., Bozkurt, B., & Özkagnici, A. (2012). Evaluation of Retinal Nerve Fiber Layer Thickness in Patients With Anisometropic and Strabismic Amblyopia Using Optical Coherence Tomography. *Journal of Pediatric Ophthalmology & Strabismus*. https://doi.org/10.3928/01913913-20121211-02

Ersoz, M. G., Pekcevik, Y., Ayintap, E., Gunes, İ. B., Mart, D. K., Yucel, E., & Türe, G. (2017). MR Imaging of the Anterior Visual Pathway in Primary Open-Angle Glaucoma: Correlation with Octopus 101 Perimetry and Spectralis Optical Coherence Tomography Findings. *Current Eye Research*, 1–7. https://doi.org/10.1080/02713683.2017.1279633

European Glaucoma Prevention Study (EGPS) Group, Miglior, S., Pfeiffer, N., Torri, V., Zeyen, T., Cunha-Vaz, J., & Adamsons, I. (2007). Predictive factors for open-angle glaucoma among patients with ocular hypertension in the European Glaucoma Prevention Study. *Ophthalmology*, *114*(1), 3–9. https://doi.org/10.1016/j.ophtha.2006.05.075

Evangelho, K., Mastronardi, C. A., & de-la-Torre, A. (2019). Experimental Models of Glaucoma: A Powerful Translational Tool for the Future Development of New Therapies for Glaucoma in Humans—A Review of the Literature. *Medicina*, *55*(6), 280. https://doi.org/10.3390/medicina55060280

Farivar, R., Zhou, J., Huang, Y., Feng, L., Zhou, Y., & Hess, R. F. (2019). Two cortical deficits underlie amblyopia: A multifocal fMRI analysis. *NeuroImage*, *190*, 232–241. https://doi.org/10.1016/j.neuroimage.2017.09.045

Federer, F., Ichida, J. M., Jeffs, J., Schiessl, I., McLoughlin, N., & Angelucci, A. (2009). Four Projection Streams from Primate V1 to the Cytochrome Oxidase Stripes of V2.

Journal of Neuroscience, *29*(49), 15455–15471. https://doi.org/10.1523/JNEUROSCI.1648-09.2009

Felleman, D. J., & Van Essen, D. C. (1987). Receptive field properties of neurons in area V3 of macaque monkey extrastriate cortex. *Journal of Neurophysiology*, *57*(4), 889–920. https://doi.org/10.1152/jn.1987.57.4.889

Fellman, R. L., Lynn, J. R., Starita, R. J., & Swanson, W. H. (1989). Clincial importance of spatial summation in glaucoma. In A. Heijl (Ed.), *Peimetry Update 1988/1989* (pp. 313–324). Kugler & Gedini.

Ferreira, S., Pereira, A. C., Quendera, B., Reis, A., Silva, E. D., & Castelo-Branco, M. (2019). Enhanced Visual Attentional Modulation in Patients with Inherited Peripheral Retinal Degeneration in the Absence of Cortical Degeneration. *Neural Plasticity*, *2019*, 1–14. https://doi.org/10.1155/2019/8136354

Field, G. D., Gauthier, J. L., Sher, A., Greschner, M., Machado, T. A., Jepson, L. H., Shlens, J., Gunning, D. E., Mathieson, K., Dabrowski, W., Paninski, L., Litke, A. M., & Chichilnisky, E. J. (2010). Functional connectivity in the retina at the resolution of photoreceptors. *Nature*, *467*(7316), 673–677. https://doi.org/10.1038/nature09424

Fiorentini, A., Maffei, L., Pirchio, M., Spinelli, D., & Porciatti, V. (1981). The ERG in response to alternating gratings in patients with diseases of the peripheral visual pathway. *Investigative Ophthalmology & Visual Science*, *21*(3), 489–493.

Fischl, B. (2012). FreeSurfer. *NeuroImage*, *62*(2), 774–781. https://doi.org/10.1016/j.neuroimage.2012.01.021

Fledelius, H. C., Christensen, A. S., & Fledelius, C. (2014). Juvenile eye growth, when completed? An evaluation based on IOL-Master axial length data, cross-sectional and

longitudinal. *Acta Ophthalmologica*, *92*(3), 259–264. https://doi.org/10.1111/aos.12107

Fortune, B., Demirel, S., Zhang, X., Hood, D. C., Patterson, E., Jamil, A., Mansberger, S. L., Cioffi, G. A., & Johnson, C. A. (2007). Comparing Multifocal VEP and Standard Automated Perimetry in High-Risk Ocular Hypertension and Early Glaucoma. *Investigative Opthalmology & Visual Science*, *48*(3), 1173. https://doi.org/10.1167/iovs.06-0561

Fracasso, A., Petridou, N., & Dumoulin, S. O. (2016). Systematic variation of population receptive field properties across cortical depth in human visual cortex. *NeuroImage*, *139*, 427–438. https://doi.org/10.1016/j.neuroimage.2016.06.048

Frezzotti, P., Giorgio, A., Motolese, I., De Leucio, A., Iester, M., Motolese, E., Federico, A., & De Stefano, N. (2014). Structural and Functional Brain Changes beyond Visual System in Patients with Advanced Glaucoma. *PLoS ONE*, *9*(8), e105931. https://doi.org/10.1371/journal.pone.0105931

Frezzotti, P., Giorgio, A., Toto, F., De Leucio, A., & De Stefano, N. (2016). Early changes of brain connectivity in primary open angle glaucoma. *Human Brain Mapping*, *37*(12), 4581–4596. https://doi.org/10.1002/hbm.23330

Frishman, L. J. (2017). Electroretinography☆. In *Reference Module in Neuroscience and Biobehavioral Psychology* (p. B9780128093245024000). Elsevier. https://doi.org/10.1016/B978-0-12-809324-5.02454-8

Fritsch, D. M., Sowden, J. C., & Thompson, D. A. (2018). Pattern Onset ERGs and VEPs Produced by Patterns Arising From Light Increment and Decrement. *Investigative Opthalmology & Visual Science*, *59*(1), 94. https://doi.org/10.1167/iovs.17-22984

Gagné, A.-M., Lavoie, J., Lavoie, M.-P., Sasseville, A., Charron, M.-C., & Hébert, M. (2010). Assessing the impact of non-dilating the eye on full-field electroretinogram and standard flash response. *Documenta Ophthalmologica*, *121*(3), 167–175. https://doi.org/10.1007/s10633-010-9242-1

Ganekal, S., Dorairaj, S., & Jhanji, V. (2013). Pattern Electroretinography Changes in Patients with Established or Suspected Primary Open Angle Glaucoma. *Journal of Current Glaucoma Practice with DVD*, *7*, 39–42. https://doi.org/10.5005/jp-journals-10008-1135

Gao, X. R., Huang, H., & Kim, H. (2019). Polygenic Risk Score Is Associated With Intraocular Pressure and Improves Glaucoma Prediction in the UK Biobank Cohort. *Translational Vision Science & Technology*, *8*(2), 10. https://doi.org/10.1167/tvst.8.2.10

Garway-Heath, D. F., Holder, G. E., Fitzke, F. W., & Hitchings, R. A. (2002). Relationship between Electrophysiological, Psychophysical, and Anatomical Measurements in Glaucoma. *Investigative Ophthalmology and Visual Science*, *43*, 2213–2220.

Gegenfurtner, K. R., Kiper, D. C., & Levitt, J. B. (1997). Functional Properties of Neurons in Macaque Area V3. *Journal of Neurophysiology*, *77*(4), 1906–1923. https://doi.org/10.1152/jn.1997.77.4.1906

Gerente, V. M., Schor, R. R., Chaim, K. T., Felix, M. de M., Ventura, D. F., Teixeira, S. H., Lottenberg, C. L., Amaro, E., & Paranhos, A. (2015). Evaluation of Glaucomatous Damage via Functional Magnetic Resonance Imaging, and Correlations Thereof with Anatomical and Psychophysical Ocular Findings. *PLOS ONE*, *10*(5), e0126362. https://doi.org/10.1371/journal.pone.0126362

Gigerenzer, G., Krauss, S., & Vitouch, O. (2004). The null ritual: What you always wanted to know about significance testing but were afraid to ask. In D. Kaplan (Ed.), *The sage*

handbook of quantitative methodology for the social sciences. SAGE PUBLICATIONS LTD.

Girkin, C. A., Fazio, M. A., Bowd, C., Medeiros, F. A., Weinreb, R. N., Liebmann, J. M., Proudfoot, J., Zangwill, L. M., & Belghith, A. (2019). Racial Differences in the Association of Anterior Lamina Cribrosa Surface Depth and Glaucoma Severity in the African Descent and Glaucoma Evaluation Study (ADAGES). *Investigative Opthalmology & Visual Science*, *60*(13), 4496. https://doi.org/10.1167/iovs.19-26645

Glezer, V. (1965). The receptive fields of the retina. *Vision Research*, *5*(9), 497–525.

Glickstein, M., & Whitteridge, D. (1987). Tatsuji Inouye and the mapping of the visual fields on the human cerebral cortex. *Trends in Neurosciences*, *10*(9), 350–353. https://doi.org/10.1016/0166-2236(87)90066-X

Glovinsky, Y., Quigley, H. A., & Dunkelberger, G. R. (1991). Retinal ganglion cell loss is size dependent in experimental glaucoma. *Investigative Ophthalmology & Visual Science*, *32*(3), 484–491.

Goense, J. B. M., & Logothetis, N. K. (2008). Neurophysiology of the BOLD fMRI Signal in Awake Monkeys. *Current Biology*, *18*(9), 631–640. https://doi.org/10.1016/j.cub.2008.03.054

Gonzalez, P., Parks, S., Dolan, F., & Keating, D. (2004). The effects of pupil size on the multifocal electroretinogram. *Documenta Ophthalmologica*, *109*(1), 67–72. https://doi.org/10.1007/s10633-004-1545-7

Goodale, M. A., & Milner, A. D. (1992). Separate visual pathways for perception and action. *Trends in Neurosciences*, *15*(1), 20–25.

Goodyear, B. G., & Menon, R. S. (2001). Brief visual stimulation allows mapping of ocular dominance in visual cortex using fMRI. *Human Brain Mapping*, *14*(4), 210–217. https://doi.org/10.1002/hbm.1053

Goodyear, B. G., Nicolle, D. A., & Menon, R. S. (2002). High resolution fMRI of ocular dominance columns within the visual cortex of human amblyopes. *Strabismus*, *10*(2), 129–136. https://doi.org/10.1076/stra.10.2.129.8140

Gracitelli, C. P. B., Abe, R. Y., & Medeiros, F. A. (2015). Spectral-Domain Optical Coherence Tomography for Glaucoma Diagnosis. *The Open Ophthalmology Journal*, *9*(1), 68–77. https://doi.org/10.2174/1874364101509010068

Graham, C. H., & Bartlett, N. R. (1939). The relation of size of stimulus and intensity in the human eye: II. Intensity thresholds for red and violet light. *Journal of Experimental Psychology*, *24*(6), 574–587.

Gregg, R. G., McCall, M. A., & Massey, S. C. (2013). Function and Anatomy of the Mammalian Retina. In S. J. Ryan (Ed.), *Retina* (5th Ed, pp. 360–400). Saunders/Elsevier.

Groppe, D. (2020). *Bonferroni-Holm Correction for Multiple Comparisons (https://www.mathworks.com/matlabcentral/fileexchange/28303-bonferroni-holm-correction-for-multiple-comparisons)* (v.1.1) [MATLAB; MATLAB Central File Exchange].

Guo, L., Salt, T. E., Luong, V., Wood, N., Cheung, W., Maass, A., Ferrari, G., Russo-Marie, F., Sillito, A. M., Cheetham, M. E., Moss, S. E., Fitzke, F. W., & Cordeiro, M. F. (2007). Targeting amyloid-beta in glaucoma treatment. *Proceedings of the National Academy of Sciences*, *104*(33), 13444–13449. https://doi.org/10.1073/pnas.0703707104

Guo, N., Ma, M., Xiong, W., Chen, L., & Jing, N. (2017). An Efficient Query Algorithm for Trajectory Similarity Based on Fréchet Distance Threshold. *ISPRS International Journal of Geo-Information*, *6*(11), 326. https://doi.org/10.3390/ijgi6110326

Guo, Z., Kwon, Y. H., Lee, K., Wang, K., Wahle, A., Alward, W. L. M., Fingert, J. H., Bettis, D. I., Johnson, C. A., Garvin, M. K., Sonka, M., & Abràmoff, M. D. (2017). Optical Coherence Tomography Analysis Based Prediction of Humphrey 24-2 Visual Field Thresholds in Patients With Glaucoma. *Investigative Ophthalmology & Visual Science*, *58*(10), 3975–3985. https://doi.org/10.1167/iovs.17-21832

Hammond, P. (1974). Cat retinal ganglion cells: Size and shape of receptive field centres. *The Journal of Physiology*, *242*(1), 99–118. https://doi.org/10.1113/jphysiol.1974.sp010696

Harris, A., Siesky, B., & Wirostko, B. (2013). Cerebral blood flow in glaucoma patients. *Journal of Glaucoma.*, *22*, s46-48.

Harrison, J. M., O'Connor, P. S., Young, R. S., Kincaid, M., & Bentley, R. (1987). The pattern ERG in man following surgical resection of the optic nerve. *Investigative Ophthalmology & Visual Science*, *28*(3), 492–499.

Harvey, B. M., & Dumoulin, S. O. (2011). The Relationship between Cortical Magnification Factor and Population Receptive Field Size in Human Visual Cortex: Constancies in Cortical Architecture. *Journal of Neuroscience*, *31*(38), 13604–13612. https://doi.org/10.1523/JNEUROSCI.2572-11.2011

Harwerth, R. S., Carter-Dawson, L., Shen, F., Smith, E. L., & Crawford, M. L. (1999). Ganglion cell losses underlying visual field defects from experimental glaucoma. *Investigative Ophthalmology & Visual Science*, *40*(10), 2242–2250.

Harwerth, R. S., Wheat, J. L., & Rangaswamy, N. V. (2008). Age-Related Losses of Retinal Ganglion Cells and Axons. *Investigative Opthalmology & Visual Science*, *49*(10), 4437. https://doi.org/10.1167/iovs.08-1753

He, D., & Fang, F. (2015). Perceptual learning reduces crowding effect and the size of population receptive field in V2. *Journal of Vision*, *15*(12), 107. https://doi.org/10.1167/15.12.107

Hendrickson, A. E., & Wilson, J. R. (1979). A difference in [14C]deoxyglucose autoradiographic patterns in striate cortex between Macaca and Saimiri monkeys following monocular stimulation. *Brain Research*, *170*(2), 353–358. https://doi.org/10.1016/0006-8993(79)90113-6

Hess, R. F., & Baker, C. I. Jr. (1984). Human pattern-evoked electroretinogram. *Journal of Neurophysiology*, *51*(5), 939–951.

Hess, R. F., & Howell, E. R. (1977). The threshold contrast sensitivity function in strabismic amblyopia: Evidence for a two type classification. *Vision Research*, *17*(9), 1049–1055. https://doi.org/10.1016/0042-6989(77)90009-8

Hirota, R., Kondo, M., Ueno, S., Sakai, T., Koyasu, T., & Terasaki, H. (2012). Photoreceptor and Post-Photoreceptoral Contributions to Photopic ERG a-Wave in Rhodopsin P347L Transgenic Rabbits. *Investigative Opthalmology & Visual Science*, *53*(3), 1467. https://doi.org/10.1167/iovs.11-9006

Hiss, P., & Fahl, G. (1991). [Changes in the pattern electroretinogram in glaucoma and ocular hypertension are dependent on stimulus frequency]. *Fortschritte Der Ophthalmologie: Zeitschrift Der Deutschen Ophthalmologischen Gesellschaft*, *88*(5), 562–565.

Holden, B. A., Fricke, T. R., Wilson, D. A., Jong, M., Naidoo, K. S., Sankaridurg, P., Wong, T. Y., Naduvilath, T. J., & Resnikoff, S. (2016). Global Prevalence of Myopia and High Myopia and Temporal Trends from 2000 through 2050. *Ophthalmology*, *123*(5), 1036–1042. https://doi.org/10.1016/j.ophtha.2016.01.006

Holder, G. E. (2001). Pattern Electroretinography (PERG) and an Integrated Approach to Visual Pathway Diagnosis. *Progress in Retinal and Eye Research*, *20*(4), 531–561. https://doi.org/10.1016/S1350-9462(00)00030-6

Holder, G. E., Brigell, M. G., Hawlina, M., Meigen, T., Vaegan, Bach, M., & for the International Society for Clinical Electrophysiology of Vision. (2007). ISCEV standard for clinical pattern electroretinography—2007 update. *Documenta Ophthalmologica*, *114*(3), 111–116. https://doi.org/10.1007/s10633-007-9053-1

Holm, S. (1979). A Simple Sequentially Rejective Multiple Test Procedure. *Scandinavian Journal of Statistics*, *6*(2), 65–70.

Holmes, G. (1918). DISTURBANCES OF VISION BY CEREBRAL LESIONS. *British Journal of Ophthalmology*, *2*(7), 353–384. https://doi.org/10.1136/bjo.2.7.353

Holopigian, K., Seiple, W., Mayron, C., Koty, R., & Lorenzo, M. (1990). Electrophysiological and psychophysical flicker sensitivity in patients with primary open-angle glaucoma and ocular hypertension. *Investigative Ophthalmology & Visual Science*, *31*(9), 1863–1868.

Hood, D. C. (2019). Does Retinal Ganglion Cell Loss Precede Visual Field Loss in Glaucoma?: *Journal of Glaucoma*, *28*(11), 945–951. https://doi.org/10.1097/IJG.0000000000001380

Hood, D. C., & Greenstein, V. C. (2003). Multifocal VEP and ganglion cell damage: Applications and limitations for the study of glaucoma. *Progress in Retinal and Eye Research*, *22*(2), 201–251. https://doi.org/10.1016/S1350-9462(02)00061-7

Hood, D. C., & Kardon, R. H. (2007). A framework for comparing structural and functional measures of glaucomatous damage. *Progress in Retinal and Eye Research*, *26*(6), 688–710. https://doi.org/10.1016/j.preteyeres.2007.08.001

Hood, D. C., Xu, L., Thienprasiddhi, P., Greenstein, V. C., Odel, J. G., Grippo, T. M., Liebmann, J. M., & Ritch, R. (2005). The Pattern Electroretinogram in Glaucoma Patients with Confirmed Visual Field Deficits. *Investigative Opthalmology & Visual Science*, *46*(7), 2411. https://doi.org/10.1167/iovs.05-0238

Hornik, K., Kleiber, C., Leisch, F., & Zeileis, A. (2001). *Strucchange: An R Package for Testing for Structural Change in Linear Regression Models*. Universitätsbibliothek Dortmund. https://doi.org/10.17877/DE290R-12194

Horton, J. C. (1991). The Representation of the Visual Field in Human Striate Cortex: A Revision of the Classic Holmes Map. *Archives of Ophthalmology*, *109*(6), 816. https://doi.org/10.1001/archopht.1991.01080060080030

Hosford, P. S., & Gourine, A. V. (2019). What is the key mediator of the neurovascular coupling response? *Neuroscience & Biobehavioral Reviews*, *96*, 174–181. https://doi.org/10.1016/j.neubiorev.2018.11.011

Howarth, C. I., & Lowe, G. (1966). Statistical Detection Theory of Piper's Law. *Nature*, *212*(5059), 324–326. https://doi.org/10.1038/212324a0

Howitt, D. (2013). *Introduction to statistics in psychology*. Pearson Education.

Hu, X., Le, T. H., & U??urbil, K. (1997). Evaluation of the early response in fMRI in individual subjects using short stimulus duration. *Magnetic Resonance in Medicine*, *37*(6), 877–884. https://doi.org/10.1002/mrm.1910370612

Hu, Y.-X., He, J.-R., Yang, B., Huang, X., Li, Y.-P., Zhou, F.-Q., Xu, X.-X., Zhong, Y.-L., Wang, J., & Wu, X.-R. (2018). Abnormal resting-state functional network centrality in patients with high myopia: Evidence from a voxel-wise degree centrality analysis. *International Journal of Ophthalmology*, *11*(11), 1814–1820. https://doi.org/10.18240/ijo.2018.11.13

Huang, D., Swanson, E., Lin, C., Schuman, J., Stinson, W., Chang, W., Hee, M., Flotte, T., Gregory, K., Puliafito, C., & et, al. (1991). Optical coherence tomography. *Science*, *254*(5035), 1178–1181. https://doi.org/10.1126/science.1957169

Huang, X., Hu, Y., Zhou, F., Xu, X., Wu, Y., Jay, R., Cheng, Y., Wang, J., & Wu, X. (2018). Altered whole-brain gray matter volume in high myopia patients: A voxel-based morphometry study. *Neuroreport*, *29*(9), 760–767. https://doi.org/10.1097/WNR.0000000000001028

Hubel, D. H., & Livingstone, M. S. (1990). Color and contrast sensitivity in the lateral geniculate body and primary visual cortex of the macaque monkey. *The Journal of Neuroscience*, *10*(7), 2223–2237. https://doi.org/10.1523/JNEUROSCI.10-07-02223.1990

Hubel, D. H., & Wiesel, T. N. (1959). Receptive fields of single neurones in the cat's striate cortex. *The Journal of Physiology*, *148*(3), 574–591. https://doi.org/10.1113/jphysiol.1959.sp006308

Hubel, D. H., & Wiesel, T. N. (1962). Receptive fields, binocular interaction and functional architecture in the cat's visual cortex. *The Journal of Physiology*, *160*(1), 106–154. https://doi.org/10.1113/jphysiol.1962.sp006837

Hubel, D. H., & Wiesel, T. N. (1965). RECEPTIVE FIELDS AND FUNCTIONAL ARCHITECTURE IN TWO NONSTRIATE VISUAL AREAS (18 AND 19) OF THE CAT. *Journal of Neurophysiology*, *28*(2), 229–289. https://doi.org/10.1152/jn.1965.28.2.229

Hubel, D. H., & Wiesel, T. N. (1968). Receptive fields and functional architecture of monkey striate cortex. *The Journal of Physiology*, *195*(1), 215–243. https://doi.org/10.1113/jphysiol.1968.sp008455

Hubel, D. H., & Wiesel, T. N. (1969). Anatomical Demonstration of Columns in the Monkey Striate Cortex. *Nature*, *221*(5182), 747–750. https://doi.org/10.1038/221747a0

Hughes, A. E., Greenwood, J. A., Finlayson, N. J., & Schwarzkopf, D. S. (2019). Population receptive field estimates for motion-defined stimuli. *NeuroImage*, *199*, 245–260. https://doi.org/10.1016/j.neuroimage.2019.05.068

Hummer, A., Ritter, M., Woletz, M., Ledolter, A. A., Tik, M., Dumoulin, S. O., Holder, G. E., Schmidt-Erfurth, U., & Windischberger, C. (2018). Artificial scotoma estimation based on population receptive field mapping. *NeuroImage*, *169*, 342–351. https://doi.org/10.1016/j.neuroimage.2017.12.010

Iannetti, G. D., & Wise, R. G. (2007). BOLD functional MRI in disease and pharmacological studies: Room for improvement? *Magnetic Resonance Imaging*, *25*(6), 978–988. https://doi.org/10.1016/j.mri.2007.03.018

Infanti, E., & Schwarzkopf, D. S. (2020). Mapping sequences can bias population receptive field estimates. *NeuroImage*, *211*, 116636. https://doi.org/10.1016/j.neuroimage.2020.116636

Jafarzadehpour, E., Radinmehr, F., Pakravan, M., Mirzajani, A., & Yazdani, S. (2013). Pattern Electroretinography in glaucoma suspects and early primary open angle glaucoma. *Journal of Ophthalmic and Vision Research*, *8*(3), 199–206.

JASP Team. (2019). *JASP (Version 0.11.1)*. https://jasp-stats.org

Je, S., Ennis, F. A., Morgan, J. E., & Redmond, T. (2015). Spatial summation of perimetric stimuli across the visual field in anisometropic and strabismic amblyopia. *Investigative Ophthalmology & Visual Science*, *56*, 2212.

Je, S., Ennis, F. A., Woodhouse, J. M., Sengpiel, F., & Redmond, T. (2018). Spatial summation across the visual field in strabismic and anisometropic amblyopia. *Scientific Reports*, *8*(1), 3858. https://doi.org/10.1038/s41598-018-21620-6

Jenkinson, M., Beckmann, C. F., Behrens, T. E. J., Woolrich, M. W., & Smith, S. M. (2012). FSL. *NeuroImage*, *62*(2), 782–790.

Jha, M. K., Thakur, D., Limbu, N., Badhu, B. P., & Paudel, B. H. (2017). Visual Evoked Potentials in Primary Open Angle Glaucoma. *Journal of Neurodegenerative Diseases*, *2017*, 1–4. https://doi.org/10.1155/2017/9540609

Jiang, F., Zeng, F.-F., Yu, C., Ye, Y.-Q., & Zeng, X.-J. (2018). Altered whole-brain gray matter volume in primary angle closure glaucoma patients: A voxel-based morphometry study. *NeuroReport*, 1. https://doi.org/10.1097/WNR.0000000000001126

Johnson, M. A., & Massof, R. W. (1982). The photomyoclonic reflex: An artefact in the clinical electroretinogram. *British Journal of Ophthalmology*, *66*(6), 368–378. https://doi.org/10.1136/bjo.66.6.368

Johnson, T. V., & Tomarev, S. I. (2010). Rodent models of glaucoma. *Brain Research Bulletin*, *81*(2–3), 349–358. https://doi.org/10.1016/j.brainresbull.2009.04.004

Jorge, L., Canário, N., Martins, R., Santiago, B., Santana, I., Quental, H., Ambrósio, F., Bernardes, R., & Castelo-Branco, M. (2020). The Retinal Inner Plexiform Synaptic Layer Mirrors Grey Matter Thickness of Primary Visual Cortex with Increased Amyloid *β* Load in Early Alzheimer's Disease. *Neural Plasticity*, *2020*, 1–11. https://doi.org/10.1155/2020/8826087

Jorge, L., Canario, N., Quental, H., Bernardes, R., & Castelo-Branco, M. (2020). Is the Retina a Mirror of the Aging Brain? Aging of Neural Retina Layers and Primary Visual Cortex Across the Lifespan. *FRONTIERS IN AGING NEUROSCIENCE*, *11*. https://doi.org/10.3389/fnagi.2019.00360

Jung, K. I., Jeon, S., Kim, Y. C., & Park, C. K. (2019). Comparison of pattern electroretinograms of glaucoma patients with parafoveal scotoma versus peripheral nasal step. *Scientific Reports*, *9*(1), 3547. https://doi.org/10.1038/s41598-019-39948-y

Junoy-Montolio, F. G., Meems, W., Janssens, M. S. A., Stam, L., & Jansonius, N. M. (2016). Lateral Inhibition in the Human Visual System in Patients with Glaucoma and Healthy Subjects: A Case-Control Study. *PLOS ONE*, *11*(3), e0151006. https://doi.org/10.1371/journal.pone.0151006

Kaas, J. H. (2000). Why is Brain Size so Important:Design Problems and Solutions as Neocortex Gets Bigger or Smaller. *Brain and Mind*, *1*(1), 7–23. https://doi.org/10.1023/A:1010028405318

Kaneko, A. (1970). Physiological and morphological identification of horizontal, bipolar and amacrine cells in goldfish retina. *The Journal of Physiology*, *207*(3), 623–633. https://doi.org/10.1113/jphysiol.1970.sp009084

Kang Li, Xiaodong Wu, Chen, D. Z., & Sonka, M. (2006). Optimal Surface Segmentation in Volumetric Images-A Graph-Theoretic Approach. *IEEE Transactions on Pattern Analysis and Machine Intelligence*, *28*(1), 119–134. https://doi.org/10.1109/TPAMI.2006.19

Kansal, V., Armstrong, J. J., Pintwala, R., & Hutnik, C. (2018). Optical coherence tomography for glaucoma diagnosis: An evidence based meta-analysis. *PLOS ONE*, *13*(1), e0190621. https://doi.org/10.1371/journal.pone.0190621

Karaśkiewicz, J., Drobek-Słowik, M., & Lubiński, W. (2014). Pattern electroretinogram (PERG) in the early diagnosis of normal-tension preperimetric glaucoma: A case report. *Documenta Ophthalmologica*, *128*(1), 53–58. https://doi.org/10.1007/s10633-013-9414-x

Karaśkiewicz, J., Penkala, K., Mularczyk, M., & Lubiński, W. (2017). Evaluation of retinal ganglion cell function after intraocular pressure reduction measured by pattern electroretinogram in patients with primary open-angle glaucoma. *Documenta Ophthalmologica*, *134*(2), 89–97. https://doi.org/10.1007/s10633-017-9575-0

Kasi, A., Faiq, MuneebA., & Chan, KevinC. (2019). In vivo imaging of structural, metabolic and functional brain changes in glaucoma. *Neural Regeneration Research*, *14*(3), 446. https://doi.org/10.4103/1673-5374.243712

Katz, J., Quigley, H. A., & Sommer, A. (1995). Repeatability of the Glaucoma Hemifield Test in automated perimetry. *Investigative Ophthalmology & Visual Science*, *36*(8), 1658–1664.

Keliris, G. A., Li, Q., Papanikolaou, A., Logothetis, N. K., & Smirnakis, S. M. (2019). Estimating average single-neuron visual receptive field sizes by fMRI. *Proceedings of the*

National Academy of Sciences, *116*(13), 6425–6434. https://doi.org/10.1073/pnas.1809612116

Kim, J. H., Taylor, A. J., Wang, D. J., Zou, X., & Ress, D. (2019). Dynamics of the cerebral blood flow response to brief neural activity in human visual cortex. *Journal of Cerebral Blood Flow & Metabolism*, 0271678X1986903. https://doi.org/10.1177/0271678X19869034

King, W. M., Sarup, V., Sauvé, Y., Moreland, C. M., Carpenter, D. O., & Sharma, S. C. (2006). Expansion of visual receptive fields in experimental glaucoma. *Visual Neuroscience*, *23*(1), 137–142. https://doi.org/10.1017/S0952523806231122

Klein, B. P., Fracasso, A., van Dijk, J. A., Paffen, C. L. E., te Pas, S. F., & Dumoulin, S. O. (2018). Cortical depth dependent population receptive field attraction by spatial attention in human V1. *NeuroImage*, *176*, 301–312. https://doi.org/10.1016/j.neuroimage.2018.04.055

Klein, B. P., Harvey, B. M., & Dumoulin, S. O. (2014). Attraction of Position Preference by Spatial Attention throughout Human Visual Cortex. *Neuron*, *84*(1), 227–237. https://doi.org/10.1016/j.neuron.2014.08.047

Kline, D. W., Culham, J. C., Bartel, P., & Lynk, L. (2001). Aging effects on vernier hyperacuity: A function of oscillation rate but not target contrast. *Optometry and Vision Science: Official Publication of the American Academy of Optometry*, *78*(9), 676–682.

Kolb, H., & Dekorver, L. (1991). Midget ganglion cells of the parafovea of the human retina: A Study by electron microscopy and serial section reconstructions. *The Journal of Comparative Neurology*, *303*(4), 617–636. https://doi.org/10.1002/cne.903030408

Kolb, H., & Marshak, D. (2003). The midget pathways of the primate retina. *Documenta Ophthalmologica*, *106*(1), 67–81. https://doi.org/10.1023/A:1022469002511

Korth, M. (1983). Pattern-evoked responses and luminance-evoked responses in the human electroretinogram. *Journal of Physiology*, *337*, 451–469.

Korth, M., Horn, F., Storck, B., & Jonas, J. (1989). The pattern-evoked electroretinogram (PERG): Age-related alterations and changes in glaucoma. *Graefe's Archive for Clinical and Experimental Ophthalmology*, *227*(2), 123–130. https://doi.org/10.1007/BF02169783

Korth, M., & Rix, R. (1989). Differences between pattern onset and pattern reversal retinal responses. *Documenta Ophthalmologica*, *72*(1), 39–46. https://doi.org/10.1007/BF00155212

Kuffler, S. W. (1953). DISCHARGE PATTERNS AND FUNCTIONAL ORGANIZATION OF MAMMALIAN RETINA. *Journal of Neurophysiology*, *16*(1), 37–68. https://doi.org/10.1152/jn.1953.16.1.37

Kumschick, I. R., Beck, L., Eid, M., Witte, G., Klann-Delius, G., Heuser, I., Steinlein, R., & Menninghaus, W. (2014). READING and FEELING: The effects of a literature-based intervention designed to increase emotional competence in second and third graders. *Frontiers in Psychology*, *5*. https://doi.org/10.3389/fpsyg.2014.01448

Kwon, M., & Liu, R. (2019). Linkage between retinal ganglion cell density and the nonuniform spatial integration across the visual field. *Proceedings of the National Academy of Sciences*, 201817076. https://doi.org/10.1073/pnas.1817076116

Lagreze, W.-D., & Sireteanu, R. (1991). Two-dimensional spatial distortions in human strabismic amblyopia. *Vision Research*, *31*(7–8), 1271–1288. https://doi.org/10.1016/0042-6989(91)90051-6

Lam, D. S. C., Leung, K. S., Mohamed, S., Chan, W., Palanivelu, M. S., Cheung, C. Y. L., Li, E. Y. M., Lai, R. Y. K., & Leung, C. K. (2007). Regional Variations in the Relationship

between Macular Thickness Measurements and Myopia. *Investigative Opthalmology & Visual Science*, *48*(1), 376. https://doi.org/10.1167/iovs.06-0426

Le, A., Mukesh, B. N., McCarty, C. A., & Taylor, H. R. (2003). Risk Factors Associated with the Incidence of Open-Angle Glaucoma: The Visual Impairment Project. *Investigative Opthalmology & Visual Science*, *44*(9), 3783. https://doi.org/10.1167/iovs.03-0077

Lee, B. B. (1996). Receptive field structure in the primate retina. *Vision Research*, *36*(5), 631–644. https://doi.org/10.1016/0042-6989(95)00167-0

Lee, J. Y., Jeong, H. J., Lee, J. H., Kim, Y. J., Kim, E. Y., Kim, Y. Y., Ryu, T., Cho, Z.-H., & Kim, Y.-B. (2014). An Investigation of Lateral Geniculate Nucleus Volume in Patients With Primary Open-Angle Glaucoma Using 7 Tesla Magnetic Resonance Imaging. *Investigative Opthalmology & Visual Science*, *55*(6), 3468. https://doi.org/10.1167/iovs.14-13902

Lelkens, A. M. M., & Zuidema, P. (1983). Increment thresholds with various low background intensities at different locations in the peripheral retina. *Journal of the Optical Society of America*, *73*(10), 1372–1378. https://doi.org/10.1364/JOSA.73.001372

Leventhal, A., Rodieck, R., & Dreher, B. (1981). Retinal ganglion cell classes in the Old World monkey: Morphology and central projections. *Science*, *213*(4512), 1139–1142. https://doi.org/10.1126/science.7268423

Levin, N., Dumoulin, S. O., Winawer, J., Dougherty, R. F., & Wandell, B. A. (2010). Cortical Maps and White Matter Tracts following Long Period of Visual Deprivation and Retinal Image Restoration. *Neuron*, *65*(1), 21–31. https://doi.org/10.1016/j.neuron.2009.12.006

Levitt, J. B., Kiper, D. C., & Movshon, J. A. (1994). Receptive fields and functional architecture of macaque V2. *Journal of Neurophysiology*, *71*(6), 2517–2542. https://doi.org/10.1152/jn.1994.71.6.2517

Li, Q., Guo, M., Dong, H., Zhang, Y., Fu, Y., & Yin, X. (2012). Voxel-based analysis of regional gray and white matter concentration in high myopia. *Vision Research*, *58*, 45–50. https://doi.org/10.1016/j.visres.2012.02.005

Li, X., Dumoulin, S. O., Mansouri, B., & Hess, R. F. (2007). Cortical Deficits in Human Amblyopia: Their Regional Distribution and Their Relationship to the Contrast Detection Deficit. *Investigative Opthalmology & Visual Science*, *48*(4), 1575. https://doi.org/10.1167/iovs.06-1021

Li, Z., Allingham, R. R., Nakano, M., Jia, L., Chen, Y., Ikeda, Y., Mani, B., Chen, L.-J., Kee, C., Garway-Heath, D. F., Sripriya, S., Fuse, N., Abu-Amero, K. K., Huang, C., Namburi, P., Burdon, K., Perera, S. A., Gharahkhani, P., Lin, Y., … Vithana, E. N. (2015). A common variant near TGFBR3 is associated with primary open angle glaucoma. *Human Molecular Genetics*, *24*(13), 3880–3892. https://doi.org/10.1093/hmg/ddv128

Lin, F.-H., Polimeni, J. R., Lin, J.-F. L., Tsai, K. W.-K., Chu, Y.-H., Wu, P.-Y., Li, Y.-T., Hsu, Y.-C., Tsai, S.-Y., & Kuo, W.-J. (2018). Relative latency and temporal variability of hemodynamic responses at the human primary visual cortex. *NeuroImage*, *164*, 194–201. https://doi.org/10.1016/j.neuroimage.2017.01.041

Liu, S., Ong, Y.-T., Hilal, S., Loke, Y. M., Wong, T. Y., Chen, C. L.-H., Cheung, C. Y., & Zhou, J. (2016). The Association Between Retinal Neuronal Layer and Brain Structure is Disrupted in Patients with Cognitive Impairment and Alzheimer's Disease. *JOURNAL OF ALZHEIMERS DISEASE*, *54*(2), 585–595. https://doi.org/10.3233/JAD-160067

Liu, T., Tang, W., Sun, X., & Qian, J. (2007). FMRI-Based Implication of Receptive Field Size Expansion and Eccentricity Distribution of Visual Cortex in Glaucoma. *Investigative Ophthalmology & Visual Science*, *48*(13), 1616–1616.

Livingstone, M. S., & Hubel, D. H. (1984a). Anatomy and physiology of a color system in the primate visual cortex. *The Journal of Neuroscience*, *4*(1), 309–356. https://doi.org/10.1523/JNEUROSCI.04-01-00309.1984

Livingstone, M. S., & Hubel, D. H. (1984b). Specificity of intrinsic connections in primate primary visual cortex. *The Journal of Neuroscience*, *4*(11), 2830–2835. https://doi.org/10.1523/JNEUROSCI.04-11-02830.1984

Logothetis, N. K. (2008). What we can do and what we cannot do with fMRI. *Nature*, *453*(7197), 869–878. https://doi.org/10.1038/nature06976

Logothetis, N. K., Pauls, J., Augath, M., Trinath, T., & Oeltermann, A. (2001). Neurophysiological investigation of the basis of the fMRI signal. *Nature*, *412*(6843), 150–157. https://doi.org/10.1038/35084005

Longhin, E., Convento, E., Pilotto, E., Bonin, G., Vujosevic, S., Kotsafti, O., & Midena, E. (2013). Static and dynamic retinal fixation stability in microperimetry. *Canadian Journal of Ophthalmology*, *48*(5), 375–380. https://doi.org/10.1016/j.jcjo.2013.05.021

Lu, P., Shi, L., Du, H., Xie, B., Li, C., Li, S., Liu, T., Feng, H., & Wang, J. (2013). Reduced white matter integrity in primary open-angle glaucoma: A DTI study using tract-based spatial statistics. *Journal of Neuroradiology*, *40*(2), 89–93. https://doi.org/10.1016/j.neurad.2012.04.001

Lu, Z., & Dosher, B. (2013). *Visual psychophysics: From laboratory to theory.* MIT Press.

Luck, S. J., Chelazzi, L., Hillyard, S. A., & Desimone, R. (1997). Neural Mechanisms of Spatial Selective Attention in Areas V1, V2, and V4 of Macaque Visual Cortex. *Journal of Neurophysiology*, *77*(1), 24–42. https://doi.org/10.1152/jn.1997.77.1.24

Luo, X., & Frishman, L. J. (2011). Retinal pathway origins of the pattern Electroretinogram (PERG). *Investigative Opthalmology & Visual Science*, *52*(12), 8571. https://doi.org/10.1167/iovs.11-8376

Maffei, L., & Fiorentini, A. (1981). Electroretinographic responses to alternating gratings before and after section of the optic nerve. *Science (New York, N.Y.)*, *211*(4485), 953–955. https://doi.org/10.1126/science.7466369

Magistretti, P. J., & Pellerin, L. (1999). Cellular mechanisms of brain energy metabolism and their relevance to functional brain imaging. *Philosophical Transactions of the Royal Society of London. Series B: Biological Sciences*, *354*(1387), 1155–1163. https://doi.org/10.1098/rstb.1999.0471

Malonek, D., & Grinvald, A. (1996). Interactions Between Electrical Activity and Cortical Microcirculation Revealed by Imaging Spectroscopy: Implications for Functional Brain Mapping. *Science*, *272*(5261), 551–554. https://doi.org/10.1126/science.272.5261.551

Marshak, D. W. (2009). Retinal Ganglion Cells: Anatomy. In *Encyclopedia of Neuroscience* (pp. 211–218). Elsevier. https://doi.org/10.1016/B978-008045046-9.00897-4

Martinez-Conde, S., Macknik, S. L., Troncoso, X. G., & Hubel, D. H. (2009). Microsaccades: A neurophysiological analysis. *Trends in Neurosciences*, *32*(9), 463–475. https://doi.org/10.1016/j.tins.2009.05.006

Masland, R. H. (2012a). The tasks of amacrine cells. *Visual Neuroscience*, *29*(1), 3–9. https://doi.org/10.1017/s0952523811000344

Masland, R. H. (2012b). The Neuronal Organization of the Retina. *Neuron*, *76*(2), 266–280. https://doi.org/10.1016/j.neuron.2012.10.002

Masters, M., Bruner, E., Queer, S., Traynor, S., & Senjem, J. (2015). Analysis of the volumetric relationship among human ocular, orbital and fronto-occipital cortical morphology. *Journal of Anatomy*, *227*(4), 460–473. https://doi.org/10.1111/joa.12364

MATLAB (9.5.0.1067069 (R2018b) Update 4). (2018). [Computer software]. The MathWorks Inc.

May, J. G., Ralston, J. V., Reed, J. L., & Van Dyk, H. J. L. (1982). Loss in Pattern-Elicited Electroretinograms in Optic Nerve Dysfunction. *American Journal of Ophthalmology*, *93*(4), 418–422. https://doi.org/10.1016/0002-9394(82)90131-3

Mayer, A. R., Toulouse, T., Klimaj, S., Ling, J. M., Pena, A., & Bellgowan, P. S. F. (2014). Investigating the properties of the hemodynamic response function after mild traumatic brain injury. *Journal of Neurotrauma*, *31*(2), 189–197. https://doi.org/10.1089/neu.2013.3069

McMonnies, C. W. (2017). Glaucoma history and risk factors. *Journal of Optometry*, *10*(2), 71–78. https://doi.org/10.1016/j.optom.2016.02.003

Medendorp, W. P., de Brouwer, A. J., & Smeets, J. B. J. (2018). Dynamic representations of visual space for perception and action. *Cortex*, *98*, 194–202. https://doi.org/10.1016/j.cortex.2016.11.013

Medina, J., Jax, S. A., & Coslett, H. B. (2019). Impairments in action and perception after right intraparietal damage. *Cortex*, S0010945219300553. https://doi.org/10.1016/j.cortex.2019.02.004

Menezes de Oliveira, M., Pang, J. C., Robinson, P. A., Liu, X., & Schira, M. M. (2019). Feasibility of functional magnetic resonance imaging of ocular dominance and orientation preference in primary visual cortex. *PLOS Computational Biology*, *15*(11), e1007418. https://doi.org/10.1371/journal.pcbi.1007418

Menon, R. S., & Goodyear, B. G. (1999). Submillimeter functional localization in human striate cortex using BOLD contrast at 4 Tesla: Implications for the vascular point-spread function. *Magnetic Resonance in Medicine*, *41*(2), 230–235. https://doi.org/10.1002/(sici)1522-2594(199902)41:2<230::aid-mrm3>3.0.co;2-o

Menon, R. S., Ogawa, S., Hu, X., Strupp, J. P., Anderson, P., & U??urbil, K. (1995). BOLD Based Functional MRI at 4 Tesla Includes a Capillary Bed Contribution: Echo-Planar Imaging Correlates with Previous Optical Imaging Using Intrinsic Signals. *Magnetic Resonance in Medicine*, *33*(3), 453–459. https://doi.org/10.1002/mrm.1910330323

Merigan, W., Katz, L., & Maunsell, J. (1991). The effects of parvocellular lateral geniculate lesions on the acuity and contrast sensitivity of macaque monkeys. *The Journal of Neuroscience*, *11*(4), 994–1001. https://doi.org/10.1523/JNEUROSCI.11-04-00994.1991

Merkel, C., Hopf, J., & Schoenfeld, M. A. (2020). Modulating the global orientation bias of the visual system changes population receptive field elongations. *Human Brain Mapping*, *41*(7), 1765–1774. https://doi.org/10.1002/hbm.24909

Michael, C. R. (1978). Color vision mechanisms in monkey striate cortex: Simple cells with dual opponent-color receptive fields. *Journal of Neurophysiology*, *41*(5), 1233–1249. https://doi.org/10.1152/jn.1978.41.5.1233

Michael, R., & Bron, A. J. (2011). The ageing lens and cataract: A model of normal and pathological ageing. *Philosophical Transactions of the Royal Society B: Biological Sciences*, *366*(1568), 1278–1292. https://doi.org/10.1098/rstb.2010.0300

Mirzajani, A., Ghorbani, M., Rasuli, B., & Mahmoud-Pashazadeh, A. (2017). Effect of induced high myopia on functional MRI signal changes. *Physica Medica-European Journal of Medical Physics*, *37*, 32–36. https://doi.org/10.1016/j.ejmp.2017.04.004

Mirzajani, A., Sarlaki, E., Kharazi, H. H., & Tavan, M. (2011). Effect of Lens-Induced Myopia on Visual Cortex Activity: A Functional MR Imaging Study. *American Journal of Neuroradiology*, *32*(8), 1426–1429. https://doi.org/10.3174/ajnr.A2551

Moradi, F., Buračas, G. T., & Buxton, R. B. (2012). Attention strongly increases oxygen metabolic response to stimulus in primary visual cortex. *NeuroImage*, *59*(1), 601–607. https://doi.org/10.1016/j.neuroimage.2011.07.078

Morgan, C., & Schwarzkopf, D. S. (2020). Comparison of human population receptive field estimates between scanners and the effect of temporal filtering. *F1000Research*, *8*, 1681. https://doi.org/10.12688/f1000research.20496.2

Morgan, J. E. (2000). Retinal ganglion cell death in experimental glaucoma. *British Journal of Ophthalmology*, *84*(3), 303–310. https://doi.org/10.1136/bjo.84.3.303

Morgan, J. E. (2002). Retinal ganglion cell shrinkage in glaucoma. *Journal of Glaucoma*, *11*(4), 365–370.

Movshon, J. A., Thompson, I. D., & Tolhurst, D. J. (1978). Receptive field organization of complex cells in the cat's striate cortex. *The Journal of Physiology*, *283*, 79–99. https://doi.org/10.1113/jphysiol.1978.sp012489

Mulholland, P. J., Redmond, T., Garway-Heath, D. F., Zlatkova, M. B., & Anderson, R. S. (2015). Estimating the Critical Duration for Temporal Summation of Standard

Achromatic Perimetric Stimuli. *Investigative Ophthalmology & Visual Science*, *56*(1), 431–437. https://doi.org/10.1167/iovs.14-15304

Murphy, M. C., Conner, I. P., Teng, C. Y., Lawrence, J. D., Safiullah, Z., Wang, B., Bilonick, R. A., Kim, S.-G., Wollstein, G., Schuman, J. S., & Chan, K. C. (2016). Retinal structures and visual cortex activity are impaired prior to clinical vision loss in glaucoma. *Scientific Reports*, *6*, 31464. https://doi.org/10.1038/srep31464

Muthukumaraswamy, S. D., Evans, C. J., Edden, R. A. E., Wise, R. G., & Singh, K. D. (2012). Individual variability in the shape and amplitude of the BOLD-HRF correlates with endogenous GABAergic inhibition. *Human Brain Mapping*, *33*(2), 455–465. https://doi.org/10.1002/hbm.21223

Nagra, M., Gilmartin, B., Logan, N. S., & Anderson, S. J. (2018). The Effects of Severe Myopia on the Properties of Sampling Units in Peripheral Retina. *Optometry and Vision Science*, *95*(4), 399–404. https://doi.org/10.1097/OPX.0000000000001199

Nauhaus, I., Busse, L., Carandini, M., & Ringach, D. L. (2009). Stimulus contrast modulates functional connectivity in visual cortex. *Nature Neuroscience*, *12*(1), 70–76. https://doi.org/10.1038/nn.2232

NEIGHBORHOOD consortium, UK Biobank Eye and Vision Consortium, Craig, J. E., Han, X., Qassim, A., Hassall, M., Cooke Bailey, J. N., Kinzy, T. G., Khawaja, A. P., An, J., Marshall, H., Gharahkhani, P., Igo, R. P., Graham, S. L., Healey, P. R., Ong, J.-S., Zhou, T., Siggs, O., Law, M. H., … MacGregor, S. (2020). Multitrait analysis of glaucoma identifies new risk loci and enables polygenic prediction of disease susceptibility and progression. *Nature Genetics*, *52*(2), 160–166. https://doi.org/10.1038/s41588-019-0556-y

Nguyen, A. H., Fatehi, N., Romero, P., Miraftabi, A., Kim, E., Morales, E., Giaconi, J., Coleman, A. L., Law, S. K., Caprioli, J., & Nouri-Mahdavi, K. (2018). Observational Outcomes of Initial Trabeculectomy With Mitomycin C in Patients of African Descent vs Patients of European Descent: Five-Year Results. *JAMA Ophthalmology*, *136*(10), 1106. https://doi.org/10.1001/jamaophthalmol.2018.2897

Nilsson, S. E. (1971). Human retinal vascular obstructions. A quantitative correlation of angiographic and electroretinographic findings. *Acta Ophthalmologica*, *49*(1), 111–133.

Nilsson, S. E., & Skoog, K. O. (1980). The ERG c-wave in vitelliruptive macular degeneration (VMD). *Acta Ophthalmologica*, *58*(4), 659–666.

Ntim-Amponsah, C. T., Amoaku, W. M. K., Ofosu-Amaah, S., Ewusi, R. K., Idirisuriya-Khair, R., Nyatepe-Coo, E., & Adu-Darko, M. (2004). Prevalence of glaucoma in an African population. *Eye*, *18*(5), 491–497. https://doi.org/10.1038/sj.eye.6700674

Odell, D., Dubis, A. M., Lever, J. F., Stepien, K. E., & Carroll, J. (2011). Assessing Errors Inherent in OCT-Derived Macular Thickness Maps. *Journal of Ophthalmology*, *2011*, 1–9. https://doi.org/10.1155/2011/692574

O'Keefe, L. P., Levitt, J. B., Kiper, D. C., Shapley, R. M., & Movshon, J. A. (1998). Functional Organization of Owl Monkey Lateral Geniculate Nucleus and Visual Cortex. *Journal of Neurophysiology*, *80*(2), 594–609. https://doi.org/10.1152/jn.1998.80.2.594

Okuizumi, K., Onodera, O., Tanaka, H., Kobayashi, H., Tsuji, S., Takahashi, H., Oyanagi, K., Seki, K., Tanaka, M., Naruse, S., Miyatake, T., Mizusawa, H., & Kanazawa, I. (1994). ApoE–ε4 and early–onset Alzheimer's. *Nature Genetics*, *7*(1), 10–11. https://doi.org/10.1038/ng0594-10b

Osman, W., Low, S.-K., Takahashi, A., Kubo, M., & Nakamura, Y. (2012). A genome-wide association study in the Japanese population confirms 9p21 and 14q23 as susceptibility loci for primary open angle glaucoma. *Human Molecular Genetics*, *21*(12), 2836–2842. https://doi.org/10.1093/hmg/dds103

Osterberg, G. A. (1935). Topography of the layer of rods and cones in the human retina. *Acta Ophthalmologica*, *6*, 1–102.

Otto, T., & Bach, M. (1997). Reproduzierbarkeit des Musterelektroretinogramms. *Der Ophthalmologe*, *94*(3), 217–221. https://doi.org/10.1007/s003470050105

Pan, F., & Swanson, W. H. (2006). A cortical pooling model of spatial summation for perimetric stimuli. *Journal of Vision*, *6*(11), 2–2. https://doi.org/10.1167/6.11.2

Papanikolaou, A., Keliris, G. A., Papageorgiou, T. D., Shao, Y., Krapp, E., Papageorgiou, E., Stingl, K., Bruckmann, A., Schiefer, U., Logothetis, N. K., & Smirnakis, S. M. (2014). Population receptive field analysis of the primary visual cortex complements perimetry in patients with homonymous visual field defects. *Proceedings of the National Academy of Sciences*, *111*(16), E1656–E1665. https://doi.org/10.1073/pnas.1317074111

Papst, N., Bopp, M., & Schnaudigel, O. E. (1984). The pattern evoked electroretinogram associated with elevated intraocular pressure. *Graefe's Archive for Clinical and Experimental Ophthalmology = Albrecht Von Graefes Archiv Fur Klinische Und Experimentelle Ophthalmologie*, *222*(1), 34–37.

Parisi, V. (2005). Electrophysiological Assessment of Glaucomatous Visual Dysfunction During Treatment with Cytidine-5'-diphosphocholine (citicoline): A Study of 8 years of Follow-up. *Documenta Ophthalmologica*, *110*(1), 91–102. https://doi.org/10.1007/s10633-005-7348-7

Parisi, V., Manni, G., Centofanti, M., Gandolfi, S. A., Olzi, D., & Bucci, M. G. (2001). Correlation between optical coherence tomography, pattern electroretinogram, and visual evoked potentials in open-angle glaucoma patients. *Ophthalmology*, *108*(5), 905–912. https://doi.org/10.1016/s0161-6420(00)00644-8

Park, H.-Y. L., Kim, J. H., & Park, C. K. (2014). Alterations of the synapse of the inner retinal layers after chronic intraocular pressure elevation in glaucoma animal model. *Molecular Brain*, *7*(1), 53. https://doi.org/10.1186/s13041-014-0053-2

Pearce, E., & Bridge, H. (2013). Is orbital volume associated with eyeball and visual cortex volume in humans? *Annals of Human Biology*, *40*(6), 531–540. https://doi.org/10.3109/03014460.2013.815272

Peichl, L., & Wässle, H. (1983). The structural correlate of the receptive field centre of alpha ganglion cells in the cat retina. *The Journal of Physiology*, *341*, 309–324. https://doi.org/10.1113/jphysiol.1983.sp014807

Perthen, J. E., Lansing, A. E., Liau, J., Liu, T. T., & Buxton, R. B. (2008). Caffeine-induced uncoupling of cerebral blood flow and oxygen metabolism: A calibrated BOLD fMRI study. *NeuroImage*, *40*(1), 237–247. https://doi.org/10.1016/j.neuroimage.2007.10.049

Petrov, Y. (2005). Two Distinct Mechanisms of Suppression in Human Vision. *Journal of Neuroscience*, *25*(38), 8704–8707. https://doi.org/10.1523/JNEUROSCI.2871-05.2005

Pfeiffer, N., Tillmon, B., & Bach, M. (1993). Predictive value of the pattern electroretinogram in high-risk ocular hypertension. *Investigative Ophthalmology & Visual Science*, *34*(5), 1710–1715.

Piéron, H. (1929). De la summation spatial des impressions lumineuses au niveau de la fovea. *L'année Psuchologique*, *30*(30), 87–105.

Pierre-Filho, P. de T., Gomes, P. R., Pierre, E. T., & Pierre, L. M. (2010). Learning effect in visual field testing of healthy subjects using Humphrey Matrix frequency doubling technology perimetry. *Eye*, *24*(5), 851–856. https://doi.org/10.1038/eye.2009.210

Piper, H. (1903). Über die Abhängigkeit des Reizwertes leuchtender Objekte von ihre Flachen-bezw. Winkelgrasse. *Zeitschrift Für Psychologie Und Physiologie Der Sinnesorgane*, *32*, 98–112.

Powers, W. J. (2016). Cerebral Blood Flow and Metabolism. In *Stroke* (pp. 28-46.e7). Elsevier. https://doi.org/10.1016/B978-0-323-29544-4.00003-7

Prabhakaran, G. T., Carvalho, J., Invernizzi, A., Kanowski, M., Renken, R. J., Cornelissen, F. W., & Hoffmann, M. B. (2020). Foveal pRF properties in the visual cortex depend on the extent of stimulated visual field. *NeuroImage*, *222*, 117250. https://doi.org/10.1016/j.neuroimage.2020.117250

Puckett, A. M., Mathis, J. R., & DeYoe, E. A. (2014). An investigation of positive and inverted hemodynamic response functions across multiple visual areas: Hemodynamic Responses in Visual Cortex. *Human Brain Mapping*, *35*(11), 5550–5564. https://doi.org/10.1002/hbm.22569

Qassim, A., Souzeau, E., Siggs, O. M., Hassall, M. M., Han, X., Griffiths, H. L., Frost, N. A., Vallabh, N. A., Kirwan, J. F., Menon, G., Cree, A. J., Galanopoulos, A., Agar, A., Healey, P. R., Graham, S. L., Landers, J., Casson, R. J., Gharahkhani, P., Willoughby, C. E., … Craig, J. E. (2020). An Intraocular Pressure Polygenic Risk Score Stratifies Multiple Primary Open-Angle Glaucoma Parameters Including Treatment Intensity. *Ophthalmology*, *127*(7), 901–907. https://doi.org/10.1016/j.ophtha.2019.12.025

Qing, G., Zhang, S., Wang, B., & Wang, N. (2010). Functional MRI Signal Changes in Primary Visual Cortex Corresponding to the Central Normal Visual Field of Patients with

Primary Open-Angle Glaucoma. *Investigative Opthalmology & Visual Science*, *51*(9), 4627. https://doi.org/10.1167/iovs.09-4834

Quigley, H. A. (2006). The number of people with glaucoma worldwide in 2010 and 2020. *British Journal of Ophthalmology*, *90*(3), 262–267. https://doi.org/10.1136/bjo.2005.081224

Quigley, H. A., Dunkelberger, G. R., & Green, W. R. (1989). Retinal ganglion cell atrophy correlated with automated perimetry in human eyes with glaucoma. *American Journal of Ophthalmology*, *107*(5), 453–564.

Quigley, H. A., & Vitale, S. (1997). Models of open-angle glaucoma prevalence and incidence in the United States. *Investigative Ophthalmology & Visual Science*, *38*(1), 83–91.

R core team. (2013). *R: A language and environment for statistical computing.* (v.3.0.2) [Computer software]. R Foundation for Statistical Computing.

R core team. (2020). *R: A language and environment for statistical computing.* (v.4.0.0) [Computer software]. R Foundation for Statistical Computing. https://www.R-project.org/

Racette, L., Medeiros, F. A., Pascual, J. P., Zangwill, L. M., Weinreb, R. N., & Sample, P. A. (2003). *Transforming the Visual Field Scale From Decibel to 1/Lambert: Does it Alter the Structure-Function Relationship? 44*(77). https://iovs.arvojournals.org/article.aspx?articleid=2412456

Rajmohan, V., & Mohandas, E. (2007). The limbic system. *Indian Journal of Psychiatry*, *49*(2), 132. https://doi.org/10.4103/0019-5545.33264

Read, S. A., Alonso-Caneiro, D., & Vincent, S. J. (2017). Longitudinal changes in macular retinal layer thickness in pediatric populations: Myopic vs non-myopic eyes. *PLOS ONE*, *12*(6), e0180462. https://doi.org/10.1371/journal.pone.0180462

Redmond, T. (2009). *SPATIAL SUMMATION AND THE STRUCTURE/FUNCTION RELATIONSHIP WITH AGE AND IN GLAUCOMA*. University of Ulster.

Redmond, T., Anderson, R. S., Russell, R. A., & Garway-Heath, D. F. (2013). Relating Retinal Nerve Fiber Layer Thickness and Functional Estimates of Ganglion Cell Sampling Density in Healthy Eyes and in Early Glaucoma. *Investigative Opthalmology & Visual Science*, *54*(3), 2153. https://doi.org/10.1167/iovs.12-10342

Redmond, T., Garway-Heath, D. F., Zlatkova, M. B., & Anderson, R. S. (2010). Sensitivity loss in early glaucoma can be mapped to an enlargement of the area of complete spatial summation. *Investigative Ophthalmology & Visual Science*, *51*(12), 6540–6548. https://doi.org/10.1167/iovs.10-5718

Redmond, T., Zlatkova, M. B., Garway-Heath, D. F., & Anderson, R. S. (2010). The effect of age on the area of complete spatial summation for chromatic and achromatic stimuli. *Investigative Ophthalmology & Visual Science.*, *51*(12), 6533–6539.

Redmond, T., Zlatkova, M. B., Vassilev, A., Garway-Heath, D. F., & Anderson, R. S. (2013). Changes in Ricco's area with background luminance in the s-cone pathway. *Optometry and Vision Science*, *90*, 66–74.

Reid, R. C., & Shapley, R. M. (2002). Space and Time Maps of Cone Photoreceptor Signals in Macaque Lateral Geniculate Nucleus. *The Journal of Neuroscience*, *22*(14), 6158–6175. https://doi.org/10.1523/JNEUROSCI.22-14-06158.2002

Ricco, A. (1877). Relazione fra il minimo angolo visuale l'intensita luminosa. *Mem R Accad Sci Lett Arti Modena*, *17*, 47–160.

Richards, W. (1967). Apparent modifiability of receptive fields during accommodation and convergence and a model for size constancy. *Neuropsychologia*, *5*(1), 63–72. https://doi.org/10.1016/0028-3932(67)90051-6

Riggs, L. A., Johnson, E. P., & Schick, A. M. L. (1964). Electrical Responses of the Human Eye to Moving Stimulus Patterns. *Science*, *144*(3618), 567–567. https://doi.org/10.1126/science.144.3618.567

Ringo, J. L. (1991). Neuronal Interconnection as a Function of Brain Size. *Brain, Behavior and Evolution*, *38*(1), 1–6. https://doi.org/10.1159/000114375

Ritter, M., Hummer, A., Ledolter, A. A., Holder, G. E., Windischberger, C., & Schmidt-Erfurth, U. M. (2019). Correspondence between retinotopic cortical mapping and conventional functional and morphological assessment of retinal disease. *British Journal of Ophthalmology*, *103*(2), 208–215. https://doi.org/10.1136/bjophthalmol-2017-311443

Rizzolatti, G., & Matelli, M. (2003). Two different streams form the dorsal visual system: Anatomy and functions. *Experimental Brain Research*, *153*(2), 146–157. https://doi.org/10.1007/s00221-003-1588-0

Rockwood, K., Song, X., & Mitnitski, A. (2011). Changes in relative fitness and frailty across the adult lifespan: Evidence from the Canadian National Population Health Survey. *Canadian Medical Association Journal*, *183*(8), E487–E494. https://doi.org/10.1503/cmaj.101271

Rountree, L., Mulholland, P. J., Anderson, R. S., Garway-Heath, D. F., Morgan, J. E., & Redmond, T. (2018). Optimising the glaucoma signal/noise ratio by mapping changes in spatial summation with area-modulated perimetric stimuli. *Scientific Reports*, *8*(1), 2172. https://doi.org/10.1038/s41598-018-20480-4

RStudio Team. (2016). *RStudio: Integrated Development for R.* (1.0.153) [Computer software]. RStudio, Inc. http://www.rstudio.com/

Rudnicka, A. R., Mt-Isa, S., Owen, C. G., Cook, D. G., & Ashby, D. (2006). Variations in primary open-angle glaucoma prevalence by age, gender, and race: A Bayesian meta-analysis. *Investigative Ophthalmology & Visual Science*, *47*(10), 4254–4261. https://doi.org/10.1167/iovs.06-0299

Salgarello, T., Giudiceandrea, A., Calandriello, L., Marangoni, D., Colotto, A., Caporossi, A., & Falsini, B. (2018). Pattern Electroretinogram Detects Localized Glaucoma Defects. *Translational Vision Science & Technology*, *7*(5), 6. https://doi.org/10.1167/tvst.7.5.6

Samarawickrama, C., Wang, J. J., Huynh, S. C., Pai, A., Burlutsky, G., Rose, K. A., & Mitchell, P. (2010). Ethnic differences in optic nerve head and retinal nerve fibre layer thickness parameters in children. *British Journal of Ophthalmology*, *94*(7), 871–876. https://doi.org/10.1136/bjo.2009.158279

Schefrin, B. E., Bieber, M. L., McLean, R., & Werner, J. S. (1998). The area of complete scotopic spatial summation enlarges with age. *Journal of the Optical Society of America. A, Optics, Image Science, and Vision.*, *15*(2), 340–348.

Schenk, T. (1997). Visual motion perception after brain damage: I. Deficits in global motion perception. *Neuropsychologia*, *35*(9), 1289–1297. https://doi.org/10.1016/S0028-3932(97)00004-3

Schenk, T., & McIntosh, R. D. (2010). Do we have independent visual streams for perception and action? *Cognitive Neuroscience*, *1*(1), 52–62. https://doi.org/10.1080/17588920903388950

Schindelin, J., Arganda-Carreras, I., Frise, E., Kaynig, V., Longair, M., Pietzsch, T., Preibisch, S., Rueden, C., Saalfeld, S., Schmid, B., Tinevez, J.-Y., White, D. J., Hartenstein, V., Eliceiri, K., Tomancak, P., & Cardona, A. (2012). Fiji: An open-source platform for

biological-image analysis. *Nature Methods*, *9*(7), 676–682. https://doi.org/10.1038/nmeth.2019

Schneider, C. A., Rasband, W. S., & Eliceiri, K. W. (2012). NIH Image to ImageJ: 25 years of image analysis. *Nature Methods*, *9*(7), 671–675. https://doi.org/10.1038/nmeth.2089

Schuman, J. S., Hee, M. R., Arya, A. V., Pedut-Kloizman, T., Puliafito, C. A., Fujimoto, J. G., & Swanson, E. A. (1995). Optical coherence tomography: A new tool for glaucoma diagnosis. *Current Opinion in Ophthalmology*, *6*(2), 89–95.

Schwarzkopf, D. S., Anderson, E. J., de Haas, B., White, S. J., & Rees, G. (2014). Larger Extrastriate Population Receptive Fields in Autism Spectrum Disorders. *Journal of Neuroscience*, *34*(7), 2713–2724. https://doi.org/10.1523/JNEUROSCI.4416-13.2014

Schwarzkopf, D. S., Song, C., & Rees, G. (2011). The surface area of human V1 predicts the subjective experience of object size. *Nature Neuroscience*, *14*(1), 28–30. https://doi.org/10.1038/nn.2706

Sehi, M., Grewal, D. S., Feuer, W. J., & Greenfield, D. S. (2011). The impact of intraocular pressure reduction on retinal ganglion cell function measured using pattern electroretinogram in eyes receiving latanoprost 0.005% versus placebo. *Vision Research*, *51*(2), 235–242. https://doi.org/10.1016/j.visres.2010.08.036

Sehi, M., Grewal, D. S., Goodkin, M. L., & Greenfield, D. S. (2010). Reversal of Retinal Ganglion Cell Dysfunction after Surgical Reduction of Intraocular Pressure. *Ophthalmology*, *117*(12), 2329–2336. https://doi.org/10.1016/j.ophtha.2010.08.049

Self, M. W., Lorteije, J. A. M., Vangeneugden, J., van Beest, E. H., Grigore, M. E., Levelt, C. N., Heimel, J. A., & Roelfsema, P. R. (2014). Orientation-Tuned Surround Suppression in

Mouse Visual Cortex. *Journal of Neuroscience*, *34*(28), 9290–9304. https://doi.org/10.1523/JNEUROSCI.5051-13.2014

Sereno, M., Dale, A., Reppas, J., Kwong, K., Belliveau, J., Brady, T., Rosen, B., & Tootell, R. (1995). Borders of multiple visual areas in humans revealed by functional magnetic resonance imaging. *Science*, *268*(5212), 889–893. https://doi.org/10.1126/science.7754376

Shao, Y., Keliris, G. A., Papanikolaou, A., Fischer, M. D., Zobor, D., Jägle, H., Logothetis, N. K., & Smirnakis, S. M. (2013). Visual cortex organisation in a macaque monkey with macular degeneration. *European Journal of Neuroscience*, *38*(10), 3456–3464. https://doi.org/10.1111/ejn.12349

Shapley, R., & Hawken, M. J. (2011). Color in the cortex: Single- and double-opponent cells. *Vision Research*, *51*(7), 701–717. https://doi.org/10.1016/j.visres.2011.02.012

Shmuel, A., Augath, M., Oeltermann, A., & Logothetis, N. K. (2006). Negative functional MRI response correlates with decreases in neuronal activity in monkey visual area V1. *Nature Neuroscience*, *9*(4), 569–577. https://doi.org/10.1038/nn1675

Shmuel, A., Yacoub, E., Pfeuffer, J., Van de Moortele, P.-F., Adriany, G., Hu, X., & Ugurbil, K. (2002). Sustained Negative BOLD, Blood Flow and Oxygen Consumption Response and Its Coupling to the Positive Response in the Human Brain. *Neuron*, *36*(6), 1195–1210. https://doi.org/10.1016/S0896-6273(02)01061-9

Shorstein, N. H., Dawson, W. W., & Sherwood, M. B. (1999). Mid-peripheral pattern electrical retinal responses in normals, glaucoma suspects, and glaucoma patients. *British Journal of Ophthalmology*, *83*(1), 15–23. https://doi.org/10.1136/bjo.83.1.15

Sihota, R., Sony, P., Gupta, V., Dada, T., & Singh, R. (2006). Diagnostic Capability of Optical Coherence Tomography in Evaluating the Degree of Glaucomatous Retinal Nerve

Fiber Damage. *Investigative Opthalmology & Visual Science*, *47*(5), 2006. https://doi.org/10.1167/iovs.05-1102

Silson, E. H., Aleman, T. S., Willett, A., Serrano, L. W., Pearson, D. J., Rauschecker, A. M., Maguire, A. M., Baker, C. I., Bennett, J., & Ashtari, M. (2018). Comparing Clinical Perimetry and Population Receptive Field Measures in Patients with Choroideremia. *Investigative Opthalmology & Visual Science*, *59*(8), 3249. https://doi.org/10.1167/iovs.18-23929

Silson, E. H., Reynolds, R. C., Kravitz, D. J., & Baker, C. I. (2018). Differential Sampling of Visual Space in Ventral and Dorsal Early Visual Cortex. *The Journal of Neuroscience*, *38*(9), 2294–2303. https://doi.org/10.1523/JNEUROSCI.2717-17.2018

Silver, M. A., & Kastner, S. (2009). Topographic maps in human frontal and parietal cortex. *Trends in Cognitive Sciences*, *13*(11), 488–495. https://doi.org/10.1016/j.tics.2009.08.005

Smith, A. T., Singh, K. D., Williams, A. L., & Greenlee, M. W. (2001). Estimating Receptive Field Size from fMRI Data in Human Striate and Extrastriate Visual Cortex. *Cerebral Cortex*, *11*(12), 1182–1190. https://doi.org/10.1093/cercor/11.12.1182

Smittenaar, C. R., MacSweeney, M., Sereno, M. I., & Schwarzkopf, D. S. (2016). Does Congenital Deafness Affect the Structural and Functional Architecture of Primary Visual Cortex? *The Open Neuroimaging Journal*, *10*(1), 1–19. https://doi.org/10.2174/1874440001610010001

So, Y. T., & Shapley, R. (1981). Spatial tuning of cells in and around lateral geniculate nucleus of the cat: X and Y relay cells and perigeniculate interneurons. *Journal of Neurophysiology*, *45*(1), 107–120. https://doi.org/10.1152/jn.1981.45.1.107

Sommer, A., Tielsch, J. M., Katz, J., Quigley, H. A., Gottsch, J. D., Javitt, J., & Singh, K. (1991). Relationship between intraocular pressure and primary open angle glaucoma among white and black Americans. The Baltimore Eye Survey. *Archives of Ophthalmology (Chicago, Ill.: 1960)*, *109*(8), 1090–1095.

Song, C., Schwarzkopf, D. S., Kanai, R., & Rees, G. (2015). Neural Population Tuning Links Visual Cortical Anatomy to Human Visual Perception. *Neuron*, *85*(3), 641–656. https://doi.org/10.1016/j.neuron.2014.12.041

Song, C., Schwarzkopf, D. S., & Rees, G. (2013). Variability in visual cortex size reflects tradeoff between local orientation sensitivity and global orientation modulation. *Nature Communications*, *4*(1), 2201. https://doi.org/10.1038/ncomms3201

Song, X., Mitnitski, A., & Rockwood, K. (2010). Prevalence and 10-Year Outcomes of Frailty in Older Adults in Relation to Deficit Accumulation: FRAILTY PREVALENCE AND OUTCOME. *Journal of the American Geriatrics Society*, *58*(4), 681–687. https://doi.org/10.1111/j.1532-5415.2010.02764.x

Song, Y., Mu, K., Wang, J., Lin, F., Chen, Z., Yan, X., Hao, Y., Zhu, W., & Zhang, H. (2014). Altered Spontaneous Brain Activity in Primary Open Angle Glaucoma: A Resting-State Functional Magnetic Resonance Imaging Study. *PLoS ONE*, *9*(2), e89493. https://doi.org/10.1371/journal.pone.0089493

Springelkamp, H., Iglesias, A. I., Cuellar-Partida, G., Amin, N., Burdon, K. P., van Leeuwen, E. M., Gharahkhani, P., Mishra, A., van der Lee, S. J., Hewitt, A. W., Rivadeneira, F., Viswanathan, A. C., Wolfs, R. C. W., Martin, N. G., Ramdas, W. D., van Koolwijk, L. M., Pennell, C. E., Vingerling, J. R., Mountain, J. E., … MacGregor, S. (2015). ARHGEF12 influences the risk of glaucoma by increasing intraocular pressure. *Human Molecular Genetics*, *24*(9), 2689–2699. https://doi.org/10.1093/hmg/ddv027

Spry, P. G. D., Johnson, C. A., McKendrick, A. M., & Turpin, A. (2001). Variability Components of Standard Automated Perimetry and Frequency-Doubling Technology Perimetry. *Investigative Ophthalmology & Visual Science*, *42*(6), 1404–1410.

Stapley, V., Anderson, R. S., Saunders, K. J., & Mulholland, P. J. (2020). Altered spatial summation optimizes visual function in axial myopia. *Scientific Reports*, *10*(1), 12179. https://doi.org/10.1038/s41598-020-67893-8

Stapley, V., Anderson, R. S., Saunders, K., & Mulholland, P. J. (2019). Investigating the Effect of Axial Myopia on Spatial Summation. *Investigative Ophthalmology & Visual Science*, *60*(9), 4370.

Stefanovic, B., Warnking, J. M., Rylander, K. M., & Pike, G. B. (2006). The effect of global cerebral vasodilation on focal activation hemodynamics. *NeuroImage*, *30*(3), 726–734. https://doi.org/10.1016/j.neuroimage.2005.10.038

Stockton, R. A., & Slaughter, M. M. (1989). B-wave of the electroretinogram. A reflection of ON bipolar cell activity. *The Journal of General Physiology*, *93*(1), 101–122. https://doi.org/10.1085/jgp.93.1.101

Stoll, S., Infanti, E., de Haas, B., & Schwarzkopf, D. S. (2020). *Flaws in Data Binning for Population Receptive Field Analyses* [Preprint]. Neuroscience. https://doi.org/10.1101/2020.12.15.422942

Strittmatter, W. J., Weisgraber, K. H., Huang, D. Y., Dong, L. M., Salvesen, G. S., Pericak-Vance, M., Schmechel, D., Saunders, A. M., Goldgaber, D., & Roses, A. D. (1993). Binding of human apolipoprotein E to synthetic amyloid beta peptide: Isoform-specific effects and implications for late-onset Alzheimer disease. *Proceedings of the National Academy of Sciences*, *90*(17), 8098–8102. https://doi.org/10.1073/pnas.90.17.8098

Stucht, D., Danishad, K. A., Schulze, P., Godenschweger, F., Zaitsev, M., & Speck, O. (2015). Highest Resolution In Vivo Human Brain MRI Using Prospective Motion Correction. *PLOS ONE*, *10*(7), e0133921. https://doi.org/10.1371/journal.pone.0133921

Sugiyama, T., Utsunomiya, K., Ota, H., Ogura, Y., Narabayashi, I., & Ikeda, T. (2006). Comparative study of cerebral blood flow in patients with normal-tension glaucoma and control subjects. *American Journal of Ophthalmology*, *141*(2), 394–396. https://doi.org/10.1016/j.ajo.2005.08.037

Susanna, R., De Moraes, C. G., Cioffi, G. A., & Ritch, R. (2015). Why Do People (Still) Go Blind from Glaucoma? *Translational Vision Science & Technology*, *4*(2), 1. https://doi.org/10.1167/tvst.4.2.1

Suzuki, Y., Iwase, A., Araie, M., Yamamoto, T., Abe, H., Shirato, S., Kuwayama, Y., Mishima, H., Shimizu, H., & Tomita, G. (2006). Risk Factors for Open-Angle Glaucoma in a Japanese PopulationThe Tajimi Study. *Ophthalmology*, *113*(9), 1613–1617. https://doi.org/10.1016/j.ophtha.2006.03.059

Swanson, W. H., Felius, J., & Pan, F. (2004). Perimetric defects and ganglion cell damage: Interpreting linear relations using a Two-Stage neural model. *Investigative Ophthalmology & Visual Science*, *45*(2), 466–472. https://doi.org/10.1167/iovs.03-0374

Szigeti, A., Tátrai, E., Szamosi, A., Vargha, P., Nagy, Z. Z., Németh, J., DeBuc, D. C., & Somfai, G. M. (2014). A Morphological Study of Retinal Changes in Unilateral Amblyopia Using Optical Coherence Tomography Image Segmentation. *PLoS ONE*, *9*(2), e88363. https://doi.org/10.1371/journal.pone.0088363

Szmajda, B. A., Grünert, U., & Martin, P. R. (2008). Retinal ganglion cell inputs to the koniocellular pathway. *The Journal of Comparative Neurology*, *510*(3), 251–268. https://doi.org/10.1002/cne.21783

Tai, T. Y. T. (2018). Visual Evoked Potentials and Glaucoma. *Asia-Pacific Journal of Ophthalmology*. https://doi.org/10.22608/APO.2017532

Tailby, C., Szmajda, B. A., Buzás, P., Lee, B. B., & Martin, P. R. (2008). Transmission of blue (S) cone signals through the primate lateral geniculate nucleus: Spatial properties of S-cone pathways. *The Journal of Physiology*, *586*(24), 5947–5967. https://doi.org/10.1113/jphysiol.2008.161893

Takeuchi, H., Taki, Y., Nouchi, R., Yokoyama, R., Kotozaki, Y., Nakagawa, S., Sekiguchi, A., Iizuka, K., Yamamoto, Y., Hanawa, S., Araki, T., Miyauchi, C. M., Shinada, T., Sakaki, K., Sassa, Y., Nozawa, T., Ikeda, S., Yokota, S., Daniele, M., & Kawashima, R. (2018). Refractive error is associated with intracranial volume. *Scientific Reports*, *8*, 175. https://doi.org/10.1038/s41598-017-18669-0

Taylor, A. J., Kim, J. H., & Ress, D. (2018). Characterization of the hemodynamic response function across the majority of human cerebral cortex. *NeuroImage*, *173*, 322–331. https://doi.org/10.1016/j.neuroimage.2018.02.061

Terry, L., Cassels, N., Lu, K., Acton, J. H., Margrain, T. H., North, R. V., Fergusson, J., White, N., & Wood, A. (2016). Automated Retinal Layer Segmentation Using Spectral Domain Optical Coherence Tomography: Evaluation of Inter-Session Repeatability and Agreement between Devices. *PLOS ONE*, *11*(9), e0162001. https://doi.org/10.1371/journal.pone.0162001

Thompson, D. A. (1987). *Spatial tuning studies of the pattern evoked electroretinogram* [Student Thesis, Aston University].

https://research.aston.ac.uk/portal/en/theses/spatial-tuning-studies-of-the-pattern-evoked-electroretinogram(05a65111-b54f-4aac-b3a4-cb0a636fb705).html

Thompson, D. A., & Drasdo, N. (1987). Computation of the luminance and pattern components of the bar pattern electroretinogram. *Documenta Ophthalmologica*, *66*(3), 233–244. https://doi.org/10.1007/BF00145237

Thorell, L. G., de Valois, R. L., & Albrecht, D. G. (1984). Spatial mapping of monkey VI cells with pure color and luminance stimuli. *Vision Research*, *24*(7), 751–769. https://doi.org/10.1016/0042-6989(84)90216-5

Thoreson, W. B., & Mangel, S. C. (2012). Lateral interactions in the outer retina. *Progress in Retinal and Eye Research*, *31*(5), 407–441. https://doi.org/10.1016/j.preteyeres.2012.04.003

Thorleifsson, G., Walters, G. B., Hewitt, A. W., Masson, G., Helgason, A., DeWan, A., Sigurdsson, A., Jonasdottir, A., Gudjonsson, S. A., Magnusson, K. P., Stefansson, H., Lam, D. S. C., Tam, P. O. S., Gudmundsdottir, G. J., Southgate, L., Burdon, K. P., Gottfredsdottir, M. S., Aldred, M. A., Mitchell, P., … Stefansson, K. (2010). Common variants near CAV1 and CAV2 are associated with primary open-angle glaucoma. *Nature Genetics*, *42*(10), 906–909. https://doi.org/10.1038/ng.661

Tiryaki Demir, S., Oba, M. E., Tuna Erdoğan, E., Odabaşı, M., Dirim, A. B., Demir, M., Can, E., Kara, O., & Şendül, S. Y. (2015). Comparison of Pattern Electroretinography and Optical Coherence Tomography Parameters in Patients with Primary Open-Angle Glaucoma and Ocular Hypertension. *Türk Oftalmoloji Dergisi*, *45*(6), 229–234. https://doi.org/10.4274/tjo.39260

Tootell, R. B. H., & Nasr, S. (2017). Columnar Segregation of Magnocellular and Parvocellular Streams in Human Extrastriate Cortex. *The Journal of Neuroscience*, *37*(33), 8014–8032. https://doi.org/10.1523/JNEUROSCI.0690-17.2017

Tootell, R. B., Mendola, J. D., Hadjikhani, N. K., Ledden, P. J., Liu, A. K., Reppas, J. B., Sereno, M. I., & Dale, A. M. (1997). Functional analysis of V3A and related areas in human visual cortex. *The Journal of Neuroscience: The Official Journal of the Society for Neuroscience*, *17*(18), 7060–7078.

Tribble, J. R., Vasalauskaite, A., Redmond, T., Young, R. D., Hassan, S., Fautsch, M. P., Sengpiel, F., Williams, P. A., & Morgan, J. E. (2019). Midget retinal ganglion cell dendritic and mitochondrial degeneration is an early feature of human glaucoma. *Brain Communications*, *1*(1), fcz035. https://doi.org/10.1093/braincomms/fcz035

Turpin, A., Artes, P. H., & McKendrick, A. M. (2012). The Open Perimetry Interface: An enabling tool for clinical visual psychophysics. *Journal of Vision*, *12*(11), 22–22. https://doi.org/10.1167/12.11.22

Uclés, P., Almárcegui, C., Fernández, F. J., & Honrubia, F. M. (1997). [Early diagnosis of glaucoma with pattern-ERG]. *Journal Francais D'ophtalmologie*, *20*(2), 90–96.

Uludağ, K., & Blinder, P. (2018). Linking brain vascular physiology to hemodynamic response in ultra-high field MRI. *NeuroImage*, *168*, 279–295. https://doi.org/10.1016/j.neuroimage.2017.02.063

Ungerleider, L. G., & Mishkin, M. (1982). Two cortical visual systems. In D. J. Ingle, M. A. Goodale, & R. J. W. Mansfield (Eds.), *Analysis of visual behaviour* (pp. 549–586). MIT Press.

Ursell, T. (2013). *Frechet Distance Calculator* (v.1.) [MATLAB Central File Exchange]. https://www.mathworks.com/matlabcentral/fileexchange/41956-frechet-distance-calculator

Usrey, W. M., & Reid, R. C. (2000). Visual physiology of the lateral geniculate nucleus in two species of New World monkey: *Saimiri sciureus* and *Aotus trivirgatis*. *The Journal of Physiology*, *523*(3), 755–769. https://doi.org/10.1111/j.1469-7793.2000.00755.x

Vaegan, & Hollows, F. C. (2006). Visual-Evoked Response, Pattern Electroretinogram, and Psychophysical Magnocellular Thresholds in Glaucoma, Optic Atrophy, and Dyslexia: *Optometry and Vision Science*, *83*(7), 486–498. https://doi.org/10.1097/01.opx.0000225920.97380.62

van den Berg, T. J., Riemslag, F. C., de Vos, G. W., & Verduyn Lunel, H. F. (1986). Pattern ERG and glaucomatous visual field defects. *Documenta Ophthalmologica. Advances in Ophthalmology*, *61*(3–4), 335–341.

Vanegas, M. I., Blangero, A., & Kelly, S. P. (2015). Electrophysiological indices of surround suppression in humans. *Journal of Neurophysiology*, *113*(4), 1100–1109. https://doi.org/10.1152/jn.00774.2014

Vassilev, A., Mihaylova, M. S., Racheva, K., Zlatkova, M., & Anderson, R. S. (2003). Spatial summation of s-cone ON and OFF signals: Effects of retinal eccentricity. *Vision Research*, *43*(27), 2875–2884. https://doi.org/10.1016/j.visres.2003.08.002

Ventura, L. M., Feuer, W. J., & Porciatti, V. (2012). Progressive Loss of Retinal Ganglion Cell Function Is Hindered with IOP-Lowering Treatment in Early Glaucoma. *Investigative Opthalmology & Visual Science*, *53*(2), 659. https://doi.org/10.1167/iovs.11-8525

Ventura, L. M., Golubev, I., Lee, W., Nose, I., Parel, J.-M., Feuer, W. J., & Porciatti, V. (2013). Head-down Posture Induces PERG Alterations in Early Glaucoma: *Journal of Glaucoma*, *22*(3), 255–264. https://doi.org/10.1097/IJG.0b013e318232973b

Ventura, L. M., & Porciatti, V. (2005). Restoration of retinal ganglion cell function in early glaucoma after intraocular pressure reduction: A pilot study. *Ophthalmology*, *112*(1), 20–27. https://doi.org/10.1016/j.ophtha.2004.09.002

Victor, J. D., Purpura, K., Katz, E., & Mao, B. (1994). Population encoding of spatial frequency, orientation, and color in macaque V1. *Journal of Neurophysiology*, *72*(5), 2151–2166. https://doi.org/10.1152/jn.1994.72.5.2151

Viswanathan, S., Frishman, L. J., & Robson, J. G. (2000). The uniform field and pattern ERG in macaques with experimental glaucoma: Removal of spiking activity. *Investigative Ophthalmology & Visual Science*, *41*(9), 2797–2810.

Volbrecht, V. J., Shrago, E. E., Schefrin, B. E., & Werner, J. (2000a). Spatial summation in human cone mechanisms from 0 degrees to 20 degrees in the superior retina. *Journal of the Optical Society of America. A, Optics, Image Science, and Vision*, *17*(3), 641–650. https://doi.org/10.1364/JOSAA.17.000641

Volbrecht, V. J., Shrago, E. E., Schefrin, B. E., & Werner, J. S. (2000b). Ricco's areas for S- and l-cone mechanisms across the retina. *Color Research & Application*, *26*(S1), S32–S35. https://doi.org/10.1002/1520-6378(2001)26:1+<::aid-col8>3.0.co;2-v

Wachtmeister, L. (1998). Oscillatory potentials in the retina: What do they reveal. *Progress in Retinal and Eye Research*, *17*(4), 485–521.

Waisbourd, M., Ahmed, O. M., Molineaux, J., Gonzalez, A., Spaeth, G. L., & Katz, L. J. (2016). Reversible structural and functional changes after intraocular pressure reduction in

patients with glaucoma. *Graefe's Archive for Clinical and Experimental Ophthalmology*, *254*(6), 1159–1166. https://doi.org/10.1007/s00417-016-3321-2

Wandell, B. A., Dumoulin, S. O., & Brewer, A. A. (2007). Visual Field Maps in Human Cortex. *Neuron*, *56*(2), 366–383. https://doi.org/10.1016/j.neuron.2007.10.012

Wang, J., Li, T., Sabel, B. A., Chen, Z., Wen, H., Li, J., Xie, X., Yang, D., Chen, W., Wang, N., Xian, J., & He, H. (2016a). Structural brain alterations in primary open angle glaucoma: A 3T MRI study. *Scientific Reports*, *6*, 18969. https://doi.org/10.1038/srep18969

Wang, J., Li, T., Sabel, B. A., Chen, Z., Wen, H., Li, J., Xie, X., Yang, D., Chen, W., Wang, N., Xian, J., & He, H. (2016b). Structural brain alterations in primary open angle glaucoma: A 3T MRI study. *Scientific Reports*, *6*(1), 18969. https://doi.org/10.1038/srep18969

Wang, L., Mruczek, R. E. B., Arcaro, M. J., & Kastner, S. (2015). Probabilistic Maps of Visual Topography in Human Cortex. *Cerebral Cortex*, *25*(10), 3911–3931. https://doi.org/10.1093/cercor/bhu277

Wang, Q., Chen, W., Wang, H., Zhang, X., Qu, X., Wang, Y., Li, T., Wang, N., & Xian, J. (2018). Reduced Functional and Anatomic Interhemispheric Homotopic Connectivity in Primary Open-Angle Glaucoma: A Combined Resting State-fMRI and DTI Study. *Investigative Opthalmology & Visual Science*, *59*(5), 1861. https://doi.org/10.1167/iovs.17-23291

Wang, Q., Qu, X., Chen, W., Wang, H., Huang, C., Li, T., Wang, N., & Xian, J. (2020). Altered coupling of cerebral blood flow and functional connectivity strength in visual and higher order cognitive cortices in primary open angle glaucoma. *Journal of Cerebral*

Blood Flow & Metabolism, 0271678X2093527. https://doi.org/10.1177/0271678X20935274

Wang, R., Tang, Z., Sun, X., Wu, L., Wang, J., Zhong, Y., & Xiao, Z. (2018). White Matter Abnormalities and Correlation With Severity in Normal Tension Glaucoma: A Whole Brain Atlas-Based Diffusion Tensor Study. *Investigative Opthalmology & Visual Science*, *59*(3), 1313. https://doi.org/10.1167/iovs.17-23597

Wang, W., Andolina, I. M., Lu, Y., Jones, H. E., & Sillito, A. M. (2016). Focal Gain Control of Thalamic Visual Receptive Fields by Layer 6 Corticothalamic Feedback. *Cerebral Cortex*, cercor;bhw376v1. https://doi.org/10.1093/cercor/bhw376

Wang, Y., Lu, W., Yan, T., Zhou, J., Xie, Y., Yuan, J., Liu, G., Teng, Y., Han, W., Chen, D., & Qiu, J. (2019). Functional MRI reveals effects of high intraocular pressure on central nervous system in high-tension glaucoma patients. *Acta Ophthalmologica*, *97*(3), e341–e348. https://doi.org/10.1111/aos.14027

Wanger, P., & Persson, H. E. (1983). Pattern-reversal electroretinograms in unilateral glaucoma. *Investigative Ophthalmology & Visual Science*, *24*(6), 749–753.

Watson, A. B. (2014). A formula for human retinal ganglion cell receptive field density as a function of visual field location. *Journal of Vision*, *14*(7). http://jov.arvojournals.org/article.aspx?articleid=2279458

Weber, A. J., Kaufman, P. L., & Hubbard, W. C. (1998). Morphology of single ganglion cells in the glaucomatous primate retina. *Investigative Ophthalmology & Visual Science*, *39*(12), 2304–2320.

Weinreb, R. N., Aung, T., & Medeiros, F. A. (2014). The Pathophysiology and Treatment of Glaucoma: A Review. *JAMA*, *311*(18), 1901. https://doi.org/10.1001/jama.2014.3192

Welbourne, L. E., Morland, A. B., & Wade, A. R. (2018). Population receptive field (pRF) measurements of chromatic responses in human visual cortex using fMRI. *NeuroImage*, *167*, 84–94. https://doi.org/10.1016/j.neuroimage.2017.11.022

Wellcome Trust Case Control Consortium 2, NEIGHBORHOOD Consortium, Gharahkhani, P., Burdon, K. P., Fogarty, R., Sharma, S., Hewitt, A. W., Martin, S., Law, M. H., Cremin, K., Bailey, J. N. C., Loomis, S. J., Pasquale, L. R., Haines, J. L., Hauser, M. A., Viswanathan, A. C., McGuffin, P., Topouzis, F., Foster, P. J., … Craig, J. E. (2014). Common variants near ABCA1, AFAP1 and GMDS confer risk of primary open-angle glaucoma. *Nature Genetics*, *46*(10), 1120–1125. https://doi.org/10.1038/ng.3079

Westner, B. U., & Dalal, S. S. (2017). Faster than the brain's speed of light: Retinocortical interactions differ in high frequency activity when processing darks and lights. *BioRxiv*. https://doi.org/10.1101/153551

White, A. J. R., Solomon, S. G., & Martin, P. R. (2001). Spatial properties of koniocellular cells in the lateral geniculate nucleus of the marmoset *Callithrix jacchus*. *The Journal of Physiology*, *533*(2), 519–535. https://doi.org/10.1111/j.1469-7793.2001.0519a.x

White, A. J. R., Sun, H., Swanson, W. H., & Lee, B. B. (2002). An Examination of Physiological Mechanisms Underlying the Frequency-Doubling Illusion. *Investigative Ophthalmology & Visual Science*, *43*(11), 3590–3599.

White, I. R., Royston, P., & Wood, A. M. (2011). Multiple imputation using chained equations: Issues and guidance for practice. *Statistics in Medicine*, *30*(4), 377–399. https://doi.org/10.1002/sim.4067

Wiesel, T. N., & Hubel, D. H. (1966). Spatial and chromatic interactions in the lateral geniculate body of the rhesus monkey. *Journal of Neurophysiology*, *29*(6), 1115–1156. https://doi.org/10.1152/jn.1966.29.6.1115

Wiggs, J. L., & Pasquale, L. R. (2017). Genetics of glaucoma. *Human Molecular Genetics*, *26*(R1), R21–R27. https://doi.org/10.1093/hmg/ddx184

Wiggs, J. L., Yaspan, B. L., Hauser, M. A., Kang, J. H., Allingham, R. R., Olson, L. M., Abdrabou, W., Fan, B. J., Wang, D. Y., Brodeur, W., Budenz, D. L., Caprioli, J., Crenshaw, A., Crooks, K., DelBono, E., Doheny, K. F., Friedman, D. S., Gaasterland, D., Gaasterland, T., … Haines, J. L. (2012). Common Variants at 9p21 and 8q22 Are Associated with Increased Susceptibility to Optic Nerve Degeneration in Glaucoma. *PLoS Genetics*, *8*(4), e1002654. https://doi.org/10.1371/journal.pgen.1002654

Willermain, F., Libert, S., Motulsky, E., Salik, D., Caspers, L., Perret, J., & Delporte, C. (2014). Origins and consequences of hyperosmolar stress in retinal pigmented epithelial cells. *Frontiers in Physiology*, *5*. https://doi.org/10.3389/fphys.2014.00199

Wilsey, L., Gowrisankaran, S., Cull, G., Hardin, C., Burgoyne, C. F., & Fortune, B. (2017). Comparing three different modes of electroretinography in experimental glaucoma: Diagnostic performance and correlation to structure. *Documenta Ophthalmologica*, *134*(2), 111–128. https://doi.org/10.1007/s10633-017-9578-x

Wilson, M. (1970). Invariant features of spatial summation with changing locus in the visual field. *The Journal of Physiology*, *207*(3), 611–622.

Wittström, E., Schatz, P., Lövestam-Adrian, M., Ponjavic, V., Bergström, A., & Andréasson, S. (2010). Improved retinal function after trabeculectomy in glaucoma patients. *Graefe's Archive for Clinical and Experimental Ophthalmology*, *248*(4), 485–495. https://doi.org/10.1007/s00417-009-1220-5

Wolfs, R. C., Klaver, C. C., Ramrattan, R. S., van Duijn, C. M., Hofman, A., & de Jong, P. T. (1998). Genetic risk of primary open-angle glaucoma. Population-based familial

aggregation study. *Archives of Ophthalmology (Chicago, Ill.: 1960)*, *116*(12), 1640–1645. https://doi.org/10.1001/archopht.116.12.1640

Womelsdorf, T., Anton-Erxleben, K., & Treue, S. (2008). Receptive Field Shift and Shrinkage in Macaque Middle Temporal Area through Attentional Gain Modulation. *Journal of Neuroscience*, *28*(36), 8934–8944. https://doi.org/10.1523/JNEUROSCI.4030-07.2008

Wong-Riley, M. (1979). Changes in the visual system of monocularly sutured or enucleated cats demonstrable with cytochrome oxidase histochemistry. *Brain Research*, *171*(1), 11–28. https://doi.org/10.1016/0006-8993(79)90728-5

Woolrich, M. W., Ripley, B. D., Brady, M., & Smith, S. M. (2001). Temporal Autocorrelation in Univariate Linear Modeling of FMRI Data. *NeuroImage*, *14*(6), 1370–1386. https://doi.org/10.1006/nimg.2001.0931

Wright, M. E., Singh, K. D., Rushton, S., Kusmia, S., Wise, R. G., Schwarzkopf, D. S., & Redmond, T. (2019). Exploring the Haemodynamic Response Function in the occipital lobe in glaucoma. *Investigative Ophthalmology & Visual Science*, *60*(9), 6110.

Wright, M. E., & Wise, R. G. (2018). Can Blood Oxygenation Level Dependent Functional Magnetic Resonance Imaging Be Used Accurately to Compare Older and Younger Populations? A Mini Literature Review. *Frontiers in Aging Neuroscience*, *10*. https://doi.org/10.3389/fnagi.2018.00371

Wu, J., Yan, T., Zhang, Z., Jin, F., & Guo, Q. (2012). Retinotopic mapping of the peripheral visual field to human visual cortex by functional magnetic resonance imaging. *Human Brain Mapping*, *33*(7), 1727–1740. https://doi.org/10.1002/hbm.21324

Wuerger, S., Powell, J., Chaudhoury, A., & Parkes, L. (2015). Comparison of fMRI measurements in LGN and Primary Visual cortex with visual deficits in Glaucoma. *Journal of Vision*, *15*(12), 257. https://doi.org/10.1167/15.12.257

Xu, J., Lu, F., Liu, W., Zhang, F., Chen, W., & Chen, J. (2013). Retinal nerve fibre layer thickness and macular thickness in patients with esotropic amblyopia: Retinal thickness in strabismic esotropic amblyopes. *Clinical and Experimental Optometry*, *96*(3), 267–271. https://doi.org/10.1111/cxo.12001

Yacoub, E., Shmuel, A., Logothetis, N., & Uğurbil, K. (2007). Robust detection of ocular dominance columns in humans using Hahn Spin Echo BOLD functional MRI at 7 Tesla. *NeuroImage*, *37*(4), 1161–1177. https://doi.org/10.1016/j.neuroimage.2007.05.020

Yildirim, F., Carvalho, J., & Cornelissen, F. W. (2018). A second-order orientation-contrast stimulus for population-receptive-field-based retinotopic mapping. *NeuroImage*, *164*, 183–193. https://doi.org/10.1016/j.neuroimage.2017.06.073

Yoshor, D., Bosking, W. H., Ghose, G. M., & Maunsell, J. H. R. (2007). Receptive Fields in Human Visual Cortex Mapped with Surface Electrodes. *Cerebral Cortex*, *17*(10), 2293–2302. https://doi.org/10.1093/cercor/bhl138

Yu, L., Xie, L., Dai, C., Xie, B., Liang, M., Zhao, L., Yin, X., & Wang, J. (2015). Progressive Thinning of Visual Cortex in Primary Open-Angle Glaucoma of Varying Severity. *PLOS ONE*, *10*(3), e0121960. https://doi.org/10.1371/journal.pone.0121960

Yu, L., Yin, X., Dai, C., Liang, M., Wei, L., Li, C., Zhang, J., Xie, B., & Wang, J. (2014). Morphologic changes in the anterior and posterior subregions of V1 and V2 and the V5/MT+ in patients with primary open-angle glaucoma. *Brain Research*, *1588*, 135–143. https://doi.org/10.1016/j.brainres.2014.09.005

Zeileis, A. (2001). *P-Values and Alternative Boundaries for CUSUM Tests*. Universitätsbibliothek Dortmund. https://doi.org/10.17877/DE290R-15221

Zhang, P., Wen, W., Sun, X., & He, S. (2016). Selective reduction of fMRI responses to transient achromatic stimuli in the magnocellular layers of the LGN and the

superficial layer of the SC of early glaucoma patients: Magnocellular Response Loss in LGN and SC. *Human Brain Mapping*, *37*(2), 558–569. https://doi.org/10.1002/hbm.23049

Zhang, S., Wang, B., Xie, Y., Zhu, S., Thomas, R., Qing, G., Zhang, C., & Wang, N. (2015). Retinotopic Changes in the Gray Matter Volume and Cerebral Blood Flow in the Primary Visual Cortex of Patients With Primary Open-Angle Glaucoma. *Investigative Opthalmology & Visual Science*, *56*(10), 6171. https://doi.org/10.1167/iovs.15-17286

Zhang, S., Xie, Y., Yang, J., Tang, Y., Li, R., Wang, N., & Zhang, C. (2016). Reduced Cerebrovascular reactivity in posterior cerebral arteries in patients with primary open-angle glaucoma. *Ophthalmology*, *120*(12), 2501–2507. https://doi.org/10.1016/j.ophtha.2013.05.017

Zhou, W., Muir, E. R., Nagi, K. S., Chalfin, S., Rodriguez, P., & Duong, T. Q. (2017). Retinotopic fMRI Reveals Visual Dysfunction and Functional Reorganization in the Visual Cortex of Mild to Moderate Glaucoma Patients: *Journal of Glaucoma*, *26*(5), 430–437. https://doi.org/10.1097/IJG.0000000000000641

Zuiderbaan, W., Harvey, B. M., & Dumoulin, S. O. (2012). Modeling center-surround configurations in population receptive fields using fMRI. *Journal of Vision*, *12*(3), 10–10. https://doi.org/10.1167/12.3.10

Appendix A – Examples of visual field plots

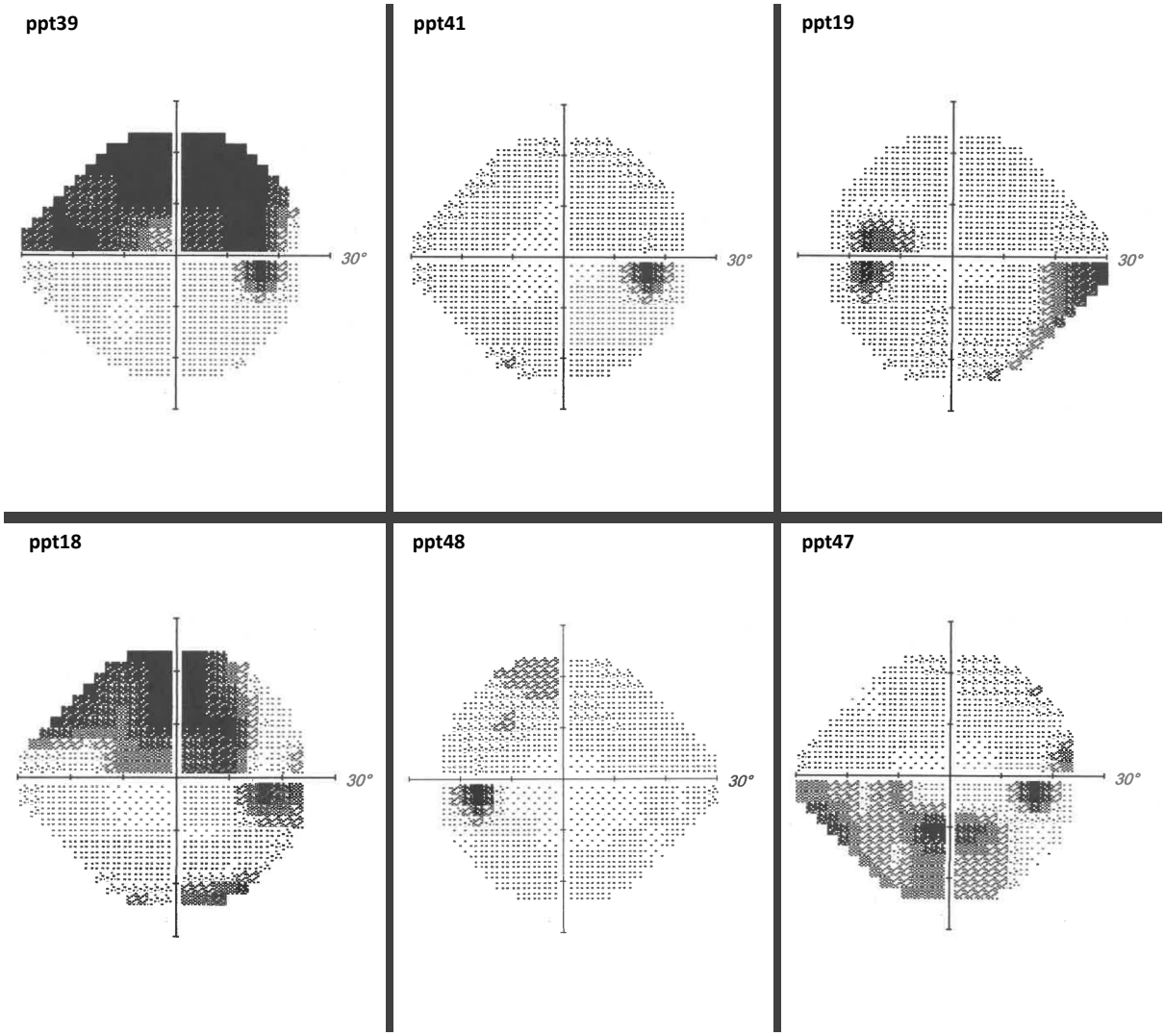

Appendix A – Examples of the visual field deficits in a representative group of glaucoma patients recruited for the studies outlined in this thesis. Greyscale values calculated and generated by the ZEISS Humphrey Field Analyser 3 perimeter.

Appendix B – Fourier analysis MATLAB code

```
function [Final] = FourierAnalysisGeneric_v1(data, ppt, Time)

% Fourier Analysis - Smooths ERG data and corrects for drift. Eyeblink
% artefacts should be already removed.
% Melissa E Wright, Tom Margrain


% Inputs:

% Data - Matrix of data to be analysed. Each column is taken as a seperate
% timecourse.
% Time - Associated timecourse
% ppt - participant (ppt id) for saving
% Produces matlab variable with timecourse and smoothed waveforms in the
% correct order, plot with amplitude of 12 harmonics, matrix with harmonic
% amplitude and phase, spatial tuning curve peaks.
% Saves in same file as data reading


% 11/01/19 - changed so produces harmonic power and ability to alter
% number of harmonics
% Fourier analysis - Currently 12 harmonics - 5Hz each harmonic (e.g.
% Harmonic one seperates power at 5Hz, Harmonic two seperates power at 10
% Hz etc...)

%% Parameters - Set these up first!

NumSteps = 1;
% Number of steps/Time courses being analysed in single participant
% (Entered in the 'data' input
Harm = 21;
% Number of harmonics wanted. The power in each of these will be plotted
Filter = 10;
% Top number of harmonics wanted in final data. This acts as a low-pass
% filter, removing those higher frequencies. For a more strict filter,
% lower this number (so only lower freuqncies with pass).
%Time = [-10:0.5:199.5]';
% Timepoints matrix.
TimeBase = 210;
% Full length of time in timecourse
Base = 200;
% Length of time post-onset


Data = [Time data];
% Puts data together. Also acts as a check that there is the corresponding
% number of datapoints to timepoints.
[row col] = size(Time);


%% Finds Averages for pre-stimulus time and final 5ms (depending on
timescale),
% then corrects to zero

StartAv= zeros(1,NumSteps);
EndAv = zeros(1,NumSteps);
```

```
if NumSteps == 1
     StartAv(:,(1)) = (mean(Data(1:20,2)));
    EndAv(:,(1)) = (mean(Data((row-20):end,2)));
else
    for i= 2:(NumSteps+1)
    StartAv(:,(i-1)) = (mean(Data(1:21,i)));
    EndAv(:,(i-1)) = (mean(Data((row-20):end,i)));
    end

end

ZeroDrift = zeros(row,NumSteps);

for i = 1:row
for dd = 2:(NumSteps+1)
ZeroDrift(i,(dd-1)) = (Data(i,dd)-StartAv(dd-1))+(Data(i,1)*(StartAv(dd-1)-
EndAv(dd-1)))/Base;
end
end

%% Find Degrees and Radians

% Change 0 in time course to 0.000001 to stop division by zero
Data(21,1)= 0.000001;

for i=1:row %length of data
Degrees (i,:) = 360*(Data(i,1)/TimeBase); %210 = time base of recording,
inc. pre-stimulus time
Radians (i,:) = 2*pi()/(360/Degrees(i,:));
end

%% Find fourier coeffecient a(n)

% a(0) or fx is the ZeroDrift data. Finding the fourier coefficient a(n)


fx = ZeroDrift;
for dd = 1:NumSteps
    a0(1,dd) = 2*(mean(fx(:,dd)));
end

for dd = 1:NumSteps % Steps
    for xx = 1:Harm % Harmonics
        for i = 1:row % Datapoints
            fxCos(i,dd,xx) = fx(i,dd) * (cos(xx * Radians(i,1)));
        end
        a(1,dd,xx) = 2* mean(fxCos(:,dd,xx));
    end
end

%% Find fourier coeffecient b(n)

% b(0) or fx is the ZeroDrift data. Need to find b(1-12) or f(xx)sim1-12x

for dd = 1:NumSteps % Steps
    for xx = 1:Harm % Harmonics
        for i = 1:row % Datapoints
            fxSin(i,dd,xx) = fx(i,dd) * (sin(xx * Radians(i,1)));
        end
        b(1,dd,xx) = 2* mean(fxSin(:,dd,xx));
```

```
    end
end

%% Rebuild filtered function

% a0 times 0.5
for dd=1:NumSteps
    for i= 1:row
        a02(i,dd) = a0(1,dd)*0.5;
    end
end

for dd=1:NumSteps
    for xx = 1:Harm
        for i=1:row
            aCos(i,dd,xx)= a(1,dd,xx) * cos(xx*Radians(i,1));
        end
    end
end

%%
for dd=1:NumSteps
    for xx = 1:Harm
        for i=1:row
            bSin(i,dd,xx)= b(1,dd,xx) * sin(xx*Radians(i,1));
        end
    end
end

%% Find amplitude and phase of each harmonic

for dd=1:NumSteps
    for xx = 1:Harm

Amplitude(1,xx,dd) = sqrt((a(1,dd,xx)^2)+(b(1,dd,xx)^2));
Phase(1,xx,dd) = atan(a(1,dd,xx)/b(1,dd,xx));

    end
end

% Plot harmonic powers

figure()
for xx = 1:NumSteps
subplot((round(NumSteps/2)), 2, xx)
bar(Amplitude(:,:,xx))
title(sprintf('Harmonic amplitude for step %d', xx))
axis([0 21 0 (max(max(Amplitude))+100)])
xlabel('Harmonic')
ylabel('Amplitude')
end


if ~exist(sprintf('/Users/Melissa/Library/Mobile
Documents/com~apple~CloudDocs/Data/PERG_data/PhaseTwo/%s', ppt), 'dir')
    mkdir(sprintf('/Users/Melissa/Library/Mobile
Documents/com~apple~CloudDocs/Data/PERG_data/PhaseTwo/%s', ppt));
end
```

```
savefig(sprintf('/Users/melissa/Library/Mobile
Documents/com~apple~CloudDocs/Data/PERG_data/PhaseTwo/%s/Harmonics', ppt));


%% Final Function

% Rebuild final data, filtering unwanted harmonics.
for dd = 1:NumSteps
   for i= 1:row
       Final(i,dd)=sum(aCos(i,dd,1:Filter)) + sum(bSin(i,dd,1:Filter)) +
...
           a02(i,dd);
   end
end

%% Find peaks

for dd = 1:NumSteps
    [Peak(1,dd) TTP(1,dd)] = max(Final(61:221, (dd))); % Find peak
amplitude ...
    % and time to peak (TTP) between 20ms and 100ms (post onset)
    TTP (1,dd) = TTP(1,dd) +60;
    TTP(1,dd) = Time(TTP(1,dd), 1);
    Trough(1,dd) = min(Final(181:341, (dd))); % Find trough
    Diff(1,dd) = Peak(1,dd) - Trough (1,dd);
end
```

Appendix C – Chapter 11 Multivariate Imputation by Chained Equations (MICE) and Linear model analysis R code

```
# Multivariate Imputation by Chained Equations (MICE) and Linear model ana
lysis
# Melissa E Wright 2020

install.packages("mice")
library("mice")

Data <- read.csv("/Users/mellissawright/Library/Mobile Documents/com~apple
~CloudDocs/Data/RAchapter/ModelData.csv")

Data <- data.frame(Data)

# MICE computation
imp <- mice(Data, method = "norm.predict", m = 30)

# Store data
data_imp <- complete(imp)


# Mixed Model - Group
library(lme4)

# Split by group
Data.glau <- Data[which(Data$Group=="1"),]
Data.con <- Data[which(Data$Group=="0"),]
data_imp.glau <- data_imp[which(data_imp$Group=="1"),]
data_imp.con <- data_imp[which(data_imp$Group=="0"),]


## Start with functional linear models

# Healthy controls
#First with no imputed data

RA.comp = lm(RA ~ PERG + V1pRF + V2pRF +
                V3pRF,
              data=Data.con)

#Then imputed

RA.imp = lm(RA ~ PERG + V1pRF + V2pRF +
                V3pRF,
              data=data_imp.con)

# Compare to ensure no bias introduced by MICE
plot(fitted(RA.comp),residuals(RA.comp))
hist(residuals(RA.comp))

plot(fitted(RA.imp),residuals(RA.imp))
```

```r
hist(residuals(RA.imp))

# Results from linear modeling (go to end of script for p-value code)
summary(RA.imp)
confint(RA.imp)

# Glaucoma
#First with no imputed data

RA.comp = lm(RA ~ PERG + V1pRF + V2pRF +
               V3pRF,
             data=Data.glau)

#Then imputed

RA.imp = lm(RA ~ PERG + V1pRF + V2pRF +
              V3pRF,
            data=data_imp.glau)


# Compare to ensure no bias introduced by MICE
plot(fitted(RA.comp),residuals(RA.comp))
hist(residuals(RA.comp))

plot(fitted(RA.imp),residuals(RA.imp))
hist(residuals(RA.imp))

# Results from linear modeling (go to end of script for p-value code)
summary(RA.imp)
confint(RA.imp)


## Now structural linear model

# Healthy controls
#First with no imputed data

RA.comp = lm(RA ~ OCT.GCIPL + V1.surf + V2.surf +
                V3.surf + V1.thickness + V2.thickness +
                V3.thickness,
              data=Data.con)

#Then imputed

RA.imp = lm(RA ~ OCT.GCIPL + V1.surf + V2.surf +
                V3.surf + V1.thickness + V2.thickness +
                V3.thickness,
              data=data_imp.con)


# Compare to ensure no bias introduced by MICE
plot(fitted(RA.comp),residuals(RA.comp))
hist(residuals(RA.comp))
```

```r
plot(fitted(RA.imp),residuals(RA.imp))
hist(residuals(RA.imp))

# Results from linear modeling (go to end of script for p-value code)
summary(RA.imp)
confint(RA.imp)

# Glaucoma
#First with no imputed data

RA.comp = lm(RA ~ OCT.GCIPL + V1.surf + V2.surf +
               V3.surf + V1.thickness + V2.thickness +
               V3.thickness,
             data=Data.glau)

#Then imputed

RA.imp = lm(RA ~ OCT.GCIPL + V1.surf + V2.surf +
              V3.surf + V1.thickness + V2.thickness +
              V3.thickness,
            data=data_imp.glau)


# Compare to ensure no bias introduced by MICE
plot(fitted(RA.comp),residuals(RA.comp))
hist(residuals(RA.comp))

plot(fitted(RA.imp),residuals(RA.imp))
hist(residuals(RA.imp))

# Results from linear modeling (go to end of script for p-value code)
summary(RA.imp)
confint(RA.imp)

################################################
# To get one-tailed P-values for all models

res <- summary(RA.imp)

# For H1: beta < 0

pt(coef(res)[, 3], RA.imp$df, lower = TRUE)


# For H1: beta > 0

pt(coef(res)[, 3], RA.imp$df, lower = FALSE)
```